BUBBLE COLUMNS

Structures or stability?

Wouter Harteveld

BUBBLE COLUMNS

Structures or stability?

PROEFSCHRIFT

ter verkrijging van de graad van doctor
aan de Technische Universiteit Delft,
op gezag van de Rector Magnificus prof. dr. ir. J. T. Fokkema,
voorzitter van het College voor Promoties,
in het openbaar te verdedigen op
maandag 12 december 2005 om 13:00 uur

door

Wouter Koen HARTEVELD

natuurkundig ingenieur
geboren te Leidschendam

Dit proefschrift is goedgekeurd door de promotoren:
Prof. dr. ir. H. E. A. van den Akker
Prof. dr. R. F. Mudde

Samenstelling promotiecommissie:

Rector Magnificus, voorzitter	
Prof. dr. ir. H. E. A. van den Akker,	Technische Universiteit Delft, promotor
Prof. dr. R.F. Mudde,	Technische Universiteit Delft, promotor
Prof. dr. ir. J. Westerweel,	Technische Universiteit Delft
Prof. dr. ir. T.H.J.J. van der Hagen,	Technische Universiteit Delft
Prof. dr. D. Lohse,	Universiteit Twente
Prof. dr. M. Lance,	Ecole Centrale de Lyon
Prof. dr. -ing. habil. C. Tropea	Technische Universität Darmstadt

The work presented in this thesis was supported financially by the Foundation for Fundamental Research on Matter (FOM).

Keywords: Bubble column, bubbly flow, turbulence, Laser Doppler Anemometry, glass fibre probe

Printed by: Ponsen & Looijen b.v., Amsterdam

ISBN: 90-64642-26-5

Aan Natalie

Contents

Summary

Bubble columns - structures or stability?
Wouter Harteveld

The aim of the present investigation is to get an improved understanding of the hydrodynamics of the gravity driven bubbly flow that can be found in a bubble column reactor. Special attention has been paid to the large scale structures that can be found in these flows, since these structures have a strong impact on the performance of a bubble column reactor (e.g., mixing, mass and heat transfer).

Particular interest has been paid to the factors leading to their creation: are the large scale fluctuations due to the inherently unstable interplay of the gas distribution and gravity, and what is the role of imperfections in the gas injection? To answer these questions, a special sparger with 559 needles has been constructed for a bubble column with 15 cm diameter that can provide both very uniform and non-uniform gas injection. The performance of and bubble formation process at this sparger have been studied in detail, revealing the importance of bubble-bubble interaction processes for the bubble diameter.

Hydrodynamics

With the very uniform gas injection obtained with this sparger, very homogeneous flow was obtained in which no large scale structures could be detected, up to the superficial gas velocity where instability sets in. For increasing levels of contamination, increasingly high critical voidages up to 55% have been obtained at which the first vortical structures appear. Several indications have been found which indicate that the onset to a flow with large dynamic structures is caused by the reversal of the direction of the lift force. Wall peaking was found for the void fraction in the case of homogeneous flow, it disappears when instability is approached. The horizontal bubble diameter observed around the onset of instability agrees well with the critical diameter suggested by Tomiyama et al. (2002) for which the lift coefficient changes sign. For increasing levels of contamination, coalescence near the sparger decreases, smaller bubbles result and the flow is stable up to higher voidages.

Sufficiently large non-uniformities in the gas injection create an entrance region with dynamic vortical cells. The strength of the associated liquid velocity fluctuations quickly dampens for higher positions in the column, until a bulk region is found with uniform properties. For U_g<0.05 m/s, the size and nature of this entrance region mainly depend on the gas injection pattern, and less on the void fraction. A data set has been generated for both a cylindrical and pseudo-2D bubble column to allow more refined validation studies of numerical work.

In addition, the strength of fluctuations due to pseudo-turbulence has been studied, as well as the turbulent properties of the flow to get a better understanding of the cascade process at scales larger than the bubble diameter. For this purpose, power spectra of the liquid velocity signal have been determined. These suffer from power added by the pseudo-turbulence obscuring the turbulent cascade process of the larger structures. Various techniques have been compared to reduce the influence of the local fluctuations. Removal of velocity samples obtained close to the bubbles only gives partial improvement, a fit of the autocorrelation function gives somewhat better results, but both require careful interpretation. The results show a power law slope close to -5/3 at intermediate frequencies for large dynamic structures both due to instability of the flow and due to non-uniform gas injection.

Measurement techniques

The study of the hydrodynamics required the improvement and evaluation of several measurement techniques. This work is summarized below.

Optical fiber probes are used for the measurement of the void fraction. A study shows that for the gas-liquid transition, the so-called Low-Level-Criterion should be used. Various error sources causing the underestimation of the void fraction are determined by studying video images of the piercing of bubbles. Errors due to the blinding, crawling and drifting effect are quantified. For the bubble velocity and size, a four point optical fiber probe is used. A study into its accuracy shows, via the analysis of both artificial piercing simulations and simplified experiments, that the major error sources are the bubble shape oscillations and probe-bubble interactions (drifting and deformation). For the data processing, the importance of curvature correction is shown. The inaccuracy for individual bubble velocity measurements (magnitude and direction) is quite high, but for ensembles of bubbles the averages are reasonably accurate.

The signal processing of Laser Doppler Anemometry (LDA) velocity time series is evaluated and improved. In order to deal properly with the random sampling and gaps in the data due to bubbles, the slotting technique and time-series analysis present no particular problems. The use of reconstruction techniques produces significant biases due to a double low-pass filter operation redistributing high-frequency power to low frequencies. The filters have a cut-off frequency that is lower than that based on theory for single phase flow, and can produce power-law slopes close to -5/3 in the absence of turbulence.

For the processing of the electronic LDA signals, a dual burst wavelet LDA processor has been developed, tested and applied to both single phase and bubbly flows. The use of this processor results in 50% smaller dead times, strong reduction of multiple validation, more accurate Doppler frequency and arrival time estimates, and provides much more insight in the data processing and on how to optimize the LDA technique. Smaller bias problems are obtained for the velocity moments compared to a commercial burst processor, the comparison suggests that the accuracy of the results of the latter processor can be improved by removal of multiple validation, the use of a coincidence window and velocity bias correction. The advantages of the wavelet processor for the estimation of power spectra are limited, due to the size of the measurement volume.

Samenvatting

Bellenkolommen - structuren of stabiliteit?
Wouter Harteveld

Het doel van het huidige onderzoek is een beter begrip te krijgen van de hydrodynamica van de zwaartekracht gedreven bellenstroming, die in een bellenkolomreactor aanwezig is. Hierbij is vooral aandacht besteed aan de grootschalige structuren die in deze stromingen gevonden kunnen worden, omdat deze structuren een grote invloed hebben op de prestaties van een bellenkolomreactor (bv. menging, en stof- en warmteoverdracht).

In het bijzonder is er gekeken naar de factoren die tot vorming van deze structuren leiden: worden deze veroorzaakt door de inherent onstabiele wisselwerking van de gasverdeling en de zwaartekracht, en wat is de rol van onvolmaaktheden in de gasinjectie? Om deze vragen te beantwoorden is er een speciale begasser gebouwd, bestaande uit 559 naalden voor een bellenkolom met 15 cm diameter. Deze begasser kan zowel zeer uniforme begassing als niet-uniforme begassing leveren. De prestaties van de begasser zijn in detail bestudeerd, samen met het belvormingsproces. Hierbij is het belang van bel-bel wisselwerkingen voor de beldiameter duidelijk geworden.

Hydrodynamica

De zeer uniforme gasinjectie, die de begasser levert, resulteert in een zeer homogene stroming, waarin geen grootschalige structuren ontdekt kunnen worden. Dit blijft het geval totdat de superficiële gassnelheid bereikt wordt waarbij instabiliteit optreedt en het transitieregime betreden wordt. Voor een toenemende vervuilingsgraad worden steeds hogere kritieke gasfracties voor transitie bereikt. Een maximale kritieke gasfractie van 55% wordt uiteindelijk gevonden. Verschillende aanwijzingen zijn gevonden die aangeven dat de verandering van een homogene stroming naar een met grootschalige structuren wordt veroorzaakt door het omkeren van de richting van de liftkracht. Wandpieken in de gasfractie zijn gevonden voor het geval van homogene stroming. De pieken verdwijnen zodra de stroming bijna instabiel wordt. De horizontale beldiameter, die wordt gemeten rond het punt waar de stroming instabiel wordt, komt overeen met de kritieke diameter zoals gesuggereerd door Tomiyama et al. (2002), waarbij de liftcoëfficiënt negatief wordt. Voor toenemende vervuilingsgraad neemt de hoeveelheid coalescentie bij de begasser af, met als gevolg kleinere bellen en een stroming die stabiel is tot een hogere gasfractie.

Voldoende grote inhomogeniteiten in de gasinjectie creëren een ingangsgebied met dynamische wervelstructuren. De sterkte van de geassocieërde vloeistofsnelheidsfluctuaties neemt snel af voor posities hoger in de kolom, totdat een bulkgebied gevonden wordt met uniforme eigenschappen. Voor U_g<0.05 m/s hangen de grootte en het type van dit ingangsgebied voornamelijk af van het begassingspatroon en minder van de gasfractie. Een dataset is gecreëerd voor zowel een

cilindrische als een pseudo-2D bellenkolom voor meer verfijnde validatiestudies van numeriek werk.

Verder is de sterkte onderzocht van de fluctuaties als gevolg van pseudo-turbulentie, evenals de turbulentie-eigenschappen van de stroming om een beter idee te krijgen van het cascade proces op schalen groter dan de beldiameter. Om deze reden zijn vermogensspectra bepaald van het vloeistofsnelheidssignaal. Deze spectra hebben last van extra vermogen toegevoegd door de pseudo-turbulentie. Dit extra vermogen verdoezelt het turbulente cascade-proces van de grotere structuren. Verschillende technieken zijn vergeleken, die de invloed van lokale fluctuaties kunnen verminderen. Het verwijderen van snelheidsrealisaties verkregen vlakbij de bellen geeft slechts een gedeeltelijke verbetering. Een fit van de autocorrelatiefunctie geeft wat betere resultaten, maar beide technieken vereisen een zorgvuldige interpretatie. De resultaten tonen een power law helling in de buurt van -5/3 rond het gebied van 1 tot 10 Hz, voor stromingen met grootschalige dynamische structuren zowel veroorzaakt door instabiliteiten in de stroming als door niet-uniforme gasinjectie.

Meettechnieken

De studie van de hydrodynamica vereist het verbeteren en evalueren van verschillende meettechnieken. Dit werk is hieronder samengevat.

Optische glasvezelprobes zijn gebruikt voor de metingen van de gasfractie. Een studie laat zien dat het zogenaamde Low-Level-Criterion moet worden gebruikt voor de gas-vloeistof overgang. Verschillende foutenbronnen voor de onderschatting van de gasfractie zijn bepaald door het bestuderen van videobeelden van het aanprikken van bellen. Onnauwkeurigheden veroorzaakt door het 'blinding', 'crawling' en 'drifting' effect zijn gekwantificeerd. Voor de belsnelheid en belgrootte is een vierpuntsglasvezelprobe gebruikt. Een studie naar diens nauwkeurigheid laat zien, via de analyse van zowel artificiële aanpriksimulaties als versimpelde experimenten, dat de belangrijkste foutenbronnen de belvormoscillaties en de probe-bel interacties ('drifting' en vervorming) zijn. Voor de dataverwerking is het belang van correctie van de belkromming aangetoond. De onnauwkeurigheid van individuele belsnelheidsmetingen (grootte en richting) is vrij groot, maar voor grotere groepen bellen zijn de gemiddelden redelijk nauwkeurig.

De signaalverwerking van Laser Doppler Anemometrie (LDA) snelheidstijdsreeksen is geëvalueerd en verbeterd. De slotting-techniek en tijdsreeksanalyse hebben geen bijzondere problemen met het willekeurig samplen van en de gaten in de data veroorzaakt door de bellen. Het gebruik van reconstructietechnieken produceert echter significante structurele afwijkingen als gevolg van een dubbele laagdoorlaatfilteroperatie, die vermogen bij hogere frequenties herverdeelt naar lagere frequenties. Deze filters hebben een afkapfrequentie, die lager ligt dan verwacht op basis van theorie voor éénfasestromingen, en kunnen power-law hellingen opleveren in de buurt van -5/3, zelfs als er helemaal geen turbulentie aanwezig is.

Voor de verwerking van electronische LDA signalen is een overlappende burst wavelet LDA processor ontwikkeld, getest en toegepast op zowel éénfasestromingen als bellenstromingen. Het gebruik van deze processor resulteert in 50% kortere dode tijden, een sterke afname van meervoudige validatie, meer nauwkeurige Doppler-frequentie- en aankomsttijdschatters en levert veel meer inzicht in de dataverwerking en hoe de LDA techniek moet worden geoptimaliseerd. De techniek levert kleinere problemen met structurele afwijkingen voor de snelheidsmomenten vergeleken

met een commerciële burstprocessor. De vergelijking suggereert dat de nauwkeurigheid van de commerciële processor kan worden verbeterd door het verwijderen van meervoudig gevalideerde metingen, het gebruik van een coïncidentievenster en correctie voor de structurele afwijking in de snelheid. De voordelen van het gebruik van de waveletprocessor voor de schatting van vermogensspectra zijn beperkt door de grootte van het meetvolume.

1. Introduction

1.1. Bubbly flow

1.1.1. Motivation

Gas-liquid bubbly flows are encountered in a large variety of applications in industry. These vary from air-lift reactors in the bio-industry, nuclear boiling water reactors, the use of the gas-lift technique for underground oil recovery, CO_2 sequestration in the ocean, to bubble column reactors in the petro-chemical industry (e.g. for the oxidation of butane or toluene). Bubble column reactors are frequently used due to their simple construction with no moving parts, which make their construction and maintenance cheap, and for their simplicity of operation and good mass and heat transfer. However, the hydrodynamic behavior of bubble columns is very complex, making a detailed description generally not feasible. Consequently, scale-up of bubble column reactors is difficult, and usually based on empirical relations. Despite several decades of research, their behavior is still far from well understood. Design, scale up, fine tuning and use of bubble columns would all strongly benefit from a better understanding of the hydrodynamics of this two-phase flow.

1.1.2. Flow regimes and vortical structures

Classically (e.g. Zahradnik et al. (1997)), the following regimes are identified for the hydrodynamic behavior (Figure 1.1):

- The homogeneous regime is characterized by a narrow bubble size distribution and radially uniform void fraction distribution. Bubble-bubble interaction is minor and liquid recirculation takes place in between the bubbles: no large scale circulation exists.

- The transition regime. If the gas flow rate is increased, the void fraction increases and the flow becomes unstable. The homogeneous behavior disappears. Instead, the bubble size distribution widens and the radial void fraction distribution is not homogeneous any more. The void fraction near the center of the bubble column is larger than the average void fraction, and large vortical structures appear with a size comparable to the column diameter. These large scale structures contribute to the large scale circulation in the bubble column with up flow in the center and down flow near the wall.

- The heterogeneous (churn-turbulent) regime exists for even higher gas throughput, when coalescence and breakup reach an equilibrium. It is marked by a wide bubble size distribution: the bubble diameter can vary an order of magnitude. The degree of mixing in the flow is very strong.

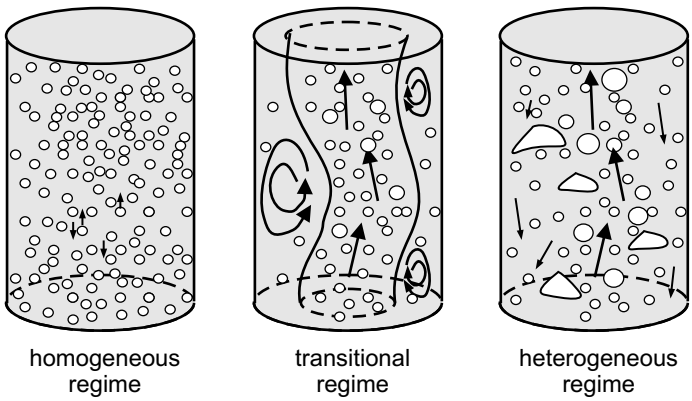

Figure 1.1.: Classical picture of flow regimes that occur in bubble columns for increasing superficial gas velocity U_g.

This classification is not unique: not all authors distinguish the transition regime, some include it in the churn-turbulent regime (e.g. Groen (2004)). The hydrodynamic behavior of bubble columns changes due to the appearance of large scale coherent vortical structures. These structures have a strong impact on the performance of a bubble column reactor (e.g. mass and heat transfer, mixing), and have therefore received a lot of of attention over the years (overviews can be found in Mudde (2005) and Joshi et al. (2002)). The level of understanding of the nature of these structures has gradually increased. Where initial investigators considered a single circulation cell for the mean flow, this concept was later replaced with that of multiple stacked circulation cells with a steady-state character (e.g. Joshi and Sharma (1979)). Later investigations (e.g. Franz et al. (1984) and Chen et al. (1994)) showed that, in fact, the flow field is formed by a meandering vortical plume surrounded by circulation cells with a very dynamic character, which are constantly moving through the column in a chaotic fashion.

Knowledge of the regime of operation and therefore of the large structures in the flow is crucial. The hydrodynamic behavior is dependent on a large number of parameters (e.g. geometry, liquid properties, sparger type). If a sparger with only a few holes is used (e.g. Ruzicka et al. (2001)), the heterogeneous regime is found for all superficial gas velocities: behavior according to the homogeneous regime is not observed. For spargers with small and closely spaced orifices, the homogeneous regime is typically reported for superficial gas velocities below 0.04 m/s (e.g. Wild et al. (2003)). The behavior suggests that the presence of a wide bubble size distribution implies the heterogeneous regime. The opposite is, however, not generally true (Mudde (2005)): a narrow bubble size distribution does not imply homogeneous flow. The large-scale circulation and vortical structures have been found at low superficial gas velocities (Mudde et al. (1997a), Mudde and Van den Akker (1999), Yuan et al. (1993), Franz et al. (1984) and Chen et al. (1994)), even though several of these authors used spargers that were claimed to provide uniform gas injection (e.g. Mudde and Van den Akker (1999) used a porous plate sparger). Various authors report non-uniform gas distribution also for moderate gas fractions (Kumar et al. (1997), Yuan et al. (1993) and Chen et al. (1994)). Chen et al. (1994), even distinguish an additional ('vortical

spiral flow') regime for superficial gas velocities in the range of 0.02-0.05 m/s. Consequently, characteristics of the behavior corresponding to the heterogeneous regime have been found for conditions where a homogeneous flow is expected based on the classical picture of the regimes. It is not clear, whether these large-scale fluctuations are due to the inherently unstable interplay of the gas distribution and gravity, or to small imperfections in the aeration pattern. This needs further clarification.

Similarly, large vortical structures were reported in numerical (Computational Fluid Dynamics) investigations, both for non-uniform and uniform gas sparging conditions (e.g. Lapin and Lübbert (1994), Sokolichin et al. (1997)). Variation of parameters in the simulation (such as models for the turbulence and the interaction forces, or numerical issues) has an important influence on the presence of coherent structures in the result, such as the grid size (Lapin and Lübbert (1994)), the discretization scheme (Sokolichin et al. (1997)), and the implementation of the added mass and/or the lift force (e.g. Monahan et al. (2005), Mudde and Simonin (1999) and Sokolichin et al. (2004)). In many of these studies, correct prediction of the presence of vortical structures is used as an indicator which models should be included. Therefore, the use of experimental data with well-defined conditions, such as carefully controlled aeration, is very important for making the correct choices.

In addition, the modeling of turbulence of the continuous phase in bubble columns is still an unresolved problem (Sokolichin et al. (2004)). It is not yet clear how the turbulence is modified by the bubbles at scales larger than the bubble diameter (e.g. Lance and Bataille (1991), Mudde et al. (1997a)) and how the pseudo-turbulence introduced by the gas phase influences the flow. Modeling would clearly benefit from additional insight in these processes.

1.1.3. Scope

The main objective in the present thesis is to determine the behavior of dynamic large scale structures in bubble columns. The work aims at answering the question whether large-scale fluctuations are due to the inherently unstable interplay of the gas distribution and gravity, or due to small imperfections in the aeration pattern. This is done via an experimental approach. Special attention is paid to the influence of the gas injector. The properties of the flow for very uniform gas injection are investigated, and the influence of non-uniformities in the gas injection on the presence of the large structures is determined. This way, a data set is created for a well-defined geometry that provides an interesting test case for numerical work. The investigation tries to find which factors determine the creation of the vortical structures, i.e. the instability of the flow.

In addition, the turbulent properties of the flow are investigated in order to get a better understanding of the cascade process of structures at scales larger than the bubble diameter. Moreover, the pseudo-turbulence introduced by the bubbles is studied to get a better idea of the strength of the fluctuations in the liquid velocity due to the local 'stirring' by the bubbles.

To accomplish the above, the present work pays a lot of attention to the application of measurement techniques to bubbly flows. In order to determine the hydrodynamical properties, reliable and accurate measurement techniques are required. The optical accessibility of bubble columns is, however, quite poor, and the flow is sensitive to disturbances. For this reason, the accuracy of optical probe techniques for the measurement of bubble properties is studied, and,

when possible, improved. In addition, the application of Laser Doppler Anemometry (LDA) to bubbly flows is investigated, and improved. The suitability of signal processing techniques for the determination of turbulence power spectra from LDA signals obtained in bubbly flows is evaluated and improved when possible.

1.2. Bubbly flow research at the Kramers Laboratorium

Gas-liquid and gas-liquid-solid bubbly flows have received a lot of attention in the research programme of the Kramers Laboratorium voor Fysische Technologie of the Delft University of Technology. Frijlink (1987) studied gassed suspension reactors. Later, Bakker (1992) investigated stirred gas-liquid dispersions, and Venneker (1999) studied these dispersions for pseudoplastic liquids. Van den Berg (1996) studied the interplay of the various time scales in bubbly flow. Groen (2004) investigated the hydrodynamics of bubble columns, his studies were followed by several publications on the topic of bubble columns and air-lift loop reactors, e.g. Mudde and Van den Akker (1999) and Mudde and Saito (2001). Numerical work on the topic of bubbly flows using the two-fluid formalism was performed by Lathouwers (1999) and Oey (2005). Finally, Guet (2004b) investigated ways to improve the gas-lift technique for underground oil recovery, and currently a follow-up project on this topic is being performed by Michael Descamps.

1.3. Project

The present project 'Hydrodynamics of gravity driven bubbly flows' was funded by the Stichting Fundamentele Onderzoek der Materie (FOM), and was part of the Dispersed Multiphase Flow program (work group FOM-D-35, project number 99MFS12).

1.4. Outline

Measurement techniques and setup

Chapter 2 discusses gas injection in bubble columns and presents the bubble column and the special gas injector that has been created for this study allowing for the investigation of the flow for both very uniform and non-uniform gas injection conditions. Chapter 3 discusses the accuracy of the use of single glass fiber probes for the measurement of void fractions. In chapter 4 the application of the four point optical fiber probe for the measurement of 3D bubble velocities and the bubble chordal length is studied, with special attention for the accuracy of this technique. Next, in chapter 5 the estimation of turbulence power spectra from LDA signals obtained in bubbly flows is studied. The chapter deals with signal processing techniques and first evaluates techniques to deal with gaps in the data introduced by bubbles and random sampling, and, second, how to deal with fluctuations due to the local flow around the bubbles. Chapter 6 considers the dual burst wavelet LDA processor that has been developed in this project to provide more accurate processing of LDA signals and assesses its performance when applied to bubbly flows.

Hydrodynamics

Before discussing the hydrodynamics of the bubble column, the bubble formation process at the sparger is discussed in section 2.3. Chapter 7 discusses the hydrodynamics of the bubble column: the stability of the flow, pseudo-turbulence, the influence of non-uniformities on the flow for both a cylindrical and a pseudo-2D column, and, finally, the turbulence power spectra that have been obtained.

2. Uniform and non-uniform gas injection in bubble columns

One of the major goals of the present study is to determine the influence of the sparger on the hydrodynamics in the bubble column, with special attention for large scale vortical structures. The present chapter discusses gas injection in bubble columns. First, a short literature overview is presented, followed by a discussion of the bubble column and the gas injector used for the present investigation. Next, the bubble formation at a single needle is studied followed by a discussion of interaction effects that are observed when multiple needles are used.

2.1. Gas injection in bubble columns

For the application of bubble columns in industry, different design parameters of interest are found which can give conflicting optimal designs (see e.g. Deckwer (1992)). For instance, a large gas-liquid interfacial area is required when the chemical reaction rate is high and the gas-liquid mass transfer rate is limiting. This may be achieved by a higher void fraction and a smaller bubble size. This means that the liquid circulation intensity is reduced, lowering the heat transfer coefficient and possibly the mass transfer coefficient for solids.

The type of gas injector that is used has a major influence on the bubble size, gas distribution, void fraction and liquid circulation intensity. The variety in design parameters has, therefore, led to a wide variety in gas injectors. The influence of the sparger on the flow is found to be generally smaller for airlift loop reactors than for bubble columns (Snape et al. (1995)).

Gas may be dispersed through pores or holes; a wide variety in number, size and distribution is found. The simplest configuration is a single orifice or tube which produces bubbles with a wide bubble size distribution: the gas is introduced in the form of a 'jet'. Larger numbers of orifices are encountered in drilled tubes, perforated plate spargers, porous plate spargers, flexible spargers and needle spargers. Drilled tubes (e.g. Tang and Heindel (2004) and Yu and Kim (1991)) and perforated plates (e.g. Kumar et al. (1997)) are commonly used in industry, with hole diameter typically in the range of 1 to 5 mm. These plates have a free area typically in the range of 0.5% to 5%. The bubble size typically gets smaller when smaller holes and larger numbers of holes are used. Porous plate spargers are often used for investigations in laboratories (e.g. Groen (2004), Mouza et al. (2005), Camarasa et al. (1999)) and provide small bubbles and generally more uniform gas injection than perforated plate spargers. Due to problems with clogging they are rarely used for process gas dispersion.

A flexible sparger (e.g. Rice and Howell (1986), Hebrard et al. (1999), Poulsen and Iversen (1999)) is a thin, elastic (usually rubber) membrane, stretched over a hoop. Holes are drilled or punctured in it. On increase of the pressure, the membrane expands and the holes increase in size. Flexible spargers are used if uniformly sized small bubbles are desired (e.g. in waste

water treatment). They have the advantage of self-cleaning properties and do not suffer from the clogging problems that rigid spargers have during periods when the aeration is stopped. However, the spargers cannot be used under conditions of high temperature and pressure, and, in addition, the bubble formation process at flexible spargers is less well understood than that at rigid spargers (Loubière and Hébrard (2003), Rice and Howell (1986), Geary and Rice (1991)).

Needle spargers are thus far not widely used, probably due to the large construction effort involved. Garnier et al. (2002) considered 271 hollow needles for the injection of bubbles in a small airlift reactor, with the goal of producing a monodisperse injection with a void fraction distribution which is as uniform as possible.

Due to its impact on the bubble column performance, the gas injector has been the subject of many studies to investigate its influence on the hydrodynamics and other properties. Several comparative studies have been published in which various spargers were compared for their influence on the hydrodynamics. Hills (1974) investigated the influence on the hydrodynamics of an increasing number of orifices in a perforated plate: for an increasing number of orifices, reduced liquid circulation and flatter void fraction profiles are obtained. Other investigations show that for perforated plates, a decrease in hole diameter, a decrease in the height-to-diameter ratio, and a reduction in the coalescing nature give an increase in the critical hold up for the transition to the heterogeneous regime. This is for instance shown by Thorat et al. (1998) and Thorat and Joshi (2004), who compare 22 different sieve plate geometries, but also by Drahos et al. (1991), Zahradnik et al. (1997) and Ruzicka et al. (2001). These latter authors showed how the homogeneous regime disappears if a perforated plate with larger hole diameter is used. Wilkinson et al. (1992) found that the influence of the sparger design on the hold up is small if the holes in the sparger are smaller than 1-2 mm and if care is taken to prevent maldistribution on the sparger. Veera and Joshi (1999) provide an overview of many sparger types presented in the literature and investigate the influence of the free area and hole diameter with five sieve plate spargers, including a single orifice sparger, on the void fraction profile that is obtained at various heights in the column. Haque et al. (1986) study the optimum gas sparger design for low height-to-diameter ratio bubble columns with respect both to minimum mixing time and maximum void fraction. Bhavaraju et al. (1978) discuss design procedures for gas injectors, focusing on the bubble sizes that are produced. Polli et al. (2002) investigated the bubble size distribution in the sparger region for various perforated plate and perforated ring type spargers. Dhotre et al. (2004) and Ranade and Tayalia (2001) used CFD simulations to simulate the effect of the sparger. Dhotre et al. (2004) consider the same spargers as Veera and Joshi (1999), Ranade and Tayalia (2001) the single and double ring tube spargers considered by Haque et al. (1986).

Several authors considered various methods to determine how the flow regime transitions change for different sparger types. Most authors make use of pressure signals. For instance, Drahos et al. (1992a) considered the fractal behavior of pressure signals, Drahos et al. (1991) autoregressive and spectral analysis of pressure signals. Lin et al. (2001) used chaotic time series analysis to find flow transitions as a function of the sparger type: two porous plate spargers and two perforated plate spargers were compared. Vial et al. (2000) and Vial et al. (2001) used the latter techniques in combination with statistical analysis and time-frequency analysis of pressure signals for the comparison of a porous plate sparger, multiple orifice sparger and a single orifice nozzle. The use of LDA for the investigation of flow patterns was considered by Kulkarni (2005b) in order to distinguish the behavior of single point and multi-point spargers.

2.2. The controlled sparger

2.2.1. Introduction

Chapter 1 mentions that the influence of the gas sparger on the hydrodynamics, in particular the presence of large scale structures, is still poorly understood. In order to investigate the influence further, a special gas injector is required that can provide well-defined very uniform gas injection as well as non-uniform gas injection in well-known patterns. This way, not only the influence on the flow can be studied, but also sparger characteristics are obtained that can be implemented in Computational Fluid Dynamics (CFD) models more easily and accurately. The present section discusses the requirements for the sparger and describes the sparger and bubble column that have been actually constructed.

2.2.2. Demands for gas injection

- The sparger should enable very uniform gas injection. This means:
  - The amount of gas injected per unit time and area is independent of the position on the sparger.
  - The bubble size that is injected is independent of the position on the sparger.
- The sparger should enable non-uniform gas injection in well-controlled patterns. This means:
  - The sparger is divided in groups, to which specified flow rates can be set.
- The sparger should be relatively easy to model.
  - A lot of gas injection points are used, consequently one can model the gas injection as a uniform inlet for each grid cell.
  - The bubble size distribution should be narrow, allowing for modeling of a monodisperse bubble ensemble for conditions where coalescence and breakup are relatively unimportant. Consequently, coalescence near the sparger should be limited.
  - Preferably, the bubble size should not vary strongly with the superficial gas velocity.
  - The amount of gas that is injected in each part of the sparger should be known.
  - The local amount of gas that is injected should be independent of time and the flow inside the bubble column, such that feedback can be ignored.
- The bubble size should be in the range of 3-5 mm since we are interested in obtaining the homogeneous regime.
- The gas injection for adjacent needles should be as uncorrelated as possible. Correlations may introduce time scales in the flow that are strongly determined by the specific sparger geometry. We are less interested in behavior that is specific only to one geometry.

No sparger geometry is available in the literature that satisfies the above demands. Especially the possibility to use well-controlled patterns is new. The choice was made to construct the sparger based on a large number of needles, which allows an easy subdivision in groups, very similar properties for all the openings, large pressure drop and uniform distribution. Special efforts were made in order to comply with the above requirements as much as possible. The next paragraph gives a description of the bubble column and the needle sparger. Subsequent sections describe the bubble formation at the needle sparger.

2.2.3. Description of the bubble column and sparger

Two bubble columns, each with a needle sparger, have been used for the work in the present thesis. The first is a cylindrical bubble column, the second a rectangular pseudo-2D column. The present section describes the bubble columns and spargers.

Cylindrical column

The cylindrical bubble column, that has been used, has a 15.0 cm inner diameter (R=0.075 m) and was filled with tap water. It is shown in Figure 2.1. The column wall is made of PMMA, and has a height of 2.0 m. A rectangular vessel filled with water is built around the column for the Laser Doppler Anemometry experiments to allow also for the measurement of the tangential liquid velocity component. It has dimensions 0.31 m x 0.20 m x 0.30 m (height x width x depth), is constructed from PMMA and can be displaced in height to allow LDA measurements at various heights. The bubble column is placed in a frame, which allows careful vertical alignment: misalignment results in circulation loops in the flow (e.g. Rice and Littlefield (1987), Rice et al. (1990), Ityokumbul (1993) and Tinge and Drinkenburg (1986)). At the bottom of the bubble column, the special needle bubble distributor is placed. It consists of 559 stainless steel needles glued in the bottom plate which is constructed of PVC. The needles have lengths of 20 cm, inner diameters 0.8 mm, the exits extend 5 mm above the bubble column bottom. The needles are placed in a triangular pattern, with a distance between the needle centers of 6 mm (Figure 2.2(a)). This picture also shows the direction of the second velocity component v. The first velocity component, u, is the axial velocity component.

In order to provide both uniform and non-uniform gas injection in well-defined patterns, the needles are connected in groups of 18 pieces. The flow system used to distribute the air to these groups is shown in Figure 2.3. The main gas stream is split into 7, 11 or 31 channels feeding the various groups, the number is depending on the operation mode of the bubble column. Eleven electronic mass flow meters (VP Instruments VPFlowmate with range 0-5 slm) were used in combination with metering valves to obtain accurate control over the flow to the groups. Upstream of each group a 'group needle' (with an inner diameter of 0.6 mm and length of 10 cm) is placed in order to obtain very uniform gas distribution over the channels to the needle groups. Due to the large pressure drop over these needles the flow rates to the various groups are independent and the volume available for pressure fluctuations is strongly reduced. This way, the flow to the various areas of the sparger should be independent of the hydrodynamics inside the bubble column. In order to obtain a narrow bubble size distribution and uniform aeration, the flow rate through the needles is limited between 1 ml/s and 3 ml/s. At lower flow rates water may enter some of the needles and uniformity is no longer guaranteed. At the higher flow rates

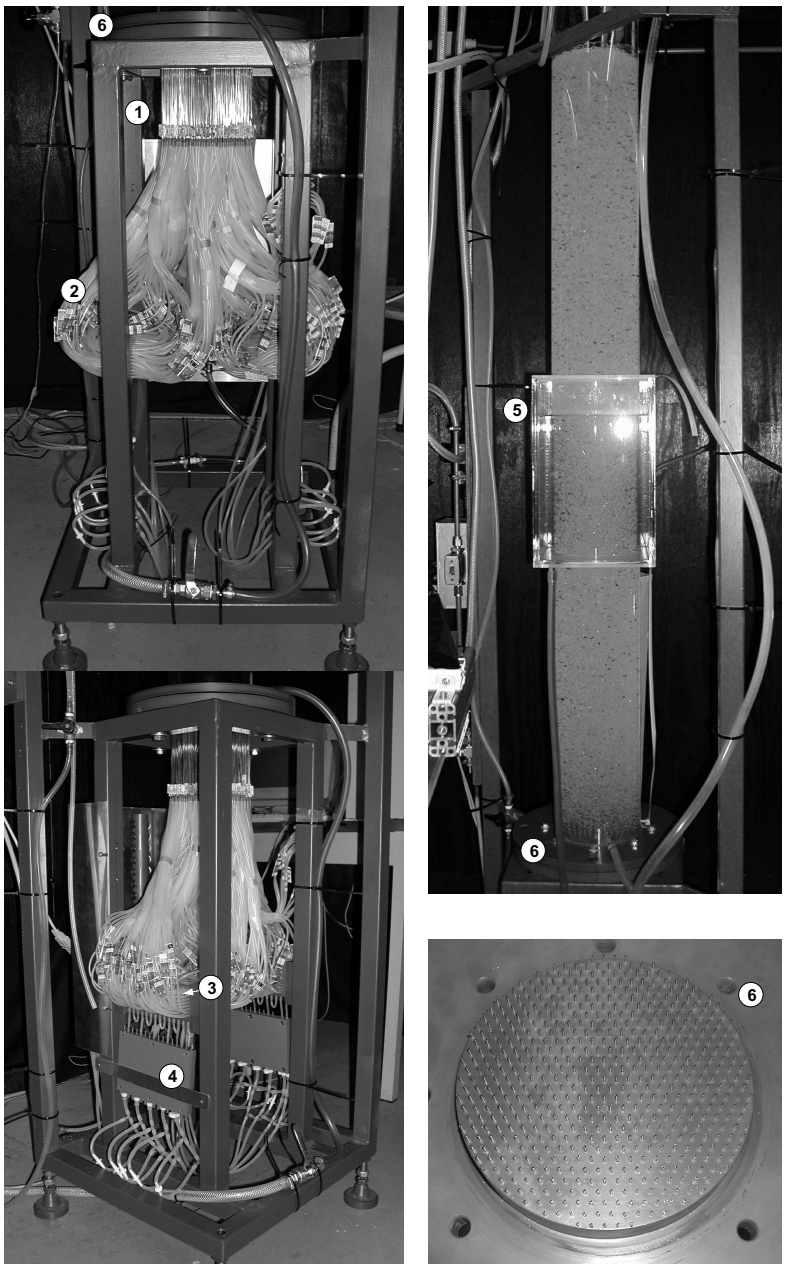

Figure 2.1.: Bubble column setup with sparger details. 1: needles, 2: hoses from group distributor to needles, 3: group distributors, 4: group needles, 5: rectangular vessel, 6: sparger.

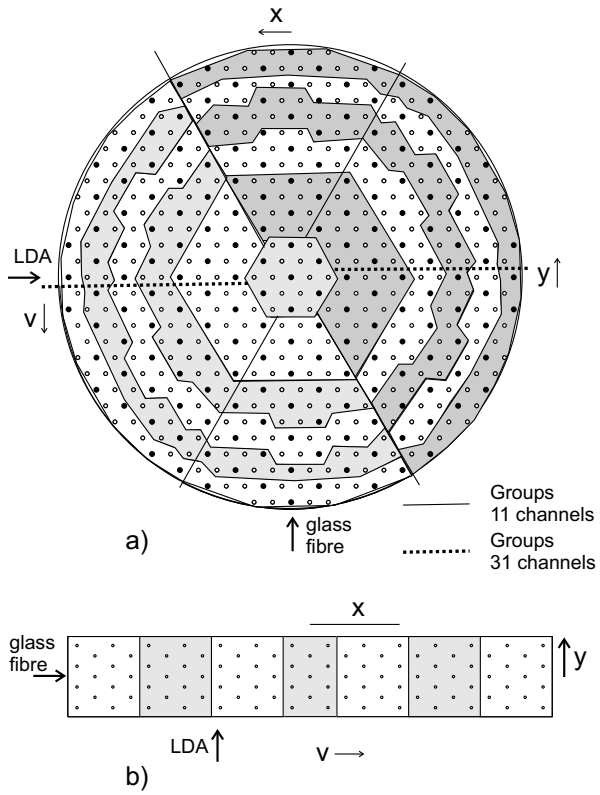

Figure 2.2.: Top view of the needle sparger for the cylindrical (a) and pseudo-2D (b) bubble column. For low superficial gas velocities only the black filled needles are used. The arrows show the position from which the LDA and void fraction profiles are obtained.

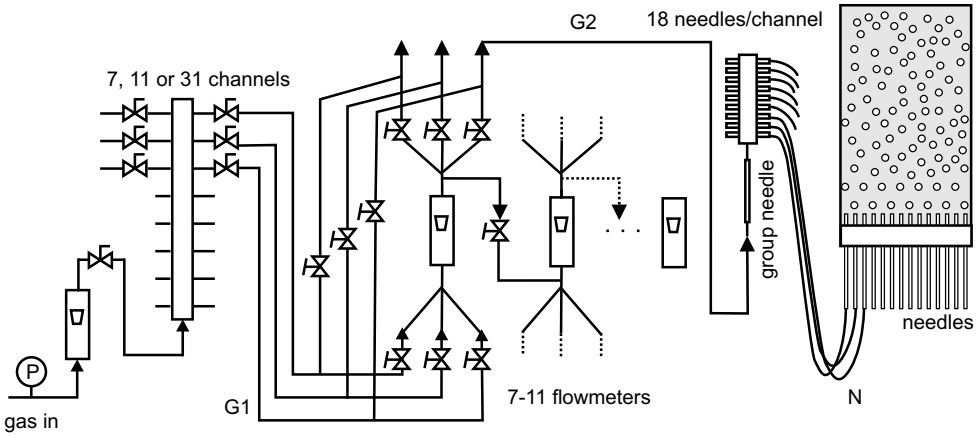

Figure 2.3.: The system used to provide the bubble column with air.

the bubble formation mechanism changes and coalescence starts to play a larger role: the bubble size distribution widens. Section 2.3 and 2.4 discuss the bubble formation process in more detail. In addition, at the larger flow rates the pressure drop in the network feeding the needles becomes large and further increase of the flow rate is no longer possible if the group needles are present. This is caused by the high pressure drop over the group needles, combined with the long hoses that are employed in the setup: hose type 'G1' (see Figure 2.3) has a length of 3 m and inner diameter of 4 mm, hose type 'G2' a length of 5 m and an inner diameter of 4 mm and hose type 'N' a length of 0.5 m and an inner diameter of 2 mm.

Therefore, only a limited range of void fractions can be investigated if all needles are used at the same time. For void fractions $\alpha > 15\%$ (superficial gas velocity beyond 0.03 m/s) all needles are used in 31 groups. For the range $5\% < \alpha < 12\%$ (superficial gas velocity 0.015 m/s - 0.027 m/s) one third of the needles is used in 11 groups: 187 needles, again in a triangular pattern (the black filled needles in Figure 2.2(a)). An example of the bubble formation in this mode is shown in Figure 2.4. The use of different numbers of needles has the advantage that the differences in the flow rates through the needles for high and low superficial gas velocities are reduced. The bubble diameter increases with this flow rate, so the differences in the bubble diameters are also reduced. For the superficial gas velocities beyond 0.055 m/s, the group needles were removed: at these flow rates the pressure drops in the hoses connecting the flow meters with the group distributors (denoted by 'G1' and 'G2' in Figure 2.3) have become large enough to ensure independent operation of the groups. This way, superficial gas velocities up to 0.10 m/s are possible.

The groups are shown in Figure 2.2(a). In the case that 187 needles are used, one central group of 7 needles and 10 groups of 18 needles forming half rings are used. If all 559 needles are used, there are one central group of 19 needles and 30 groups of 18 needles forming one sixth of a ring. Since only 11 flow meters are available for the experiments, a switching panel was used to allow the measurement of the flow rate of 31 channels (Figure 2.3). The same panel allowed

Figure 2.4.: Picture showing bubble formation with one third of the needles in operation.

the series connection of the flow meters to provide a regular calibration to compensate for the effects of drift (e.g. temperature) in the meters. Finally, the bubble column has to be operated with care to prevent water from entering the needles. Therefore, it is slowly filled with water from a supply near the bottom at a sufficiently large gas flow rate.

Figure 2.2(a) shows the lines over which experiments were performed in the bubble column: LDA experiments were performed over the line y=0, most void fraction measurements over the line x=0 (a small number over the line y=0).

Rectangular pseudo-2D column

The rectangular column dimensions are a 50% scaled-down version of those used by Becker et al. (1994). The column has a width of 24.3 cm (R_{2D}=0.122 m, hydraulic diameter 0.069 m), a depth of 4.0 cm (R_{depth}=0.020 m) and a height of 99 cm. The sparger for this column is made of 95 needles, again placed in a triangular pattern with distance between the needle centers of 1.04 cm (Figure 2.2(b)). This is almost the same pattern that is used in the cylindrical column when 187 needles are employed. Seven needle groups are created: one central group of 11 needles and six groups of 14 needles. LDA experiments are done from the front (probe aligned with the y-axis), such that the distance that has to be covered by the laser beams into the bubbly flow is short. Glass fiber probe experiments were performed over the line y=0.

Construction

In order to ensure that the needles had very similar lengths, diameters and openings, the needles were cut to the appropriate length and mechanically deburred in the factory. In addition, the needles were handled carefully during construction to prevent buckling which would dramatically affect the pressure drop. The length of the needle which extends from the bottom plate into the liquid is very similar for all needles (inaccuracy much smaller than 1 mm) to prevent static pressure differences at the exits of the needles that can translate to somewhat different flow rates.

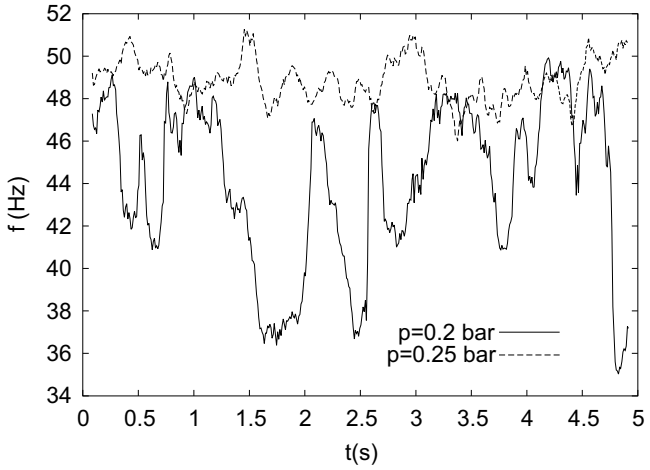

Figure 2.5.: Bubble formation frequency fluctuations due to liquid circulation for two pressures.

Performance of the sparger components

Tests have been performed to evaluate the performance of the sparger and its separate components. The individual bubbling frequencies are compared for small and high flow rates. At small flow rates the bubbling frequency is a good indicator for the flow rate changes. Variations in the bubbling frequencies around the mean are within a band of 3%, indicating a good accuracy. In addition, tests are performed to compare the group needles. A needle is placed at the bottom of a tube filled with water, the water flows out through the tube. The time is determined which the liquid column with a height of 2.0 m requires in order to drop 0.5 m in height. Differences are around 0.3%, i.e. the needle diameters are very similar and very similar flow rates and pressure drops to the groups are obtained.

2.3. Bubble formation at a single needle - the influence of bubble-bubble interactions

2.3.1. Motivation

Understanding the behavior of the bubbles, with the formation process as an important element, is of key importance for the study of bubble columns. The size of the bubbles can have a strong effect on the hydrodynamical behavior. The size is strongly influenced by the conditions at which the bubble column is operated, e.g. the number of active needles, the gas injection pattern, the superficial gas velocity and the flow regime. In order to investigate this relationship better, the bubble formation process is studied in more detail. Quite surprising behavior was found in the presence of large scale vortical structures at the sparger. The present section discusses this behavior. If the needle sparger is operated in the presence of large scale vortical structures, a strongly fluctuating liquid velocity is present at the needles. This influences the

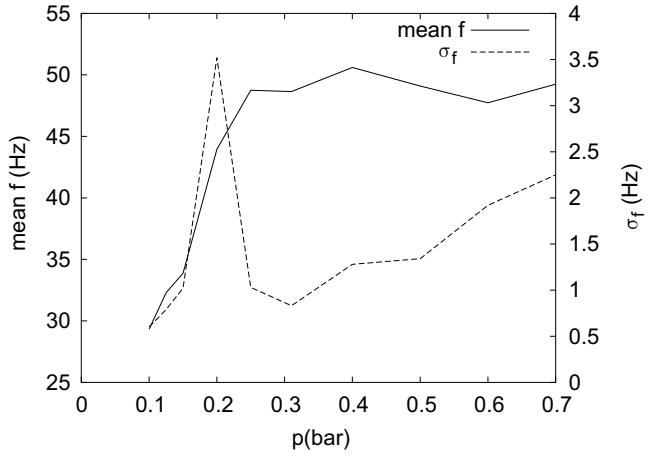

Figure 2.6.: Variation of mean and standard deviation σ_f of bubble formation frequency with pressure for a needle in a flow with varying liquid velocities.

bubble formation process, and, consequently, the bubble size that is produced. The bubble formation in the presence of a fluctuating liquid velocity is studied by aerating a bubble column with a small group of 17 needles (with the same properties as the needle sparger), placed in the center of the bottom of the 15 cm diameter bubble column. A liquid height of 20 cm is used, this way a dynamic liquid circulation loop is obtained with a typical timescale for the liquid velocity fluctuations of 1 second. The bubble formation process has been studied with the use of high speed video recordings. It is quite difficult to obtain an accurate estimate of the fluctuating bubble size from the images. Therefore, instead, the bubble formation frequency was determined via the autocorrelation function of the intensity of the pixels at the location of the bubble formation. The flow rate through the group of needles was set by varying the pressure p in the chamber volume before these needles: no flow meter was available at the time for the relevant range of flow rates. Figure 2.5 shows this time-dependent bubbling frequency for two different pressures. For only a small increase in the pressure, the magnitude of the fluctuations strongly drops. Figure 2.6 shows the mean and standard deviation of the bubbling frequency for various pressures p. For $p<0.15$ bar the frequency increases with p. For $p \approx 0.2$ bar the standard deviation shows a strong peak, for higher pressures the standard deviation drops and slowly increases, the mean of the frequency is more or less constant.

Obviously, the strong frequency fluctuations are accompanied by strong bubble size fluctuations, since the pressure drop over the needle has a considerable magnitude. These fluctuations occur at very relevant flow rates: if all 559 needles are used, these occur around a superficial gas velocity of 0.035 m/s. For this reason, the phenomenon is studied in more detail. Since the use of multiple needles is not essential for the understanding of the behavior, the bubble formation at a single needle is studied.

The bubble formation at a needle or at an orifice has been the subject of a wide range of studies. Many studies have presented experimental results and modeled the bubble formation

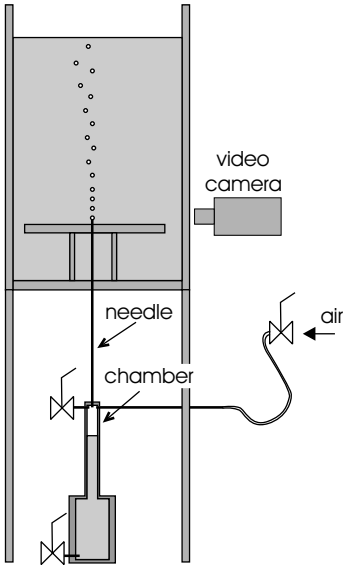

Figure 2.7.: The experimental setup

with simplified models based on force balances, which were gradually extended to incorporate additional effects, e.g. Davidson and Schüler (1960a,b); Ruff (1972); la Nauze and Harris (1972); Wraith (1971); Oguz and Prosperetti (1993). These models generally assume a simplified bubble shape (e.g. spherical) and an empirical criterion for the detachment of the bubble. In addition, the role of the chamber volume, that strongly determines the time-dependent flow through the orifice or the needle, was studied by various authors, e.g. Ramakrishnan et al. (1969); Satyanarayan et al. (1969); Khurana and Kumar (1969); Park et al. (1977). More complicated bubble shapes without empirical criteria for the detachment were considered by Oguz and Prosperetti (1993); Oguz and Zeng (1997); Longuet-Higgins et al. (1991); Hooper (1986); Pinczewski (1981). Despite the large amount of literature available, no previous report of the presented phenomenon could be found. For this reason, the bubble formation has been investigated in more detail with experiments and a modeling study to get a better idea of the physical phenomena responsible for the behavior.

2.3.2. Experimental setup

The bubble formation has been studied in a series of experiments in the setup shown in Figure 2.7. The water container has a horizontal cross-section of 0.18 m x 0.35 m and is filled with tap water of at least several days old. The needle dimensions correspond to those used in the needle bubble column sparger. A 20 cm long needle made of stainless steel extends 5 mm from the bottom, the water height above the needle tip is 20 cm. The inner diameter of the needle is 0.8 mm, the outer diameter 1.3 mm. Air is fed to the needle through a chamber with a volume that can be varied by changing the liquid level in it. Volumes V_c ranging from 0.2 ml-75 ml are possible

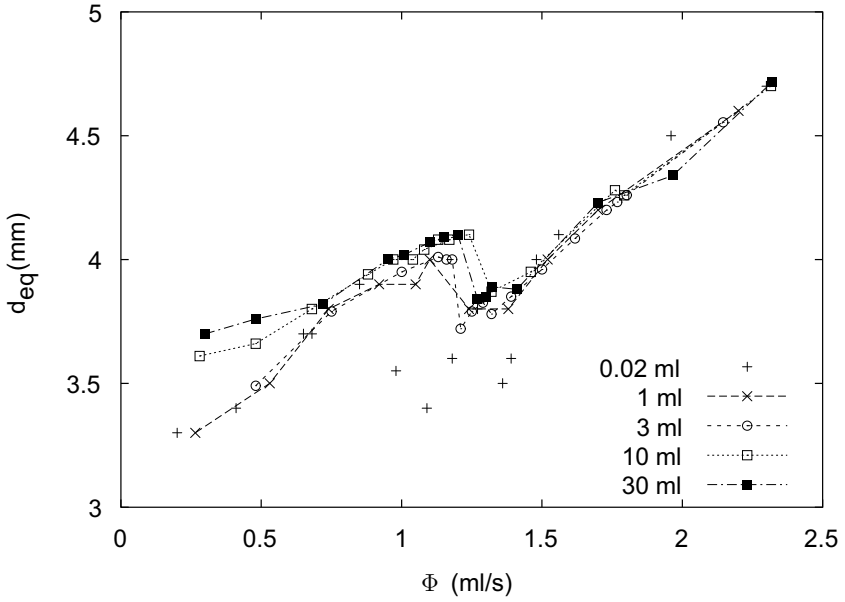

Figure 2.8.: Equivalent bubble diameters for various chamber volumes.

with an accuracy of about 0.1 ml. Air is fed to the chamber through a needle of 0.2 m length, with 0.8 mm inner diameter, in which an iron wire is placed with slightly smaller diameter. A large pressure drop with order of magnitude of 0.4 bar results. Consequently, a constant gas flow to the chamber results. For experiments with virtually constant flow conditions, the chamber is removed and the narrow needle is almost directly connected to the bubbling needle, giving a chamber volume of around 0.02 ml.

A high speed digital video-camera is used to record the bubble-formation. Frame rates up to 900 Hz at 256x256 resolution are possible. Direct measurement of the bubble size from the video images is inaccurate, therefore the bubble volume is determined from the ratio of the gas flow rate and the bubbling frequency: $V_b = \Phi/f$. The bubbling frequency f was determined from the video recordings by determining the number of bubble detachments over a period of about 1 second. This way, in the case of coalescence, the bubbling frequency before coalescence is determined. The air flow rate Φ has been determined at the exit of the needle in the period between the video recordings. This has been done using a volumetric method: a volumetric flask has been used to collect the bubbles released from the needle, and the time required to fill a well-known volume is determined. Flow rates, that have been studied, are in the range of 0-3 ml/s.

2.3.3. Bubble formation at a single needle: observations

The variation of the equivalent bubble diameter d_{eq} with the gas flow rate is shown in Figure 2.8 for a number of chamber volumes. A few characteristics draw the attention. First, the diameters for V_c=0.02 ml are very scattered in the range Φ =1-1.5 ml/s. Second, there is a quick decrease in diameter around $\Phi = 1.2$ ml/s for $V_c \geq 1$ ml. Third, for low gas flow rates, the bubble size increases with the chamber volume, for higher gas flow rates there is little difference. The first point will now be discussed before studying the more interesting second and third observations in more detail.

Coalescence

For small chamber volumes ($V_c < 0.75$ ml) coalescence occurs occasionally for flow rates in the range of 1-1.5 ml/s. This causes the bubble diameter to deviate from the value without coalescence. In Figure 2.8 smaller sizes are observed. This is due to the fact that the bubble frequency and size, before coalescence takes place, are determined, and the coalescence results in earlier detachment. Additionally, since the bubble frequency was determined over a limited number of bubbles and the coalescence occurs randomly, scatter is seen in the plots in Figure 2.8 for the range of 1-1.5 ml/s. This explains why the bubble diameters with $V_c = 0.02$ ml deviate from the values for larger V_c. For the small chamber volumes, there is an almost constant gas flow through the needle. Consequently, there is no delay time in between the formation of two bubbles (the period during which pressure builds up in the chamber volume before a new bubble can start growing). Bubble growth commences immediately after detachment of the previous bubble, and the previous bubble has traveled only a very small distance when the next bubble starts growing. Additionally, the flow rate in the earliest stages of bubble growth is larger than in the case of larger chamber volumes, resulting in higher velocities for the top of the growing bubble. The collisions between the bubbles are stronger and last for a longer period, making the chance of rupture of the film between the bubbles bigger. Therefore, the smallest volumes have larger probabilities of coalescence than bigger volumes and for the sparger a not too small volume should be used. For chamber volumes larger than 0.75 ml, coalescence is observed mainly at gas flow rates above 2.6 ml/s. At lower gas flow rates coalescence is very rare.

Bubble formation: observations of interaction effects

To investigate the origin of the sharp decrease in the bubble size occurring at flow rates close to 1.2 ml/s, the bubble formation process is studied by tracking the height of the top and the base of the growing bubble and the last bubble that has detached. From these results also the distance between the bubbles is known. Results are shown in Figures 2.9 and 2.10 for $V_c = 3$ ml. Video recordings of the bubble formation process are shown in Figure 2.11.

When the results are inspected, it is observed that the bubble formation process is quite different for flow rates below 1.20 ml/s (Fig. 2.11(a) and (b)) and flow rates above 1.20 ml/s (Fig. 2.11(c)), this will be explained further in the text. When the gas flow rate is increased, the bubbling frequency increases and the delay time decreases. As a result, the distance between the bubble base of the departing bubble and the top of the growing bubble becomes smaller (Fig. 2.9). When the distance gets sufficiently small (in the order of 1 mm) interaction with

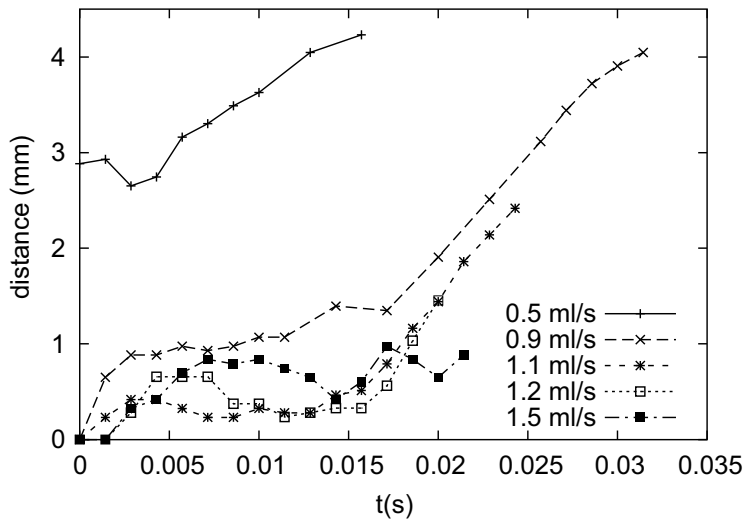

Figure 2.9.: The distance between the top of the growing bubble and the base of the previous bubble as a function of time (V_c =3 ml).

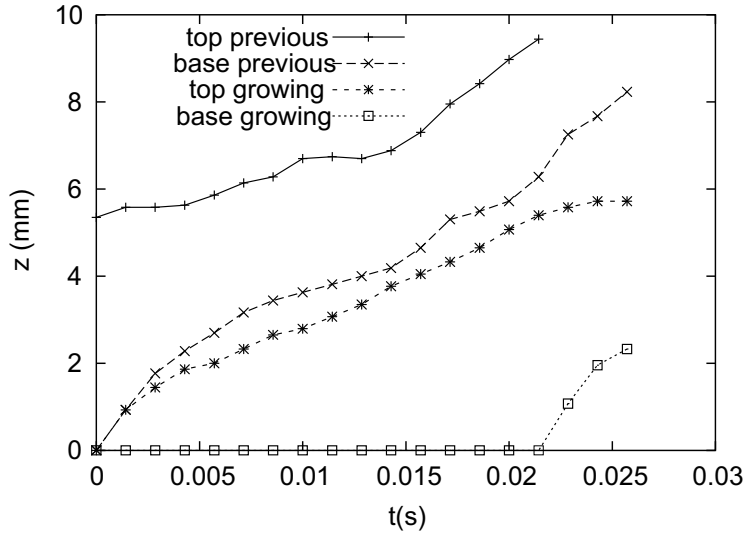

Figure 2.10.: The vertical position of the top and base of the previously formed bubble and the growing bubble as a function of time ($\Phi = 1.5$ ml/s, V_c =3 ml).

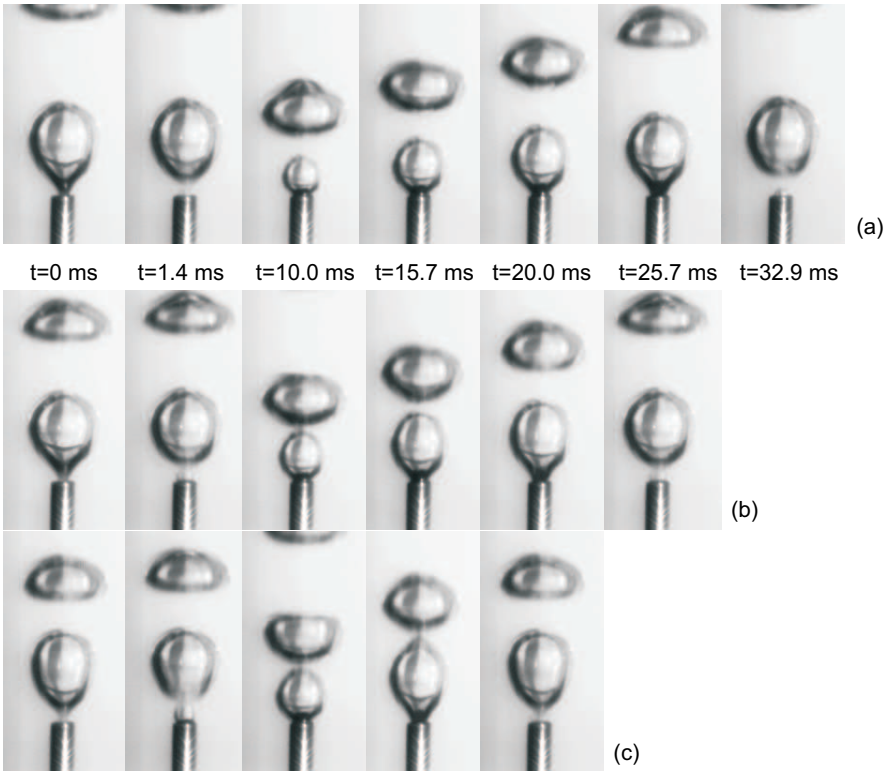

Figure 2.11.: Bubble growth process for (a) 0.9 ml/s, (b) 1.1 ml/s and (c) 1.2 ml/s gas flow rate (V_c =3 ml).

the previously formed bubble starts to influence the final bubble size. When the delay time has become very short, the departing bubble will start to block the growing bubble. With increasing frequency, the blocking time will increase. The blocking time can extend to the part of the formation process when the upward forces would be larger than the downward forces had the blocking bubble not been there. In this stage, the bubble would have lifted off while remaining connected to the needle with a neck, leading to an earlier detachment. Instead, bubble lift off starts later, the bubble formation can last longer and the bubble may reach a larger size. For flow rates below 1.20 ml/s bubble growth continues for a while when the distance between the two bubbles has started increasing (Fig. 2.11(b) $t > 18$ ms). For flow rates higher than 1.20 ml/s, however, the bubble detaches almost immediately after the instant when the distance starts increasing (Fig 2.10 and 2.11(c)). This is most likely caused by an extra force that acts on the growing bubble when the distance between the bubbles is small and the previously formed bubble tries to get away from the growing bubble: the departing bubble tries to pull the growing bubble away from the needle.

The bubble formation at higher flow rate is often modeled as inertia and/or drag-dominated in literature (e.g. Davidson and Schüler (1960a) and Davidson and Schüler (1960b)). In the current investigation it is found that the bubble formation for the higher flow rates is indeed inertia and drag-dominated, but here the inertia and drag of the previously formed bubble are dominating, not those of the growing bubble. This was not found in literature. The importance of the consideration of bubble-bubble interaction is clear.

The bubble sizes for flow rates above 1.2 ml/s are virtually independent of the chamber volume (Fig 2.8). For lower flow rates, the bubble size increases with the chamber volume. This agrees with trends reported in literature (e.g. Khurana and Kumar (1969); Park et al. (1977)). For a larger chamber volume the delay time in between the bubble formations increases and extra air is stored in the chamber. The conditions in the chamber tend more towards constant pressure for the larger chamber sizes. Therefore, the flow rate is higher during bubble growth and bubbles grow larger. For the higher flow rates there is no delay time and the differences between the bubble sizes produced with different chamber volumes disappear.

Figure 2.12 and Figure 2.13 show results for the bubble diameter for different needle diameters and for water-glycerol mixtures with higher viscosities μ_l up to 13 mPas. Whereas the needle used for the experiments for Figure 2.8 was originating from the same batch used for the construction of the needle bubble column sparger, the needles for the Figures 2.12 and 2.13 were manually cut, and consequently their openings had different shapes. The differences in the results for the 0.8 mm needle show that reproducibility is difficult. The lengths of the needles with different needle diameters were chosen to get similar pressure drops as in the case of the 0.8 mm needle. The results show that the discontinuity for the bubble diameter also occurs for the different needle diameters, but the magnitude of the discontinuity is somewhat smaller for the larger diameter, and the flow rate at which the discontinuity occurs increases with the diameter. The latter effect is due to the fact that a larger needle diameter leads to larger bubbles and consequently the bubbling frequency at which interaction effects start to play a role is only achieved at a higher flow rate. The increase in viscosity leads to a decrease in the magnitude of the discontinuity: for $\mu_l \approx 13$ mPas the discontinuity has disappeared. This effect is probably due to the different nature of the attraction by the departing bubble: in the case of a higher viscosity the attraction will not be limited to small distances between the bubbles and the sharp decrease in the diameter

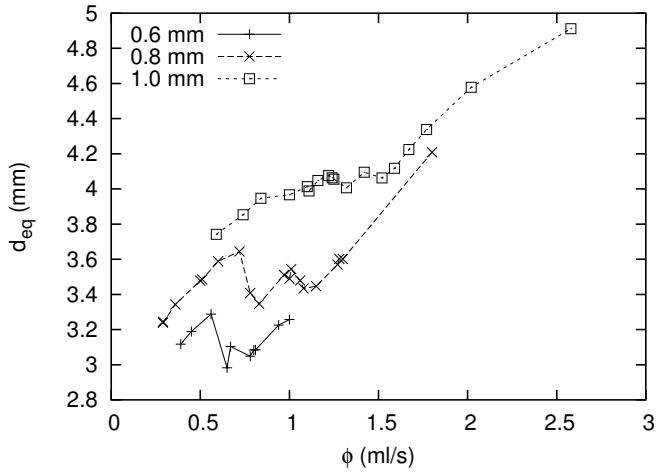

Figure 2.12.: Effect of the needle diameter on the bubble diameter (V_c =1 ml).

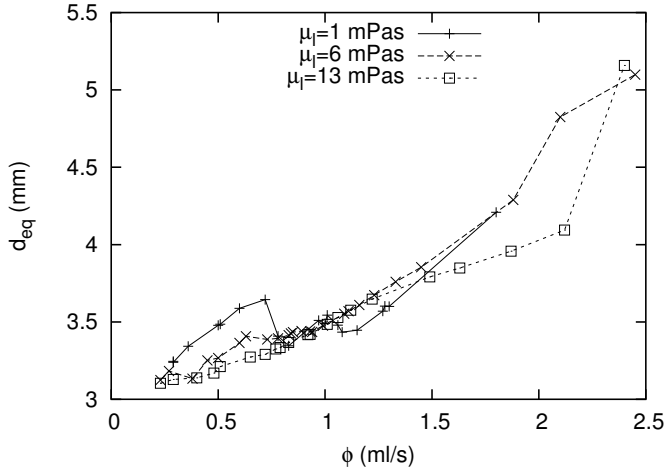

Figure 2.13.: Effect of the liquid viscosity on the bubble diameter (V_c =1 ml, needle diameter 0.8 mm).

is smeared over a larger range in flow rates.

2.3.4. Bubble formation model

The previous section discussed that bubble-bubble interaction effects are probably responsible for the effects leading to the strong bubble frequency fluctuations that are observed. The flow rate at which the fluctuations are observed, matches exactly with the flow rate at which the discontinuity in the bubble size is found. Next, a modeling study is performed to check whether we can recapture such a size discontinuity by including the bubble-bubble interaction effects, and to find out if it is possible to get rid of this discontinuity since a narrow bubble size distribution is preferred.

In the literature on bubble formation, bubble-bubble interactions and effects due to the wake of the bubble have been considered in several studies, but generally for different conditions than encountered here. For instance, in most cases bubble-bubble contact will lead to coalescence (Kyriakidis and Kastrinakis (1997)) and not to blocking. The low-pressure region under the bubble has been considered for studies of pairing and weeping. Pairing is the generation of a second bubble which quickly joins the previous bubble (McCann and Prince (1971), Zhang and Shoji (2001)), weeping is the flow of liquid through the needle or orifice to the gas chamber volume (e.g. Zhang and Tan (2000), McCann and Prince (1969)). Snabre and Magnifotcham (1998) consider the drag reduction due to the presence of the bubble stream. Chuang and Goldschmidt (1970) do consider the wake of the previous bubble for the assistance in the detachment.

First, the general idea behind the model is discussed. Next, details of the model are described, paying particular attention to the interaction effects.

Model setup

A full theoretical analysis of the bubble growth, motion and liquid motion as well as the interaction with the previously formed bubble would be very complicated. Therefore, a simplified bubble formation model is studied which contains all the major effects. A quite common method in literature (e.g. Ruff (1972) or Zhang and Shoji (2001)) is to consider bubble formation in several stages, modeling the equation of motion of the bubble with a force balance and to check for detachment with an empirical criterion. This approach is followed here as well.

The simplified model considers the following situation (see Figure 2.14). A bubble is growing on top of a vertical, thin-walled cylindrical needle with inner radius R_n. The needle extends 5 mm into the liquid (water). Gas is fed to the needle from a chamber with volume V_c containing gas (air) with pressure p_c and gas mass m_c. A constant gas mass flow $\phi_{M,c}$ is feeding the chamber and a time dependent gas mass flow $\phi_{M,b}$ feeds the bubble via the needle.

The model should be able to predict the effect of the chamber volume, i.e. the study of both constant flow conditions and intermediate conditions. This is handled by including models for the dynamic gas flow through the needle and the pressure fluctuations in the chamber.

Oguz and Prosperetti (1993) show that the bubble detaches from the needle when the distance z_b from its center to the needle tip is approximately equal to the bubble radius R_b plus the needle radius R_n. This is used as the detachment criterion in the model. So, in order to model the detachment, the motion of the bubble has to be tracked. This is done by considering the force

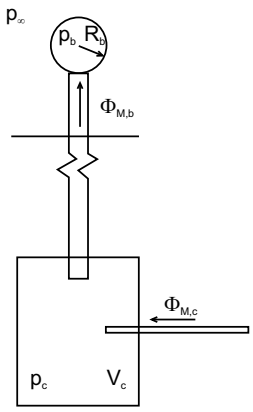

Figure 2.14.: Situation modeled.

balance over the bubble. To study the influence of bubble-bubble interactions, the corresponding forces are incorporated in the force balance. This also requires tracking of the last bubble that has detached.

The growth and motion of the bubble is modeled in stages, similar to Khurana and Kumar (1969), see Figure 2.15, which also shows the forces acting on the bubble. Stage 1 represents the delay time: pressure in the chamber has to build up before the rapid bubble growth can commence, see Figure 2.18. The bubble grows slowly from an almost flat surface to a hemisphere with the same radius as the needle. Once the pressure in the chamber is large enough, above $p_{c,min}$, the bubble can grow further: stage 2 is entered. During stage 2, the bubble grows as a sphere with its base attached to the needle. Upward and downward forces are balanced. Once upward forces become larger than the downward forces, stage 3 is entered. In stage 3, the bubble base starts to rise. The bubble continues growing, gas flows to the bubble through a neck that connects it with the needle. When the base of the bubble has traveled a distance equal to the needle radius, the bubble detaches and stage 4 is obtained: the bubble is no longer growing and leaves the needle. Before discussing the stages in more detail, the forces acting on the bubble will be discussed.

Forces

Several forces are taken into account (shown in Figure 2.15). For stages 2 and 3 these are the forces caused by buoyancy, F_b, surface tension, F_σ, liquid inertia by virtual mass, $\frac{d}{dt}(M_b v_b)$, (M_b is the virtual mass, v_b the velocity of the center of the bubble), bubble-bubble interactions, F_{b-b} and drag, F_d. For stage 4 only the buoyancy, liquid inertia and drag forces play a role. The force exerted due to the bubble mass and via the gas momentum give negligible contributions.

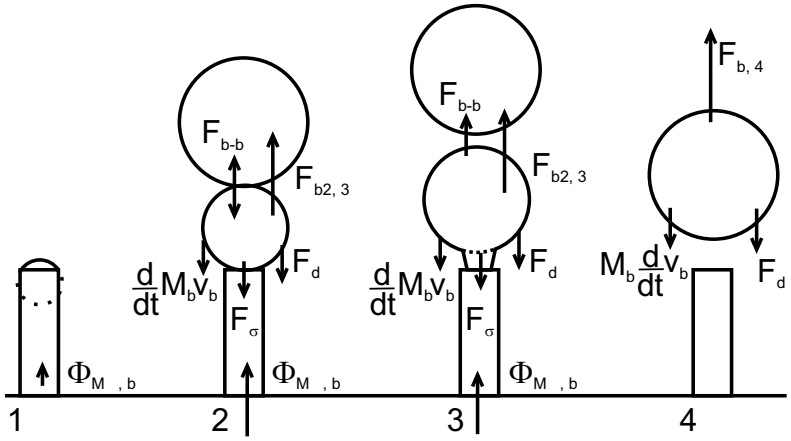

Figure 2.15.: The various stages in the model with acting forces.

Buoyancy force

The buoyancy force for a bubble with volume V_b that has detached (stage 4) is given by $F_{b4} = \rho_l g V_b$. Here ρ_l is the density of the liquid and g the acceleration due to gravity. When calculating the buoyancy force for stages 2 and 3, however, a small correction has to be made for the fact that the bubble is not surrounded by liquid at the position of the tube mouth in stages 2 and 3 (Chesters (1977)):

$$F_{b2,3} = \rho_l g V_b + \pi R_n^2 (2\sigma/R_b - g2R_b\rho_l) \tag{2.1}$$

with σ the surface tension. The surface tension force $F_\sigma = 2\pi R_n \sigma cos\theta$ (θ is the contact angle) increases during stage 2 until it reaches a maximum value of $F_{\sigma,max} = 2\pi R_n \sigma$, which it keeps during stage 3. The change with time of the contact angle during stage 2 is determined by the force balance, but is actually not relevant for the model.

Virtual mass

The virtual mass of the bubble is given by:

$$M_b = C_A \rho_l V_b \tag{2.2}$$

with the added mass coefficient C_A equal to $\frac{1}{2}(1 + \frac{3}{8}(R_b/z_{wall})^3 + O(R_b/z_{wall})^5)$ (Lamb (1932)). z_{wall} is the distance from the center of mass of the bubble to the wall (bottom). For a 4 mm diameter bubble with $z_{wall} = 7$ mm, we get $C_A = 0.50$: the wall plays a negligible role, so we simply use the value 0.5. Furthermore, the liquid inertia force can be rewritten as:

$$\frac{d}{dt}(M_b v_b) = M_b \frac{dv_b}{dt} + v_b \frac{dM_b}{dt} = M_b \frac{dv_b}{dt} + v_b C_A \frac{\rho_l}{\rho_b} \phi_{M,b} \tag{2.3}$$

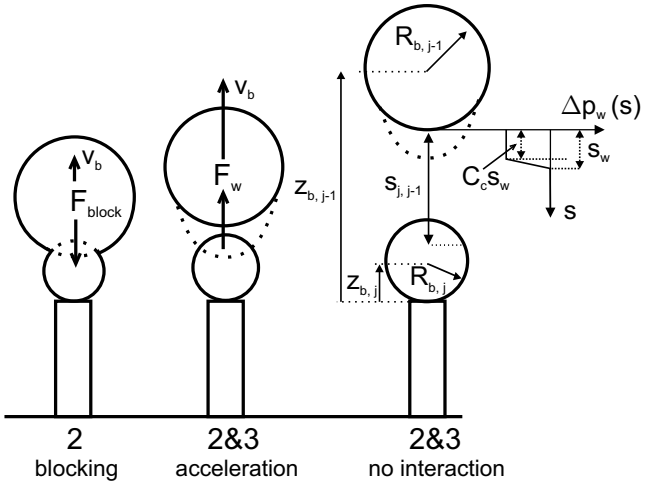

Figure 2.16.: Possible bubble-bubble interactions with stage numbers in which they can occur.

with ρ_b the density of the gas in the bubble which is assumed constant, a reasonable assumption in the later stages of the bubble formation when the virtual mass becomes important.

Bubble-bubble interaction force

The bubble-bubble interaction force, F_{b-b}, is the force acting on the growing bubble, exerted by the last bubble that has detached. This force comes into play for high bubble formation frequencies. Two types of interaction are modeled. First, if the last bubble has not had the time to move away far enough from the needle, it can block the growing bubble and exert a downward force, F_{block} (Fig. 2.16, left). This way the blocking can result in larger bubbles. Second, if the leading bubble has traveled somewhat further and it is moving away from the growing bubble, it is no longer blocking the growing bubble. Instead, it exerts an upward force F_w (see Figure 2.16, center) and accelerates the departure of the growing bubble. This is caused by the low-pressure region in between the bubbles. The presence of this upward force can lead to smaller bubble sizes. F_w only considers the upward force that is present for small distances between the bubbles. The effect of the long range drag reduction and liquid circulation induced by the bubble plume leading to a higher terminal velocity is included in the drag force. Combining the forces F_{block} and F_w we get $F_{b-b} = F_{block} - F_w$ with direction downwards.

In the model, blocking is present whenever the distance between the base of the upper spherical bubble and top of lower spherical bubble is less than, or equal to, zero (i.e. there is 'overlap'). In reality, overlap will not occur due to deformation. The blocking force is only taken into account implicitly with a kinematic criterion by keeping the base of the growing bubble attached to the needle as long as the previous bubble is blocking its path. In other words, as long as the blocking continues, the formation remains in stage 2. The reacting force on the leading bubble is neglected in the model.

A model is required for the extra upward force F_w for the case of two bubbles with a small distance in between, the trailing bubble fixed in position, and the leading bubble accelerating away. In the literature, considerable attention has been paid to the interaction of two bubbles, frequently with special attention for conditions relevant for coalescence. For example, the case of bubbles rising in line has been studied extensively (e.g. Ruzicka et al. (2000a), Katz and Meneveau (1996), Zhang and Fan (2003), Harper (1997), and Bhaga and Weber (1980)). Most of this work concerns, however, the interaction of bubbles at distances of at least several diameters, and for developed flow. Zhang and Shoji (2001) and Chuang and Goldschmidt (1970) model the drag force reduction for the growing bubble with an average upward velocity due to the wake that is experienced by the growing bubble. This velocity is proportional to the power -2/3 of the axial distance. This way, a force with a long range is obtained, which is quite unrealistic for a bubble which has just started moving. In addition, this assumes a fully developed wake. Zhang and Tan (2000) use a wake model for the prediction of weeping, their model has a relatively short range. The studies by Yuan and Prosperetti (1994) and Sankaranarayan et al. (2002) do investigate the interaction at smaller distances. Both present results for developed flow. Yuan and Prosperetti (1994) also study the impulsive motion of bubbles, but only for the case when both bubbles are moving. The results by Yuan and Prosperetti (1994) show that the drag reduction rapidly increases if the distance between the bubbles is smaller than a distance with the order of magnitude of the bubble radius. This is exactly the effect that is represented by the interaction force F_w.

The force F_w is especially important in the later stages of the bubble growth and for relatively high bubbling frequencies, since it may result in an earlier detachment of the bubble and therefore a size reduction. For these conditions, the departing bubble has traveled a distance of typically no more than one bubble diameter, the bubble is rapidly deforming from the spherical to an ellipsoidal shape, and the flow around the bubble and in its wake is still developing. The distance between the growing and the departing bubble is still quite small, so the growing bubble will affect the flow around the departing bubble considerably. Nevertheless, the velocity of the departing bubble has already reached a considerable fraction of the terminal velocity, and, typically, Re has values of at least 500. Although very little data is available for these circumstances, a rough qualitative model is constructed to study the effect of F_w on the bubble diameter. Due to the inaccuracy of this model its effect will be checked by turning the force F_w on and off, and by comparison with an alternative wake model. A more detailed model would require an extensive study of the flow field around the bubble, and the deformation of the bubbles. This approach is presently not pursued.

The local flow and the developing wake lead to a low pressure field below the departing bubble. The resulting pressure difference over the growing bubble generates the additional force F_w. For simplicity, the pressure reduction experienced by the growing bubble is determined only for the mean height of the upper end of the bubble (i.e. $s = s_{j,j-1} = z_{b,j-1} - R_{b,j-1} - z_j - R_{b,j}/2$) and assumed constant over the rest of the upper side of the bubble. The lower side of the bubble experiences no pressure drop. This way, the extra force on the growing bubble is calculated with:

$$F_w = \pi R_{b,j}^2 \Delta p_w(s_{j,j-1}) \tag{2.4}$$

The presence of the growing bubble will further lower the pressure in between the bubbles since

it hampers the flow around the departing bubble. The precise characteristics of this pressure field are not known, but Johnson and Patel (1999) give an idea of the pressure drop: in the wakes behind spheres with velocity v_{sphere} and Re up to 300, the pressure drop is $C_1(1/2)\rho_l v_{sphere}^2$ where C_1 has a typical value around 0.25. The pressure drop reduces to zero over a distance $s_w = C_w R_{b,j-1}$ away from the base of the bubble. Indices j and $j-1$ refer to the growing bubble and last detached bubble, respectively. Over a length $C_c s_w$ from the bubble base, the pressure reduction is constant. These observations are used to construct the model for F_w (see Figure 2.16). The leading bubble has below it a region with reduced pressure, the reduction is given by $\Delta p_w(s)$. s is the distance to the base of the leading bubble. At distances up to $C_c s_w$ below the bubble base the pressure drop is constant: $\Delta p_w(s) = C_1 \frac{1}{2}\rho_l v_{b,j-1}^2$, at distances from $C_c s_w$ up to $s_w = C_w R_{b,j-1}$ the pressure drop decreases linearly to zero. C_1 is taken 0.25 after the observations by Johnson and Patel (1999). The drag reduction observations by Yuan and Prosperetti (1994) suggest that C_w is of the order of magnitude 1. Since no further information is available, the value 1 is taken. This gives a good match with the experimental results, the results are not very sensitive with respect to the exact value. C_c is taken as 0.75.

To check the sensitivity, a comparison is made with the results obtained with an alternative model for $\Delta p_w(s)$. For this purpose, the model by Zhang and Tan (2000) is used who considered the drop in pressure below a departing bubble for the study of weeping:

$$\Delta p_w(s) = \frac{6}{\mathrm{Re}_{j-1}} \left(\frac{\rho_l v_{j-1}^2 R_{b,j-1}^2}{2(s + R_{b,j-1})^2} \right) + \left(\frac{\rho_l v_{j-1}^2 R_{b,j-1}^3}{2(s + R_{b,j-1})^3} \right) \tag{2.5}$$

where Re_{j-1} is the Reynolds number of the departing bubble. The first term is usually very small.

Drag force

The drag force needs to be calculated for a bubble with radius R_b and velocity v_b. Most models in literature use Stokes drag, e.g. Satyanarayan et al. (1969) and Ruff (1972). This is not correct for the present situation, since relatively high velocities are attained. Similar to Chuang and Goldschmidt (1970), the drag force is modeled with: $F_d = C_d(Re) \cdot \pi R_b^2 \cdot \frac{1}{2}\rho_l (v_b - v_{liquid})^2$, where $Re = \frac{\rho_l |v_b - v_{liquid}| 2R_b}{\mu_l}$. μ_l is the viscosity of the liquid. v_{liquid} is the velocity of the liquid around the bubble. It is included to incorporate the effect of long range drag reduction and liquid circulation induced by the bubble plume. The results in Zhang and Fan (2003) show that this is a reasonable good approximation for the description of the interaction at longer distances between the bubbles. The main consequence on the model outcome of the inclusion of this effect is a more accurate prediction of the terminal velocity of the departing bubble.

Most papers in literature providing correlations on the drag coefficient of bubbles, give values obtained in situations where the bubble velocity is near the terminal velocity v_∞. In the case of bubble formation, the bubble velocity may be considerably lower, the deformation to ellipsoid shape has not yet taken place and the mobility of the surface is still changing. In addition, the wake may not have developed to the same extent as in cases where the terminal velocity has almost been reached. Therefore, the use of these correlations may not be entirely appropriate. However, due to the lack of better data, a correlation for the drag coefficient based on terminal

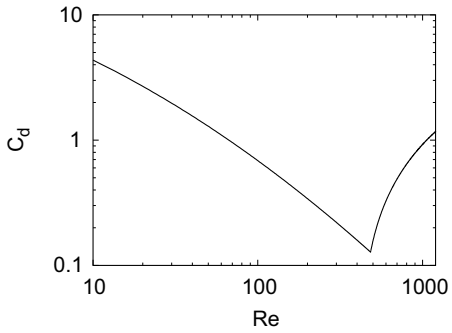

Figure 2.17.: Drag coefficient model used.

velocity data is used.

A model for the drag coefficient (Figure 2.17) is constructed from terminal velocity data for a range of bubble diameters found in Clift et al. (1978)(eq. (7-3) and Fig. 7-3), using $C_d = \frac{\frac{8}{3} R_b g}{v_\infty^2}$. The terminal velocities given by Clift et al. (1978) (around 0.24 m/s for bubbles with sizes around 4 mm) agree well with the experimental values. Other models are not as well able to predict the terminal velocity of a single bubble for this experiment, for instance the model by Karamanev (1994) underpredicts the terminal velocity with $0.02 - 0.03$ m/s. Tests show that the sensitivity with respect to the exact value of the drag coefficient for low to intermediate Reynolds numbers is quite small. Results are sensitive with respect to the value of the terminal velocity that is attained by the bubble, however, since it has a major influence on the bubble blockage interaction.

Since the bubbles are rising in line, drag reduction as well as liquid circulation occurs and the bubble terminal velocity is higher. Experiments show that for the present conditions, the velocity increases approximately linearly with the bubbling frequency from the velocity of a single bubble (0.25 m/s) at low bubbling frequencies to a velocity around 0.31 m/s for the highest bubbling frequencies. The combined drag reduction and circulation are accounted for by including the liquid velocity v_{liquid}. For flow rates smaller than 1.2 ml/s the bubbling frequency increases approximately linearly with the flow rate, beyond the flow rate of 1.2 ml/s the bubbling frequency is more or less constant. Consequently, the liquid velocity is modeled with a linear increase from 0 to 0.06 m/s with the gas flow rate for flow rates up to 1.2 ml/s. For flow rates higher than 1.2 ml/s the liquid velocity is set to a constant value of 0.06 m/s.

Stages

Next, the stages will be discussed in more detail. During stage 1, pressure is building up in the chamber. Assuming adiabatic behavior in the gas chamber, the following equation is obtained for the pressure in the chamber (based on Park et al. (1977)):

$$\frac{m_c}{\gamma p_c} \frac{dp_c}{dt} = \Phi_{M,c} - \Phi_{M,b} \tag{2.6}$$

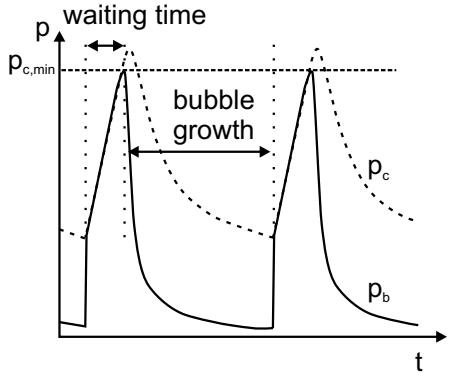

Figure 2.18.: Schematic pressure build up in chamber and bubble with time.

with $\gamma = C_p/C_v \approx 1.4$ and $p_c/m_c^\gamma = p_c(t=0)/m_c^\gamma(t=0)$. $\Phi_{M,b}$ is the gas mass flow rate through the needle from the chamber to the bubble and is given by (Oguz and Prosperetti (1993), assuming isothermal flow):

$$\phi_{M,b} = \frac{\pi}{16}\frac{R_n^4}{l_n \mu_g}\frac{p_c^2 - p_b^2}{\mathcal{R}T_e} \tag{2.7}$$

Here l_n is the length of the needle, T_e the temperature of the environment, μ_g the viscosity of the gas and $\mathcal{R}$ the specific gas constant.

During stage 1, the bubble is modeled as a spherical cap with radius of curvature R_b (see Fig. 2.15). The pressure in the bubble p_b during stage 1 is described with:

$$p_b = p_\infty + 2\sigma/R_b \tag{2.8}$$

A mass balance tracks the mass of gas in the bubble. The relation between the gas mass of the bubble m_b and the pressure in the bubble is given by:

$$p_b = m_b \frac{\mathcal{R}T_e}{V_b} \tag{2.9}$$

With these equations the mass evolution, and therefore the bubble size evolution is specified. The gas-liquid interface starts almost flat (large R_b). When the pressure in the chamber increases due to inflow of gas, the bubble will slowly grow to a hemisphere. During the growth, the bubble radius of curvature decreases to the minimum value of R_n. At that moment there is a maximum pressure drop over the interface (see Figure 2.18), giving a minimum value for the chamber pressure before bubble growth enters the next stage (Oguz and Prosperetti (1993)):

$$p_{c,min} = p_\infty + 2\sigma/R_n \tag{2.10}$$

If the pressure in the chamber increases further, the bubble radius of curvature will increase

again and stage 2 is entered. So, the criterion for stage 1 to end is:

$$R_b = R_n \tag{2.11}$$

During stage 2, the bubble is assumed to be spherical with its base attached to the needle: $z_b = R_b$. Its growth is described by the Rayleigh-Plesset equation.

$$R_b\ddot{R}_b + \frac{3}{2}\dot{R_b}^2 = \frac{1}{\rho_l}\left(p_b - \frac{2\sigma}{R_b} - p_\infty\right) \tag{2.12}$$

where ρ_l is the density of the liquid. Consequently the velocity of the bubble is given by $v_b = \dot{R}_b$. The chamber and bubble pressure are given by equations 2.6 and 2.9.

The end of stage 1 gives the initial conditions for stage 2 and 3. $R_b = R_n$; for $\dot{R}_b$ the velocity of the top of the bubble at the end of stage 1 is taken. When switching from stage 1 to stage 2 the bubble volume makes a small jump since the change from a hemisphere to a full sphere is made. The amount of air required for this is removed from the chamber.

During stage 2, the bubble is growing as a sphere with its base connected to the needle. The upward and downward forces are balanced, the relevant forces are shown in Figure 2.15. Stage 2 ends when the upward forces get bigger than the downward forces and the bubble will accelerate away from the needle. In the absence of blocking, the upward buoyancy and wake forces and the downward drag and liquid inertia forces can be evaluated, and F_σ follows from a force balance. Since F_σ can not exceed $F_{\sigma,max}$, stage 2 ends when the force balance produces $F_\sigma > F_{\sigma,max}$. When the bubbling frequency increases, the blocking force needs to be taken into account. However, no explicit formulation is used for the blocking force. Instead, a kinematic criterion is used: stage 2 can not end as long as the leading bubble is blocking, i.e. as long as the spherical bubbles overlap in the model. When the blocking ends, the blocking force disappears. Hence, stage 2 ends if the two resulting conditions are satisfied:

$$F_{b2,3} + F_w \geq F_{\sigma,max} + F_d + M_b\frac{dv_b}{dt} + v_b C_A \frac{\rho_l}{\rho_b}\phi_{M,b} \tag{2.13}$$

$$z_{b,j-1} - R_{b,j-1} > z_{b,j} + R_{b,j} \tag{2.14}$$

The model assumes that in the case of a blocking event, the fluid is able to sustain a film between the two bubbles, otherwise coalescence would occur. During the blocking event the bubbles will deform. Experimental observation shows that the condition of no coalescence is actually met most of the time in the experiment: for most experimental conditions that were considered, coalescence only occurred occasionally. For certain conditions (e.g. very small chamber volume), however, the condition is not met. Consequently, the model will not predict the bubble size correctly for these cases.

During stage 3, the upward forces are bigger than downward forces and no bubble is blocking. The base of the spherical bubble moves away from the needle exit. The bubble growth is again given by equations 2.6, 2.9, and 2.12. Newton's second law of motion determines the ascent of the bubble. The following equation of motion applies:

$$M_b\frac{dv_b}{dt} = F_{b,23} + F_w - F_d - F_{\sigma,max} - v_b C_A \frac{\rho_l}{\rho_b}\phi_{M,b} \tag{2.15}$$

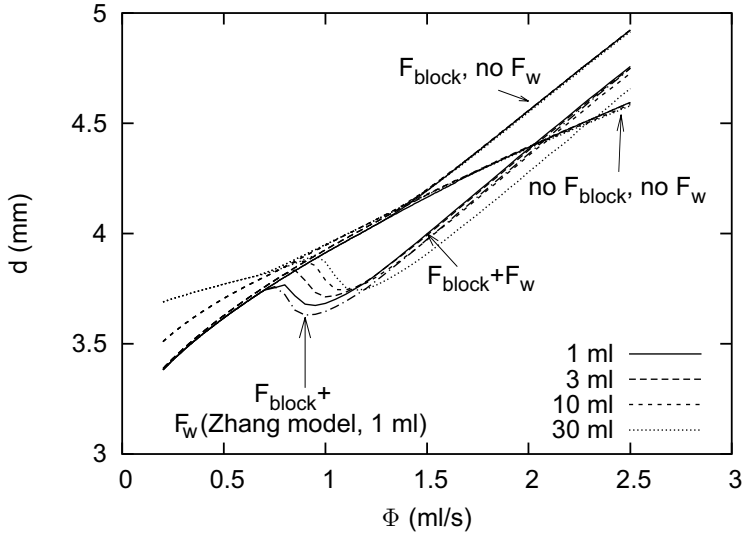

Figure 2.19.: Model predictions for bubble diameter as a function of gas flow rate for various chamber volumes. Three different realizations for different bubble-bubble interaction models are shown.

Stage 3 may be entered at an earlier time due to the force F_w. This force may level off in strength very soon in stage 3 due to the departure of the leading bubble. In this case, the acceleration and velocity of the bubble may become negative. Therefore, the bubble base can return to, and even sink below the needle exit in stage 3. If the bubble sinks below the needle exit, the model returns to stage 2 and fixes the bubble base to the needle. Stage 3 ends when the bubble detaches. This happens when the base of the bubble has traveled a vertical distance R_n from the needle exit (Oguz and Prosperetti (1993)): $z_b \geq R_b + R_n$. When stage 3 ends, immediately a new bubble is generated which enters stage 1: weeping is ignored.

The detached bubble is no longer growing in stage 4. F_w can be ignored since the distance between two consecutive bubbles is big. The equation of motion is:

$$M_b \frac{dv_b}{dt} = F_{b4} - F_d \tag{2.16}$$

2.3.5. Model predictions: comparison with experimental results

Predictions for the bubble diameter by the model are shown in Figure 2.19. The effect of the bubble interactions on the bubble size is checked by including or excluding the forces induced by the previous bubble: F_w and F_{block} (the latter implemented via eq. 2.14). Four different model predictions are shown: the first includes both F_w and F_{block}, the second only F_{block}. The third includes neither F_w nor F_{block} and the fourth shows the outcome with a different model for F_w. Up to a flow rate around 0.75 ml/s no differences concerning the forces F_w and F_{block} are observed. At higher flow rates, the distance between bubbles has significantly decreased and

interactions start to play a role. The models with F_{block} included have much higher slope for the higher flow rates: due to the blocking of the growing bubbles, bubbles can grow for a longer time (stage 2 lasts longer). The predictions without the force F_w do not show the diameter drop that was observed in the experiments. There is simply no mechanism present in the model that can give bubble size reduction for increasing gas flow rate. When the force F_w is incorporated, this force is present. In the later instants of stage 2, when upward and downward forces are almost balanced, the extra force F_w can lead to an earlier lift-off of the bubble base. Additionally, a higher acceleration in stage 3 may result. This can give an earlier detachment of the bubble, and therefore smaller bubbles. These results shows the importance of incorporating bubble-bubble interaction effects in the model. The difference between the predictions obtained with the two different models for F_w are quite small. This shows the results are not very sensitive to the precise details of this model.

The experimental values for the bubble diameter are compared to the predictions using the model with the force F_{block} and F_w included (Fig 2.20). The slope of the curves for high flow rates agrees quite good with the experimental value. When comparing to the predictions for the model without F_{block}, the relevance of the inclusion of bubble blockage in the model is clear. The diameter prediction is quite reasonable, except close to the drop in diameter. The gas flow rate where the drop occurs is underpredicted, and it is more smooth than in the experiment. This can simply be explained by the qualitative nature of the model for F_w. The effect of the previous bubble on the growing bubble is complicated, and in order to get more accurate results the flow between the bubbles, much more extensive modeling efforts are required. Additionally, bubble deformation is present which again complicates matters. Finally, we saw that the exact gas flow rate where the drop occurs is strongly dependent on the shape of the needle opening.

Similar to the experimental results, bubble sizes are independent of the chamber volume for flow rates above 1.2 ml/s. Also, for low flow rates, the bubble size increases with increasing chamber volume. The sizes predicted for low gas flow rates by the model agree reasonably well with the experimental values. Only the values for the smallest chamber volumes of 1 ml and 3 ml are somewhat overpredicted.

Figure 2.21 compares the diameters obtained with the model with those obtained in the experiments for three different needle diameters. Rough agreement is obtained: similar trends are observed for the change in the flow rate at which the diameter discontinuity is observed. The reduction in the magnitude of the drop for the needle with 1.0 mm diameter is not predicted correctly by the model.

2.3.6. Bubble frequency oscillations

The peaking of the standard deviation of the bubbling frequency reported in section 2.3.1 can now be explained as follows, see Fig. 2.22. The solid line represents the bubble size without liquid flow. The presence of the liquid flow induces an extra force on the bubbles. This force tries to move the bubble away from the needle. Detachment of the bubbles occurs earlier: smaller bubbles and higher bubbling frequencies result. The dashed line represents this smaller bubble size for the case with liquid flow. With higher frequencies, bubble-bubble interaction will play a role at a lower gas flow rate, resulting in a diameter jump at lower gas flow rate. If the bubble column is operated at a flow rate corresponding to point 3 and 4, small diameter and frequency

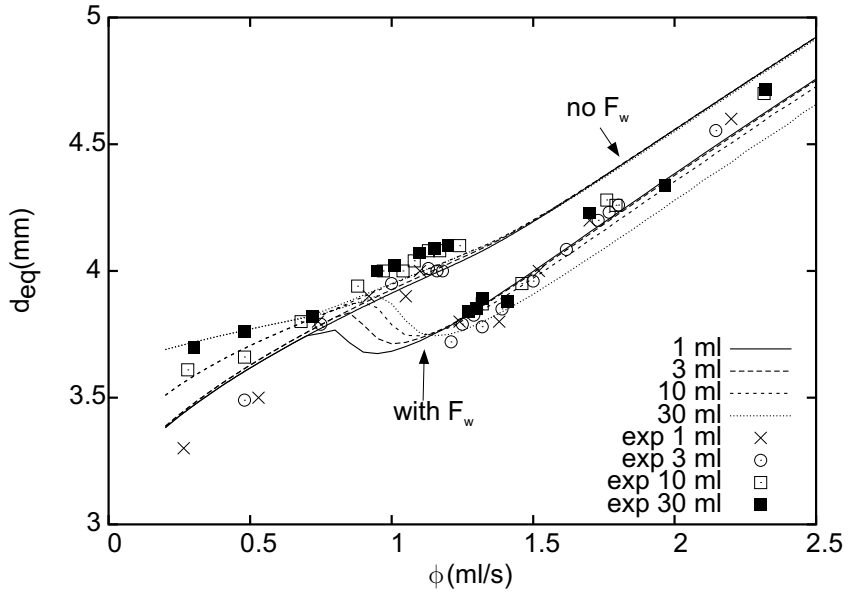

Figure 2.20.: Comparison of model predictions for the bubble diameter with experimental values.

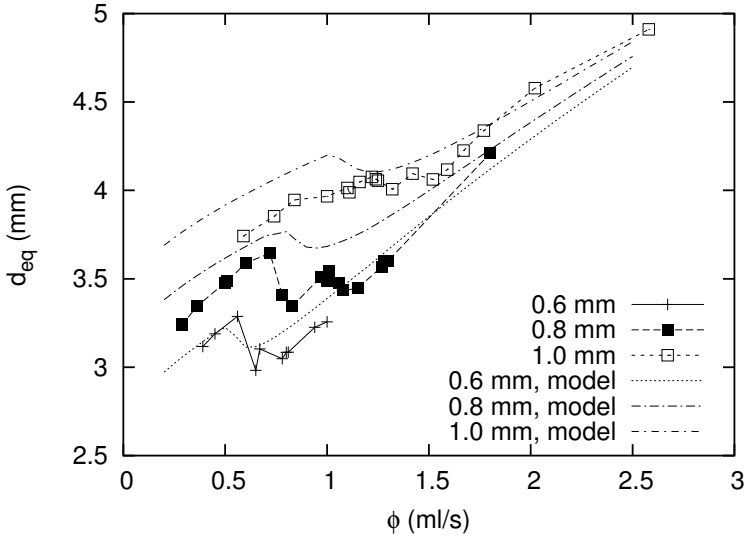

Figure 2.21.: Comparison of model predictions for the bubble diameter with experimental values for various needle diameters.

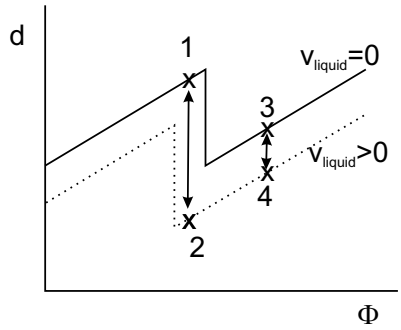

Figure 2.22.: Explanation for strong frequency fluctuations near diameter jump.

fluctuations result when the liquid velocity fluctuates. For flow rates close to the flow rate where the diameter jump occurs (point 1 and 2), large diameter and frequency fluctuations result. Unfortunately, the experimental study and the modeling study did not provide useful clues as how to reduce the effect. For instance, the use of needles with a larger diameter could reduce the magnitude somewhat, but these needles need to be significantly longer to get a similar pressure drop (equation 2.7) and they would produce larger bubbles. This prevents practical application. The magnitude of the chamber volume has very little effect. Reduction of the liquid velocity along the needles is not feasible either: this would require, e.g., the placement of a honeycomb-like structure. For modeling studies intending to simulate the setup, however, this would require a special model for the boundary condition at the sparger. In addition, the honeycomb would probably quickly fill-up with gas due to the small distance between the needles, strongly affecting the bubbling behavior.

2.4. Interaction effects for bubble formation with multiple needles

The previous section discussed the creation of bubbles with a single needle. For the bubble column sparger up to 559 needles are used to introduce bubbles. These needles are closely spaced, each needle is fed with air through a system of which parts are shared with other needles. Due to the close spacing, interaction effects via the liquid phase may play a role in the bubble formation process. The mutual volumes may lead to different bubble volumes since the pressure fluctuations in the volumes are altered. These factors may, therefore, influence the way bubbles are introduced and alter the dynamics of the bubble column. For this reason, a study to possible interaction effects was performed.

Only little attention has been paid in the literature to these possible interaction effects which may lead to altered or correlated bubble formation. Titomanlio et al. (1976) found that the presence of a second orifice basically leads to an effective halving of the volume of the common gas chamber. Ruzicka et al. (2000b) studied the simultaneous bubbling of two orifices with a common gas chamber, for various distances between the orifices. Various interaction effects were reported: synchronous bubbling, asynchronous bubbling and intermittent behavior. The gas flow rate had a strong effect on the type of regime. Ruzicka et al. (1999) studied the various modes of

bubble formation for larger numbers of orifices placed in various patterns. For both latter studies, the orifices were holes with diameter 1.6 mm in a plate with thickness of 3 mm. Consequently, larger bubbles were obtained than in the present study and a relatively smaller pressure drop was present over the orifice than for the present needle sparger. Therefore, pressure fluctuations play a much larger role than for the needle sparger. As a result, the dynamic behavior may differ due to the interplay of the interaction effects in the liquid with the pressure fluctuations in the chamber volume.

Influence of common chamber volumes

In the present study the influence of the mutual chamber volumes is relatively small due to the needle length and relatively small chamber volumes employed, therefore different behavior will be obtained than that reported in the work by Ruzicka. The results in section 2.3 show that the influence of the chamber volume is very small for flow rates per needle beyond 0.75 ml/s, and, consequently, the influence of pressure fluctuations in the common volume on the bubble formation is quite small. For flow rates per needle around and below 0.75 ml/s the chamber volume does play a role, consequently pressure fluctuations and a possible delay time are important. After bubble detachment, extra pressure needs to be built up in order to generate a new bubble. In addition, water may enter the needle for a small distance, resulting in a need for an even larger extra pressure. For the lower flow rates, this extra pressure may not be created: each group has 18 needles, and at any time a bubble is growing at a large number of the other needles. Consequently, these needles provide a much easier way out for the air, the extra pressure may not be built up and the needle may cease operation. Observations show that, indeed, part of the needles cease operation at flow rates per needle around 0.75 ml/s. As a result, the bubble column is not operated at flow rates where the chamber volume plays a significant role. Alterations or correlation in the bubble formation due to interaction via pressure fluctuations in the common volumes will therefore not be very important for the relevant operation conditions. This is confirmed by tests: no correlation was found for the bubble formation at needles operated in two separated compartments. This leaves interactions in the liquid as the only possible significant source for interactions.

Interactions via the liquid phase

As a next step, a study was performed to find out if correlated bubble formation can occur in the needle sparger due to interactions in the liquid phase. Several geometries with small numbers of needles were studied and several types of correlated bubble formation were observed. The type and strength of interaction were depending of the geometry of the needles. Bubble formation was more or less uncorrelated if the needles were not direct neighbors (i.e. the distance in between was larger than 1 cm). If bubbles were generated by two adjacent needles, correlated bubble formation was observed. Both synchronous and a-synchronous (alternating) bubble formation were observed, the type depending on the flow rate through the needle. If multiple needles were placed in a linear row, the correlation strength increased further. Figure 2.23 shows the behavior for the row of needles. Asynchronous (alternating) bubble formation was observed for flow rates per needle in the range $\phi_{transition}/3 < \phi < \phi_{transition}$ with $\phi_{transition} \approx 1.2$ ml/s, the flow rate at which transition to smaller bubble sizes occurs. For flow rates per needle beyond $\phi_{transition}$,

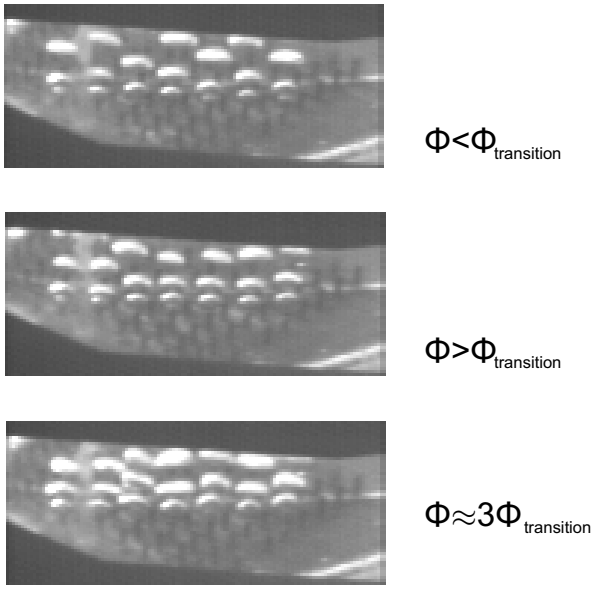

Figure 2.23.: Synchronous and asynchronous bubble formation.

synchronous bubble formation was observed. For flow rates around $3\phi_{transition} \approx 3.6$ ml/s, 'drafting, kissing and tumbling' behavior of the detached bubbles is observed quite close to the needle, as well as coalescence close to the needle. For these flow rates the behavior returns to asynchronous (alternating) bubble formation, though less stable than for the low flow rates. The interaction patterns were surprisingly stable for a row of needles: the phase difference of the bubble formation at needles separated by several other needles was not much larger than that for adjacent needles. In fact, the stability even increases with the number of needles. Figure 2.24 shows how a sudden change in the bubbling frequency of one needle (due to e.g. a coalescence event) is quickly followed by a matching frequency change in the neighboring needle.

A possible explanation for the alternating and synchronous bubble formation is sketched in Figure 2.25. For ϕ somewhat smaller than $\phi_{transition}$ the detached bubble ('1') rises away from the needle, and exerts a force via its wake on the growing bubbles at the needle at which the bubble was formed ('2') and the closest neighboring needles ('3'). The bubble '2' is, however still firmly attached to the needle due to its small size, and therefore does not detach earlier by this extra force. The extra force can, however, lead to earlier detachment of bubble '3'. Vice versa, the bubbles departing other needles (e.g. bubble '3') can result in earlier detachment of bubble '2'. This way, the bubbling frequencies of neighboring needles will quickly match, though with opposite phase. For ϕ larger than $\phi_{transition}$, the detachment of bubble '2' is determined by the moment when bubble '1' has moved away far enough (see the previous section). Consequently, the wake of bubble '1' will accelerate the detachment of both bubbles '2' and '3' and synchronous bubbling results.

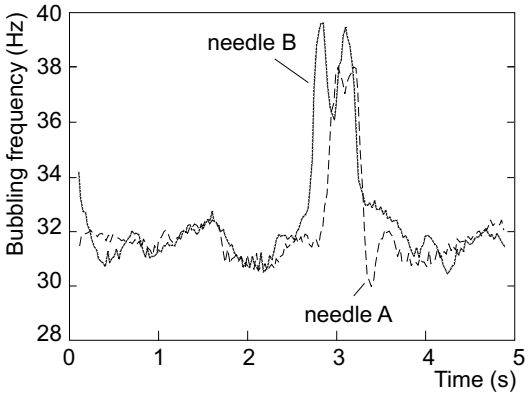

Figure 2.24.: Bubbling frequencies for two neighboring needles ($\phi < \phi_{transition}$, alternating bubble formation).

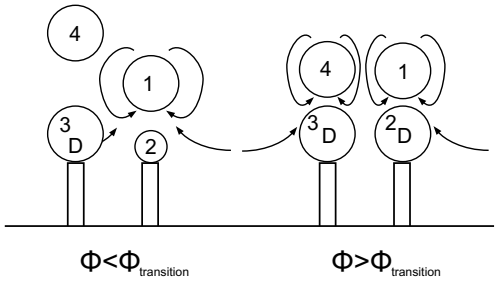

Figure 2.25.: Schematics interaction effects for two neighboring needles. 'D': bubble about to detach.

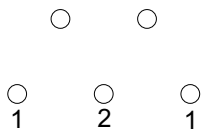

Figure 2.26.: 2D grid with bubble formation order: 1=first, 2=second.

The correlation for only two needles was much weaker. Small differences between the needles (which were manually cut for the study) result in different bubbling frequencies for the individual needles. The extra upward interaction force can reduce the difference between the bubbling frequencies, but only small differences can be fully reduced. If a small frequency difference remains, the phase difference of the bubble formation will slowly drift until a very quick phase jump to the next cycle occurs: i.e. more or less synchronous bubble formation is interrupted by short periods of asynchronous bubble formation.

In 2D needle configurations, such as those encountered in the bubble column, alternating bubble formation such as shown in Figure 2.23 is very unstable since each needle has more than two direct neighbors which should all have opposite phase. This is not possible in the 2D geometry for all the needles (Figure 2.26). Synchronous bubble formation is also not very stable. The interaction effects are quite weak, and in the full sparger each needle has six nearest neighbors. A disruption in only one of these neighbor needles may break the synchronization, a fluctuating liquid velocity field has a similar result. Observations in the final bubble column sparger confirm this: negligible synchronization is observed.

2.5. Conclusions

Bubble formation at a single needle

The bubble formation at a needle has been studied. Experiments were performed and a bubble formation model was developed to study the influence of bubble-bubble interaction mechanisms on the bubble size. Two important bubble-bubble interaction mechanisms are identified: the previously formed bubble which is still in the vicinity of the growing bubble can either give a blocking effect on the growing bubble or accelerate its departure. These effects have an delaying and accelerating effect, respectively, on the instant of detachment and consequently give larger and smaller bubble sizes, respectively. Both effects are found to have a significant impact on the bubble size. The acceleration of the next bubble was found to cause a very rapid bubble diameter decrease for a small increase in gas flow rate beyond a critical value. The bubble diameter drop is insensitive to the size of the chamber volume. The effect of the chamber volume can only be found for small gas flow rates. Results of the model that was developed show reasonable agreement with the experimental results.

If the needles are used for a sparger in a bubble column with a dynamic liquid flow field, strong bubble size and frequency fluctuations can occur for specific gas flow rates. The present investigation has shown that these are caused by changes in the critical flow rate where the sharp decrease in bubble diameter occurs: liquid flow fluctuations can have a major impact on the subtle interplay of the bubble-bubble interaction forces with the other forces present.

Interaction effects for multiple needles

A short study has shown that interaction effects due to mutual chamber volumes can be neglected for all flow rates of interest: interaction effects only take place at low gas flow rates, and for these flow rates some of the needles cease operation, rendering the sparger ineffective. Interaction via the liquid phase is mainly important for linear configurations of needles and can produce both synchronous and alternating bubble formation. For 2D configurations the synchronization is easily broken due to the larger number of needles involved.

Acknowledgements

The author wishes to thank Anouk de Jong and Sam van der Zwan for their help in running the experiments described in section 2.3.

List of symbols

Roman symbols

C_1	coefficient for the pressure drop behind a sphere	-
C_A	added mass coefficient	-
C_c	scaling coefficient for constant pressure region	-
C_d	drag coefficient	-
C_w	scaling coefficient for s_w	-
d_{eq}	equivalent bubble diameter	m
F	force	$kg\ m\ s^{-2}$
F_{b-b}	bubble-bubble interaction force	$kg\ m\ s^{-2}$
$F_{b2,3}$	buoyancy force during stages 2 and 3	$kg\ m\ s^{-2}$
F_{b4}	buoyancy force during stage 4	$kg\ m\ s^{-2}$
F_d	drag force	$kg\ m\ s^{-2}$
F_σ	surface tension force	$kg\ m\ s^{-2}$
$F_{\sigma,max}$	maximum surface tension force	$kg\ m\ s^{-2}$
F_{block}	bubble blockage force	$kg\ m\ s^{-2}$
F_w	upward force exerted by previous bubble on growing bubble	$kg\ m\ s^{-2}$
f	bubble formation frequency	s^{-1}
g	acceleration of gravity	$m\ s^{-2}$
l_n	needle length	m
M_b	virtual mass of bubble	kg
m_c	mass of gas in chamber volume	kg
p	pressure	$kg\ m^{-1}\ s^{-2}$
p_b	pressure inside bubble	$kg\ m^{-1}\ s^{-2}$
p_c	pressure inside chamber volume	$kg\ m^{-1}\ s^{-2}$
$p_{c,min}$	minimum pressure chamber volume before stage 2 is entered	$kg\ m^{-1}\ s^{-2}$
p_∞	pressure in liquid at needle exit height	$kg\ m^{-1}\ s^{-2}$
$\mathcal{R}$	specific gas constant	$m^2\ s^{-2}\ K^{-1}$
R	cylindrical bubble column radius	m

R_{2D}	half width of pseudo-2D bubble column	m
R_b	bubble radius	m
R_{depth}	half depth of pseudo-2D bubble column	m
R_n	needle radius	m
Re	Reynolds number	-
s	distance from lower side of departing bubble	m
$s_{j,j-1}$	distance s at which the force F_w is evaluated	m
s_w	distance s over which reduced pressure is observed behind the bubble	m
T_e	environment temperature	K
t	time	s
x	horizontal coordinate	m
y	horizontal coordinate	m
V_b	bubble volume	m^3
V_c	chamber volume	m^3
v_b	velocity of bubble center of mass	$m\ s^{-1}$
v_{liquid}	velocity of liquid close to the bubble	$m\ s^{-1}$
v_{sphere}	velocity of sphere	$m\ s^{-1}$
v_∞	terminal bubble velocity	$m\ s^{-1}$
z	axial coordinate	m
z_b	distance of bubble center to the needle exit	m
z_{wall}	distance of bubble center to the wall	m

Greek symbols

γ	polytropic coefficient	-
Δp_w	pressure drop behind departing bubble	$kg\ m^{-1}\ s^{-2}$
θ	contact angle	rad
μ_g	dynamic viscosity gas	$kg\ m^{-1}\ s^{-1}$
μ_l	dynamic viscosity liquid	$kg\ m^{-1}\ s^{-1}$
ρ_b	bubble gas density	$kg\ m^{-3}$
ρ_l	liquid density	$kg\ m^{-3}$
σ	surface tension	$kg\ s^{-2}$
σ_f	standard deviation of the bubble formation frequency	s^{-1}
Φ	gas volumetric flow rate through needle	$m^3\ s^{-1}$
$\Phi_{M,b}$	gas mass flow rate through needle to bubble	$kg\ s^{-1}$
$\Phi_{M,c}$	gas mass flow rate feeding chamber volume	$kg\ s^{-1}$
$\Phi_{transition}$	gas volumetric flow rate through needle where transition occurs	$m^3\ s^{-1}$

Subscripts

j	growing bubble
$j-1$	previously formed bubble

3. On the accuracy of the void fraction measurements using optical probes in bubbly flows [1]

3.1. Introduction

For the investigation of bubbly gas-liquid flows, local phase detection probes have become widely applied sensors. These intrusive probes, often based on impedance or optical phenomena, can provide estimates for, e.g., the phase indicator functions, void fraction, and dispersed phase velocity (Cartellier and Achard, 1991). Optical probes have the advantage of the simplicity of the setup, easy interpretation of the results, and the fact that the signal is not coupled to the flow. In optical probes, light is emitted into one extreme of an optical fiber. At the other extreme, the tip, some light is reflected back. The reflected intensity is determined. Its value depends on the refractive index of the phase surrounding the probe tip. This way, the detection of bubbles is enabled by the different refraction indices of the gas and liquid phases. A good introduction and overview of the principles of this technique can be found in Cartellier and Achard (1991) and Cartellier and Barrau (1998a).

The use of optical probes for the investigation of small non-uniformities in the void fraction distribution of bubbly flows (chapter 7) puts high demands on the accuracy of the void fraction estimate. This requires a good understanding of the signal produced by the probe and the intrusive nature of the probe. From this, a more accurate residence time of the probe in the bubble can be determined, and the difference between the measured residence time and the residence time for a 'virtual probe' (an imaginary probe having no intrusive nature) is clarified. Regarding these points, two issues are important. First, the moments in the signal that the probe enters and exits the bubble must be correctly identified. Second, the interaction of the probe with the bubble interface has to be understood: the probe induced deformation of the bubble, its deceleration, and the drifting of its trajectory should be identified.

A considerable amount of work on optical probes has been published. Most studies on the accuracy of the void fraction (Cartellier and Achard, 1991; Cartellier, 1992; Barrau et al., 1999; Zŭn et al., 1995; Carrica et al., 1995) consider the total error in the void fraction by comparing with a global technique, such as vertical ducts with fast closing valves (Cartellier and Achard, 1991; Cartellier, 1992; Barrau et al., 1999; Zŭn et al., 1995). These studies provide little clue to the individual contributions of all error sources. The identification in the signal of the moments of entrance and exit of the probe in the bubble has been the subject of many studies on the signal shape and signal analysis (Cartellier and Achard, 1991; Barrau et al., 1999; Zŭn et al.,

[1] Reprinted with permission from Rev. Sci. Instr. 76, 035103 "On the accuracy of the void fraction measurements using optical probes in bubbly flows", Copyright 2005, American Institute of Physics.

1995; Cartellier, 1990; Schmitt et al., 1995). The main focus in these investigations was on the transition of the probe from the liquid phase into the gas phase, as well as the selection of appropriate thresholds for an accurate algorithm. There is still uncertainty on the point in the signal which corresponds to the moment that the probe crosses the undisturbed air-water interface at the end of the bubble. Especially criteria for lower amplitude signals without a plateau are unclear (Cartellier, 1992; Barrau et al., 1999). The possible effects of the probe on the bubble shape, velocity, and trajectory were first classified by Serizawa et al. (1984) for a hot film probe. This was refined later for optical probes by Barrau et al. (1999). Investigations on the modification of the bubble shape by the probe have generally been focused on the piercing of a flat surface (Cartellier and Achard, 1991; Liju et al., 2001) or are based on assumptions about the piercing behavior (Carrica et al., 1995). Only the work by Barrau et al. (1999) and Sene (1984) attempt to quantify the contribution of the interaction effects, but their conclusions are partially contradicting and incomplete.

The present article considers the inaccuracy of the optical probe technique in a bubbly flow. The first objective is to find proper criteria for the signal analysis that give the best correspondence with the actual crossing of the probe through the undisturbed interface. The second objective is to find the effects of the probe on the bubble that are responsible for inaccuracies in the void fraction, and to quantify them. For both objectives, special attention is given to the dependence of the behavior on the radial position of the piercing event. This way, especially low-amplitude signals are studied in more detail and the effect of curvature is considered. The approach toward finding these criteria and interaction effects is experimental. The piercing of a single bubble is studied under dynamic conditions by comparing probe signals and charge coupled device (CCD) images with and without piercing and investigating these for possible interaction effects. Sections 3.2 and 3.3 discuss the literature regarding the subject and the experimental facilities and processing techniques used in this work, respectively. Section 3.4 presents the results on the identification of the interfaces in the probe signal and Section 3.5 analyzes the results obtained on the probe-bubble interaction.

3.2. Literature overview

3.2.1. The probe signal

Cartellier and Achard (1991); Cartellier (1990, 1992) provide a general sketch of the piercing event of a bubble by an optical fiber. The papers give an overview of literature on optical probes. Controlled quasi-steady piercing experiments of a probe penetrating a plane water-air interface are described and appended with an overview of literature on related techniques such as resistivity probes. This provides a picture of the penetration of a bubble by an optical probe.

Figures 3.1 and 3.2 sketch the bubble piercing process and the corresponding bubble signal for an ideal case. The probe is fixed, the bubble is moving upward with constant velocity U_b. If the bubble is penetrated in the center, generally, five stages can be distinguished during the piercing process:

- Stage 1: Perturbation of the bubble interface (Figure 3.1a); when the probe tip approaches the bubble surface a deformation is produced due to the probe-induced liquid pressure

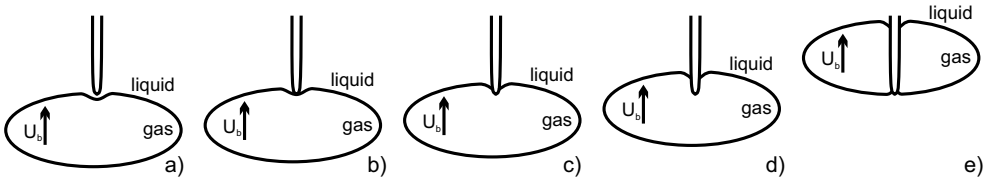

Figure 3.1.: Sketch of the piercing phenomena.

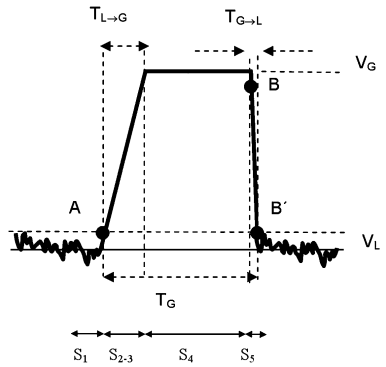

Figure 3.2.: Optical probe signal generated by an ideal bubble.

over the bubble: the 'surge effect'. The film between the tip and the interface is drained laterally. The amplitude of the deformation depends on the bubble velocity, tip diameter and geometry, and fluid characteristics. Calculations using boundary element methods and potential flow assumption (Liju et al., 2001) show that, in general, the amplitude of this deformation is much smaller than the tip radius. During this stage, the optical probe signal level equals V_L (Figure 3.2 - S_1).

- Stage 2: Rupture of the bubble interface (Figure 3.1b). Once the film has become very thin due to the lateral film draining, it ruptures due to direct force interactions between the solid surface and the interface. The optical probe signal starts increasing (point A in Figure 3.2 - S_2).

- Stage 3: Movement of the three-phase contact line along the probe tip (Figure 3.1 c). The tip enters the bubble, and an increasingly larger area of the tip starts reflecting light. As a result, the probe signal gradually reaches the gas level V_G (Figure 3.2 - S_3).

- Stage 4: Bubble passage (Figure 3.1d). The tip is almost dry. In the case of a silica tip, it is never completely dry because the clean silica has a natural wettability due to the hydrogen bonding to surface silanol (Si-OH) groups produced by the hydrolysis of the silica surface in aqueous environment (Fordham et al., 1999). In this stage, the optical probe signal level is V_G (Figure 3.2 - S_4).

- Stage 5: Gas-liquid transition (Figure 3.1e). When the tip contacts the rear part of the bubble, the liquid quickly creeps up along the solid surface and a new deformation is produced due to surface tension. In this stage, the optical probe signal level drops to V_L (Figure 3.2-S_5). The exact signal point that identifies the interface transition is not yet clear in this case.

The duration of the signal rise for the liquid to gas transition ($T_{L\rightarrow G}$) is much longer than the duration of the signal drop for the gas to liquid phase transition ($T_{G\rightarrow L}$). There are two reasons for this. First, the amplitude of the interface deformation is much smaller for the case of gas-liquid transition than for the liquid-gas transition: the low gas inertia allows a quick lateral drainage when pushed by the tip, and the remaining gas layer encounters a higher inertia medium which resists its penetration. Second, when the probe is applied to bubbles, it usually encounters a concave interface for the gas-liquid transition. When the probe pierces the interface, the curvature keeps its sign until breaking. As a result, the gas-liquid transition occurs more rapidly than the liquid-gas transition which has a convex surface. For bubbles pierced in the center, the de-wetting is complete and a plateau exists in the signal if the tip penetrates far enough into the bubble, i.e., deeper than the probe latency length. If the bubble is pierced further away from its center, the de-wetting process of the probe may not be completed before the re-wetting occurs at the gas-liquid interface. In this case, a smaller amplitude signal is obtained without a plateau, the signal usually has a bell-shape. The signal drop associated with re-wetting now has a much larger duration. Imperfections in the tip shape may give deviations from the ideal signal shape (Cartellier and Barrau, 1998a). One common example is the occurrence of a pre-signal. Before the probe touches the interface, a primary peak of low amplitude may be observed in the signal (Cartellier, 1992), depending on the probe that is used. This 'pre-signal' is attributed to reflection of light back into the probe by the interface before contact. The identification of the points in the signal associated with the crossing of the interface has been done so far by investigating quasi-steady situations with flat interfaces, and by using the results obtained with resistivity probes (Cartellier and Achard, 1991). Ignoring the possible pre-signal, the beginning of the signal rise corresponds to the detection of the disturbed liquid-gas interface (Cartellier and Barrau, 1998a; Cartellier, 1990; Cartellier and Barrau, 1998b). For the gas-liquid interface, no tests under dynamic conditions are available (Cartellier and Achard, 1991). Cartellier and Achard (1991) and Barrau et al. (1999) performed experiments under quasi-steady conditions on a plane gas-liquid interface. Very accurate measurements of the surface deformations combined with expectations based on the results for resistivity probes (Cartellier and Achard, 1991) suggest that the transition takes place at the start of the falling slope, the so-called high level criterion (HLC, point B in Figure 3.2). In these experiments, a sharp signal drop was obtained at the instant that the probe touches the lower gas-liquid interface. The rapid wetting of the probe results in a very fast transition. Other authors (Schmitt et al., 1995) propose a criterion based on the end of the falling slope for the gas-liquid transition, the so-called low level criterion (LLC), see point B' in Figure 3.2. However, the motivation for this choice is based more on algorithm simplification than on experimental evidence, since the calculation of the point B is difficult for some types of signals, especially in the case of high gas fractions.

3.2.2. Probe-bubble interaction mechanisms

Serizawa et al. (1984) performed for hot film probes the first classification of the effects that occur during the bubble piercing process and that can induce measurements errors. This classification was refined later for optical probes by Barrau et al. (1999):

- Blinding effect: since the probe detects the disturbed interface position, the local interface deformation during probe impact contributes to the error. This leads to the existence of a blind zone or, equivalently, to an effective shape detected by the probe.
- Crawling effect: the whole bubble is decelerated and/or deformed during the interaction.
- Drifting effect: the trajectory of the bubble is altered leading to either the detection of a smaller chord or to no detection at all.

Both the blinding effect and the crawling effect contain deformation effects. The deformation for the blinding effect is mainly related with a local deformation zone located in the bubble interface which may for instance be produced by both the probe induced liquid pressure over the bubble and the direct hitting itself. The crawling effect considers the deformation of large parts of the bubble. The relative influence of these effects on the final residence time estimate results, as well as their absolute magnitude, is not yet clear (Barrau et al., 1999). Carrica et al. (1995) identified the blind zone for resistivity probes as a membrane over the bubble interface of width equal to the probe tip radius. If the tip center is inside this zone, no bubble is detected, leading to underestimation of the void fraction. For optical probes, however, the work claims that these probes can detect bubbles touched by only a part of the tip. This would lead to overestimation. For bubbles, however, generally underestimation is observed. Barrau et al. (1999) reverse the explanation for optical probes by Carrica et al. (1995) and attribute the systematic underestimations observed in the optical probes measurements to the blinding effect. Similar to the explanation for resistivity probes by Carrica et al. (1995), a blind zone near the bubble perimeter is identified where the corresponding chords are not perceived or underestimated. The size of this region is based on a critical dimensionless radial coordinate for the piercing, instead of the tip radius. Experiments to determine the value of this coordinate were only done for a viscous liquid ($\nu = 20 \cdot 10^{-6} m^2/s$), and showed a value of 0.7. Outside the blind zone, the underestimation of the chord length is very small since the surge effect (Liju et al., 2001) only gives a small deformation. In addition, other authors (Sene, 1984) claim that the crawling effect can play an important role in bubble piercing interaction, but the experimental evidence in this case is still weak.

3.3. Experimental setup and processing

3.3.1. Introduction

In order to determine the void fraction, the probe signal must be analyzed by an appropriate signal processing algorithm. This algorithm must identify the points in the signal that correspond to the crossing of the liquid-gas and gas-liquid bubble interface by the probe tip. The

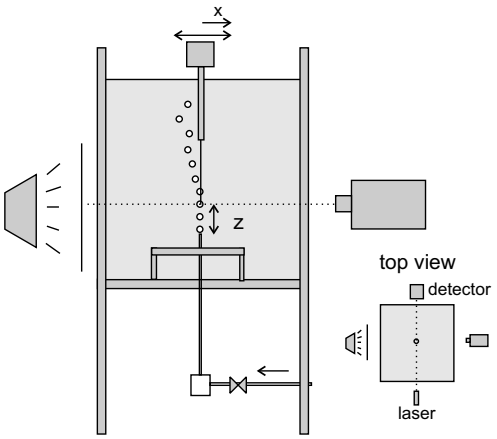

Figure 3.3.: Single bubble experimental setup.

identification of the points in the signal associated with the crossing of the interface for a dynamic situation requires the simultaneous recording of the probe signal and the position of the probe tip with respect to the interface. The relative importance of the probe-bubble interaction mechanisms can be investigated by studying the differences between the original (not-pierced) and the pierced bubbles. The residence times obtained from the optical probe signal are compared with the residence times obtained from CCD images with and without piercing. These two types of experiments will be referred to as the synchronous experiments and the residence time experiments respectively.

3.3.2. Experimental setup

A train of bubbles is analyzed using both the optical probe technique and digital image processing techniques. Figure 3.3 shows a sketch of the system. The basic configuration is composed of a water tank, 30 cm x 30 cm x 50 cm, where a train of bubbles with very constant shapes is produced at a constant flow rate by a single needle (inner diameter 0.8 mm, length 20 cm). With the flow rates used in these experiments, the bubbles have ellipsoidal shapes and a wobbling behavior when they have traveled a few centimeters from the needle. The synchronous experiments and the major part of the residence time experiments have been performed with bubbles having 4.8 mm major axis (equivalent diameter D_{eq}=3.7 mm). Additional residence time experiments have been performed with bubbles of D_{eq}=2.8 mm (major axis 3.8 mm) and D_{eq}=5.2 mm (major axis 5.8 mm). The diameter variations were obtained by changing the flow rate through the needle. The image acquisition system is composed of a CCD camera (DALSA, resolution 256x256) and a continuous light source. The residence time recordings were performed at the highest possible frame rate of 900 fps (image resolution of 36 pixels per mm). In the synchronous experiments, the instant when the bubble interface is pierced has to be determined accurately. For this purpose, a higher temporal resolution is needed. Therefore, a triggering system is used. A small laser beam is aligned through the bubble plume at an optical detector, which provides a trigger pulse.

This trigger pulse is delayed with a variable amount of time. Two pulses are derived: one for starting the image capture and one for ending the image capture (capture time 30 μs). The evolution of the piercing of the bubble is investigated by varying the delay. The optical probe system is composed of an optical probe (stretched type, R_f=100 μm, latency length=75 μm), a multichannel analog-digital converter (ADC) card and a XYZ traversing system with a precision of 1 μm. The probe is placed vertically in the tank, parallel to the bubble trajectory. The signal of the optical probe is recorded simultaneously with the trigger signals using the ADC card. For the synchronous experiments, a sampling rate of 200 kHz is used, for the residence time experiments 100 kHz. The study of the influence of the position of puncture and the evolution of the piercing at various vertical positions of the bubble requires that all of the bubbles are very constant in both shape and trajectory and that no coalescence occurs. Different experiments verify that the constant shape and trajectory is only obtained in the zone near to the needle (at a distance in between 1 cm and 3.5 cm in this work). In this range, the bubble trajectories are straight and very reproducible (maximum variation of 1.5 pixels over 8 hours). In addition, the bubble surface exhibits some shape oscillations. These are again very reproducible (maximum variation of 1 pixel). The coalescence can be prevented by varying the volume of the pressure chamber under the needle and the flow rate. The single CCD camera allows for only a two-dimensional view of the axisymmetric piercing process. The probe is aligned in the plane parallel to the CCD image plane that passes through the bubble center. This alignment is done by traversing the probe perpendicular to the image plane and finding the maximum of the probe residence time from its signal.

3.3.3. Processing of residence time experiments

The differences between the original and pierced bubbles are studied. In this set of experiments, three different residence times are determined: first, the tip residence times inside the bubble are obtained from the optical probe signal. Second, the residence times from the sequence of images without piercing (virtual tip) are obtained and third, the residence times are obtained from image sequences with piercing. The latter two residence times are obtained using digital image processing techniques. The analysis is done at various probe locations. Kiambi et al. (2003) also perform virtual tip measurements but do not distinguish for piercing location, Sene (1984) also compared images and probe signals but with a rather low accuracy. Comparison between the various results is possible due to the fact that the bubble shape (including oscillations) and trajectory are very constant in time. Additionally, information about the bubble deformations or decelerations is obtained. The analysis of these results for a complete bubble scan will provide us with valuable information of the different effects during piercing and their contribution to void fraction (i.e. residence times) measurement errors.

Processing of Charge Coupled Device (CCD) images

The initial step of the digital image processing consists of the bubble segmentation process. First, the background of the image is subtracted. Next, a simple threshold technique is used to identify the bubble pixels in the image. The threshold level is chosen from the histogram of the bubble image. Once the bubble pixels are identified, two different calculations are performed. First, geometrical calculations are carried out to obtain the center of gravity and bubble boundary

coordinates from a sequence of images. Velocities are determined of the top, the rear, and the center of gravity of the bubble. In addition, other bubble geometrical parameters are calculated, such as the bubble height and the maximum and minimum axis length. By comparing the set of results from two sequences of images, with and without piercing, it is possible to obtain information about the bubble deceleration and/or deformation during the piercing process for different piercing positions. Additional calculations are performed to calculate the residence times inside the bubble without piercing (virtual tip) from a sequence of images. The trajectories of the front and rear side of the bubble are determined for all radial piercing coordinates using linear interpolation between the images. These trajectories are used to calculate the time elapsed between the arrival of the upper part of the bubble at the virtual tip position and the departure of the rear part of the bubble from this position. This way, a complete scan of residence times over a radial line over the bubble is obtained.

Optical Fiber Signal Processing

The signal processing software is similar to that used by Barrau and Cartellier (Cartellier, 1992; Barrau et al., 1999). The actual analysis is done as post-processing on a PC on the sampled data. Therefore, the algorithm speed is not an issue. First, the liquid and gas phase signal levels V_L and V_G are determined from the signal probability density function (pdf). The levels are re-determined every second to handle possible drift. Subsequently, the approximate locations of the bubble signatures are determined by using a threshold level $V_L + 0.1(V_G - V_L)$. Very short signatures due to noise are discarded. Next, for every bubble, the entry and exit time are determined. For every individual bubble, the plateau level is determined by finding its corresponding maximum in the signal pdf. For bell-shaped signals, the maximum level is determined. This level is named V_i. A pre-signal could be observed in some bubble piercing events near the bubble center where the piercing is almost perpendicular to the interface. For piercing events with non-perpendicular piercing, this mirror effect is not present and no pre-signal is observed. Because of the pre-signal, the criterion for bubble entry can not be based on the noise level (which works well for all signals without pre-signal). Instead, its threshold is set to 10% of the bubble plateau level. This way, the pre-signal is not included in the residence time. For bubbles without plateau, 10% of the maximum level is taken. This gives: $V_{entry,i} = V_L + 0.1(V_i - V_L)$. For the gas-liquid transition, both residence times obtained using the HLC and the LLC are determined. These are located, respectively, at 90% and 10% of the signal plateau, or maximum (for incomplete signatures): $V_{exit,i}^{LLC} = V_L + 0.1(V_i - V_L)$, $V_{exit,i}^{HLC} = V_L + 0.9(V_i - V_L)$.

3.4. Identification of interfaces in the signal

Figure 3.4 shows signals acquired at various distances X from the bubble center. When piercing occurs in the central area (X/R<0.88), full-amplitude signals with a plateau are obtained. The probe tip gets enough time to dry completely.

When piercing occurs close to the bubble edge (X/R>0.88), full de-wetting is not obtained. As a result, 'incomplete' signals are obtained: these have smaller amplitudes, no plateau, and are usually bell-shaped. When piercing occurs further from the center, the rising flanks get a longer duration. In the region with approximately X/R>0.8, the falling flanks also get a

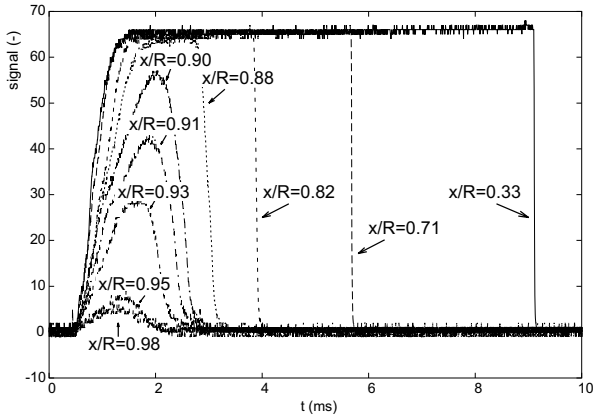

Figure 3.4.: Signal shape as a function of piercing position.

longer duration. As a result, away from the center, the choice for the criterion for the gas-liquid transition becomes much more important for accurate void fraction measurements: the difference in the residence times can be up to 50%. The shape of the signals is investigated further by recording simultaneously the probe signal and images of the bubble and probe. Figure 3.5 shows the results for bubbles with velocities of 0.24 m/s; the instants when capture is started and ended of the corresponding images are shown in the signals as vertical lines. The (invisible) probe tip is visualized in white.

Figures 3.5 a-c show the piercing of a bubble providing full-amplitude signals (X/R=0.56). The arrival of the probe at the gas-liquid interface corresponds to the first 5% rise of the signal. This agrees with the classical use of the LLC for the liquid-gas transition. Distinction between the undisturbed and disturbed interface position can not be made, since the magnitude of the surge effect is of the order of magnitude of 5 μm (Liju et al., 2001), which is smaller than the spatial resolution used. In addition, this deformation cannot be visualized due to the perspective of the images. The temporal resolution for the gas-liquid transition is not sufficient to select the most appropriate criterion: the fall-time is very close to the image capture time. More interesting are the small-amplitude signals (Figures 3.5 d-h, with X/R=0.93). Again, the signal rise starts as soon as the liquid-gas interface position is reached. The signal starts to fall before the full dry-tip signal level is reached. The fully wet-tip signal level is reached before the probe tip reaches the undisturbed gas-liquid interface position. A more detailed study showed that this happens for all positions where small-amplitude signals are obtained. This can be explained using Figures 3.6 and 3.7.

Figure 3.6 shows the schematic piercing of a bubble close to its side. The undisturbed interface is shown; this is the interface that is perceived with the CCD 2D side view. In addition, the schematic disturbed interface and the probe signal are shown. The instances of the sketches are marked in this signal. The interface is pierced under a relatively small angle between the tip and the bubble interface. Due to this small angle the gas-liquid-probe contact line returns over the tip before it has proceeded far enough to give a fully dry tip. The bump that is created in the

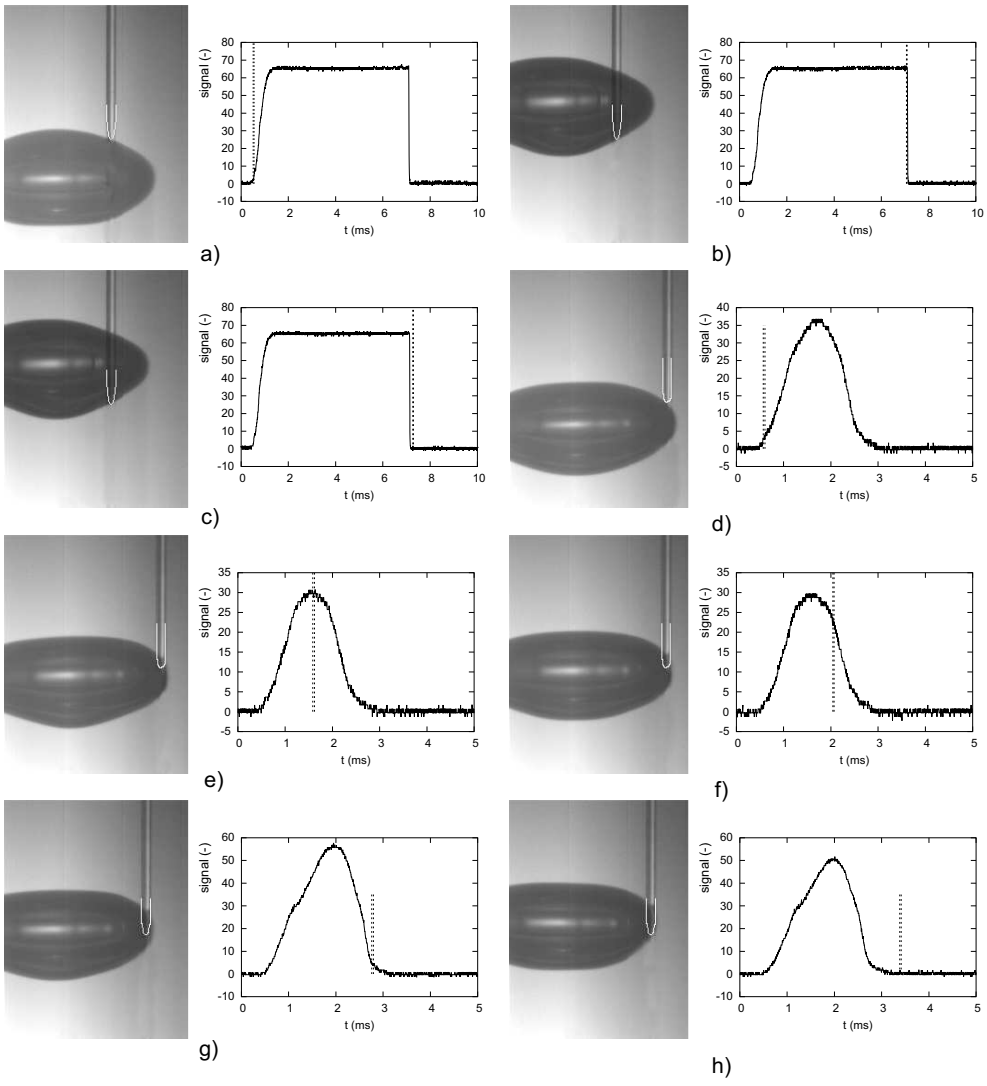

Figure 3.5.: Images of piercing events with corresponding moment of capture in the signal (U_{cg}=0.24 m/s).

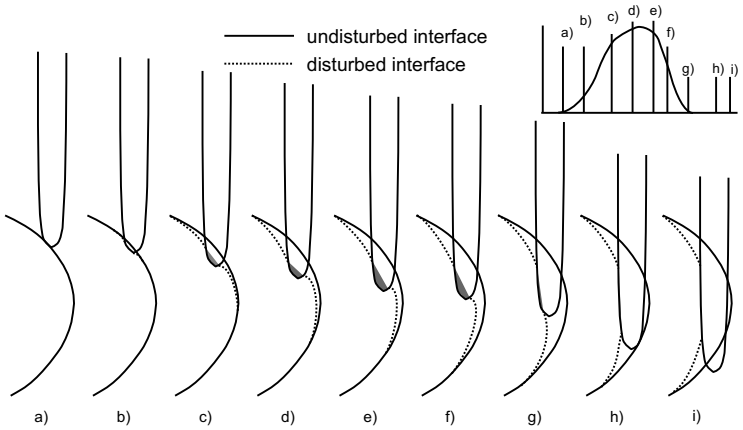

Figure 3.6.: Schematic piercing of a bubble close to its side leading to smaller amplitude signals and blinding effect.

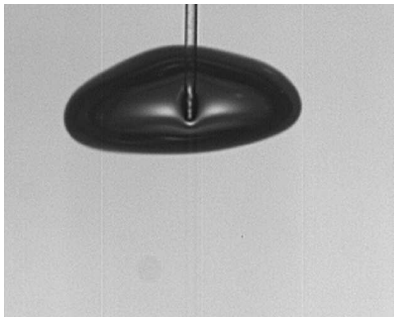

Figure 3.7.: Picture of the bump generated when a bubble is pierced close to its side.

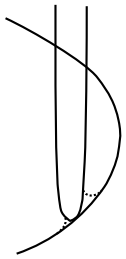

Figure 3.8.: Schematic explanation of the longer gas-liquid transition signal fall-time.

bubble is shown in Figure 3.7, which gives a front view of a bubble 'pierced' at the sides. The probe tip is clearly only partially de-wetted. The sidewards wetting of the tip by the moving contact line occurs relatively slowly since the probe-interface angle varies relatively slowly. The tip is fully wetted again before the undisturbed gas-liquid interface is reached. Therefore, if the probe hits the bubble with a small angle between the probe and the interface, the following effects can occur:

- A small-amplitude signal is obtained.
- Both the rise time and fall time of the signal increase since the progress of the contact line over the probe is much slower.
- A partial 'blinding'-effect can occur: part of the undisturbed chord length is not seen by the probe.

Thus, the most appropriate gas-liquid transition criterion for the processing of the smaller-amplitude signals is therefore the LLC. This way, the underestimation of the residence time of small-amplitude signals is minimized. Also, for full-amplitude signals, the fall-time may be increased if the gas-liquid interface is hit under an angle (sketch in Figure 3.8): not the point, but the side is the first part of the probe tip that touches the gas-liquid interface.

As a result, the signal starts dropping before the extreme of the probe tip has reached the undisturbed gas-liquid interface. In addition, the wetting of the probe tip may be only partial, giving the longer fall-time. This was confirmed by the results from Figure 3.4 for $X/R>0.8$. This extra fall-time should be associated with the residence time inside the bubble. This is accomplished by the use of the LLC. Therefore, typically in about 40% of all bubble hits the LLC gives the closest approximation to the undisturbed residence time. In the case of more spherical (smaller) bubbles, this percentage would probably increase even further (for the probe that was used in this investigation). The fall-time in the case of perpendicular piercing is very small (a maximum of 1%, but typically 0.3% of the total residence time). In addition, close to the sides of the bubble, the LLC is the most appropriate one. These arguments lead to the choice of the LLC for the processing of all bubble signals. Tests in a very uniform bubble column (7.5% void fraction) show that by using the LLC, typically the underestimation of the void fraction is reduced from about 15% to about 10%.

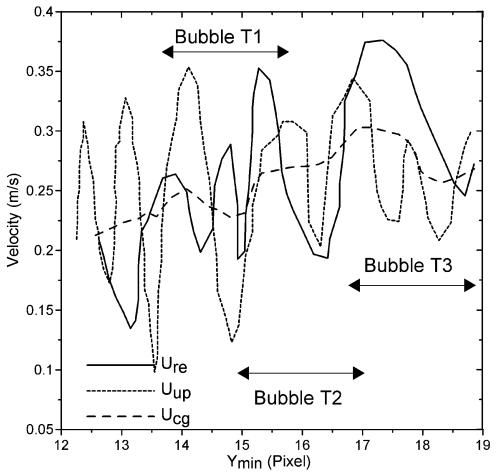

Figure 3.9.: Bubble types and their velocity development.

3.5. Probe-bubble interaction effects

In order to study the bubble modifications during the piercing process, a bubble scan is performed at 30 radial positions over a line through the bubble center perpendicular to the fiber orientation and parallel to the CCD image plane. The residence times are measured with the optical probe. These measurements are compared with the residence times obtained from a sequence of CCD images without (virtual tip) and with tip for different parts of the bubble. For the piercing experiments, it is necessary to define the angle α between the probe and the bubble short axis. The angle α was varied in the experiments. Both the bubble motion and bubble orientation are parallel to the vertical axis, since the wobbling behavior has not started yet. In the first set of experiments it is observed that the analyzed bubbles have strong velocity oscillations due to the relatively small distance that has been traveled since they were generated at the needle. The oscillations can affect the piercing phenomena and, consequently, the comparison of the results. Figure 3.9 shows the upper (U_{up}), rear (U_{re}), and gravity center (U_{gc}) velocities of the bubble with respect to the distance of the lower side of the bubble to the needle that generates the bubbles (Y_{min}).

Piercings at three different phases of the oscillations are considered. The oscillations at the beginning of the piercing are summarized in Table 3.1.

3.5.1. Perpendicular piercing ($\alpha = 0$)

Figure 3.10 shows the comparison of the residence times given by the optical probe using both the LLC and the HLC, and the results from the virtual probe CCD images analysis. This was done for a scan over a line for bubble T1. Comparison of the results of the two gas-liquid criteria

Bubble type	Upper part velocity	Rear part velocity	Gravity center velocity
T1	Near a minimum and increasing	Near a maximum and decreasing	Almost constant
T2	Increasing	Near a minimum and increasing	Slightly increasing
T3	Near a maximum and decreasing	Near a minimum and increasing	Slightly decreasing

Table 3.1.: Oscillation schemes for the different bubble types

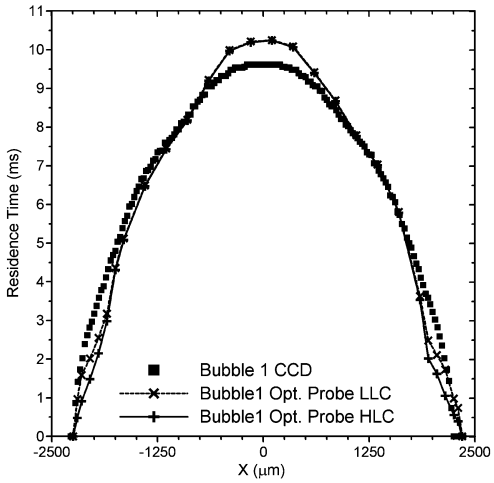

Figure 3.10.: Residence time comparison for bubble T1.

and of the CCD is facilitated by considering the absolute and relative differences between the residence time from the probe and the residence time from CCD images (Figure 3.11 for bubble T1).

There are two different zones for the bubble piercing. In the central zone of the bubble ($|X/R| < 0.5$), the residence time is overestimated. In the bubble sides ($|X/R| > 0.5$), an underestimation is observed. Both criteria give similar results for the overestimation zone. This is not surprising since signals with a plateau are obtained in this zone and bubble interfaces are pierced almost perpendicularly, giving a quick signal drop at the gas-liquid transition. The underestimation in the region with $|X/R| > 0.5$ is smaller when the LLC is used, in agreement with the results from section 3.4. The cross-sectional area of the bubble where the LLC gives a smaller underestimation is about 75% of the total cross-sectional area, again stressing the importance of the use of the best criterion for the void fraction estimate. From this point on, only the results for the LLC will be considered.

Comparison of the residence time for piercing obtained from the probe signal and the images with piercing is shown in Figure 3.12. Although only a 2D projection is obtained, the images give a good impression of the total bubble deformation. Therefore, the graph gives a good idea of the part of the bubble that is not seen by the probe due to local interface deformations, such as the surge effect and deformations close to the bubble sides, like those described in Figures 3.6 and 3.7. In other words, it shows the magnitude of the blinding effect. In the central region, there is a very small difference ($<$0.05 ms, that is $< 0.5\%$): the blinding effect is negligible compared to the other effects. This agrees with the calculations by Liju et al. (2001) that the surge effect is small. In the outer regions, however, an underestimation is observed which agrees with the results from section 3.4. This shows that for these bubbles in water, the blinding effect is only important in the outer regions of the bubble, and that it results in the underestimation of chordal lengths. The behavior described by Barrau et al. (1999) (which was discussed in section 3.2.2, and is sketched in Figure 3.13a), where chords near outer regions are not detected at all, is not observed.

Instead, a new behavior is observed, shown schematically in Figure 3.13b. The difference may be caused by the lower viscosity in the current experiment. The underestimation in the outer bubble regions that remains with the use of the LLC, can be caused by the blinding effect as well as the crawling effect (deformation). An example of this deformation effect on a larger scale is shown in Figure 3.14.

The outer part of the bubble is squeezed due to the piercing. As a result, the residence time is underestimated. In the central bubble region, the overestimation is very likely caused by a deceleration of the bubble by the probe. So, in all regions, the crawling effect is expected to play an important role. The trajectory of the bubble center of gravity is investigated for the situations with and without piercing, for various positions of the probe. This gives information about the bubble drifting induced by the piercing. The results show that no drifting effect is present with perpendicular piercing, since the biggest difference in mass center coordinates is around 1 pixel (which corresponds to about 0.03 mm). The changes in residence time due to the crawling effect can be estimated. For various piercing positions, bubble deformation and deceleration are determined by comparing CCD recordings of bubble passages with piercing and without piercing. These are translated to residence time differences using the average velocity of the bubble center of gravity. Figure 3.15 shows the results for bubble T1. It is observed that if the bubble is pierced

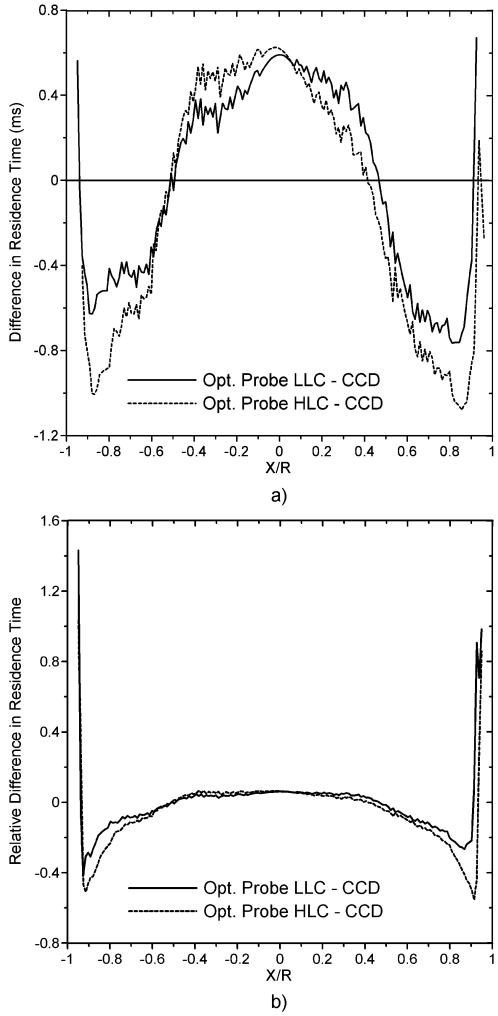

Figure 3.11.: Residence time differences comparison for bubble T1 using LLC and HLC, a) absolute and b) relative units.

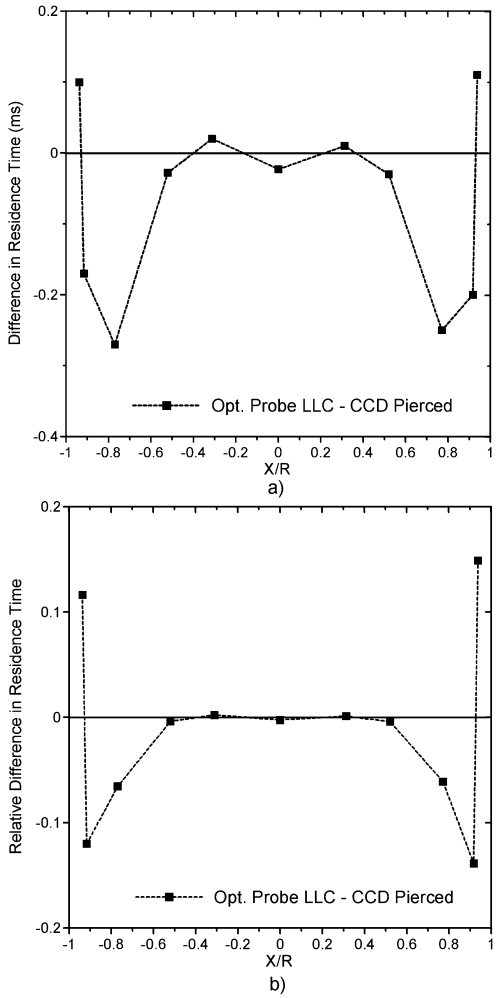

Figure 3.12.: Difference in residence time from optical signal and the images for pierced bubble T1, a) absolute and b) relative units.

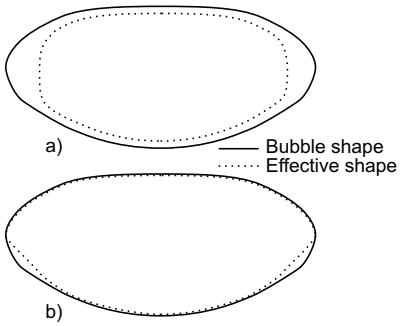

Figure 3.13.: Schematic representation of the blinding effect. a) behavior according to Barrau et al. (1999) b) behavior observed in current investigation.

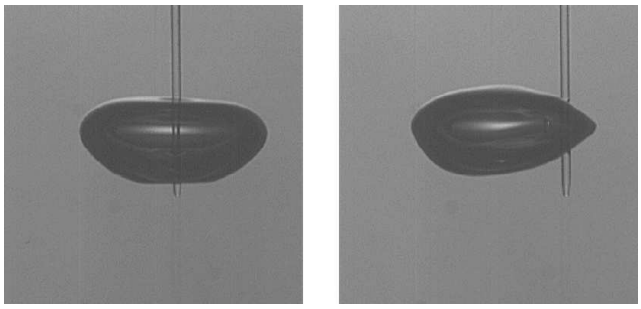

Figure 3.14.: Deformation of the bubble shape induced by piercing.

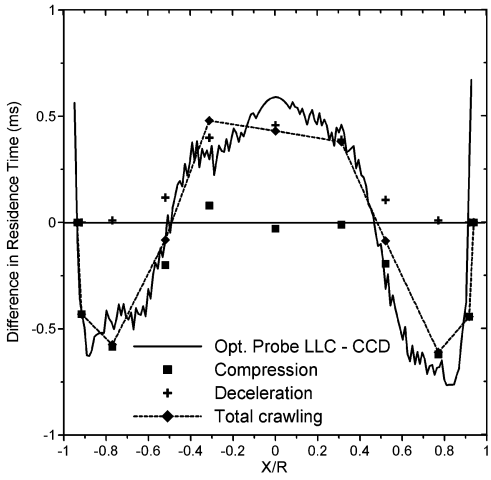

Figure 3.15.: Crawling effects in bubble T1.

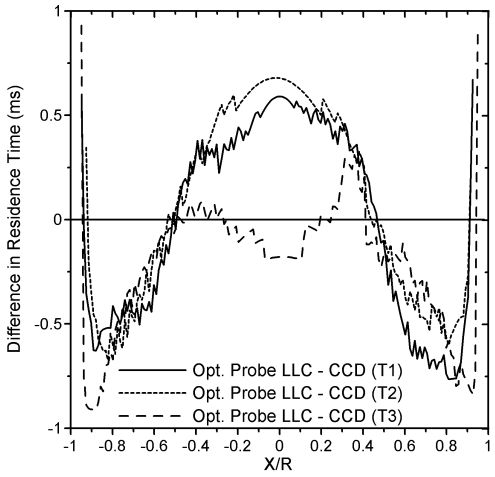

Figure 3.16.: Residence time differences comparisons for the three bubble types.

in the central zone, the bubble deceleration causes a residence time overestimation. In the outer zone, bubble compression is found, resulting in a decrease of the residence time. Combination of the estimates of the residence time differences due to the deformation, deceleration, and the blinding effect would give a good explanation for the observed residence time differences. A minor overestimation of the residence time differences in the outer part of the bubble is obtained. This may be explained with the assumption of a constant velocity and height of the bubble during its passage. Additional tests have been done with bubbles T2 and T3 with similar results. Therefore, the crawling effect can be considered the major effect producing residence time differences, and the blinding effect a minor effect. It is, however, necessary to distinguish between deceleration (important in the center) and compression effects (important near the sides). Figure 3.16 shows the residence time differences for the three bubble types using the LLC.

The underestimation zones are quite constant in both position ($|X/R| > 0.5$) and underestimation magnitude. However, the overestimation zone presents important differences between the first two types of bubbles (T1 and T2) and the third one (T3). This fact seems to be connected to the velocity of the upper part of the bubble at the start of the piercing process, this velocity has the biggest value for bubble T3. The residence times $T_{residence}$ can be translated to bubble volume by assuming axial rotational symmetry and a constant velocity U_{gc}:

$$V = U_{gc} \int_{-R}^{R} T_{residence}(x)|x|\pi dx \tag{3.1}$$

Table 3.2 summarizes the differences $((V_{piercing} - V_{virtualprobe})/V_{virtualprobe})$ between the volumes obtained with the optical probe signal and the 'virtual probe' CCD images for the three bubble types and the two different criteria. A systematic underestimation is found with the LLC giving more accurate results for all cases. Figure 3.17 shows the results obtained for the residence time differences for different bubble diameters.

Bubble type	Volume difference (%) (LLC)	Volume difference (%) (HLC)
T1	-3.66	-8.41
T2	-2.77	-5.88
T3	-6.49	-10.75

Table 3.2.: Volume differences for the three bubble types

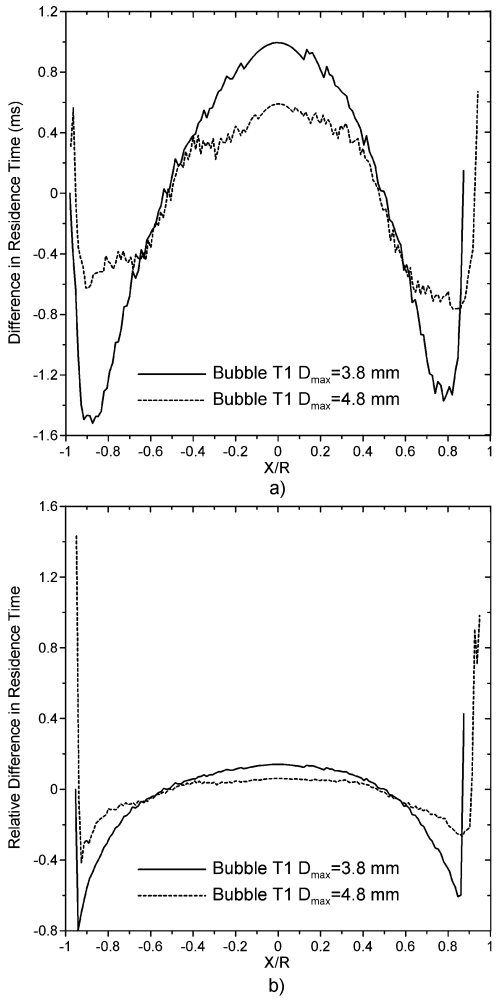

Figure 3.17.: Residence time differences comparisons for different bubble diameters, a) absolute and b) relative units.

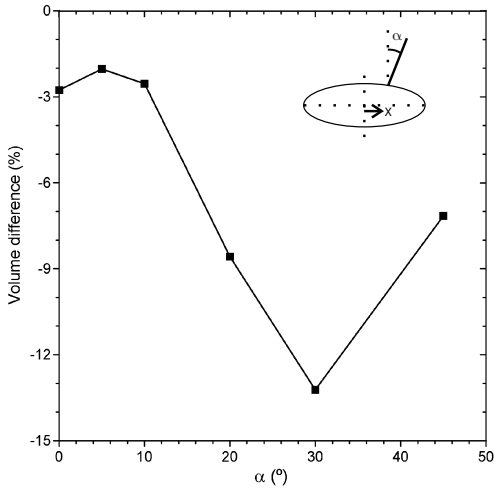

Figure 3.18.: Bubble volume difference with different α (bubble T2).

The shape of the graphs is the same. The relative size of the underestimation ring is constant. The magnitude of the underestimation and overestimation increases with smaller diameters: there is apparently more deformation and deceleration for smaller diameters.

3.5.2. Non-perpendicular piercing ($\alpha \neq 0$)

Similar experiments were performed with variation of the impact angle α for bubble T2. Figure 3.18 shows the difference in the volumes obtained with the probe and the virtual probe experiments.

α ranged from 0° to 45°. Notice that for non-perpendicular piercing, the bubble axial symmetry is lacking and this assumption in the volume calculation can only give a first approximation of the true volume. A systematic volume underestimation is found for all the angles, but its value is not constant. For $\alpha \in [0°, 10°]$ the underestimation is almost constant, for $\alpha \in [10°, 30°]$ the underestimation is drastically enlarged, and for $\alpha = 45°$ the underestimation is reduced again. Figure 3.19 shows the residence times differences for the particular cases of $\alpha = 0°$,30° and 45°.

The tip is inclined toward the positive x coordinate values. Significant differences are observed between the non-perpendicular cases and the perpendicular cases. For $\alpha = 30°$, the overestimation zone is bigger and both overestimation and underestimation zones are no longer symmetrical. The underestimation zone ($X < -2000\ \mu m$) is reduced considerably in size, and the underestimation zone ($X > 1250\ \mu m$) is stretched and increased in magnitude. In the case of $\alpha = 45°$, the overestimation zone is bigger in amplitude. The underestimation in the region $X < -1250\ \mu m$ is much larger, but the underestimation at $X > 1250\ \mu m$ has disappeared. Figure 3.20 shows the residence time differences calculated from the deceleration and compression effects for the $\alpha = 30°$ case.

The overestimation zone is properly described by the deceleration effect, but the bubble

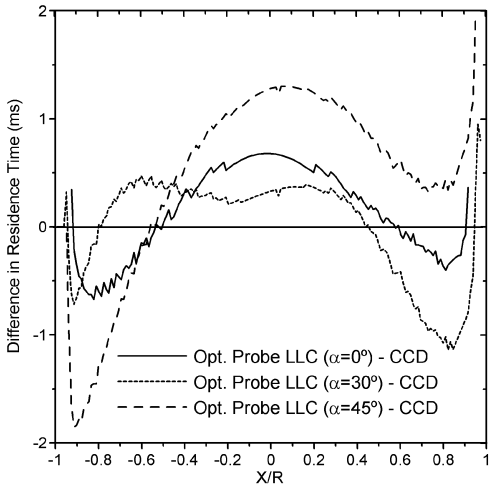

Figure 3.19.: Residence time differences comparisons for bubble T2 and different α.

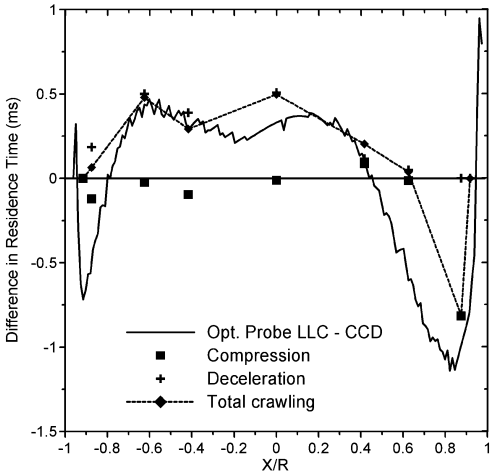

Figure 3.20.: Deceleration and compression effects for the bubble T2 and $\alpha = 30°$.

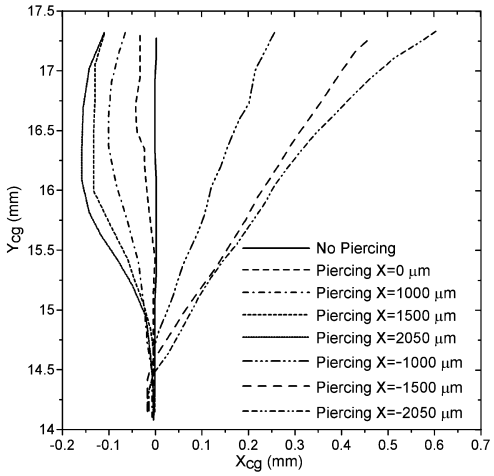

Figure 3.21.: Drifting effect for bubble T2 and $\alpha = 30°$.

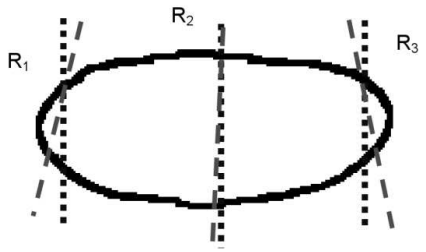

Figure 3.22.: Bubble T2 contour before piercing and the pierced bubble trajectories.

compression only justifies part of the peak at $X > 1250\ \mu m$; the underestimation peak at $X < -1750\ \mu m$ cannot be explained. Apparently, some effect is missing. In order to explain this second underestimation zone, it is necessary to take into account the drifting effect. This effect is negligible for $\alpha < 10°$, but it becomes important for bigger impact angles.

Figure 3.21 shows the drifting trajectory observed for the bubble T1 with a piercing angle $\alpha = 30°$ at different piercing positions, where X_{cg} and Y_{cg} represent the horizontal and vertical bubble mass center coordinates, respectively, during the piercing process. In this case, if the bubble is pierced in its part with $X > 0$, a small drifting is observed opposite to the tip direction, this behavior is due to a slight bubble rotation. However, if the bubble is pierced in its part with $X < 0$, a big drift is produced toward the tip direction. The consequences of the drifting effect on the residence time differences are schematically shown in Figure 3.22.

When the bubble is pierced at its center (R_2), the drifting effect has a negligible effect on the residence time. However, if the piercing takes place in the sides (R_1 and R_3), the drifting effect results in underestimation of the residence time because the path length inside the bubble

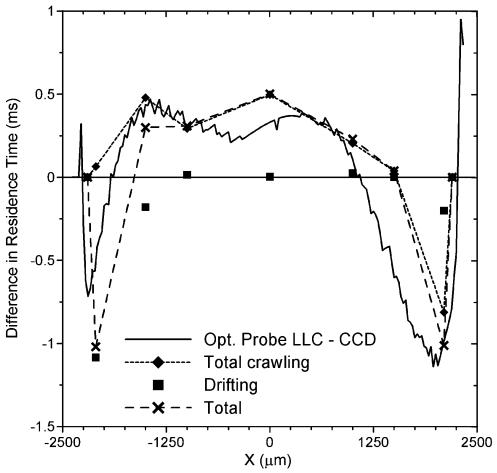

Figure 3.23.: Residence time differences taking into account the drifting effect (Bubble T2 and $\alpha = 30°$).

is reduced. It is possible to calculate this effect in the residence time assuming constant velocity during the piercing process. Figure 3.23 shows the results of the residence time errors including the drifting effect. The underestimation at $X/R < -0.65$ and part of the underestimation at $X/R > 0.4$ are due to the drifting effect. Figure 3.24 shows the results obtained for $\alpha = 45°$. The conclusions obtained from this graph are very similar to the $\alpha = 30°$ case. It is possible to explain all of the differences in the residence times with the two crawling effects (deformation and deceleration) and the drifting effect. From similar calculations for the other α cases, the following conclusions are extracted. For $0° < \alpha < 10°$, the residence times differences can be explained with only the crawling effect, since no noticeable drifting effect is present. For $10° < \alpha < 30°$, an increment in the size of the overestimation zone is found due to the bigger deceleration effect produced by the bigger tip-bubble contact zone. Also, the deformation effect decreases in magnitude for X<0. However, this fact is compensated for by the appearance of drifting. If all of the effects are summed, the total underestimation increases in this range of α. For $\alpha = 45°$, a slight increment in the magnitude and size of the overestimation zone due to a further enhancement of the deceleration is observed. Also, the underestimation zone at X>0 due to the compression effect disappears. The underestimation at X<0 by deformation grows. The influence of the drifting effect seems not to grow beyond $\alpha = 30°$. When all effects are summed, the total underestimation decreases for these angles.

3.6. Summary and conclusions

The accuracy of the measurement of the void fraction in bubbly flows using an optical probe has been investigated. Experiments were performed in tap water with ellipsoidal-shaped air bubbles with equivalent diameters and velocities in the range of 2.8 - 5.2 mm and 0.22 - 0.28 m/s.

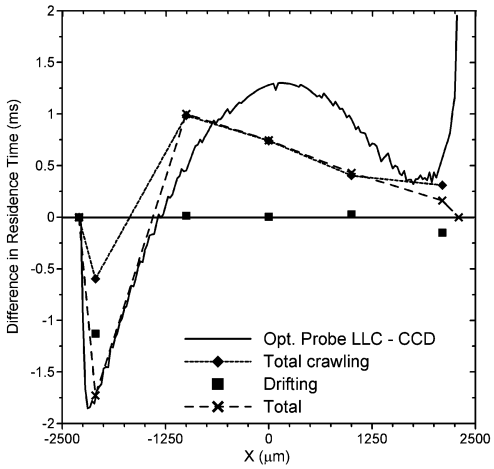

Figure 3.24.: Residence time differences taking into account the drifting effect (Bubble T2 and $\alpha = 45°$).

Comparison of Charge Coupled Devices (CCD) images of dynamic bubble piercing events with optical probe signals shows that for piercing in the area around the bubble side, the so-called low-level criterion gives the best agreement with the actual gas-liquid transition for the undisturbed bubble. In addition, residence time underestimation due to a partial blinding effect is observed in the outer regions of the bubble. Residence times of the probe inside the bubble are obtained from the probe signal and from CCD images of the undisturbed bubble. These are compared to study the relevance of various probe-bubble interaction effects. The crawling effect is found to play an important role. For perpendicular piercing, the experiment shows that in the central area of the bubble deceleration effects induced by the probe lead to local overestimation of residence times. In the outer region of the bubble, large-scale deformation leads to local underestimation of residence times. The larger cross-sectional area associated with the underestimation leads to a net underestimation of the total bubble volume. For non-perpendicular piercing, the probe inclination is found to generate an additional drifting effect, creating an additional source of underestimation. The exact levels of underestimation and overestimation strongly depend on the angle under which the bubble hits the probe, the radial position of the hit, the bubble size and oscillation phase, making quantitative prediction of the total error for practical situations difficult.

List of symbols

Roman symbols and abbreviations

D_{eq}	equivalent bubble diameter	m
D_{max}	horizontal bubble diameter	m
HLC	High Level Criterion	-

LLC	Low Level Criterion	-
R_f	radius of optical fiber	m
T_{G-L}	duration change from gas signal level to liquid signal level	s
T_{L-G}	duration change from liquid signal level to gas signal level	s
$T_{residence}$	estimated residence time of the probe tip in the bubble	s
U_{cg}	velocity of bubble center of gravity	$m\ s^{-1}$
U_{re}	velocity of bubble top	$m\ s^{-1}$
U_{up}	velocity of bubble bottom	$m\ s^{-1}$
V	bubble volume	m^3
V_{entry}	signal threshold for bubble entry	-
V_{exit}	signal threshold for bubble exit	-
V_G	signal level corresponding to gas phase	-
V_i	maximum or plateau signal level for individual bubble	-
V_L	signal level corresponding to liquid phase	-
$V_{piercing}$	bubble volume estimated from probe measurement	m^3
$V_{virtualprobe}$	bubble volume estimated from CCD (virtual probe) experiment	m^3
X	horizontal coordinate, distance to bubble center	m
X_{cg}	horizontal coordinate bubble center of gravity	m
Y_{cg}	axial coordinate bubble center of gravity	m
Y_{min}	axial distance of bubble bottom to needle exit	pixels

Greek symbols

α	probe-bubble impact angle	$^\circ$
ν	kinematic viscosity liquid	$m^2\ s^{-1}$

4. Bubble velocity and size measurement using a four point optical fiber probe

The measurement of bubble size and 3D velocity with the use of a four point optical fiber probe is studied. The accuracy of the technique is evaluated, and ways to improve the technique are investigated.

4.1. The four point probe

4.1.1. Introduction

In order to understand the behavior of the flow in the bubble column better, we are interested in the bubble velocity and bubble size. For the measurement of these quantities in practical bubble columns, thus far the only method is by using probes, the most common being conductivity probes and optical probes. Optical probes have the advantage of simplicity of the setup, easy interpretation of the results and the fact that the signal is not coupled to the flow (for more information, see chapter 3). These are therefore used in the present investigation.

Various types of optical probes have been employed by various authors for the measurement of the bubble velocity and diameter, as well as the interfacial area and volume fraction. The main difference between these probes lies in the number of tips employed. In the case of a single tip, the axial velocity component is measured by estimating the rise time of the signal, i.e. the time required for the active part of the probe to de-wet when it enters the gas phase (e.g. Cartellier (1992) and Cartellier and Barrau (1998a)). If the size of this active part, the so-called reference length, is known, the velocity can be determined from the rise-time. Cartellier (2001) and Cartellier and Barrau (1998b) considered and optimized various tip shapes to get improved accuracy with this technique.

In the case of two-point tips (e.g. Kiambi et al. (2001)), the axial velocity component is determined from the difference in the arrival times of the bubble at the two tips that are placed some distance apart. For both one-point and two-point probes, a problem occurs when the bubble velocity is not aligned with the probe orientation. Xue (2004) showed that an overestimation of the velocity component occurs if the velocity direction differs from the probe axial direction. This overestimation can be as large as 100% at an angle of 45°. Hence, single probes and two point probes are only suited for situations where all bubbles move in one direction (e.g. cocurrent pipe flows). In bubble columns, however, this cocurrent flow is not present and the zig-zag or rocking motion of the bubbles as well as the presence of liquid vortical structures cause a general mismatch between the direction of the velocity and the probe axial direction.

Four-point probes were developed to resolve this problem (Frijlink (1987) (optical probes) and Burgess and Calderbank (1975) (resistivity probes)). With these probes, it is possible to

recognize and remove from the data set the bubbles with motion direction deviating from the probe axial direction. Figure 4.1 shows the geometry of the four point probe used in the current investigation, with $\Delta s = 1.6$ mm and $d_p = 0.6$ mm. The probe consists of four fibers, the tips of three of these fibers are located in a plane at a distance Δs above the central tip. For each fiber, the instant t_i when the bubble hits the probe tip i is determined (see section 3.3 for a description of the method). Next, the times of flight $\Delta t_i = t_i - t_0$ (i=1,2,3) of the bubble between the central tip (tip 0) and the three other tips located downstream, are determined. In addition, the residence time T_i of tip i inside the bubble is estimated. Two different approaches are taken by different authors to estimate the velocity:

- Mudde and Saito (2001), Guet et al. (2003) and Frijlink (1987):

$$u = \frac{\Delta s}{\Delta t} = \frac{\Delta s}{\frac{1}{3}\sum \Delta t_i} \tag{4.1}$$

  The measurement has to satisfy

$$|\frac{\Delta t_i - \Delta t}{\Delta t}| < \beta_t \ \forall i \in \{1, 2, 3\} \tag{4.2}$$

- Xue (2004):

$$u = \frac{1}{3}\sum_{i=1}^{3} u_i = \frac{1}{3}\sum_{i=1}^{3} \frac{\Delta s}{\Delta t_i - \frac{T_0 - T_i}{2}} \tag{4.3}$$

  Where the term $\frac{T_0 - T_i}{2}$ is used to correct for the curvature of the bubble. It will be discussed in more detail in the following sections. The measurement has to satisfy

$$|\frac{u_i - u}{u}| < \beta_u \ \forall i \in \{1, 2, 3\} \tag{4.4}$$

Some small differences exist in the approaches taken by the various authors, e.g. Guet et al. (2003) and Frijlink (1987) correct for the bubble shape in Δs, whereas Mudde and Saito (2001) do not perform this correction. The criteria in equations 4.2 and 4.4 are used to check if the bubble was pierced by the probe under a small enough angle to allow accurate measurement. This way, only the velocities of part of the total pierced bubble population can be determined, namely those traveling under a small angle with the probe axial direction. It remains questionable how representative this sample is for the entire bubble population. Xue (2004) showed how a larger portion of the bubbles can be accepted by increasing the threshold level. This is, however, a trade-off with the accuracy of the bubble velocity component estimate.

4.1.2. Advanced four point probe algorithms

A method allowing for bubbles arriving under an angle with the probe axial direction would be strongly preferred. With this method, no longer a large part of the measured data needs to be rejected. In addition, information about the bubble velocity orientation is helpful for the understanding of the importance of the lift-force in regions of the flow with strong gradients.

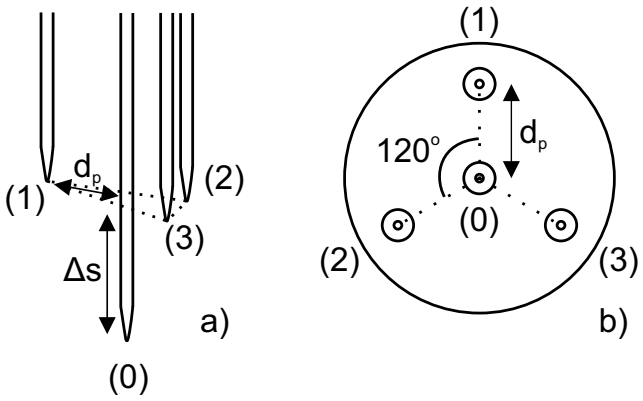

Figure 4.1.: Four point probe geometry. a) Side view b) Front view.

More refined algorithms for the processing of four-point probe signals, that also determine the velocity direction, have been presented by Rensen (2003), Guet (2004b) and Luther et al. (2004) as well as Xue (2004) and Xue et al. (2003) for optical probes and Mishra et al. (2002) and Lucas and Mishra (2005) for conductivity probes. The idea of these methods is that much more information than a single velocity component and chord length is contained in the measurements of the times that the four probes enter and exit the bubble. Based on a model of the bubble, the three time differences $\Delta t_i (i = 1, 2, 3)$ and four residence times $T_i (i = 0, 1, 2, 3)$ are used to estimate several bubble properties. The model of Mishra et al. (2002) was developed for spherical droplets and bubbles and is therefore not suited, the other techniques allow for ellipsoidal bubbles and are discussed in more detail.

Rensen's algorithm

Rensen (2003) estimates the magnitude of the velocity, the two angles that give the orientation of the velocity vector with respect to the probes axial direction, two angles defining the radial positions of piercing and finally the semimajor and semiminor axis lengths of the bubble. In order to do this, the assumption is made that the bubble can be modeled as an ellipsoid and that the velocity vector $\vec{u}$ is directed parallel to the minor axis. The estimation is performed with a constrained non-linear least squares minimization of the error between the actual measurements and the measurements predicted by the model for a given set of parameters. This means that actually seven parameters have to be determined from seven measurements. This suggests that there may be a risk of ill-posedness of this reconstruction problem: i.e. relatively small deviations from the assumptions made about the bubbles or inaccuracies in the measurements may lead to large errors in the parameter estimates. In this respect, it is important to realize that the common four point probe geometry was not optimized for the measurement of e.g. the semimajor axis length of the bubble. The shape of the bubbles in the bubble column generally deviates from the ellipsoidal shape: many surface oscillations and some flattening of the bubble are observed. Therefore, the local surface curvature generally differs from that of the ellipsoidal curvature.

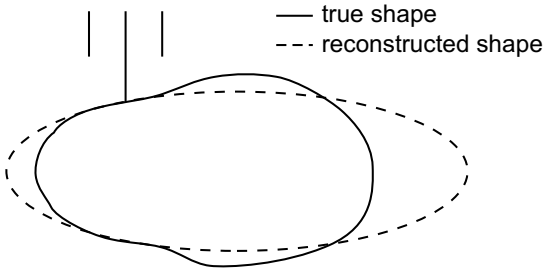

Figure 4.2.: Reconstruction of non-ellipsoidal bubbles.

With the relatively small transversal distance between the probe tips, this can lead to large errors in the aspect ratio. This is illustrated with an example in Figure 4.2. Rensen (2003) typically tests the technique for bubbles with horizontal size of 3 mm and mentions an increase of the inaccuracy with increasing bubble size due to flattening on top, as well as failure for bubbles in the wobbling regime. In addition, Guet (2004a), who works with bubbles in the size range 3-10 mm mentioned that the use of this technique resulted in the requirement to reject a very large fraction (more than 90%) of the bubbles to get results. The probability of rejection is dependent on the bubble size and the phase of the shape oscillations. This again leads to questions how representative the result is for the total bubble ensemble. For this reason, we decide not to use this technique.

Xue's algorithm

Xue (2004) presents a different reconstruction technique that enables determination of the three velocity components and does not require selection of bubbles that hit the probe: the entire population can be used. The technique is employed in bubble columns for bubble sizes in the range 2 mm-20 mm. This technique will also be used for the measurements in the present investigation. It is in fact equivalent to the reconstruction technique used by Lucas and Mishra (2005) for conductivity probes, who apply it to water-air systems with bubbles with their major axis in the range of 5-8 mm. In order to allow for the reconstruction, the assumptions are made that the velocity vector is parallel to the semiminor axis, and (implicitly) that the shape of the bubble has mirror symmetry with respect to the plane perpendicular to the velocity vector passing through the centroid of the bubble. The technique estimates the velocity magnitude u and the angles of the velocity vector with respect to the probe axial direction (Figure 4.3). Given the locations of the probe tips (x_{ti},y_{ti},z_{ti}) in the xyz coordinate system (defined by the probe), the coordinates of the tips in the coordinate system x'y'z' (defined by the bubble velocity vector) can be obtained with a simple transformation (section A.1). For the piercing times the following

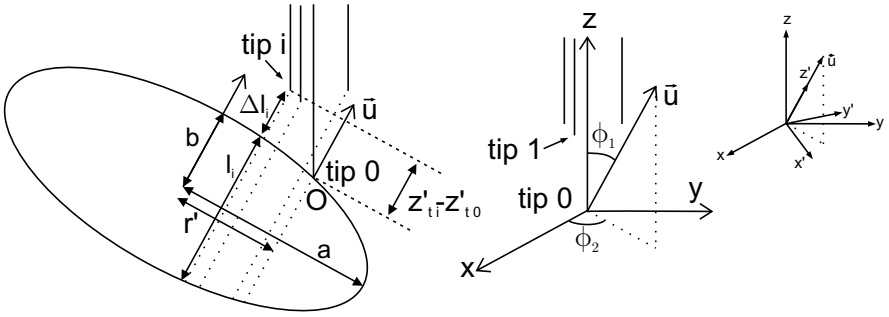

Figure 4.3.: Probe tips, the bubble and coordinate systems

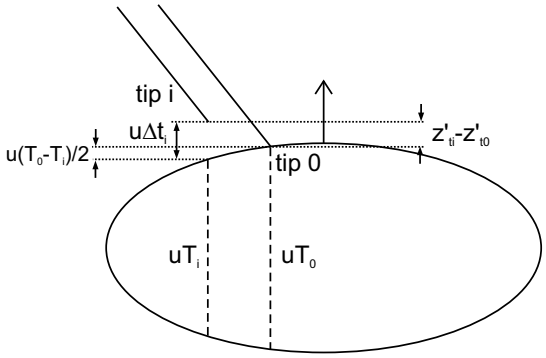

Figure 4.4.: Curvature correction for velocity reconstruction

equations are obtained:

$$\Delta t_1 - \frac{T_0 - T_1}{2} = \frac{z'_{t1} - z'_{t0}}{u} = \frac{x_{t1}sin(\phi_1)cos(\phi_2) + y_{t1}sin(\phi_1)sin(\phi_2) + z_{t1}cos(\phi_1)}{u} \tag{4.5a}$$

$$\Delta t_2 - \frac{T_0 - T_2}{2} = \frac{z'_{t2} - z'_{t0}}{u} = \frac{x_{t2}sin(\phi_1)cos(\phi_2) + y_{t2}sin(\phi_1)sin(\phi_2) + z_{t2}cos(\phi_1)}{u} \tag{4.5b}$$

$$\Delta t_3 - \frac{T_0 - T_3}{2} = \frac{z'_{t3} - z'_{t0}}{u} = \frac{x_{t3}sin(\phi_1)cos(\phi_2) + y_{t3}sin(\phi_1)sin(\phi_2) + z_{t3}cos(\phi_1)}{u} \tag{4.5c}$$

where the term $\frac{T_0-T_1}{2}$, etc. correct for the bubble curvature (explained in Figure 4.4). These equations for u, ϕ_1 and ϕ_2 are solved numerically using the Newton-Raphson method.

4.1.3. Probe manufacture

In order to get precise velocity information it is necessary that the bubble is not strongly deformed due to the piercing. In addition, precise information about the locations of the probe tips is required. The classical method for probe manufacture is to first pass the fibers through a capillary. Next, alignment is obtained by passing the fibers through a jig, followed by fixation

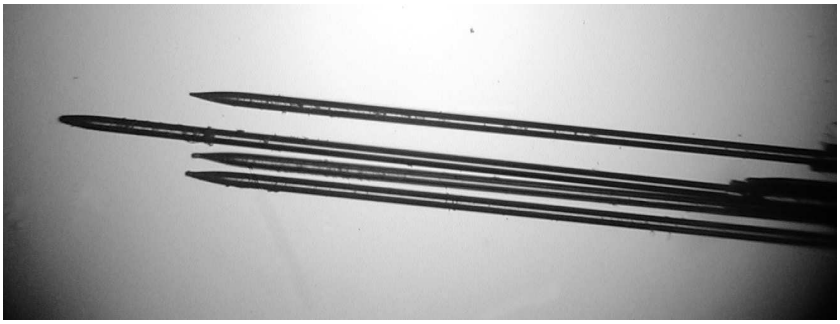

(a)

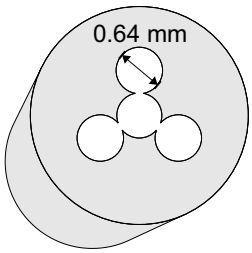

(b)

Figure 4.5.: (a) Picture of the four point probe and (b) sketch of the jig used for the alignment.

with glue. When the glue has dried, the jig is removed. With this method, it is difficult to keep the fibers parallel over a long distance: after removal of the jig, some of the fibers may get an inclination due to tension in the fibers, leading to a deviation of the desired geometry. Consequently, the accuracy of the technique may deteriorate for certain velocity directions. For this reason, a different manufacturing method was used in order to maintain sufficient distance between the capillary holder with the glue and the three upper tips. Again, a jig was used (Figure 4.5 (b)). This jig has a length of 0.7 cm, its diameter is identical to that of the capillary (3 mm). Openings are created in the jig with the use of electrical discharge machining. These openings (0.64 mm diameter) are only slightly larger than the cladding of the fibers (0.6 mm). The fibers are glued right in front of the jig and the jig is no longer removed after the glue has dried. This way, the alignment of the fibers is strongly improved, and the uncladded fibers extend over a length of 1 cm. The result is shown in Figure 4.5 (a).

After production and after longer periods of use, the tips of the probe get contaminated. This affects the shape of the signal (Figure 4.6(a)). Extra peaks occur right before the arrival of the tips at the liquid-gas ('presignal') and the gas-liquid interface. Also, the gas phase-level may show trends instead of being constant. The signal shape is altered in a different way for each probe, consequently the inaccuracy in the piercing times and velocity reconstruction increases strongly. For this reason, the tips are regularly cleaned with ethanol and ultrasonic cleaning. The signal shape after cleaning is shown in Figure 4.6(b). Not only the shape of the signal is

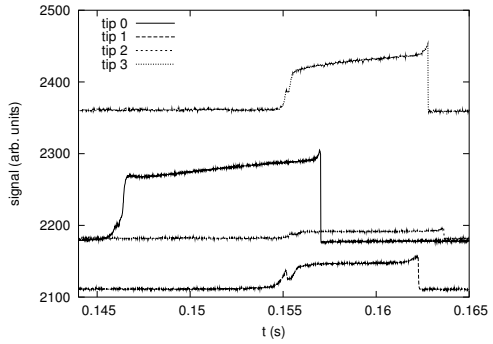

(a)

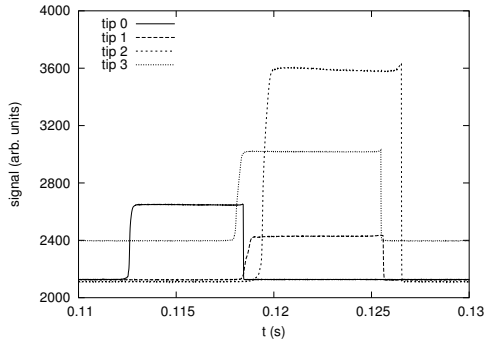

(b)

Figure 4.6.: (a) Signals for contaminated probe tips. (b) Signals for clean tips.

changed, but also the amplitude is increased considerably, especially by the ultrasonic cleaning.

4.2. Accuracy analysis of 3D bubble velocity vector estimation: non-intrusive effects

In order to evaluate the experimental observations, information is required about the accuracy of the measurement technique. This requires insight in the various error sources involved and their relative importance. This information may also be used to further improve the measurement technique. Previous investigations (e.g. Guet et al. (2003), Mudde and Saito (2001)) focused on the accuracy of the probe with the 1D algorithm. Little attention was paid to the individual error sources. In addition, the study usually focused on bubbles close to a location of formation with piercing close to the axis of symmetry. These conditions are probably not very representative for the conditions inside the bubble column. Lucas and Mishra (2005) only consider the inaccuracy due to errors in the times t_i when the bubble interface is pierced. Xue (2004) presents only a brief study for the accuracy of the 3D reconstruction technique with respect to measurement

inaccuracies, for different conditions than encountered in the cylindrical bubble column. The conclusions from Xue's study do not agree with the results obtained in initial tests with the four point probe in the present study. In addition, the effect of only one assumption is investigated: the assumption that the velocity vector is parallel to the minor axis. In practice, there is a wide variety in error sources: inaccuracy of the tip positions, tip shapes, bubble shape oscillations, shape of the bubble and various probe-bubble interactions. Consequently, it is not clear what the accuracy is of the estimate of the velocity and its direction, and which error sources dominate.

For this reason, we investigate the performance of the four point probe in combination with the Xue algorithm in more detail. Study of the accuracy for the conditions encountered inside the bubble column is difficult, since visual observation of the bubbles is complicated and many error sources are involved simultaneously. For this reason, a combined experimental and modeling study is performed. In the modeling study, artificial piercing events are simulated, this way the conditions in the bubble column can be mimicked. An order of magnitude of the inaccuracy can be determined and the individual error sources can be studied separately. The present section 4.2 studies the error sources due to non-intrusive effects, the next section 4.3 discusses the error sources due to the probe-bubble interaction. Section 4.4 studies the combined error.

4.2.1. Generation of artificial signals

Artificial data is generated by calculating the times when the tips enter and exit bubbles for artificial piercing events. Both bubbles with fixed shape and size, and bubbles with dynamic shape oscillations are considered. For most calculations, ellipsoidal bubbles with semimajor axis length a and semiminor axis length b are considered. For the calculations where the influence of the shape is investigated, also non-ellipsoidal bubbles are considered. The bubbles have velocity u parallel to the minor axis (Figure 4.3). The direction of the velocity is given by the angles ϕ_1 and ϕ_2. The tip positions x_{ti}, y_{ti}, z_{ti} are transformed from the probe coordinate system (x,y,z) to the bubble coordinate system (x',y',z'), this gives tip positions $x'_{ti}, y'_{ti}, z'_{ti}$. This is done using the transformations described in appendix A.1. The path of the tips through the bubbles is shown in Figure 4.3 with the dotted lines parallel to the velocity (i.e. the z'-axis) that pass through the point x'_i, y'_i, z'_i. The intersections of these lines with the bubble are determined, which gives the distances Δl_i and l_i. This provides $\Delta t_i = \Delta l_i / u$ and $T_i = l_i / u$. Next, inaccuracies may be added and reconstruction is performed.

4.2.2. Tip position and shape

If exact data is used of ellipsoidal bubbles with the velocity vector parallel to the semiminor axis, and the reconstruction is performed with the exact probe positions, very high accuracy in the estimates of u, ϕ_1 and ϕ_2 is obtained. The accuracy is independent of the radial position of piercing $r' = \sqrt{x'^2 + y'^2}$ and the velocity direction (ϕ_1 and ϕ_2).

Tip position accuracy

An actual probe will never have the exact dimensions mentioned in section 4.1. A deviation does not present a problem if the actual measured positions of the tips are used for the reconstruction. Artificial data is used to investigate the required accuracy in the measured tip positions to get

reliable velocity (direction) information. Virtual ellipsoidal bubbles are pierced with $a = 2.58$ mm, $b = 1.71$ mm (d_{eq}=4.5 mm). For the reconstruction, tip positions (x_{tri}, y_{tri}, z_{tri}) (i=0,1,2,3) are used. These were obtained by displacing the exact tip positions (x_{ti},y_{ti},z_{ti}) over a distance δr_t each in a different random three-dimensional direction. For this purpose, a large number of virtual bubble-probe interactions N ($5 \cdot 10^4$ or more) were simulated with velocity u_j=0.2 m/s, random angles ϕ_{1j} ($0° \leq \phi_{1j} \leq 90°$) and ϕ_{2j} ($0° \leq \phi_{2j} < 360°$) and random radial piercing location. For each interaction, different random directions were used for the tip displacement δr_t to get an idea about the order of magnitude of the error induced by this inaccuracy. Of course, the error in the reconstruction for a given probe will not have a random nature, but will manifest itself as a systematic deviation. The error for the velocity is estimated from the velocity estimates $\hat{u}_j$ as:

$$\delta_u = \sqrt{\sum_{j=1}^{N} \frac{(\hat{u}_j - u_j)^2}{N}} \tag{4.6}$$

Similar definitions are used for the angles. Again, no dependence of the accuracy on the radial piercing location is found. The accuracy, however, does depend on the angle ϕ_1 (Figure 4.7). Figure 4.7(a) shows how the inaccuracy of the velocity increases with ϕ_1 for various values of δr_t. This increase is due to the geometry of the probe: $d_p < \Delta s$: the relative error in the 'distance of flight' increases. The inaccuracy of the estimated angles ϕ_1 and ϕ_2 decreases with ϕ_1 (Figure 4.7(b) and Figure 4.7(c)). For small angles ϕ_1 the angle ϕ_2 is very inaccurate as may be expected (obviously, ϕ_2 becomes less relevant for ϕ_1 approaching 0°). The inaccuracy of the distances between the tips of a real probe is of the order of magnitude of 0.01 mm. This shows that the accuracy of the tip positions is sufficient to allow accurate reconstruction.

Tip shape

The actual reconstruction of experimental data is performed using the measured geometry of the tip. The distances between the fiber ends are measured from microscope photographs with an accuracy of approximately 5-10 μm. This inaccuracy is quite small, but there is an additional inaccuracy that needs to be taken into account: the effect of the finite size of the probe extreme. The probe tip is not a single point, but, instead, is a region with a certain size. For the reconstruction, the part that first touches the bubble is of primary importance. The probe tip shapes vary from fiber to fiber (Figure 4.8(a)), the radii of curvature vary typically from 25 to 40 μm. The inaccuracy caused by the differences in curvature is illustrated in Figure 4.8(b) for a flat gas-liquid interface. If two probe tips with curvature R_1 and R_2 are used, the probes will not pierce the gas-liquid interface with their extreme, but pierce it with another part of the rounded tip. As a result, the interface will travel a distance l' instead of the distance l for an infinitely sharp tip. The difference is $|l - l'| = |R_1 - R_2|cos(\phi_1)$. For non-zero angles between the velocity vector and the fiber, this gives inaccuracies in the reconstruction. The variations in R_i are in the range of 5-15 μm and therefore the magnitude of this effect is similar to the effect caused by the uncertainty in the position of the probe tips. Therefore, the effect on the accuracy is small, and it can be neglected.

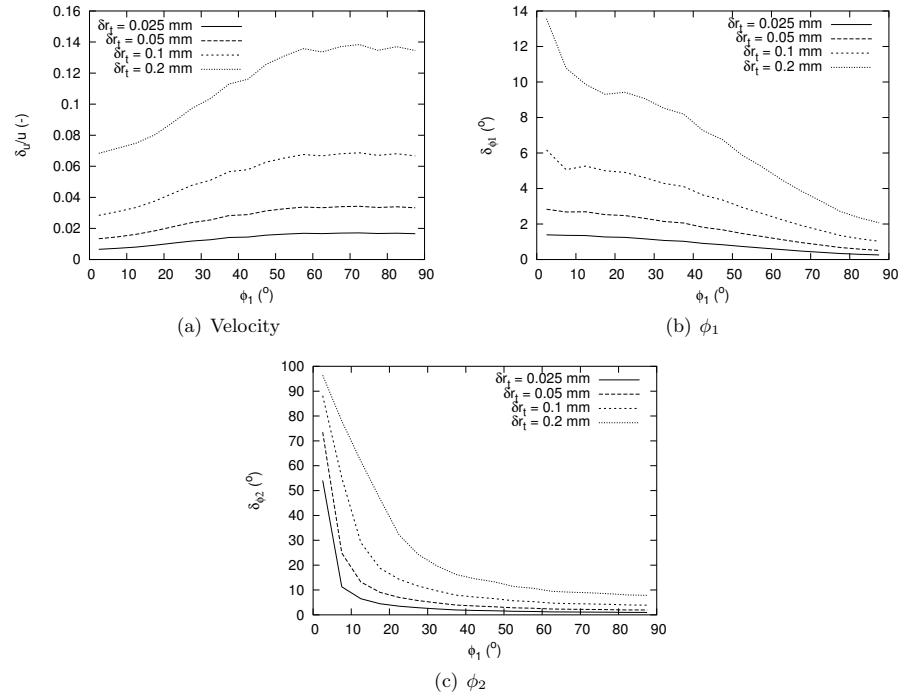

(a) Velocity

(b) ϕ_1

(c) ϕ_2

Figure 4.7.: Influence of inaccuracy in the tip positions on the accuracy of the velocity magnitude and velocity angle estimates.

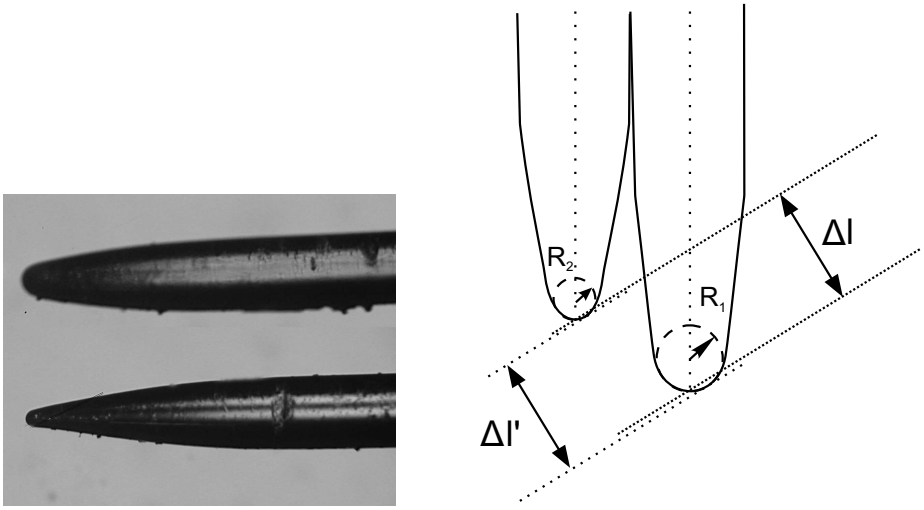

(a) (b)

Figure 4.8.: (a) Tip shapes. (b) Effect of probe tip curvature on accuracy (not to scale).

Figure 4.9.: Bubble shapes close to the wall in the cylindrical bubble column.

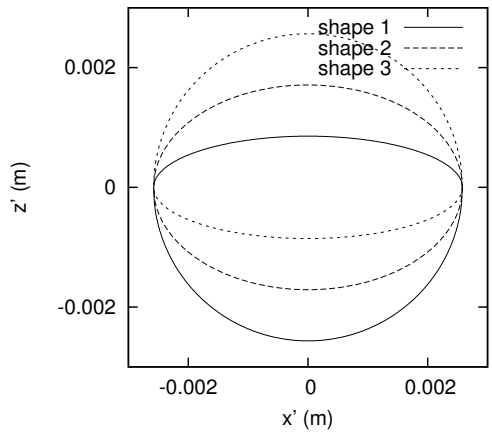

Figure 4.10.: Bubble shapes used for generation of artificial data.

4.2.3. Non-ellipsoidal shape, shape oscillations and curvature correction

Non-ellipsoidal shape

Due to the fact that bubbles do not have flat interfaces, but, instead, are rounded, a correction for the curvature is required to get accurate velocity information. In equations 4.5a-c the correction terms $\frac{T_0-T_i}{2}$ are used, which were illustrated in Figure 4.4. This correction is only precise if the bubble has mirror symmetry with respect to the plane, perpendicular to the velocity vector, which passes through its centroid. In the case of the wobbling regime, many bubble shapes are encountered which do not have this symmetry. This is also observed for our bubble column (Figure 4.9). Even if the average bubble shape is ellipsoidal, shape oscillations cause deviations from the symmetry for individual bubbles. The effect of this deviation is investigated with an example, by considering the accuracy of the reconstruction if the bubble shape is varied. Figure 4.10 illustrates the shapes used to generate artificial signals. The shape is given by the curves $z = b^+\sqrt{1 - r'^2/a^2}$ and $z = -b^-\sqrt{1 - r'^2/a^2}$ where $2b = b^+ + b^-$ ensuring that the volume is constant. An ensemble of bubbles with different shapes is considered. First, dynamic shape oscillations are neglected. The constant b^+ is varied according to a sinusoidal probability distribution between $0.5b$ and $1.5b$ from bubble to bubble, but kept constant during the entire piercing process, simulating bubble shapes around an average ellipsoidal shape. The deviations from the symmetry result in inaccuracies in the estimates for u, ϕ_1 and ϕ_2. For bubbles where the top is more flattened (like shape 1 in Figure 4.10), the curvature correction (with $\frac{T_0-T_i}{2}$) gives overcorrection; for bubbles with more rounded top (like shape 3 in Figure 4.10) the curvature correction gives a correction with is too small.

The order of magnitude of the inaccuracy is investigated. The results are shown in Figure 4.11 ('no selection'). Figure 4.11(a) shows that close to the sides of the bubble, where the curvature is strongest, the inaccuracy is largest. Figure 4.11(b), Figure 4.11(c) and Figure 4.11(d) show that the bubble deformations result in errors with magnitudes around 5% for u and 8° for ϕ_1.

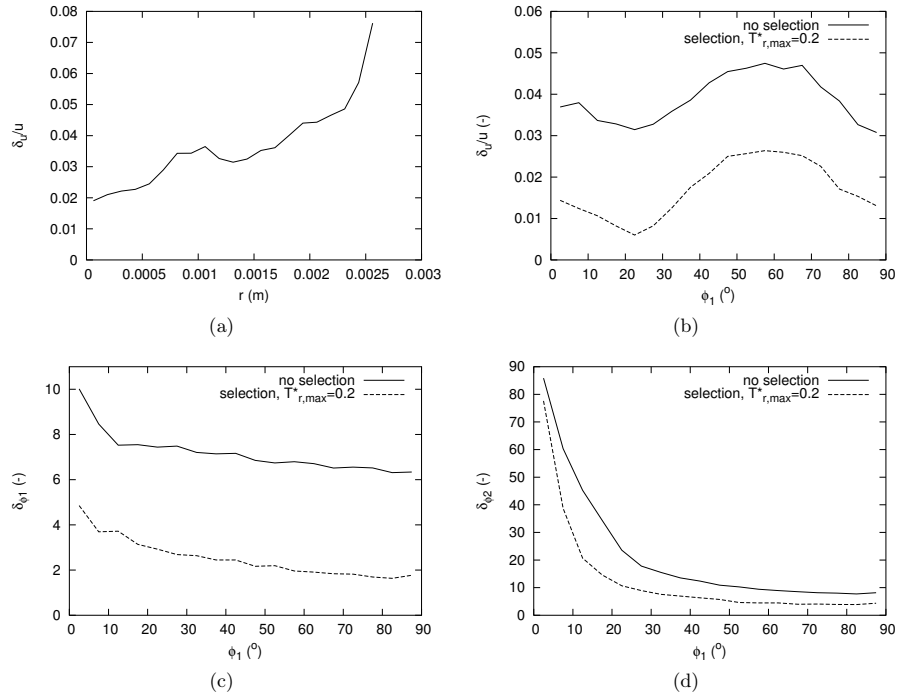

Figure 4.11.: Influence of the bubble shape on the accuracy of the velocity magnitude and velocity angle estimates.

ϕ_2 has an inaccuracy of about 10° for $\phi_1 > 30^\circ$, for smaller ϕ_1 the inaccuracy increases rapidly.

The results suggest that improvements in the accuracy may be obtained by rejecting measurement taken close to the bubble edges. This is performed by setting the condition

$$T_r^* = max\Big(\frac{|T_i - T_0|}{T_0}\Big) < T_{r,max}^* \tag{4.7}$$

for acceptance of measurements. Figure 4.11 shows the effect on the accuracy of using this selection criterion with $T_{r,max}^* = 0.2$. For the present example, this criterion effectively results in rejection of piercing events with $r'/a > 0.7$. Tests with experimental data (section 4.4), however, show little improvement in the results. Apparently, many measurements close to the sides of the bubble are already rejected due to, e.g., deformation. In addition, the errors in the residence time due to deformations, etc. may make the criterion less effective for distinguishing measurements taken close to the bubble sides. For this reason, this criterion is not used in the experiments.

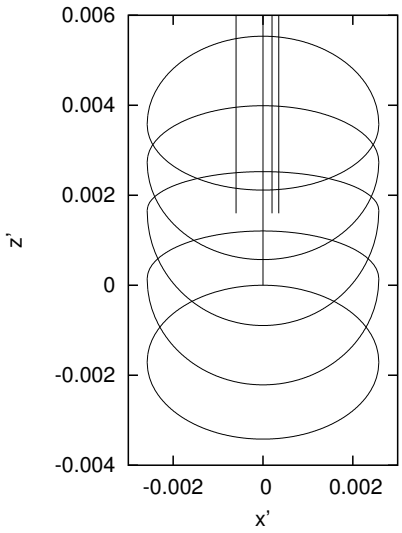

Figure 4.12.: Oscillating bubble shapes (f_{osc}=20 Hz).

Shape oscillations and curvature correction

If dynamic shape oscillations are included, the bubble is no longer 'frozen' while passing the probe tips. This has an additional negative effect on the accuracy since the interface velocities differ from the velocity of the center of gravity. Again an order of magnitude estimate is obtained with synthetic data. Virtual bubbles arrive from random directions and are pierced at random radial positions. The center of gravity of the virtual bubbles moves with a constant velocity. The shape is defined with respect to the centroid by the curves

$$z'^{+}(t) = \frac{3}{4}(b - b^{+}(t)) + b^{+}(t)\sqrt{1 - \frac{r'^2}{a^2}} \tag{4.8}$$

and

$$z'^{-}(t) = -\frac{3}{4}(b - b^{+}(t)) - (2b - b^{+}(t))\sqrt{1 - \frac{r'^2}{a^2}} \tag{4.9}$$

with

$$b^{+}(t) = b(1 + \frac{1}{2}cos(2\pi f_{osc}t + \phi_{osc})) \tag{4.10}$$

with f_{osc} and ϕ_{osc} the frequency and (random) phase of the oscillations. An example of a bubble passage is shown in Figure 4.12. The effect of the oscillations on the velocity accuracy is shown for various oscillation frequencies f_{osc} in Figure 4.13(a). The accuracy of the velocity estimate drops with increasing oscillation frequency. The increasing inaccuracy is caused by the increasingly closer match between the half oscillation period (10 ms for 50 Hz) and the travel times Δt_i (8 ms for u=0.2 m/s and ϕ_1=0°). The accuracy in ϕ_1 is nearly independent of the

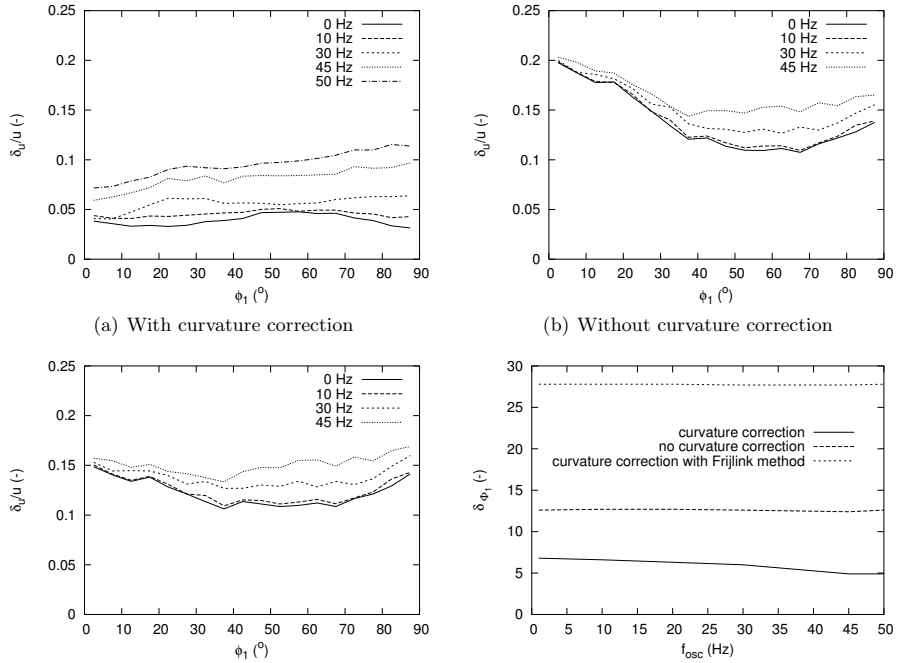

(a) With curvature correction

(b) Without curvature correction

(c) Curvature correction with eq 4.12

(d) Accuracy for ϕ_1 estimate for ϕ_1=0.

Figure 4.13.: Influence of oscillations in the bubble shape on the accuracy of the velocity magnitude and ϕ_1 estimates for various oscillation frequencies f_{osc}, with and without curvature correction.

oscillation frequency (Figure 4.13(d)).

Frijlink (1987) discourages the use of the curvature correction with the term $(T_0 - T_i)/2$ for the 1D reconstruction algorithm. The author mentions that in the case of shape oscillations and movement under an angle, the correction may result in large distortion of the results. For this reason, we compare the results of the reconstruction with (Figure 4.13(a)) and without (Figure 4.13(b)) curvature correction. For the latter, the equation

$$\Delta t_i - T_{correct} = \frac{z'_{ti} - z'_{t0}}{u} = \frac{x_{ti}sin(\phi_1)cos(\phi_2) + y_{ti}sin(\phi_1)sin(\phi_2) + z_{ti}cos(\phi_1)}{u} \tag{4.11}$$

is solved for i=1,2,3 with $T_{correct} = 0$. The results show that the inaccuracy is larger if the correction is left out. Frijlink (1987) suggests an alternative curvature correction, which is also used by Guet (2004b) (both authors only consider 1D velocity reconstruction with removal of bubbles which do not move in the axial direction). The author assumes a spherical bubble, for which the curvature correction is estimated with $\hat{d}_b/2 - \sqrt{\hat{d}_b^2/4 - d^2}$. $\hat{d}_b$ is an estimate of the bubble diameter, which is determined by obtaining a first velocity estimate by solving equation 4.11 with $T_{correct} = 0$. We get $\hat{d}_b = u \cdot max(T_i)$. Next, a curvature correction is estimated with:

$$T_{correct} = \frac{\hat{d}_b/2 - \sqrt{\hat{d}_b^2/4 - d_p^2}}{u} \tag{4.12}$$

Subsequently, equation 4.11 is solved for i=1,2,3 using equation 4.12. The results are shown in Figure 4.13(c). This shows that for small ϕ_1 a small improvement over the results without any correction is obtained. The results with the correction $T_{correct} = (T_0 - T_i)/2$ (Figure 4.13(a)) remain superior. These conclusions also hold if the selection criterion from equation 4.7 is used. The accuracy of the ϕ_1 estimate is also best with the curvature correction and decreases if the curvature correction is left out. In the case of correction with equation 4.12 a very large error is obtained.

Further study with artificial as well as experimental signals shows that, generally, the best results are obtained if the curvature correction term is based on the average shape of the bubbles. Since the average shape of the actual bubbles is closer to a ellipsoid than a bubble with a flat top, in general better results are obtained if the correction terms $(T_0 - T_i)/2$ are included than when these are left out.

4.2.4. Aspect ratio oscillations and vertical probe dimensions

The bubbles in the bubble column not only exhibit shape oscillations, but aspect ratio oscillations as well. These contribute even stronger to the errors, since not only the vertical dimensions vary, but the apparent cross-section of the bubble as well. This generates larger errors when the bubbles are pierced near the edges: the horizontal movement of the interface can give much larger changes in the times of piercing than vertical movement of the interface alone. Observation of the bubbles in the cylindrical bubble column and a plume shows that the frequency of the most important oscillation mode is in the range of 30-40 Hz. This agrees with the order of magnitude

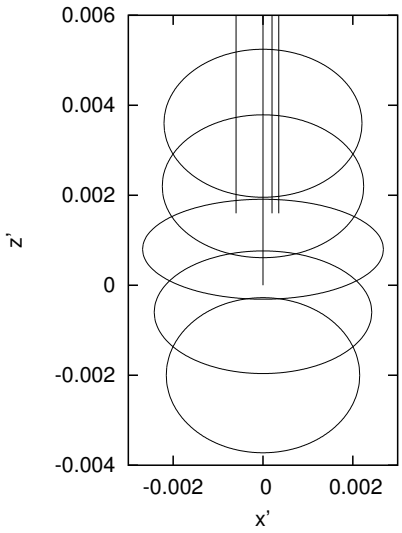

Figure 4.14.: Oscillating bubble shapes (f_{osc}=40 Hz).

given by (Lamb, 1932):

$$f_{lamb} = \frac{1}{\pi}\big[(k+1)(k-1)(k+2)\frac{2\sigma_l}{\rho_c d_{eq}^3}\big]^{\frac{1}{2}} \tag{4.13}$$

which was derived analytically for small oscillations around a spherical shape. k is the order of the oscillation, σ_l the surface tension, and ρ_c the liquid density. A frequency of 44 Hz is obtained for the most important oscillation with order $k = 2$ in the case of bubbles with d_{eq}=4.5 mm. Observations in the bubble column show that the aspect ratio varies between 0.4 and 0.8.

Artificial signals are generated for bubbles with oscillating aspect ratio. Piercing is simulated of an ellipsoidal bubble (d_{eq}=4.5 mm) which has an aspect ratio which is oscillating sinusoidally in time in between the extremes 0.4 and 0.8. Only ϕ_1=0° is considered. Figure 4.15 shows the inaccuracy for the estimate of the velocity and ϕ_1 for various radial piercing positions in the case f_{osc}=40 Hz. Overall, the performance of the reconstruction with curvature correction is superior and the errors are largest for piercing near the bubble sides. The average inaccuracy in ϕ_1 (averaged over all accepted realizations) is independent of f_{osc} for 20 Hz$<f_{osc}<$80 Hz and has the value 14.5° with curvature correction, and 18.8° without curvature correction. A histogram of ϕ_1 is shown for f_{osc}=40 Hz in Figure 4.16(b). This shows that also very large values (up to 60°) are obtained.

Figure 4.16(a) shows the mean inaccuracy for the velocity measurements for increasing oscillation frequency and two different probe dimensions (Δs=1.6 mm being the standard configuration, other dimensions are left unchanged). The inaccuracy increases with f_{osc}, a maximum is reached around f_{osc}=50 Hz for Δs=1.6 mm. For Δs=0.8 mm the inaccuracy still increases for $f_{osc}>$50 Hz. The magnitude of the inaccuracy is determined by the ratio of the displacement of the interface due to the oscillations and the displacement due to the bubble velocity.

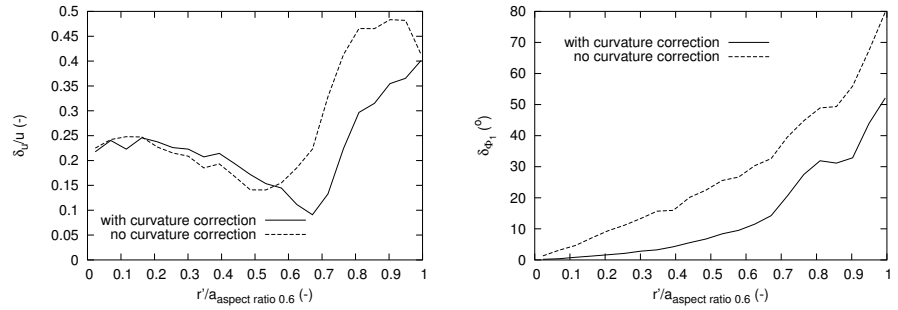

(a) Velocity accuracy (b) Accuracy of ϕ_1

Figure 4.15.: Influence of oscillations in the aspect ratio on the accuracy of the velocity magnitude and ϕ_1 estimates for various radial piercing locations, with and without curvature correction, f_{osc}=40 Hz.

For lower oscillation frequencies the technique effectively determines an average of the local interface velocity on the upper side and the lower side of the bubble. For very small oscillation frequency the errors caused on the upper side and the lower side cancel out since the oscillation is symmetric. The phases of the oscillations on the lower side and the upper side differ more for increasing frequency. Therefore, the error in the velocity increases for frequency increases up to approximately 50 Hz. Although a reduction in Δs results in a smaller interface displacement due to the oscillations, this does not help to reduce the error in the velocity, since the decrease in the displacement is approximately proportional to the reduction in Δs: the technique will continue to determine an average of the local interface velocities. Consequently, for $f_{osc}<$30 Hz, the inaccuracy is more or less independent of the vertical probe dimensions.

The maximum near 50-60 Hz for Δs=1.6 mm follows from the probe dimensions. The mean time in between the piercing event by the central tip and the other tips is approximately $\Delta s/u$=0.008 s. This time corresponds to the half period of an oscillation with frequency of 62 Hz, i.e. for frequencies around 62 Hz the interface oscillation displacement in between the piercing events typically reaches a maximum value (the exact result depends on the phase of the oscillation). For frequencies beyond 62 Hz, part of the oscillation during piercing averages out and the inaccuracy drops. For the smaller probe size Δs, the maximum inaccuracy is reached for a higher frequency. Therefore, the inaccuracy continues to increase for $f_{osc}>$50 Hz. Consequently, reduction of the size of the probe (Δs) will not help in reducing the inaccuracies due to the bubble surface oscillations.

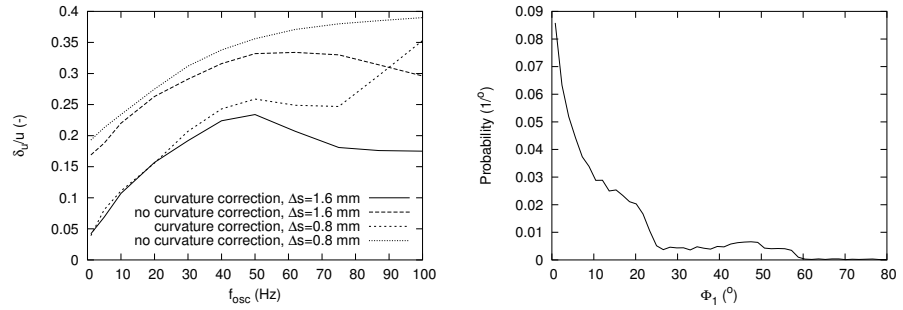

(a) (b)

Figure 4.16.: Inaccuracy results for aspect ratio oscillations. (a) Influence of the frequency of oscillations in the aspect ratio on the accuracy of the velocity magnitude with and without curvature correction, for two different probe dimensions. (b) Histogram of ϕ_1 estimates. f_{osc}=40 Hz, curvature correction.

4.3. Accuracy analysis of 3D bubble velocity vector estimation: probe-bubble interaction

4.3.1. Probe-bubble interactions

In chapter 3, various interaction effects of the bubble with the fiber were discussed. These were the blinding effect, the crawling effect (i.e. deformation and deceleration of the bubble), and the drifting effect, where the fiber induces lateral movement and/or a change in the velocity orientation of the bubble. Similar effects are observed for the four point probe, but their magnitude and relative importance is different.

Figures 4.17 and 4.18 shows the piercing of a relatively small bubble near its center. Some of the differences with the piercing by a single fiber, that may occur are:

- Up to four piercing events occur instead of one. Consequently, the total force involved is much bigger.

- The upper three tips pierce an interface that is already deformed by the piercing due to the central tip. Perpendicular piercing due to the upper tips is therefore unlikely. Consequently, the lateral component of the interaction forces is larger, and the drifting effect may play a role, whereas it is negligible for a single fiber if the probe and bubble velocity orientation are aligned ($\alpha = 0°$, section 3.5). In addition, the total deformation may be much larger than for a single fiber (e.g. compare Figure 3.14 and Figure 4.17).

- The deformation of the upper side of the bubble is relatively unimportant for a single probe, the deformation of the lower side is mainly responsible for the inaccuracies. For a four point probe, however, the deformation of the upper side may also play an important role for e.g. the times of flight Δt_i.

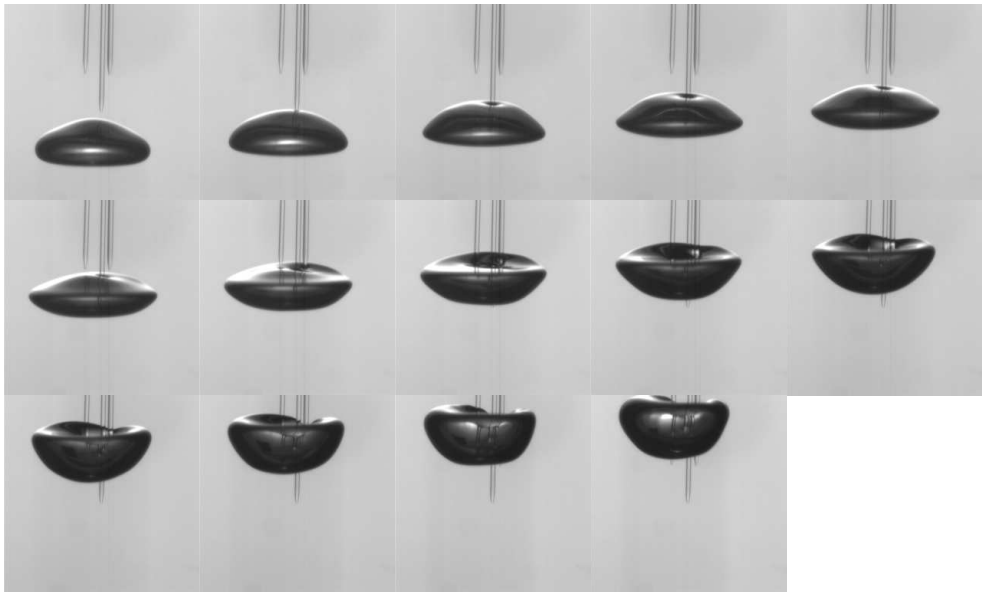

Figure 4.17.: Images of piercing of a bubble by a 4 point probe. Time between frames 1.4 ms, bubble size 3.3 mm.

- The delay between the piercing by the central and the other tips provides the deformations with more time to grow and to have more impact on the measurement.

In the next sections, the drifting effect and deformation effect (crawling and blinding) due to the probe-bubble interaction are studied in more detail, since these play the most important role for the accuracy. The study is performed via observations of the interaction of a bubble and a probe in a bubble plume. The experimental setup that was used for this investigation was described in section 3.3.2. The deceleration of the bubble by the probe has been the subject of more studies (e.g. Guet et al. (2003), Mudde and Saito (2001)) and is therefore only considered briefly. Observation of piercing of bubbles in the present research shows that for perpendicular piercing the bubble velocity is reduced by typically 10% during the entire piercing process. This means that in general the bubble velocity is underestimated by about 5%, a value which agrees with the results presented in Guet (2004b).

4.3.2. Drifting effect

If the bubble is not pierced in its center, the probe not only exerts a force component in the axial direction but also in the lateral direction (Figure 4.19). This results in the acceleration of the bubble in this direction: drifting occurs. The velocity direction of the bubble changes with an angle ϕ_d during the time from the instant when the central tip enters the bubble, until the instant when the last upper tip exits the bubble (Figure 4.20).

For piercing further away from the bubble center, the lateral interaction force component

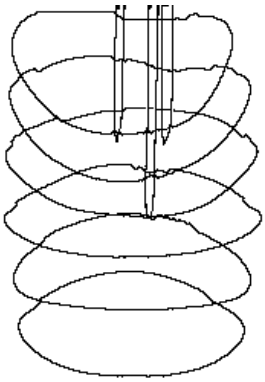

Figure 4.18.: Bubble contours of bubble piercing by a 4 point probe. Time between contours 4.1 ms, bubble size 3.3 mm.

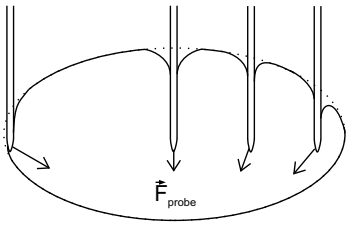

Figure 4.19.: Local bubble deformation at different radial positions and the induced interaction force.

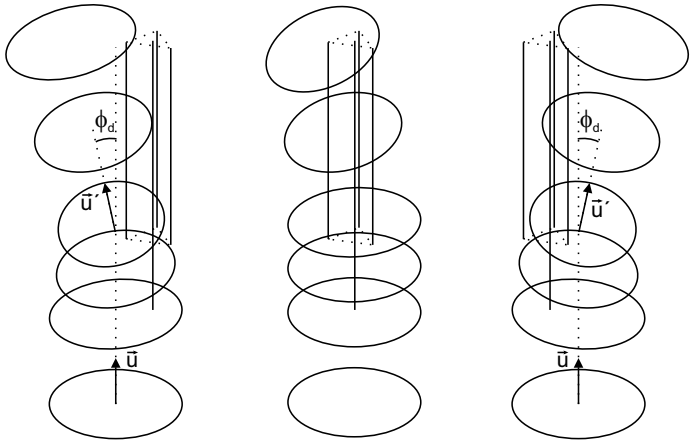

Figure 4.20.: Bubble drifting effect for piercing at various radial locations.

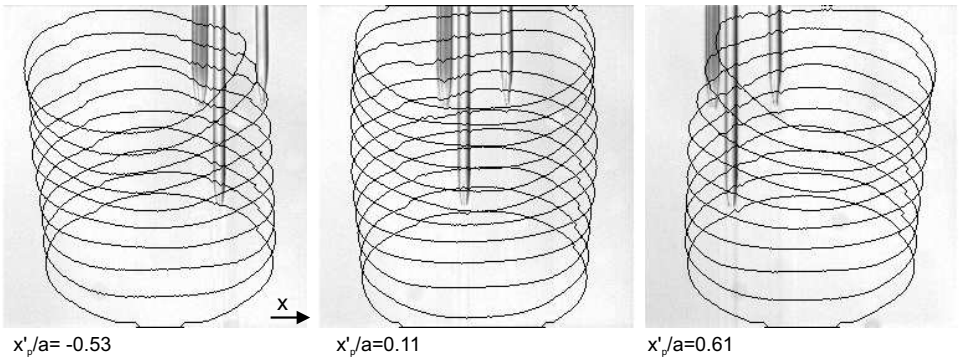

Figure 4.21.: Bubble contours showing drifting effect for case A (d_{eq}=3.0 mm), interval between contours 1.4 msec.

increases as well as the total force magnitude, due to the larger inclination of the interface locally at the tips. Consequently, the magnitude of ϕ_d increases for piercing further away from the center. This variation is investigated using a bubble plume by studying the piercing of a bubble a few diameters away from the location of formation. The use of a plume allows simple visual observation of alterations of the direction of the velocity by the interaction, and allows accurate control of the radial position of piercing. On the other hand, the use of a bubble plume has the drawback that the path of the bubbles is somewhat altered by the wake of the previous bubble. This effect is minimized by keeping the bubbling frequency low. Consequently, the influence is small. Bubbles are pierced with the probe axial direction parallel to the bubble velocity ($\phi_1 = 0$). Three cases are considered: A) d_{eq}=3.0 mm, aspect ratio 0.56, u=0.24 m/s, piercing at 8 mm from the needle where the bubble is formed (needle opening diameter 0.8 mm), B) d_{eq}=3.0 mm, aspect ratio 0.4, u=0.26 m/s, piercing at 15 mm from the needle (needle opening diameter 0.8 mm) and C) d_{eq}=4.3 mm, aspect ratio 0.31, u=0.30 m/s, piercing at 17 mm from the needle (needle opening diameter 1.6 mm). The piercing is performed for various radial positions x'_p over the line y=0 (sketch in Figure 4.23(a)).

Video images of the bubble piercing were processed with image processing software. The bubble contour and location of the center of mass were determined for each image. Figure 4.21 shows the sequence of bubble contours for case A for three radial piercing locations. The path of the center of mass of the bubble was calculated from the images, the result is shown for case A in Figure 4.22. The actual bubble path is 3D, therefore the probe is aligned with its central tip in the bubble plane of symmetry parallel to the CCD imaging plane, minimizing movement of the bubble toward or away from the camera.

Figure 4.23(b) plots the drift angles ϕ_d versus $sin(\alpha_d)$, with α_d the angle describing the surface inclination. Data is shown for the three cases and the various radial piercing locations. For $|sin(\alpha_d)|$<0.2 the angle ϕ_d is approximately proportional to $sin(\alpha_d)$, suggesting that the force on the bubble is directed perpendicular to the interface and approximately constant in magnitude. From the data the following relation is derived:

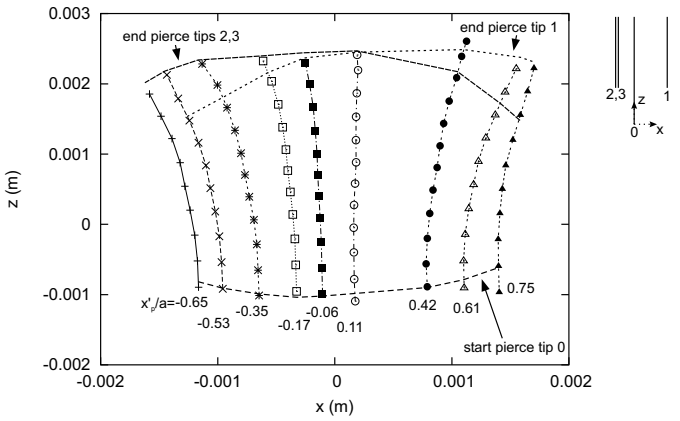

Figure 4.22.: Trajectory of bubble center of mass with respect to the central tip position during piercing for case A (d_{eq}=3.0 mm), interval between locations 1.4 msec. The lines show the instants when the measurements start and end.

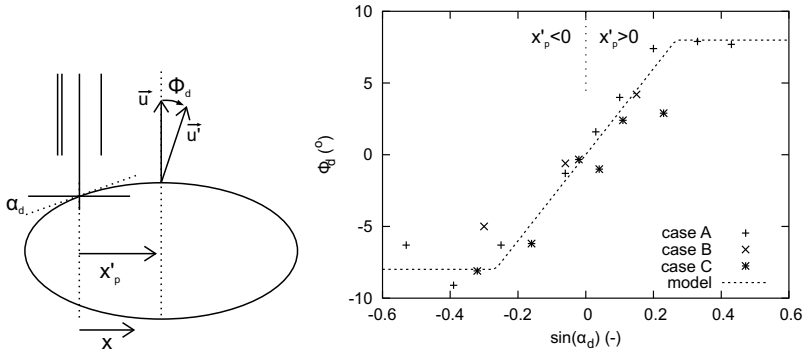

(a) Drifting effect.

(b) Measured effect of surface inclination on measured drift angle.

Figure 4.23.: Drifting effect.

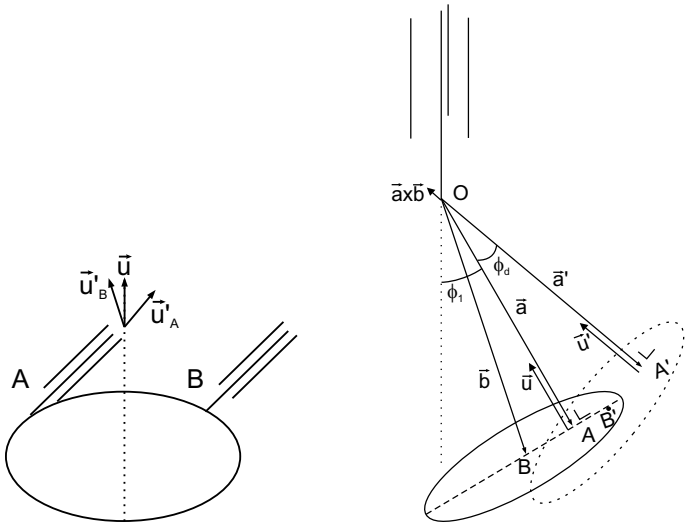

(a) Drifting effect for non-perpendicular piercing

(b) Modeling of the bubble velocity drifting effect

Figure 4.24.: Non-perpendicular piercing and drifting effect model

$$\phi_d = \min(8, 30sin(\alpha_d)) \tag{4.14}$$

If the bubble velocity vector is not aligned with the probe, the drifting effect may increase in magnitude (section 3.5.2). This is illustrated in Figure 4.24(a). For piercing on the left side (A) the three phase contact line is longer than for piercing on the right side, and consequently the force involved and ϕ_d are larger (see also Figure 3.21). This effect is, however, not studied further, and equation 4.14 is used for the generation of artificial signals. For this purpose, the drifting effect is simplified and the velocity direction is rotated before the actual artificial piercing takes place. This is implemented as follows (Figure 4.24(b)). The position of the bubble center is given by the vector $\vec{b}$, the vector $\vec{a}$ constitutes the path of the location on the bubble where piercing will take place. The drifting effect is modeled by determining the radial position where the bubble will be pierced, calculating α_d, and next rotating the bubble and its velocity vector over an angle ϕ_d around the rotation axis $\vec{a} \times \vec{b}$. This way, only the effect on the bubble velocity orientation is modeled, inaccuracies in the velocity magnitude are not taken into account, these will give a small overestimation of the velocity.

4.3.3. Bubble deformation

Once the first fiber touches the bubble, the bubble starts to deform. The deformation is again an interplay between inertia forces and surface forces, similar to the natural shape oscillations. Therefore, the deformation has a timescale which is of the same order as the half period of the bubble shape oscillations. Consequently, it closely matches the bubble passage time, as was

discussed in section 4.2.4. Close to the sides, the radius of curvature of the bubble is usually smaller. As a result, the surface forces involved are bigger and the size of the deformations and the speed with which they grow increase closer to the sides (this can be observed in Figure 4.21).

Observation shows that when the bubble is pierced, it is deformed both locally and on the scale of its diameter (Figures 4.17 and 4.21). On the upper side the bubble becomes usually more flattened, on the lower side the interface usually becomes more inclined. In addition, the aspect ratio of the bubble increases. As a result, inaccuracies in the magnitude and direction of the bubble velocity are obtained. The effect on the velocity direction is very similar to that of the drifting effect: a bubble pierced on the left side will appear to move to the right.

Since the deformation effect is accompanied by natural shape oscillations and the drifting effect, accurate estimation is made more difficult. Analysis is easier relatively close to the point of bubble formation where surface oscillations are relatively weak, consist out of few modes and are very reproducible from bubble to bubble. The CCD image sequences of the piercing of cases A and B are used to study the increase in aspect ratio after the start of piercing. The aspect ratio is determined as the ratio of the vertical distance between the imaged bubble top and bottom, and the horizontal distance between the imaged left and right sides of the bubble. In addition, the time dependent change of the aspect ratio for a bubble, which is not pierced, is determined ('virtual piercing'). This serves as a reference. First, the difference is determined in the aspect ratio evolution with time between the cases with and without piercing (Figure 4.25(a), where t=0 corresponds to the moment when either the real of virtual piercing starts):

$$aspect\_ratio_{deform}(t) = aspect\_ratio_{piercing}(t) - aspect\_ratio_{virtualpiercing}(t) \tag{4.15}$$

Next, the average change in time of $aspect\_ratio_{deform}(t)$ is determined as a function of the radial piercing position (Figure 4.25(b)). It can well be approximated by:

$$d(\text{aspect\_ratio}_{deform})/dt = \min(15, 2 + 18r'/a) \tag{4.16}$$

where the numerical constants have dimension s^{-1}. The change with time is limited to a maximum of 15 s^{-1} since no data is available for $|x'_p|/a > 0.7$: the bubble is no longer pierced by all fibers. Equation 4.16 is used to model the deformation effect and to study its influence on the accuracy of the probe technique. This simple model can of course only present an order of magnitude estimate for the inaccuracy. The precise deformation will be dependent on many parameters, such as the bubble size, aspect ratio and bubble velocity direction, and also consists of local deformation. A model that accurately predicts the effect of all these parameter variations is, however, outside the scope of the current investigation.

For the generation of artificial signals, the instant t_{first} when the first tip touches the interface is determined. The radial piercing position of the central tip r' provides $d(\text{aspect\_ratio}_{deform})/dt$ via equation 4.16. At time $t > t_{first}$ the aspect ratio due to the deformation is given by:

$$\text{aspect\_ratio}(t) = \text{aspect\_ratio}_{\text{no deformation}}(t) + (t - t_{first})d(\text{aspect\_ratio}_{deform})/dt \tag{4.17}$$

with $\text{aspect\_ratio}_{\text{no deformation}}$ the aspect ratio in the absence of deformation. Figure 4.25(a) suggests that the linear increase of the contribution due to deformation is a reasonable approximation.

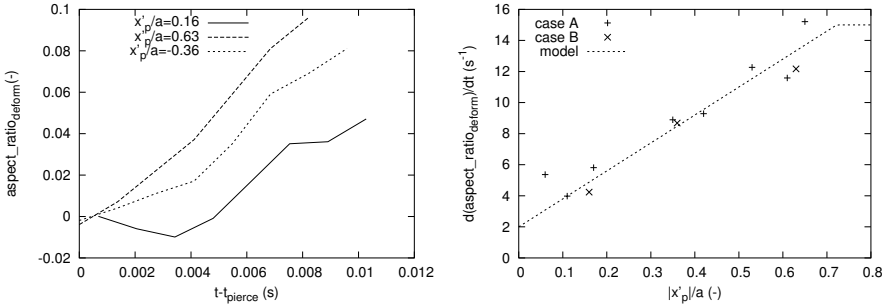

(a) (b)

Figure 4.25.: Observations of the aspect ratio in the case of bubble piercing. (a) Difference in aspect ratio between a bubble which is pierced and a bubble which is not pierced for case B. t_{pierce} is the time when the first tip pierces the bubble. (b) Change of aspect ratio with time due to piercing.

In Figure 4.26 the estimate of ϕ_1 obtained with the simulated piercing is compared with the values obtained from experiments. The order of magnitude is predicted reasonably well. This shows that the aspect ratio deformation is responsible for the largest part of the observed deviation in ϕ_1. Local deformations are responsible for the differences between the simulated piercing and the experiments, these are especially important in the center of the bubble and close to the sides.

4.4. Inaccuracy in the bubble column

In the previous sections the focus was put on the separate error sources. The present section starts with the estimation of the total error magnitude and identification of the major error sources with the use of artificial piercing simulations. Next, a comparison of simulation results is made with probe data from a pseudo-2D bubble column from Xue (2004). Subsequently, the accuracy of the measurements obtained in the cylindrical bubble column is analyzed, with a focus on the effect of a large angle between the velocity vector and the probe's axial direction. Finally, possibilities for improvement of the measurement technique are discussed.

4.4.1. Artificial piercing: total error

In the previous sections many error sources were considered. The present section compares these and tries to provide an estimate for the total error. In section 4.2, the inaccuracies due to differences in tip shapes and uncertainties in the tip positions were found to be small compared to those due to other error sources. The inaccuracy due to shape oscillations is significant. The largest contribution was found to originate from aspect ratio oscillations. The drifting and deformation effect were found to give significant contributions for the inaccuracy in the velocity direction. For the total error, only the largest error sources are considered: shape oscillations, drifting and deformation. The study is performed for conditions encountered in bubble columns.

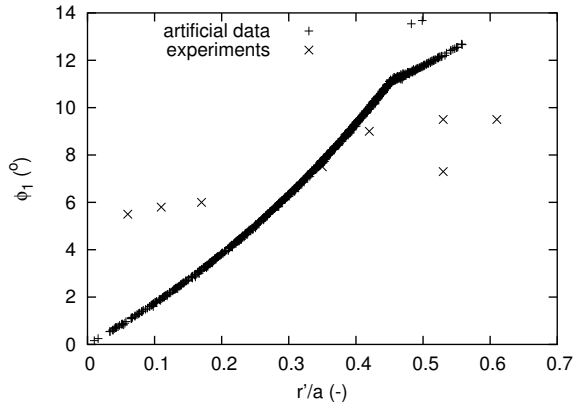

Figure 4.26.: Comparison of estimates for ϕ_1 obtained from simulated piercing and experiment (case A). U=0.24 m/s, d_{eq}=3.0 mm, the aspect ratio variation with time without piercing is modeled after experimental observations.

Of course, the approach taken here via the modeling of the error sources can only provide an order of magnitude of the inaccuracy.

The following settings are used: d_{eq}=4.5 mm, u=0.2 m/s, the aspect ratio is constant at 0.6 (if the oscillations are ignored) or fluctuates between 0.4 and 0.8 with f_{osc}=40 Hz. The piercing of 10000 bubbles is simulated, typically 4000 events produce a bubble velocity estimate (in the other cases one or more tips miss the bubble). Four different cases are considered for the exact bubble velocity distribution (Figure 4.27), with $p(\phi_1)$ describing the probability density function of ϕ_1:

- A1: Vertical motion with ϕ_1=0^o
- A2: Zig-zag motion: for $\phi_1 < \phi_{1,max}$ ($\phi_{1,max}$=25 ^{o}, after Fan and Tsuchiya (1990), see also

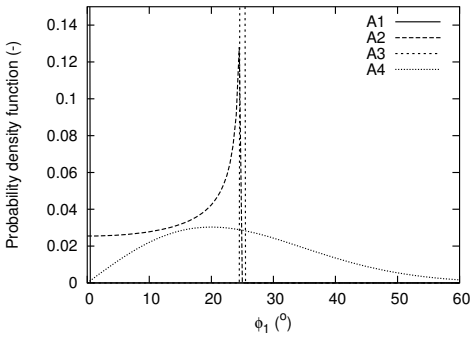

Figure 4.27.: Exact bubble velocity angle ϕ_1 distributions.

	$\mu_{\phi_1}^{A1}(^\circ)$	$\sigma_{\phi_1}^{A1}(^\circ)$	$\mu_{\phi_1}^{A2}(^\circ)$	$\sigma_{\phi_1}^{A2}(^\circ)$
Exact	0	0	15.9	7.7
DR	7.1	1.7	15.9	7.3
DR+DF	13.0	5.2	18.4	8.8
DR+DF+OSC	15.5	13.0	21.6	12.4
OSC	16.2	17.1	25.8	18.7
	$\mu_{\phi_1}^{A3}(^\circ)$	$\sigma_{\phi_1}^{A3}(^\circ)$	$\mu_{\phi_1}^{A4}(^\circ)$	$\sigma_{\phi_1}^{A4}(^\circ)$
Exact	25.0	0	24.5	12.8
DR	23.0	4.7	23.6	12.4
DR+DF	23.4	9.0	25.3	13.0
DR+DF+OSC	26.7	11.7	28.1	15.8
OSC	33.0	18.9	32.8	21.5

Table 4.1.: Mean (μ_{ϕ_1}) and standard deviation (σ_{ϕ_1}) of ϕ_1 for various effects in simulated piercing. DR=drifting effect, DF=deformation effect, OSC=shape oscillations.

appendix A) :

$$p(\phi_1) = \frac{1}{\frac{\pi}{2}\phi_{1,max}\sqrt{1-\phi_1^2/\phi_{1,max}^2}} \tag{4.18}$$

- A3: Spiraling motion: ϕ_1=25^o
- A4: Gaussian distribution of the velocity direction. The velocity direction is distributed with standard deviation b_{ϕ_1} around the average velocity vector with ϕ_1=0^o. This distribution is close to that obtained via measurements with the probe inside the cylindrical bubble column. b_{ϕ_1} is taken as 20^o, this value is obtained from measurements in the cylindrical bubble column for U_g=0.034 m/s.

$$p(\phi_1) = \phi_1 \frac{e^{-\phi_1^2/2b_{\phi_1}^2}}{b_{\phi_1}^2} \tag{4.19}$$

For all cases ϕ_2 is a random number, uniformly distributed between 0^o and 360^o. The magnitude and direction of the velocity of the center of gravity of the bubble are constant during the bubble piercing: accelerations are not taken into account.

The results of the simulated piercings are shown in Tables 4.1 and 4.2 and in the Figures 4.28 and 4.29(a). Figures 4.28(a) and 4.28(e) show how the combination of the drifting and the deformation effect gives an inaccuracy in ϕ_1 of typically 15°. The effect on u is very small (Figure 4.28(e)). The oscillation effect (Figure 4.28(d)) alone produces large errors, with a magnitude of typically 24° (the total error: the combination of the systematic and random errors). The piercing close to the sides produces a very long tail with values for ϕ_1 up to 60°. The inaccuracy in the velocity u due to the oscillations is about 0.05 m/s.

Combination of the drifting, deformation and shape oscillations produces somewhat smaller errors than the shape oscillations alone. The inaccuracy of ϕ_1 is around 20°, the inaccuracy in u is about 0.04 m/s. This shows that the shape oscillations produce the largest contribution to the total error. The error for the combined oscillation and interaction effects is even somewhat

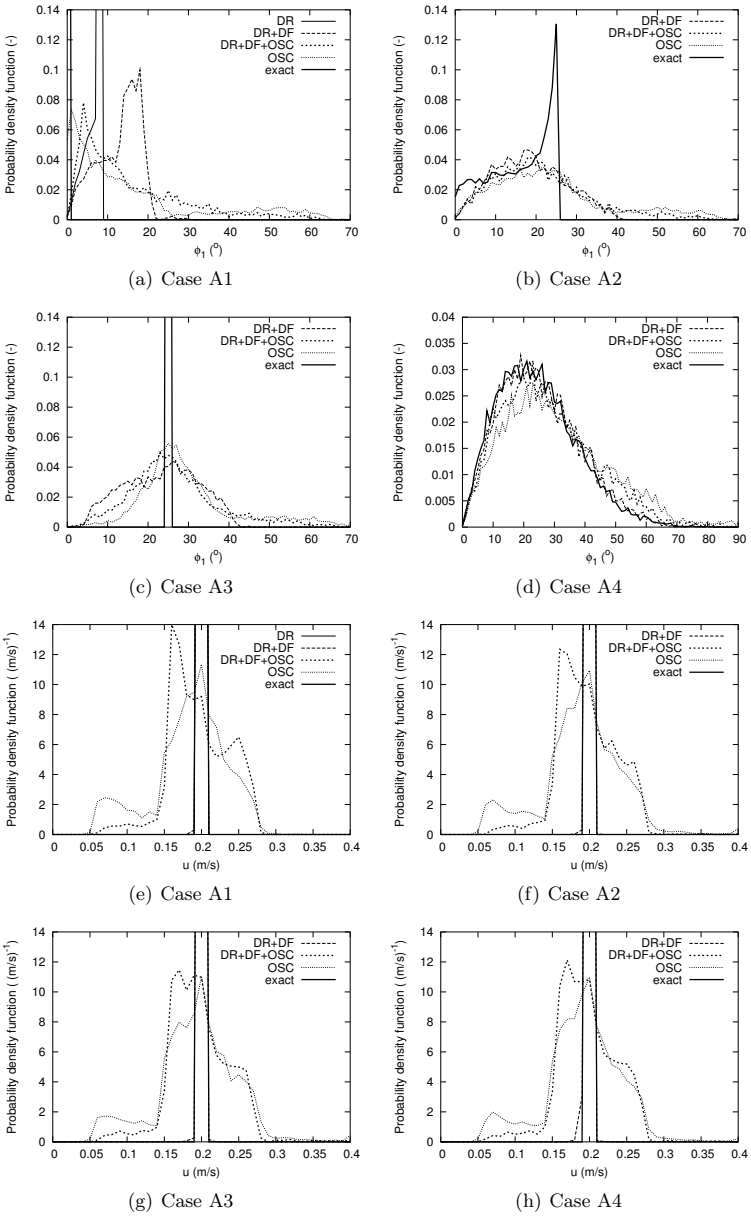

(a) Case A1 (b) Case A2

(c) Case A3 (d) Case A4

(e) Case A1 (f) Case A2

(g) Case A3 (h) Case A4

Figure 4.28.: Histograms of artificial estimates of velocity angle ϕ_1 and u. DR=drifting effect, DF=deformation effect, OSC=shape oscillations.

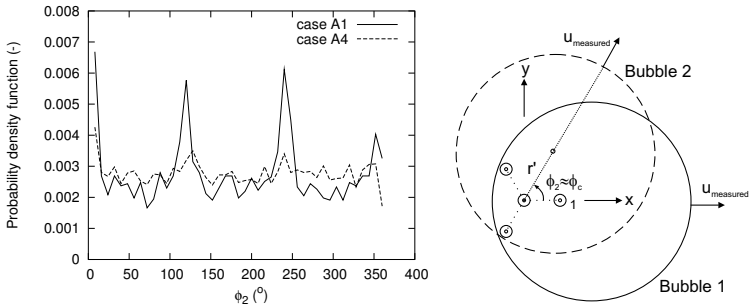

(a) Simulated probability density functions for ϕ_2

(b) Geometrical explanation dependence inaccuracy on ϕ_2 (top view).

Figure 4.29.: Dependence measurement inaccuracy on ϕ_2

	$\mu_u^{A1}(\frac{m}{s})$	$\sigma_u^{A1}(\frac{m}{s})$	$\mu_u^{A2}(\frac{m}{s})$	$\sigma_u^{A2}(\frac{m}{s})$
Exact	0.200	0.000	0.200	0.000
DR	0.200	0.000	0.200	0.000
DR+DF	0.200	0.001	0.200	0.001
DR+DF+OSC	0.196	0.040	0.196	0.039
OSC	0.184	0.051	0.189	0.055
	$\mu_u^{A3}(\frac{m}{s})$	$\sigma_u^{A3}(\frac{m}{s})$	$\mu_u^{A4}(\frac{m}{s})$	$\sigma_u^{A4}(\frac{m}{s})$
Exact	0.200	0.000	0.200	0.000
DR	0.200	0.000	0.200	0.000
DR+DF	0.199	0.001	0.199	0.002
DR+DF+OSC	0.197	0.041	0.196	0.039
OSC	0.193	0.055	0.191	0.052

Table 4.2.: Mean (μ_u) and standard deviation (σ_u) of u for various effects in simulated piercing.

reduced compared to the error due to the oscillations alone. This is due to the fact that measurements close to the bubble sides are rejected more often: the additional deformation may result in a bubble miss by one or more tips. Nevertheless, a significant part of the error due to the shape oscillations remains, since the shape oscillations can also cause relatively large errors in the center. The latter is caused by the following: due to the oscillations, the interface velocities are different from the bubble centroid velocity. Due to the high frequency of the oscillations the error contributions from the upper and lower interface do not cancel.

For the zig-zag and spiraling motion (Figures 4.28(b) and 4.28(c)) the inaccuracy produces a strong smearing in the probability distribution for ϕ_1. The effect for the Gaussian distribution (Figure 4.28(d)) is relatively small: the width of the distribution was already large due to the true distribution of velocity vectors.

Figures 4.28e-h show that the inaccuracy in the velocity seems virtually independent of the exact velocity direction distribution. In reality this may not be the case: if the probe is not aligned with the bubble velocity the longer contact line will affect the forces involved. An example of this behavior will be given in section 4.4.4.

Figure 4.29(a) shows the probability density function of ϕ_2 for case A1 and A4. For case A1 three peaks are observed. These can be explained by the probe geometry (Figure 4.29(b)). The location where the central tip pierces the bubble is specified with r' and ϕ_c. Two bubbles are shown, one with $\phi_c \approx 0°$, and one with $\phi_c > 0°$. If the bubbles are rising vertically (case A1), $\phi_2 \approx \phi_c$ for both bubbles due to the drifting and deformation effects (Figure 4.20). For $\phi_c \approx 0, 120, 240°$ and therefore for $\phi_2 \approx 0, 120, 240°$ piercing is possible up to smaller distances from the central tip to the side of the bubble due to the probe geometry. Consequently, the peaks in Figure 4.29(a) result. Especially these measurements close to the bubble sides contribute strongly to the tails in e.g. Figure 4.28(a). For case A4 the correlation of the inaccuracy with ϕ_2 is obscured by the wide distribution of velocity directions.

Chord length measurements

One or more estimate(s) for the bubble vertical chord length can be determined with (Guet et al. (2003), Mudde and Saito (2001)):

$$d_c^c = uT_0 \tag{4.20}$$

or (Frijlink (1987)):

$$d_c^{max} = u \cdot \max(T_i, i = 0, 1, 2, 3) \tag{4.21}$$

or by determining one estimate for each tip (Xue (2004)):

$$d_c^i = uT_i, i = \{0, 1, 2, 3\} \tag{4.22}$$

Interpretation of the results is strongly facilitated if the chord length estimate approaches $2b$. Since the bubble tips usually do not pierce the bubble in its center, smaller chordal lengths are obtained. At the same time, shape oscillations give inaccuracies in the velocity and residence time. These inaccuracies are usually correlated: an overestimation in the velocity (aspect ratio decreasing) is often accompanied by an overestimation in the residence time, and vice versa. This gives an overestimation of the chordal length that is actually pierced.

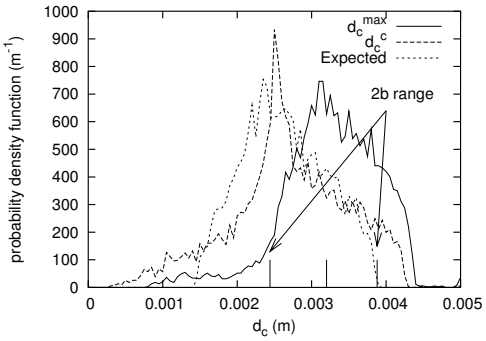

Figure 4.30.: Simulated chord length estimate probability density functions for case A4.

The use of equation 4.22 results in more measurements obtained from the bubble sides, and, consequently, strong smearing of the chordal length distribution occurs. Therefore this method is not considered further. If equations 4.20 and 4.21 are used, the chordal length is calculated with residence times obtained closer to the center of the bubble. The latter is, however, not necessarily true for larger ϕ_1 and for equation 4.20. Therefore, the use of equation 4.21 is preferred over equation 4.20 for velocity distributions with large ϕ_1.

Figure 4.30 shows the simulated chordal length probability density functions and compares it with the range of $2b$ values encountered for the given shape oscillations. The 'expected' probability density function for d_c^c is also shown. It is based on the distribution of chord lengths that are obtained for piercing at random radial position, accounting for the range of aspect ratios and the fact that the region close to the bubble sides does not produce velocity realizations. Comparison of the 'expected' distribution and the actual distribution of d_c^c shows the overestimation due to the oscillations and an underestimation of the true range of $2b$. The distribution of d_c^{max} produces the best match with the range of 2b. For all estimates, a wide distribution of d_c is obtained. This makes the measurement of an actual bubble diameter distribution more difficult.

4.4.2. Pseudo-2D column (Xue (2004))

Xue (2004) presents data for a pseudo-2D bubble column with relatively low gas fraction. The small gas fraction and bubble size with d_{eq}=3.6 mm provides a reasonable match with the conditions under which the various models for the simulated piercing were created. This is therefore a good test for the reliability of the simulated predictions. Artificial piercing events are simulated for the conditions under which this data was obtained: u=0.365 m/s (due to liquid circulation in the column), d_{eq}=3.6 mm, the aspect ratio fluctuates between 0.4 and 0.8 with frequency f_{osc}=40 Hz. The latter values for the oscillations were obtained from observations in the cylindrical bubble column used in the present investigation. Due to the relative low gas fraction, the bubble-bubble interaction is relatively small and the bubble motion is consequently modeled as a zig-zag path with maximum angle 25° (Fan and Tsuchiya (1990), see also appendix A). The bubble velocity direction varies sinusoidally in time. For each bubble, a random direction is

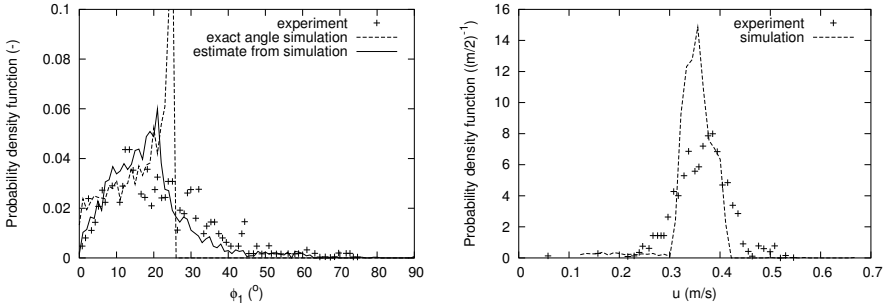

Figure 4.31.: Comparison simulated piercing data and experimental data from Xue (2004) for d_{eq}=3.6 mm.

picked from the sinusoidal distribution. During the piercing process the velocity direction is kept constant to facilitate the computations. Shape oscillations, the drifting effect and deformations are taken into account.

Figures 4.31(a) and 4.31(b) compare the results of the simulation and the results from Xue (2004). The agreement for ϕ_1 is quite good. This suggests that the model does a reasonable job and that the shape of the distribution that is measured should be interpreted with care: the tails are measurement artifacts, the location of the maximum of the distribution is altered strongly by the measurement inaccuracies. The standard deviation of the simulated velocity estimates (Figure 4.31(b)) is approximately a factor 0.6 smaller than the experimental standard deviation. The difference can probably be contributed to the true variations in the velocity. This indicates that a large part of the measured bubble velocity fluctuations are due to measurement inaccuracies.

When the results of the simulation are considered, the agreement between the camera observations and probe measurements in Xue (2004) is surprising. A test with a pseudo-2D bubble column with a depth of 1.3 cm shows that the movement of bubbles is strongly three dimensional, and therefore the bubble inclination angle ϕ_1 is generally not aligned in the plane of the camera projection. Estimation of the angle ϕ_1 using observations from a single camera is therefore inaccurate (Rensen (2003)). For example, the projection of the velocity vector gives estimated values ϕ_1' with the camera that are smaller than the actual values ϕ_1. The reduction can be up to a value 0.65, if a random angle ϕ_2 is assumed. Bubbles with velocity vector aligned towards or away from the wall will appear more rounded and the inaccuracy in ϕ_1' may increase further. This may explain why Xue (2004) finds good agreement for ϕ_1 whereas the simulations presented in the current investigation indicate a larger inaccuracy.

4.4.3. Bubble identification

In the experimental signals, it is crucial to correctly match the bubble piercings for the various fibers. The matching is performed in the following way (Figure 4.32). For each bubble pierced by the central tip, a search is performed in the signals of the other tips for the bubble with the

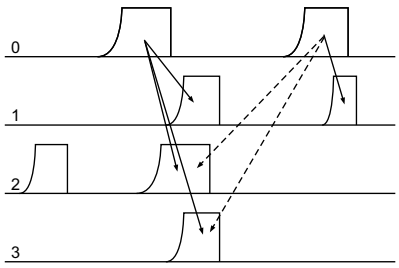

Figure 4.32.: Matching of bubbles detected with various fibers.

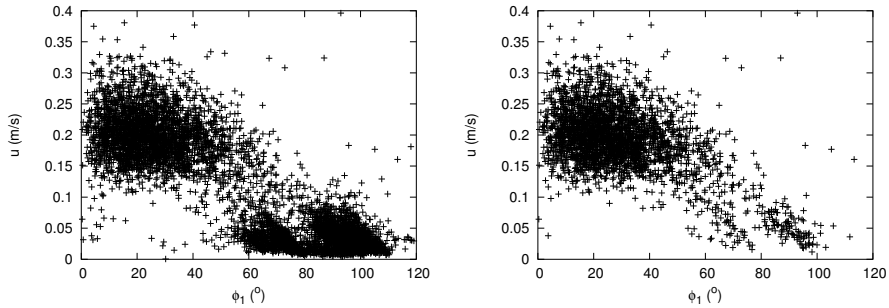

(a) No validation (b) Validation

Figure 4.33.: Effect of the extra validation on bubble output. U_g=0.034 m/s (α=17%), probe aligned vertically in the center of the column.

arrival time closest to the arrival time for the central tip. For many interactions, not all of the four fiber tips are pierced by the bubble. Consequently, an incorrect match will result (dashed line in Figure 4.32). This incorrect match results in an erroneous velocity measurement. An example is shown in Figure 4.33(a): the outliers are perceived by the probe as bubbles with ϕ_1 in the range 60°-110°, with u<0.1 m/s. As a result, the estimation of velocities for relatively slow bubbles with ϕ_1 in the range 60°-110° is complicated. For higher void fractions, the time between the arrival of subsequent bubbles at the probe decreases and the range of outliers may grow, further increasing the problem. For this reason, an extra check is performed on the bubble pair. For the selected bubble in channel i a check is performed whether the matched bubble in channel j is indeed the closest. If not, the measurement is discarded. This check is performed for all possible channel combinations. The result is shown in Figure 4.33(b). This way, most of the outliers are removed without affecting the correct measurements. Further improvements may be obtained by selecting regions of interest for u and ϕ_1 based on knowledge of the flow properties.

4.4.4. Accuracy in the cylindrical bubble column - effect of probe inclination

In the previous sections, the accuracy of the four point probe measurements was analyzed using artificial signals. For the generation of the signals, models were used based on observations of

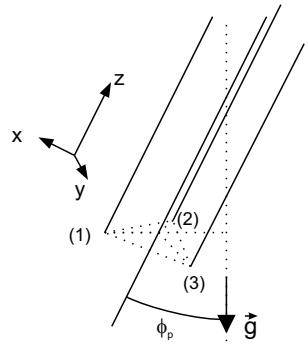

Figure 4.34.: Rotation of probe.

probe-bubble interactions for small ϕ_1. If ϕ_1 is large, the bubble is not pierced perpendicularly and the inaccuracies may be larger. In addition, the asymmetric piercing (Figure 4.24(a)) may produce a bias in the average velocity direction. These effects are studied by measuring the velocity distribution inside the bubble column with a four point probe rotated over an angle ϕ_p in the x-z plane (Figure 4.34).

The use of ϕ_1 and ϕ_2 for the analysis of the average velocity estimate direction is impractical for small ϕ_1: if the mean of ϕ_1 is nonzero, this does not necessarily mean that the average velocity direction is non-vertical. Instead, two new parameters are used (see Figure 4.35(a)):

$$\phi_x = \phi_1 cos(\phi_2) \tag{4.23}$$

$$\phi_y = \phi_1 sin(\phi_2) \tag{4.24}$$

With these parameters, a plot of (ϕ_x,ϕ_y) gives a much clearer idea of the distribution of the velocity direction with respect to the probe orientation. The line from the origin to (ϕ_x,ϕ_y) has the same orientation as (u_x,u_y), and its length denotes the angle ϕ_1. Measurements are performed close to the center of the cylindrical bubble column, for U_g=0.034 m/s and uniform gas injection. For these conditions no large scale structures are present, and therefore the average bubble velocity vector has ϕ_1=0°, so ϕ_x=0° and ϕ_y=0°. ϕ_p is varied in between -40° and +40°. The measured velocity vectors are transformed back to the laboratory frame of reference to check the influence of ϕ_p.

First, the measurements for ϕ_p=0° are discussed. Figure 4.36 compares the velocity probability density function with the simulated piercing result from Figure 4.28 (drifting, deformation and oscillation for case A4). This suggests that a large part of the variation in the velocity is due to the shape oscillations of the bubble. Figure 4.35(b) shows the probability density function for ϕ_x and ϕ_y for ϕ_p=0°. The shape is clearly Gaussian and symmetric.

Next, ϕ_p is varied, the velocity vectors are transformed back and ϕ_x and ϕ_y are determined. Since the rotation of the probe is performed in the x-z plane, only ϕ_x changes significantly. Figure 4.37(a) shows the probability density function for ϕ_x for very distinct values of ϕ_p. Whereas the distribution is clearly symmetric for ϕ_p=0°, it is skewed for $\phi_p \neq$0° and its mean, μ_{ϕ_x}, nonzero.

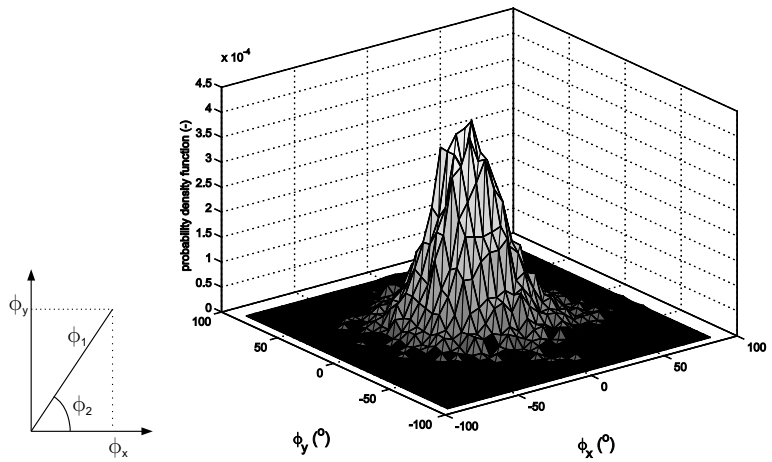

(a) (b)

Figure 4.35.: (a) Definition of ϕ_x and ϕ_y. (b) Probability density function for ϕ_x and ϕ_y, ϕ_p=0°.

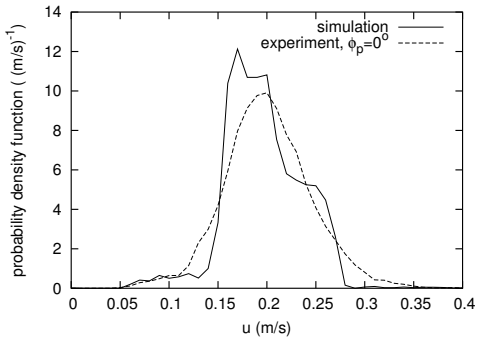

Figure 4.36.: Probability density functions for velocity u, comparison experiment and simulated piercing.

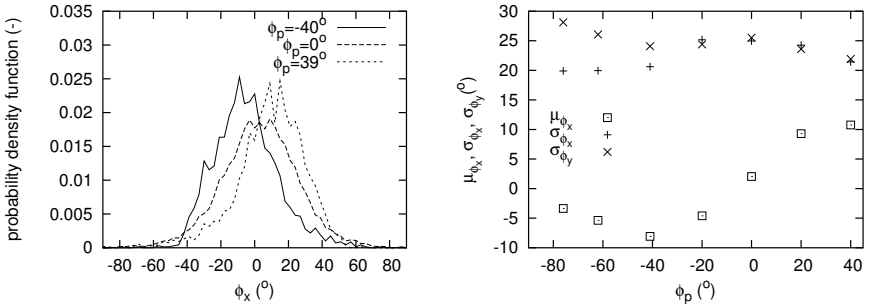

(a) Probability density function for ϕ_x (b) Mean and standard deviation for ϕ_x and ϕ_y

Figure 4.37.: Probability density function and mean for ϕ_x for various probe inclinations.

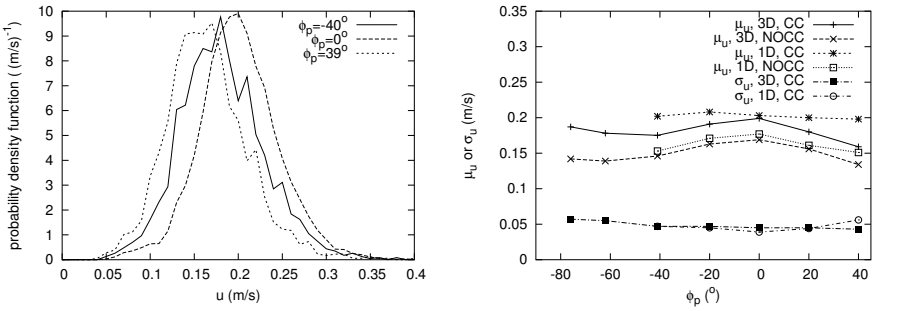

(a) Probability density function for u

(b) Mean and standard deviation for u. CC=curvature correction, NOCC=no curvature correction

Figure 4.38.: Probability density function and mean for u for various probe inclinations.

The mean is shown as a function of ϕ_p in Figure 4.37(b). Approximately for $\phi_p > 0°$ we find $\mu_{\phi_x} > 0°$; for $\phi_p < 0°$ we find $\mu_{\phi_x} < 0°$. This bias increases with $|\phi_p|$ for $|\phi_p|$<40° and reduces with $|\phi_p|$ for $|\phi_p|$>40°. The same effect is observed if the probe is rotated in another plane than the x-z plane. The small offset observed in Figure 4.37(b) is, however, not reproduced in these cases and is probably due to a small inaccuracy in the alignment or in the probe tip positions. The observations suggest that there is an asymmetric drifting and/or deformation effect. For the single fiber also an asymmetric drifting effect was observed (Figure 3.21, explained in Figure 4.24(a)), but with an opposite trend than observed here (movement of bubbles toward the fiber, i.e. bias to smaller or more negative μ_{ϕ_x} for $\phi_p > 0°$). Therefore, the asymmetry is probably produced by an asymmetric deformation effect. Apart from the small bias, no effect is observed on the standard deviations σ_{ϕ_x} and σ_{ϕ_y}: these are almost identical and independent of ϕ_p (Figure 4.37(b)). The result suggests that the average velocity direction can be determined quite well, and if the bubble ensemble has on average a non-vertical direction this can be measured.

The effect of ϕ_p on the velocity magnitude u is shown in Figures 4.38(a) and 4.38(b) (3D,

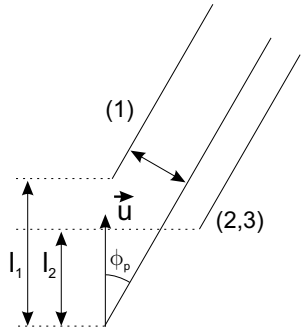

Figure 4.39.: Path lengths of interaction for piercing under an angle ϕ_p.

CC curves). It is clear that the use of no curvature correction ('NOCC') results in much smaller values for μ_u than if curvature correction is employed, the offset is approximately constant. In section 4.2.3 the improved accuracy obtained with curvature correction was discussed, for this reason only results with this correction are discussed from this point. A bias in μ_u to smaller velocities is observed for $\phi_p \neq 0$, the standard deviation σ_u is almost independent of ϕ_p. This bias in the mean is probably caused by a stronger deceleration of the bubble by the probe if the fiber direction is not aligned with the bubble velocity. Moreover, if ϕ_p increases, the bubble is hit by a second, and usually also a third tip before the last tip is hit. The instant when this occurs, becomes earlier in time for a larger ϕ_p (decrease of l_2 in Figure 4.39). Therefore, more deceleration is obtained during the measurement. A maximum deceleration is obtained for $|\phi_p| \approx 40°$. For larger angle the bias decreases again. This can be explained with the more or less constant duration of the interaction (constant l_1) for $0° < |\phi_p| < 40°$. For $|\phi_p| > 40°$ l_1 rapidly drops, leaving less time for drifting and deformation effects, and the bias reduces. The bias is investigated in more detail by determining the correlation between ϕ_1 and the velocity (Figure 4.40(a)). For a measurement with given ϕ_p, the mean velocity $\overline{u}_{\phi_{1,i}}$ is determined for the measurements with $\phi_{1,i} - \Delta\phi_1 < \phi_1 \leq \phi_{1,i} + \Delta\phi_1$. $\Delta\phi_1$ is taken as 5°. Values for $\overline{u}_{\phi_1}$ are determined for ϕ_p=-76°, -62°, -41°, -20°, 0°, 20° and 40°. The trends in $\overline{u}_{\phi_1}$ are very similar to the trend in $\mu_u(\phi_p)$ and are therefore clearly for a large part a measurement artifact. This shows that it is not possible to investigate weak variations of the velocity with ϕ_1.

Not only the inaccuracy in ϕ_1 and u obtains a maximum value for bubbles approaching the probe with an angle of 45° ($|\phi_p| \approx 45°$), but also the amount of rejected bubble piercings has its maximum value for bubbles traveling under this angle (Figure 4.40(b)). Finally, Figure 4.40(c) compares the relative underestimation for the velocity with that of the bubble chord length (with respect to the measurement at $\phi_p = 0°$). This shows that for $|\phi_p| \leq 40°$ the relative underestimation of the chord length is about half of that of the velocity: part of the underestimation due to the deceleration cancels due to the longer residence time. The results show that, although the probe can measure bubbles coming from angles in the range 0-90°, a bias occurs which is dependent on the direction of the bubble. The performance for a probe under 90° seems actually relatively good. This suggests a very interesting application of the probe, where both positive and negative axial bubble velocities can be measured reasonably accurately.

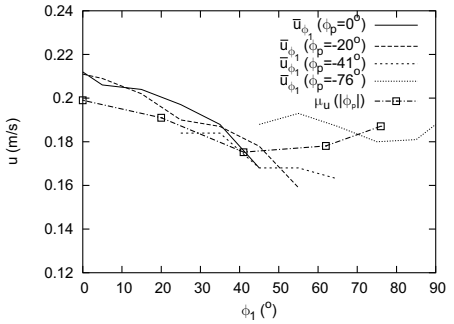

(a) Comparison of $\overline{u}_{\phi 1}$ and μ_u

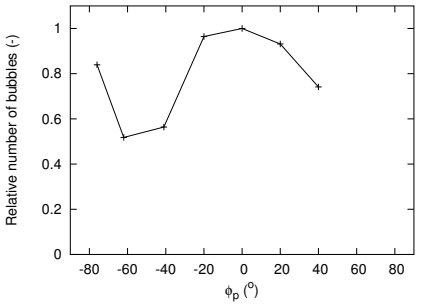

(b) Change in number of measurements with ϕ_p

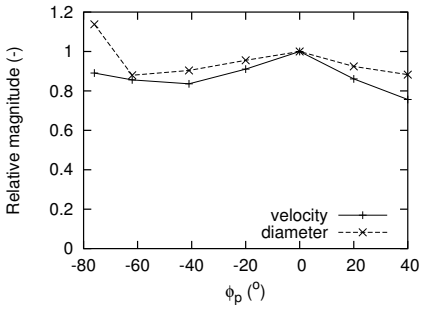

(c) Change in magnitude of the velocity and diameter estimates with ϕ_p (normalized with the values for $\phi_p = 0^\circ$)

Figure 4.40.: Velocity bias, diameter bias and variation in number of measurements for increasing ϕ_p

1D algorithm vs 3D algorithm

A comparison between the results of the 1D algorithm (equations 4.1 and 4.3) and the 3D algorithm is made. A first test with both experimental and simulated signals shows that the use of either equation 4.1 or equation 4.3 gives no significant differences if the same type of curvature correction is used. For this reason, equation 4.3 is used from this point on.

Figure 4.38(b) also shows the velocity estimate obtained with the 1D algorithm ($\beta_u = 0.1$). Due to the large spread in velocity directions, there are always some bubbles that pierce the probe in its axial direction (for $|\phi_p|$ up to 40°) and sufficient bubbles remain after selection in the case of the 1D algorithm. Figure 4.40(a) suggested earlier that the velocity has at most a weak dependence on the bubble velocity direction. Consequently, the velocities measured using the 1D algorithm are more or less independent of ϕ_p and are very close to the curvature corrected 3D measurements for small ϕ_p. Therefore, it seems that the 3D algorithm provides no significant improvement over the 1D algorithm if one is only interested in the velocity magnitude and/or bubble diameter and if the technique is applied in flows where there is a preferential direction of movement for the bubbles and no significant correlation between the velocity magnitude and direction occurs. For flows where this is not the case, the 3D algorithm should be used.

4.4.5. Gas fraction accuracy

If the void fraction is estimated using a single fiber probe generally a net underestimation is obtained (Chapter 3 and Barrau et al. (1999)), for the stretched fiber type typically around 10%. The overestimation by the deceleration of the bubble by the interaction with the fiber is smaller than the underestimation caused by the deformation and other interaction effects. If a four point probe is used, however, the deceleration is enhanced by the upper three tips. Xue (2004) compares void fraction measurements of Computed Tomography and a four point probe, and find agreement within ±15%. Guet et al. (2003) present void fraction measurements of a single fiber probe and a four point fiber probe. The four point fiber probe gives about 10-15% higher void fraction estimates than the single fiber probe. These results suggest that at least partially the underestimation and overestimation effects cancel, thus the intrusive effects observed do not make the four point fiber probe technique unsuited for void fraction measurements. The accuracy, however, will be dependent on, for example, the bubble size.

4.4.6. Improvement of the four point probe technique

The previous analysis considered the various factors responsible for the inaccuracies in the bubble properties if the four point probe technique is used. The inaccuracy in the velocity magnitude and orientation distribution and the diameter distribution can be quite big, especially for the lower bubble velocity (around 0.2 m/s) encountered in the bubble column. A large part of the inaccuracy is dominated by the shape oscillations. Of course, these shape oscillations cannot be altered and therefore the improvements that can be achieved are limited. Unfortunately, the frequency of these shape oscillations is very unfavorable (section 4.2.4), and therefore a change in the probe dimensions (Δs and d_p) will probably not give improvements. A smaller probe (reduction of Δs) could even increase the inaccuracy due to higher mode oscillations. The results in Figure 4.38(b) (for ϕ_p=90°) suggest that the size reduction could reduce the effect

of deformations and drifting somewhat. This would have a positive effect on e.g. the bias in the mean of the velocity. A larger probe (increase of Δs) could in theory average out some of the fluctuations due to shape oscillations, but in the bubble column these oscillations are less periodic and the larger scale would increase the total piercing time. This would provide more time for the probe-bubble interactions to deform the bubble or alter the velocity (direction) of the bubble.

Some improvement may be expected if thinner fibers are used. This would reduce the magnitude of the forces involved in the probe-bubble interaction. Especially the measurement of bubbles traveling under a relatively large angle with the bubble may benefit. Since the stiffness of the probe decreases with the diameter, glass is a preferred material over plastic fibers, since the position of the tips has to be known with a high precision. The thinner fiber may be achieved by either using fibers with smaller diameter (e.g. with a core diameter of 50 μm) or etching of fibers with larger diameter (with core diameters of 100-200 μm). Etching (e.g. Wong et al. (2002), Buchholz and Auracher (2002)) would also allow for better defined and more reproducible tip shapes, facilitating the measurement of an accurate piercing time. If a 3C (Cone-Cylinder-Cone) tip shape (like Cartellier and Barrau (1998b)) would be used, additional axial velocity component information can be obtained from the rise-time of the signal: eight arrival times are available instead of four. This extra information may be used to improve the accuracy of the technique. A first test shows that the width of the velocity distribution may be significantly reduced. Some improvement may also be obtained with a coating on the fiber (except the active part). This way the contact angle may be increased, reducing the deformation of the bubble. Finding an optimal contact angle is difficult, however, since the inclination of the interface with respect to the probe and therefore the deformation varies strongly with the velocity direction and radial piercing position.

Considering the difficulties associated with the improvement of the accuracy of the four point probe technique, it would be interesting to test endoscopic methods for the measurement of e.g. the bubble size and aspect ratio. With this technique, local probe-interaction effects play a much smaller role and horizontal dimensions can also be determined. However, image processing for bubbles in dense flows is difficult and the flow around the imaging device could be altered strongly, making it probably less suited for, e.g., the analysis of the velocity vector orientation.

4.5. Conclusions

The inaccuracy of the estimation of velocity magnitude and direction in a bubble column with a four point optical probe has been investigated via experiments and simulations of modeled piercing. The simulations indicate that the errors due to inaccuracies in probe geometry are much smaller than other inaccuracies. If the probe pierces a curved interface, curvature correction is required to get accurate estimates. This correction should be based on the average bubble shape that is encountered, also in the case of dynamic shape oscillations. The best choice for a curvature correction criterion is therefore probably based on an ellipsoidal shape. Deviation from the ellipsoidal shape due to shape oscillations cause inaccuracies in the velocity magnitude estimate of typically 5%. If these shape oscillations have high frequencies (typically 40 Hz), this inaccuracy increases to typically 10%. Aspect ratio oscillations produce even larger errors:

typically 20% of the velocity magnitude, and are therefore the dominant error source. The most important probe-bubble interactions are the drifting effect and deformation of the bubble. These effects create significant inaccuracies in the estimate of the velocity direction. Analysis of the total error shows that the magnitude of bubble velocity fluctuations should be interpreted with care: a large part of the fluctuations can be due to measurement inaccuracy. The typical uncertainty in the velocity angle ϕ_1 is around 20^o. This means that for individual bubbles the velocity direction estimate is not very precise. Nevertheless, the mean direction of a large number of bubbles can be estimated quite accurately, although for non-vertical movement a bias exists towards larger ϕ_1 values. It obtains a maximum value around ϕ_1=45°. A bias exists for the velocity magnitude as well: for bubbles that do not move in the probe's axial direction the velocity is underestimated, the underestimation increases with ϕ_1. Possibilities for improvement of the probe technique are discussed: an increase in the accuracy is expected if thinner fibers are used, nevertheless the dominant error due to shape oscillations cannot be avoided.

List of symbols

Roman symbols

$\vec{a}, \vec{b}$	vectors for calculating the drift effect	-
a	bubble semimajor axis length	m
$aspectratio$	time dependent aspect ratio	-
b	bubble semiminor axis length	m
b^+, b^-	constants defining bubble shape	m
b_{ϕ_1}	strength of the fluctuations of ϕ_1	rad
d_c^c	bubble chord length calculated from T_0	m
d_c^{max}	bubble chord length calculated from maximum residence time	m
d_{eq}	equivalent bubble diameter	m
d_p	radial distance between central tip and other tips	m
$\hat{d}_b$	initial bubble size estimate	m
F_{probe}	force of probe acting on the bubble	$kg\ m\ s^{-2}$
f_{lamb}	Lamb oscillation frequency	s^{-1}
f_{osc}	bubble oscillation frequency	s^{-1}
k	Lamb oscillation mode	-
l	chordal piercing length	m
N	number of (artificial) measurements	-
p	probability density function ϕ_1	rad^{-1}
R	tip radius of curvature	m
r'	radial position of piercing	m
T	residence time	s
$T_{correct}$	curvature correction	s
T_r^*	dimensionless residence time difference	-
$T_{r,max}^*$	dimensionless residence time difference selection threshold	-
t	time when tip is hit	s
t_{first}	instant when the first tip touches the interface	s

U_g	superficial gas velocity	$m\ s^{-1}$
u	velocity	$m\ s^{-1}$
x, y, z	coordinates in probe frame of reference	m
x', y', z'	coordinates in bubble velocity frame of reference	m
x'_p	piercing coordinate	m

Greek symbols

α	probe-bubble impact angle	rad
α_d	local surface inclination with respect to the bubble major axis	rad
β_t	selection criterion based on time of flight	-
β_u	selection criterion based on velocity	-
Δl	distance tip to the interface when tip 0 enters the bubble	m
$\Delta l'$	Δl plus deviation due to tip shape	m
Δs	axial distance between central tip and other tips	m
Δt	time of flight	s
δ	inaccuracy	various
δr_t	random tip displacement for error analysis	m
μ	mean	various
ρ_c	liquid density	$kg\ m^{-3}$
σ_l	surface tension	$kg\ s^{-2}$
σ	standard deviation	various
ϕ_1	angle between probe axial direction and velocity vector	rad
$\phi_{1,max}$	maximum for ϕ_1	rad
ϕ_2	angle of projection of the velocity vector on the xy plane to the x-axis	rad
ϕ_c	angle where bubble is pierced	rad
ϕ_d	drift angle	rad
ϕ_{osc}	bubble oscillation phase	rad
ϕ_p	probe inclination angle	rad
ϕ_x	bubble velocity angle	rad
ϕ_y	bubble velocity angle	rad

Subscripts

deform	due to deformation effect
no deformation	due to shape oscillation
i	tip index
j	(artificial) measurement index
t	tip
tr	tip with error in location

5. Estimation of power spectra of LDA signals in bubbly flows [1]

The accuracy of the estimation of turbulence power spectra from Laser Doppler Anemometry (LDA) signals obtained in bubbly flows is studied. Special attention is paid to the effect of the random sampling and the gaps in the signal created by the bubbles. Suitable signal processing techniques to deal with these effects are selected. Next, the influence of the local flow field around the bubbles on the power spectra is investigated, and the techniques to reduce this influence are evaluated.

5.1. Introduction

The hydrodynamics of bubbly flows are characterized by a wide range of scales. First, (pseudo)-turbulence is found at the scale of the bubble diameter and at smaller scales, caused by the flow around the bubbles and the wakes of bubbles. At the same time, density gradients generate vortical structures at the scale of the equipment diameter, while turbulent cascade processes break down the vortices to smaller scales. The understanding of these processes in bubbly flows, such as found in bubble columns, is still incomplete. The measurement of accurate turbulence power spectra of the liquid velocities in these flows will help in the understanding of the interplay of all these phenomena. Accurate estimates of the slopes in the power spectra can give more information on the nature of the cascade process, and, e.g., the influence of large scale structures on this process. In literature different values for the slope are reported (-8/3 in Lance and Bataille (1991), -5/3 in Mudde et al. (1997a)), but little attention is paid to accuracy, in particular possible bias sources in the signal processing.

The most commonly used techniques for measurement of the liquid velocity in bubbly flow are Laser Doppler Anemometry (LDA), Particle Image Velocimetry (PIV) and hot film anemometry. Particle Image Velocimetry has limited temporal resolution, and is limited to small equipment scales and/or very low void fractions due to the restricted optical access. Hot film anemometry, on the other hand, has sufficient temporal resolution, is not limited to measurements in small equipment or small distances to the wall, but disturbs the flow and the bubbles. In addition, its signal processing is complicated, since bubble signatures need to be removed from the signal (Rensen et al. (2005)). LDA has the advantage that the flow is not disturbed, and the technique does not require removal of velocity realizations due to the bubbles, since the velocity realizations are originating predominantly from the liquid seeding (Mudde et al., 1997a). LDA has limits with respect to the optical accessibility: the laser beams can be blocked by the bubbles. However,

[1] Parts of the sections 5.1-5.7 have been published as W.K. Harteveld, R.F. Mudde and H.E.A. van den Akker, "Estimation of turbulence power spectra for bubbly flows from Laser Doppler Anemometry signals", Chem. Eng. Sci. (60), 2005, pp. 6160-6168

compared to PIV it has a higher temporal resolution and measurements are possible up to relatively high void fractions and larger equipment scale.

For the estimation of power spectra from LDA velocity signals, however, particular difficulties in the signal processing are encountered. First, noise levels are relatively high due to the small amounts of light detected. Furthermore, the signal is randomly sampled, which is due to the random distribution of seeding particles.

Consequently, no obvious equivalent to the Discrete Fourier Transform is available as a computational algorithm. For single phase flows, a wide range of estimators has been developed over the years to deal with the random sampling. Several classes of techniques can be identified. A first class reconstructs the signal and resamples it equidistantly. This is usually done with interpolation techniques, e.g. Sample and Hold (Adrian and Yao, 1987) or the Shannon algorithm (Veynante and Candel, 1988). An overview of reconstruction techniques is presented by Britz and Antonia (1996). The reconstruction is followed by spectral estimation employing the periodogram (i.e. the FFT) or nonlinear spectral estimation. Another class employs a slot correlation (Benedict et al., 2000) followed by a cosine transform. The approach taken by Van Maanen and Oldenziel (1998) is to fit a general model to the slot correlation coefficients; the estimated power spectrum is the Fourier transform of the fitted model. In addition, estimation via time series analysis has been extended for non-equidistant data (Bos et al. (2002)). The final class of techniques comprises the Lomb-Scargle method (Lomb, 1974; Scargle, 1989) which originates from astrophysics. This technique was especially developed for the estimation of narrow peaks in the power spectrum and is not suited for the estimation of the distribution of power over the frequencies (Broersen et al., 2000). For this reason, this latter technique is a poor choice for the estimation of turbulence spectra and is not considered further in the present investigation.

In the case of bubbly flow, the random sampling is further complicated by the presence of the bubbles (Figure 5.1). The measurement volume only exists if none of the laser beams is blocked by a bubble. This results in the creation of large gaps in the data, which may influence the properties of the signal processing. Moreover, this gives a decrease in the data rate (see appendix D), increasing the variance and making the higher frequency information in the power spectrum less reliable. At the moments when a bubble crosses the measurement volume, the liquid velocity is not defined, which raises philosophical questions to the interpretation of the power spectrum. At distances beyond 1-2 bubble diameters from the wall, most gaps, however, originate from blocking at other locations than the measurement volume.

The multiple reflection of the laser beams by bubbles behind the measurement volume, combined with the use of the backscatter mode results in relatively high noise levels for LDA in bubbly flow. The passage of the bubbles near or through the measurement volume generates additional liquid velocity fluctuations which add power the spectrum, especially at higher frequencies. The study of the cascade of large structures in the flow to smaller structures is complicated by these fluctuations.

The present work investigates the problems encountered when calculating power spectra for measurements obtained using LDA, paying particular attention to (i) the effects and problems introduced by the presence of the bubbles generating gaps in the data and (ii) the effect of the velocity fluctuations due to the local flow around the bubbles on the spectra. Various signal processing techniques are compared and their suitability for application to signals obtained in bubbly flows is studied. The approach taken is to generate synthetic signals with known spectra,

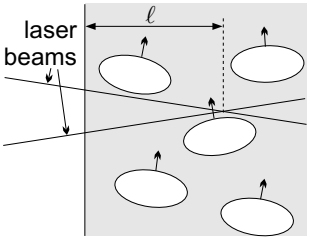

Figure 5.1.: LDA in bubbly flow.

which are randomly sampled using a Monte Carlo technique mimicking the sampling process in a bubbly flow. Finally, techniques are considered for the removal of the velocity realizations which contain the strongest contributions of the local flow around the bubbles.

5.2. Generation of synthetic signals of LDA in bubbly flow

In order to study the performance of the spectral estimators, synthetic data is required which has typical properties of the real bubbly flow signals. An equidistant velocity time series with a known turbulent power spectrum is generated at a high frequency. This is obtained by convolution of white noise with the impulse response of a digital low-pass filter with specified power spectrum. Next, the passage of seeding particles with a specified particle rate $\dot{N}_p$ is simulated by generating random particle arrival times t_i. The random intervals between the arrival of particles have a Poisson distribution, and are generated with $\Delta t_p = -\frac{1}{\dot{N}_p} ln(RND)$. RND is a random number uniformly distributed between 0 and 1. The velocity u_i at the time t_i is determined from the high-frequency equidistant velocity time series via interpolation.

Next, the passage of bubbles is simulated. Two laser beams are considered. These originate from a backscatter probe with focal length 35 cm and beam distance 5 cm before the lens. The beams pass through a transparent wall to form a measurement volume at a distance l from the wall inside the bubbly flow (see Figure 5.1). For each instant t_i, the algorithm determines whether any of the laser beams is blocked by a bubble (more details can be found in appendix A). Around the laser beams and the measurement volume, a control volume is considered. Virtual bubbles are inserted at random positions at the bottom of the control volume, at random times with intervals which have a Poisson distribution. The void fraction α is assumed constant throughout the flow. In order to obtain a realistic bubble blockage duration distribution, the motion and shape of the bubbles is modeled in detail. Each bubble has an ellipsoidal shape with equivalent diameter of 4.5 mm and aspect ratio of 0.65. The bubble follows a zig-zag trajectory with a velocity of 0.2 m/s. The rocking angle of the bubble varies sinusoidally with time, with a maximum of 25° (based on Fan and Tsuchiya (1990)). The minor axis of the bubble is parallel to its path, consequently its path is specified by the time evolution of the rocking angle. The initial phase and plane of zig-zag motion is chosen randomly for each bubble. Possible blockage of the laser beams by a bubble is determined for each bubble by determining the intersections of the bubble surface and the lines that follow the undisturbed laser beam paths. If an intersection

is found between the wall and the measurement volume at the time t_i, the velocity realization (t_i, u_i) is removed from the series.

The present technique generates signals with a realistic distribution of the data arrival times. The properties of the artificial velocity signal that is obtained correspond to a certain extent to those found in true bubbly flow signals. In sections 5.3-5.8 the local flow around the bubble is not included in the model. It is included in the sections starting from 5.9. In addition, the fact that the liquid velocity signal is actually not defined when the bubbles cross the measurement volume is not taken into account. The signal does, however, have well-defined statistical properties that allow an accurate evaluation of the estimated spectra and the performance of the signal processing techniques with respect to the non-equidistant nature of the signals. In addition, the shapes of the chosen spectra resemble those reported in, e.g., Groen (2004).

5.3. Sample and Hold technique

A commonly applied technique is to reconstruct the signal with the use of interpolation techniques, and resample it at equidistant time intervals at a high frequency. Standard FFT techniques can subsequently be applied for the estimation of the power spectrum. The most common reconstruction technique is the zeroth-order interpolation or Sample and Hold (S&H) method. The method is illustrated in Figure 5.2. A stationary, zero mean velocity record $u(t)$ is considered, which is sampled randomly at intervals t_k. The reconstructed signal $r(t)$ is obtained via the Sample and Hold reconstruction technique: the sampled value obtained at t_k is kept constant until t_{k+1}. Next, equidistant resampling is performed with frequency f_e. This means that $r(t_i) = u(t_k)$ for $t_k \leq t_i < t_{k+1}$ and $t_i = iT_e$ ($T_e = 1/f_e$).

The work by Adrian and Yao (1987) investigated the effect of the reconstruction with S&H on the power spectra. For data with Poisson distributed interarrival times (encountered in single phase flows without velocity bias) they arrived at the following expectancy for the spectrum:

$$E[\hat{S}(f)] = \frac{1}{1 + f^2/(\dot{N}_p/2\pi)^2} \left(S(f) + \int_0^\infty R'(\tau) e^{-\dot{N}_p \tau} d\tau \right) \tag{5.1}$$

with $\hat{S}(f)$ the estimated power spectrum, $S(f)$ the true power spectrum, $\dot{N}_p$ the particle rate, i.e. the mean number of particles passing the measurement volume per unit time and $R(\tau)$ the autocovariance function of the velocity series. The effect of the reconstruction is the addition of white noise (so called 'step noise', the second term in the brackets) and a low-pass filtering operation with low pass cut-off frequency of $\dot{N}_p/(2\pi)$. This results in a redistribution of energy from high frequencies to low frequencies. Consequently, the shape of the power spectrum is no longer reliable for $f > \dot{N}_p/(2\pi)$, and the absolute values are unreliable for the entire frequency range. This indicates that for bubbly flows, where the particle rate $\dot{N}_p$ is relatively low, only the shape of the power spectra can be estimated up to relatively low frequencies.

Correction technique

Equation 5.1 suggests that if the step noise level and the particle rate are known, it is possible to get an unbiased estimate of the power spectrum via a correction method. Nobach et al. (1998a)

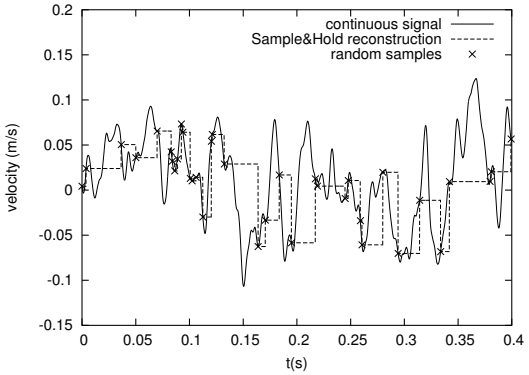

Figure 5.2.: Sample and Hold reconstruction technique.

and Simon and Fitzpatrick (2004) present techniques to perform this correction. Nobach et al. (1998a) correct the autocovariance function that is obtained via S&H reconstruction. This was one of the two recommended techniques in the overview of a benchmark of spectral estimators presented by Benedict et al. (2000). Simon and Fitzpatrick (2004) directly correct the biased power spectrum estimate. For discrete time signals resampled with frequency f_e (which may be freely chosen) the Power Spectral Density function (PSD), of the reconstructed signal is given by:

$$S_{rr}(f_k) = |L(f_k)|^2 (S_{uu}(f_k) + S_{ss}) \tag{5.2}$$

with $f_k = f_e k/N_f$, $k \in [0, N_f - 1]$ (N_f is the number of Discrete Fourier Transform (DFT) points), where $S_{uu}(f)$ is the PSD of the original signal $u(t)$ and S_{ss} the step noise. For discrete signals, a slightly different low-pass filter is obtained than the result by Adrian and Yao (1987). If the arrival of velocity realizations occurs randomly, i.e. the arrival times are a homogeneous Poisson process, the expression for the low-pass filter is given by (Simon and Fitzpatrick, 2004):

$$|L(f_k)|^2 = \frac{T_e \dot{N}_p}{2} \frac{1 - e^{-2T_e \dot{N}_p}}{1 - 2cos(2\pi \frac{k}{N_f}) + e^{-T_e \dot{N}_p} + e^{-2T_e \dot{N}_p}} \tag{5.3}$$

provided $f_e = \frac{1}{T_e} \gg 2 f_{max}$, where f_{max} is the maximum frequency for which we want to estimate. Using the fact that the variance of the original signal $u(t)$ and the reconstructed signal $r(t)$ are identical, the step noise can be estimated with (Simon and Fitzpatrick, 2004):

$$\hat{S_{ss}} = \frac{1}{N_f} \left(\sum_{k=0}^{N_f - 1} \frac{S_{rr}(f_k)}{|L(f_k)|^2} - \sum_{k=0}^{N_f - 1} S_{rr}(f_k) \right) \tag{5.4}$$

A corrected PSD can be estimated with:

$$S_{cc}(f_k) = \frac{S_{rr}(f_k)}{|L(f_k)|^2} - \hat{S_{ss}} \tag{5.5}$$

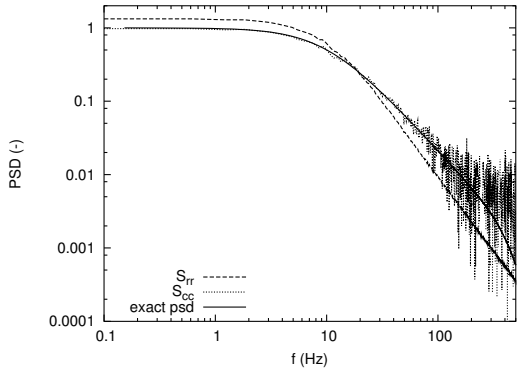

Figure 5.3.: Results of correction procedure for artificial signals. 300000 velocity samples, $\dot{N}_p = 100Hz$, $f_e = 10^4 Hz$, $N_f = 16384$

The performance of the correction is illustrated with an artificial signal. Reconstruction of the irregularly sampled signal is performed using the Sample and Hold technique. The PSDs are calculated with the periodogram (Welch window, 50% overlap and no zero padding). An example is shown in Figure 5.3. The shape of the PSD without correction is not reliable above the cut-off frequency of 16 Hz, and the PSD level below this frequency is not reliable due to transfer of energy from high to low frequencies by the Sample and Hold energy redistribution. The PSD with correction, however is reliable up to approximately $\dot{N}_p$, which is a significant improvement.

Dead time and multiple validation

Application of this method to bubbly flow has a number of complications. The use of equation 5.3 requires an accurate estimate of the mean data rate $\dot{N}_{tot}$. $\dot{N}_{tot}$, the mean data rate, is the average number of velocity realizations that is acquired per unit time. It may differ strongly from the mean particle rate $\dot{N}_p$, i.e. the number of particles passing the measurement volume that can scatter enough light for detection. Possible causes for the difference are multiple validation, a dead time in the processor (Nobach et al. (1998a)) and the presence of bubbles. The influence of the multiple validation and dead time on the correction technique is investigated in the present section. The effect of the bubbles is investigated in subsequent sections.

The effect of dead time and multiple validation is simulated. The dead time is realized by removing all bursts which follow a previous burst within a time interval with length T_{dead}. Multiple validation is simulated by insertion of extra velocity realizations for some of the bursts. If $RND < P_{mv}$, the burst located at t_k is replaced by a burst pair located at times $t_k - \Delta T_{mv,k}$ and $t_k + \Delta T_{mv,k}$. Both have velocity $u(t_k)$, the effect of increased noise levels is ignored. RND is a random number with uniform distribution between 0 and 1, P_{mv} is the probability of multiple validation and $\Delta T_{mv,k} = |\sigma_{mv} G|$, with $\Delta T_{mv,k} < T_{k+1} - T_k$, and $\Delta T_{mv,k} < T_k - T_{k-1}$. σ_{mv} is the time scale over which multiple validation is important and G is a random number with Gaussian distribution, standard deviation 1 and zero mean.

An example of the data interarrival time distribution with dead time and multiple validation

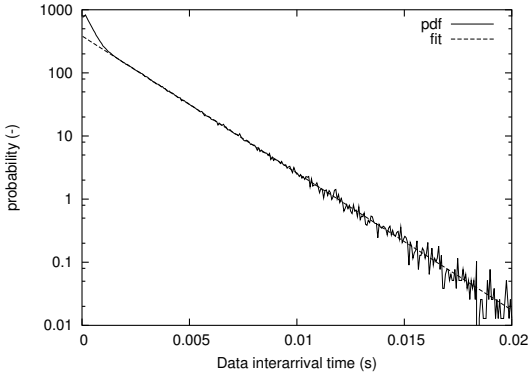

Figure 5.4.: Data interarrival time distribution for artificial multiple validation and dead time. $T_{dead} = 0.1ms$, $\sigma_{mv} = 0.5ms$, $P_{mv} = 0.3$. Data rate with multiple validation is 618 Hz, particle rate is 500 Hz.

is shown in Figure 5.4, the multiple validation is visible at intervals shorter than 1 ms. The effect on the estimated PSD is shown in Figure 5.5. If the correction is performed using the data rate $\dot{N}_{tot}$ with multiple validation (618 Hz) there is significant bias: the slope of the PSD is estimated incorrectly, as was mentioned by Nobach et al. (1998a). An estimate of the true particle rate (500 Hz) can, however, be obtained from a fit to the data interarrival time distribution for intervals where the multiple validation does not affect the distribution (Figure 5.4). If the correction is performed using this true particle rate (500 Hz), the result is close to that of the time series without multiple validation. This is probably caused by the fact that only very short intervals are perturbed, which affect frequencies outside the range of interest. Once a larger range of intervals is perturbed, the bias in the PSD estimate increases. The effect is similar to that of an inaccurate arrival time estimate.

5.4. Data interarrival time distribution for bubbly flow

If bubbles are present, the blockage of laser beams results in relatively large gaps in the time series. The deviation of the data interarrival time distribution from the Poisson distribution can become large. The time intervals that are affected are much larger than in the case of multiple validation, and, consequently, relatively low frequencies are affected. The modifications in the data interarrival time distribution by the presence of bubbles are studied below.

As a first approximation, a single beam is considered and the bubbles are assumed to give identical blockage durations T_d. Bubbles arrive randomly at the laser beam with an average interarrival interval T_a. Before the blockage by bubble i ends, bubble $i+1$ may arrive and the blockage continues, etcetera. A blocking event with total blockage time T_{bt} results. Examples of the distribution of T_{bt} are shown in Figure 5.6(a). The shape of the blockage time distribution is characterized by $P(T_{bt}) = f(\frac{T_{bt}}{T_d}, \frac{T_a}{T_d})$. A sharp peak of single bubble blockage events is located at $T_{bt} = T_d$, for $\frac{T_{bt}}{T_d} > 2$ the distribution has the shape $exp(-\frac{T_{bt}}{T_d} f_o(\frac{T_a}{T_d}))$. These are the overlapping

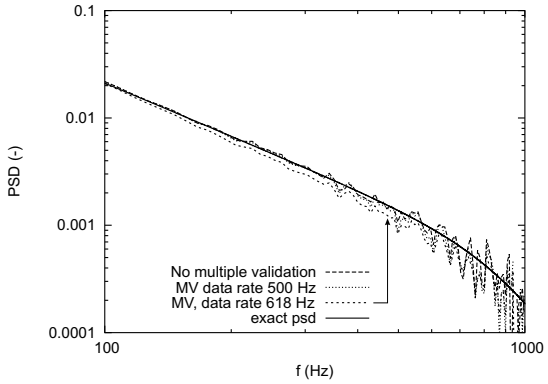

Figure 5.5.: Effect of multiple validation (MV) on spectral estimation.

bubbles. The length of the overlapping event scales with the individual blockage duration T_d. If the ratio of the average interarrival time and the blockage duration T_a/T_d decreases, the amount of overlapping increases and the length of the overlapping events increases. This trend is given by $f_o(\frac{T_a}{T_d})$, which is shown in Figure 5.6(b). Consequently, the slope decreases if e.g. the void fraction is increased. The ratio of the number of blocking events and the number of bubbles crossing the laser beam is shown in Figure 5.6(c).

Similar to the case of the random arrival of particles, the probability of a short interval in between two blockage events is relatively large. If the particle rate with LDA is relatively low, the probability that no seeding particle arrives during this interval is large. Consequently, the length of the intervals without bursts are generally longer than the blockage durations due to the bubbles. The effect of the combination is shown in Figure 5.6(d). The strong overlap of the blockage duration distribution and the particle interarrival time distributions result in the smearing of the peak and different slopes than for particles or bubbles alone. Exponential decay with two slopes and a bend are obtained. The slope for long intervals ($\Delta T > 2T_d$) decreases, the slope for short intervals ($\Delta T < T_d$) increases. The change in slope decreases with increasing particle rate and decreasing bubble rate. The presence of bubbles makes estimation of the particle rate from the distribution of the data interarrival times, therefore, difficult.

In the case of bubbles, the blockage duration T_d is not constant, but dependent on the position of the bubble. Figure 5.7 shows the data interarrival time distributions obtained with Monte Carlo calculations. This shows that a similar shape as in the case of the simplified model is obtained. The probability density function $p(\Delta T)$ can be approximated by

$$p(\Delta T) = Ae^{-\dot{N}_1 \Delta T} + Be^{-\dot{N}_2 \Delta T} \tag{5.6}$$

where $\frac{A}{\dot{N}_1} + \frac{B}{\dot{N}_2} = 1$ and $\frac{A}{\dot{N}_1^2} + \frac{B}{\dot{N}_2^2} = \frac{1}{\dot{N}_{tot}}$ with $\dot{N}_{tot}$ the data rate of the signal with the bubbles. We pose $\dot{N}_1 > \dot{N}_2$. The complex interaction of the blockage duration distribution and the particle interarrival time distribution at the measurement volume makes it difficult to provide a simple model for A, B, $\dot{N}_1$ and $\dot{N}_2$. For this reason, these parameters are determined from the Monte

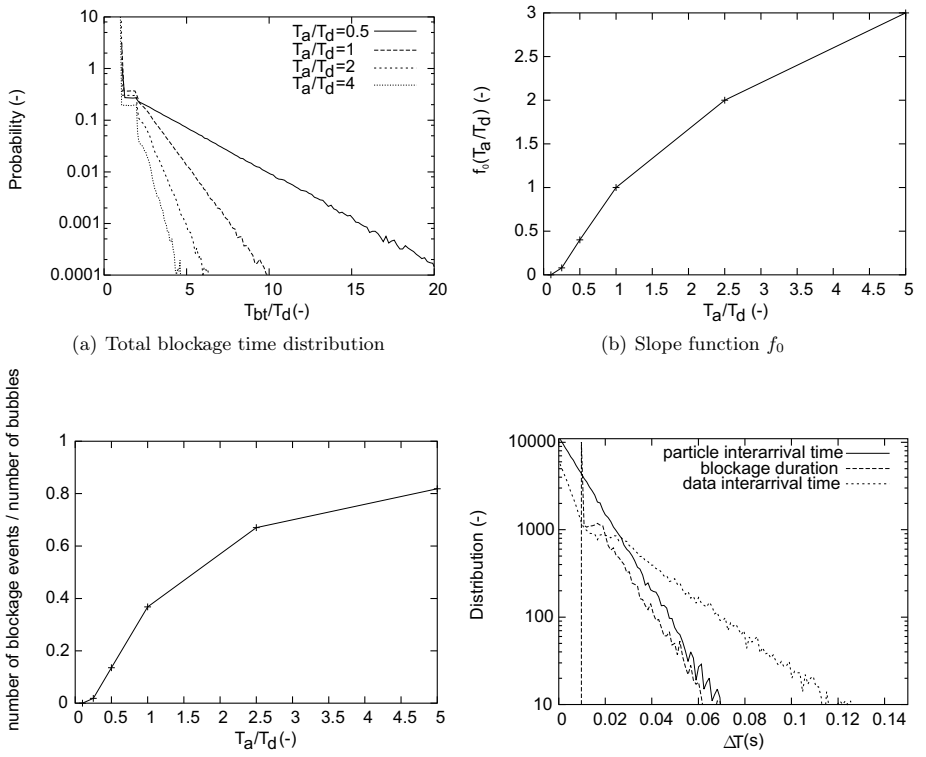

(a) Total blockage time distribution

(b) Slope function f_0

(c) Number of blockage events

(d) Data interrival time distribution if particles and bubbles are combined ($T_d = T_a = 0.01$ s, particle rate 100 Hz).

Figure 5.6.: Bubble blockage duration distribution properties

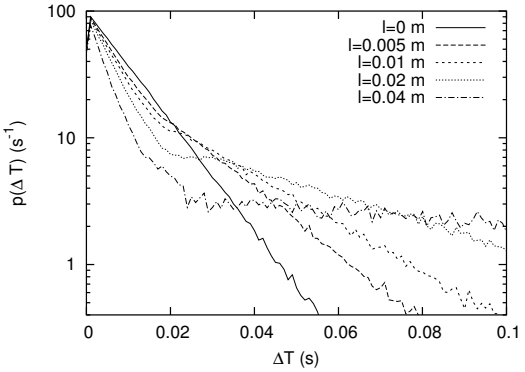

Figure 5.7.: Data interarrival time probability distributions for combination of particles and bubbles calculated with Monte Carlo technique for various distances to the wall. $\alpha = 0.1$, particle rate $\dot{N}_p$=100 Hz.

Carlo simulation results.

Not only the probability distribution of the data interarrival time is altered by the presence of the bubbles, but also the probability of having a velocity realization in the interval $\{\tau, \tau+d\tau\}$ after the previous arrival of a data point. This probability is shown in Figure 5.8 for a bubbly flow and for random arrival of particles (with Poisson distributed interarrival times). Due to the bubbles, the probability that more velocity realizations are obtained shortly after the acquisition of a previous realization, is larger than for the case of random acquisition of the velocity realizations (i.e. the single phase case).

These changes in the statistics of the arrival times of velocity realizations modify the effect of the reconstruction step on the power spectra and also affect the correction procedure. The next section investigates these effects.

5.5. Influence of bubbles on the spectral estimation employing Sample and Hold reconstruction

The effect of the bubbles on the spectrum can be evaluated if the spectrum is calculated after resampling of the signal using Sample and Hold. Adrian and Yao (1987) evaluate the effect for random arrival times with a Poisson distribution. A similar approach is followed here for arrival times with extra gaps due to the bubbles.

The irregularly sampled signal $u(t_i)$ is reconstructed using the Sample and Hold technique. The effect of the reconstruction on the signal properties can be analyzed by investigating the autocovariance function of the resampled data $R_R(\tau)$ and expressing it in terms of the original autocorrelation function $R_{uu}(\tau)$ (which is equal to $E[u(t_1)u(t_2)]$).

$$R_R(\tau) = E[u_R(t_1)u_R(t_2)] = E[u(\xi_0)u(\xi_n)] \tag{5.7}$$

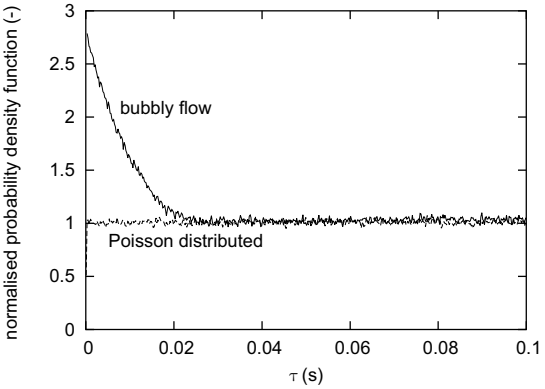

Figure 5.8.: Probability of velocity realizations in the interval $[\tau, \tau + d\tau]$ after the previous arrival of a data point.

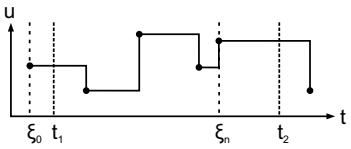

Figure 5.9.: Time instants used in the derivation of the autocorrelation function of the resampled signal

with $\tau = t_2 - t_1$. $u(\xi_0)$ is used to reconstruct $u_R(t_1)$, $u(\xi_n)$ is used to reconstruct $u_R(t_2)$ (Figure 5.9). n is the number of measured data points in the interval $[t_1, t_2]$, $n \geq 0$. We have

$$R_R(\tau) = P_{1point}(\tau) R_{uu}(0) + \int_0^\infty R_{uu}(\eta) f_{multi}(\eta, \tau) d\eta \tag{5.8}$$

with P_{1point} the probability that n=0: a single point ξ_0 is used to reconstruct both $u_R(t_1)$ and $u_R(t_2)$. $f_{multi}(\eta, \tau)d\eta$ is the probability that two different points are used for the reconstruction for given τ, i.e. $n \geq 1$, with interval $\eta = \xi_n - \xi_0$.

For LDA in bubbly flow, the distribution of the time between subsequent velocity realizations of the unevenly sampled data $p(\Delta T)$ is modeled with equation 5.6. $P_{1point}(\tau)$ is given by the probability that no particle arrives during the interval $[t_1, t_2]$:

$$P_{1point}(\tau) = \dot{N}_{tot} \int_{-\infty}^{t_1} \int_{t_2}^{\infty} p(\xi_1 - \xi_0) d\xi_1 d\xi_0 = \dot{N}_{tot} [\frac{A}{\dot{N}_1^2} e^{-\dot{N}_1 \tau} + \frac{B}{\dot{N}_2^2} e^{-\dot{N}_2 \tau}] \tag{5.9}$$

$f_{multi}(\eta)$ is given by

$$f_{multi}(\eta, \tau) = \sum_{n=1}^{\infty} f_{(n)}(\eta, \tau) \tag{5.10}$$

where $f_{(n)}(\eta, \tau)d\eta$ is the probability that exactly n particle(s) are present in the interval $[t_1, t_2]$

with $\eta = \xi_n - \xi_0$ for given τ. For a Poisson process, the probability of finding a particle at a time ξ is independent of what events preceded this time. This is, however, not the case with the particle interarrival time distribution in equation 5.6. Due to the bubbles, the probability of finding new particles is larger shortly after the arrival of a particle than at a random moment in time (see also Figure 5.8). Therefore, the probability of finding a particle at time ξ_n depends on $\xi_n - \xi_0$ and $\xi_n - t_1$. In total, n particles arrive during the interval $[t_1, t_2]$ with arrival times ξ_i $(i = 1..n)$ where we have $\xi_0 < t_1 < \xi_1 < \xi_2 < ... < \xi_i < ... < \xi_n$. The probability that this occurs is given by

$$\begin{aligned}
&f_{(n)}(\xi_0, \xi_1, .., \xi_i, .., \xi_n) d\xi_0 d\xi_1 .. d\xi_i .. d\xi_n = \\
&\text{Prob(particle arrival during } [\xi_0, \xi_0 + d\xi_0]) \times \text{Prob(interval of length } \xi_1 - \xi_0) \times ... \times \\
&\text{Prob(interval of length } \xi_i - \xi_{i-1}) \times ... \times \text{Prob(interval of length } \xi_n - \xi_{n-1}) \times \\
&\text{Prob(interval with length } > t_2 - \xi_n) = \\
&\dot{N}_{tot} d\xi_0 p(\xi_1 - \xi_n + \eta) d\xi_1 .. p(\xi_i - \xi_{i-1}) d\xi_i .. p(\xi_n - \xi_{n-1}) p_{no}(t_2 - \xi_n) d\xi_n
\end{aligned} \tag{5.11}$$

with $p_{no}(\Delta T)$ the probability of no velocity realization during a time ΔT after arrival of a particle:

$$p_{no}(\Delta T) = \int_{\Delta T}^{\infty} p(\Delta T') d\Delta T' = \frac{A}{\dot{N}_1} e^{-\dot{N}_1 \Delta T} + \frac{B}{\dot{N}_2} e^{-\dot{N}_2 \Delta T} \tag{5.12}$$

The conditional probability density function for n particles that the points t_1 and t_2 are reconstructed from two points with lag η is obtained by integrating over all the possible combinations that generate this lag:

$$\begin{aligned}
&f_{(n)}(\eta, \tau) = \dot{N}_{tot} \int_{t_1}^{min(t_1+\eta, t_2)} p_{no}(t_2 - \xi_n) \int_{t_1}^{\xi_n} .. \int_{t_1}^{\xi_{i+1}} .. \int_{t_1}^{\xi_2} p(\xi_1 - \xi_n + \eta) .. \\
&p(\xi_i - \xi_{i-1}) .. p(\xi_{n-1} - \xi_{n-2}) p(\xi_n - \xi_{n-1}) d\xi_1 .. d\xi_i .. d\xi_{n-1} d\xi_n
\end{aligned} \tag{5.13}$$

The actual integration of equation 5.13 is complicated. For this reason, only part of the solution is presented here: combination of equations 5.8, 5.9, 5.10 and 5.13 yields

$$\begin{aligned}
&R_R(\tau) = \tfrac{A\dot{N}_t}{2\dot{N}_1} \int_{-\infty}^{\infty} R_{uu}(\eta) e^{-\dot{N}_1 |\eta - \tau|} d\eta + \tfrac{B\dot{N}_t}{2\dot{N}_2} \int_{-\infty}^{\infty} R_{uu}(\eta) e^{-\dot{N}_2 |\eta - \tau|} d\eta \\
&+ \tfrac{A\dot{N}_t}{\dot{N}_1^2} e^{-\dot{N}_1 \tau} \int_0^{\infty} R'_{uu}(\eta) e^{-\dot{N}_1 \eta} d\eta + \tfrac{B\dot{N}_t}{\dot{N}_2^2} e^{-\dot{N}_2 \tau} \int_0^{\infty} R'_{uu}(\eta) e^{-\dot{N}_2 \eta} d\eta + \text{cross terms}
\end{aligned} \tag{5.14}$$

and

$$\begin{aligned}
&S_{rr}(f) = \tfrac{A\dot{N}_t}{\dot{N}_1^2} \tfrac{1}{1 + f^2/(2\pi\dot{N}_1)^2} \left[S_{uu}(f) + \int_0^{\infty} R'_{uu}(\eta) e^{-\dot{N}_1 \eta} d\eta \right] \\
&+ \tfrac{B\dot{N}_t}{\dot{N}_2^2} \tfrac{1}{1 + f^2/(2\pi\dot{N}_2)^2} \left[S_{uu}(f) + \int_0^{\infty} R'_{uu}(\eta) e^{-\dot{N}_2 \eta} d\eta \right] + \text{cross terms}
\end{aligned} \tag{5.15}$$

Ignoring the cross terms, we see that the combination of seeding and bubbles results in an additive white noise component followed by low pass filter operation, similar to the results by Adrian and Yao (1987) for a Poisson process. In the present case, however, two different white noise terms are found and two second order low pass filters operate on the spectrum, one with cutoff frequency $\dot{N}_1/2\pi$ and another with (lower) cutoff frequency $\dot{N}_2/2\pi$. The difference between these frequencies increases with α, l and the particle rate. The relative influence of each filter is dependent on the values of A,B, $\dot{N}_1$ and $\dot{N}_2$. Nevertheless, the second term (with $\dot{N}_2$) is usually dominant for the lower frequencies. The effect will be demonstrated with examples.

If the analysis of Adrian and Yao (1987) would hold, one would expect (i) a single cutoff frequency around $\dot{N}_{tot}/2\pi$ due to the signal processing and (ii) that the shape of the spectrum will be reliable up to higher frequencies by increasing the data rate $\dot{N}_{tot}$. Figure 5.10(a) shows the spectrum for a bubbly flow with a white noise signal and $\alpha = 0.1$ and l=0.02 m (the equivalent bubble diameter is 4.5 mm for all artificial signals in this chapter), where the particle rate $\dot{N}_p$ is increased from 100 Hz to 1000 Hz. For $\dot{N}_p$=1000 Hz the two cutoff frequencies are clearly visible. The first cutoff frequency (at $\dot{N}_2/2\pi$) is clearly located at a lower frequency than $\dot{N}_{tot}/2\pi$, the difference increasing for increasing $\dot{N}_p$. An increase of the particle rate $\dot{N}_p$ (and therefore $\dot{N}_{tot}$) with a factor of 10 produces an increase in the lower cutoff frequency $\dot{N}_2/2\pi$ by only a factor of 2.

This behavior is independent of the true spectrum. This is illustrated in Figure 5.10(b). In this example, the true spectrum has a -5/3 slope (on a log scale), as is often encountered in single phase isotropic turbulence. Spectral estimates are shown for both a single phase flow signal (i.e. Poisson distributed data) and a bubbly flow signal generated with the same exact spectrum S_{uu}. The changes in the spectral estimates are shown for an increase in the particle rate with a factor of 10. For the single phase flow, the range over which the spectral estimate is reliable increases with a factor of 10. For the bubbly flow, this increase is again only a factor of 2. This clearly shows that improvement of the LDA equipment and an increase in the seeding density do not help much in order to obtain more reliable spectra if Sample and Hold is used: the bottleneck is clearly the signal processing, unless the measurement is performed very close to the wall. Even for very high data rates, the gaps due to the bubbles will never disappear.

The difference in the cutoff-frequencies $\dot{N}_2/2\pi$ and $\dot{N}_{tot}/2\pi$ can give an incorrect impression of the nature of the flow. This is illustrated with the following example. Figure 5.11 illustrates the effect of increasing bubble blockage by an increasing distance l of the measurement volume to the wall. Increasing the void fraction would give similar effects. The true spectrum S_{uu} is that of white noise. For increasing l, the data rate $\dot{N}_{tot}$ decreases. $\dot{N}_2$ decreases faster than $\dot{N}_{tot}$. The result is that an increasingly large part of the spectrum with frequencies below $\dot{N}_{tot}/2\pi$ becomes unreliable. The example shows that it is possible to obtain a -5/3 slope for frequencies around and even below $\dot{N}_{tot}/2\pi$. This suggests a turbulence cascade process, whereas the true spectrum contains only white noise. The -2 slope that is expected based on the results for Poisson processes is only observed for frequencies well beyond $\dot{N}_{tot}/2\pi$ (i.e. beyond $\dot{N}_1/2\pi$).

The exact behavior depends strongly on α, l, $\dot{N}_p$ and S_{uu}. Nevertheless, the behavior in the example in Figure 5.11 does not only hold for white noise signals, but also occurs in more realistic signals. Figure 5.12(b) shows the S&H spectra for the two signals. Figure 5.12(a) shows the exact spectra for these signals: the signals are generated by the addition of white noise to a noiseless artificial signal. The spectrum of the first noiseless artificial signal has a slope of -5/3, the second has a slope -2. The exact -5/3 slope is visible for f>10 Hz in the noiseless artificial signal, however, the extra noise results in somewhat lower slope for the noisy signal. Both signals are dominated by noise only for the frequencies beyond the range of interest. Nevertheless, due to the extra noise, the S&H spectra both get a -5/3 slope in the range below 10 Hz (whereas the mean total data rate $\dot{N}_{tot}$ suggests a single phase cutoff frequency at 30 Hz). This shows that the slope obtained with S&H is not very reliable and that interpretation of spectra obtained using the Sample and Hold reconstruction technique with bubbly flow requires, therefore, even more care than results for single phase flows.

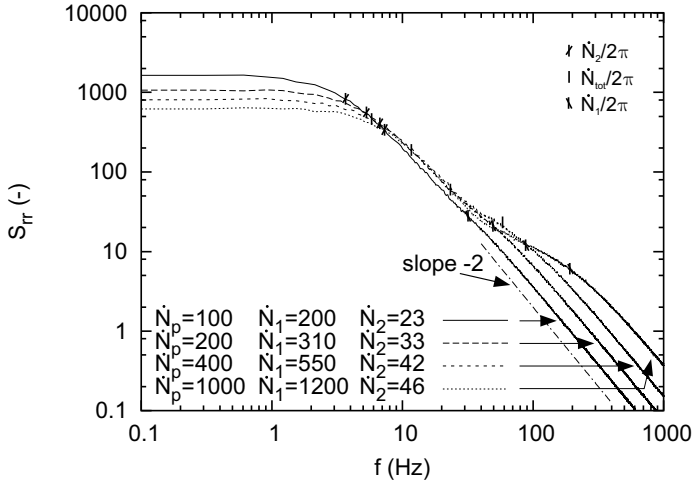

(a) Effect bubbles on shape of spectrum for a white noise signal (α=0.1, l=0.02 m)

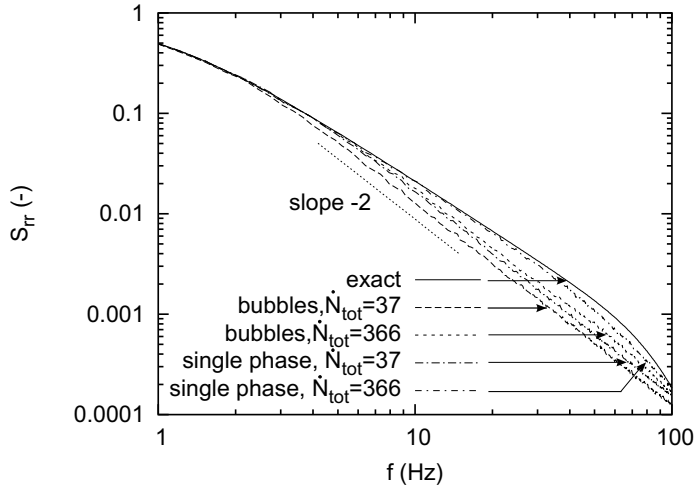

(b) Comparison with single phase behavior for a spectrum with -5/3 slope (bubbly flow: α=0.1, l=0.02 m, $\dot{N}_p$ increased from 100 Hz to 1000 Hz). Spectra normalized at 1 for low frequency.

Figure 5.10.: Effect of Sample and Hold on spectra, obtained in bubbly flow with $\alpha = 0.1$ and $l = 0.02$ m.

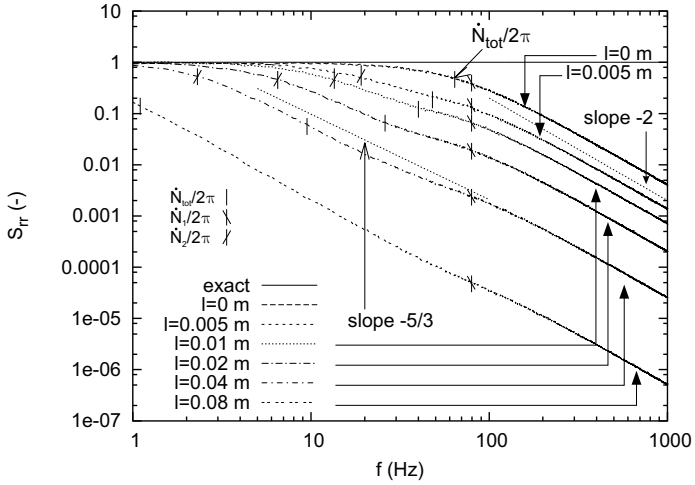

Figure 5.11.: Effect of distance to wall l on spectra for a white noise signal. Spectra normalized at 1 for low frequency. $\dot{N}_p$=400 Hz, α=0.1.

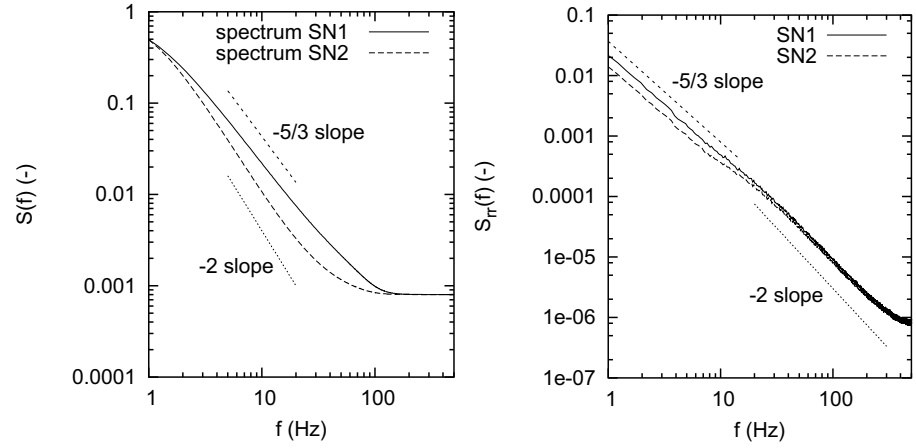

(a) Exact spectra

(b) Spectra obtained with S&H.

Figure 5.12.: Effect bubbles on shape of spectrum for a turbulence-like signal with noise(α=0.1, l=0.02 m, particle rate 400 Hz, $\dot{N}_{tot}$=186 Hz).

Sample and Hold correction of bubbly flow signals

Consequently, the effect of the Sample and Hold reconstruction on the spectrum is no longer the addition of a white noise term and a low pass filter. If this were true, equation 5.2 would be valid, and the low pass filter can be estimated using artificial signals with this equation. Nevertheless, a test is carried out to see whether or not equation 5.2 can be used to improve the estimated spectrum. An artificial signal with known spectrum $S_{uu}(f)$ is generated. It is sampled with non-equidistant intervals distributed according to equation 5.6. The signal is reconstructed with S&H and the spectrum $\hat{S}_{rr}(f)$ is calculated. Using the knowledge that $L(0) = 1$, the step noise can be estimated via:

$$\hat{S}_{ss} = \hat{S}_{rr}(0) - S_{uu}(0) \tag{5.16}$$

and the low pass filter can be estimated via:

$$|\hat{L}(f)|^2 = \frac{\hat{S}_{rr}(f)}{S_{uu}(f) + \hat{S}_{ss}(f)} \tag{5.17}$$

If equation 5.2 would be valid, different input spectra $S_{uu}(f)$ would give the same low pass filter estimate. The results for the input spectra in Figure 5.13(a) are shown in Figure 5.13(b). The low pass filter estimates for the various input spectra (with identical interarrival time distribution) are different, showing that equation 5.2 is not valid if bubbles are present. The difference grows for $f > \dot{N}_1/2\pi$. Although the differences look small (on a log scale), very different estimates for the step noise are obtained if equation 5.4 is used. The problem originates from the fact that the spectrum of the reconstructed signal can no longer be written as the operation of a single filter on the sum of the original spectrum and white noise: equation 5.2 is no longer valid. Instead, multiple filters act and multiple noise terms originate. It is, however, not possible to estimate multiple noise terms, since only one equation (similar to equation 5.4) is available for their estimation. Therefore, a correction method that reduces the bias significantly up to higher frequencies, similar to that by Simon and Fitzpatrick (2004), is not possible. For the same reason, it is not possible to construct a correction technique using a convolution sum such as was done by Nobach et al. (1998a).

At best, a partial correction can be performed. Examples for the spectra 2 and 4 from Figure 5.13(a) are shown in Figure 5.14. Since the spectrum $S_{uu}(f)$ is generally unknown, the shape of the low pass filter is estimated from an artificial white noise signal using equations 5.16 and 5.17. Next, the corrected spectrum is determined with equations 5.4 and 5.5. The performance is quite poor, the inaccurate step noise estimates can even produce negative power spectrum values. The main improvement is observed in the shape of the spectrum at low frequencies up to $\dot{N}_2/2\pi$. Improvement of the spectrum up to $\dot{N}_{tot}$, which can be obtained for single phase flow, is not obtained (Figure 5.15). A different approach is required.

Summarizing, the results show that the use of Sample and Hold reconstruction gives poor results when applied to bubbly flow data. A similar conclusion will hold for other reconstruction techniques (Benedict et al., 2000), since the velocity in the reconstructed signal will always be strongly correlated to the velocity at the points that were used for the reconstruction, i.e. the correlation extends over similar time spans as for Sample and Hold (Van Maanen, 1999). Consequently, the estimation at higher frequencies encounters similar problems.

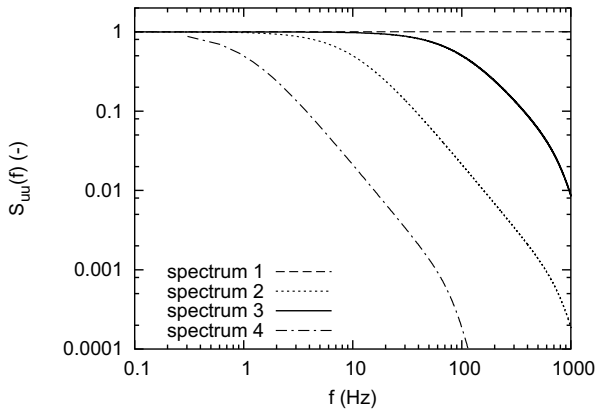

(a) Input spectra artificial signals

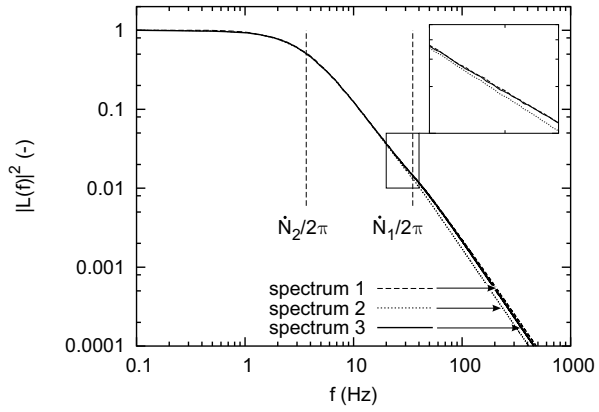

(b) Filters reconstructed from artificial signals

Figure 5.13.: Reconstruction of Sample and Hold low pass filter from artificial signals. Data interarrival time distributed according to eq. 5.6 with A=92.62, B=12.35, $\dot{N}_1 = 200$ Hz, $\dot{N}_2 = 23$ Hz.

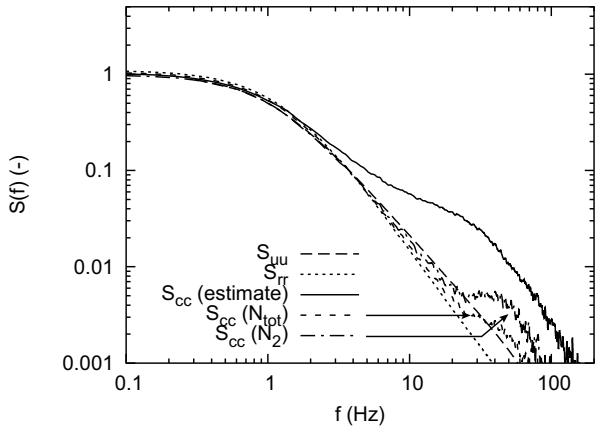

(a) S&H correction for input spectrum 4

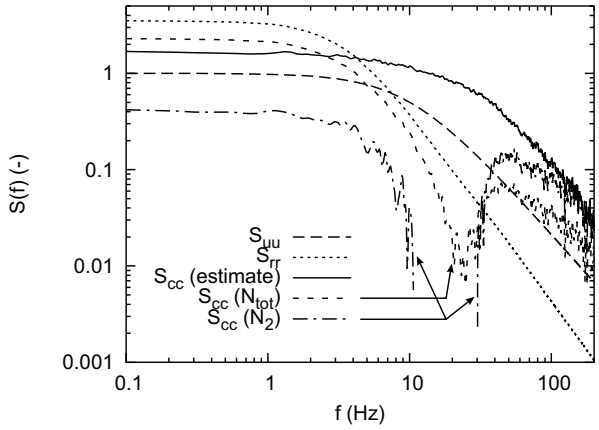

(b) S&H correction for input spectrum 2

Figure 5.14.: Effect of correction procedure on spectra. $S_{cc}(estimate)$ uses the filter estimated via equation 5.17, $S_{cc}(N_{tot})$ and $S_{cc}(N_2)$ use equation 5.3 with estimates of $\dot{N}_{tot}$ and $\dot{N}_2$

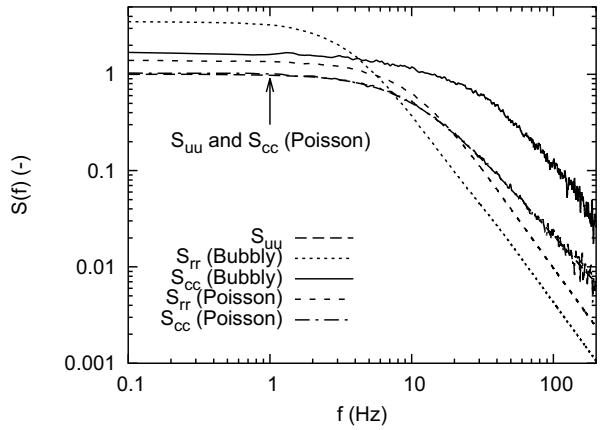

Figure 5.15.: Comparison correction procedure bubbly vs single phase flow ($\dot{N}_{tot}$=39 Hz) for input spectrum 2.

5.6. Slotting techniques

Slotting techniques form a second important class of techniques for the estimation of power spectra from LDA data. The classic slotting correlation technique was introduced by Mayo et al. (1974). In this technique, the slotting autocovariance estimate $\hat{R}_k$ is calculated from cross-products with time lags falling in a slot with width $\Delta\tau$:

$$\hat{R}_k = \hat{R}(k\Delta\tau) = \frac{\sum_{i=1}^{N}\sum_{j=i+1}^{N} u_i u_j b_k(t_j - t_i)}{\sum_{i=1}^{N}\sum_{j=i+1}^{N} b_k(t_j - t_i)} \tag{5.18}$$

and

$$b_k(t_j - t_i) = \begin{cases} 1 & \text{for } |(t_j - t_i)/\Delta\tau - k| < 1/2 \\ 0 & \text{otherwise} \end{cases} \tag{5.19}$$

Power spectra calculated from the autocovariance functions determined with the slotting technique suffer only very mildly from a low-pass filtering effect if a small slot size is used, especially compared to reconstruction techniques (Broersen et al., 2000). This effect is therefore ignored. The variance of the spectrum estimate, on the other hand, is an important issue (Benedict et al., 2000). For this reason a number of improvements were introduced to reduce the variance of the slot correlation estimate. One of these distributes the cross-products over two neighboring slots: fuzzy slotting (Nobach et al., 1998b):

$$b_k(t_j - t_i) = \begin{cases} 1 - |(t_j - t_i)/\Delta\tau - k| & \text{for } |(t_j - t_i)/\Delta\tau - k| < 1 \\ 0 & \text{otherwise} \end{cases} \tag{5.20}$$

Additional reduction in the variance is obtained by using 'local normalization' with an individual estimate of the variance for each slot (Van Maanen and Tummers, 1996; Van Maanen et al., 1999):

$$\hat{\rho}_k = \hat{\rho}(k\Delta\tau) = \frac{\sum_{i=1}^{N}\sum_{j=i+1}^{N} u_i u_j b_k(t_j - t_i)}{\left[\left[\sum_{i=1}^{N}\sum_{j=i+1}^{N} u_i^2 b_k(t_j - t_i)\right]\left[\sum_{i=1}^{N}\sum_{j=i+1}^{N} u_j^2 b_k(t_j - t_i)\right]\right]^{1/2}} \tag{5.21}$$

This technique has the additional advantage that the influence of velocity bias is reduced (Tummers (1999), Tummers and Passchier (2001)).

Nobach (2002b) pointed out that a processor delay may lead to a gradient in the probability density function of the time lags. As a result, correlation estimates are dominated by cross-products with larger time-lags than the time lag in the middle of the bin. In bubbly flow, there is in addition a gradient in the probability density function of the time lags (Figure 5.8). For $\tau < \tau_{bubble}$ shorter lags occur more often due to the gaps in the data created by the bubbles. τ_{bubble} is the typical duration of a bubble passage through the laser beams. Consequently, correlation estimates are dominated by cross-products with shorter time-lags than the time lag in the middle of the bin, if $\Delta\tau$ is of the order τ_{bubble}. The solution proposed by Nobach (2002b) is to calculate a more appropriate time lag ('local time estimate') for each correlation estimate $\hat{R}(k)$ using:

$$\hat{\tau}_k = \frac{\sum_{i=1}^{N-1}\sum_{j=i+1}^{N}(t_j - t_i)b_k(t_j - t_i)}{\sum_{i=1}^{N-1}\sum_{j=i+1}^{N} b_k(t_j - t_i)} \tag{5.22}$$

where b_k may be determined via equation 5.19 or equation 5.20. The auto correlation function (ACF) at $\tau = 0$ is extrapolated from a fit of the data with $\tau > 0$. For this fit, a model similar to that suggested by Benedict et al. (2000) is used:

$$\rho_k = a_{fit} e^{-b_{fit}\tau_k^{c_{fit}}} \tag{5.23}$$

After calculating the correlation coefficients, the normalized power spectrum is calculated with a cosine transform:

$$\hat{S}(f) = \mathcal{F}\{\hat{\rho}(\tau)\}(f) = 2\int_0^\infty w(\tau; f)\hat{\rho}(\tau)cos(2\pi f\tau)d\tau \tag{5.24}$$

$S(f)$ can be calculated directly by assuming $w(\tau; f) = 1$. A significant improvement can be obtained by using a variable window as suggested by Tummers and Passchier (1996). The use of a Tuckey-Hanning window results in a strong decrease of the variance of the spectral estimates. This window is given by:

$$w(\tau; f) = \begin{cases} \frac{1}{2} + \frac{1}{2}cos(\pi f\tau/\kappa) & \text{for } f\tau < \kappa \\ 0 & \text{otherwise} \end{cases} \tag{5.25}$$

Figure 5.16(a) shows the comparison of the power spectrum estimates obtained with the direct transformation and the transformation with variable window ($\kappa = 3$). The spectrum using the direct transformation is reliable up to the frequencies around the data rate (39 Hz), whereas the spectrum using the variable window is reliable up to frequencies approximately 10-15 times the

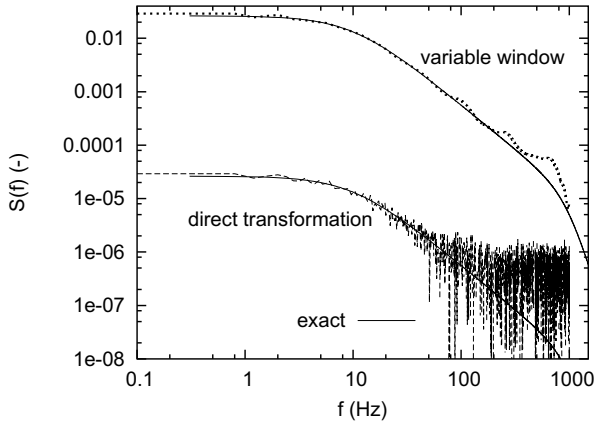

(a) Comparison calculation via direct transformation and variable window technique for classic slotting technique, $\Delta\tau$=0.5 ms. The spectrum for the direct transformation and the exact spectrum with which it is compared, are offsetted for comparison purposes.

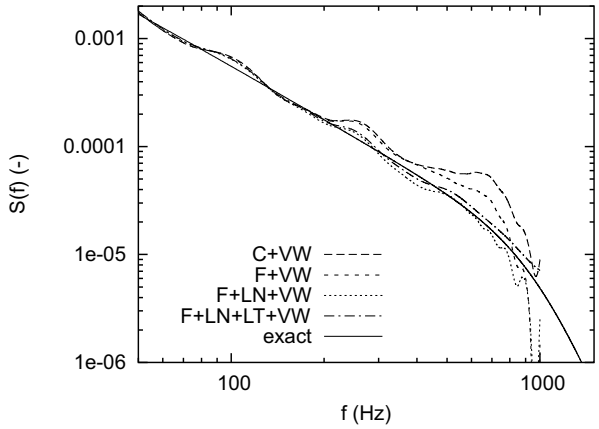

(b) Comparison various refinements of slotting technique. C=classic, F=fuzzy, LN=local normalization, LT=local time estimate, D=direct transformation, VW=variable window.

Figure 5.16.: Assessment of various slotting techniques. Data for bubbly flow with α=0.1, l=0.02 m and $\dot{N}_{tot} = 39$ Hz.

data rate. The result of the use of the various improvements of the slotting technique is shown in Figure 5.16(b) that zooms in on the higher frequencies. The variance of the technique clearly decreases: the oscillations around the true spectrum become much smaller.

Van Maanen and Oldenziel (1998) and Van Maanen (1999) proposed to obtain power spectra with higher accuracy up to high frequencies by using a curve fit of the correlation coefficients. The model chosen to describe the normalized power spectrum is:

$$S(f) = S_a(0)[1 + (f/f_0)^2] \prod_{k=1}^{n_k} \frac{1}{1 + (f/f_k)^2} \tag{5.26}$$

where f_i, $i = 0...n_k$ are the parameters and $S_a(0)$ the static gain of the spectrum. The corresponding autocorrelation function is given by:

$$\rho(\tau) = S_a(0) \sum_{k=1}^{n_k} \left[e^{\frac{-2\pi|\tau|}{\tau_{fk}}} \left(1 - \frac{\tau_{f0}^2}{\tau_{fk}^2}\right) \frac{1}{\tau_{fk}} \prod_{l=1|l\neq k}^{n_k} \left(\frac{\tau_{fk}^2}{\tau_{fk}^2 - \tau_{fl}^2}\right) \right] \tag{5.27}$$

with fit parameters $\tau_{fk} = \frac{1}{f_k}$, $i = 0...n_k$. These parameters are determined by minimizing a weighted mean square error:

$$L_{fit} = \sum_{k=0}^{N} w_k \left[\rho_k - \rho(\hat{\tau}_k, \tau_{f0}, \tau_{f1}, .., \tau_{f_{n_k}})\right]^2 \tag{5.28}$$

More details can be found in Van Maanen (1999). Figure 5.17(a) compares the results for the variable window technique and the fit technique for a very long signal (5000 s). The performance is more or less similar. The variable window technique shows some oscillations around the true spectrum. The differences between the spectrum estimate with the fit technique and the exact spectrum are mainly due to the inadequacy of the general model to fit the data exactly. Both techniques are not very well able to see the second change in slope in the spectrum, which is located at 25 times the mean data rate. Figure 5.17(b) shows the same comparison for a shorter signal with duration of 300 s. The shorter signal duration results in stronger oscillations for the variable window technique. The result for the fit technique is affected less. Consequently, the use of the slotting technique with its improvements in combination with the variable window technique or the fit technique is well suited for the estimation of power spectra of LDA signals obtained in bubbly flow, if the velocity fluctuations are fully dominated by the turbulence. Section 5.9.1 will show that for flows with pseudo-turbulence due to the bubbles, the fit technique is less appropriate.

5.7. Tests with experimental signals

Finally, the performance of the signal processing techniques is evaluated with real data. LDA signals were obtained in a 15.0 cm diameter cylindrical bubble column, in which air is injected with the use of 559 needles. With these conditions a very homogeneous gas distribution is obtained, the void fraction is constant in the bulk up to 5 mm distance from the wall. The bubble

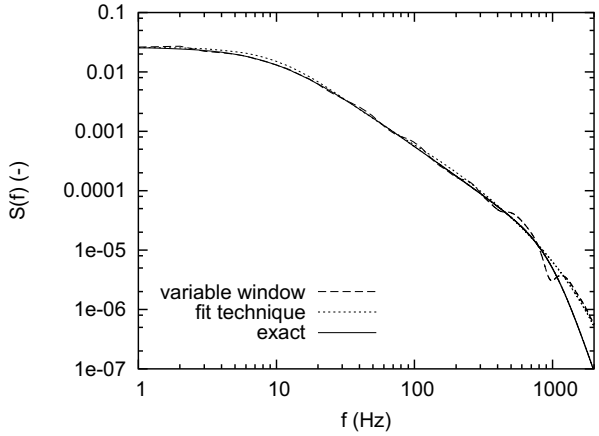

(a) Long signal (duration of 5000 s).

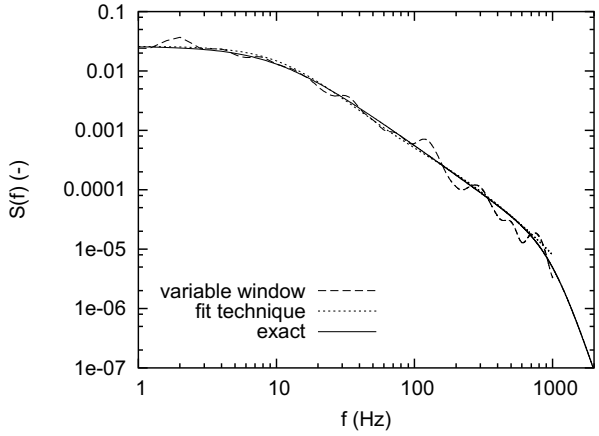

(b) Short signal (duration of 300 s).

Figure 5.17.: Comparisons variable window and fit techniques. α=0.1, l=0.02 m, $\dot{N}_{tot}$=39 Hz

column is filled with tap water up to a height of 1.2 m, experiments are performed at a void fraction of 15% (superficial gas velocity 0.031 m/s), at which a very homogeneous bubbly mixture is obtained without large scale vortical motion and a bubble equivalent diameter around 4-4.5 mm. For more details on the bubble column, see section 2.2.3. The LDA equipment consists of a 4W Spectra-Physics AR^+ laser and a TSI 9201 colorburst multicolor beam separator. A preshift frequency of 500 kHz is used. Beam pairs are focused with a 122 mm lens, the measurements were performed in the backscatter mode. Detected light is sent to a TSI 9203 color link, and bursts are processed with the use of processor type IFA-750. The data rate close to the wall is close to 500 Hz, signals are collected over a period of 180 seconds at a height of 0.65 m.

Measurements were performed at various distances l to the wall, in the range of 1.3 mm to 4 cm. Since the flow has very homogeneous properties, the true power spectra will only vary in the region very close to the wall (i.e. up to approximately l=5 mm) and be more or less constant in the bulk region, especially for the higher frequencies. Figure 5.18(a) shows the spectra obtained with the use of Sample and Hold and the Welch periodogram (resample frequency 5000 Hz). Figure 5.18(b) shows the results obtained with the slotting technique with variable window. The results in Figure 5.18(a) clearly show how the cutoff frequency due to the bubble gaps $\dot{N}_2/2\pi$ moves to lower frequencies for increasing l. For l <0.04 m only for the higher frequencies, beyond $\dot{N}_1/2\pi \approx 100$ Hz, a slope of -2 is observed. At the intermediate frequencies (typically around 10 Hz) the slope approaches -5/3, especially for l close to 0.02 m. This slope is caused by the double cut-off behavior of the Sample and Hold filter, and is very similar to that observed in Figure 5.11(a), obtained with artificial signals. Again, the slope is close to -5/3 at frequencies below $\dot{N}_{tot}/2\pi$, showing the need for careful interpretation of Sample and Hold spectra. The results for the slotting technique (Figure 5.18(b)) display a much weaker dependence on l. The slope is smaller than -5/3 for all frequencies. Since the flow is very homogeneous, only a weak dependency on l is expected. The measurement at l=0.0013 m is recorded very close to the wall, i.e. the local void fraction is smaller than in the bulk, the amount of fluctuations due to the bubble passages is also smaller, and the effect of the wall is noticed. Consequently, the power at higher frequencies increases if l increases. The results for l=0.02 m and l=0.027 m are very close, whereas they show great differences for the Sample and Hold reconstruction. This confirms that the slotting technique deals much better with the non-equidistant nature of the signal and the gaps due to the bubbles. No results are shown for l >0.027 m. For these distances to the wall the amount of data is insufficient for the present signal duration of 180 seconds, and the variance of the spectrum increases strongly. The results for the experimental signals confirm the results obtained with the artificial signals: the slotting technique is more reliable than the reconstruction techniques.

5.8. Time series analysis

For the estimation of regular (i.e. equidistant) time series, time series analysis provides a tool for the investigation of power spectra that is able to produce accurate estimates for much smaller amounts of data than traditional periodogram techniques (Broersen (2002)). The technique tries to find the coefficients for the autoregressive (AR), moving average (MA) or autoregressive moving average (ARMA) model that gives the best match in terms of statistical properties with

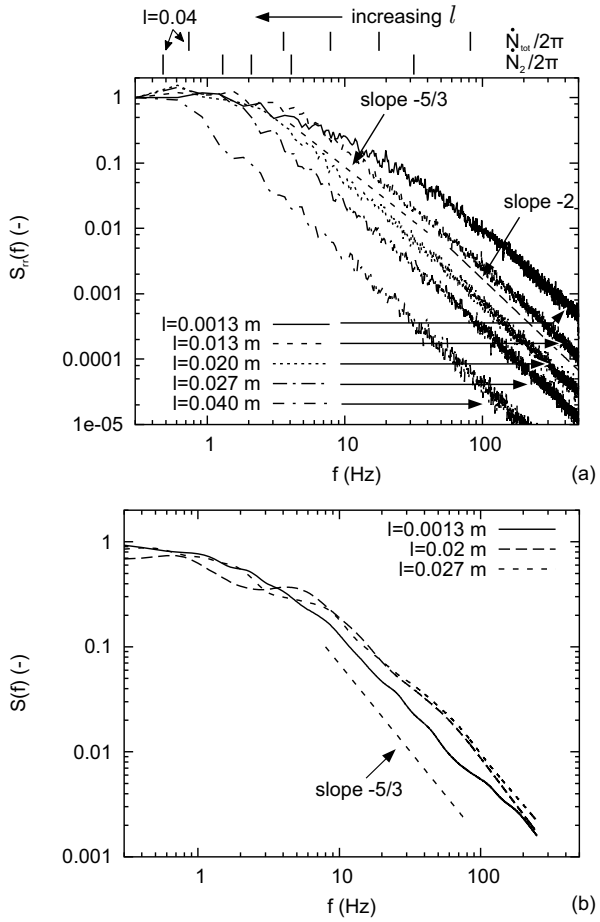

Figure 5.18.: Spectrum estimates for experiment signals ($\alpha = 0.15$), normalized to similar levels at low frequency. (a) Reconstruction via Sample and Hold. The markers above the figure indicate the cutoff-frequencies $\dot{N}_2/\pi$ and $\dot{N}_{tot}/2\pi$, from right to left for increasing values of l. (b) Fuzzy slotting with local normalization, local time estimation and variable window ($\kappa = 3$).

the signal that is analyzed. This technique has been extended for signals with missing data by Broersen et al. (2004) and for irregular data by Bos et al. (2002). The latter technique requires typically 200000 observations for reliable results, but recent improvements in the technique by Broersen (2005) have reduced the number of required observations strongly.

At the time that this thesis is being written, the new algorithms for spectral estimation are not available yet for general application to data, but some preliminary results are given in Figure 5.19 to demonstrate the potential of this new technique, especially for short signals. The figure compares the results for spectra obtained from time series analysis with those obtained with the slotting technique with variable window and fit. The artificial signal from the previous section is used, truncated to short data segments with lengths of 133 and 13 seconds. The variable window technique produces quite strong oscillations in the spectrum which are due to the small number of observations. The fit technique and time series analysis provide good estimates of the power spectrum for 133 seconds of data. Whereas the fit technique provides a slightly better approximation up to 500 Hz for $\Delta\tau$=1 ms, it cannot predict the power spectrum at higher frequencies than 500 Hz since this requires a smaller slot width. However, for this smaller slot width convergence problems were encountered for the numerical optimization. The time series analysis has some problems approximating the power spectrum shape for frequencies around 200 Hz due to the use of a small number of AR coefficients. The bend at 1000 Hz, however, is reproduced very well. Even if only 13 s of data is available, the time series analysis provides a reasonably good estimate of the power spectrum. This shows that time series analysis performs very well for short data segments. An additional advantage is that the time series analysis technique makes less assumptions about the shape of the power spectrum than the slotting fit technique and may have less convergence problems. Although for real data, where the velocity and arrival time suffer from inaccuracies, the results will be less accurate, the technique seems promising.

5.9. Effect of the bubble local flow field on the power spectrum

The previous sections showed how the bubbles can have an effect on the estimated spectra due to the gaps introduced in the signal. The bubbles also have another effect: the flow around the bubbles and in the wakes introduces sharp fluctuations in the velocity which can affect the spectra (Groen et al. (1999), Kulkarni et al. (2001a), Rensen (2003)). The present section investigates the changes introduced by these fluctuations.

First, the spectrum is investigated of bubbly flows with only the potential flow around the bubbles present, no turbulence is present. This is, again, performed using artificial signals. Next, the combination of turbulence and potential flow around the bubbles is considered. Special attention is paid to the slopes in the spectrum.

5.9.1. Power spectrum for bubbly flows with local flow around the bubbles only

In the homogeneous regime, and especially for uniform gas injection, large scale structures are usually weak. This means that the turbulence production in the flow is small and the velocity fluctuations are dominated by the local flow field around the bubbles. Investigation of the cascade of the various structures is, therefore, severely hampered. This problem is not limited to LDA,

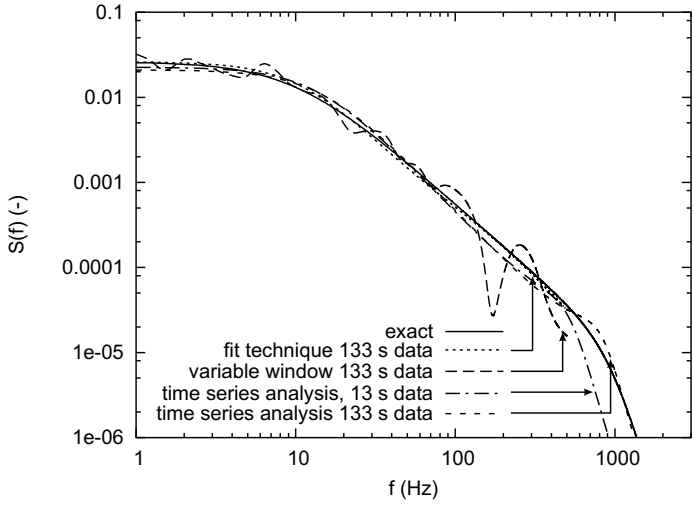

Figure 5.19.: Comparison of slotting technique and results from time series analysis.

but will also affect spectra determined from velocity signals measured with, e.g., hot film probes. The effect on the power spectrum is investigated with artificial signals. The flow field due to the bubbles is simulated as follows. The flow around each bubble is modeled as potential flow around an ellipsoidal bubble, which is given in Moore (1965). As a first approximation, the total flow field is taken as the sum of the potential flow of the individual bubbles. The following conditions are used: bubbles with d_{eq}=4.5 mm, and aspect ratio 0.66, u=0.2 m/s. The bubbles rise rectilinear. Velocity realizations are generated equidistantly with sample period 1 ms. This way, the influence of the random sampling due to the random arrival of particles is ignored in this stage. Gaps in the data appear if the bubble crosses the measurement volume. The influence of additional gaps due to bubbles passing the laser beams outside the measurement volume is studied in subsequent sections. Figure 5.20 shows an example of an artificial signal. Sharp changes in the velocity before the passage of a bubble through the measurement volume are visible.

The estimation of the power spectrum of the bubbly potential flow signal is studied for signals with a length of 500 s. The potential flow signal contains gaps due to the passage of bubbles. Consequently, in parts of the signal no data is available. The problem is, however, different from the more general class of ´missing data´ problems for which dedicated signal processing techniques exist such as those discussed in Broersen et al. (2004). In the present case, however, the signal simply is not defined during the bubble passage through the measurement volume: no liquid velocity can be defined during this period. Since signal processing techniques generally are intended for statistically stationary signals (i.e. without non-defined parts), the outcome should be interpreted with care.

The spectrum of the artificial signal is determined with the use of the techniques discussed in sections 5.3 and 5.6. By studying the outcome with artificial signals for the various techniques,

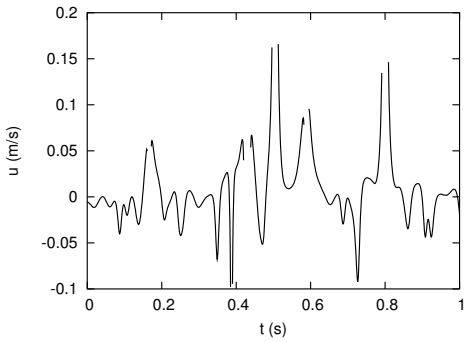

Figure 5.20.: Artificial velocity signal of potential flow around bubbles (α=0.1)

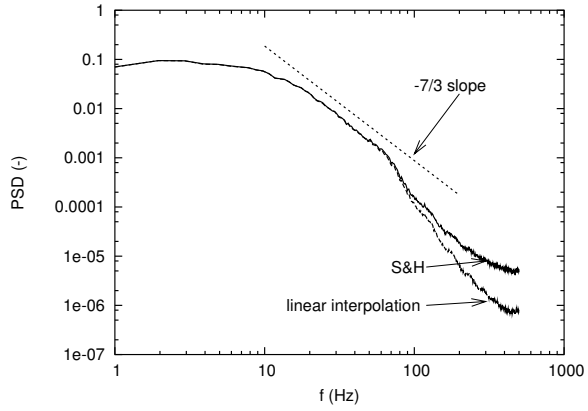

Figure 5.21.: Spectra for potential flow signal obtained with reconstruction techniques (α=0.1).

interpretation of experimentally obtained power spectra is facilitated. Figure 5.21 shows the result for the reconstruction techniques. The gaps due to the bubbles in the signal are reconstructed with Sample & Hold and linear interpolation, with resampling interval 1 ms (which is the original sampling interval for the other parts of the signal).

For frequencies below 10 Hz a more or less constant power is observed, in the frequency range 20-60 Hz a constant slope is observed with a value close to -7/3. For frequencies beyond 100 Hz more rapid decay is observed, the rate depending on the reconstruction technique. The shape is dependent on the bubble velocity: slower bubbles induce steeper slopes, and vice versa. The presence of a wake has a similar result as a lower velocity: a steeper slope is obtained.

In addition, the autocorrelation function is estimated with the slotting technique (Figure 5.22(a)). Two distinct features are visible: a sharp decrease in $\rho(\tau)$ for $\tau < 0.015$ s which is caused by the self-correlation of the high velocities before or after the bubble passage. In addition a peak is observed around τ=0.02 s, corresponding roughly to the residence time of the bubbles in the measurement volume. This is, therefore, the correlation of the high velocities before the passage with the high velocities after the passage of the bubble. This peak in the autocorrelation estimate produces oscillations in the power spectrum (Figure 5.22(b)). If reconstruction techniques are used, extra high velocity points are added and the peaks in the autocorrelation function are smeared and widened (Figure 5.22(a)). Therefore the oscillations are not visible in the spectrum for the reconstruction techniques. Consequently, the slotting technique provides a different shape of the power spectrum for frequencies beyond 20 Hz.

The difference between the power spectrum estimate of the slotting technique obtained with direct transformation and that obtained with the variable window technique is relatively small: the high frequency at which the data was generated gives only a small variance in the power spectrum estimate. Some smearing of the power spectrum with the variable window technique is observed for f>70 Hz. The use of the fit technique by Van Maanen and Oldenziel (1998) faces a problem due to the peak in the autocorrelation function estimate: equation 5.27 can not fit peaks. In Van Maanen (1999) this problem is solved by removing periodic components. For the present signal, the peak is not caused by a periodic component in the signal, but simply by the shape of the potential flow field, combined with the signal gap. Removal would require the removal of the potential flow field, i.e. this is not an option. Nevertheless, an idea of the shape of the power spectrum at high frequencies without the presence of the 'periodic' component can be obtained by performing a fit over the range $\tau < 0.012$ s ('fit' in Figure 5.22(a)). The spectrum that is obtained ('fit' in Figure 5.22(b)) has a similar trend as the oscillations in the slotting results without fitting. This suggests that the decay for f>20 Hz is determined by the shape of the velocity gradients right before and after the passage of the bubble and will be strongly affected by the bubble velocity and presence of a wake.

5.9.2. Combination of turbulent flow and the bubble flow field

As the next step, the combination of a turbulent flow with local flow around the bubbles is considered. The combination is made by superposition, which is obviously only a rough approximation of reality. The following velocity time series is considered:

$$u_{mix}(t_i) = u_{potential flow}(t_i) + C_{mix} u_{turbulence}(t_i) \tag{5.29}$$

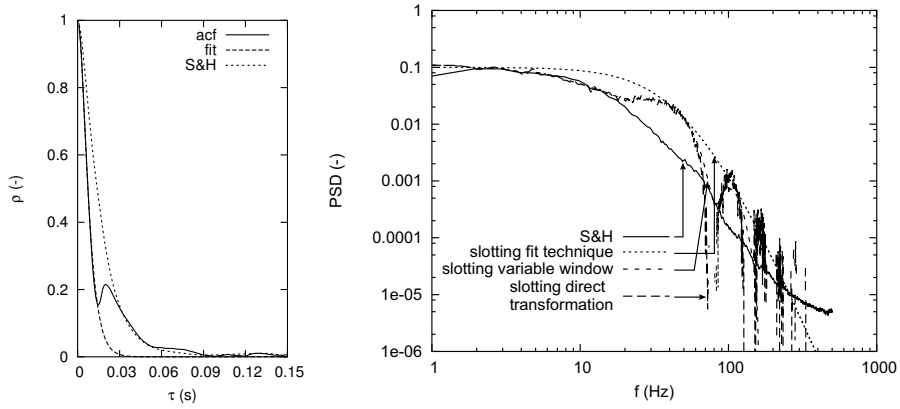

(a) (b)

Figure 5.22.: (a)Autocorrelation estimate slotting technique (fuzzy slotting, local normalization, $\Delta\tau$=1 ms). (b) PSD estimate for slotting techniques and S&H technique, normalized to get similar values at low frequency. $\kappa = 3$. The signal only contains potential flow around the bubbles (α=0.1).

with $u_{mix}(t_i)$ the combined flow signal, $u_{potentialflow}(t_i)$ the flow field due to potential flow only, $u_{turbulence}(t_i)$ the flow field due to turbulence only, and C_{mix} a constant determining the relative strength of the flow fields. The approximation of potential flow underestimates the strength of the fluctuations (De Vries (2001), Van Wijngaarden (1998) and Mudde and Saito (2001)). Nevertheless, a reasonable idea of the effect of the combination of the two signals on the power spectrum can be obtained by selecting C_{mix} such that the ratio of the velocity variances

$$C_{power} = \frac{C_{mix}^2 \sigma_{turbulence}^2}{\sigma_{potentialflow}^2} \tag{5.30}$$

of the two signals is similar to that observed in experimental signals. An idea of this ratio can be obtained by comparing the variance of the velocity fluctuations for similar void fractions in the case of a homogeneous flow and in the case of a heterogeneous flow. A range of values of C_{mix} (and thus C_{power}) is investigated to study the effect on the power spectrum.

Artificial signals with two different exact spectra are considered for $u_{turbulence}$: the spectra 2 and 4 from Figure 5.13(a), both with -5/3 slope at intermediate frequencies but with different cutoff frequencies (10 and 1 Hz respectively). The standard deviations of these signals are 0.044 m/s (spectrum 2) and 0.014 m/s (spectrum 4), versus 0.038 m/s for the potential flow signal ($\alpha = 0.1$). Figure 5.23 shows the results for spectrum 2 for the S&H reconstruction technique and the slotting technique with variable window. In Figures 5.23(a) and 5.23(b) the estimated power spectrum converges to the true turbulence spectrum if C_{mix} increases and the signal is progressively dominated by the turbulence. The convergence is more or less complete for C_{mix}=4 for both techniques (C_{power}=22), for the S&H technique a small difference with the true spectrum is reminiscent: a small bias occurs due to the gaps.

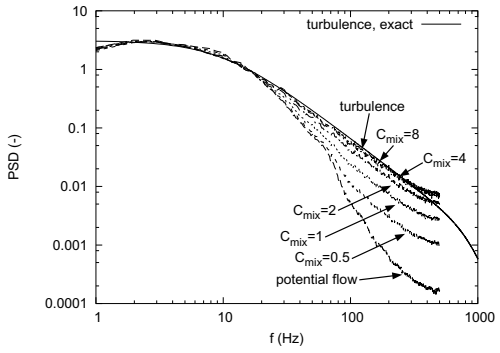

(a) Spectra obtained with S&H reconstruction.

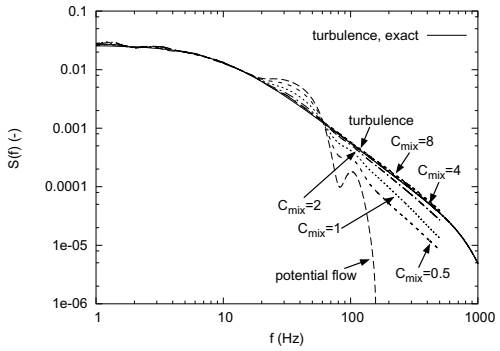

(b) Spectra obtained with fuzzy slotting technique with local normalization and variable window technique ($\Delta\tau$= 1 ms, κ=3).

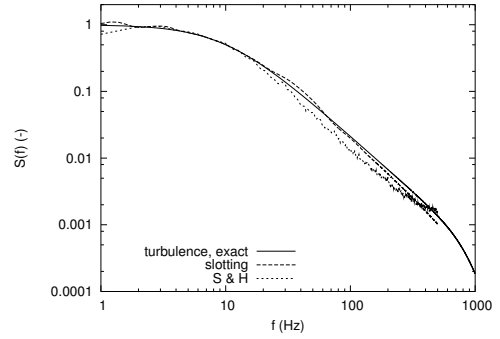

(c) Comparison spectra with S&H technique and slotting technique (C_{mix}=2).

Figure 5.23.: Evaluation of estimated power spectrum for increasing turbulence strength, normalized to get similar values at low frequency. (α=0.1, exact spectrum 2).

The convergence is much faster for the slotting technique than for the S&H technique and for given C_{mix} the power spectrum obtained with the slotting technique is a better approximation of the turbulence spectrum (Figure 5.23(c)). This can be explained by the behavior that was discussed in section 5.9.1 for the Figure 5.22(a). The use of reconstruction adds additional high velocities to the bubble velocity 'spikes' that are present in the signal, increasing their influence on the spectrum. This once again demonstrates that the slotting technique is to be preferred over the reconstruction techniques for the estimation of spectra of signals obtained from bubbly flows. The shape of the power spectrum is determined by C_{mix}. If we ignore the absolute power in the signal, an increase in C_{mix} corresponds to an increase in the turbulence (e.g. transition from homogeneous regime to heterogeneous regime), or a decrease of the void fraction while the coherent structures do not change in strength. If the S&H technique is used (Figure 5.23(a)) a decrease in C_{mix} results in a gradual increase of the slope in the frequency range 20-60 Hz from the value of -5/3 to -7/3. This is quite similar to the behavior reported by Lance and Bataille (1991), who investigated the power spectrum using reconstruction techniques for a turbulent flow (turbulence generated with a grid) in which bubbles are injected. The authors report that the classic -5/3 slope is progressively replaced by another power law of exponent -8/3 when the void fraction increases and the turbulence level is maintained constant. Similarly, Rensen (2003) reported for hot film flow signals that a slope of approximately -5/3 is obtained if the bubble spikes are removed from the signal. A slope of approximately -8/3 is obtained if the spikes are left in the signal. In fact, the behavior reported by Rensen (2003) (Figure 6.14) is very similar to that observed for the spectrum 4 in Figure 5.24(a).

Figure 5.24 shows similar results for the spectrum 4. The turbulent cut-off of the spectrum of this signal occurs at a smaller frequency, increasing the influence of the bubbles on the spectrum. Even for C_{mix}=8 the estimated power spectrum has not approached the turbulence spectrum yet fully. Again, the deviation from the turbulence spectrum is larger for the S&H technique than for the slotting technique (Figure 5.24(c)).

Tests with the slotting fit technique show similar problems as for the potential flow: equation 5.26 is not able to model the oscillations in the power spectra that arise due to the velocity spikes. This means that the fit technique is not able to give a reliable idea about the shape of the power spectrum. Tests were performed with a hybrid combination of the fit technique and the variable window technique: in these techniques the autocorrelation function is fitted only for $\tau < 0.01\ s$, the rest of the autocorrelation function is left unaffected. This technique does not give improved performance over the variable window technique, partly also since the function incorrectly extrapolates the autocorrelation function for the times shorter than the local time estimate of the first slot. Improved results may be obtained by modifying the model in equation 5.26 by adding an extra term like $[1 + (f/f_0)^2]$ in the numerator. This approach is, however, not pursued further and the fit technique is, therefore, not considered further.

5.9.3. Combined effect of the local flow around the bubbles and the gaps due to intersections of bubbles with laser beams

Next, the combined effect is considered of the local flow around the bubbles, turbulence and the gaps in the signal due to intersections of bubbles with the laser beams. This way two problems occur: the measurement of the turbulence spectrum is obscured by the velocity fluctuations due

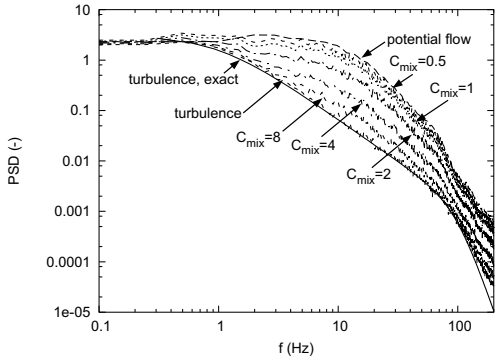

(a) Spectra obtained with S&H reconstruction.

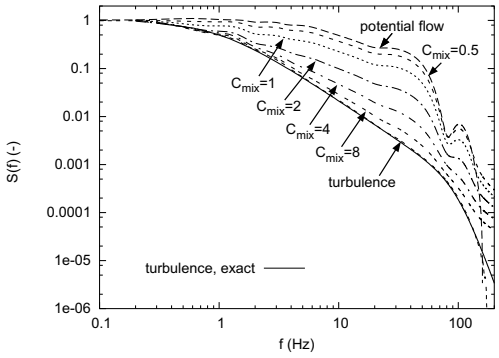

(b) Spectra obtained with fuzzy slotting technique with local normalization and variable window technique ($\Delta\tau$= 1 ms, κ=3).

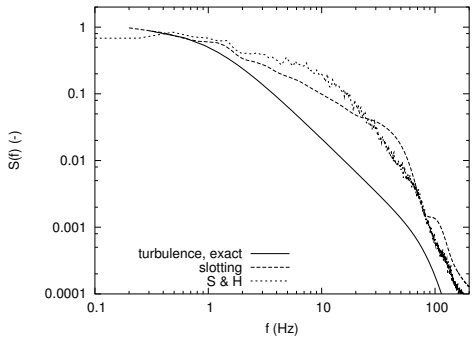

(c) Comparison spectra with S&H technique and slotting technique (C_{mix}=2).

Figure 5.24.: Evaluation of estimated power spectrum for increasing turbulence strength, normalized to get similar values at low frequency. (α=0.1, exact spectrum 4).

to the flow around the bubbles and the signal processing is complicated by the gaps in the signal. An artificial signal is used with a realistic length of 900 s and a particle rate $\dot{N}_p$ of 400 Hz. Figure 5.25 shows the results in the case of only potential flow around the bubbles for Sample and Hold reconstruction and the slotting technique. Figure 5.25(a) shows that if l increases, cutoff in the spectrum due to the gaps occurs at a lower frequency. For $l > 0.01$ m the slope and shape of the spectrum are not reliable for the S&H technique. Much better results are obtained with the slotting technique: for l up to 0.04 m a good impression of the spectrum can be obtained. For the measurements close to the center of the bubble column ($l = 0.08$ m) only a rough idea of the shape of the spectrum is obtained. Some improvement may be obtained by using a smaller value for κ (e.g. 1). For signals containing both the local flow around the bubbles and turbulence with spectrum 2 (Figure 5.13(a)), similar results are obtained (Figure 5.26(a)). The same holds for the results for spectrum 4 in Figure 5.26(b). The gaps have no influence on the bias that was observed in Figure 5.24(b): for all values of l the spectrum deviates similarly from the turbulence spectrum.

5.10. Noise removal from velocity time series

Experimental data is always accompanied by noise, which will obscure the higher frequency information. Therefore, this noise needs to be removed as far as is possible. The present section discusses two techniques for noise removal.

5.10.1. Noise removal via wavelets

Kulkarni et al. (2001a) use wavelet analysis to identify and remove noise from the bubbly LDA signal, based on the work by Roy et al. (1999). The use of wavelets gives the advantage over traditional Fourier techniques that the velocity signal can be studied both in time and at various structure scales. It has been applied in various other investigations to study bubbly flows (e.g. Mudde and Van den Akker (1999), Kulkarni et al. (2001c) and Kulkarni et al. (2001b)). For more information, the reader is referred to Farge (1992), Farge et al. (1996), Kulkarni et al. (2001a) and Meneveau (1991).

The Discrete Wavelet Transform (DWT) of the signal x_i provides wavelet coefficients $W_{j,k}$ at dyadic scales in j and displacements k and is defined as:

$$W_{j,k} = \frac{1}{\sqrt{N}} \sum_i x_i \psi_{j,k}(i) \tag{5.31}$$

for $j \in [0, p]$, $k \in [1, 2^p]$ with $p = \log N / \log(2)$ corresponding to the dyadic scale. Small j refers to fine scales, large j to coarse scales. $\psi_{j,k}$ is the selected wavelet basis. In the current investigation, Daubachies Db4 wavelets are taken, following Kulkarni et al. (2001a).

Kulkarni et al. (2001a) use the following procedure to remove noise from the velocity time series. Since the wavelet transform requires an equidistant time signal, the signal is first reconstructed and resampled with interval T_e. This gives the equidistant signal r_i, consisting of N points. The resampled velocity-time series r_i is differentiated to give r_i^d using the central differences method with fourth order correction. This way, unwanted noise components move

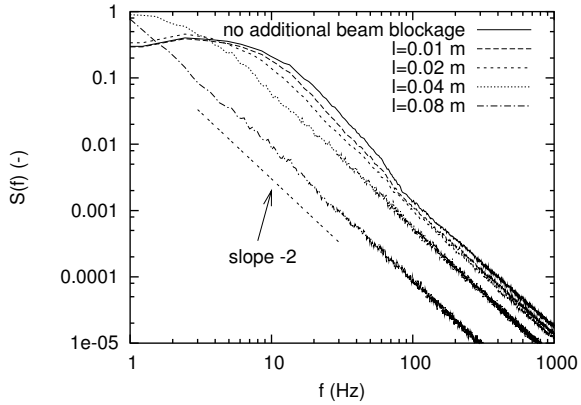

(a) Spectra obtained with S&H reconstruction.

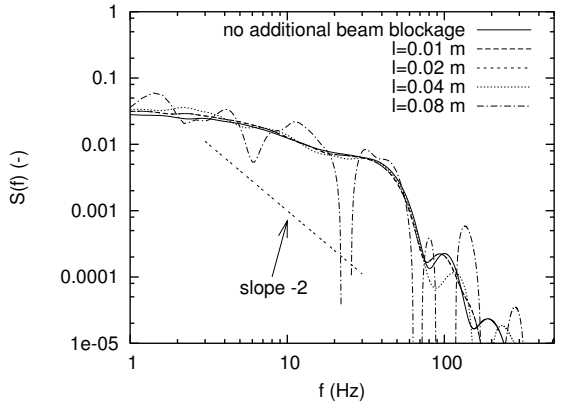

(b) Spectra obtained with fuzzy slotting technique and variable window. κ=3.

Figure 5.25.: Evaluation of spectral estimates for artificial signals with potential flow around the bubbles and gaps due to bubbles interrupting the laser beams (α=0.1)

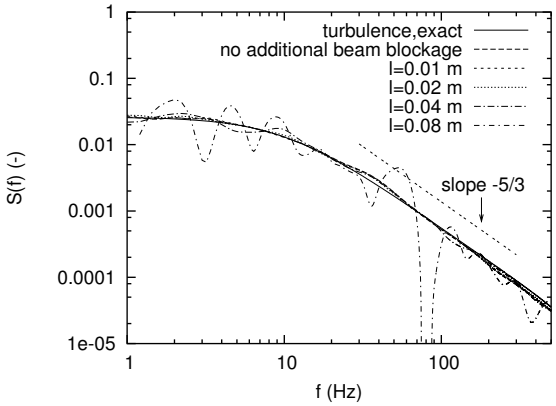

(a) Spectral estimation for exact spectrum 2, $C_{mix} = 2$.

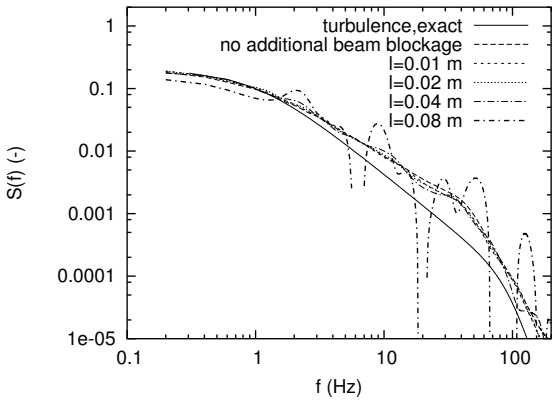

(b) Spectral estimation for exact spectrum 4, $C_{mix} = 4$.

Figure 5.26.: Evaluation of spectral estimates for artificial signals with combined potential flow and turbulence as well as gaps due to bubbles interrupting the laser beams. (α=0.1) Spectra obtained with fuzzy slotting technique and variable window. κ=3.

toward smaller scales. Next, the differentiated data is subjected to wavelet analysis, the wavelet coefficients are calculated. For each dyadic scale j, the power P_j is estimated via:

$$P_j = \sum_k |W_{j,k}|^2 \tag{5.32}$$

By plotting P_j versus j, the scale j_m is identified at which the power due to noise falls off rapidly. The noise is suppressed by zeroing the wavelet coefficients corresponding to the finest scales: $W_{j,k} = 0$ for $j \in [0, j_m]$. Finally, the denoised signal is obtained with the use of the inverse wavelet transform and subsequent integration of the denoised differentiated signal.

This method has been tested by Roy et al. (1999) for application to equidistant signals only. It is, therefore, not clear how the outcome is affected by the non-equidistant nature of the signal and the gaps due to bubbles. As was mentioned, the wavelet analysis requires first a reconstruction step. The previous sections showed that application of Sample and Hold reconstruction may lead to bias in the spectrum; energy from higher frequencies is redistributed to lower frequencies. For this reason, the technique is evaluated with an artificial signal.

The signal with spectrum SN1 (containing a white noise contribution) from Figure 5.12(a) is used to test the denoising routine (α=0.1, l=0.02 m, $\dot{N}_p$=400). The signal is reconstructed with Sample and Hold and resampled at a frequency of 1000 Hz. Figure 5.27(a) shows the scale wise power distribution for the reconstructed signal before and after differentiation. Next, j_m has to be determined, the gradual decay of the scale wise power makes the selection quite subjective. Following Kulkarni et al. (2001a), j_m is chosen at 3, close to what the authors name the "inflexion point" (which is not further specified by the authors) of the scale wise power of the differentiated data. The resulting power spectrum estimate is shown in Figure 5.27(b). The gaps due to the bubbles give a bias from the exact spectrum due to the reconstruction, as was discussed in the previous sections. The denoising operation suppresses power in the frequencies beyond 30 Hz, whereas the noise only becomes apparent in the true spectrum around 100 Hz. In addition, the spectrum of the signal after denoising does not approximate the spectrum of the signal without noise any better than the spectrum of the signal before denoising. A different choice of j_m does not give improvements. This suggests that the wavelet denoising technique does not work for signals with significant gaps. Apparently, the gaps obscure the noise in the combined reconstruction step and wavelet analysis. No advantage over traditional Fourier Transform-based filtering techniques is observed. This technique is therefore discarded.

5.10.2. Noise removal in slotting autocorrelation function

If the slotting technique is used, uncorrelated noise can be recognized relatively easily since it will result in a discontinuity $\Delta\rho$ in the autocorrelation function at τ=0 (see, e.g. Tummers and Passchier (2001)). If $\Delta\rho$ is determined accurately, e.g. via a fit, the discontinuity can be eliminated via:

$$\rho_c(k\Delta\tau) = \frac{\rho(k\Delta\tau)}{1 - \Delta\rho} \tag{5.33}$$

where ρ_c is the corrected autocorrelation function. The value at τ=0 is put to 1 for the corrected autocorrelation function. Figure 5.28(a) shows the result for an artificial signal (signal SN1 from Figure 5.12(a)). For this signal, a fit of the autocorrelation function with equation 5.23 gives

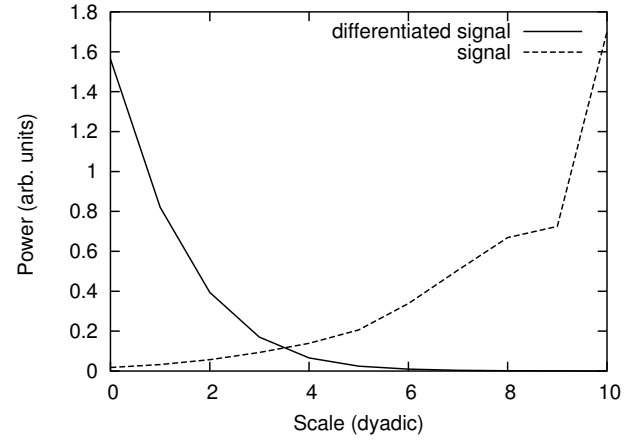

(a) Scale wise power distribution (normalized).

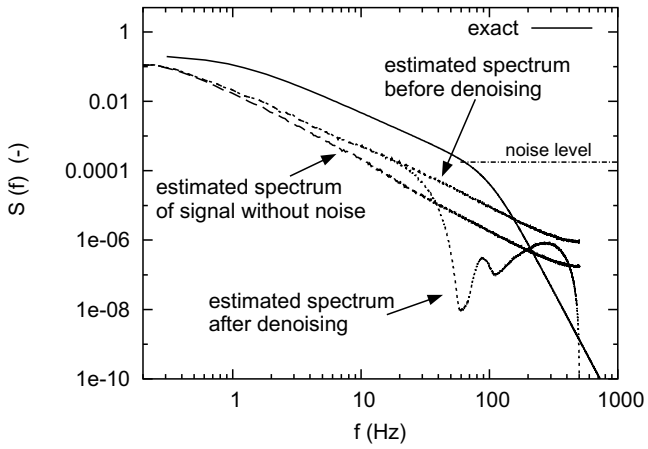

(b) Spectra

Figure 5.27.: Evaluation of wavelet denoising. All spectra shown were obtained from the reconstructed signals with the Welch periodogram (except exact).

good results (Figure 5.28(b), which has $\Delta\rho$=0.17). The maximum frequency up to which the spectrum is reliable is approximately doubled, the spectrum is estimated accurately down to somewhat below the noise level. Tests with signals containing both the local flow around the bubble and turbulence gives similar results: the use of equation 5.23 is also suited for these signals.

5.11. Reduction of the impact of the flow field around the bubble on the spectral estimate: removal of velocity realizations

Section 5.9 showed that the local flow field around the bubbles can have a major impact on the spectra. In order to study the cascade process of the large scale structures, however, a spectrum of the turbulent nature of the flow is required, without the modifications due to the bubbles. The results in Rensen (2003) suggest that removal of bubble signatures from the velocity time series can give a better understanding of the turbulent nature. One possible way to achieve this, is by identification and removal of the velocity realizations which are most dominated by the local flow around the bubbles, followed by estimation of the spectrum via, e.g, the slotting technique. This way, the estimated power spectrum may give a better idea of the turbulent cascade process. The present section first considers the question how much improvement can be obtained by removing the velocity realizations which are dominated by the local flow, and, second, how the removal may be obtained in practice.

5.11.1. Effect of the removal of velocity realizations on the spectrum

Two types of bubble passages can be identified (Figure 5.29). In the first, the bubble crosses the measurement volume, leaving a gap in the data and producing a rapid velocity increase before and a rapid velocity decrease after crossing the measurement volume. In the second, the bubble does not cross the measurement volume, and produces small velocity increases and a larger negative velocity peak.

The first type of interaction can be identified due to the gap signature in the data accompanied by sharp velocity gradients right before and after the gap. The second type of interaction is much harder to identify. No gap is produced, the gradients are much smaller and therefore resemble those due to the turbulence. No suitable technique is known to identify reliably the velocity realizations that are dominated by this type of interaction. Identification of the first interaction type is much more feasible, and, in the presence of wakes, the first type of interaction is relatively more important. Therefore, the focus in the present investigation is put on removal of velocity realizations due to the first type of interaction.

First, the change in the estimated power spectrum is considered if velocity realizations obtained close to the bubbles passing the measurement volume are removed from the series. An artificial signal is considered, with $\alpha = 0.1$, $l = 0.02$ m, d_{eq}=4.5 mm, aspect ratio 0.66, $\dot{N}_p$= 400 Hz and a lens with focal length of 12.2 cm. The signal contains a mix of the turbulence signal (spectrum 4 from Figure 5.13(a)) and potential flow with C_{mix}=4. For this signal, the exact times of the bubble passage through the measurement volume are known. This knowledge is used to determine the effect of the removal of velocity realizations. The bubble starts crossing the measurement volume at time $T_{cross,start}$; the crossing ends at time $T_{cross,end}$. The

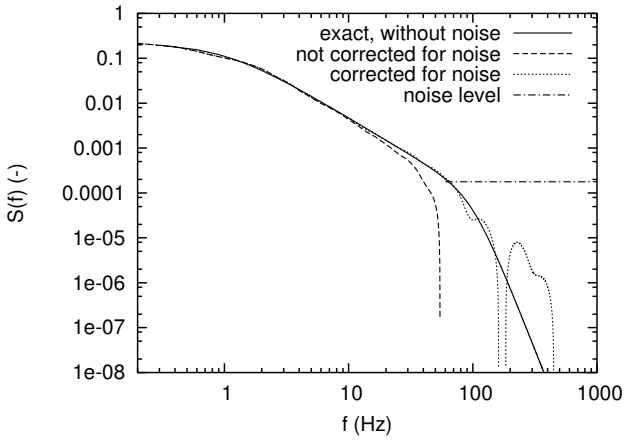

(a) Spectral estimates

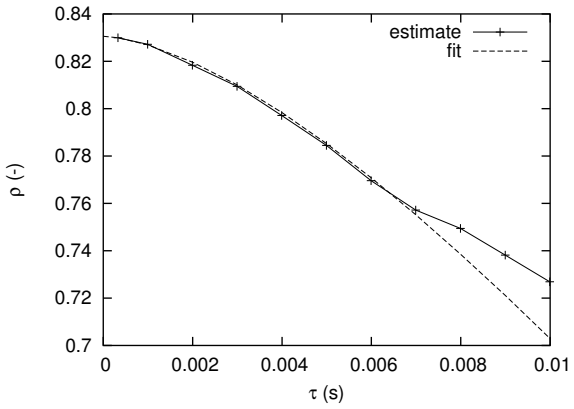

(b) Uncorrected autocorrelation function estimate with fit

Figure 5.28.: Spectral estimation with slotting technique and noise correction. Variable window technique, κ=3, $\Delta\tau$=1 ms, scaled to get similar level at low frequency.

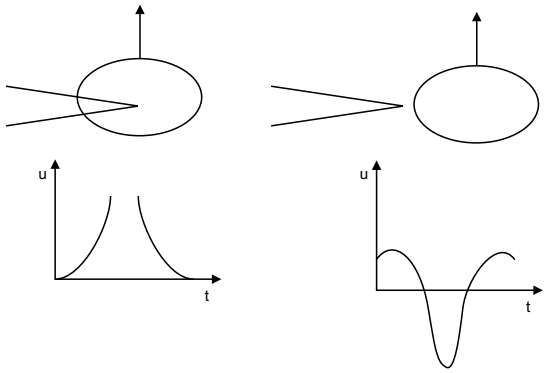

Figure 5.29.: Two types of bubble passage at the measurement volume, with the typical velocity signature that results.

velocity realizations obtained during the time period $[T_{cross,start} - T_{removal,start}, T_{cross,start}]$ and $[T_{cross,end}, T_{cross,end} + T_{removal,end}]$ are removed from the series. For the present work on artificial signals $T_{removal,start} = T_{removal,end} = T_{removal}$. Results for the spectrum and autocorrelation function are shown in Figure 5.30. The power spectrum obtained after removal with $T_{removal}$=0.01 s is a better approximation to the turbulence spectrum for f<10 Hz. A further increase of $T_{removal}$ beyond 0.01 s gives no further improvement. Differences between the estimated spectrum and the turbulence spectrum remain, however, especially for f>10 Hz no improvement is found. Similar effects are observed for the autocorrelation function. The partial improvement can be explained by the second type of bubble passages from Figure 5.29. The bubble signatures due to these interactions are not removed. This shows that in practice it is never possible to fully separate the local flow due to the bubbles, although the performance will be somewhat different in the presence of wakes.

5.11.2. Identification and removal of velocity realizations dominated by the local flow around the bubble

In practice, it is not known when bubbles pass the measurement volume. Therefore, a selection has to be made of the data points that need to be removed. The present section considers techniques to perform this removal.

Removal based on gap length

The simplest technique is based only on the duration of gaps in the data. The interval $\Delta T = t_i - t_{i-1}$ between the measurements obtained at t_i and t_{i-1} is attributed to the passage of a bubble if $\Delta T > T_{mingap}$. The assumption is made that this bubble has passed through the measurement volume, and data obtained in the interval $[t_{i-1} - T_{removal,start}, t_{i-1}]$ and $[t_i, t_i + T_{removal,end}]$ is rejected.

Often, the assumption that this gap corresponds to the passage of a bubble through the measurement volume is not true. We therefore investigate the nature and length of the gaps in

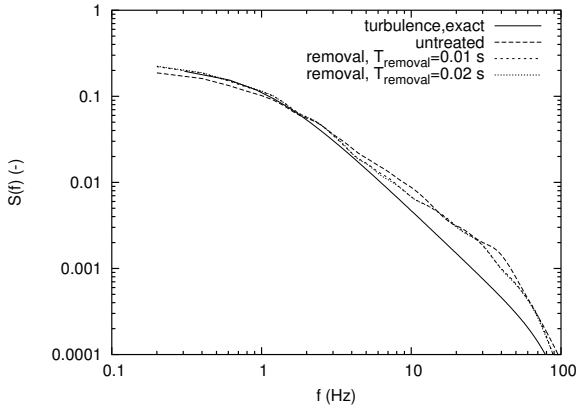

(a) Spectral estimates

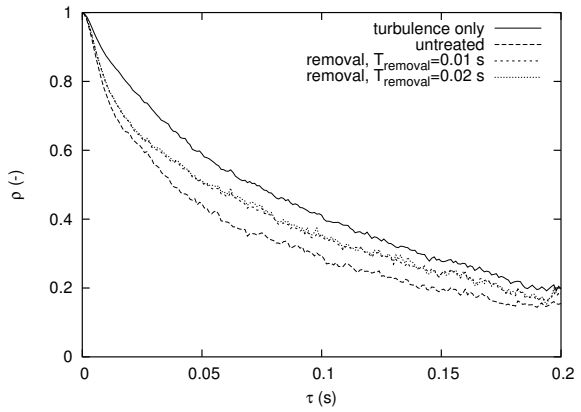

(b) Autocorrelation function estimates

Figure 5.30.: Influence of removal of velocity realizations attributed to local flow on the estimate of the power spectrum and the autocorrelation function. Variable window technique, κ=3, $\Delta\tau$=1 ms.

the signal. In the signals, gaps occur due to various events:

- The random nature of the arrival of seeding particles. Gaps due to the random arrival may be misinterpreted as bubbles, especially for low particle rates. Kulkarni et al. (2001a) also attempt the identification of bubbles via gaps in the signal from forward scatter measurements, and employ data rates in the range of 150-440 Hz. In the present investigation backscatter is used and data rates close to the wall of typically 400 Hz are obtained. Although occasionally large gaps may be expected do to the Poisson nature, this is therefore only a minor problem.
- A bubble crosses the measurement volume. This effect will dominate very close to the wall.
- One or more bubbles block one or both of the laser beams in between the wall and the measurement volume, without actually intersecting the measurement volume. This effect will dominate, more and more, further away from the wall.
- Two or three of these events occur simultaneously.

The relative importance of these effects is investigated with artificial data. The arrival times for both the axial and tangential components are determined for a measurement with $\alpha = 0.1$, $l = 0.02$ m, bubble size 4.5 mm. The arrival times of the axial and tangential components are combined and a lens with shorter focal length (12.2 cm) is used (i.e. blockage for the axial and tangential components is less correlated). With these improvements, less and shorter gaps due to the blockage outside the measurement volume and random particle arrival are obtained. Figure 5.31(a) shows histograms of the gap lengths observed in the signal ('LDA velocity series') and the actual distribution of the duration of the passage of the bubbles through the measurement volume ('measurement volume'). This shows that the number of gaps in the signal is much larger than that can be attributed to passage of bubbles through the measurement volume. In addition, much overlap of blockage events occurs, leading to longer intervals. Figure 5.31(b) compares the actual phase that is present in the measurement volume with the arrival times that are obtained. From the arrival times, identification of the gaps at the measurement volume is very difficult, the actual gaps that are observed are generally larger than the true passage duration of the bubble through the measurement volume. This shows that for the conditions in the present investigation, with bubbles of sizes with order of magnitude of 5 mm, the longer gaps in the signal are dominated by the passage of bubbles in between the wall and the measurement volume. This is already the case for l>0.01 m. Kulkarni et al. (2001a) claim that the overlap of bubble blockage events is only a problem in the case of a wide bubble size distribution and a small bubble passing through the measurement volume. The present data suggests otherwise. Kulkarni et al. (2004) use the gaps in the data for the estimation of bubble sizes. The present observations of the bubble blockage overlap suggests that application of this technique to flows with bubbles with sizes around 4-5 mm is not possible.

The technique with identification based solely on the length of the gaps will therefore often lead to incorrect rejection of velocity realizations. Since the incorrect rejection occurs more or less randomly, this will not give an extra bias. Nevertheless, the variance of the spectrum will increase due to the smaller number of data points available for the estimation. This is illustrated with the artificial signal example from section 5.11.1. The results are shown in Figure 5.32. If

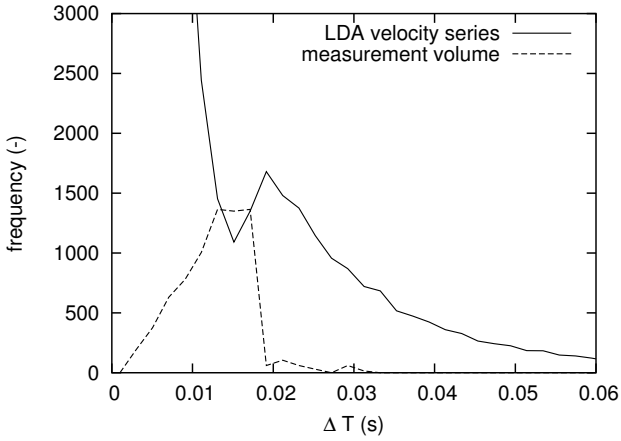

(a) Histogram of time between velocity realizations and the time during which the bubbles block the measurement volume (900 s duration).

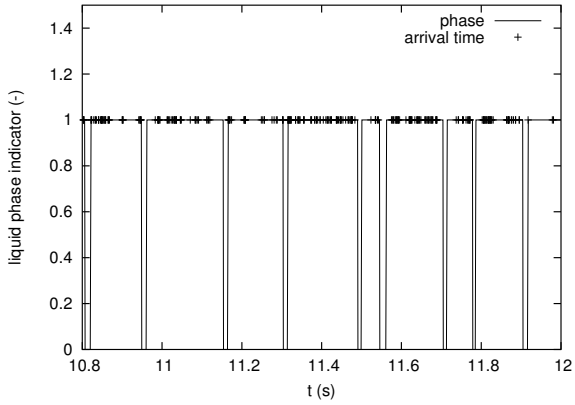

(b) Comparison of the combined arrival times of the axial and tangential component and the phase at the measurement volume (1=liquid, 0=bubble)

Figure 5.31.: Evaluation of gaps in the time signal for the detection of bubbles at the measurement volume.

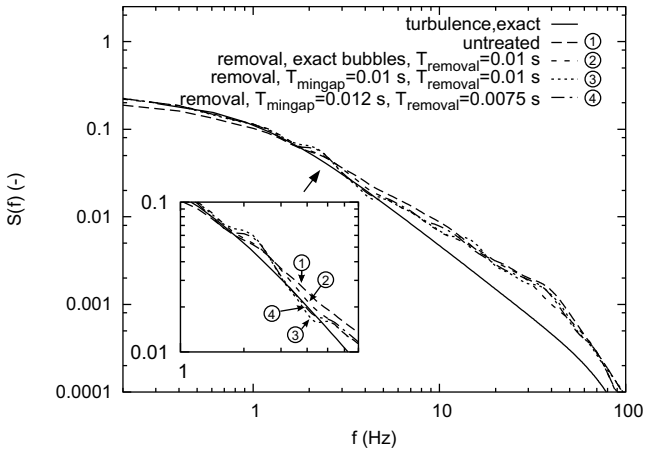

Figure 5.32.: Spectra for various methods of removal of velocity realizations corresponding to local flow around bubbles. Exact bubbles refers to removal based on exact knowledge of bubble removal, otherwise the removal is based on the gap length.

the gaps are detected based on the arrival times of the axial component alone, 81% of the data is thrown away for T_{mingap}=0.01 s and $T_{removal}$=0.01 s, leading to a large variance. The use of both the arrival times of the axial and tangential component results in a rejection of 66% of the data. The random arrival of the particles leads to incorrect estimation of the times when the bubble starts and ends crossing the measurement volume. Consequently, it is justified to use a smaller value for $T_{removal}$ than in the case when exact bubble arrival times are available. Therefore, the values of $T_{removal}$=0.0075 s and T_{mingap}=0.012 s give a good compromise between the reduction in bias and the increase in variance.

The results show that it is possible to get similar reduction in bias as in the case when the exact bubble passage times are known. For practical data, the value of $T_{removal}$ has to be chosen according to what is known about the local flow around the bubble. The values for T_{mingap} and $T_{removal}$ can be varied to study the effect on the spectrum. For increasing l, the rejection of data will increase and consequently, the variance will increase strongly, eventually making spectral estimation impossible.

5.11.3. Identification based on gaps in data and velocity gradients

The previous results showed that a closer approximation to the turbulence spectrum can be obtained by removing velocity realizations around large gaps in the data, but that this occurs at the expense of an increase in the variance. Many velocity realizations are, however, thrown away wrongfully since very frequently the start and end of the gaps do not correspond to the moments when a bubble enters or exits the measurement volume. If, therefore, it is possible to remove the velocity realizations in a more sophisticated way, the increase in variance may be limited. In the following, two methods are described and evaluated, both are based on the occurrence of a gap which is preceded or followed by strong velocity fluctuations.

LIM-technique

Kulkarni et al. (2001a) and Kulkarni et al. (2004) suggest the use of wavelet analysis in combination with a quantity named the Local Intermittency Measure (LIM) for the identification. The velocity fluctuations that follow a bubble passage appear as bursts of energy in the signal. The LIM has been used earlier for the investigation of intermittency in turbulence by e.g. Farge (1992), Meneveau (1991) and Camussi and Guj (1997). In addition, Kulkarni et al. (2001c) use it to find large coherent structures in the signal. Wavelet analysis is particularly suitable for the identification of these bursts, since they are localized both in time and scale.

The LIM gives an idea of rapid changes in the velocity at a specific moment in time and for a certain scale j. Kulkarni et al. (2001a) define the LIM as:

$$\mathrm{LIM}_j(i) = \frac{|x_j(i)|^2}{< |x_j(i)|^2 >_i},\ i = 1, 2, 3, ..., N \tag{5.34}$$

where $<>_i$ denotes averaging over i. $x_j(i)$ is the reconstructed signal for scale j, obtained with the inverse wavelet transform of the wavelet coefficients, after setting the coefficients not corresponding to scale j equal to zero. For more details about the wavelet transform, see section 5.10.1. The definition for LIM is notably different from the original definition used by Farge (1992) and Camussi and Guj (1997), who use

$$\mathrm{LIM}_j(i) = \frac{|W_{j,i}|^2}{< |W_{j,i}|^2 >_i},\ i = 1, 2, 3, .., 2^p \tag{5.35}$$

A graphical representation of the $LIM_j(i)$ can display the velocity gradients and therefore also the bubble passage by using a threshold value. Kulkarni et al. (2001a) tune this threshold value for a number of points to get a good match with the void fraction.

Kulkarni (2005a) mentions that the technique is tested primarily on simple flows, e.g. a bubble plume. In this case, it is reasonable to expect that all strong velocity gradients can be attributed to the bubbles. In the case of a bubbly flow where also other hydrodynamic effects may play a role, e.g. turbulence, peaks in the LIM may also be due to other phenomena. For this reason, we investigate the technique for its suitability for bubble identification in more complex flows.

The test signal from the previous section is used. With tests, we find that the LIM definition in equation 5.35 provides a more straightforward interpretation than equation 5.34, in which also the shape of the basis functions plays a role (although the results are similar for both definitions). Figure 5.33(a) shows the artificial signal, with its Sample and Hold reconstruction, the phase which is present in the measurement volume and the LIM. The values of LIM are considered for the scale which has the closest correspondence to the duration of the typical velocity gradient. The example shows that peaks are observed in the LIM right before and after gaps in the signal due to bubbles passing the measurement volume, but that, also, strong peaks are observed at other instants. Inspection shows that these peaks are caused by turbulent fluctuations, often accompanied by a gap in the data. As a result, the reconstructed signal exhibits a strong jump, which produces the LIM peak. This happens even more frequently for signals with gaps due to bubbles crossing the laser beams (Figure 5.33(b)). The gaps are much longer, and therefore

the jumps introduced by the S&H reconstruction are also larger. As a result, peaks in the LIM are quite general behind a long gap. These do not necessarily coincide with the moments when the local flow around the bubble is measured. Due to the S&H reconstruction, usually a much stronger peaking occurs for the measurements behind the gap than for those before the gap. The example in Figure 9 in Kulkarni et al. (2001a) seems to confirm this behavior. Here, it seems as if the gaps are selected that have the longest duration. In fact, taking into account the length of the gaps (50 ms) and velocities (0.4-1.0 m/s) in their example, the gaps would have to correspond to very large bubbles of 2-6 cm which seems quite unlikely for the conditions that are reported (sintered plate, superficial gas velocities in the range of 1.7-3.8 cm/s, column diameter 15 cm).

Consequently, it seems very difficult to use the LIM technique accurately for the identification of velocity realizations around the bubbles, especially for measurements deeper in the bubble column.

Local fluctuations

An alternative for the LIM technique is, therefore, required. Improvements may be obtained by using linear interpolation instead of Sample and Hold: this would reduce the number of false alerts. However, in the present section a technique is considered that searches strong velocity gradients, while taking into account the non-equidistant nature of the signal. If a gap is found in the signal with duration longer than T_{mingap}, the Local Fluctuation Measure (LFM) is determined for the instants corresponding to t_{last}, the last velocity realization before the gap and t_{first}, the first realization after the gap. The LFM is given by:

$$LFM(t) = \frac{s^2(t)}{< s^2(t) >} \tag{5.36}$$

The deviations $s^2(t)$ and $m(t)$ of the local velocity realizations from the local mean are given by:

$$s^2(t) = \frac{1}{N_{local}} \sum_{i=1}^{N_{local}} (u_{local,i} - \mu_{local}(t))^2 \tag{5.37}$$

$$m(t) = \frac{1}{N_{local}} \sum_{i=1}^{N_{local}} (u_{local,i} - \mu_{local}(t)) \tag{5.38}$$

$s^2(t)$ and $m(t)$ and $\mu_{local}(t)$ are determined with two windows. The first, and smallest, window spans from either $t_{last} - T_{local}$ to t_{last}, or from t_{first} to $t_{first} + T_{local}$. The velocity realizations in the first window are located, their number is given by N_{local}, the velocities are given by $u_{local,i}$ ($i \in [1, N_{local}]$). $s^2(t)$ and $m(t)$ are calculated with this window. The second, and largest, window is centered around time t_{last} or t_{first}. It has duration $T_{\mu,local}$. The mean velocity μ_{local} is determined from the velocity realizations that are located in the second (large) window, but not in the first (small) window.

We assume that we can identify a piece of the signal corresponding to the local flow around a bubble, if a gap was found, LFM(t) exceeds a certain threshold LFM_{min} and $m(t) > m_{threshold}$. The latter constraint serves to prevent the detection of strong negative fluctuations, which more frequently correspond to turbulent fluctuations than bubble passages. If these constraints are

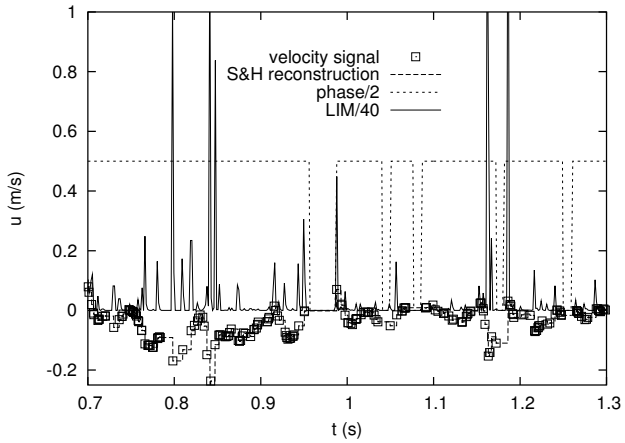

(a) Signal with only large gaps due to bubbles crossing the measurement volume

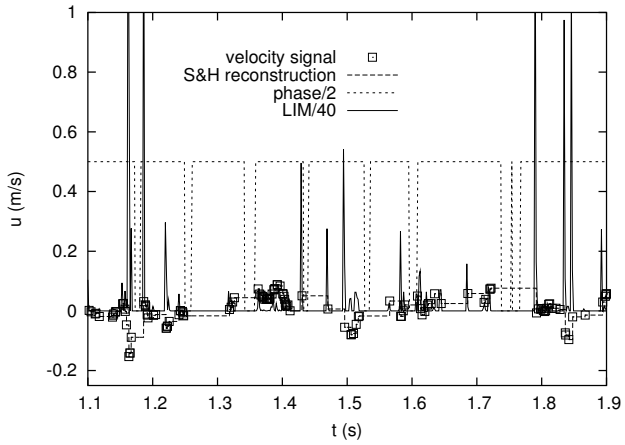

(b) Signal with also gaps due to bubbles crossing the laser beams

Figure 5.33.: LIM for two signals. Phase indicates the phase which is present at the measurement volume at a given instant (1=water, 0=gas), phase and LIM are scaled.

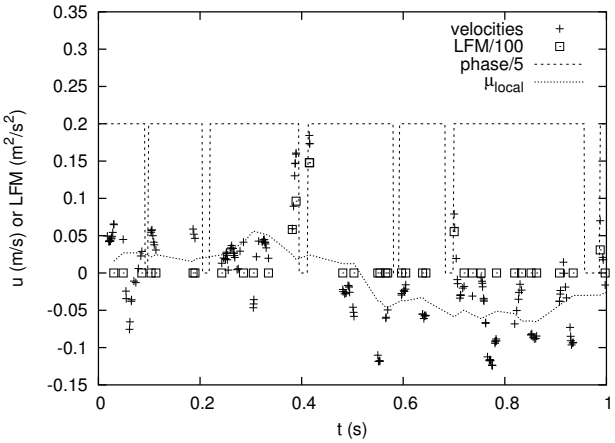

(a) Example of the LFM

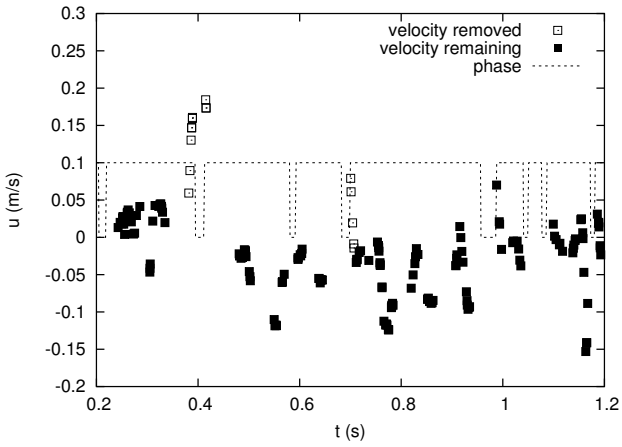

(b) Example of the effect of velocity realization removal using the LFM (LFM_{min}=5)

Figure 5.34.: Example of the LFM use.

satisfied, velocity realizations in a segment of the signal near t_{last} or t_{first} over a duration $T_{removal}$ are removed.

Figure 5.34(a) shows an example of the LFM for an example signal. For clarity, in this example, LFM is set to zero if $m(t) < m_{threshold}$. For this example, the following values were used: T_{local}=0.007 s, T_{mingap}=0.01 s, $T_{\mu,local}$=0.25 s and $m_{threshold}$=0.05 m/s. The combined arrival times of the axial and tangential component are used for the gap lengths. There is a reasonable correspondence of the highest LFM values with the velocity realizations right before and after bubble passage. Visual inspection is, however, not an objective way of setting the threshold. Kulkarni et al. (2001a) and Kulkarni (2005a) mention that the threshold is set to get a good match with the void fraction. The void fraction α^{LDA} is estimated with:

$$\alpha^{LDA} = \frac{\frac{1}{2}\sum_{bubbles}\Delta T_i}{\sum_{short}\Delta T_i + \sum_{bubble}\Delta T_i} \tag{5.39}$$

where the summation $\sum_{bubbles}$ is only over the gap lengths ΔT_i for which the adjacent velocity realizations were removed. The summation $\sum_{short}$ is only performed over the gap lengths ΔT_i shorter than T_{mingap}. The factor $1/2$ is used since gaps can be identified twice (the points before and after the gap are considered separately). LFM_{min}=5 gives the best match for the void fraction. The result with this threshold and $T_{removal}$=0.01 s is shown in Figure 5.34(b).

The result for the power spectrum is illustrated in Figure 5.35 for various values of LFM_{min}. For LFM_{min}=5, the value suggested by the void fraction analysis, the power spectrum provides the best approximation to the true turbulence power spectrum. The result is quite similar to that obtained using the brute force approach, where data around each gap is rejected. With the removal based on the LFM technique, only 5% of the data is rejected, and a smaller variance is obtained. However, the value of LFM_{min} has a strong effect on the power spectrum, especially around 6 Hz. For smaller values of LFM_{min} too many spikes are thrown away: also those due to turbulent fluctuations, generating a new bias. On the other hand, a value of LFM_{min} which is too high results in too little removal. This shows that a reliable result depends on a careful selection of LFM_{min}.

Although the present example suggests that the void fraction presents a good verification method, we previously saw that in fact the number and length of the gaps changes if measurements are performed deeper in the column, and that the gap length cannot be directly coupled to the duration of the intersection of the bubble with the measurement volume. In addition, visual inspection may suggest a different optimal value for LFM_{min}. Tests with artificial signals obtained much closer to the wall shows similar results, but a different threshold LFM_{min} is found via the void fraction technique. This suggests that it is not possible to select a threshold for one condition, and apply it to different conditions. For the present example, we see that the settings of the threshold to get a match with the void fraction results in the removal of approximately the correct amount of peaks from the signal. Inspection shows, that not all of these peaks originate from the local bubble flow, and that part of the peaks due to the local flow are left intact. The performance is, therefore, probably strongly dependent on the conditions (e.g. void fraction, turbulence intensity, particle rate) and the results should be interpreted with care. A safe approach is to use various methods and threshold levels for the removal of the bubble signatures. Comparison can give an idea of the sensitivity of the results to the details of the

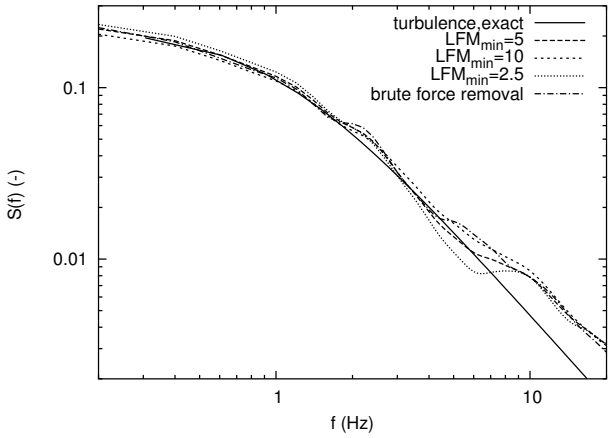

Figure 5.35.: Power spectrum estimates for removal with the LFM criterion.

removal technique.

Further refinements

The technique for removal of velocity realizations can be further refined using various techniques. First, the estimation of the gap lengths could be improved by attempts to further increase the data rate. In the case that the wavelet processor is used (see Chapter 6), additional information from the detector and processor can be used, e.g. the arrival time of rejected bursts is taken into account to further close the gaps due to the random arrival of particles. This will, however, only give a relatively small improvement and this option is therefore not pursued further.

Other methods for improvement can be based on additional properties of the signal. Kulkarni and Joshi (2004b) and Kulkarni et al. (2004) mention a third check of the cross-correlation of the two measured fluctuating velocity components, which is further clarified by Kulkarni (2005a). This is performed as follows: for coincident measurements the cross correlation is calculated (i.e. the product of u' and v', the fluctuating components of the velocities). If a bubble has just passed the measurement volume, the liquid flows in radially, and also high axial velocities are found. Consequently, the cross-correlation shows a peak value. An experimental test is performed to study the potential of this technique. The velocity signal is acquired close to the wall at a distance of 4.5 mm, using a lens with 12.2 cm focal length (beam distance 5 cm), for a void fraction of 15.6% and uniform gas injection. The IFA-750 processor is used, and a data rate of 430 Hz is obtained. Coincident axial and tangential velocity realizations are located, these have a data rate of 210 Hz. A local average of both velocity components is determined by averaging the velocity realizations in a window with duration 0.25 s. The velocity fluctuations u' and v' are now determined by subtracting the local means from the velocity estimates, and their product is calculated. In addition, for each velocity realization, the local gap duration is determined, i.e. the maximum duration of the gaps before and after the velocity realization. Figure 5.36 shows a

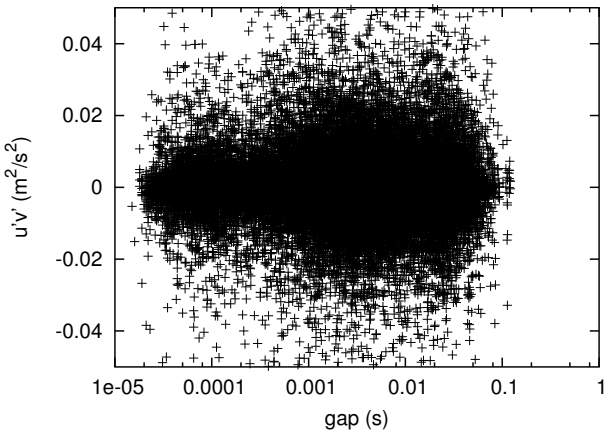

Figure 5.36.: Scatter plot of the gap length versus u'v'.

scatter plot of these two quantities. The measurement was performed close to the wall, i.e. most large gaps can be attributed to bubbles passing the measurement volume. Nevertheless, no clear correlation of the gap length and u'v' is observed. Modifications of the method of calculation, e.g. clustering of small groups of data, gives no improvement. In addition, the number of data points available for the detection is usually much smaller, since coincident measurement of two components is required. Therefore, the use of the cross-correlation technique does not seem suited for the detection of bubbles passing through the measurement volume.

5.12. Conclusions

Effect of bubble gaps on signal processing

The performance of reconstruction and slotting techniques for the estimation of turbulence power spectra of bubbly flow signals obtained with LDA has been investigated. The blockage of laser beams by bubbles leads to extra gaps in the LDA signal. This results in changes in the shape of the data interarrival time distribution, i.e. the overrepresentation of short and long intervals. Spectra of LDA signals calculated with reconstruction techniques suffer from step noise addition and low-pass filtering. The nature of these biases for bubbly flows signals, however, differs significantly from the biases for single phase flow signals. For bubbly flows, the spectrum is reliable up to a cut-off frequency much smaller than the cut-off frequency for a single-phase flow signal with identical data rate. This cut-off frequency is mainly determined by the void fraction α and distance to the wall l and decreases if these parameters are increased. In total, two cut-off frequencies are obtained, their interaction may result in (log-log) decay slopes close to -5/3 in the signal if no turbulence is present at all. Correction for these signal processing artifacts is not possible for bubbly flow signals. The gaps created by the bubbles do not lead to particular problems if slotting techniques or time series analysis are employed. The use of variable window

techniques combined with several improvements in the slotting technique allows for estimation of the spectra well beyond the mean data rate. The application of the fit technique introduced by Van Maanen and Oldenziel (1998) gives similar results for long signals as the variable window technique, but superior results for shorter signals, although it is less suited in the presence of pseudo-turbulence. The use of wavelet techniques for the analysis of the bubbly signal also suffers from problems due to need of signal reconstruction.

Effect of local bubble flow on the power spectrum

The local flow around the bubbles and the wakes of the bubbles generate additional velocity fluctuations in the signal which obscure the turbulence cascade process. Furthermore, no liquid velocity is defined at the moments when bubbles cross the measurement volume, creating problems with the interpretation of spectra. The fluctuations due to local flow generate extra power in the power spectrum, especially at higher frequencies. The amount of extra power is larger for the case of reconstruction techniques than for the slotting technique. The influence of the extra power on the spectrum is strongly dependent on the exact shape of the turbulence spectrum and the turbulence intensity. Results for the combination of gaps in the data and velocity fluctuations due to local bubble flow, show that the use of reconstruction techniques for the study of bubbly flow signals is, generally, not suited. The use of slotting techniques shows a superposition of the deviation due to local flow and an increased variance due to the gaps in the data. The influence of local flow on the power spectrum may be reduced by removing velocity realizations that were produced right before and after the intersection of a bubble with the measurement volume. The removal requires identification of these velocity realizations, which can be based on the associated gap in the data, and also on the strong velocity gradients that are produced close to the bubble. Removal based only on the gap length gives a better approximation of the turbulence spectrum. The improval is, however, only partial since not all fluctuations are localized and accompanied by an intersection event. In addition, the improvement occurs at the cost of a strong increase in the variance. The increase in variance is limited if information about velocity gradients is used, but correct removal is more difficult.

List of symbols

Roman symbols

A, B	constants data interarrival time distribution	-
$a_{fit}, b_{fit}, c_{fit}$	constants for autocorrelation fit	-
b	slot weight function	-
C_{mix}	constant for mixed flow signal	-
C_{power}	ratio strength fluctuations due to turbulence and potential flow	-
d_{eq}	bubble equivalent diameter	m
E	expectancy	
f	frequency	s^{-1}
f_e	resampling frequency	s^{-1}
f_{max}	maximum frequency to be estimated	s^{-1}

$f_{multi}(\eta,\tau)$	probability density function of having two different points with interval η for reconstruction of an interval with duration τ	s^{-1}
$f_{(n)}(\eta,\tau)$	probability density function of having exactly n particles for reconstruction	s^{-1}
f_o	scaling function total bubble blockage duration	-
j_m	dyadic scale where wavelet power drops off	-
L	low pass filter due to reconstruction	-
L_{fit}	least squares error of fit	-
LFM	Local Fluctuation Measure	-
LFM_{min}	Local Fluctuation Measure threshold	-
LIM	Local Intermittency Measure	-
l	distance measurement volume to the wall	m
m	average local deviation of the velocity from the mean	$m\ s^{-1}$
$m_{threshold}$	threshold for m	$m\ s^{-1}$
$\dot{N}_1, \dot{N}_2$	frequency scales for bubbly flow data interarrival time distribution	s^{-1}
N_f	number of DFT/FFT points	-
N_{local}	number of points to calculate s^2	-
$\dot{N}_p$	mean particle rate	s^{-1}
$\dot{N}_{tot}$	mean data rate	s^{-1}
n	number of velocity realizations in interval	-
n_k	number of power spectrum model parameters	s
P	power in wavelet scale	$m^2\ s^{-2}$
$P_{1point}(\tau)$	probability of having no particles in interval τ	-
P_{mv}	probability of multiple validation	-
p	number of displacements for wavelet transform	-
$p_{no}(\Delta T)$	probability of having no velocity realizations during interval ΔT after arrival of a particle	-
r	reconstructed velocity signal	$m\ s^{-1}$
R	autocovariance function	$m^2\ s^{-2}$
R_R	autocovariance function reconstructed signal	$m^2\ s^{-2}$
R_{uu}	original autocovariance function	$m^2\ s^{-2}$
RND	uniformly distributed random number between 0 and 1	-
S	power spectrum	various
S_a	static gain power spectrum model	various
S_{cc}	corrected power spectrum	various
S_{nn}	step noise	various
S_{rr}	reconstructed power spectrum	various
S_{uu}	original power spectrum	various
s^2	local deviation of velocity fluctuations from mean	$m^2\ s^{-2}$
T_a	average interarrival time bubbles	s
T_{bt}	cumulative bubble blockage duration	s
$T_{cross,start}$	time bubble starts crossing measurement volume	s
$T_{cross,end}$	time bubble ends crossing measurement volume	s
T_d	bubble blockage duration	s

T_{dead}	dead time	s
T_e	resampling interval	s
T_{local}	local averaging period for calculating s^2 and m	s
$T_{\mu,local}$	local averaging period for calculating μ_{local}	s
$T_{removal,start}$	duration signal segment removed from the signal before bubble arrival	s
$T_{removal,end}$	duration signal segment removed from the signal after bubble arrival	s
T_{mingap}	minimum gap duration in order to associate gap with bubble	s
t	time	s
t_{first}	time first velocity realization after gap	s
t_{last}	time last velocity realization before gap	s
u	velocity	$m\ s^{-1}$
u', v'	axial and tangential velocity fluctuations	$m\ s^{-1}$
u_{local}	short segment of velocity signal	$m\ s^{-1}$
u_{mix}	combined flow velocity signal	$m\ s^{-1}$
$u_{potentialflow}$	potential flow velocity signal	$m\ s^{-1}$
$u_{turbulence}$	turbulence velocity signal	$m\ s^{-1}$
u_R	reconstructed velocity	$m\ s^{-1}$
W	wavelet coefficients	$m\ s^{-1}$
w	window function for PSD calculation	-

Greek symbols

α	void fraction	-
α^{LDA}	void fraction determined with the use of LDA	-
ΔT	data interarrival time	s
ΔT_{mv}	multiple validation time	s
Δt_p	interval between particle arrivals	s
$\Delta\tau$	slot width	s
κ	variable window constant	-
μ_{local}	velocity mean over small signal segment	$m\ s^{-1}$
ξ_i	time instant velocity realization i	s
ρ	autocorrelation function	-
ρ_c	autocorrelation function corrected for noise	-
σ_{mv}	multiple validation time scale	s
$\sigma_{potentialflow}$	strength fluctuations potential flow signal	$m\ s^{-1}$
$\sigma_{turbulence}$	strength fluctuations artificial turbulence signal	$m\ s^{-1}$
τ	lag	s
τ_{bubble}	typical duration of bubble passage through laser beams	s
τ_f	power spectrum model parameters	s
Ψ	wavelet basis	-

6. Dual burst wavelet LDA processor implemented and tested on real flows [1]

The accurate measurement of turbulence spectra up to high frequencies requires data with high accuracy in both the Doppler frequency and the burst arrival time, as well as a short processor delay time, even in the presence of high noise levels which can be encountered in e.g. bubbly flows. In addition, measurement of the mean and standard deviation of the velocity in a bubbly flow can suffer strongly from bias problems. The present chapter considers the implementation of a dual burst wavelet processor for the processing of LDA signals, in order to get more accurate velocity time series. The processor is described, as well as various tests to check its performance. A comparison is made with the IFA-750 processor that is used for most standard LDA experiments described in the present thesis.

6.1. Introduction

The use of Laser-Doppler Anemometry (LDA) for turbulence research requires accurate estimates of both the frequency of the Doppler burst (which is directly related to the velocity of the tracer particle) and its arrival time. Through the years, considerable attention has been given to the determination of the frequency (an overview can be found in Albrecht et al. (2003)), since the noise in the signal leads to an error in the estimation of the frequency of the Doppler burst and thus in the estimation of the velocity. This, on its turn, translates into a noise floor in the turbulence power spectra. Less attention has been paid to the accurate estimation of the arrival time of the burst. However, for, e.g. velocity signal reconstruction and turbulence power spectrum measurement, the arrival time is very important. This can be clarified in two ways. First, an inaccuracy in the arrival time can be interpreted as an additional error in the velocity estimate because the flow is turbulent:

$$\Delta u \approx \frac{du}{dt}\Delta T_a \tag{6.1}$$

in which Δu is the additional uncertainty in the velocity estimation, u is the measured velocity component, t time and ΔT_a the uncertainty in the arrival time. Alternatively, the uncertainty in the arrival times of two tracer particles results in an uncertainty in the time difference between the two velocity estimates. This translates into an error in the estimation of the auto correlation function of the turbulent velocity fluctuations. Especially for the estimation of the spectrum at the higher frequencies, corresponding to the shortest time scales, this error in the time difference

[1] Parts of this chapter were previously published as W.K. Harteveld, R.F. Mudde, H.E.A. van den Akker, "Dual burst wavelet LDA processor implemented and tested on real flows", proc. 12th int. symposium on application of laser techniques to fluid mechanics, Lisbon, Portugal, 2004

can lead to significant errors in the spectrum at these time scales.

More refined estimators (Benedict et al., 2000; Broersen et al., 2000) allow the determination of the spectra at higher frequencies, but these also require more accurate estimation of the arrival time. In addition, the larger the number of Doppler bursts processed, the lower the variance in the turbulence power spectrum is. Therefore, as many Doppler bursts as possible should be validated.

A practical problem is the "delay time" (or "dead time") of the processor: when a Doppler burst is being processed, no other Doppler burst will be accepted, whether the burst being processed will be validated or not. Because of the exponential time interval distribution, however, there is a significant probability that two Doppler bursts are not separated in time but are (partly) overlapping. Most processors are unable to process such overlapping Doppler bursts correctly, leading to a large number of rejected bursts and a relatively large delay time, which severely hampers the estimation of the turbulence power spectrum at the smaller scales and increases the variance of the turbulence properties, derived from the remaining estimates. To improve the results a processor should therefore be able to:

- Estimate the frequency of the Doppler burst with the highest possible accuracy;
- Estimate the arrival time of the Doppler burst with the highest possible accuracy;
- Be able to process overlapping Doppler bursts and still be able to obtain the best estimators for their frequencies and arrival times.

The development of such a processor, software based, will be described below.

Van Maanen (1999), Nobach and van Maanen (2001) and Van Maanen and Nijenboer (1996) have previously shown that a very reliable technique to estimate accurately both the Doppler frequency and the arrival time is by using wavelets, i.e. by fitting a model of the burst to the data. This technique uses the a priori information about the Gaussian burst envelope shape to provide a high accuracy for these estimates. Nobach and van Maanen (2001) used artificially generated data to show how the noise in the signal is effectively suppressed and that for many cases the accuracy of the Doppler frequency and arrival time estimates approaches the Cramér-Rao lower bound. This technique by itself, however, still assumes the presence of a single burst and does not solve the delay time problem. Nobach (2002a) has considered the option to improve the signal validation by allowing for dual-burst signals. A signal processing technique is proposed where three estimators are used. The first estimator assumes a single burst is present and processes it as such. The other processors assume a dual-burst is present. The first dual-burst processor attempts a separation in the time domain after evaluation of the envelope. The second dual-burst processor attempts the separation in the spectral domain. Finally, for each burst the 'best' estimate is selected. The study pays little attention to the effect of noise in the signal.

The present work considers the combination of the wavelet technique (WT) with the dual-burst approach to a 'dual-burst wavelet processor'. This combination should provide both a short processor delay time, and good performance in the presence of noise: accurate arrival time estimates and Doppler frequency estimates.

The development of the processor is performed especially for use with LDA in bubbly flows, although its use is not limited to this flow type. The application of other measurement techniques

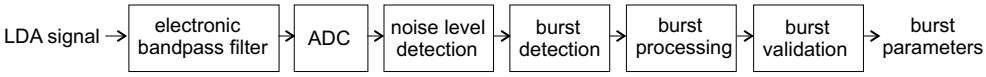

Figure 6.1.: Procedure of LDA signal processing

to bubbly flows has severe limitations. For instance, PIV is not possible at higher void fractions and larger scale equipment due to the limited optical accessibility. Hot film probes suffer from their intrusive nature and their liquid velocity signals contain contributions from the bubble which need to be identified and removed. LDA does not have these problems as predominantly the seeding velocity is measured. Nevertheless, the use of LDA in bubbly flow also has its complications. The reflections and scattering by the bubbles give a much higher noise level. The higher noise level may lead to multiple validation: bursts corresponding to a single particle appear more than once in the final velocity signal. Bubbles crossing the laser beams create gaps in the data (see chapter 5). The flow in a bubble column is characterized by no net liquid flow. If very uniform gas injection is used, the mean axial liquid velocity is low (typically in the range -0.05 m/s to 0.05 m/s) but the fluctuations are much larger (e.g. in the range -0.4 m/s to 0.4 m/s). This may lead to relatively large deviations in the moments due to the various bias sources. The application of the dual-burst wavelet processor may help in dealing with the problems created by the high noise levels, low data rate etc. For instance, the seeding density may be further increased. In addition, by storing the entire LDA signals and use flexible processing via software, extra insight can be gained about problems associated with the use of LDA in the bubbly flows.

The present chapter describes the implementation of the algorithms for the dual burst wavelet processor. In particular, attention is paid to the combination of the dual-burst approach and wavelet approach. The application of the processor to real data is discussed, in particular for bubbly flow. Most algorithms were developed using test bursts obtained experimentally in these bubbly flows. The chapter first discusses the general approach to the burst processing, followed by the algorithms for the processing of single bursts. Next, the processing of dual bursts is discussed, followed by a discussion of the algorithms for detection and validation. The experimental setup used for the tests and the results obtained are discussed. A comparison with the commercial IFA-750 processor is made, followed by conclusions.

6.2. Dual burst wavelet processing

The process of the estimation of burst parameters is composed of a number of steps shown in Figure 6.1.

These will be discussed in more detail in the rest of the chapter. First, an electronic bandpass filter is applied which serves as an anti-aliasing filter and removes the pedestal and noise. The LDA signal is sampled continuously at a high frequency resulting in data files of several GBytes. Next, the signal is processed offline via the use of software written in C++. First, the noise level is determined. This is done to allow automatic setting of the detection parameters and processing parameters. Next, the approximate burst locations are determined by the burst

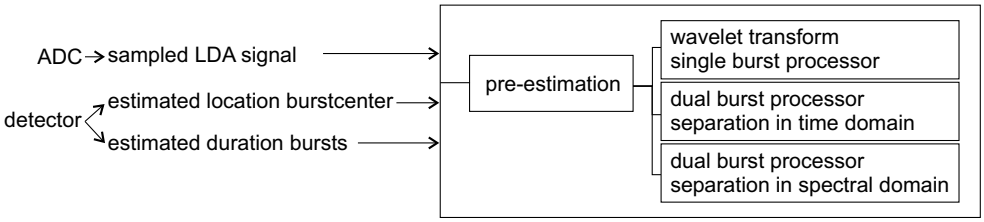

Figure 6.2.: Procedure of LDA signal processing

detector. The burst processor estimates various parameters of the burst. Finally, a separate validation procedure is performed which removes outliers. The separate validation procedure allows quick study of the effect of validation parameters, without the need of re-running the computationally intensive burst processing algorithms.

For the dual-burst processing, an approach similar to that by Nobach (2002a) is taken. For every burst (pair) the parameters are determined in parallel by three processors (see Figure 6.2). This is done since a priori it is not known whether a single or dual burst is present. The first processor considers the signal fragment as a single burst, the other two processors consider the signal fragment as a dual burst. The decision which estimate should be used is made in the validation step. Since the single burst processor is based on the iterative wavelet transform, a pre-estimation is required for several burst parameters. In the following sections the algorithm components are discussed in more detail.

6.3. Single burst processing using the Wavelet transform

The single burst processor processes bursts using the wavelet technique. The present section discusses this technique. The wavelet technique requires pre-estimates for the Doppler frequency and the transit time. For this reason, the techniques used to provide these pre-estimates are also discussed.

6.3.1. Wavelet transform technique

The processing of single bursts with the wavelet transform technique is considered. For more details, the reader is referred to Van Maanen and Nijenboer (1996), Nobach and van Maanen (2001) and Van Maanen (1999). A detected burst is passed to the processors. Its signal $y(t)$ is mean-free, has N points and has been sampled with frequency f_s at times $t_i = i\Delta t$ ($i = 0 \ldots N-1$; $\Delta t = 1/f_s$). The wavelet transform tries to fit the following signal model to this burst (arrival time T_a, transit time T_t, Doppler frequency f_D, phase ϕ and amplitude A):

$$s(t_i) = Ae^{-\frac{8(t_i-T_a)^2}{T_t^2}} \cos(2\pi f_D t_i + \phi) \tag{6.2}$$

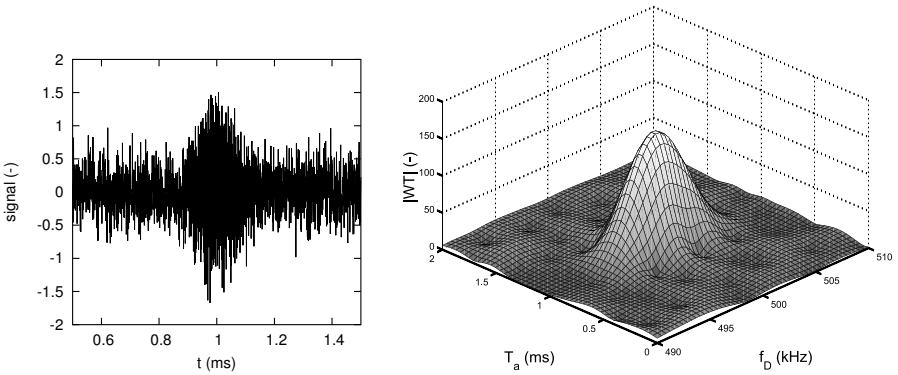

(a) (b)

Figure 6.3.: Example burst (a) and its wavelet transform (b). The Doppler frequency of the burst is 500 kHz, the arrival time 1 ms.

The Wavelet Transform (WT) in complex notation of $y(t)$ is given by:

$$\begin{aligned} \mathrm{WT}\{y\}(f_D, T_a) &= \sum_{i=0}^{N-1} y(t_i) e^{-\frac{8(t_i - T_a)^2}{T_t^2}} e^{-2\pi j f_D t_i} \\ &= \sum_{i=0}^{N-1} y(t_i) E(t_i; T_a) C(t_{i;} f_D) \end{aligned} \tag{6.3}$$

with transform kernels $E(t_i; T_a) = e^{-\frac{8(t_i - T_a)^2}{T_t^2}}$ and $C(t_{i;} f_D) = e^{-2\pi j f_D t_i}$. Figure 6.3 shows an example of a burst and its wavelet transform. In the absence of noise, the wavelet transform of the burst has its maximum at the location of the exact Doppler frequency and arrival time. If noise is present in the signal, a deviation from this location will occur.

The estimates of the Doppler frequency $\hat{f}_D$ and arrival time $\hat{T}_a$ are determined by maximizing the magnitude of the wavelet coefficient:

$$(\hat{f}_D, \hat{T}_a) = \max(|\mathrm{WT}\{y\}(f_D, T_a)|) \tag{6.4}$$

The maximization is performed iteratively. A pre-estimation algorithm determines a first estimate of $\hat{f}_D$ and $\hat{T}_t$: $\hat{f}_{D,pre}$ and $\hat{T}_{t,pre}$. The estimate for the transit-time is held constant during the following calculations. Next, the algorithm calculates the wavelet coefficients for all discrete arrival times at the fixed frequency $\hat{f}_{D,pre}$ and determines the value of the arrival time where their magnitude is maximized:

$$\hat{T_a} = \max\left\{|\mathrm{WT}\{y\}(\hat{f}_{D,pre}, T_a)|\right\} \tag{6.5}$$

Nobach and van Maanen (2001) showed how the wavelet coefficients can be efficiently calculated for a fixed frequency. With $E_0 = e^{-\frac{8t_i^2}{T_t^2}}$, the coefficients at $T_a = k/f_s$ (k=0 ... $N-1$) are

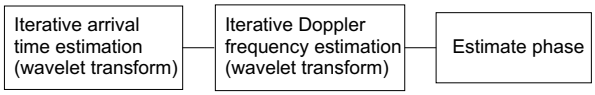

Figure 6.4.: Wavelet transform single burst processor

obtained using:

$$\mathrm{DFT}\left\{\mathrm{WT}\{y\}(f_D, k/f_s)\right\} = \mathrm{DFT}\left\{y \cdot C\right\} \cdot \mathrm{DFT}\left\{E_0\right\} \tag{6.6}$$

with DFT the Discrete Fourier Transform. The Doppler frequency is found at the location of the maximum:

$$\hat{f}_D = \mathrm{argmax}\left\{\left|\mathrm{WT}\{y\}(f_D, \hat{T}_a)\right|\right\} \tag{6.7}$$

The wavelet coefficients can be calculated via the DFT, since:

$$\mathrm{WT}\{y\}(f_D, \hat{T}_a) = \mathrm{DFT}\{y \cdot E(t_i, \hat{T}_a)\} \tag{6.8}$$

The estimate $\hat{f}_D$ is obtained from the coefficients using a three-point Gaussian interpolation algorithm. The phase estimate $\hat{\phi}$ is required for validation purposes. It is estimated from the FFT of the signal using the method described in Nobach and van Maanen (2001). The same authors showed that one frequency iteration and one arrival time estimate are sufficient. This is due to the symmetry of the Gaussian peak in the two-dimensional (f_D, T_a) domain. Consequently, we obtain the algorithm shown in Figure 6.4.

The wavelet transform provides improved accuracy in the Doppler frequency and arrival time estimates by optimal weighing of the signal. If, for instance, the Doppler frequency is determined, the effective windowing operation of the wavelet transform provides the optimal peak-to-noise level ratio in the wavelet coefficients, better than can be achieved with traditional DFT-techniques. A priori knowledge about the peak shape can give a further increase in accuracy via peak fitting. The wavelet transform preserves the Gaussian peak shape, which is not the case for DFT techniques with other window shapes or clipping.

6.3.2. Improved Doppler frequency accuracy due to the wavelet transform

By comparing the power spectrum and the wavelet transform (for fixed arrival time estimate) of a burst immersed in noise, an idea can be obtained why the WT gives higher accuracy for the Doppler frequency estimate than traditional DFT techniques. If the signal of a burst $s(t)$ immersed in noise $n(t)$ is measured during time T_w, a total signal $s(t) + n(t)$ is obtained. From Monte-Carlo investigations it was found that the variance of the DFT coefficients and WT coefficients of the total signal is proportional to the ratio $\sqrt{(n_{\mathrm{DFT}}/s_{\mathrm{DFT}})}$ and $\sqrt{(n_{\mathrm{WT}}/s_{\mathrm{WT}})}$ respectively, with $s_{\mathrm{DFT}} = |\mathrm{DFT}\{s(t)\}(f_D)|^2$, $n_{\mathrm{DFT}} = \mathrm{mean}(|\mathrm{DFT}\{n(t)\}(f)|^2)$, $s_{\mathrm{WT}} = |\mathrm{WT}\{s(t)\}(f_D)|^2$ and n_{WT}= mean($|\mathrm{WT}\{n(t)\}(f)|^2$).

The following noiseless burst is considered:

$$s_1(t_i) = A_1 e^{-\frac{8(t_i - T_{a1})^2}{T_{t1}^2}} \cos(2\pi f_{D1} t_i + \phi_1) \tag{6.9}$$

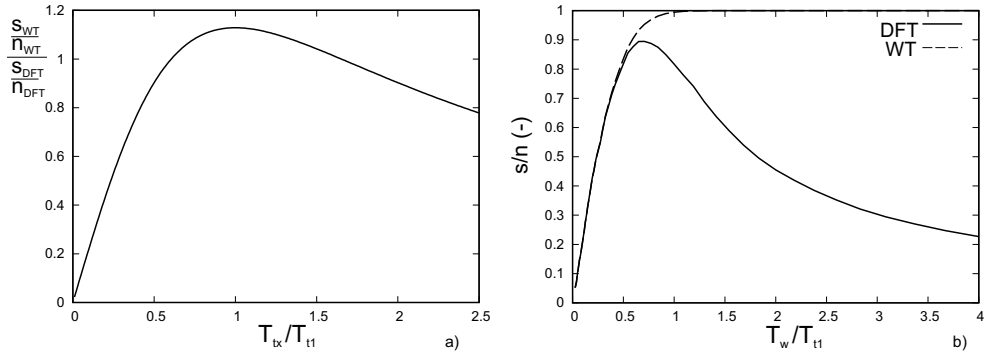

Figure 6.5.: a) s/n ratio for T_w=T_{t1} b) Comparison of s/n for DFT and WT.

With η_1=$8/\mathrm{T}_{t1}^2$, the DFT of the burst is given by (ignoring clipping):

$$|\mathrm{DFT}\{s_1\}(f_k)|^2 = \frac{\pi A_1^2 f_s^2}{4\eta_1} e^{-\frac{2\pi^2}{\eta_1}(f_{D1}-f_k)^2} \tag{6.10}$$

The wavelet coefficients for fixed arrival time T_{a1}, are calculated with a window with width T_{tx} ($\eta_x = 8/T_{tx}^2$):

$$|\mathrm{WT}\{s_1\}(f_k)|^2 = \frac{\pi A_1^2 f_s^2}{4(\eta_1+\eta_x)} e^{-\frac{2\pi^2}{\eta_1+\eta_x}(f_{D1}-f_k)^2} \tag{6.11}$$

The noise signal $n_1(t_i)$ with white Gaussian noise with standard deviation σ_{n1} has $n_{DFT} = \sigma_1^2 N$ and $n_{WT} = \sigma_1^2 N\sqrt{(\pi/2)}/(T_w\sqrt{\eta_x})$. N is the number of data points. With $c_x = T_{tx}/T_{t1}$ we get:

$$\frac{\frac{s_{\mathrm{WT}}}{n_{\mathrm{WT}}}}{\frac{s_{\mathrm{DFT}}}{n_{\mathrm{DFT}}}} = \frac{4}{\sqrt{\pi}} \frac{c_x^2}{1+c_x^2} \frac{T_w}{T_{t1}} \tag{6.12}$$

that has a maximum for c_x=1 (see Figure 6.5(a)), i.e. the maximum accuracy for the WT is obtained with $T_{tx} = T_{t1}$, as was expected.

The effect of clipping is taken into account by calculating the normalized $s_{\mathrm{WT}}/n_{\mathrm{WT}}$ and $s_{\mathrm{DFT}}/n_{\mathrm{DFT}}$ for artificial bursts for a range of measurement durations T_w. The result is shown in Figure 6.5(b). $s_{\mathrm{DFT}}/n_{\mathrm{DFT}}$ first increases with T_w/T_{t1} since a larger part of the burst is used. When T_w/T_{t1} >0.7 relatively more extra noise than extra signal is included and $s_{\mathrm{DFT}}/n_{\mathrm{DFT}}$ drops. The wavelet coefficients have a larger s/n ratio than the DFT coefficients for all measurement durations T_w. This shows that the wavelet transform will provide more accurate frequency estimates. Another way of obtaining improved accuracy for the Doppler frequency estimate is to use the knowledge that a Gaussian burst produces a Gaussian peak in the power spectrum or wavelet coefficients, and fit a Gaussian curve to the peak. Clipping of the burst ($T_w < T_{t1}$) gives a non-Gaussian shape, and may therefore result in reduced accuracy. The WT, however, maintains the Gaussian shape as well as a high s/n.

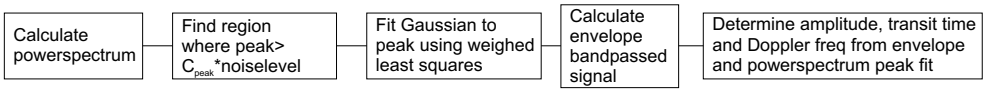

Figure 6.6.: Pre-estimation procedure

6.3.3. Pre-estimation

The iterative wavelet transform requires a pre-estimate for the transit time and the Doppler frequency. This is provided by the pre-estimation algorithms (Figure 6.6). These also provide parameters for validation afterwards, such as the amplitude.

The Doppler frequency is determined from the peak in the power spectrum. A common technique for improving the accuracy is spectral peak interpolation, such as peak fitting (Matovic and Tropea (1991)). The peak in the power spectrum of a Gaussian burst has again a Gaussian shape. From a Gaussian fit of the spectral peak not only the Doppler frequency, but also the transit time can be estimated. The power spectrum peak is fitted over the range [i_1,i_2] by minimizing the weighted least squares criterion

$$L(\hat{T}_{t,pre1}, \hat{f}_{D,pre1}, \hat{K}) = \sum_{i=i_1}^{i_2} \frac{(\ln(|\mathrm{DFT}\{y_1\}(f_i)|^2) + \frac{\pi^2 \hat{T}_{t,pre1}^2}{4}(f_D - \hat{f}_{D,pre})^2 - \hat{K})^2}{\sigma^2_{\ln(|\mathrm{DFT}\{y_1\}(f_i)|^2)}} \tag{6.13}$$

with respect to the estimates for the logarithm of the peak amplitude $\hat{K}$, the transit time $\hat{T}_{t,pre1}$ and the Doppler frequency $\hat{f}_{D,pre}$. The fit requires information about the accuracy of $ln(|\mathrm{DFT}\{y_1\}(f_i)|^2)$, which has been investigated via a semi-empirical analysis of artificial bursts. This shows that if a signal $y_1(t)$ is composed of a noiseless burst $s_1(t)$ and random noise $n_1(t)$, i.e. $y_1(t) = s_1(t) + n_1(t)$, the variance of $ln(|\mathrm{DFT}\{y_1\}(f_i)|^2)$ is approximately given by:

$$\sigma^2_{\ln(|\mathrm{DFT}\{y_1\}(f_i)|^2)} \approx 2.21 \frac{\mathrm{mean}(|\mathrm{DFT}\{n_1\}(f)|^2)}{|\mathrm{DFT}\{s_1\}(f_i)|^2} \tag{6.14}$$

for $\frac{\mathrm{mean}(|\mathrm{DFT}\{n_1\}(f)|^2)}{|\mathrm{DFT}\{s_1\}(f_i)|^2}$ <0.4. However, since $|\mathrm{DFT}\{s_1\}(f_i)|^2$ is not known, $|\mathrm{DFT}\{y_1\}(f_i)|^2$ is used. This leads in general to underestimation of $\sigma^2_{\ln(|DFT\{y_1\}(f_i)|^2)}$, especially for the weaker parts of the burst peak. The underestimation of $\sigma^2_{\ln(|\mathrm{DFT}\{y_1\}(f_i)|^2)}$ in the part of the burst where $|\mathrm{DFT}\{y_1\}(f_i)|^2$ approaches $|\mathrm{DFT}\{n_1\}(f)|^2$, can lead to erroneous fits, usually resulting in an underestimation of $\hat{T}_{t,pre1}$. Therefore, the fit region $i_{fit1} \leq i \leq i_{fit2}$ is chosen according to

$$|\mathrm{DFT}\{y_1\}(f_i)|^2 > \mathrm{mean}(|\mathrm{DFT}\{n_1\}(f)|^2) + C_{peak}(\max(|\mathrm{DFT}\{y_1\}(f)|^2) - \mathrm{mean}(|\mathrm{DFT}\{n_1\}(f)|^2)) \tag{6.15}$$

The region has a minimum size of three points. C_{peak} was chosen after tests with real bursts, with a typical value of 0.1 for strong bursts. Tests with artificial bursts show that the technique is fast and gives much higher accuracy and smaller bias for $\hat{f}_{D,pre}$ and $\hat{T}_{t,pre1}$ than traditional three point Gaussian fits. Typical improvements for the standard deviation of the Doppler frequency and transit time estimates are a factor 5 and 10 respectively.

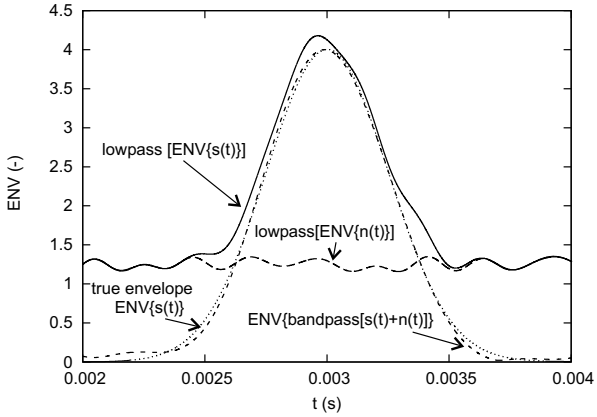

Figure 6.7.: Comparison of various envelope estimates. Lowpass and bandpass refer to lowpass and bandpass filtering operations.

If the bursts are not exactly Gaussian, the transit time estimate can be biased. In addition the noise may cause underestimation. For these reasons, the transit time is also determined from the envelope. The envelope is not only required for the transit time estimation, but is also required for the dual burst processors (e.g. arrival time estimation). The envelope of the signal y(t) is obtained with the use of the Hilbert Transform (HT) (Nobach and van Maanen (2001)):

$$\mathrm{ENV}\{y(t)\} = \left|\mathrm{IDFT}\{\mathrm{HT}^{+}\{\mathrm{DFT}\{y(t)\}\}\}\right| \tag{6.16}$$

where DFT is the discrete Fourier Transform, IDFT its inverse and

$$\mathrm{HT}^{+}\{x\}_i = \left\{ \begin{array}{ll} x_i & \text{for i} \in (0;\mathrm{N}/2) \\ 2x_i & \text{for } 0<\mathrm{i}<\mathrm{N}/2 \\ 0 & \text{for } \mathrm{N}/2<\mathrm{i} \leq \mathrm{N}\text{-}1 \end{array} \right\} \tag{6.17}$$

A low-pass filter can be applied to the envelope to remove oscillations caused by noise. It is important to consider the effect of noise on the envelope estimate. Figure 6.7 (obtained with an artificial burst with $A_1 = 4$ and $\sigma_{n1}^2 = 1$) illustrates that:

$$\mathrm{ENV}\{s(t) + n(t)\} < \mathrm{ENV}\{s(t)\} + \mathrm{ENV}\{n(t)\} \tag{6.18}$$

Therefore, for accurate estimation of the amplitude, transit time and arrival time of bursts, it is important to apply a bandpass filter to the signal before determining the envelope. This bandpass filter should only pass the frequencies where the signal power is larger than the noise power. The envelope of this band passed signal is shown in Figure 6.7, its shape is close to the true envelope. The bandpass filtering is performed by setting the Fourier coefficients outside the region $i_{fit1} \leq i \leq i_{fit2}$ to zero. This was found to render good results.

The transit time can also estimated iteratively from the envelope of the bandpass filtered

signal (extending the approach of Nobach and van Maanen (2001)):

$$\hat{T}^{(k)}_{t,pre2} = \sqrt{\frac{8}{\pi}} \frac{\sum_i \mathrm{ENV}\ \{y_1\ \}\ (t_i)}{f_s \max(\mathrm{ENV}\{y_1\}\ (t_i))} \tag{6.19}$$

where k denotes the iteration. For the first summation (k=0), summation is performed over the total signal. The presence of some reminiscent noise will in general lead to an overestimation of the transit time. Therefore, the estimate is refined in a second iteration (k=1), with the summation over a region with duration $\frac{5}{4}\hat{T}_{t,pre2}$ centred around the maximum of the envelope.

Two estimates of the transit time are available: one from the fit of the power spectrum, another one from the envelope. The estimate based on the spectral peak can suffer from underestimation, the estimate from the envelope can suffer from some overestimation. Therefore, in initial tests the average of these transit times was used as the final estimate:

$$\hat{T}_{t,pre} = \frac{\hat{T}_{t,pre1} + \hat{T}^{(1)}_{t,pre2}}{2} \tag{6.20}$$

For weak bursts, the estimate $\hat{T}_{t,pre1}$ is less reliable. Furthermore, in cases where there is part of a second burst in the segment provided by the burst detector, the peak shape in the power spectrum may be strongly affected. Consequently, the estimate $\hat{T}^{(1)}_{t,pre2}$ is found to be more reliable for practical data and it is therefore selected as the final estimate:

$$\hat{T}_{t,pre} = \hat{T}^{(1)}_{t,pre2} \tag{6.21}$$

The amplitude of the burst $\hat{A}_1$ is estimated from the band passed envelope:

$$\hat{A}_1 = \max(\mathrm{ENV}\{y_1\}(t_i)) \tag{6.22}$$

6.4. Dual bursts processing

In the dual burst processors, the following signal model is fitted to the data:

$$s(t_i) = A_1 e^{-\frac{8(t_i - T_{a1})^2}{T_{t1}^2}} \cos(2\pi f_{D1} t_i + \phi_1) + A_2 e^{-\frac{8(t_i - T_{a2})^2}{T_{t2}^2}} \cos(2\pi f_{D2} t_i + \phi_2) \tag{6.23}$$

Wavelet transform applied to dual bursts

Doppler frequencies may be estimated by fitting the peak of the coefficients obtained via the DFT or the WT. Similarly, the arrival time may be estimated via a fit of the peak obtained with the wavelet transform or the peak in the estimate of the envelope of the burst. The shapes of the peaks obtained with these techniques differ, however. The shapes of the peak obtained with the |WT| and the $|\mathrm{DFT}|^2$ are given by:

$$|\mathrm{WT}\{s_1\}(f_D, T_a)| \propto A_1 T_{t1} e^{-4\frac{(T_a - T_{a1})^2}{T_{t1}^2}} e^{-\frac{\pi^2 T_{t1}}{16}(f_{D1} - f_k)^2} \tag{6.24}$$

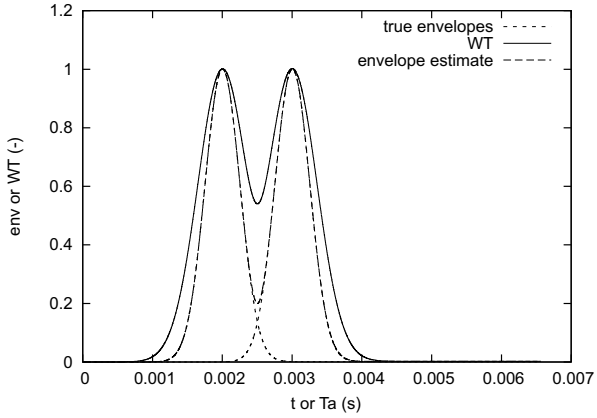

Figure 6.8.: Comparison envelopes and wavelet coefficients for a dual burst

$$|\mathrm{DFT}\{s_1\}(f_k)|^2 = \frac{\pi A_1^2 T_{t1}^2 f_s^2}{32} e^{-\frac{T_{t1}^2 \pi^2}{4}(f_{D1}-f_k)^2} \tag{6.25}$$

Comparison of equations (6.24) (squared) and (6.25) shows that the use of the WT results in a spectral peak that is a factor $\sqrt{2}$ wider than the spectral peak that is obtained with the DFT. Similarly, comparison of equations (6.24) and (6.23) shows that the temporal width of $|\mathrm{WT}\{s\}(f_D, T_a)|$ is also a factor $\sqrt{2}$ larger than the width of the burst envelope. The increase of the widths may lead to problems if a dual burst is measured where the two bursts have almost the same Doppler frequency and arrival time. Whereas a minor peak overlap may be obtained with the DFT or envelope based estimation techniques, a larger peak overlap is obtained using the WT technique. This is illustrated in Figure 6.8 for two artificial bursts with equal frequency and a small arrival time difference. An initial minor temporal overlap in the envelope becomes a severe overlap in the wavelet coefficients. The increased overlap can create a larger bias for the estimate of the Doppler frequency and arrival time. For even larger overlaps, it may even make the detection of the second peak impossible. Therefore, direct use of the wavelet transform for the estimation of dual bursts is not suitable and an alternative approach is taken incorporating only elements of the wavelet transform.

Tests with artificial bursts show that the variance of the arrival time estimate using the envelope of the band passed signal is only slightly larger than the variance using the wavelet transform. Therefore, the dual burst processor with temporal separation uses this envelope to estimate the arrival time instead of the wavelet transform. For the dual burst processor employing spectral separation, drift and detectability of the Doppler frequency may also improve by using the original power spectrum instead of the frequency iteration of the wavelet transform. However, this advantage is only present for bursts with very strong temporal overlap (i.e. two particles at almost exactly the same time in the measurement volume) and Doppler frequencies which are very close. These bursts provide little additional information anyway. Therefore, the Doppler frequency is estimated using the frequency iteration of the wavelet transform where maximum noise suppression is obtained. For bursts with strong overlap in time and frequency, further

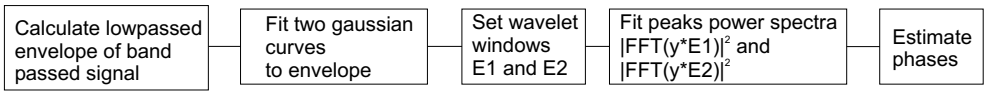

Figure 6.9.: Dual burst processor with separation in time

improvements may be obtained by incorporating a third dual-burst processor which uses window shapes which suppress noise effectively, try to suppress the peak by the other burst, but have a smaller widening effect on the peak shape. This is not performed in the current investigation, however.

6.4.1. Dual burst processor with separation in time

Bursts with overlap in the spectral domain may be separated if their overlap in time is small. The basic idea is to cut the signal at the point of overlap and process the two parts separately, similar to Nobach (2002a). The current processor, however, employs a multiplication by a wavelet window to suppress the other burst and noise. Some measures are implemented to allow for some temporal overlap. Figure 6.9 shows the algorithm schematically.

First, the signal $y(t)$ (an example is given in Figure 6.10a) is filtered with a bandpass filter. The pass regions of the filter are based on the amplitude in the power spectrum. The threshold requires an estimate of the noise level and the peak height. Therefore, the frequency f_{max} and height P_p of the highest peak in the power spectrum $P(f)$ are determined. Next, the locations of the adjacent minima at frequencies $f_{min,s}$ and $f_{min,e}$ are determined. The region $[f_{ps}, f_{pe}]$ around the highest peak is identified: this is the region $[\min(f_{min,s}, f_{max} - f_{width}/2),\ \max(f_{min,e}, f_{max} + f_{width}/2)]$, where f_{width} is the spectral peak width based on a burst duration timescale obtained from the noise detector. The noise level P_n is the average power spectrum level outside region $[f_{ps}, f_{pe}]$.

The pass regions of the filter are determined. For this purpose, the threshold level $P_{threshold} = 0.2(P_p - P_n) + P_n$ is used. The frequencies f_i in the power spectrum $P(f)$ with $P(f_i) > P_{threshold}$ are identified. Around each of these frequencies f_i, a region is identified which extends from f_i up to the closest local minima in the power spectrum. All these regions are combined and form the pass regions for the band pass filter (the combined regions are not necessarily connected). (Figure 6.10b). The bandpass filter is set to pass all of the frequencies in these regions, the Fourier coefficients of all other frequencies are zeroed. This gives the filtered signal $y_f(t)$. Next, the envelope $\mathrm{ENV}_{bandpass}$ of the bandpass filtered signal is determined using the Hilbert transform. A lowpass filter is used to remove the remaining oscillations from the envelope, providing $\mathrm{ENV}_{lowpass}$. The lowpass filter passes frequencies up to $2\pi/T_{gap}$ with T_{gap} the estimate for the burst duration from the noise detector. Fourier coefficients corresponding to frequencies outside this range are zeroed. Examples of the envelopes are shown in Figure 6.10c.

Next, the highest peak in the envelope is identified. A Gaussian curve $G_1^{DT}(t) = \hat{A}_1^{DT} e^{-\frac{8(t-\hat{T}_{a1}^{DT})^2}{(\hat{T}_{t1}^{DT})^2}}$ is fitted to three points to determine the estimates for amplitude $\hat{A}_1^{DT}$, arrival time $\hat{T}_{a1}^{DT}$ and transit time $\hat{T}_{t1}^{DT}$ of the burst with the largest amplitude. The three points used in the fit are the maxi-

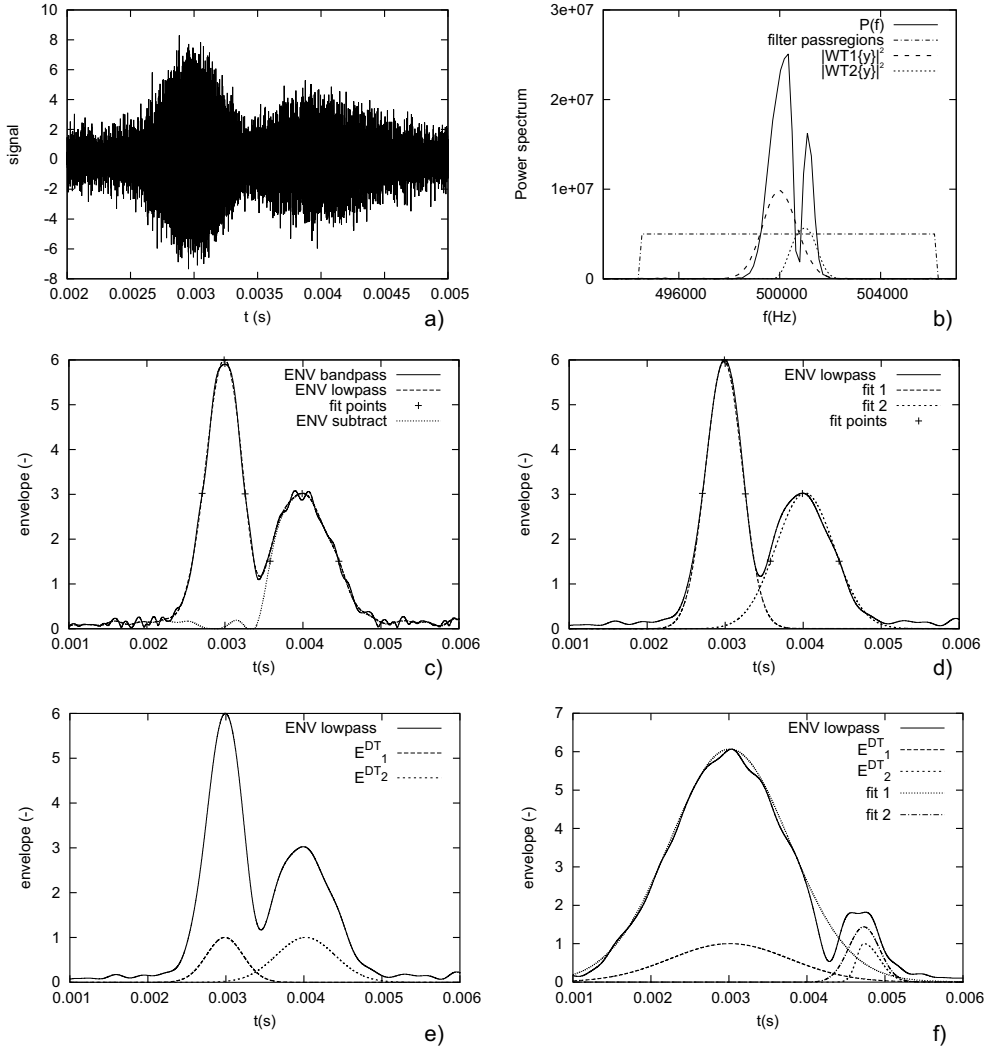

Figure 6.10.: Steps in dual burst processing with temporal separation. a) Signal b) Power spectra c) Envelopes d) Fits of envelopes e) Wavelet windows f) Wavelet windows for burst pair with stronger overlap

mum, and the points at the flanks where the threshold level min(ENV$_{lowpass}$)+0.5(max(ENV$_{lowpass}$)-min(ENV$_{lowpass}$)) is crossed. For bursts where the separation is feasible, these three points will belong to a single burst. The fit is followed by the removal of the fitted burst from the envelope via:

$$\mathrm{ENV}_{subtract}(t) = \max(\mathrm{ENV}_{lowpass}(t) - G_1^{DT}(t), 0) \tag{6.26}$$

The amplitude $\hat{A}_2^{DT}$, arrival time $\hat{T}_{a2}^{DT}$ and transit time $\hat{T}_{t2}^{DT}$ of the second burst are estimated in the same way, via fitting $G_2^{DT}(t) = \hat{A}_2^{DT} e^{-\frac{8(t-\hat{T}_{a2}^{DT})^2}{(\hat{T}_{t2}^{DT})^2}}$ to three points of ENV$_{subtract}$. The fitting procedure is illustrated in Figure 6.10c) and d). The Doppler frequencies are estimated with the use of the frequency iteration step of the wavelet transform. The influence of a possible temporal overlap on the peak of the wavelet coefficients is investigated. The noisy signal $y(t)$ is assumed to be composed of two bursts having noiseless signals s_1(t) and s_2(t). If a window with transit time T_{tx} is used, we get (with $\eta_i = 8/T_{t,i}^2$ and $\eta_x = 8/T_{t,x}^2$):

$$|WT\{s_i\}(f_D, T_a)| = \frac{\sqrt{\pi} A_i f_s}{2\sqrt{\eta_i + \eta_x}} e^{-\frac{\pi^2}{\eta_i+\eta_x}(f_{Di}-f_D)^2} e^{-\frac{\eta_i\eta_x}{\eta_i+\eta_x}(T_{ai}-T_a)^2} \tag{6.27}$$

The peak associated with burst j is estimated using a window with $T_a = T_{aj}$ and $T_{tx} = T_{tj}$. The wavelet coefficients will contain peaks due to both bursts. The ratio of the amplitudes of the peaks corresponding to burst i and burst j is given by the "overlap criterion":

$$OC_{ij} = \frac{|WT\{s_i\}(f_{Di}, T_{aj})|}{|WT\{s_j\}(f_{Dj}, T_{ai})|} = \frac{A_i}{A_j}\sqrt{\frac{2\eta_j}{\eta_i + \eta_j}} e^{-\frac{\eta_i\eta_j}{\eta_i+\eta_j}(T_{ai}-T_{aj})^2} \tag{6.28}$$

If OC_{ij} >0.5 the overlap is too big, and the window is made more narrow to reduce the influence of overlap with:

$$\hat{T}_{tj}^{DT*} = \max(2|\hat{T}_{aj}^{DT} - \hat{T}_{ai}^{DT}| - \hat{T}_{ti}^{DT}, \frac{\hat{T}_{tj}^{DT}}{10}) \tag{6.29}$$

If OC_{ij} <0.5 the standard wavelet transform Doppler frequency iteration method is used for burst j: the overlap is small enough to ensure detection of the correct peak. This gives $\hat{T}_{tj}^{DT*} = \hat{T}_{tj}^{DT}$.

The following window is obtained (for simplicity, we assume that $\hat{T}_{aj} < \hat{T}_{ai}$):

$$E_j^{DT}(t_i; \hat{T}_{aj}^{DT}) = \begin{cases} e^{-\frac{8(t_i-\hat{T}_{aj}^{DT})^2}{(\hat{T}_{tj}^{DT})^2}} & \text{for } t_i \le \hat{T}_{aj}^{DT} \\ e^{-\frac{8(t_i-\hat{T}_{aj}^{DT})^2}{(\hat{T}_{tj}^{DT*})^2}} & \text{for } t_i > \hat{T}_{aj}^{DT} \end{cases} \tag{6.30}$$

An example is shown in Figure 6.10 e). In this example, the overlap is small and the window has not been narrowed. In the example in Figure 6.10 f), a different burst pair is considered with stronger overlap. Consequently, the window is narrowed for burst 2. The Doppler frequency of burst j ($\hat{f}_{D,j}^{DT}$) is determined using a Gaussian three-point fit of the maximum of $|\mathrm{WT}_j^{DT}\{y\}|^2$ (see Figure 6.10c), which is determined with:

$$\mathrm{WT}_j^{\mathrm{DT}}\{y\}(f_D, \hat{T}_{aj}^{DT}) = \mathrm{DFT}\{y \cdot E_j^{DT}(t_i, \hat{T}_{aj}^{DT})\} \tag{6.31}$$

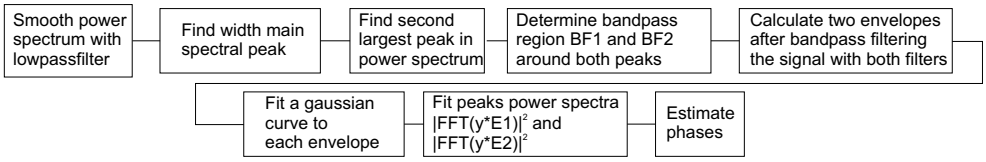

Figure 6.11.: Dual burst processor with spectral separation.

6.4.2. Dual burst processor with spectral separation

The dual burst processor tries to perform the separation in the frequency domain by finding the peaks in the power spectrum due to both bursts and selectively process these using digital filtering. This is again similar to Nobach and van Maanen (2001) but using wavelet techniques and other measures to reduce the influence of noise. A schematic overview of the method is shown in Figure 6.11.

First, the two largest peaks in the power spectrum have to be identified, as well as reliable bandpass regions around these peaks for the digital filters. Due to noise, the power spectrum contains oscillations which hamper the correct identification of these peaks and bandpass regions. For this reason, the power spectrum is smoothed using a Gaussian lowpass filter. The transit time estimate of the largest-amplitude burst with temporal separation $\hat{T}_{t1}^{DT}$ is used to set the minimum frequency scale $f_w = 4\sqrt{2}/(\pi\hat{T}_{t1}^{DT})$ that should be passed. The filter has transfer function e^{-i^2/N_c^2} with $N_c = f_{p,max}/(2f_w)$, where $f_{p,max}$ is the maximum frequency in the power spectrum. After searching the largest-amplitude power spectrum peak (located at f_{max1}), the second largest peak (located at f_{max2}) has to be found in the power spectrum. For this purpose, the algorithm determines the frequency range $[f_{ps1}, f_{pe1}]$ of the main peak that should be excluded from the search. Minima adjacent to the maximum are located: $f_{min1,s}$and $f_{min1,e}$.

The exclusion region $[f_{ps1}, f_{pe1}]$ is now taken as $[\min(f_{min1,s}, f_{max}-0.7f_w),\ \max(f_{min1,e}, f_{max}+0.7f_w)]$. The bandpass filter frequency ranges are set: for peak j the bandpass filter BF_j^{DF} has frequency pass range $[f_{bpsj}, f_{bpej}]$. The range is determined in the same way as the search exclusion zone discussed before. For peak j, the minima adjacent to the peak are determined: $f_{minj,s}$ and $f_{minj,e}$. If the peaks are not close (i.e. $|f_{max1} - f_{max2}|/f_w > 2$), the peak width $[f_{wj,s}, f_{wj,e}]$ is estimated from the timescale with: $f_{wj,s}= f_{max,j}$-$0.75f_w$ and $f_{wj,e}= f_{max,j}$+$0.75f_w$. Otherwise, $f_{wj,s}= f_{max,j}$-$0.5f_w$ and $f_{wj,e}= f_{max,j}$+$0.5f_w$. Finally, $f_{bpsj} = \min(f_{minj,s},\ f_{wj,s})$ and $f_{bpej} = \min(f_{minj,e},\ f_{wj,e})$. Figure 6.12 illustrates the procedure.

For each peak, the signal is bandpass filtered and the envelope is determined:

$$\mathrm{ENV}_j^{DF}(t) = \mathrm{ENV}(\mathrm{BP}_j^{\mathrm{DF}}(y(t))) \tag{6.32}$$

Next, each envelope ENV_j^{DF}(t) is fitted with a Gaussian curve G_j^{DF}(t) (Figure 6.12c), from which the estimates for amplitude $\hat{A}_j^{DF}$, arrival time $\hat{T}_{aj}^{DF}$ and transit time $\hat{T}_{tj}^{DF}$ are obtained. The fitting procedure is identical to that for the dual burst processor with temporal separation. Subsequently, the Doppler frequencies are estimated with the use of the frequency iteration step

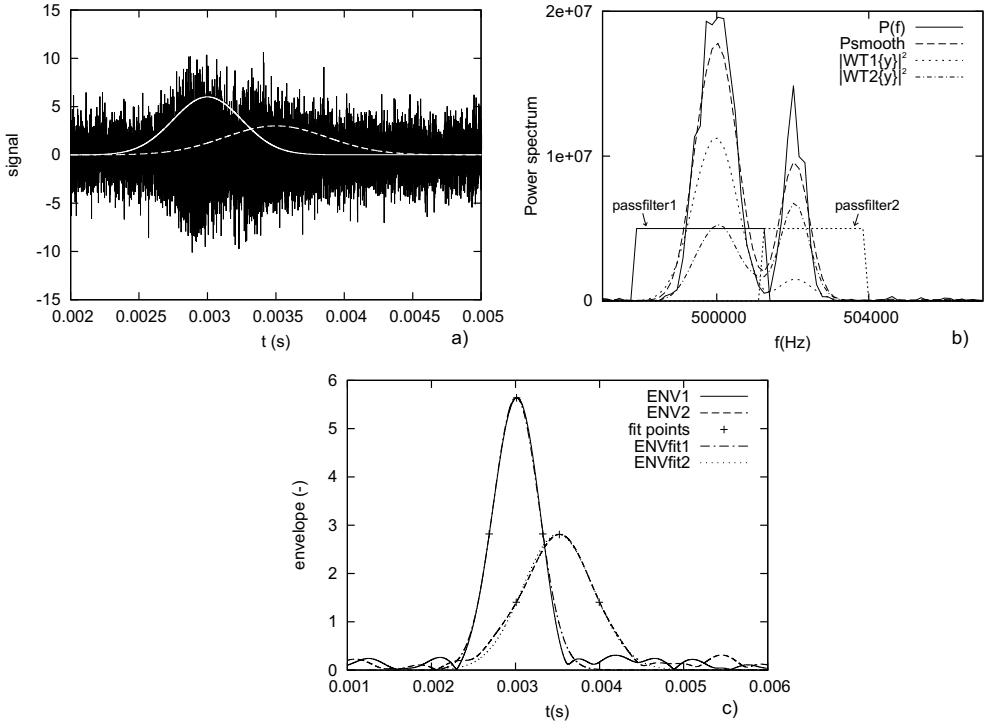

Figure 6.12.: Steps in dual burst processing with spectral separation. a) Signal b) Power spectra, raw and smoothed with bandpass filter ranges and $|WT|^2$ for both bursts c) Envelope fits.

of the wavelet transform. With $E_j^{DF}(t_i;\hat{T}_a) = e^{-\frac{8(t_i-\hat{T}_{aj}^{DF})^2}{\hat{T}_{tj}^2}}$:

$$\mathrm{WT}_j^{\mathrm{DF}}\{y\}(f_D,\hat{T}_{aj}^{DF}) = \mathrm{DFT}\{y\cdot E_j^{DF}(t_i,\hat{T}_{aj}^{DF})\} \tag{6.33}$$

The Doppler frequency of burst j ($\hat{f}_{D,j}^{DF}$) is determined using a Gaussian three-point fit of $|\mathrm{WT}_j^{DF}\{\mathrm{y}\}|^2$ of the maximum located in the range $[f_{bpsj}, f_{bpej}]$.

6.5. Detection and validation

6.5.1. Noise level detection and burst detection

The noise level detection and burst detection are discussed only briefly. An extensive discussion can be found in appendix B. An estimate of the noise level of the LDA signal is required for automatic setting of threshold levels in the burst detector as well as for the burst processing. A

rough estimate for this noise level is found by calculating the standard deviation after removal of the bursts from the signal. The bursts are removed by an iterative algorithm based on the probability density function of a small part of the signal. If a large fraction of the points differs significantly from the mean, the part of the signal is considered to be part of a burst.

The burst detector is based on an autocorrelation technique, which has similarities with the algorithm by Jenson (1992). The detector should detect bursts with frequencies inside a given range. Delays are selected that correspond to the location of the first maximum at nonzero lag of the autocorrelation of signals with these frequencies. A small window is shifted over the signal. The autocorrelation coefficients for these delays are calculated for this window. The maximum autocorrelation coefficient is selected: $A_{acf}(\mathrm{t})$. Burst candidates are found by locating the parts of the signal where $A_{acf}(\mathrm{t})$ exceeds a threshold level $A_{acf,threshold}$. False detection is reduced by rejecting burst candidates with duration shorter than a certain threshold, as well as candidates with mean and maximum $A_{acf}(\mathrm{t})$ levels lower than certain thresholds. Thresholds are set automatically, based amongst others on the burst duration and the noise level, to minimize the occurrence of multiple validation, false detection and bias in the burst duration. In addition, the algorithm and sampling rate are optimized to prevent a Doppler frequency dependent probability of detection. At this moment, the settings of the detector have been set sensitive to avoid possible bias. This results, however, in a somewhat higher rate of false detection, leading to larger computational loads for the processor. Tests show that the automated setting of detection thresholds works well: no user input or tweaking is required.

The detector outputs the start positions and end positions of the possible bursts. These segments are subsequently read by the processor. Since the processor uses FFT routines, the length of the segment is extended to the nearest larger power of two. A window is used to suppress the signal in the parts which have been added due to the segment extension.

6.5.2. Validation

After processing the detected bursts, the estimated parameters for the three processors are passed to the validation algorithm. The validation algorithm has two main purposes: first, to remove outliers from the time series, and second, to select which of the three processor outputs will be used.

Three possible criteria are considered for the removal of outliers, these will be evaluated for their suitability. If

$$SNR_k = \frac{\hat{P}_P^k}{\hat{P}_N^k C_a(\hat{f}_D^k)^2} > SNR_{threshold} \tag{6.34}$$

or

$$SNR_k^{(3)} = \frac{\hat{P}_{P3}^k}{\hat{P}_N^k C_a(\hat{f}_D^k)^2} > SNR_{threshold}^{(3)} \tag{6.35}$$

or

$$\frac{A_k}{C_a(\hat{f}_D^k)} > A_{threshold} \tag{6.36}$$

is not satisfied, the burst is rejected. $\hat{P}_P^k$ is the height of the power spectrum peak. $\hat{P}_{P3}^k$ is the sum of the heights of the power spectrum peak and its two neighbor points. $\hat{P}_N^k$ is the mean

noise level in the power spectrum. C_a(f) is a frequency dependent amplification factor that is necessary to compensate for imperfections in the photo multiplier tube and electronics used in the experiments. The initial experiments performed, used the amplifier and bandpass filters in the TSI IFA-750 burst processor. Tests with the TSI equipment showed that its amplification factor may vary up to a factor of 2 over the frequency range inside the specified bandpass filter range (appendix C). Obviously, this causes a bias for measurements with a large variation in the Doppler frequency (e.g. bubble columns). For this reason, a correction is included in the validation criterion. Appendix C discusses the measurement of C_a(f). In order to reduce the problems related to the use of the IFA-750 amplifier and filters, dedicated amplifiers and filters were built. Their use made the requirement for correction obsolete.

Apart from the removal of outliers, the rejection via the SNR criterion also serves a second purpose. Especially for measurements close to the wall, a local maximum is observed in the power spectrum at the preshift frequency. This is caused by light scattered by impurities at the wall. For this reason, bursts with a frequency close to the preshift frequency and small SNR are rejected. In section 6.6.2 the criteria for outlier removal are discussed in more detail.

After the removal of outliers, the remaining burst estimates correspond to actual coherent signals. Nevertheless, the individual processor estimates may be inaccurate since the actual number of bursts differs from the number of bursts that the processor can handle. E.g., the single burst processor may produce inaccurate results if a dual burst is present, similarly both the single and dual burst processors may produce inaccurate results if more than two bursts are present. A simple test to check for the presence of these additional bursts is by checking the 'peak ratio' P_{ratio} of the second largest maximum and the largest maximum in the power spectrum or wavelet transform. If a second burst is present, this ratio is large. The peak ratios for the various processors are given by:

$$P_{ratio}^{single} = \frac{\max 2|DFT\{y\}(f)|^2}{\max|DFT\{y\}(f)|^2} \tag{6.37}$$

$$P_{ratio,j}^{DT} = \frac{\max 2(\mathrm{WT}_j^{DT}(f_)))}{\max(\mathrm{WT}_j^{DT}(f_)))} \tag{6.38}$$

$$P_{ratio,j}^{DF} = \frac{\max 2(\mathrm{WT}_j^{DF}(f_)))}{\max(\mathrm{WT}_j^{DF}(f_)))}, \text{ with } f \in [f_{bpsj}, f_{bpej}] \tag{6.39}$$

where max2 denotes the second largest maximum. The search for the dual burst processor with spectral separation is only performed over the band pass regions. If

$$P_{ratio} > P_{ratio,threshold} \tag{6.40}$$

is satisfied for one of the burst estimates, it is rejected. The value of $P_{ratio,threshold}$ is typically set to 0.2. With this value, reliable rejection of multiple bursts is performed. If smaller values are used, the use of the criterion gets a similar character as the signal-to-noise ratio criteria (e.g. $SNR^{(3)}$): it removes the bursts that have a higher inaccuracy due to the noise in the signal.

After these two checks, the estimates with the largest inaccuracies have been removed from the data set. There is, however, the possibility that the dual burst processor has mistaken a

single burst for a dual burst due to e.g. oscillations in the envelope. In addition, the overlap of the bursts may have been so strong that a large inaccuracy in the arrival time results. The probability of correct detection by the dual burst processors can, however, be estimated. For the dual burst processor with temporal separation, the separation in time using the envelopes is the most crucial step: if the bursts cannot be correctly distinguished in the envelope, the results are inaccurate. The criterion

$$OCT_{ij} = \frac{\int_0^T \mathrm{ENV}_i(t)\mathrm{ENV}_j(t)dt}{\int_0^T (\mathrm{ENV}_j(t))^2 dt} \approx \frac{\sqrt{2}A_i}{A_j} \frac{T_{ti}}{\sqrt{T_{tj}^2 + T_{ti}^2}} e^{-\frac{8(T_{aj}-T_{ai})^2}{T_{tj}^2+T_{ti}^2}} \tag{6.41}$$

gives information about the impact of the overlap by burst i on burst j. Tests with artificial bursts show that if OCT_{ij} >0.15 the location of burst j has probably been misdetected. Consequently, if OCT_{12} >0.15 or OCT_{21} >0.15 the burst pair is rejected.

Similarly, the dual burst processor with spectral separation only produces useful results if the spectral peaks can be distinguished. If the spectral overlap criterion

$$OCF_{ij} = \frac{\int_0^{f_s/2} P_i(f)P_j(f)df}{\int_0^{f_s/2} (\mathrm{P}_j(f))^2 df} \approx \frac{A_2^2 T_{t2}^2}{A_1^2 T_{t1}^2} \frac{\sqrt{2}}{\sqrt{T_{t1}^2 + T_{t2}^2}} e^{-\frac{\pi^2 T_{t1}^2 T_{t2}^2 (f_{d1}-f_{d2})^2}{4(T_{t1}^2+T_{t2}^2)}} \tag{6.42}$$

exceeds 0.1 for one of the two bursts the burst pair should be rejected since the spectral peak of burst j has likely been misdetected. If the smallest amplitude burst of a burst pair outputted by a dual burst processor is strongly clipped (it overlaps with the start or end of the signal block), the pair is also rejected. In addition, bursts corresponding to possible stray signals are rejected as well as burst pairs with strong temporal overlap (which originate from two particles present at the same time in the measurement volume).

After these checks, the best processor estimate is selected from the remaining estimates: the processor estimate is chosen that has the smallest least squares norm:

$$L_k = C_{L,k} \sum_{i=0}^{N-1} (s^k(t_i) - y(t_i))^2 \tag{6.43}$$

L_k is the least squares norm, $C_{L,k}$ a constant and $s^k(t)$ is the model signal for processor k (equations 6.9 and 6.23); $y(t)$ is the input signal. Tests show that the accuracy of the phase estimate is sufficient to allow a correct choice. In addition, tests show that if two bursts are present in the signal, L_k will be significantly smaller for the dual burst processor estimates than the single burst processor estimate if both remain after the previous checks. Consequently, the dual burst processor output will be chosen. If, however, a single burst is present, sometimes small oscillations in the envelope may be interpreted as a second burst by the dual burst processor. In this case, the L_k norm for the dual burst processors is slightly smaller than that of the single burst processor (in the order of 1%). For this reason, the constant $C_{L,k}$ has been introduced. It

is typically set to 0.9 for the single burst processor and to 1 for the dual burst processors. This way the single burst processor output will be preferred in this case.

When all bursts have been outputted, these are sorted by arrival time and a final search is made for bursts strongly overlapping in time. For signal segments where the bursts are very closely packed, the burst detector may output two directly adjacent intervals. If a (second) burst is present at the edges of these intervals, it may be processed and outputted twice. If such a burst pair is found, the estimate with the largest signal-to-noise ratio is selected and the other discarded.

6.6. Test experiments

Several tests were performed to evaluate the performance of the new combination of detector, processor and validation. The present section discusses the setups used, an evaluation of the criteria for removal of outliers in the validation step, improvements in the data rates and the accuracies that are achieved as well as the delay time reduction.

6.6.1. Setup

Experiments to test the processor performance were performed in a laminar single phase flow and a bubbly flow. The LDA equipment consists of a 4W Spectra-Physics Ar^+ laser and a TSI 9201 colorburst multicolor beam separator. Beam pairs are focused using a backscatter probe. Detected light is sent to a TSI 9230 colorlink. For comparison purposes and setting of the equipment, bursts are processed with processor type IFA-750 (TSI), controlled by a 486 PC. Initially, the electronic signals were amplified and bandpass filtered using the filters present in the IFA 750 equipment. Many problems were encountered which could be traced back to these amplifiers and filters (see appendix C). For this reason, dedicated filters and amplifiers were developed to filter and amplify the signals. Acquisition of the signals is performed using a dual channel fast analog digital convertor (Spectrum MI.3011) which is built in an Adlon 1700+PC with 4 striped harddisks with a total storage capacity of 160 GByte. This system allows for 8 or 12 bits acquisition of two channels at sampling frequencies up to 20 MHz each. Combined with the processing software, this provides a cheap (euro 5000 + costs of the PC) yet a powerful LDA processing unit. The software was written in standard C++ and its application is therefore not limited to a windows or linux platform. Tests (sample frequency 2.5 MHz) show that typical computation times for the Adlon 1700+ machine are in the range of 3-10 times the measurement time, which is acceptable. Since software is used for the processing, scaling of the processing power is easily achieved by using more PCs.

Two flows were investigated. The first is a laminar pipe flow. A pipe (diameter 0.05 m) containing a glycerol-water mixture with a viscosity around 35 mPas was used (for more details, see section C.2.1). The second flow is a bubbly flow. Air is injected into a rectangular container with dimensions 0.04 m x0.24 m x1.0 m (dxwxh), void fractions are in the range of 10% and bubble sizes around 4 mm.

6.6.2. Outlier removal

The removal of outliers should conform to two demands:

- As many correct bursts should be passed as possible to get a high data rate.
- The fraction of bursts that are passed should not depend on e.g. the velocity of the particles.

These two demands can be conflicting: the probability of detection may depend on the velocity of the particle. Therefore, if the second demand has to be satisfied, this may mean that a significant part of the correctly detected and estimated bursts has to be rejected to prevent a bias.

Special care was taken to prevent a possible bias in the detector. This is discussed in appendix B. In addition, appendix C discusses the efforts involved in removing sources of bias in the electronic equipment (amplifiers, bandpass filters). Due to these efforts, the use of the correction factor $C_a(\hat{f}_D^k)$ in equations 6.34-6.36 is no longer required. The present section focuses on the use of the criteria in equations 6.34-6.36, selection of the threshold level for validation and the influence of the criteria on the data rate and possible bias.

The criteria are tested with the use of experiments in the laminar pipe flow of the glycerol-water mixture. A pre-shift frequency of 500 kHz was used with electronic filter range 100-1000 kHz, sampling frequency of 2.5 MHz and a backscatter probe with a lens with focal length 0.122 m. With this setup, the liquid velocity is constant in time, and only the axial velocity component is nonzero. Consequently, the data rate should be proportional to the axial velocity component, if bias due to the processor is not present (of course, velocity bias remains). By determining the data rate for different velocities, the effect of the various criteria for outlier removal is investigated.

The velocity of the liquid is varied by changing the flow rate. A velocity signal is acquired both using the IFA-750 processor and the dual burst wavelet processor. This velocity time series is chopped in small segments of 500 velocity realizations, the data rate and mean velocity is determined for each segment. Two different experiments are performed. In the first experiment, the variation of the flow rate is performed on a short time scale (10-20 seconds) to prevent inaccuracy due to e.g. drift in the photo multiplier tubes (see also appendix C). A second experiment is performed to determine the data rate corrected for multiple validation (i.e. the multiple detection of a single burst). This data rate is determined from the slope of the data interarrival time distribution. This requires longer measurement intervals with constant velocity. For this reason, the flow rate is varied stepwise and kept constant during 30 second intervals.

Figure 6.13 shows a scatter plot of the $SNR^{(3)}$ criterion versus the Doppler frequency. Erroneously detected and/or processed bursts form a cloud of points with small $SNR^{(3)}$ values and wide distribution of f_D. The threshold for validation is taken just above this cloud. This threshold was found to vary only slightly for different experiments in different flows.

The results for the data rate are shown in Figure 6.14. The IFA processor typically suffers from multiple validation, the amount increasing for lower velocities. Consequently, the trend of the data rate with multiple validation exhibits an offset for small velocities. After correction for the multiple validation (the data rate from the slope of the data interarrival distribution), the data rate no longer exhibits this offset. Nevertheless, a sharp change in the slope is observed for velocities around 0.1 m/s. This suggests that a potential source of bias exists for the velocity moments if a wide velocity range is present inside the flow and the IFA-750 processor is used. The

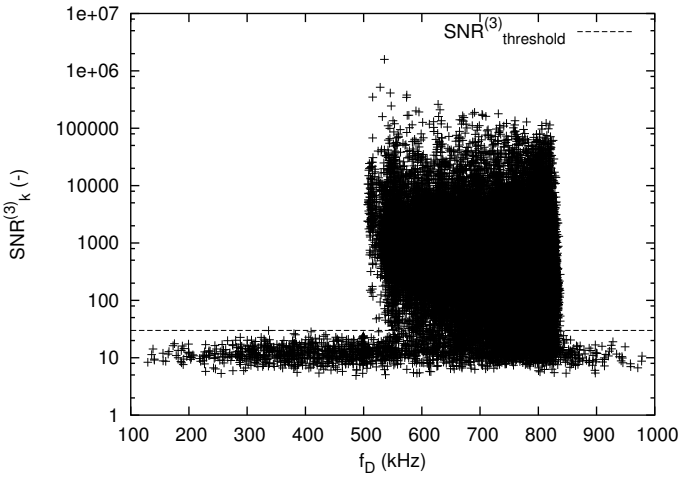

Figure 6.13.: Scatter plot of the validation criterion $SNR^{(3)}$ versus the Doppler frequency with the threshold for validation.

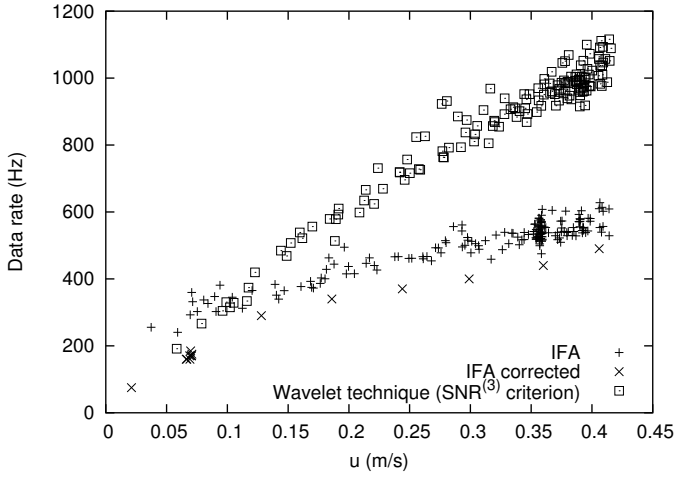

Figure 6.14.: Data rate as a function of the liquid velocity, for the IFA processor both with and without correction for multiple validation, and for the wavelet technique.

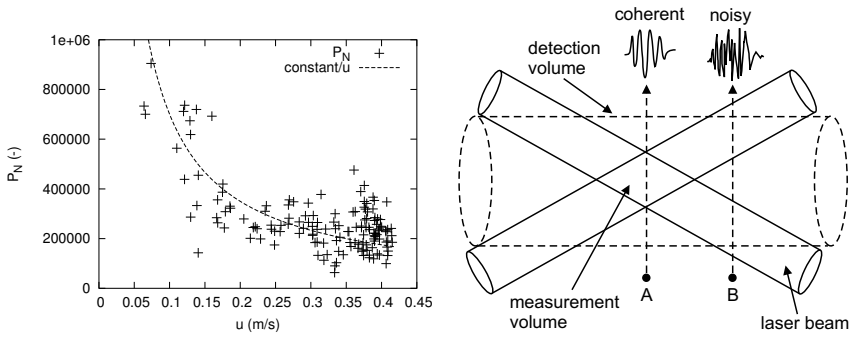

(a) Variation of average P_N with u for small groups of velocity realizations.

(b) Origin of extra noise with Gaussian envelope.

Figure 6.15.: Variation of noise level with transit time; explanation with light scattering by particles right outside the measurement volume.

use of the wavelet technique with the $SNR^{(3)}$ criterion from equation 6.35 results in higher data rates (Figure 6.14) and a more linear increase of the data rate with the velocity. Consequently, the bias is smaller. Nevertheless, some non-linearity remains. This can be explained as follows.

Equation 6.25 gives:

$$\hat{P}_P^k \propto A_k^2 T_{t,k}^2 \text{ and } \hat{P}_{P3}^k \propto A_k^2 T_{t,k}^2 \tag{6.44}$$

The measurements (Figure 6.15(a), considering that $T_t \propto 1/u$) suggest that:

$$\hat{P}_N^k \propto T_{t,k} \tag{6.45}$$

This can be explained as follows (Figure 6.15(b)). Light from the so-called detection volume is focused on the receiving fiber in the backscatter probe. This means that particles crossing one of the laser beams inside this detection volume ('B' in the figure) produce an incoherent signal, which has a Gaussian envelope. This produces the largest contribution to the noise in the signal. If a particle passes the measurement volume ('A' in the figure), the detector notices this and provides the processor with a small segment of the signal. The length of this segment is proportional to the transit time. If another particle crosses a single laser beam inside the detection volume and within this time interval, the noise level is increased and detection of the coherent burst becomes more difficult. The probability that this occurs is approximately proportional to the transit time, and, therefore, inversely proportional to the velocity, as Figure 6.15(a) suggests. Similarly, the amount of power added to the spectrum by noise due to other (e.g. electronic) sources is also proportional to the length of the selected signal interval, i.e. to the transit time. Equations 6.44 and 6.45 suggest that

$$SNR_k \propto A_k^2 T_{t,k} \text{ and } SNR_k^{(3)} \propto A_k^2 T_{t,k} \tag{6.46}$$

This suggests that for faster particles, which have shorter transit time, the probability of validation decreases. This is exactly the behavior observed in Figure 6.14.

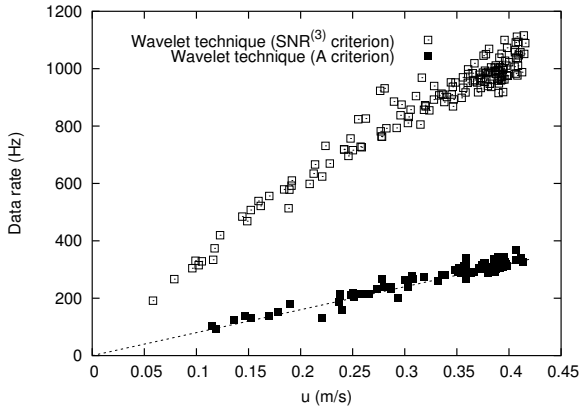

Figure 6.16.: Comparison of data rate-velocity dependence for validation using criteria 6.35 and 6.36.

The criteria in equations 6.34 and 6.35 are both based on the detectability of the bursts, these therefore produce a high data rate, at the cost of a small possible bias. Comparison tests with these criteria using artificial and experimental signals shows a slightly better performance for the criterion of equation 6.35, therefore the criterion in equation 6.34 is not considered further. The criterion of equation 6.36 uses the amplitude of the burst to decide whether the burst should be validated. The amplitude of a burst will, in general, not be correlated with the velocity of the particle. The use of this criterion should therefore provide a smaller bias than the use of equation 6.35. This is illustrated in Figure 6.16. The data rate with equation 6.36 is linearly dependent on the velocity. This improvement is, however, obtained at the cost of a strong decrease in the data rate.

The most suitable validation criterion is, therefore, dependent on the application. The bias problem is only significant in flows if the velocity fluctuations are significant with respect to the mean velocity. This is, however, always the case for a bubbly flow. For the velocity moments, a high data rate is not essential, and the use of the amplitude based criterion in combination with velocity bias correction will render the best results. For the measurement of turbulence spectra, a high data rate is important and velocity bias is usually not taken into account in the signal processing. Therefore, in this case the use of the SNR based criterion is preferred.

6.6.3. Data rate, accuracy and dead time

The performance of the processor is tested by a further investigation of the measurements in the laminar glycerol pipe flow. The data rate and relative standard deviation of the velocity fluctuations were determined for both the single burst wavelet processor (with the $SNR^{(3)}$ validation criterion) and the IFA-750 processor. The signals were recorded simultaneously. Since the measurements were obtained in the center of the pipe, and the flow rate varies only little during the measurement, the standard deviation of the liquid velocity is a good measure for the accuracy of the processor.

u (m/s)	σ_u/μ_u (%) Wavelet	σ_u/μ_u (%) IFA	Data rate (Hz) Wavelet	Data rate (Hz) IFA (corrected for multiple validation)	Multiple validation IFA (%)
0.070	1.8	4.3	255	170	54
0.129	1.6	2.9	400	290	10
0.244	1.9	2.7	551	380	11
0.301 (settings A)	1.9	2.4	612	400	14
0.05 (settings B)	5.3	6.8	100	30	15

Table 6.1.: Results of tests with laminar flow

Table 6.1 shows the results. Settings A refer to a backscatter probe with focal length of 0.122 m, pre-shift frequency of 500 kHz, bandpass filter range 100-1000 kHz. Settings B refer to a backscatter probe with focal length of 0.25 m, pre-shift frequency of 200 kHz, bandpass filter range 30-300 kHz. The noise level was much higher for the case with settings B, due to smaller laser power, higher PMT voltage and poorer alignment of detection volume and measurement volume.

The results for settings A show that the data rate for the wavelet processor is always higher than that of the IFA-750 processor, if the data rate for the IFA-750 processor is corrected for multiple validation. In the results from the wavelet processor, no indications for multiple validation are found. Multiple validation is, however, a serious problem if the IFA-750 processor is used. With this processor at least 10% of the measured velocity realizations are due to multiple validation, the fraction rapidly increasing for u<0.1 m/s. Velocities in the range 0-0.1 m/s are very common in the bubble column, indicating the relevance of the prevention of multiple validation. The accuracy of the wavelet measurement is also generally better than that of the IFA processor. The inaccuracy of the IFA-processor rapidly increases for smaller velocities. The wavelet technique gives much better accuracy, up to a factor 2.4. The improved performance has two origins. The increased inaccuracy of the IFA processor at low velocities is due to the increased multiple validation. Of course, improvements may be obtained by correction for multiple validation, this is considered in a later stage. The wavelet technique does not suffer from significant multiple validation, therefore this increase does not occur. The higher data rate for the wavelet processor provides somewhat better accuracy (for a given measurement time), particularly for the measurements deeper in the column. In addition, the wavelet technique uses the entire burst for the estimation. For lower velocities a longer transit time occurs and, consequently, the accuracy improves. This shows that the wavelet technique can deal very well with the wide distributions of transit times that occur in bubble columns.

The use of the settings A with laminar flow and measurement in the center of the flow results in a good signal-to-noise ratio. Under these conditions, the detection of the bursts is relatively easy. Consequently, the data rate of the wavelet processor is larger than the data rate of the IFA-750 processor, but the difference does not exceed a factor of 2. A different behavior is observed

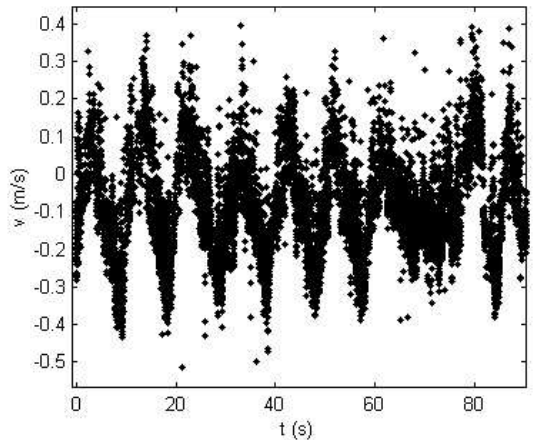

Figure 6.17.: Axial velocity time signal for bubbly flow (wavelet processor).

for conditions with worse signal-to-noise ratio. The results for the settings B in table 6.1 are an example of this behavior. In this case, an increase in the data rate with a factor of 3 is obtained with a small improvement in the accuracy of the velocity. Similar results were obtained for these settings for other velocities in the range 0-0.1 m/s. An improvement with a factor of 2-3 in the data rate was found to be quite typical for many practical applications. Another example is the use of the wavelet technique for the study of turbulent water pipe flow by Daalmans (2005) who finds similar improvement in data rates and improved results close to the wall.

Bubbly flow

The effect of the inclusion of the dual-burst processors is tested by using a bubbly flow: the more or less periodic liquid velocity in a flat bubble column is determined (Figure 6.17) as well as the velocity signal in the homogeneous cylindrical bubble column. These experiments used a 500 kHz pre-shift frequency, an electronic bandpass range of 100-1000 kHz and a backscatter probe with a 0.122 m lens. The $SNR^{(3)}$ validation criterion was used.

The initial tests in the flat bubble column showed that the use of the dual-burst wavelet processor increases the data rate again by a factor of 2-3 compared to the TSI IFA-750 output. The IFA processor output suffered from much multiple validation, whereas multiple validation for the dual-burst wavelet processor was negligible. In this situation, the signal-to-noise ratio was quite poor. The experiments in the cylindrical bubble column were performed in a later stage, after maintenance and optimization of the optical components. In addition, a larger laser power was used (1W vs 0.4 W). With these changes, the performance of the IFA-processor improved, and the data rates of the wavelet processor and the IFA processor are similar. Nevertheless, the IFA output still suffers from much multiple validation. Figure 6.18 shows the distribution of the data interarrival time for the IFA-750 processor, for the dual-burst wavelet processor and for wavelet processing only (dual burst processors switched off). The random arrival of seeding

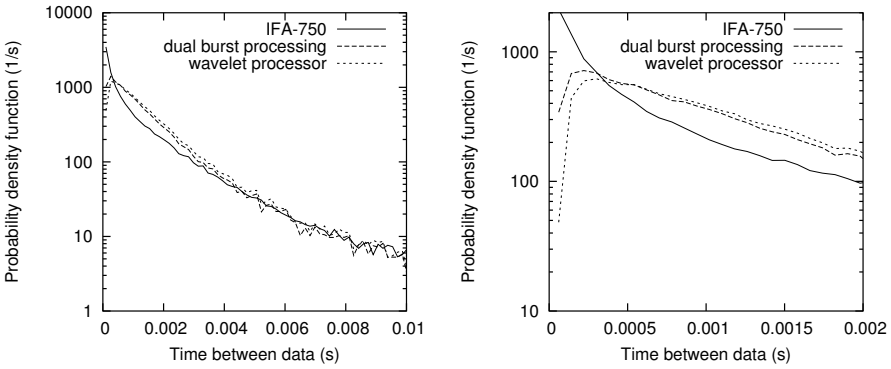

Figure 6.18.: a) Particle interarrival time distribution. b) Zoom into smaller timescales. Obtained in the cylindrical bubble column, α=0.15, at 0.9 cm from the wall.

particles should give a straight line on a semi-log plot, with some curvature due to the presence of the bubbles for longer time intervals (longer than 5 ms), see section 5.4 for more details. The IFA-750 output shows a strong increase for time intervals shorter than 1 ms, this is caused by multiple validation. In addition, its output is curved for all interarrival times, which is probably caused by a combination of multiple validation and inaccuracies in the arrival time. The multiple validation is not observed for the dual-burst and wavelet processors. In addition, the distribution shows a straight line on a logscale for intervals up to 4 ms. This shows that the estimate of the arrival time is much more accurate than for the IFA processor.

Figure 6.18(b) shows the distribution at the shortest relevant time intervals. Using only wavelet processing, a delay time of approximately 0.3 ms is observed. This corresponds to the mean transit time of the bursts. Since the transit time has a relatively wide distribution (a wide velocity distribution is obtained due to the bubbles), the cutoff is not sharp. If the dual burst processors are used, the delay time is further reduced to approximately 0.2 ms: partial overlap of the bursts is allowed. The distribution shows a straight line up to these short intervals. This shows that using the dual-burst processors we may be able to estimate turbulence spectra up to higher frequencies and that the seeding density may be increased further.

The performance can also be tested via the fuzzy slotted autocorrelation function with local normalization and local time estimation (see section 5.6). The signals corresponding to Figure 6.18 are used. The result is shown in Figure 6.19(a). Section 5.10 discussed that uncorrelated noise is visible as a discontinuity at τ=0 in the slotting autocorrelation function. If multiple validation is present, this discontinuity can be smeared to larger time intervals. In addition, Tummers (1999) discussed that the finite size of the measurement volume obscures the acf behavior at the smallest time scales and results in an extra increase at these smallest time scales. Similar behavior is observed in Figure 6.19(a). For both processors a discontinuity is observed, which is slightly smaller for the dual burst processor: i.e. the noise level is somewhat smaller for this processor. Similar to the approach discussed in section 5.10, a corrected autocorrelation function is determined (Figure 6.19(b)). This shows that for both processors the discontinuity

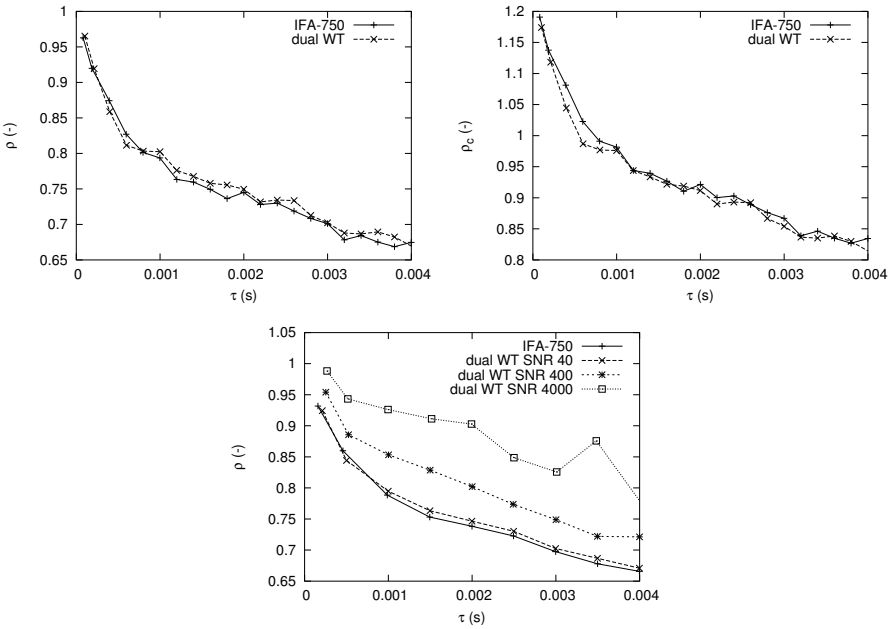

Figure 6.19.: (a) Slotting autocorrelation function for IFA-750 processor and dual burst wavelet processor ($\Delta\tau$ = 0.2 ms, 134 seconds data). (b) autocorrelation function after correction (c) Effect of increase of the $SNR^{(3)}_{threshold}$ ($\Delta\tau$=0.5 ms)

exists up to larger time intervals. For the IFA-750 processor result it extends up to 0.9 ms, for the dual burst processor up to 0.6 ms. In the case of the IFA-750 processor, multiple validation is probably the main source of this problem. For the dual burst processor, the precise origin is not clear, but probably the size of the measurement volume gives a major contribution. In Figure 6.19(c) the effect of an increase of $SNR^{(3)}_{threshold}$ from 40 to 400 and 4000 is shown. The noise level in the velocity estimates decreases strongly. This occurs, however, at the cost of a strong drop in data rate: respectively 53% and 89% of the data is rejected due to this increase. The point where the extra increase in the acf occurs is not altered by the increase in threshold. This result shows that an improvement in the autocorrelation function is obtained due to the more accurate arrival time and strong reduction in the multiple validation. The finite size of the measurement volume, however, limits the improvement.

6.6.4. Mean and standard deviation: evaluation of bias

The accuracy of the mean and standard deviation of the axial liquid velocity inside the bubble column is evaluated with the use of profile measurements. Test measurements were performed in the cylindrical bubble column with homogeneous bubbly flow with void fraction 15.3% and superficial gas velocity of 0.029 m/s at a height of 0.65 m (ungassed liquid height 1.0 m). The

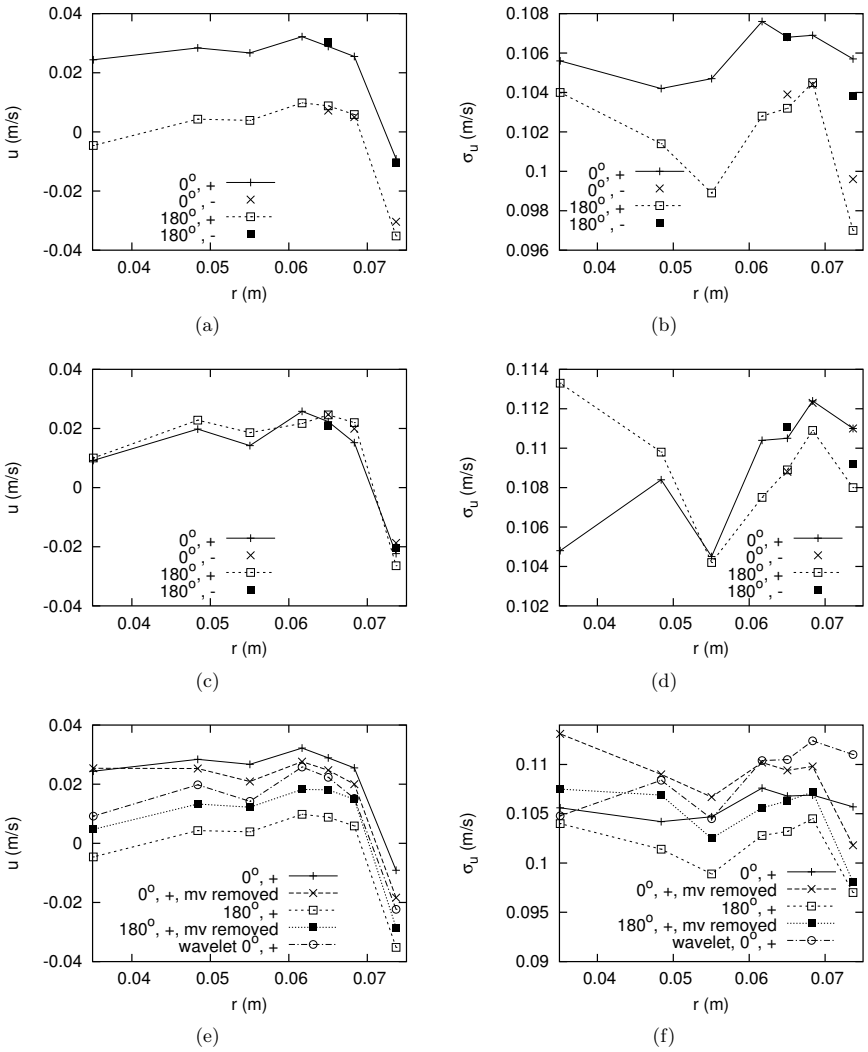

Figure 6.20.: Results for mean and standard deviation of the axial velocity for probe rotation with 180° (a), (b) IFA-750 result, (c), (d) Dual burst wavelet processor ($SNR^{(3)}$ criterion), (e), (f) IFA-750 result with removal of multiple validation (denoted by 'mv removed').

LDA settings were: laser power 1 W, focal length 0.122 m for the lens of the backscatter probe, preshift frequency 500 kHz, bandpass filter range 100-1000 KHz. The measurement duration with the IFA-750 processor was 300 s, the duration with the wavelet technique was 134 s. This way, typically Doppler frequencies in the approximate range of 300-800 kHz are obtained. If the backscatter probe is rotated around its axis by 180°, the mean velocity should only change sign in the absence of bias, and not change in magnitude. This way, Doppler frequencies are obtained in the range 200-700 kHz. The probability of validation may be frequency dependent, comparison of the means before and after rotation is, therefore, a good test for potential bias.

Figure 6.20 show the results for the probe under two orientations (0° and 180°). In addition, the rotation can also be mimicked electronically with the use of the electronic downmixers in the TSI model 9230 colorlink: the optical preshift frequency is in fact fixed at 40 MHz, a preshift frequency of 500 kHz is obtained by electronic downmixing with either 39.5 MHz or 40.5 MHz, this 'swaps' the velocity sign, and is denoted by '+' and '-'. The results of the electronic and physical rotation are very similar. A clear bias is observed for the probe orientation: the means for the two probe orientations differ by approximately 0.02 m/s for all radial positions. If homogeneous flow is studied, this bias has the same order of magnitude as the mean axial velocities. For the standard deviation, a clear difference is observed as well. Two possible reasons can be pointed out. First, the electronic bandpass filters of the IFA-equipment have a response which is not uniform (see appendix C), and second, the results of the IFA-750 processor suffer from multiple validation. The probability of multiple validation depends on the transit time and the frequency of the burst. Bursts with distinctly different Doppler frequencies are sampled at different frequencies, leading to a frequency dependent probability of detection: bursts with higher frequency suffer relatively more from multiple validation. For the settings '0°, +' and ' 180°, -' high, positive, axial velocities correspond to high frequencies (around 700-800 kHz), i.e. a bias to higher positive velocity is obtained. For the other settings the negative velocities correspond to high frequencies, i.e., a bias toward lower velocity is obtained.

The results obtained with the dual burst wavelet processor do not suffer from this effect (Figures 6.20(c) and 6.20(d)): the profiles for both probe orientations are very close. This is due to the fact that the results with the wavelet processor suffer from very little multiple validation, and strongly improved electronic bandpass filters are used. Figures 6.20(e) and 6.20(f) show the results of the IFA-750 processor after removal of multiple validation. The removal is performed by locating groups of velocity realizations with intervals in between the bursts shorter that 1 ms, and replacing the group with a single realization which has the average arrival time and average velocity of the group. Other methods of removal, e.g. removal of all realizations except the first in the group, give similar results. The removal reduces the bias: the difference between the mean velocities obtained from the two probe orientations is halved. The results for the wavelet processor remain superior, however, and do not need correction for multiple validation. The standard deviation estimate is increased: multiple validation occurs relatively more frequently for low velocities, leading to a bias to lower values in the uncorrected results. This is also clearly observed in Figure 6.21. The difference in standard deviation for the two probe orientations remains similar, however. The electronic bandpass filters of the IFA-processor are probably responsible for this behavior.

The use of the wavelet processor is, however, not free from bias either: although there is no bias due to any frequency-dependence, there is still the possibility of a bias due to different

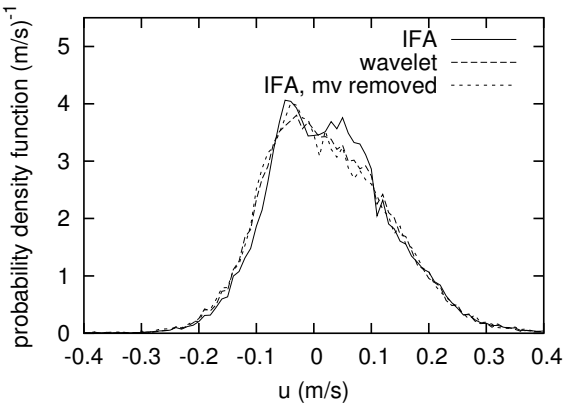

Figure 6.21.: Probability density function for axial velocity for the different processors. r=0.065 m. 'mv removed' denotes removal of multiple validation.

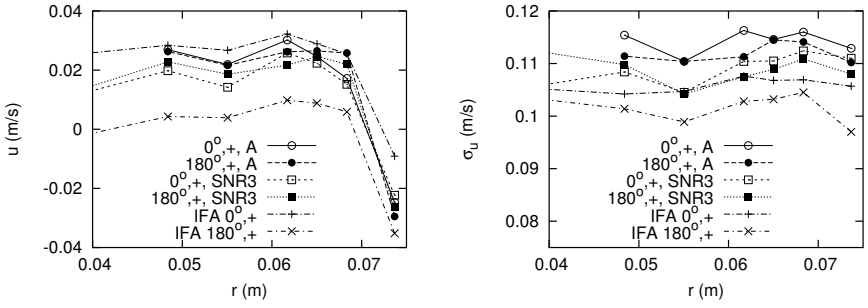

(a) (b)

Figure 6.22.: Results for mean and standard deviation of the axial velocity obtained with the wavelet processor (two criteria, A=amplitude based, SNR3 based on signal to noise ratio) and IFA processor for probe rotation with 0° and 180°.

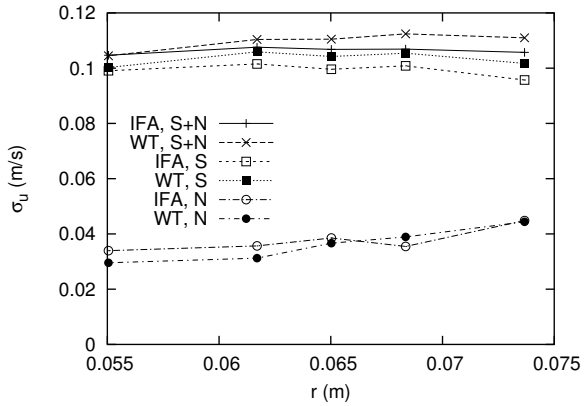

Figure 6.23.: Standard deviation for the velocity signals obtained with the IFA-750 processor and the wavelet processor (signals obtained in the 0°,+ mode). S+N=total signal, S=standard deviation due to velocity fluctuations only, N=standard deviation noise estimate

signal-to-noise ratios for bursts with different transit times (see section 6.6.2). If the $SNR^{(3)}$ criterion is used, bursts with long transit time, often corresponding to low velocities, are somewhat overrepresented. This will lead to an underestimation of the mean velocity (due to the asymmetry of the velocity pdf), and an underestimation of the standard deviation. The use of an amplitude-based criterion should give more accurate results, although at the expense of a reduction in data rate by typically 50-60%. The comparison of the results with these criteria is shown in Figure 6.22. The differences between the results for the two probe orientations are similar for both criteria. Analysis shows that the differences for the standard deviations are caused by different noise levels: since the amplitude of the signal changes with the distance to the wall, a threshold has to be set manually, giving larger variations in the noise levels for the amplitude criterion than for the $SNR^{(3)}$ criterion.

The use of the slotting technique allows the estimation of the signal-to-noise ratio of the signal (see section 5.10) by fitting the autocorrelation function. This way, the standard deviation of the measured velocity series can be split into a component due to the true velocity fluctuations and a component due to the noise. The result is shown in Figure 6.23, noise level estimation could be performed reliably up to 2 cm from the wall. Typically, 10-15% of the variance of the signal is due to noise. The noise level is independent of the probe orientation. Removal of the noise contribution results in a small reduction of the standard deviation of 5-10%. Whereas the total standard deviation has a weak decrease towards the center of the bubble column, this trend is reduced by the noise removal. The noise level is highest close to the wall, probably due to scattered light originating from the positions where the laser beams cross the wall. For the IFA-750 results the noise level is more or less constant further away from the wall, for the wavelet technique a weakly decreasing trend is observed. If the correction for noise and the correction for multiple validation are considered, the results show that these corrections cannot fully remove the differences between the IFA-results and the wavelet processor results.

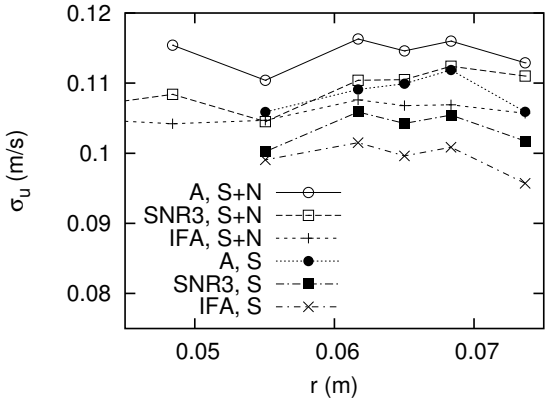

Figure 6.24.: Standard deviation for the velocity signals obtained with the IFA-750 processor, the wavelet processor with validation based on the $SNR^{(3)}$ criterion and the amplitude (signals obtained in the 0°,+ mode). S+N=total signal, S=standard deviation due to velocity fluctuations only

Results obtained with noise removal for the wavelet processor output with the two different criteria are shown in Figure 6.24. These show that the standard deviation for the wavelet output with amplitude validation gives the highest values. Of course, correction for velocity bias is still required. The results with velocity bias correction are shown in Figure 6.25. Close to the wall, the wavelet processor results for the mean axial velocity with the two validation criteria are very similar, in the center a slightly higher value is obained with the amplitude criterion (which is the most accurate result). For the standard deviation, the values obtained with the amplitude criterion are typically about 5% larger. The results obtained with the IFA-750 processor give reasonable agreement with the wavelet results with the amplitude criterion. Apparently, the subsequent operations of multiple-validation removal and velocity bias removal with its requirement for coincident data remove most of the velocity realizations contributing strongest to the bias. An underestimation of the standard deviation of the signal of typically 5% is obtained. The experiments in this thesis that use the IFA-750 processor are performed in the $0°, +$ mode, for most of the experiments the relevant corrections have been applied. Consequently, the bias for the mean velocity and normal stress is quite small.

6.7. Conclusions

The accurate measurement of turbulence spectra up to high frequencies requires data with high accuracy of both the Doppler frequency and the burst arrival time, as well as a short processor delay time, even in the presence of high noise levels. The procedure pursued in the present work is to limit the influence of noise and improve the accuracy of the Doppler frequency estimate and arrival time estimate by using the wavelet technique, i.e. a model of the burst is fitted to the data. The shorter delay time is achieved by allowing for dual bursts (i.e. overlapping bursts)

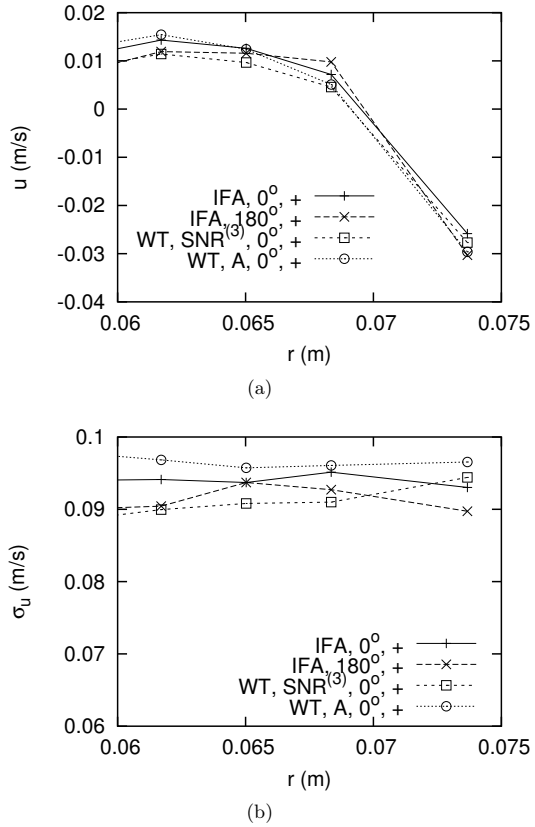

Figure 6.25.: Mean and standard deviation for the signals after velocity bias correction, for the IFA-signals multiple validation was removed before the velocity bias correction. A=ampltiude based criterion, $SNR^{(3)}$: signal to noise ratio-based criterion.

by separating bursts either in the temporal or spectral domain. The direct use of the (iterative) wavelet technique for dual burst processing is limited by the peak broadening, resulting in more difficult burst separations. Therefore, elements of the iterative wavelet technique were combined with separation techniques using the power spectrum and envelope of the band passed signal, providing good results for both the burst separation and noise suppression. Tests show that the combination of the software burst detector, processor and validation routines allows either for a small increase in the data rate with an improvement in the accuracy, or increased data rates with similar accuracy when compared with a traditional commercial hardware processor (TSI IFA-750). The variation of the data rate with the velocity shows smaller bias problems with respect to a commercial hardware processor due to the transit time dependency. By using an amplitude based validation criterion, this bias can be even further reduced at the cost of some loss in data rate. The particle interarrival time distribution shows that the processor delay time is effectively halved by the inclusion of the dual burst processors, allowing the investigation of turbulence spectra up to higher frequencies. In addition, the use of the wavelet technique gives more accurate arrival times. In practice, the advantage is limited due to the finite size of the measurement volume. Tests with the commercial hardware reveal problems with frequency bias for bubbly flows, mainly due to multiple validation and poor electronic bandpass filters. The wavelet technique does not have these problems. The bias present in the IFA-750 is reduced by removal of multiple validation, application of a coincidence window and velocity bias correction.

List of symbols

Roman symbols

A	amplitude	-
A_{acf}	maximum of the autocorrelation coefficients	-
$A_{acf,threshold}$	threshold for A_{acf} for burst detection	-
$A_{threshold}$	validation threshold for burst amplitude	-
BP	bandpass filter	
C	spectral transform kernel	-
C_a	correction factor frequency dependent amplification	-
C_l	constant for least squares norm	-
C_{peak}	threshold constant for finding the peak in the power spectrum	-
c_x	ratio window duration and burst duration	-
DFT	Discrete Fourier Transform	
E	transform kernel: WT temporal window	-
E_0	transform kernel	-
ENV	envelope	-
$ENV_{bandpass}$	envelope of bandpass filtered signal	-
$ENV_{lowpass}$	envelope after lowpass filtering	-
$ENV_{subtract}$	envelope after subtraction fitted burst	-
f_{bps}, f_{bpe}	frequency region that should be passed by bandpass filter	s^{-1}
f_D	Doppler frequency	s^{-1}
f_{max}, f_{max1}	frequency corresponding to the maximum of the PSD	s^{-1}

f_{max2}	frequency corresponding to the second largest maximum of the PSD	s^{-1}
$f_{min,s}, f_{min,e}$	frequency corresponding to the location of minima next to the maximum of the PSD	s^{-1}
$f_{p,max}$	maximum frequency in PSD	s^{-1}
f_{ps}, f_{pe}	frequency exclusion region for calculation mean noise level	s^{-1}
f_s	sampling frequency	s^{-1}
f_w	minimum frequency scale to pass with lowpass filter for PSD	s^{-1}
f_{ws}, f_{we}	frequency range around peak calculated from time scale	s^{-1}
f_{width}	spectral peak width based on noise detector output	s^{-1}
G	Gaussian curve fit	-
HT^+	Hilbert transform	
IDFT	Inverse Discrete Fourier Transform	
i_{fit1}, i_{fit2}	indices start and end DFT peak fit region	-
K	amplitude estimate	-
L	least squares criterion	-
N	number of signal points	-
n	noise	-
n_{DFT}	mean $\|DFT\|^2$ level noise	-
n_{WT}	mean $\|WT\|^2$ level noise	-
OC	overlap criterion	-
OCF	overlap criterion frequency	-
OCT	overlap criterion time	-
P	power spectrum	-
P_n	mean noise level in the PSD	-
P_P	maximum of the PSD	-
P_{P3}	sum of maximum of the PSD and the two neighboring points	-
P_{ratio}	ratio height biggest peak and second biggest peak	-
$P_{ratio,threshold}$	validation threshold for P_{ratio}	-
$P_{threshold}$	threshold level PSD for locating bandpass regions	-
r	radial position in bubble column	m
SNR	SNR based on P_P	-
$SNR^{(3)}$	SNR based on P_{P3}	-
$SNR_{threshold}$	validation threshold for SNR based on P_P	-
$SNR^{(3)}_{threshold}$	validation threshold for SNR based on P_{P3}	-
s	noiseless signal	-
s_{DFT}	mean $\|DFT\|^2$ level signal	-
s_{WT}	mean $\|WT\|^2$ level signal	-
T_a	arrival time	s
T_{gap}	estimated burst duration from noise detector	s
T_t	transit time	s
T_w	measurement time	s
u	velocity	$m\ s^{-1}$
t	time	s

WT	wavelet transform	
y	noisy signal	-
y_f	bandpass filtered signal	-

Greek symbols

α	void fraction	-
Δt	sampling interval	s
ΔT_a	inaccuracy arrival time	s
Δu	error velocity estimate	$m\ s^{-1}$
$\Delta\tau$	slot width	s
η	amplitude temporal decay constant	s^{-2}
μ	mean	
σ	standard deviation	
σ_n	noise standard deviation	-
ϕ	phase	rad

Superscript and subscript

DF	processors with spectral separation
DT	processors with separation in time
pre	pre-estimate
$single$	single burst processor
x	wavelet window

7. Dynamic large scale vortical structures in bubble columns [1]

The present chapter discusses the results for the hydrodynamics of the bubble column. First, some general aspects of the measurement techniques, and the setup are discussed. This is followed by results for uniform gas injection, which focus on the stability of the flow. Subsequently, results on the strength of the fluctuations due to pseudo-turbulence are discussed. Next, non-uniform gas injection is discussed for both the cylindrical and rectangular bubble column. Finally, the results for the power spectra, obtained from LDA data, are discussed.

7.1. Setup and experimental techniques

7.1.1. The sparger: gas injection patterns

The gas injection pattern was varied to study its influence on the hydrodynamics. Results are presented in sections 7.4 and 7.5. The patterns are described in Tables 7.1 and 7.2, and are depicted in Figure 7.1. The superficial gas velocity was kept constant when the pattern was varied. The void fraction α_{height} was determined from the hydrostatic pressure difference over the column.

7.1.2. Experimental techniques

Careful and accurate experiments are required to investigate the influence of the gas injection. Various experimental techniques have been used to investigate the flow properties. For the liquid velocity, Laser Doppler Anemometry (LDA) is used (employing the TSI IFA-750 processor).

[1] Parts of this chapter have previously been published as W.K. Harteveld, R.F. Mudde, H.E.A. van den Akker, "Dynamics of a bubble column: influence of gas distribution on coherent structures", Can. J. Chem. Eng 81, 2003, pp.389-394 and W.K. Harteveld, J.E. Julía, R.F. Mudde, H.E.A. van den Akker, "Large scale vortical structures in bubble columns for gas fractions in the range of 5% to 25%", proc. 16th Int. Conf. on chemical and process engineering (CHISA), Prague, Czech Republic, August 2004

Pattern	Description gas injection	Needles used ($\alpha < 15\%$)	Needles used ($\alpha > 15\%$)	Relative area aerated zone	Aeration for r/R
C1	Uniform	187	559	100%	≤ 1
C2	1 ring off	151	451	81%	≤ 0.89
C3	2 ring off	115	343	62%	≤ 0.77
C4	3 rings off	79	235	42%	≤ 0.63
C5	Center off	108	324	58%	> 0.63

Table 7.1.: Gas injection patterns for the cylindrical column

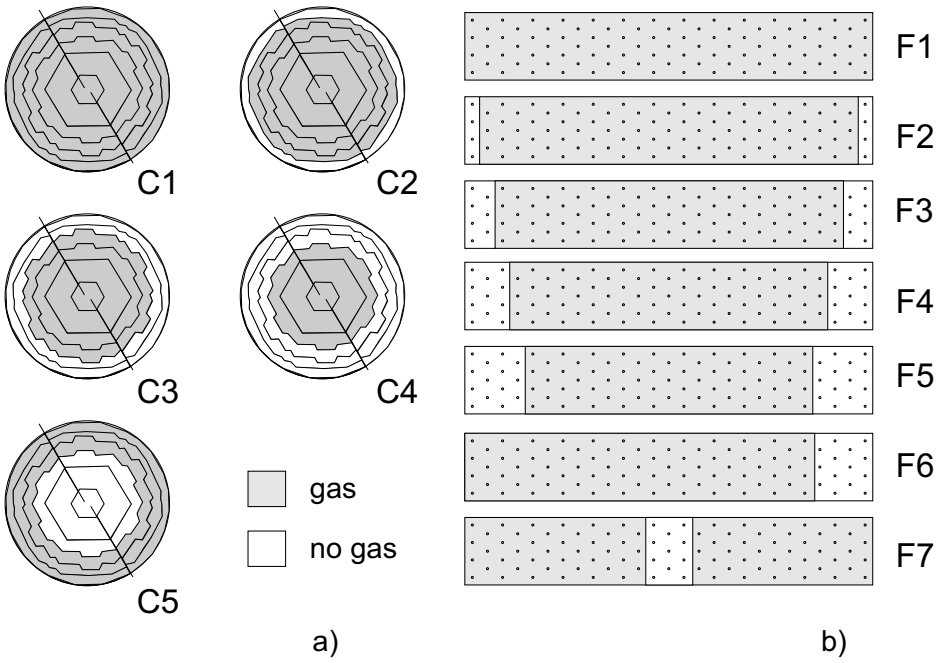

Figure 7.1.: Gas injection patterns for the cylindrical bubble column (a) and the pseudo-2D column (b).

Pattern	Description gas injection	Needles used	Rel. area aerated zone	Aeration for	α_{height} (%)
F1	Uniform	95	100%	$\lvert x\rvert/R_{2D}$ <1.00	7.3
F2	Central, 1 wall row off	87	93%	$\lvert x\rvert/R_{2D}$ <0.93	7.2
F3	Central, 2 wall rows off	81	85%	$\lvert x\rvert/R_{2D}$ <0.85	7.0
F4	Central, 3 wall rows off	73	78%	$\lvert x\rvert/R_{2D}$ <0.78	6.8
F5	Central, 4 wall rows off	67	70%	$\lvert x\rvert/R_{2D}$ <0.70	6.7
F6	Asymmetric, 4 wall rows off	81	85%	x/R_{2D} <0.70	7.0
F7	Wall, 3 central rows off	84	89%	$\lvert x\rvert/R_{2D}$ >0.11	7.1

Table 7.2.: Gas injection patterns for the pseudo-2D column

Large scale structures in the pseudo-2D column are investigated with the use of Particle Image Velocimetry (PIV, for the bubble velocities) and Particle Tracking Velocimetry (PTV, for the liquid tracers). The volume averaged void fraction is determined from the hydrostatic pressure difference over the bubble column. Local void fractions are determined with the use of single point glass fiber probes. Bubble properties (size, velocity) are studied with the use of four point glass fiber probes.

Several problems may be encountered when applying these techniques to the bubble column. The chapters 3, 4, 5 and 6 discussed some of these problems. For instance, especially for homogeneous flow the fluctuations in the liquid velocity are much larger than the actual mean liquid velocities (the standard deviation can be up to 5-10 times larger than the mean of the velocity). Consequently, the accurate measurement of the mean liquid velocities can be quite complicated. For example, the results in section 6.6.4 indicate how sensitive the mean of the velocity measured with Laser Doppler Anemometry is to bias sources. The present section discusses some of the problems encountered for the accurate measurements in the bubble column that were not discussed in previous chapters. More detailed information about the measurement techniques, that is not directly related to the application to the bubbly flow, can be found in appendix E. In addition, the Short Time Frequency Transform is discussed that is used to detect the presence of vortical structures.

7.1.3. Velocity measurements

The application of LDA in bubbly flows is hampered by the strong reduction in data rate due to the blockage of the laser beams by the bubbles. The data rate is approximately proportional to $exp(-c\frac{l\alpha}{d_b})$ where c is a constant in the range 1.5-3, l is the distance of the measurement volume to the column wall, α is the void fraction and d_b the bubble diameter (see appendix D for more details). Typical data rates for void fractions near 10% are 150-400 Hz near the wall, and 0.8 Hz in the column center (cylindrical column). This shows the difficulty of the experiments deeper inside the column, especially at the higher void fractions, where experiments in the center are no longer possible. Moreover, velocity bias correction is needed, which requires the use of a coincidence window for the axial and tangential components. The blockage of the beams used for measuring the axial and tangential component shows little correlation, especially further away from the wall, since the beam paths are different. As a result, the data rate with the use of the coincidence window drops even faster than for the single component alone, the constant c is nearly doubled and the maximum distance to the wall where experiments are possible is approximately halved.

Figure 7.2 shows mean velocity and normal stress profiles for the axial component for z=0.9 m and U_g=0.025 m/s (cylindrical column). At this void fraction (11%), the data rate in the center of the unprocessed velocity series is about 1 Hz. Application of the coincidence window, which is required for velocity bias correction, results in an even further reduction of the data rate, and there is no longer enough data to provide reliable estimates of the bias corrected mean velocity and stress. Nevertheless, velocity bias correction is very important, since for homogeneous flow the bias (overestimation) in the mean axial velocity is of the same order of magnitude as the mean, and the bias in the stress value is considerable as well (order of magnitude: 20% overestimation). Therefore, an approximate correction is performed. The magnitude of the velocity bias correction

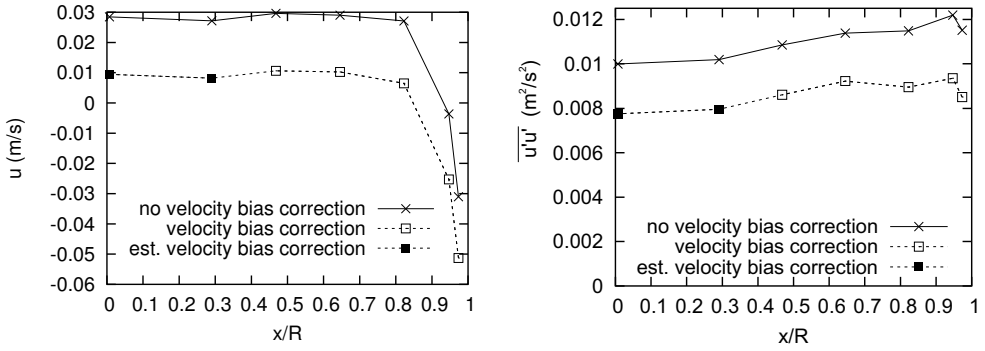

(a) (b)

Figure 7.2.: Mean axial velocity (a) and axial normal stress (b) for α=11% (U_g=0.025 m/s) and z=0.9 m.

is strongly correlated with the shape of the velocity pdf, which is quite constant in the inner regions of the bubble column (Figure 7.3). Consequently, the velocity bias correction has a more or less constant magnitude in the inner regions (this can be observed in Figure 7.2). With this knowledge the velocity bias correction can be estimated by a constant offset imposed on the uncorrected velocity mean, and a constant factor imposed on the stress. The result is shown in Figure 7.2 ('estimated velocity bias correction'). The resulting profile shows a very low mean velocity in the inner regions of the bubble column with liquid down flow very close to the wall. The mean liquid velocity, if the profile is integrated with:

$$\int_0^R (1-\alpha(r))u(r)2\pi r dr/\pi R^2 \tag{7.1}$$

is about -0.0007 m/s which agrees well with the lack of a net liquid flow in a bubble column. The stress decreases slowly toward the center of the column. Section 6.6.4 showed that a large part of this decrease can be explained by a decrease in the noise level in the LDA experiments if the measurement volume is moved inward.

7.1.4. Short time frequency transform

LDA data is investigated for the presence of coherent structures using the Short Time Frequency Transform technique (STFT, Mudde et al. (1997a)). This technique provides time-frequency plots where vortical structures appear as peaks at low frequencies. After making the time series equidistant using Sample & Hold, it is windowed using a Gaussian window $\gamma(t)$ centered around time T, truncated at its e^{-2} decay width. The corresponding spectrum is then obtained from:

$$STFT(T,f) = |\int u(t)\gamma(t)e^{2\pi i f t}dt|^2 \tag{7.2}$$

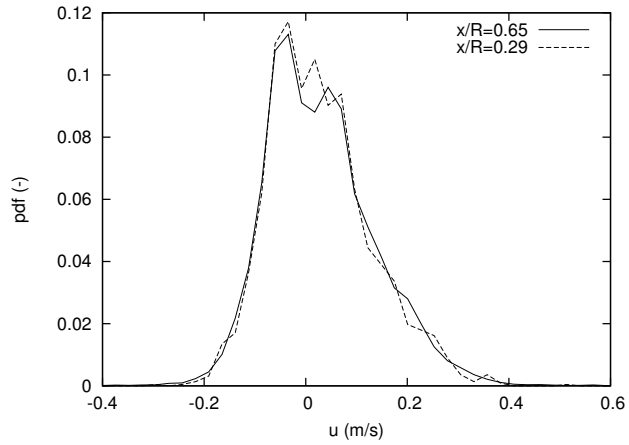

Figure 7.3.: Pdf of axial velocity (unprocessed) at two radial positions (U_g=0.025 m/s and z=0.9 m).

When the time window is slided over the time series, the evolution of the frequency content of the velocity time series is obtained. The Short Time Frequency Transform (STFT) technique is widely used for equidistant signals. For application to bubbly flows, resampling is required, which, as was discussed in chapter 5, leads to redistribution of power from high to low frequencies. Consequently, a sudden increase in the power at high frequencies will also result in a power increase at the lower frequencies, and this may lead to incorrect interpretation. For instance, for measurements further away from the wall, long gaps may occur that are followed by a measurement in the wake (i.e. a high velocity realization results). The reconstruction will, consequently, generate low-frequency power. The magnitude of this effect depends strongly on the value of $\dot{N}_2$ (see section 5.5). In the present chapter, the measurements are taken not too far from the wall, usually at a distance of 1.3 cm. This way, the effect does not provide big problems for the lower void fractions: the power due to the large structures is generally located at frequencies smaller than 1 Hz, and the re-distributed high frequency power will predominantly produce an extra offset for the low-frequency power. This does not give strong problems for the interpretation. For the higher void fractions, however, problems may be encountered. Tests show that the STFT is reliable for the detection of large scale structures for void fractions up to 15% (for the distance of 1.3 cm from the wall). For higher void fractions, many strong low-frequency artefacts are caused by large gaps in the data.

7.1.5. Column inclination angle

Rice and Littlefield (1987), Rice et al. (1990), Ityokumbul (1993) and Tinge and Drinkenburg (1986) showed that small departures from vertical alignment result in the increase of the axial dispersion in a bubble column due to the creation of a large circulation loop. The study of large scale structures in a bubble column, therefore, requires very accurate alignment. The work by Tinge and Drinkenburg (1986) shows that the required accuracy of the alignment increases with

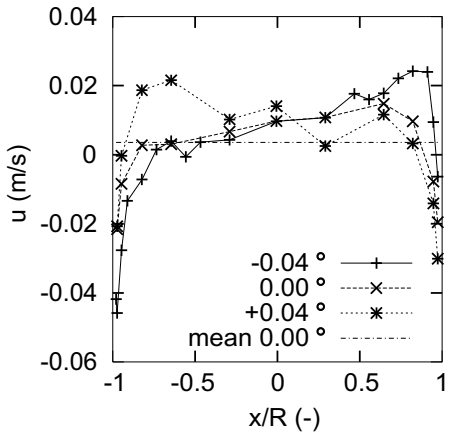

Figure 7.4.: Effect of small departures from vertical alignment on the axial liquid velocity profile ($\alpha = 8.1\%$).

the column scale. Extrapolation of their results shows that for a column with a diameter of 0.15 m, the axial dispersion increases rapidly for inclination angles larger than 0.05°. In the present study, this was checked by first optimizing the inclination visually (i.e. the presence of the large circulation loop was determined by visual comparison of the bubble velocities on both sides). Subsequently, the influence of small variations of the inclination angle on the liquid velocity profile was checked. The variations had a size of about 0.04°, which is about 1 mm horizontal deviation over a height of 1.5 m. The test was performed with an ungassed liquid height of 1.3 m and a void fraction of 8.1%, the result is shown in Figure 7.4. The effect on the velocity profile is clearly noticeable and indicates that the circulation loop is also present for smaller angles than those predicted by Tinge and Drinkenburg (1986). This can be explained by the uniformity of the flow (which is illustrated in the next section), and the resulting small variations in the velocity profile, which make small deviations very visible. It can be concluded that the investigation of uniform aerations requires very sensitive alignment. The flat bubble column, which has a horizontal width of 23.4 cm, therefore requires even more accuracy in the alignment.

7.2. Uniform gas injection: flow stability

The present section focuses on the properties of the flow in the bubble column for uniform gas injection, with a focus on the occurence of large scale vortical structures. First, observations on the presence of these structures are reported, followed by a discussion of literature on the stability of bubbly flows and bubble columns in particular. Next, the results for the flow properties of homogeneous flow are discussed. The focus is put on the mechanism responsible for the transition to a flow with large scale (dynamic) structures.

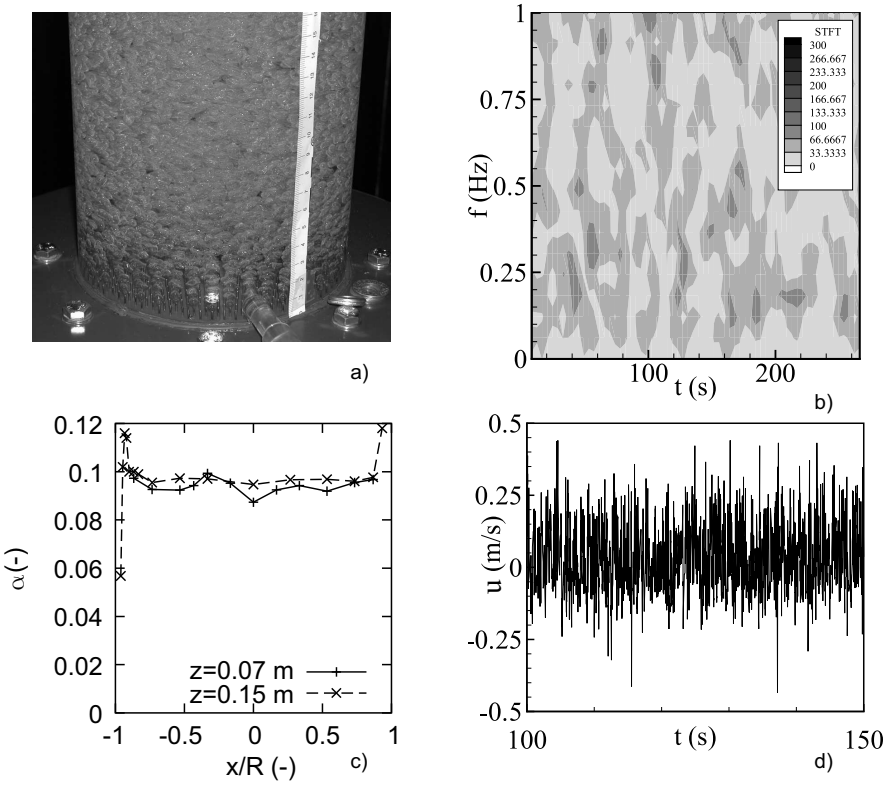

Figure 7.5.: Flow for uniform gas injection (U_g=0.023 m/s, ungassed liquid height 1.3 m). (a) Flow impression (b) STFT (c) Void fraction profile for the entrance region (d) axial velocity signal

7.2.1. Presence of structures

First, the flow for uniform gas injection is investigated for relatively low superficial gas velocities. Figure 7.5(a) shows an image of the flow for uniform gas injection for U_g=0.023 m/s. Visual inspection of the flow shows no large scale dynamics: all bubbles rise more or less similarly, the largest scale in the flow that is observed occurs at a scale similar to the bubble-bubble distance. Inspection of LDA velocity time series (Figure 7.5(d)) and the Short Time Frequency Transform of this time series (Figure 7.5(b)) does not reveal any large scale motion either. The same holds for the other quantities that are measured, such as the void fraction profiles (Figure 7.5(c)). Consequently, we find that uniform gas injection results, for low superficial gas velocities, in a flow without large scale structures. This holds also for the region close to the sparger.

Next, an investigation is performed whether the absence of the dynamic structures holds for increased superficial gas velocities, and how this compares to other results from the literature. Figure 7.6(a) compares the void fraction as a function of the superficial gas velocity for the

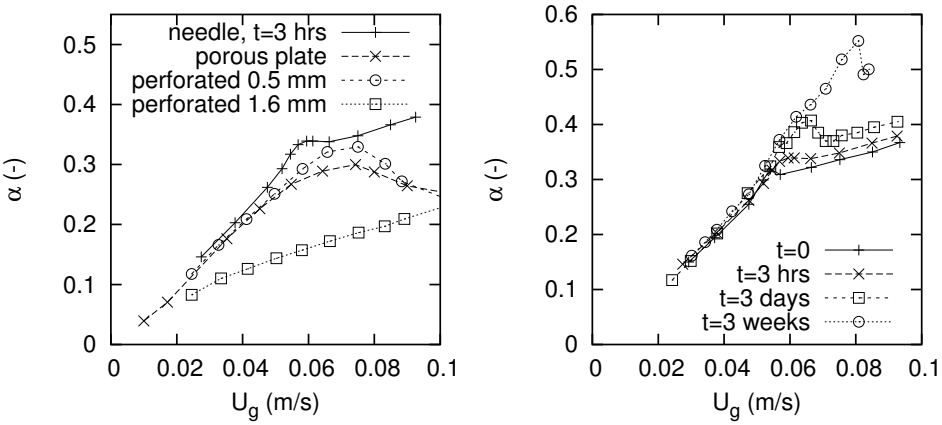

(a) (b)

Figure 7.6.: Comparison of void fractions obtained with the needle sparger, a porous plate sparger (Groen (2004)) and perforated plate spargers with two pore sizes (Drahos et al. (1992b)) (a) and evolution of void fraction with time t after filling the bubble column with fresh tap water for the needle sparger (b).

needle sparger with that obtained with porous plate and perforated plate spargers (porous plate sparger: data for a 0.15 m diameter bubble column from Groen (2004), constructed from sintered polyethylene with porosity 40%, and average pore diameter of 40 μm, perforated plate sparger: data from Drahos et al. (1992b) for a 0.14 m diameter bubble column, orifice size 0.5 mm or 1.6 mm, free plate area ratio 0.2%). For the perforated plate (0.5 mm pores), the increase in the void fraction flattens for U_g>0.06 m/s, the authors (Drahos et al. (1992b)) report the presence of macro scale eddies for U_g>0.04 m/s. For the perforated plate with 1.6 mm pores, heterogeneous regime behavior is reported for all gas velocities. For the porous plate, the increase in α flattens if U_g is larger than 0.04-0.05 m/s, indicating the transition to the heterogeneous regime. The author (Groen (2004)) reports the presence of large scale dynamical structures also for the lower superficial velocities. For the needle sparger, for U_g<0.057 m/s, no indications for large dynamical structures or significant large scale circulation are found. The slope of the void fraction curve starts decreasing for U_g>0.057 m/s and reaches a constant value in the range 0.059 m/s<U_g<0.066 m/s. The initial slope decrease corresponds to the conditions where a strongly increased liquid down flow is observed close to the wall in the top of the bubble column, but no large scale dynamic motion is observed. The strong liquid down flow is visible since the bubbles closest to the wall move upward with a small axial velocity for U_g=0.057 m/s. When U_g is somewhat further increased, the upward bubble velocity approaches zero, and weak unstable behavior is observed in the region near the free surface, with alternating upward and downward motion of the bubbles closest to the wall. The spatial scale of these disturbances is much smaller than the column diameter: dynamic large scale structures at the scale of the column diameter are not observed. For U_g>0.059 m/s, large dynamic structures are observed in the top of the

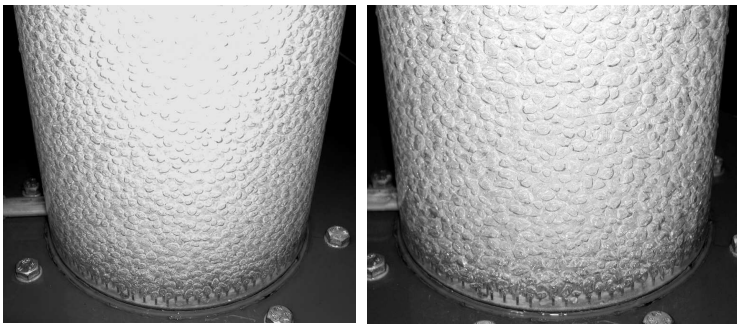

Figure 7.7.: Picture of the flow in the bubble column for contaminated water and high void fractions

bubble column. These exhibit a more or less periodic (intermittent) behavior: the structures gradually become stronger (over a period of 5-10 seconds), the local void fraction decreases until, apparently, the local mixture density has increased enough and the structures 'fall' to lower regions. The structures are dampened in the lower regions, and the bubble column becomes more or less homogeneous again, until the process repeats itself. If the superficial gas velocity is increased, the intermittent behavior changes. First, the 'heterogenous' behavior extends in space: not only the top region contains dynamic structures, but these structures are also able to reach increasingly lower parts of the column for increasing superficial gas velocities, until, finally, the sparger region is reached. If the superficial gas velocity is increased further, the time scale at which the structures are generated decreases, and the column contains dynamic structures for an increasing fraction of time. An increase of the presence of the structures in time and space has been reported earlier by Ruzicka et al. (2001). The change from a very homogeneous behavior to one with intermittent behavior appears less smooth for the needle sparger than for the other spargers: the change in slope in Figure 7.6(a) is much faster for the needle sparger. In addition, the void fraction at the onset of the structures is larger. The differences may be explained by the very uniform gas injection and possibly a narrower bubble diameter distribution for the needle sparger.

Similar to what was reported by Groen (2004), the superficial gas velocity for which the onset of large dynamical motion is observed, increases with time after filling the bubble column with fresh tap water (Figure 7.6(b)). The tap water is contaminated naturally. This reduces coalescence, and increases the maximum void fraction that is achieved before large scale structures appear. Eventually, a flow without large scale structures is found for void fractions up to 55% (see Figure 7.7 for an impression of the sparger region). The change from a homogeneous flow to a flow with large dynamic structures occurs much faster for the contaminated tap water than for 'fresh' tap water. Once large dynamic structures occur, they are able to reach the lower sparger region for only a small additional increase in the superficial gas velocity, whereas a much larger additional increase is required for the cleaner water. The 'intermittency factor' (see Ruzicka et al. (2001)) appears to increase much faster with the superficial gas velocity than for cleaner

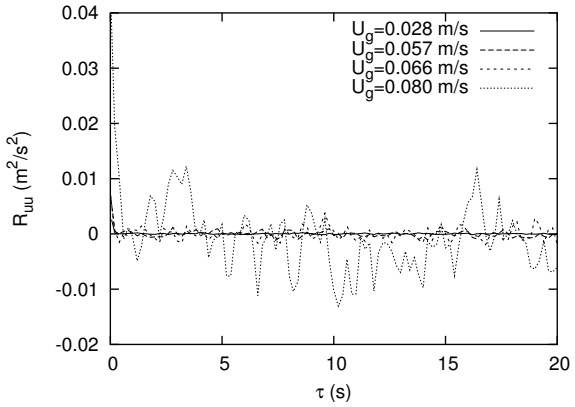

Figure 7.8.: Autocovariance function for increasing superficial gas velocities (slotting technique).

water.

The 'age' of the tap water that is used for the experiments clearly has a big impact on the behavior, in particular on the transition. The exact superficial gas velocity where the onset of vortical structures occurs, varies somewhat from experiment to experiment since regularly fresh water needs to be added to compensate for evaporation. Therefore, some differences occur between experiments owing to a change in the water quality. For this reason, the critical superficial gas velocity, where the onset of dynamic large structures occurs, is given in addition to the age of the tap water that was used, when appropriate.

The STFT is not suited for the detection of large structures in the signal for the highest void fractions: the gaps in the signal, combined with the Sample and Hold reconstruction, suggest much low-frequency power, which is non-existing in reality (see sections 5.5 and 7.1.4). Instead, the autocovariance function is determined with the use of the slotting technique. Figure 7.8 shows the results for the contaminated water of three weeks old. For U_g=0.08 m/s, the amount of long-term correlation (τ>1 s) strongly increases due to the large dynamic structures, although there is much scattering due to the low data rate. The correlation for the lower superficial gas velocities is limited to short intervals: no large dynamic structures are present.

7.2.2. Stability: literature

The observations in the previous section showed that the homogeneous flow contains no large scale structures for uniform gas injection. A transition to a flow with large structures is observed for void fractions in the range of 30%-55%. Various authors have attempted to predict this transition with various approaches. Biesheuvel and Gorissen (1990), Léon-Becerril and Liné (2001) and Léon-Becerril et al. (2002) focused on the occurence of gas fraction waves with a one-dimensional model for the axial direction. This way, instability is typically predicted for void fractions around 35% for spherical bubbles. For ellipsoidal bubbles, such as found in the present investigation, the critical voidage drops to typically 25% (Léon-Becerril and Liné (2001)). The

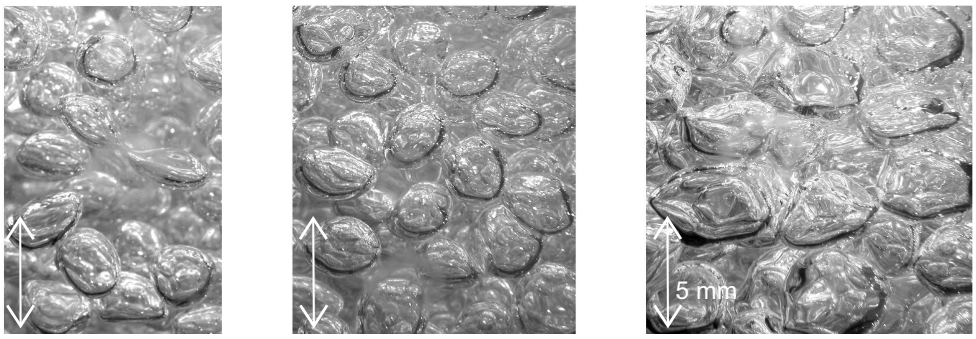

Figure 7.9.: Images of bubbles close to the wall for increasing void fraction (contaminated water of three weeks old).

approach is not able to explain the very high void fractions found in the present investigation, possibly since the behavior and shape of bubbles is strongly altered at high void fractions (see Figure 7.9) and some damping effects are not taken into account. Bhole and Joshi (2005) do account for effects of contamination (which act mainly on the added mass coefficient and bubble terminal velocity in their analysis), and predict the possibility of homogeneous flow at high void fractions, but only for very small bubbles, similar as was found in the experiments by Oels et al. (1978), who found a transition around a critical void fraction of 55% for bubbles smaller than 1 mm. In addition, a one-dimensional approach does not consider radial non-uniformities in the void fraction, which are the main driving force for the creation of large liquid vortical structures.

Ruzicka et al. (2001) and Ranade and Joshi (1987) consider the fact that every bubble carries with it a certain amount of liquid in its wake. This liquid has to flow downwards when the bubble reaches the free surface. The down-flow area for this liquid continues to decrease with increasing void fraction. The authors associate the instability with the point where the decrease has reached a critical point. Instability is predicted for void fractions in the range of 40% to 50%. The approach requires, however, an empirical value for the amount of liquid carried by each bubble.

Ruzicka and Thomas (2003) studied the analogy with thermal convection to provide a criterion for stability. This analogy is, however, only valid for bubbles with very small slip velocity (i.e. very small bubbles). Shnip et al. (1992) considered in a two-dimensional stability analysis the continuity equations and momentum balances and included the effect of the sparger. A maximum void fraction of around 35% was predicted this way. Monahan et al. (2005) studied the instability with the use of Computational Fluid Dynamics and the two-fluid model, focusing on various model aspects, such as the interaction forces and bubble induced turbulence, in order to find

their importance for predicting correctly the properties of homogeneous flow and the onset to transition. A comparison with experiments presented in the current chapter was made by the authors. This showed qualitative agreement and the importance of the lift force model for the stability.

Lucas et al. (2005) study the influence of the lift force on the stability of the flow in a bubble column via a linear stability analysis. The study shows that the sign of the lift force coefficient C_L can be used as a measure for the stability of the flow: if $C_L<0$, bubbles experience a force directed to the column center, and turbulent diffusion is too weak to counteract it. Tomiyama et al. (2002) suggested that $C_L<0$ for bubbles larger than a critical diameter. This suggests that primarily the bubble size determines the stability of the flow instead of the void fraction, and it agrees with the occurence of a pure heterogeneous regime if a single orifice (producing large bubbles) is employed.

The next two sections discuss the results of the study into the properties of the homogeneous flow and the change in properties at the onset to the transition. The focus is put on the mechanisms responsible for the transition, with special attention for the lift force. Direct measurement of the lift force on bubbles is not feasible in a dynamic flow such as the present bubble column: this requires the accurate measurement of both the path of the bubbles and detailed knowledge of the flow fields in which the bubbles are immersed. Optical accessibility is, however, strongly limited. Kulkarni and Joshi (2004a) attempt to determine the lift force sign with an indirect method from the gradient of the liquid velocity. For the evaluation, assumptions are required about the relation between the drag force and the lift force. The validity of these assumptions is not clear, and therefore this method is not pursued here. Instead, the present study focuses on the measurement of liquid velocity profiles, void fraction profiles and bubble diameters.

7.2.3. Homogeneous flow and transition

The hydrodynamics are investigated in more detail. Special attention is paid to the influence of the degree of water contamination on the results.

Void fraction profiles: wall peaking

Void fraction profiles were determined with single glass fiber probes for various superficial gas velocities at various heights in the column. Figure 7.5(c) gives an impression of the uniformity of gas injection that is achieved with the needle sparger. The profile was measured with a single fiber probe to avoid inaccuracies due to differences between the probes. The result shows that the void fraction profile contains small non-uniformities at z=0.07 m, introduced by imperfections in the sparger, but that these non-uniformities quickly even out: at z=0.15 m the void fraction distribution is very uniform. This shows that the needle sparger can provide very uniform gas injection. Small peaks are observed in the void fraction at distances of 5 mm from the wall (about one bubble diameter). At smaller distances to the wall, the void fraction drops more or less linearly. The drop near the wall may be explained with a local force driving bubbles away from the wall, such as modeled by Antal et al. (1991). This model is employed quite frequently in modeling studies for the estimation of, e.g., void fraction profiles for bubbly pipe flow or bubble columns (Guet (2004b), Krepper et al. (2004)). It is not clear, however, if such a force

U_g (m/s)	α (-)	No. of needles
0.015	6.1%	187
0.017	7.6%	187
0.025	11%	187
0.032	16%	559
0.039	20%	559
0.049	25%	559

Table 7.3.: Superficial gas velocities for the various gas fractions studied in the cylindrical column (uniform gas injection).

is really present: the derivation by Antal et al. (1991) is performed for small bubble Reynolds numbers. The work by Takemura and Magnaudet (2003) and De Vries (2001) suggest that, instead, for larger bubble Reynolds numbers, bubbles may be attracted to and bounce against the wall. An alternative explanation for the drop in void fraction near the wall may be the fact that bubbles cannot overlap with the wall. This way, their shape determines the variation in void fraction. A check with the assumption of an ellipsoidal shape shows that this gives a reasonable approximation to the decrease in void fraction near the wall.

Next, the shape of the void fraction profile is investigated for various heights, superficial gas velocities and water contamination levels. Since the gas injection is very uniform, the non-uniformities observed in the profiles are due to hydrodynamic effects and not due to the sparger. First, results are shown for tap water of several days old (large vortical structures occur for U_g>0.06 m/s), and an ungassed liquid height of 1.3 m. The superficial gas velocities that have been used are shown in Table 7.3. This table also shows the number of needles that have been used. The flow rates through the needles for these conditions give equivalent bubble diameters in the size range 3.5 mm-5.0 mm. If the superficial gas velocity is increased from 0.015 m/s to 0.025 m/s the bubble size increases due to the larger flow rates through the needles (see chapter 2). If the superficial velocity is increased further, the number of needles is tripled, the flow rate through the needles decreases and the bubble diameter drops again. As a result, the bubble diameter variation over the entire void fraction range is reduced, and attains a local maximum value for α=11%.

Figure 7.10 shows void fraction profiles for superficial gas velocities of 0.015 m/s and 0.049 m/s. Figure 7.11 shows more profiles for the superficial gas velocities without large scale structures for z=1.2 m and z=0.6 m. The figures show that the inside of the bubble column is very uniform for all superficial velocities, except close to the surface for α=25%. The low superficial gas velocities show a wall peaking behavior for all heights. The same peaking behavior is observed for U_g>0.035 m/s (α>18%) for z<0.9 m, in higher parts of the column the peak disappears. A small dip occurs near x/R=0.7 for all experiments with U_g>0.03 m/s. This small dip is probably due to inaccuracies in the correction factors for the glass fiber probe experiments which were determined for void fractions in the range 6-11%.

Additional void fraction profiles for more contaminated tap water of two weeks old are shown in Figure 7.12. For all the experiments from this point on, the ungassed liquid height was 1.0 m, unless noted otherwise. The behavior is similar to that observed in Figures 7.10 and 7.11. For the superficial gas velocities, that are significantly below the critical superficial gas velocity where

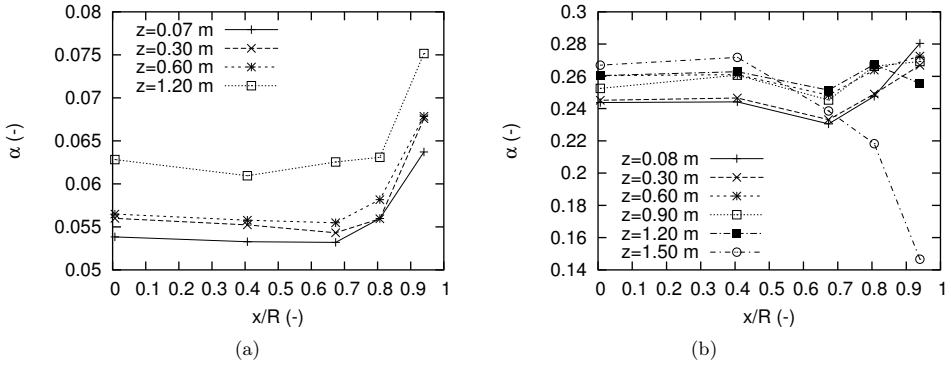

Figure 7.10.: Void fraction profiles for 6.1% void fraction (U_g=0.015 m/s) (a) and 25% void fraction (U_g=0.049 m/s) (b). Tap water several days old.

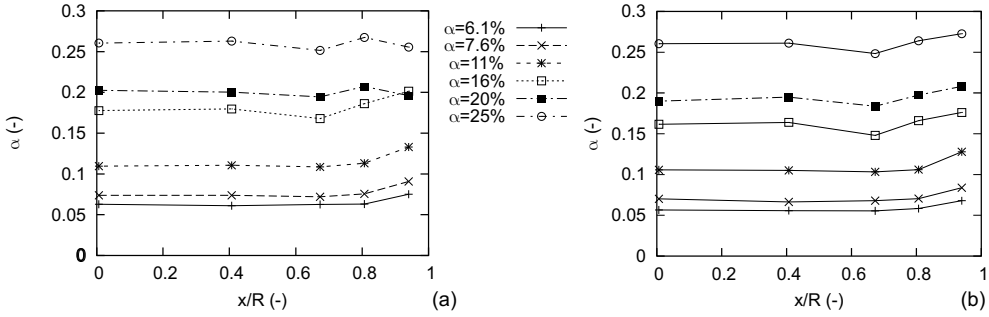

Figure 7.11.: Void fraction profiles for various gas fractions at z=1.2 m (a) and z=0.6 m (b). Tap water several days old.

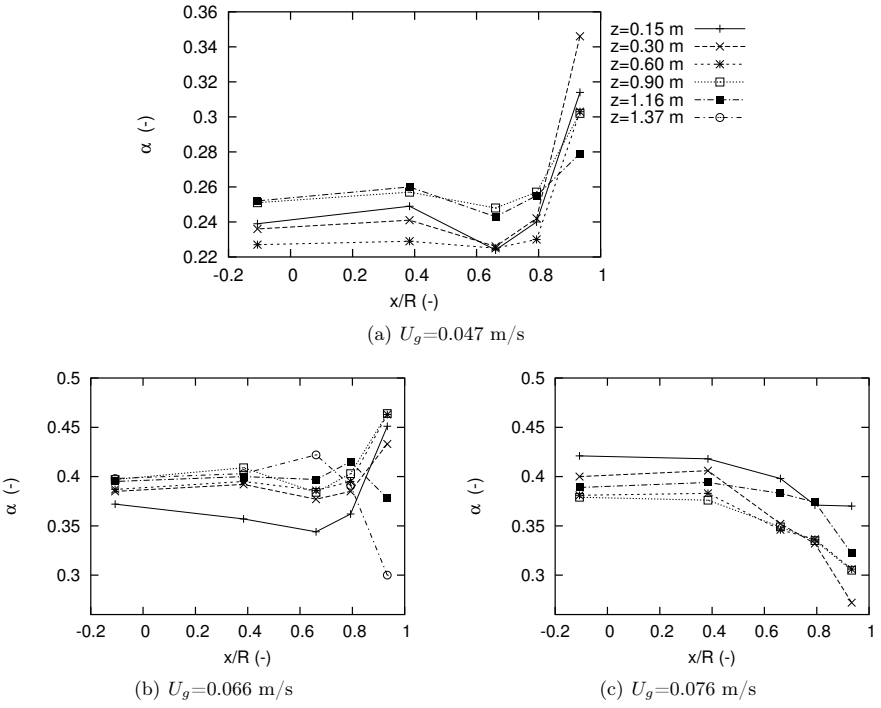

(a) U_g=0.047 m/s

(b) U_g=0.066 m/s

(c) U_g=0.076 m/s

Figure 7.12.: Void fraction profiles for tap water of 2-3 weeks old. Large scale structures for U_g>0.07 m/s.

the onset of vortical structures occurs (e.g. U_g=0.047 m/s), again wall peaking is observed for all heights. For the superficial gas velocities somewhat below the critical superficial gas velocity (U_g=0.066 m/s), the wall peaking disappears near the top of the bubble column. For the case where dynamic large scale structures are present (U_g=0.076 m/s), the familiar core-peaking void fraction profile is found. In this case, an additional underestimation of the void fraction is present: bubbles rising downwards have a smaller probability of being pierced (Groen (2004)).

Wall peaking behavior has been reported for bubbly pipe flows by e.g. Serizawa et al. (1975). Similar void fraction wall peaking is observed in model predictions for bubble columns and pipe flow by Guet (2004b). The behavior is explained by the effect of the lift force, which causes accumulation of small bubbles (i.e. smaller than 5 mm) in the negative velocity part of the flow, which is close to the wall. The position where the peaking is observed in the current experiments is at 5 mm from the wall. The lift force acting on the bubbles at this location is signicant since these bubbles experience a shear due to the down flow close to the wall, as the subsequent observations of the liquid velocity profile will show.

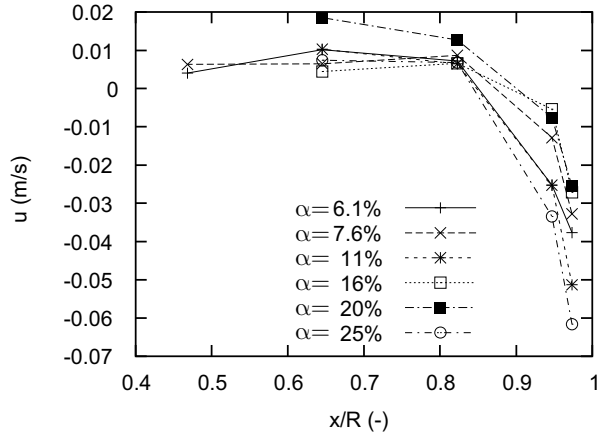

Figure 7.13.: Mean axial liquid velocity profile for various void fractions. Tap water of several days old. Ungassed liquid height 1.3 m.

Axial liquid velocity profiles

Mean axial liquid velocity profiles for various gas fractions are shown in Figure 7.13 and Figure 7.4. The profiles show that for all superficial gas velocities up flow occurs in the central region with $|x|/R<0.9$ with a typical very small velocity around 0.01 m/s. Down flow occurs for $|x|/R>0.9$ and has a typical velocity of around -0.04 m/s. The down flow is probably caused by the low void fraction very close to the wall (due to bubble interaction with the wall), which causes a density difference between the inner bubble column regions and the wall region. Most publications on bubble columns (e.g. Mudde et al. (1997a), Hills (1974)) report that the inversion point (i.e. the point where =0) is located around $|x|/R=0.7$, whereas the present study finds the inversion point near $|x|/R=0.9$. This shows the very strong homogeneity for the present flow. The difference is most likely caused by the absence of any large scale structures in the flow. This absence is caused by the very homogeneous gas injection combined with a more narrow bubble size distribution at the sparger. For the other studies, the gas injection may not have been uniform enough. The results close to the wall show no trend with U_g. This is probably due to the presence of a strong preshift frequency bleedthrough in the signal for measurements near the wall. This affects the mean velocity. In addition, since the wall location is determined by locating positions where zero velocity is found, a small error in the radial alignment is created, which manifests itself strongest close to the wall where the velocity gradient is largest.

Extra measurements have been performed to determine the velocity profile close to the wall more accurately (using very clean walls, etc.). The results are shown in Figure 7.14. For the measurements in the transitional regime (U_g=0.076 m/s), the homogeneous flow and flow with structures alternate. Consequently, the void fraction varies, generating extra variations in the data rate in addition to the variations due to velocity bias. This introduces additional bias, which increases with the distance to the wall. For this reason, the mean velocity is not only calculated with 2D+ velocity bias correction, but also with Sample and Hold. Generally, the down flow

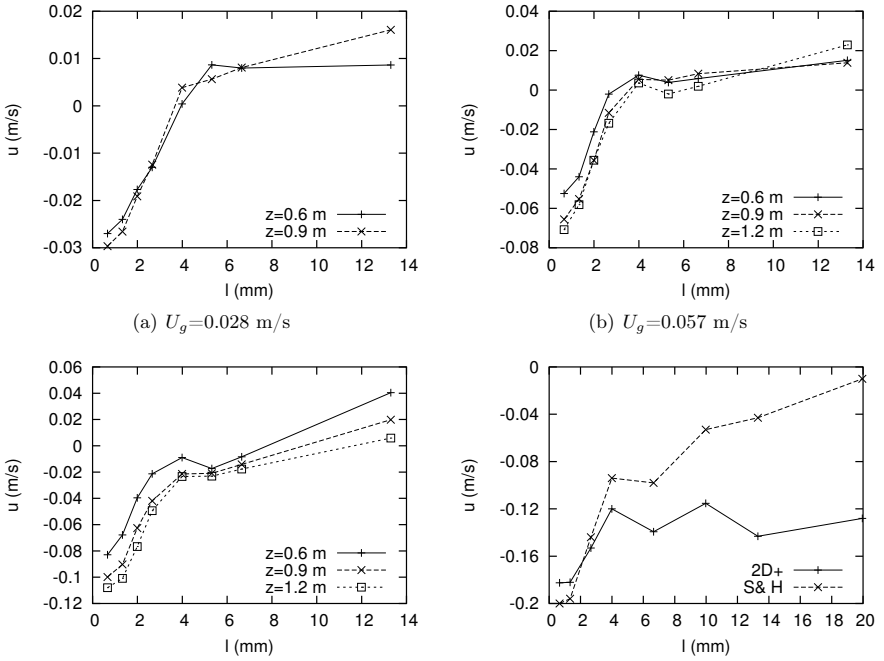

(a) U_g=0.028 m/s

(b) U_g=0.057 m/s

(c) U_g=0.066 m/s. Flow with visible strong down flow close to the wall.

(d) U_g=0.076 m/s, two velocity bias correction methods. Flow with intermittent dynamic large scale structures.

Figure 7.14.: Mean axial liquid velocity profiles close to the wall. Ungassed liquid height 1.0 m, tap water of 1 week old, large dynamic structures for U_g>0.070 m/s.

close to the wall is strongest close to the wall in a region with a thickness of approximately 4 mm. The maximum downward velocity increases with z and U_g. This agrees with the observation that the strongest down flow is observed in the top parts of the bubble column. For the superficial gas velocities approaching the onset of large vortical structures, the maximum downward liquid velocity close to the wall approaches the bubble slip velocity (which is about 0.15 m/s), agreeing with the observation of very slow rising bubbles close to the wall.

Axial normal stresses

The axial normal stresses of the liquid velocity provide a useful tool for evaluating the distribution of large scale structures along the axial direction z. Figure 7.15 shows this distribution for tap water of 3-9 hours old. In the homogeneous parts of the bubble column, the stress levels are constant and have a low value, with a typical order of magnitude around 0.01 m^2/s^2. Strong liquid down flow is observed near the wall for z>1.1 m for $U_g \approx 0.057$ m/s. This is accompanied by a small increase in the axial normal stresses. Weak dynamic structures are observed for z>0.9 m for $U_g \approx 0.061$ m/s, again accompanied by a small increase in the stresses in this region. A

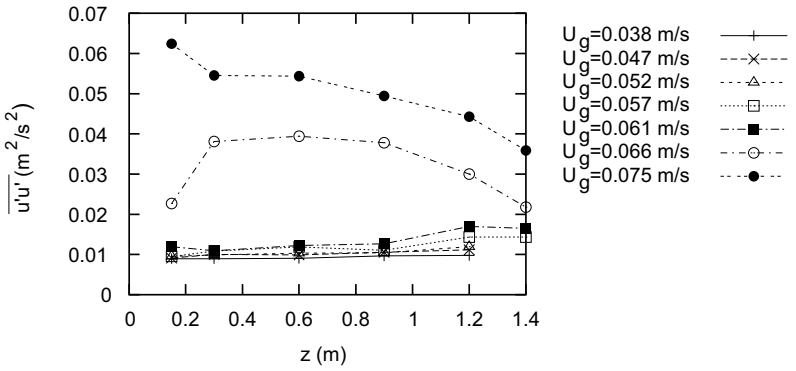

Figure 7.15.: Axial normal stresses for the liquid velocity as a function of the height z for increasing U_g. Tap water of 3-9 hours old. Ungassed liquid height 1.0 m, x/R=0.82.

sudden large increase in the stress level is obtained at the onset of intermittent dynamic large scale structures, which are observed for $U_g \geq 0.066$ m/s. The stress level is highest at intermediate heights z for $U_g \approx 0.066$ m/s. The structures are dampened when they approach the sparger, consequently the stress level drops close to the sparger. If the gas flow rate is increased further ($U_g \approx 0.075$ m/s) all structures are able to reach the bottom of the bubble column.

Bubble properties

In the previous sections, several indications were found that the lift force may be important. Wall peaking of the void fraction profiles was found, which is generally associated with a lift force driving the smaller bubbles closer to the wall. Close to the wall a narrow region with liquid down flow is found, providing a velocity gradient that can produce a significant lift force. In the higher parts of the column, and for the higher superficial gas velocities approaching the critical gas velocity where the first large structures are observed, the velocity of the down flow increases. Nevertheless, for these conditions, the wall peaking disappears. This indicates that the lift force towards the wall is decreasing in magnitude. Since the actual velocity gradient is increasing, the decrease in the lift force is probably caused by a decrease of the lift coefficient, which may possibly even reach a negative value. The results by Tomiyama et al. (2002) show that the lift coefficient decreases if the horizontal bubble diameter approaches a critical value, which is approximately 5.8 mm for air-water. If the bubble diameter increases beyond this critical value, negative values are obtained for the lift coefficient due to the asymmetry generated in the wake (Sousa et al. (2005)). The results, therefore, indicate that the mechanism for the transition that was proposed by Lucas et al. (2005) probably plays an important role. In order to investigate this further, the properties of the bubbles are investigated in more detail.

The bubble velocity and size are estimated with the use of the four point optical fiber probe (see chapter 4). Two types of flow are analyzed: homogeneous flow, where the bubbly motion is preferentially vertical, and flow with structures, where bubbles frequently hit the probe under angles that deviate significantly from the vertical direction. For the flow with structures, three-

dimensional reconstruction is prefered to get a more representative impression of the flow. On the other hand, the results in section 4.4.4 show that for bubbles hitting the probe under an angle with the vertical, an underestimation of the velocity and the chordal length occurs (see Figure 4.40(c)). The underestimation is relatively large for the velocity. For the axial velocity, we are mainly interested in values for the homogeneous regime, since the bubble velocity estimate is strongly biased for the heterogeneous regime anyway for ϕ_p=0°. This is due to the effect that most bubbles traveling downward do not produce validated measurements (for ϕ_p=0°). For this reason, the axial bubble velocity is determined with the 1D reconstruction algorithm with curvature correction (equation 4.3, β_u=0.2). The performance is checked by comparing the total gas flow rate measured with the probe ($\int_0^R \alpha u_b 2\pi r dr$) and the gas flow rate that is measured with the flow meter. The gas flow rate measured with the probe underestimates that of the flow meter by typically 10%-15% for U_g in the range 0.038 m/s to 0.057 m/s.

The underestimation is smaller for the chordal length. Therefore, the three-dimensional reconstruction algorithm is used in combination with equation 4.21. Two corrections are applied: measurements with ϕ_1>60° or with bubble velocity smaller than 0.05 m/s are discarded since these contain the largest error (see section 4.4.3), and, in addition, a correction for the underestimation is perfored based on linear interpolation of the data in Figure 4.40(c). This way, the results are very similar to those obtained with the 1D algorithm for homogeneous flow (with $\phi_p = 0°$), and the accuracy for flows with structures is much better than if the 1D algorithm is used, which gives a strong underestimation in the bubble chordal length estimate. The bubble chordal length gives an impression of the minor axis length of the bubble. In addition, both the major and minor axis lengths are determined from photographs taken at the bubble column wall. For each condition and position, two or three photographs are analyzed manually, this way the mean and standard deviation of the major axis length and minor axis length are determined for at least 30 bubbles. Figure 7.16 compares the chordal length that is measured with the probe in the bubble column center and the minor length determined from the photographs. A typical difference of 5% is found.

Figure 7.17 shows the axial bubble velocity in the bubble column center for several cases where homogeneous flow is observed. The axial liquid velocity at this position is not known, however, Figure 7.13 suggests it is in the range 0.01 m/s - 0.02 m/s. Consequently, the slip velocity is only slightly lower than the axial velocity and probably changes similarly with the void fraction. The results suggest that the velocity is independent of the level of contamination of the liquid. Similar to what has been observed by other authors (e.g. Garnier et al. (2002)), the velocity of the bubbles decreases with an increasing void fraction due to an increased resistance. Garnier et al. (2002) show that this decrease scales well with the decrease in the bubble-bubble distance, which varies as $d_b/\alpha^{1/3}$. However, for the present results the velocity appears constant for α>35%. No data is presented by Garnier et al. (2002) for this range. The constant velocity may be caused by a change in the structure of the relative bubble placement: the more or less random bubble positions at lower void fractions become more ordered (see Figure 7.9). Consequently, the average bubble-bubble distance may decrease more slowly than according to $d_b/\alpha^{1/3}$. In addition, the relative bubble positions may change such that increased in-line drag reduction (such as described by e.g. Yuan and Prosperetti (1994)) cancels the increased mutual hindrance.

Figure 7.18 shows radial profiles for the axial bubble velocity for two heights. This confirms the observations in Figures 7.13 and 7.14, that in the case of the homogeneous regime the velocity

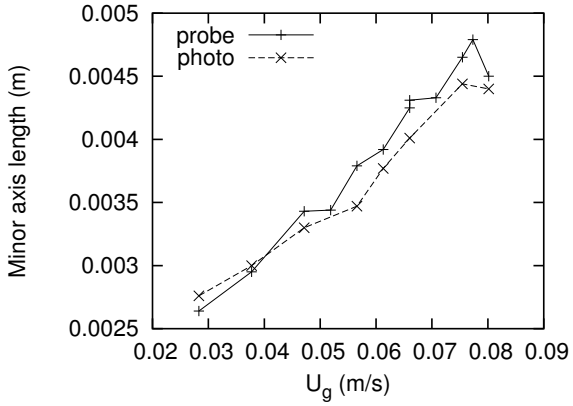

Figure 7.16.: Comparison of the bubble pierced chordal length in the center of the column and major axis estimated from images at the column wall. Contaminated water of three weeks old, z=0.15 m.

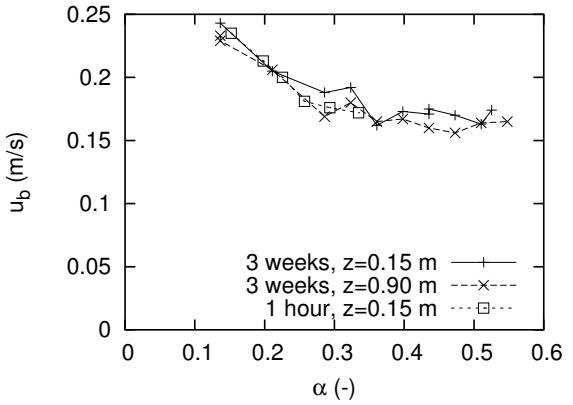

Figure 7.17.: Bubble axial velocity as a function of the void fraction for tap water of various ages.

profile is more or less flat for $|x|/R<0.8$, and that lower velocities are measured close to the wall. Once large scale structures appear, the velocity differences become more pronouced. Once should notice that for measurements in the heterogeneous regime, the velocity is biased to higher values since downward moving bubbles are not measured.

Guet (2004b) measured an average inclination of bubbles close to the wall that was oriented towards the wall for wall peaking conditions. In addition, the inclination for bubbles was found to become more orientated towards the column center for smaller aspect ratios. This behavior was associated with the migration of large bubbles towards the center due to the lift coefficient sign reversal. Figure 7.19 gives an impression of the radial variation of the average horizontal bubble velocity component towards the wall. Close to the wall, the average bubble motion is directed towards the wall, and a similar observation is made for the bubble inclination angle (ϕ_x). The behavior is found both in the presence of wall peaking and in the absence of wall peaking and is therefore not consistent with the explanation of Guet (2004b). The effect is possibly a measurement artefact caused by the altered motion of bubbles when pierced by the probe nearby the column wall, which may have an effect on the chordal length estimate as well.

The radial profiles for the vertical bubble chordal length measured with the probe are shown in Figure 7.20. The chordal length is more or less constant for $|y|/R<0.7$, but shows a small increase close to the wall. The increase is observed in the same part of the flow where the strongest velocity gradient in the liquid velocity is present. Perhaps, this gradient induces a different bias locally. This bias may be associated with the bias observed in Figure 7.19.

The change in chordal length with height is plotted in Figure 7.21. The increase of the bubble chordal length with z is quite small, but cannot fully be explained with the diameter difference in hydrostatic pressure (about 2% over 0.9 m height). This shows that there is relatively little coalescence in the bulk region. When large scale structures appear in the flow, the axial mixing is strongly enhanced and the variations in the chordal length with z become even smaller.

Figure 7.22 shows the variation of the chordal length with the superficial gas velocity for tap water of various ages. The results show almost no dependency on the level of water contamination. A strong increase with the superficial gas velocity is observed. This result can not explain how the lift force sign reversal occurs at different superficial gas velocities for different levels of water contamination. However, for the lift force the length of the major axis $2a$ is important, not the length of the minor axis $2b$, an estimate of which is obtained with the probe. Figure 7.23 shows the means and standard deviations for the major and minor axis lengths of the bubbles obtained with the photographic technique. For the horizontal diameter, clear differences are observed between the case of 'fresh' tap water and the case of contaminated tap water. For the relatively clean water, the horizontal bubble size is increasing for $U_g<0.05$ m/s, whereas it is more or less constant for the contaminated water. In this range, the bubble shape for the contaminated water is more or less ellipsoidal, whereas the bubbles in the relatively 'clean' water have much more irregular shapes and exhibit strong shape oscillations. As soon as the horizontal diameter reaches a value around 5.8 mm in the region near the free surface, the increase levels off and strongly increased liquid down flow is observed close to the wall in the top regions of the bubble column ('A'). If the superficial gas velocity is increased slightly further, large scale instability is observed, first in the top parts of the column ('B'), and for a small further increase in the entire bubble column ('C').

The results suggest that the lift-force direction reversal mechanism suggested by Lucas et al.

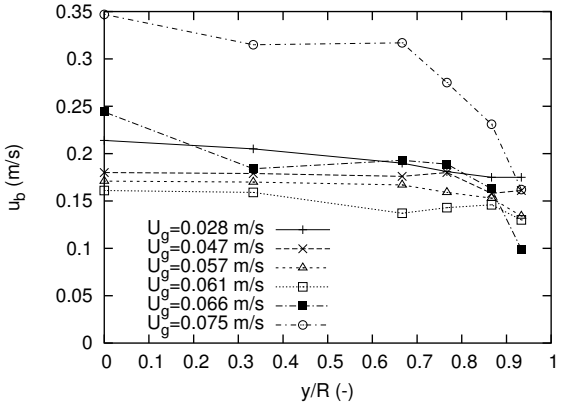

(a) z=0.15 m

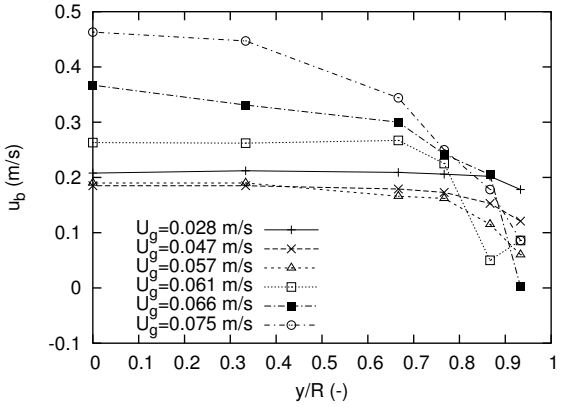

(b) z=0.9 m

Figure 7.18.: Bubble axial velocity. Tap water of 3-9 hours old. First weak vortical structures for $U_g \approx 0.061$ m/s for $z \geq 0.9$ m.

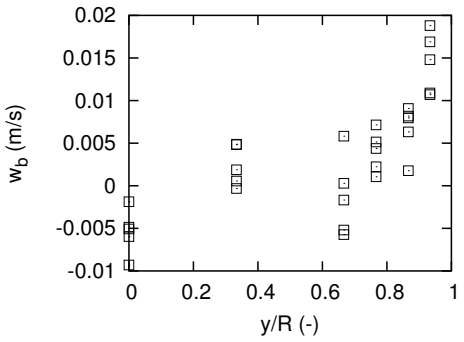

Figure 7.19.: Horizontal bubble velocity towards the wall at z=0.9 m for superficial gas velocities in the range 0.028 m/s - 0.057 m/s. Tap water of 3-9 hours old.

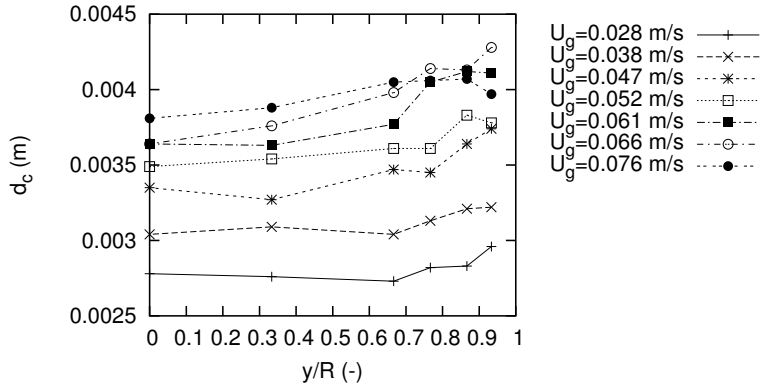

Figure 7.20.: Bubble pierced chordal length for z=0.9 m, tap water of 3-9 hours old. Onset of large dynamic vortical structures around U_g=0.061 m/s.

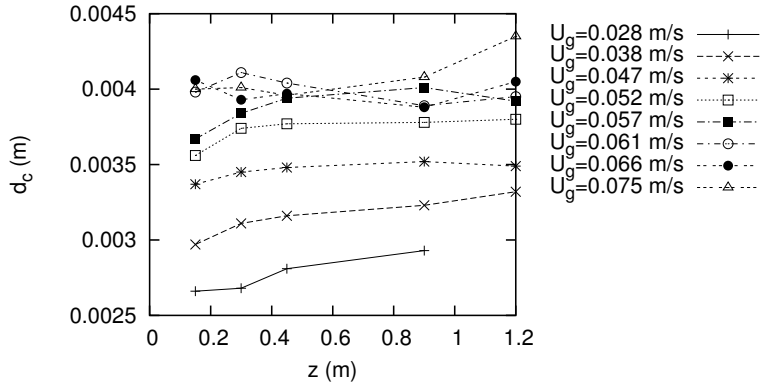

Figure 7.21.: Bubble pierced chordal length in the center for various heights, tap water of 1 day old. Dynamic large scale structures for U_g>0.06 m/s.

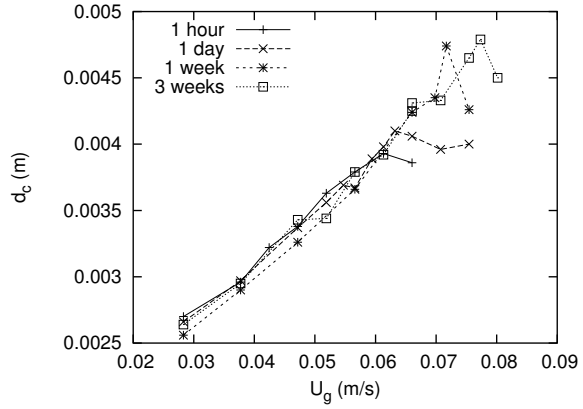

Figure 7.22.: Comparison of the bubble pierced chordal length in the center of the column for tap water with various ages. z=0.15 m

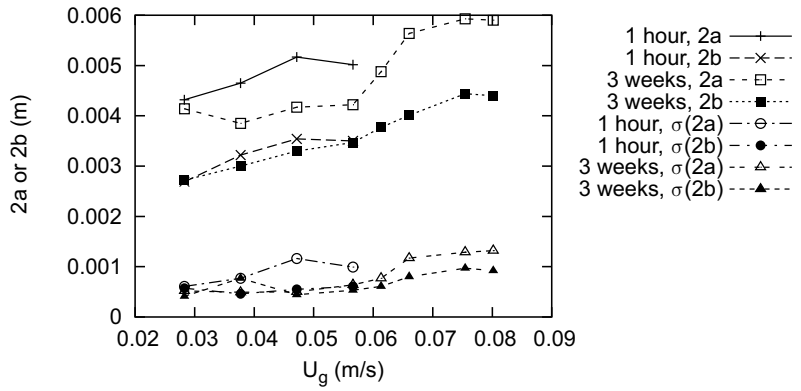

(a) Bubble sizes at z=0.15 m

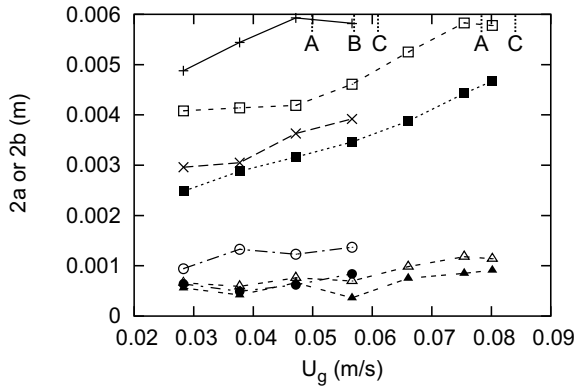

(b) Bubble sizes in the top of the bubble column (obtained in the region 15-30 cm below the free surface)

Figure 7.23.: Evolution of mean and standard deviation of the major and minor bubble axis lengths for two levels of water contamination. The dimensions were obtained with the photographic technique.

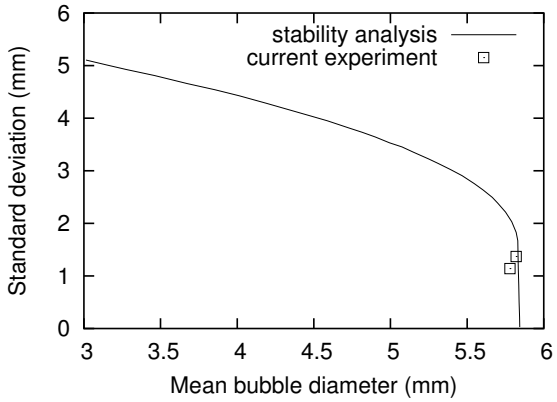

Figure 7.24.: Comparison of the maximum stable standard deviation of the bubble diameter according to Lucas et al. (2005) and the conditions in the current experiment at the onset of transiton.

(2005) plays an important role for the transition. The graph in Figure 7.24 reproduces the results of the stability analysis by Lucas et al. (2005) for a Gaussian bubble size distribution. If the standard deviation of the bubble diameter exceeds a certain critical value, the flow becomes unstable. This critical standard deviation is a function of the mean bubble diameter. The mean and standard deviation that were observed in the present experiments at the onset of dynamic large scale structures are also plotted in the same figure. The agreement with the result of the stability analysis is good, although the good match is not very sensitive to the precise value of the standard deviation for the present conditions. In addition, the result shows that the width of the bubble diameter distribution is quite small in terms of lift force behavior.

Equivalent bubble diameters were obtained from photographs with the assumption $d_{eq} = (8a^2b)^{1/3}$, which is only a rough approximation since the axial symmetry is absent, especially for the bubbles with strong shape oscillations. Figure 7.25 compares the estimated equivalent bubble diameters with those obtained in the single needle experiment described in section 2.3 (which was performed with tap water of at least one week old). For ϕ<2 ml/s, the bubble size obtained with the contaminated water matches the diameter obtained in the single needle experiment. If the flow rate is increased further, coalescence close to the needle due to the collision of growing bubbles with previously formed bubbles increases the bubble size. Observation of the bubble formation at high void fraction (i.e. 30%-50%) with a CCD camera shows that there is very little space for newly formed bubbles to enter the dispersion: the bubbles need some time to accelerate, and consequently the local bubble velocity is lower close to the needles. As a result, the local void fraction is significantly higher than in the bulk, and the probability of coalescence is, therefore, higher than in the bulk. Consequently, for conditions where the probability of coalescence in the bulk is small, this probability is not necessarily small near the sparger. For the relatively clean tap water, coalescence starts to play an important role at much lower gas injection velocities, and consequently the bubble size starts increasing at a smaller flow rate. As a result, the critical diameter, required for the onset to a flow with dynamic large structures, is

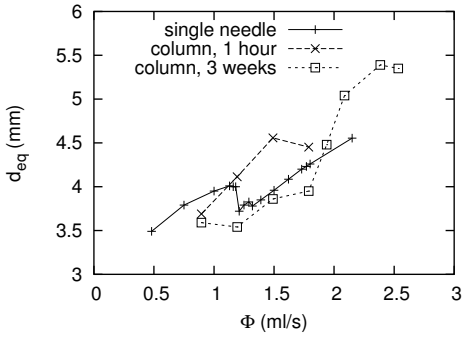

Figure 7.25.: Comparison equivalent bubble diameter for bubble formation at a single needle and bubble size in the bubble column for two levels of water contamination for various gas flow rates Φ per needle (z=0.15 m).

reached at a lower value of U_g.

7.2.4. Transition: mechanism and intermittency

The previous observations suggest that the mechanism for the onset to transition is dominated by a reversal in direction of the lift force. The following impression of the phenomena leading to the creation of large dynamic structures is obtained. At low superficial gas velocities, gas is injected uniformly in the form of bubbles with equivalent diameters in the range of 3 to 4 mm, creating a flat void fraction profile. Close to the wall, either due to interaction effects or the fact that bubbles cannot overlap with the wall, a smaller void fraction exists. The density difference with the core region of the bubbly flow creates a circulation with weak up flow in the center and down flow in a narrow region close to the wall. Due to the resulting velocity gradient, the bubbles close to the wall experience a lift force that is oriented towards the wall. This produces a void fraction profile with wall peaks. When the superficial gas velocity is increased, the bubble size increases due to the effect of inertia and drag during bubble formation. In addition, due to the increase in the frequency of bubble formation and the void fraction close to the needles, coalescence near the sparger increases. This effect becomes more important at lower gas input if the liquid contains less impurities. Coalescence in the bulk is limited, but nevertheless generates slightly bigger bubbles in the top parts of the bubble column, especially for the 'fresh' tap water. At the same time, the void fraction in the bulk increases, and the density difference with the wall region increases, enhancing the down flow near the wall. Eventually, the bubble size approaches the critical diameter where a zero lift coefficient is obtained, and the stabilizing effect of the lift force becomes weaker. Consequently, the wall peaking in the void fraction becomes weaker. As a result, the density difference increases further and strong down flow is observed close to the wall. The bubble axial velocity close to the wall becomes much smaller. If the gas flow rate is increased even further, the average bubble size becomes larger than the critical size. At the same time, a significant velocity gradient is present near the wall, and the large bubbles experience a lift force oriented towards the column center. The void fraction close to the wall decreases

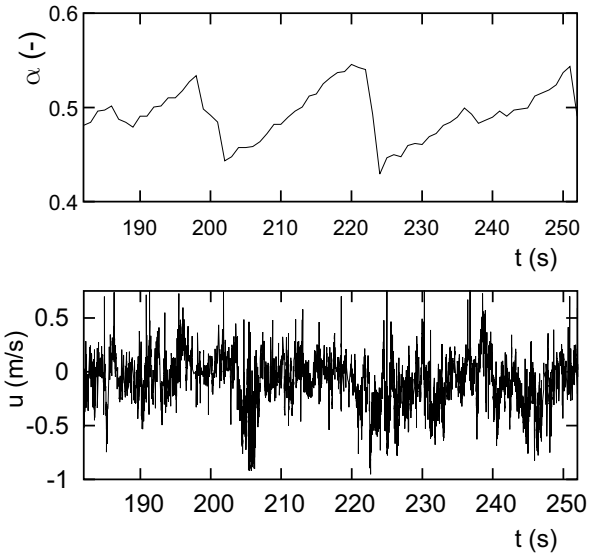

Figure 7.26.: Alternating regimes in the bubble column for uniform gas injection, U_g=0.076 m/s. Time-dependent volume-average void fraction (a) Axial velocity signal (b)

and the local down flow close to the wall increases. This void fraction disturbance is convected to the top part of the bubble column if it is not created there, and can grow close to the free surface. This way large scale structures are created near the top. This is further enhanced by a possible bubble size gradient due to coalescence and the hydrostatic pressure gradient, due to which the bubbles near the top are largest. Once a large enough fraction of the bubbles has a size larger than the critical diameter, the large scale structures become strong enough, such that the local void fraction drops. If the local density becomes significantly bigger than that in the lower column parts, the structure can move to the lower column parts. For the relatively clean water, there is a significant bubble size gradient with z. The properties in the upper part of the bubble column may allow instability to occur, whereas the lower part may still be homogeneous and not allow for instabilities to grow. Consequently, the structures that move downward are dampened more when they reach a lower level than in the case of the contaminated water, where the bubble size near the sparger is similar to that near the free surface. As a result, a smaller increase in the superficial gas velocity is required for the contaminated water before large dynamical structures can reach the sparger. When the structures also fill the lowest parts of the bubble column, they will interact with the bubble formation. The extra drag force oriented away from the needle that is acting on the bubbles during formation, will reduce their size. In addition, bubbles are transported away from the needles much faster and coalescence close to the needles reduces. Quite rapidly the bubble column is filled with smaller bubbles and the flow stabilizes: it becomes homogeneous again. Once the large dynamical motion near the sparger has ceased, the sparger produces large bubbles again. The large bubbles rise to the top parts of the bubble column, a new instability can grow and intermittent behavior results.

The latter behavior is illustrated with Figure 7.26, where the volume average void fraction is shown as a function of time. When the instability is created, it rapidly progresses through the column, and the void fraction rapidly drops. The passage of the structures clearly produces strong fluctuations in the LDA signal. Once the sparger produces small bubbles (the size difference is clearly visible by the eye), these will be quickly mixed by the large scale structures. The flow becomes homogeneous, vortical structurse are killed and, again, large bubbles will be generated at the sparger. The column is slowly filled with the high void fraction bubbly mixture, and the volume averaged void fraction increases linearly with time until the big bubbles reach the free surface and a new instability can grow.

The change of the time scale of the intermittent behavior is determined with the slotting technique for LDA signals obtained close to the wall, and for axial bubble velocity signals obtained with the four point probe placed under an angle ϕ_p of 90°. This way, both upward and downward bubble velocities can be measured. Examples of the signals are shown in Figure 7.27. The passage of the vortical structures is both visible by the increased amplitude of the fluctuations, and by the higher density of the velocity realizations for the bubble probe signal. The autocorrelation functions that were obtained for the LDA signal are shown in Figure 7.28(a). For U_g=0.061 m/s, when the first vortical structures are observed, a weak peak is observed around τ=12 s. For U_g=0.066 m/s the periodic behavior is much stronger and this peak becomes much more pronounced. If the superficial gas velocity is further increased, the periodic behavior becomes more irregular (U_g=0.075 m/s), and the time scale drops (U_g=0.085 m/s): the homogeneous regime exists for shorter periods. Figure 7.28(b), similarly, shows the autocorrelation function for the axial bubble velocity signals. Since a very large difference in 'datarate' (number of validated bubbles hitting the probe) exists between the periods with homogeneous flow and the periods with structures, Sample and Hold reconstruction is used to get a more even distribution of the amount of data with time, similar to velocity bias correction for LDA signals. This way, weak peaks become visible in the autocorrelation function. Comparison with the LDA results obtained close to the walls indicate that the time scale in the center is somewhat smaller than the time scale near the wall. This may be caused by a scale for the structures that is somewhat smaller than the column diameter.

7.3. Pseudo-turbulence: kinetic fluctuations

The motion of the bubble relative to the liquid causes small scale velocity fluctuations in the latter. This is named pseudo-turbulence and provides a strong contribution to the mixing at the smaller scales. The pseudo-turbulence has been investigated by several authors in order to provide relations for the extra kinetic energy introduced by the bubbles. The focus has been both on the magnitude of the kinetic energy $\overline{u_E'^2} = \overline{u'^2 + v'^2 + w'^2}$ and the magnitude of the axial normal stress: $\overline{u'^2}$.

Figure 7.29 shows the axial normal stress levels close to the wall for various gas fractions. The stress level looks constant for x/R≤0.95 but is different close to the wall (x/R=0.98). For void fractions smaller than 15%, the stress level is lower near the wall. This can be explained by the low void fraction near the wall. If the void fraction is lower, there is less 'local stirring' by the bubbles and therefore the stress level drops. The higher stress level for the void fractions

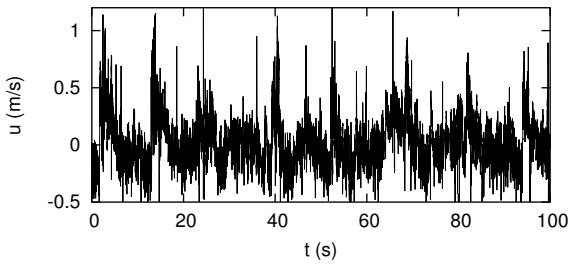

(a) LDA velocity time signal, x/R=0.91.

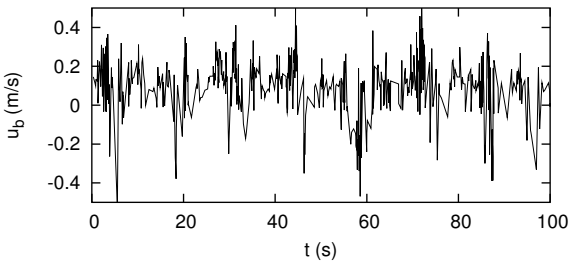

(b) Four point probe axial bubble velocity signal, x/R=0.73.

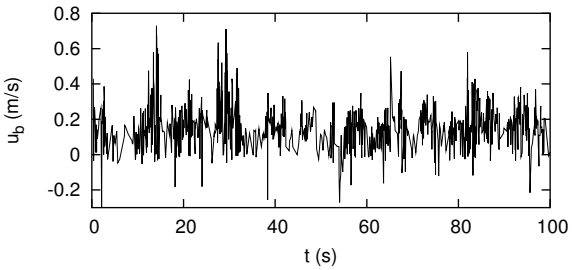

(c) Four point probe axial bubble velocity signal, x/R=0.47.

Figure 7.27.: Time signals showing the alternating regimes that occur in the bubble column (not synchronous). U_g=0.066 m/s, z=0.6 m. Tap water of 3-9 hours old with onset of vortical structures for U_g=0.058 m/s.

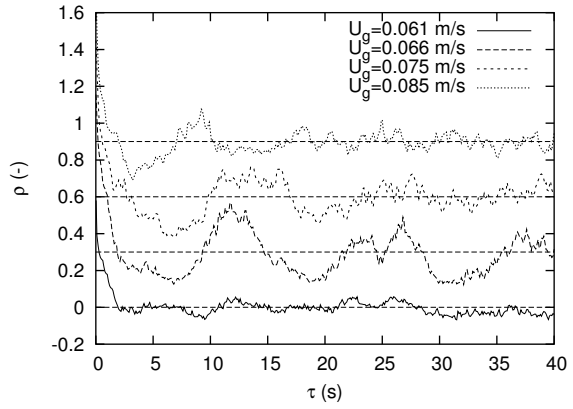

(a) LDA velocity time signals, x/R=0.91, z=0.6 m, slotting technique.

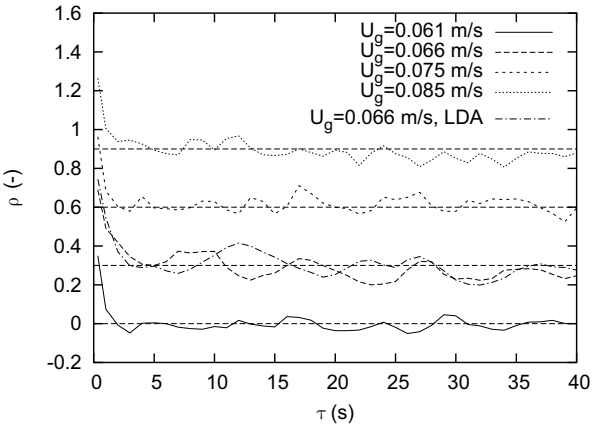

(b) Four point probe axial bubble velocity signals, x/R=0.47, z=0.6 m, Sample and Hold technique.

Figure 7.28.: Autocorrelation functions for increasing superficial gas velocity. Onset of vortical structures for U_g=0.058 m/s. Tap water of 3-9 hours old.

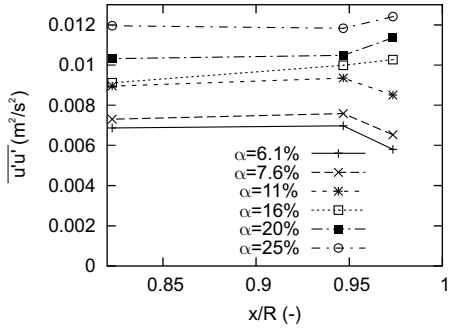

Figure 7.29.: Axial normal stresses near the wall for increasing void fraction (z=0.9 m)

Study	D_{column}	U_{g1} (m/s)	$\overline{u'u'}$ (m^2/s^2) for U_{g1}	U_{g2}	$\overline{u'u'}$ (m^2/s^2) for U_{g2}
CARPT	0.14 m	0.024	0.012	0.048	0.032
LDA, Mudde	0.15 m	0.027	0.015-0.02	0.045	0.045-0.075
LDA, present	0.15 m	0.025	0.009	0.049	0.012

Table 7.4.: Stress levels reported in the study by Mudde et al. (1997a) and the present study.

larger than 15% is not clear. This may be due to an increase in the noise level. For the purpose of further analysis stress level measurements at x/R=0.83 are used. This way, the wall has no effect on the level.

First, a comparison is made with other results published in literature. Mudde et al. (1997a) compared the stress levels obtained with LDA in a 0.15 m column with stress levels obtained from filtered data sets obtained by Dudukovic and coworkers with CARPT. This was done for two superficial gas velocities, their results are compared with results from the present study in Table 7.4. The stress levels in the present study are significantly lower. This is probably due to the very uniform gas injection obtained with the needle sparger. The CARPT and LDA experiments in the paper by Mudde et al. (1997a) were obtained using porous plate spargers which may provide less uniform gas injection (this is discussed in a subsequent section). The CARPT stress levels are probably smaller than the LDA experiments for the porous plate because of the larger inertia of the CARPT tracer particle: LDA is more suited to measure high-frequency fluctuations. In addition, the difference of the current experiments with the LDA experiments by Mudde et al. (1997a) is further enlarged by the lack of velocity bias correction in the results by Mudde et al. (1997a).

Next, the level of the kinetic fluctuations is investigated. Inviscid theory provides the following estimate for the dilute limit (Van Wijngaarden (1998)):

$$\overline{u'^2_{E,pot}} = C_k \alpha U_R^2 \tag{7.3}$$

and

$$\overline{u'^2_{pot}} = C_{k,a} \alpha U_R^2 \tag{7.4}$$

with U_R the relative velocity of the bubble with respect to the liquid, and C_k is the added mass coefficient for the inviscid flow. C_k=1/2 for a spherical bubble. Van Wijngaarden (1998) presents a relation how C_k varies with the aspect ratio and gives C_k=1 for an ellipsoidal bubble of 3 mm. For the present case of a bubble of approximately 4 mm with aspect ratio 0.65, it gives C_k=0.83. The coefficient for the axial normal stress, $C_{k,a}$, equals 0.2 for a spherical bubble and approximately 0.33 for the 4 mm ellipsoidal bubbles considered in the present work.

A second contribution comes from the wakes of the bubbles and the vortices generated by the bubbles. The fluctuation level due to these small structures can be estimated with a similar approach as that used by Mudde and Saito (2001). We consider ellipsoidal bubbles with equivalent diameter d_{eq} of 4 mm and aspect ratio 0.65 (from observations): the length of the semi-major axis is a, the length of the semi-minor axis is b. Similar to Lance and Bataille (1991), the wake contribution to the kinetic energy can be roughly estimated from the dissipation rate, which is estimated from the drag force experienced by the bubbles:

$$\epsilon_w \approx \frac{3}{8}\frac{\alpha}{1-\alpha}\frac{C_D}{b}U_R^3 \tag{7.5}$$

Similar to Lance and Bataille (1991), the relation $\frac{(\overline{u_w'^2})^{3/2}}{l_w} \propto \epsilon_w$ may be used to get an estimate of the magnitude of the fluctuations due to the wake. Assuming that the velocity fluctuations associated with this dissipation have a length scale l_w equal to $2a$, and introducing a proportionality constant C_p, we get:

$$\frac{(\overline{u_w'^2})^{3/2}}{2a} \approx C_p\epsilon_w \approx C_p\frac{3}{8}\frac{\alpha}{1-\alpha}\frac{C_D}{b}U_R^3 \tag{7.6}$$

C_D is estimated with $C_D = (1-\alpha)(8/3)(b/U_R^2)g$, where the $1-\alpha$ term is motivated by the pseudo-hydrostatic effect (Barnea and Mizrahi (1973)). We get (neglecting correlations between the fluctuations due to the potential flow and the wake):

$$\overline{u_E'^2} = \overline{u_{E,pot}'^2} + \overline{u_w'^2} \approx C_k\alpha U_R^2 + (2C_p\alpha a g U_R)^{2/3} \tag{7.7}$$

and

$$\overline{u'^2} < \overline{u_{pot}'^2} + \overline{u_w'^2} \approx C_{k,a}\alpha U_R^2 + (2C_p\alpha a g U_R)^{2/3} \tag{7.8}$$

An alternative approach is taken by Garnier et al. (2002) and De Vries (2001). Both investigations propose a scaling similar to that for inviscid flow:

$$\overline{u_E'^2} = C_{kin}\alpha U_R^2 = C_{kin}\alpha U_\infty^2(1-C_u\alpha^{1/3})^2 \tag{7.9}$$

where the second step is introduced by Garnier et al. (2002) to account for the effect of "mutual hindrance" (the data in Garnier et al. (2002) suggests a value of $C_u = 1$). De Vries (2001) does not account for this effect and assumes a constant velocity U_R with respect to α. A similar scaling is used for the axial normal stresses, with scaling constant $C_{kin,a}$. De Vries (2001) estimates the second contribution by considering the formation of 'vortex blobs' by the bubbles: each 'blob' is rearranged as Hill's spherical vortices, and an estimate for the number of vortices is obtained in order to provide a number for C_{kin}. An upper limit is obtained by considering the time that is required to generate new vorticity at the bubble surface after releasing a 'vortex blob'. A lower

limit is given by twice the natural frequency of the path of the bubble. This gives a value for C_{kin} in the range 1.35-3.1 for a 3 mm bubble at low void fraction. For the larger bubbles considered in the present study, a somewhat higher upper limit is expected due to the longer life-time of the vortical structures (which get a bigger size). In the model of the author, however, the fraction of space occupied by these vortical structures is typically in the range of 10-50 times the bubble void fraction. For the high void fractions considered in the present investigation, this space is lacking, and the results can therefore not be applied directly.

Experimental data at relatively low void fractions is provided by Theofanous and Sullivan (1982) (0-15%), as well as Lance and Bataille (1991) (up to 3% void fraction). In both investigations, a net liquid flow is present: pipe flow for Theofanous and Sullivan (1982), combined with grid turbulence for Lance and Bataille (1991). Garnier et al. (2002) present data up to void fractions of 40%. However, the authors report the presence of large scale structures for the higher void fractions, resulting in a large scatter for the high void fractions. The data reported in the present investigation does not suffer from this effect.

The kinetic energy is estimated from the LDA measurements, the normal stress of the third (radial) velocity component perpendicular to the wall, which has not been measured, is taken identical to the second (tangential) component: $\overline{u_E'^2} = \overline{u'^2} + 2\overline{v'^2}$. The measurements are scaled in two different ways: first according to equation 7.7 ('dissipation method', Figure 7.30(a)), second according to equation 7.9 ('inviscid flow', Figure 7.30(b)). For the scaling, the relative velocity is estimated from experiments for the contaminated water of 3 weeks old. Figure 7.17 gives information about the axial bubble velocity in the bubble column center. The high void fractions do not allow the accurate measurement of the axial velocity in the column center using LDA. However, the liquid velocity profiles in Figures 7.13 and 7.14 suggest that the axial liquid velocity profile is close to 0.015 m/s for all conditions. This value is used for the calculation of the slip velocity. A fit of the results is used for the scaling (for $\alpha < 28\%$: $U_R = 0.273 - 0.4072\alpha$ and for $\alpha \geq 28\%$: $U_R = 0.174 - 0.0554\alpha$, constants have unit m/s). Similarly, the mean bubble major axis length is obtained from a fit of the results in Figure 7.23: for U_g<0.05 m/s: $2a = 5.84 \cdot 10^{-3} U_g + 3.92 \cdot 10^{-3}$ and for $U_g \geq$0.05 m/s: $2a = 64.68 \cdot 10^{-3} U_g + 0.96 \cdot 10^{-3}$ (constants have units s and m respectively). A similar procedure is followed for the axial normal stresses measured in tap water that was one hour old.

The first scaling suggests a value around 1.3 for C_p and a value around 0.5 for $C_{p,a}$. The value 1.3 is somewhat bigger than the unity value found by Lance and Bataille (1991) for void fractions up to 3%. The actual difference is even somewhat bigger since these authors did not subtract the inviscid flow contribution. The second scaling suggests a value of C_{kin} in the range 3-3.5 and a value for $C_{kin,a}$ around 1.3. The latter value for $C_{kin,a}$ agrees with the findings of Garnier et al. (2002), who report values close to unity. The value for C_{kin} roughly agrees with the upper limit suggested by De Vries (2001). The two methods for the scaling seem more or less equally appropriate: the relative amount of variation in the relevant constants for the different void fractions is roughly similar. Possibly, C_{kin} shows a larger variation with the bubble diameter: equation 7.9 does not explicitly take this parameter into account, whereas equation 7.7 does.

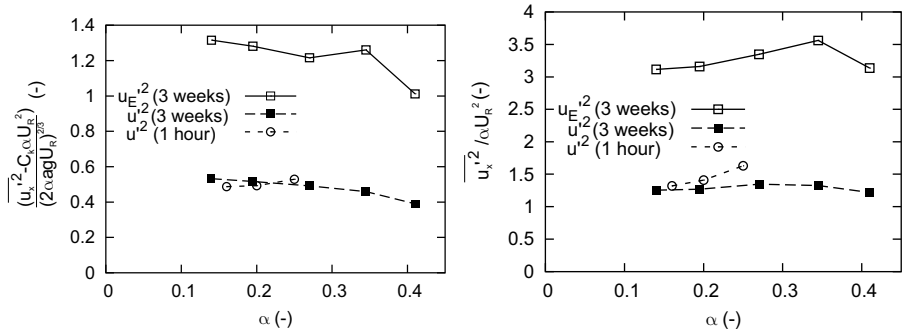

(a) (b)

Figure 7.30.: Kinetic energy scaled according to dissipation method (a) or inviscid flow method (b). Tap water, 3 weeks and 1 hour old, z=0.9 m.

7.4. Non-uniform gas injection in the cylindrical bubble column

The influence of non-uniformities in the gas injection on the flow properties is investigated for the cylindrical bubble column. First, experiments for tap water of several days old are performed for superficial gas velocities below the point where the transition occurs. No large scale structures are observed inside the bubble column when the uniform gas injection pattern is used (C1). Non-uniformities are introduced by creating non-aerated zones in the sparger (patterns C2-C5). Pictures of the lowest region of the bubble column for void fractions in this range are shown in Figure 7.31. Introduction of a small non-aerated ring near the wall (pattern C2) gives only a few weak circulation cells with fixed positions, no dynamic behavior was observed either visually or in the LDA time series. The circulation cells can be observed in the void fraction profiles in Figure 7.32(a). A diffuse plume is observed, which meanders from the center (z=0.07 m), to the wall (z=0.15 m) and back to the center (z=0.30 m). Subsequently, it gets more diffuse. The stationary recirculation cells between which the plume moves have very stable positions: these gas fraction profiles could be reproduced on different days and are apparently fixed by imperfections in the sparger. If the non-aerated zone is enlarged further (patterns C3 and C4), dynamic behavior results: circulation cells are observed in a very dynamic entrance region that extends visually up to approximately z=0.6 m. The structures move around dynamically with a typical timescale of 10 s. The void fraction profile (Figure 7.32(b)) shows the familiar core-peaking shape. Higher up in the bubble column (z=0.9 m), the profile is uniform. The behavior does not change if the void fraction is increased to 20% (Figure 7.33). In the upper column parts, again wall peaking is observed. Gas injection pattern C5, with gas injection near the wall, but not in the center, gives a strong recirculation near the sparger with up flow near the wall and down flow in the center, and a small bubble-free region in the center. No dynamic behavior is observed, however. This is illustrated with the STFT in Figure 7.34: the difference with the STFT plot for the uniform case is small, whereas the measurement for pattern C3 shows much power for the lower frequencies. Finally, Figure 7.31 also shows an impression of the behavior with a porous plate sparger (that was used by Groen (2004)). With this sparger, a dynamic

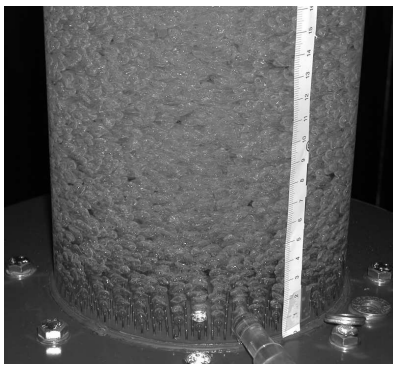

(C1)

(C2)

(C3)

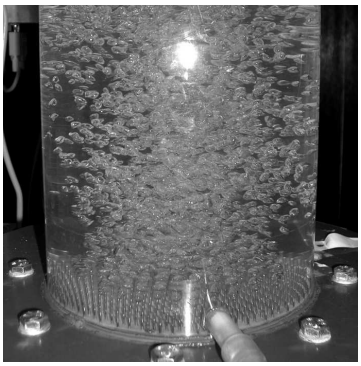

(C4)

(C5)

(Porous plate)

Figure 7.31.: Flow in the lower parts of the bubble column (images for α around 9%).

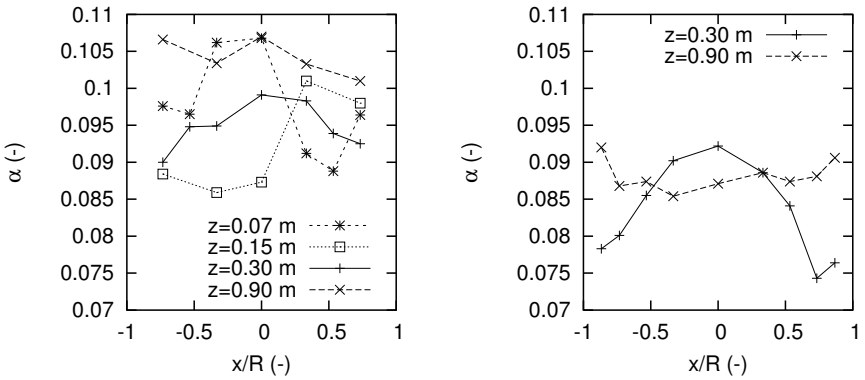

(a) Void fraction profile for injection pattern C2, U_g=0.020 m/s.

(b) Void fraction profile for injection pattern C3, U_g=0.023 m/s.

Figure 7.32.: Void fraction profiles for injection patterns C2 and C3.

entrance region is obtained. Apparently, the porous plate sparger does not provide very uniform gas injection.

Figure 7.35 shows the change in void fraction in the column center for various injection patterns. If the gas mass fraction is assumed constant, there is only a small variation due to the change in hydrostatic pressure. A weak linear dependence on z results, which is plotted for α=9.1% ('hydrostatic'). The uniform gas injection shows no entrance effect, whereas the other patterns do. The entrance effect for the case C3 extends up to z=0.6 m. The effects for the patterns C2 and C5 extend up to z=0.45 m. This is caused by the static circulation cells near the sparger for these patterns.

For all non-uniform gas injection patterns, the strength of large scale structures decays with height. This is best observed by considering the axial normal stress level for the liquid velocity, which is shown in Figure 7.36 for U_g=0.017 m/s (α=7.6%) and U_g=0.039 m/s (α=20%), normalized by the mean level for the uniform gas injection case. The highest stress levels are found near the sparger and these quickly decay with z. For pattern C3, the stress level has decayed to the uniform level for z=0.6 m. For pattern C4, the decay is complete near z=0.9 m. In the higher regions of the bubble column, no differences with the case for uniform gas injection are observed. This agrees with the observations for the void fraction profiles. The case with wall injection (C5) only has increased stress levels close to the sparger (z<0.3 m). The decay of the stress levels is more or less the same for the different void fractions. Apparently, the turbulent kinetic energy contained in the structures scales with the energy input into the column (which is proportional to the void fraction). The size of the entrance region has a small dependency on U_g, and a much bigger dependency on the injection pattern.

Figure 7.37 shows radial profiles of the axial liquid velocity for z=0.9 m. This shows that for patterns C2, C3 and C5 the liquid circulation is weak in the upper column parts, and again that the flow properties are very similar to that for the case of uniform gas injection. Only for pattern C4 a slightly increased circulation is observed. This agrees with the somewhat bigger

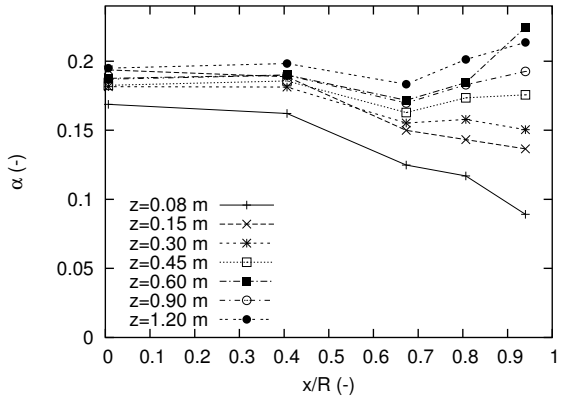

Figure 7.33.: Void fraction profile for injection pattern C4 (20% void fraction)

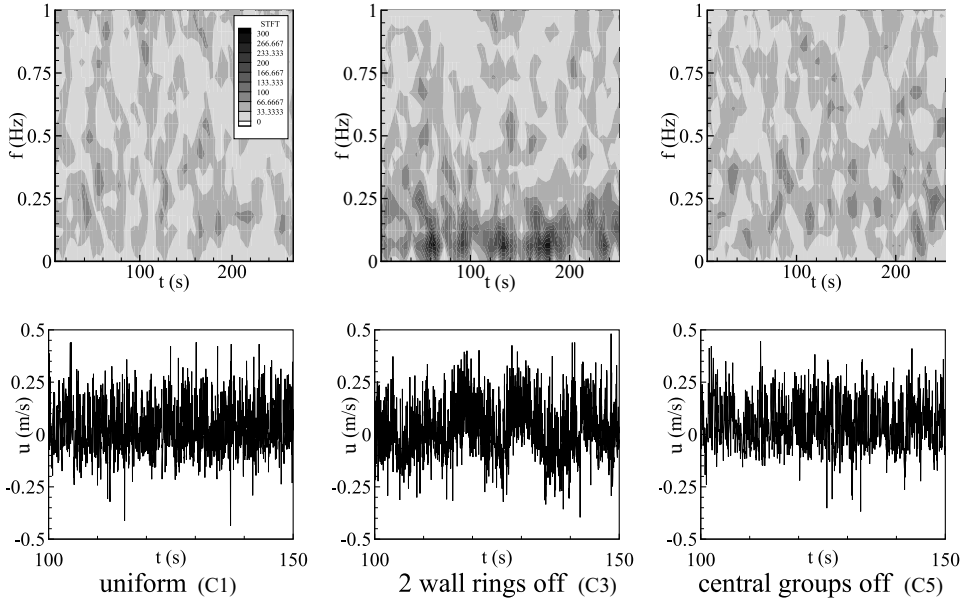

Figure 7.34.: Short Time Frequency Transform and axial liquid velocity time signals for three aeration patterns. Measurement positions: z=0.45 m, x/R=0.82. Gaussian window with e^{-2} decay width T of 16.4 s.

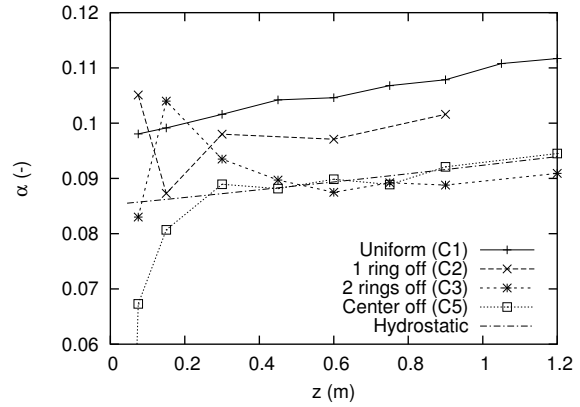

Figure 7.35.: Gas fraction at column center (pattern C1 and C2: U_g=0.023 m/s, patterns C3 and C5: U_g=0.020 m/s.

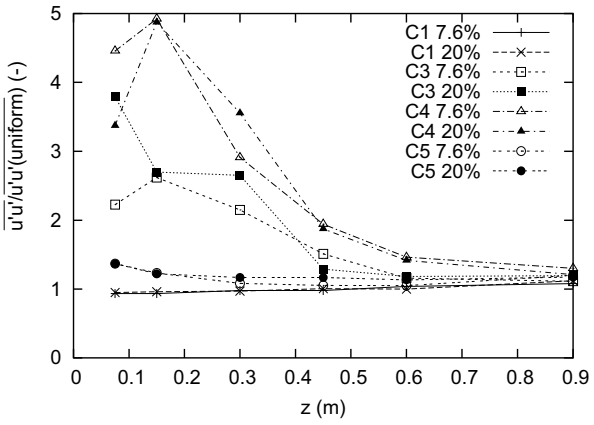

Figure 7.36.: Normalized axial normal stresses as a function of z for various gas injection patterns at x/R=0.83.

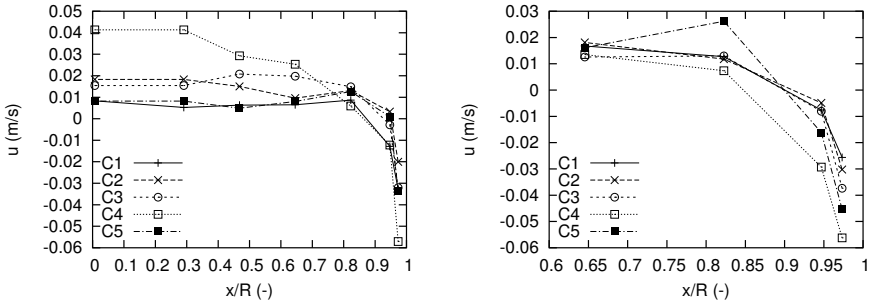

(a) α=0.076, U_g=0.017 m/s. (b) α=0.20, U_g=0.039 m/s.

Figure 7.37.: Axial liquid velocity profiles for the various injection patterns. z=0.9 m, tap water of several days old.

entrance region that was observed for this pattern in Figure 7.36.

The stress levels reported in the present study for z>0.6 m are much lower than those reported generally (e.g. Mudde et al. (1997a)), even if the gas injection is made non-uniform. A reason for the difference may be the non-dynamic behavior of the sparger. In the current setup, a large pressure drop over the sparger has been obtained by using needles. By grouping the needles and providing an additional large pressure drop for each group, the flow to the sparger is made even more independent of possible pressure fluctuations inside the bubble column. The more constant flow rate will also result in a more constant bubble size. As a result, the feedback of the hydrodynamics on the sparger is strongly limited. Most studies reported in the literature, however, make use of, e.g., perforated plate spargers or porous plate spargers. These have a smaller pressure drop and may, therefore, exhibit larger variations in the bubble size. As a result, the hydrodynamics may have a feedback effect on the local flowrate and/or the bubble size in the sparger. Consequently, large structures may be re-enforced and the size of the entrance region may grow. For instance, comparison of the flow patterns observed in the present study with those reported in Chen et al. (1994) shows significant differences. Chen et al. (1994) reported the presence of the dispersed bubble flow regime up to U_g=0.017 m/s. This regime is characterized by no coalescence and more or less straight downward liquid flow in between the bubbles. For 0.017 m/s<U_g<0.049 m/s, the vortical-spiral flow regime was reported. This regime is characterized by a spiraling central bubble plume and vortical structures near the wall. The present study does not reveal this 'vortical-spiral' behavior up to U_g=0.049 m/s, even for non-uniform gas injection. Instead, the dispersed bubble flow regime is observed for all superficial gas velocities up to the point where transition occurs. The difference may be caused by the different spargers used: Chen et al. (1994) used a tube-orifice type of distributor. The difference in pressure drop may again give a more dynamic behavior displayed by the sparger. The bubble size, which is quite uniform for a needle sparger, may vary much more for the sparger used by Chen et al. (1994), possibly promoting coalescence, which was reported by these authors for U_g>0.021 m/s. Dynamic effects of the sparger are only considered in few modeling studies (e.g. Ranade (1993)).

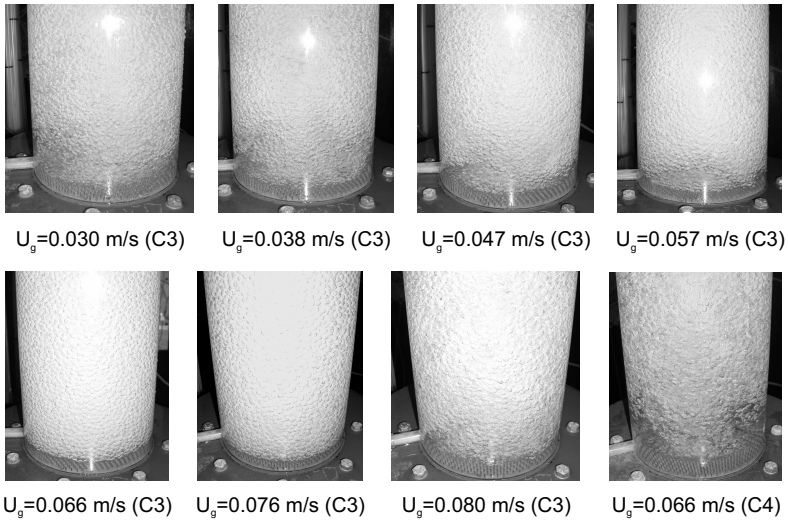

Figure 7.38.: Images of entrance region for patterns C3 and C4 for increasing U_g. Contaminated water: 3 weeks old. Ungassed liquid height 0.9 m.

Next, the influence of the gas injection patterns is studied for tap water of several weeks old. Figure 7.38 gives an impression of the sparger region for increasing superificial gas velocities. For pattern C3 and U_g<0.05 m/s, the behavior is similar to what was reported before for pattern C3. For U_g>0.05 m/s, the behavior for pattern C3 changes. The circulation at the sparger sides due to the non-uniform gas injection eventually becomes stronger, until the down flow close to the wall is so fast that bubbles are dragged downwards. For U_g=0.057 m/s a wavy motion is observed, for U_g>0.060 m/s the down flow results in homogeneous distribution of the bubbles, even close to the sparger and the dynamic behavior is killed. This is also visible in the normal stress levels (Figure 7.39): a local minimum is observed for U_g=0.066 m/s. Eventually, transition occurs in a similar fashion as in the case with uniform gas injection, but at a higher superficial gas velocity (U_g=0.08 m/s). Apparently, the local circulation at the sparger results in smaller bubbles, and the lift force sign reversal is delayed to a higher gas input. For the pattern C4, this behavior is not observed. The dynamic behavior remains present (Figure 7.40) for all superficial gas velocities. The upper parts of the bubble column are no longer homogeneous for U_g>0.050 m/s. This is probably caused by increased coalescence near the sparger: only 42% of the sparger area is available for the bubble generation, leading to strongly increased bubbling frequencies and very high local void fraction. As a result, much bigger bubbles are produced, and the lift force reversal occurs at a lower gas input, resulting in transition. Nevertheless, again, an entrance region and a bulk region can be identified. Inside the bulk region, the strength of the vortical structures is independent of z: the flow is well developed. If U_g is increased further, the relative difference between these two regions decreases.

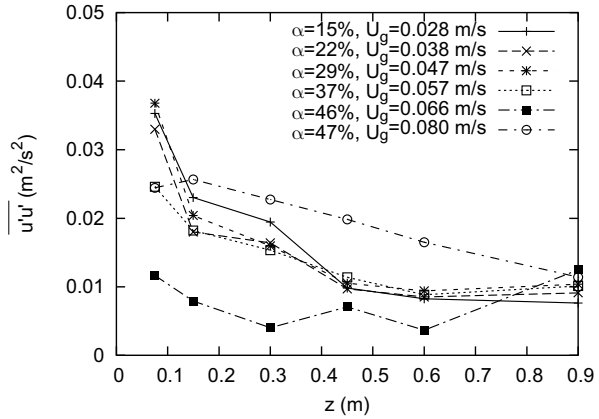

Figure 7.39.: Axial normal stress for the liquid velocity for pattern C3 as a function of the height z for increasing U_g. Contaminated water: 3 weeks old. Ungassed liquid height 0.9 m.

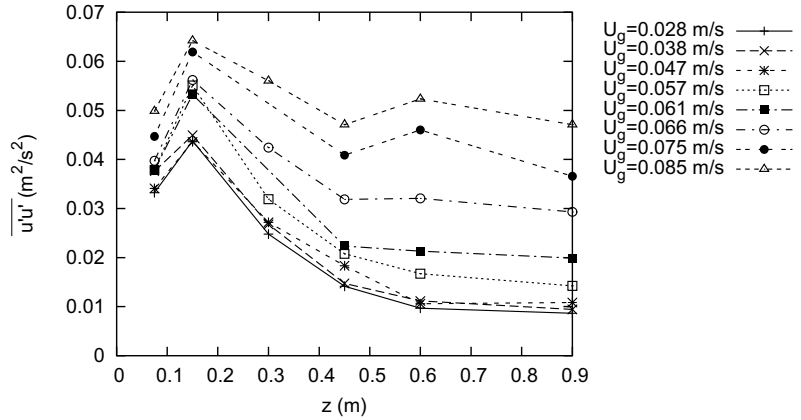

Figure 7.40.: Axial normal stress for the liquid velocity for pattern C4 as a function of the height z for increasing U_g. Contaminated water: 3 weeks old. Ungassed liquid height 0.9 m.

7.5. Pseudo 2D column

The limited optical accessibility of the cylindrical column makes it hard to study the dynamic behavior. For this reason, the influence of small non-uniformities on the large scale dynamics of the rectangular bubble column is studied. In addition, the rectangular geometry provides interesting data for validation studies since rectangular geometries are often still preferred for CFD modeling studies. The data presented in the present section was used for validation purposes in Monahan et al. (2005) and Monahan and Fox (2005). The influence of the gas injection pattern on the dynamics is studied by visual observation, PIV of the bubbles, PTV on the liquid tracers (where one should consider the slip velocity of the particles of 0.09 m/s for the interpretation, see appendix E), LDA for the mean liquid velocities and glass fiber probes for the void fraction profiles. Images of the flow combined with PIV and PTV results are shown in Figures 7.41-7.44. Visual observation of the bubbly flows shows a similarity with the behavior in the cylindrical column. For uniform gas injection and relatively small non-aerated areas in the column (F1-F4), no dynamic large scale structures are observed. Moreover, no large structures are observed (F1, F2), or these structures, if present, have a fixed position (F3,F4). If the non-aerated area near the wall is increased from 22% to 28% (from F4 to F5), suddenly very dynamic large structures are obtained with periodic behavior. Introduction of a non-aerated zone in the center leads to two circulation cells near the sparger with up flow near the walls. These cells display some weak irregular motion, but no large structures are observed in the higher parts of the column.

The hydrodynamics are now discussed in more detail. LDA axial liquid velocity profiles of the flow for uniform gas injection (F1) are shown in Figure 7.45. Horizontal velocities are not shown: these are in the range -0.015 m/s to 0.015 m/s. The axial velocity profile in the upper parts of the column has great similarity with that in the cylindrical column: down flow is only present very close to the walls, the velocity away from the walls is quite uniform. The down flow near the walls is again probably caused by a thin region near the wall where the void fraction drops. A big difference with the cylindrical case, however, is that the total area of the walls is much bigger for the pseudo-2D column. As a result, the relative volume where a lower void fraction is present, is larger (by a factor of 2 if the thickness of the region is assumed constant). This may lead to an increased circulation. The velocity profile indeed shows a slightly bigger upward velocity (2 cm/s compared with 1 cm/s for the cylindrical case). Another important difference is the relative amount of wall area, which is bigger near the two column ends (large |x|). As a result, the local driving force for the circulation increases near the ends and the void fraction near the y=0 line will be higher near the ends than in the central parts of the column (x=0). A small circulation results with up flow for large |x|. The circulation is clearly present in the LDA profiles for z=0.05-0.1 m. The difference in void fraction rapidly disappears due to the circulation and for z>0.1 m the column is very uniform. In order to obtain even more uniform gas injection, one would have to consider the presence of the low void fraction region near the wall: the amount of gas introduced near the wall per unit area of the sparger should be slightly lower. This may partially explain why only a small difference in hydrodynamics is obtained if a small area near the wall is not aerated for the cylindrical column.

Next, a small non-aerated zone near the column ends is introduced, which is gradually enlarged (F2-F5). F2 results in a weak circulation cell near the column ends with up flow in the center (Figure 7.46). Further enlargement of the non-aerated zone results in a stronger up flow

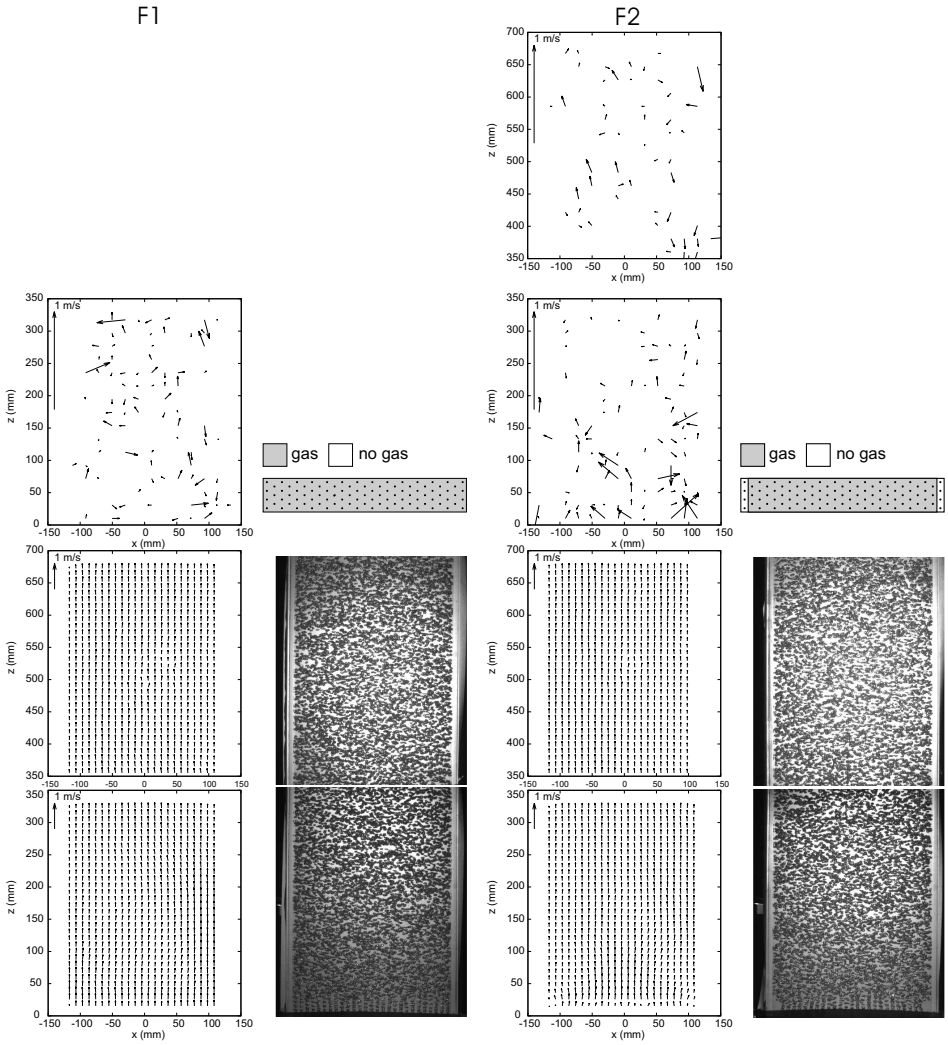

Figure 7.41.: Pseudo 2D column: Images of bubbly flow, PIV results for the bubble velocity field (bottom) and PTV results for the liquid tracers (top) for gas injection patterns F1 and F2.

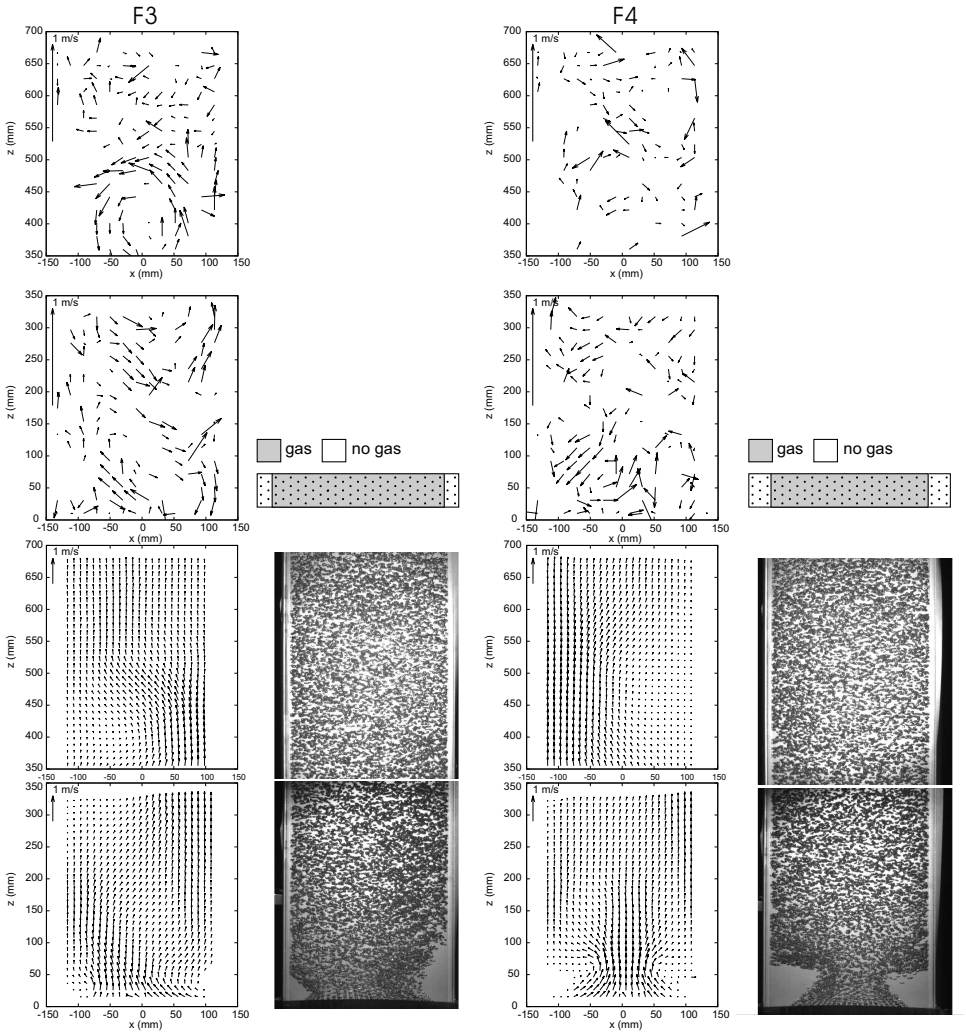

Figure 7.42.: Pseudo 2D column: Images of bubbly flow, PIV results for the bubble velocity field (bottom) and PTV results for the liquid tracers (top) for gas injection patterns F3 and F4.

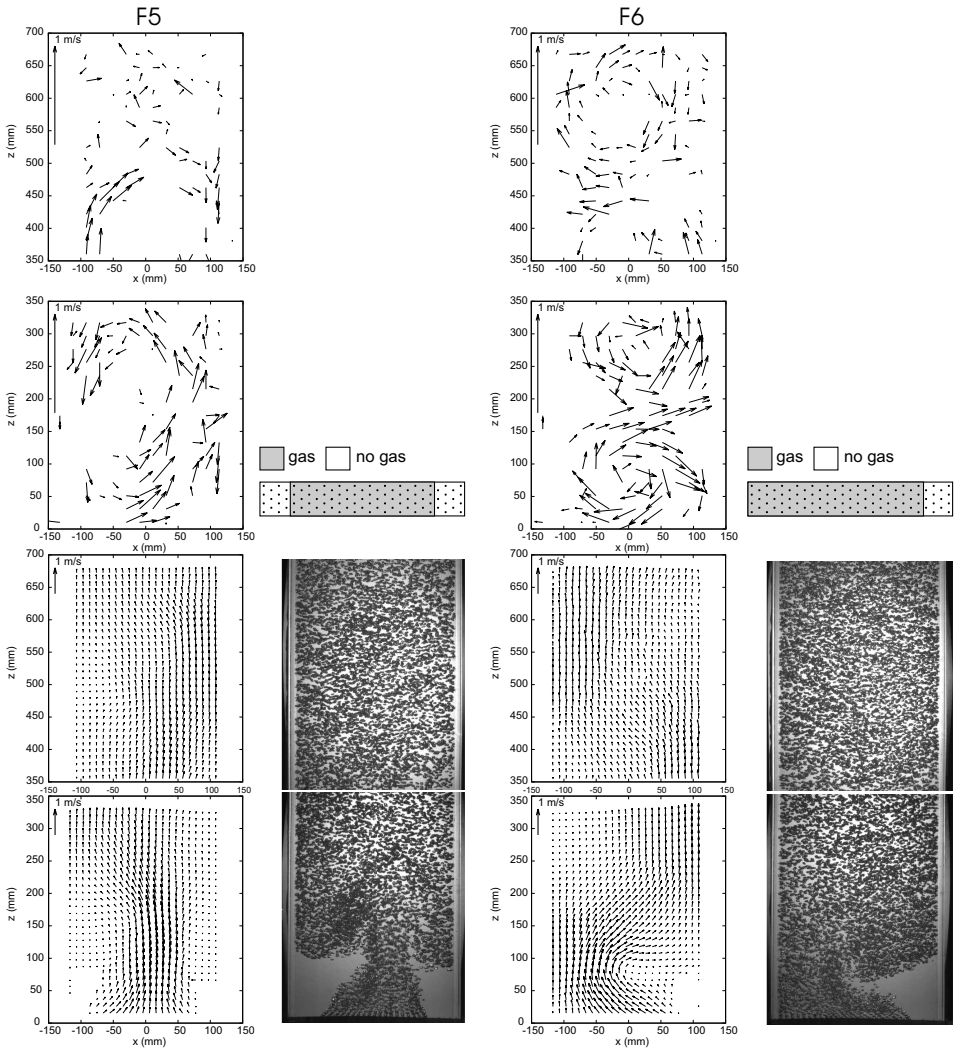

Figure 7.43.: Pseudo 2D column: Images of bubbly flow, PIV results for the bubble velocity field (bottom) and PTV results for the liquid tracers (top) for gas injection patterns F5 and F6.

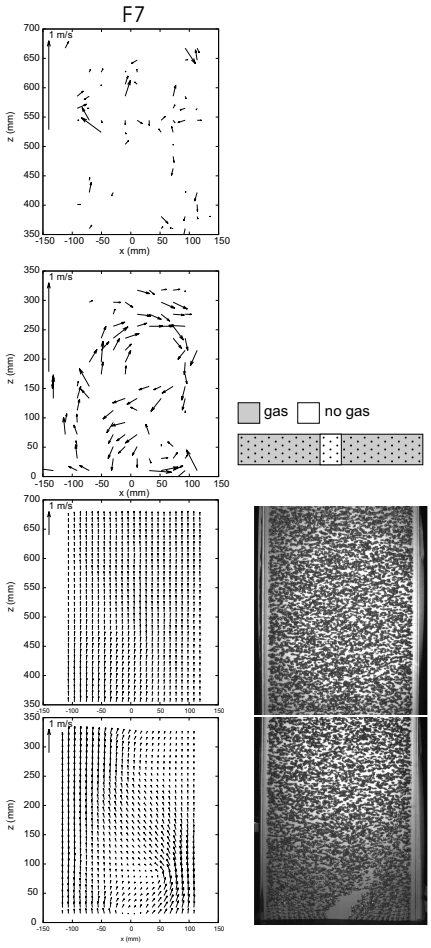

Figure 7.44.: Pseudo 2D column: Images of bubbly flow, PIV results for the bubble velocity field (bottom) and PTV results for the liquid tracers (top) for gas injection pattern F7.

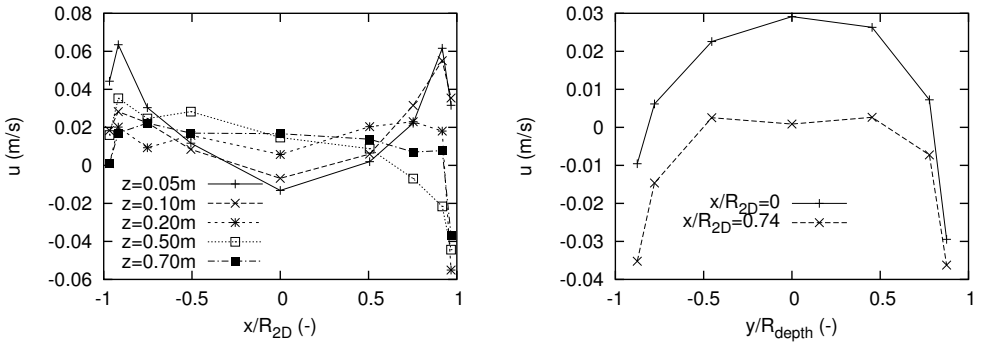

Figure 7.45.: LDA velocity profiles for uniform gas injection (pattern F1) over the center line with y=0 (a) and over two lines in the y-direction (z=0.5 m) (b).

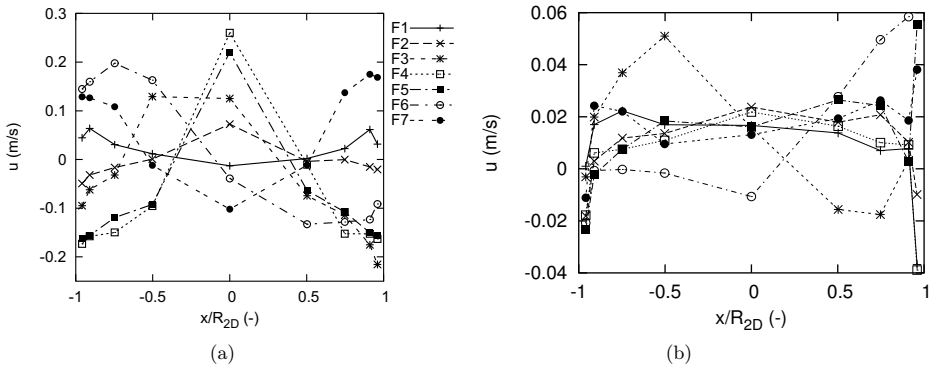

Figure 7.46.: LDA axial velocity profiles for the various gas injection patterns at z=0.05 m, y=0 (a) and z=0.7 m, y=0 (b).

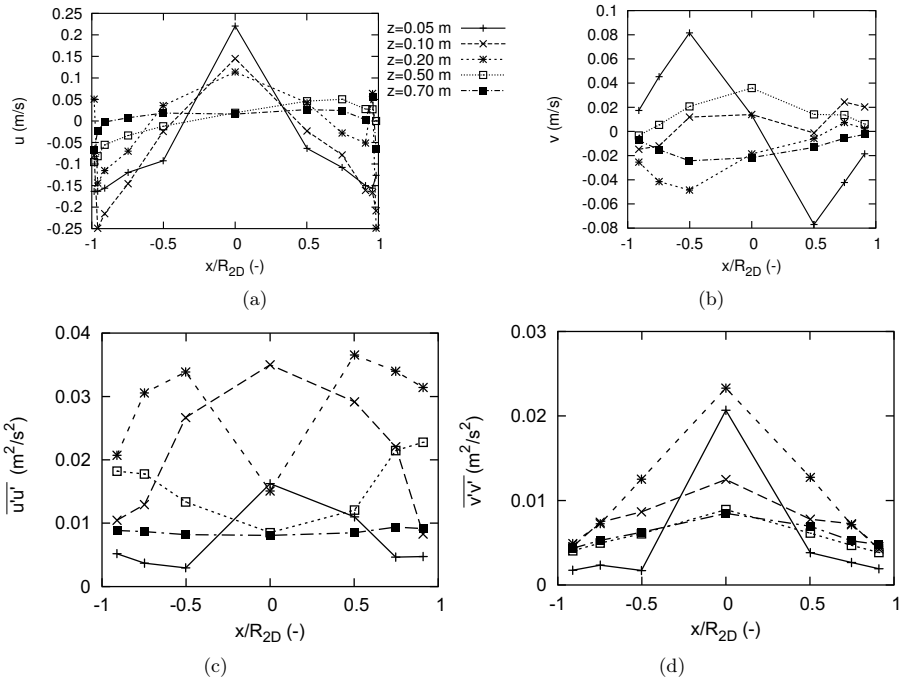

Figure 7.47.: LDA axial (a) and horizontal (b) mean velocities and normal ((c) and (d)) stresses for pattern F5.

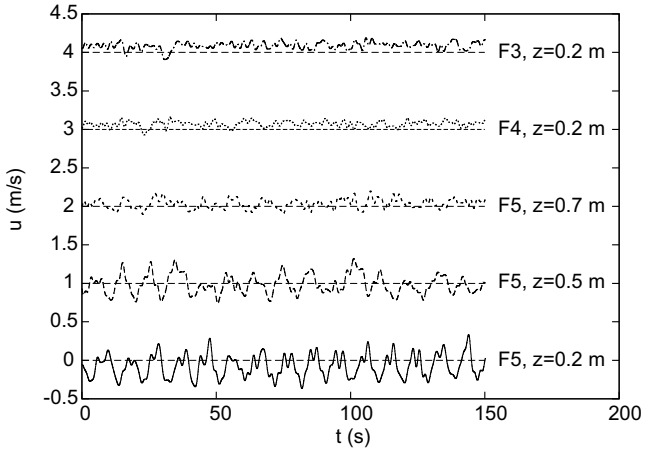

Figure 7.48.: Low-pass filtered LDA axial velocity time series for various gas injection patterns. The signals are offsetted by a constant, the lines show the offset value.

in the center for z<0.2 m (Figure 7.46(a)). Multiple stacked circulation cells are obtained with F3 and F4. These are clear in the PIV/PTV velocity fields. These cells, however, have a static nature: their position is more or less fixed. Case F5, finally, gives dynamic behavior. Large scale structures move around the column in a very periodic way, similar to what was reported by Mudde et al. (1997b). The transition from static to dynamic behavior seems to occur when the liquid down flow velocity near the wall reaches the same magnitude as the bubble slip velocity. The mean velocities and normal stresses for both the axial and horizontal direction for pattern F5 are shown in Figure 7.47. The mean velocities show the average circulation cells, and how these become weaker higher in the column. The normal stresses are very non-uniform in the lower regions and quite uniform at z=0.7 m. The axial normal stress near the sparger peaks in the center, at the position of gas injection, but peaks in the region 0.2 m≤z≤0.5 m closer to the walls: in this region the large structures have scales close to the column diameter, and the maximum axial velocities occur near the walls. The horizontal normal stresses peak near the center: the meandering vortical structures have their maximum horizontal velocity near the center.

Figure 7.48 shows LDA time series after resampling and low-pass filtering (cutoff frequency 0.5 Hz). The series were obtained at x/R_{2D}=-0.78, y=0. It is important to realize that the results from chapter 5 show that the amplitude of these filtered signals may be an overestimation: the Sample-and-Hold operation that is required transfers power from the higher frequencies to the lower frequencies. The time signals for pattern F5 clearly show the periodic behavior with period 9.4 s. The amplitude is dampened with the height z. Patterns F3 and F4 do not show a clear slow oscillation which can be associated with large structures. Study of the autocorrelation of the velocity time series shows that there is a very weak oscillatory behavior with time scale close to 10 s at z=0.2 m. The correlation coefficient is a factor 50 smaller than that for pattern F5. The oscillatory behavior is probably a weak meandering movement of the up flow in the center. Despite the dynamic behavior obtained with pattern F5, the void fraction profile is quite flat for z>0.2 m (Figure 7.49), and no significant difference with the void fraction profile for uniform injection (F1) can be observed for z=0.7 m. The asymmetric pattern F6 was found to produce a number of stacked, fixed, circulation cells. Gas injection near the wall, but not in the center (F7) was found to give some vortical structures which exhibit some weak irregular dynamic motion. No large scale structures were found in the higher parts of the column (z>0.2 m). The dynamic behavior is also studied via the axial normal stresses. Figure 7.49(b) shows these stress levels for various heights and various injection patterns. The levels were determined by taking the average stress level for all x-coordinates at a certain height z over the line y=0. For uniform gas injection, the axial normal stress in the rectangular column is around 0.007 m^2/s^2 (α=7.3%). This agrees well with the values found in the cylindrical column (for α=7.6% also around 0.007 m^2/s^2). For the horizontal velocity, the normal stress is around 0.004 m^2/s^2.

If gas injection patterns with dynamic behavior are used (F5, F7), the stress levels increase. For the top region of the column, the difference with the uniform gas injection pattern is small. The decay cannot be compared with the decay observed in the cylindrical column due to the smaller aspect ratio for the pseudo-2D column: the height where the stress has decayed to the uniform level is very close to the free surface.

More information about the dynamics of the large structures can be obtained from the shear stress $\overline{u'v'}$ (Mudde et al. (1997b)). Static large structures will not contribute to the mean shear

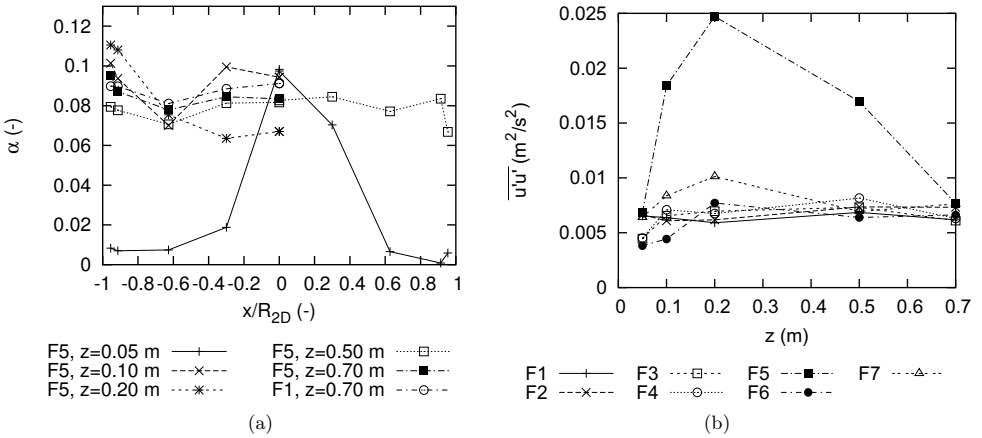

Figure 7.49.: Void fraction profiles for pattern F1 and F5, over the line y=0 (a) and axial normal stresses for the various injection patterns (b).

stress averaged over a longer period. The same holds for the bubble wakes, where the various contributions will cancel after averaging. Instead, the largest contribution comes from the dynamical motion of the large structures. Mudde et al. (1997b) mentions that the contributions from vortical structures exhibiting circular motion that travel through the column cancel. Therefore, non-zero values must come from vortical structures that are dynamic, that may have preferential locations, or lack symmetry in their direction of motion. The latter points are very clear for the sparger region. The measured shear stress values for the uniform gas injection and pattern F2 are in the range -$4 \cdot 10^{-4} m^2/s^2$- $4 \cdot 10^{-4} m^2/s^2$. Clearly, the average correlation between the two fluctuating components is very small: the structures producing the fluctuations are much smaller than the equipment size and therefore do not have a preferential location with respect to the measurement volume (except very close to the walls). For patterns F3 and F7 slightly increased values are observed in the range -$6 \cdot 10^{-4} m^2/s^2$- $6 \cdot 10^{-4} m^2/s^2$. The increased values can be contributed to weak meandering of the static circulation cells which have more or less fixed places. Figure 7.50 shows the shear stress values for patterns F4 and F5. The values are much larger for the pattern F5, reflecting the very dynamic nature of the large structures for this pattern, whereas the dynamics for pattern F4 are much weaker. For pattern F5 the vortical structures have clear preferential locations in the lower corners. The typical velocity direction in the region z<0.2 m and the region 0.2 m≤z≤0.5 m are very distinct, leading to oppositely signed values for the shear stress. For z=0.70 m the shear stress values have decayed, but not completely to the values of uniform gas injection: there is still some weak meandering motion. The results indicate that the shear stress is an interesting quantity for validation studies: correct prediction may be quite tough.

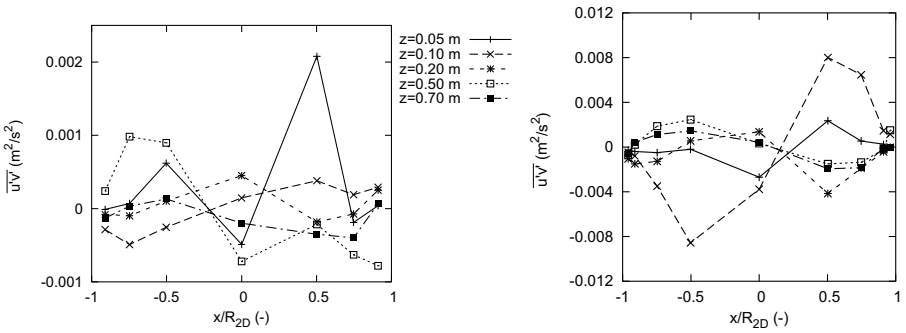

(a) (b)

Figure 7.50.: Shear stress for gas injection patterns F4 (a) and F5 (b).

7.6. Power spectra in bubbly flow: experiments and fit of autocorrelation function

The present section discusses the autocorrelation functions and power spectra obtained experimentally in the cylindrical column.

7.6.1. The local flow field

The section 5.9 considered the reduction of the impact of the flow field around the bubble on the spectral estimate via the removal of velocity realizations close to gaps. An improvement was obtained for artificial signals with potential flow contributions. The improvement was only partial since:

- The disturbance due to the flow field around the bubble is not limited to a region with specified size.
- Not all disturbances due to the local flow field are accompanied by a gap in the data.

In actual flows, the situation differs from potential flow due to the presence of the wake and the bubble-bubble interactions. A schematic impression of the local flow around the bubbles is shown in Figure 7.51. The strongest part of the velocity flow field around the bubble extends further away in the presence of a wake than for potential flow. In addition, a large part of the fluctuations are found in region 'A' on the lower side of the bubble, whereas the distribution was more symmetric with the artificial potential flow signals: fluctuations in front of the bubble were equally strong. The presence of the other bubbles influences the local flow field: it is confined to a smaller region in space.

An idea about this local flow around the bubbles and its potential influence on the spectra is obtained experimentally. The axial and tangential velocity signals are measured during 900 s (the data rate close to the wall is in the range 400-500 Hz) in a homogeneous flow with void fractions of 15%, 26% and 38%, at a distance of 7 mm from the wall. At this distance, the

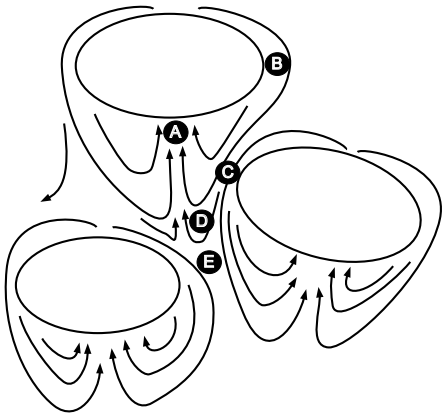

Figure 7.51.: Schematic impression of the local flow field in between the bubbles.

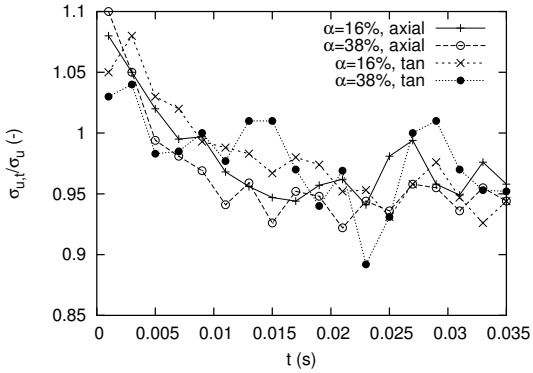

Figure 7.52.: Strength of fluctuations in the signals as a function of the time t after the end of the gap that was associated with a bubble. T_{mingap}=0.01 s.

spectrum of the signal is very similar to the spectrum obtained at larger distances from the wall, but the amount of gaps in the data is still limited. Figure 7.52 shows the strength of the velocity fluctuations as a function of the time after the presumed bubble passage. Gaps in the signal longer than 0.01 s were associated with bubble passages, the variation of the velocity realizations was determined as a function of the time after the end of the gap. Gaps were located in the combined set of arrival times from both the axial and tangential components. Larger deviations from the mean are observed right after a gap, i.e. after the bubble passage. The deviations decay in strength and have more or less disappeared around $t = 0.015$ s. These fluctuations probably correspond to region 'A' in Figure 7.51. If a bubble velocity of around 0.2 m/s is assumed, this corresponds to a region with a size of 3 mm, somewhat smaller than the bubble diameter, which is around 4 mm. The higher levels after the gaps confirm the idea that it is possible to reduce the impact of the local flow with the removal of velocity realizations after gaps. In addition, Figure 7.52 provides information for the selection of the value of $T_{removal}$. A similar study of the strength of the fluctuations before the gap does not show increased levels: the fluctuations in this area are probably of a similar magnitude as those in the other regions around the bubble and in between the bubbles.

The slotting autocorrelation functions of the axial and tangential velocity signal components are shown in Figures 7.53(a) and 7.53(b). Here, a clear decay is seen as well, the autocorrelation values are significant for lags up to 0.05-0.1 s for the axial component and 0.02 s for the tangential component. The decay for the tangential component is faster than that for the axial component. This agrees with findings by Bunner and Tryggvason (2002) for autocorrelation functions obtained from direct numerical simulations: the horizontal components become uncorrelated sooner after the bubble passage. Probably, the correlation in the horizontal fluctuations originates mostly from the wake region right below the bubble ('A'), whereas the vertical fluctuations extend further in space: also below the primary wake and in the regions near the sides of the bubbles (e.g. regions 'B', 'C' and 'D'). The decrease of the tangential component is more or less independent of the void fraction. Somewhat further away from the bubble ('D'), the wake is no longer stable: vortical structures shed by the bubble can be found here. In addition, the flow is affected more and more by the neighboring bubbles. Therefore, the velocity in these structures is still correlated with that in the structures in region 'A', but the correlation decreases with the distance. At distances comparable to the bubble-bubble distance ('E') the correlation becomes negligible. These distances correspond to the time interval of 0.05-0.1 s. The maximum time lag T_{local} up to which the local correlations are important will scale according to $T_{local} \approx d_{b-b}/u_b$. Here, u_b is the typical bubble velocity (estimated from Figure 7.17) and d_{b-b} is the typical bubble-bubble distance. The bubble-bubble distance is expected to scale approximately with $\alpha^{-1/3}$. Figure 7.53(c) also presents a scaled version of the autocorrelation function. This shows that the length of the area containing correlated velocities decreases with the void fraction, and the decrease is faster than according to $\alpha^{-1/3}$ for the lower void fractions. Similar behavior is observed in the results of Bunner and Tryggvason (2002).

The results confirm, again, that the removal of velocity realizations can only provide a partial improvement: the influence of the local flow is not limited to a subset of the velocity signal, but in fact affects the entire data set, especially for the high void fractions considered here.

Finally, the power spectra that are obtained for the bubbly flow are presented in Figure 7.54. The spectra are very similar, except for the spectrum measured at 1.3 mm distance from the

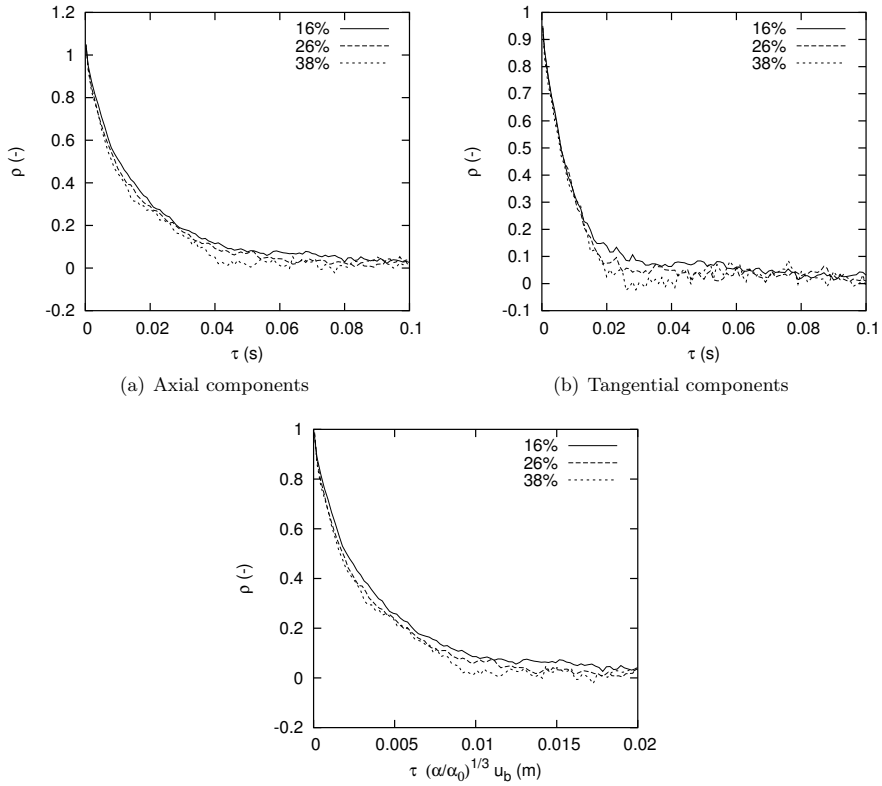

(a) Axial components

(b) Tangential components

(c) Axial components, scaled. α_0=16%.

Figure 7.53.: Slotting autocorrelation functions measured in homogeneous flow at 7 mm from the wall, corrected for noise.

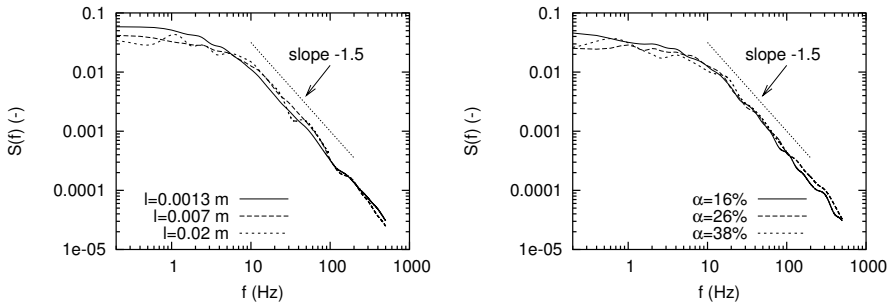

(a) Influence of l. U_g=0.032 m/s, α=0.16

(b) Influence of α, l=0.01 m.

Figure 7.54.: Power spectra for homogeneous bubbly flow.

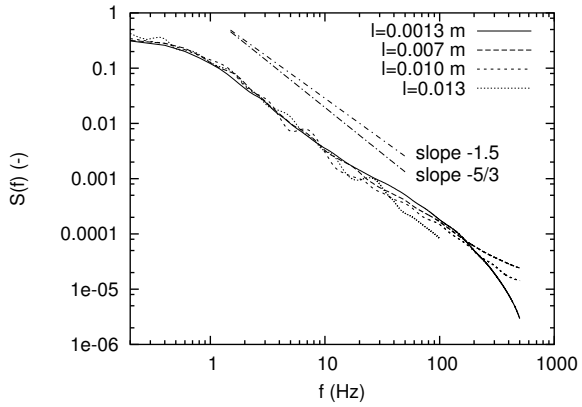

Figure 7.55.: Power spectra for bubbly flow with vortical structures (uniform gas injection). U_g=0.093 m/s, z=0.65 m.

wall, which has slightly larger values for the lowest frequencies. Cutoff occurs at a frequency around 10 Hz, beyond this frequency a power-law behavior with slope -1.5 is observed. The cut-off frequency corresponds to the bubble-bubble distance, which seems to be therefore the largest scale at which structures with relevant power are observed. At lower frequencies, the spectrum is more or less flat. For the corresponding long timescales, the autocorrelation function resembles a Dirac's delta function located at τ=0. This means that for the longer time scales the local bubble velocity field has a 'white noise' character, creating a 'noise floor' in the power spectrum for f<5-10 Hz. If the power spectrum is determined for flows containing large scale structures, this noise floor may obscure their behavior. The oscillatory nature of power spectrum that was observed in Figure 5.22(b) is not seen here. The correlation of liquid velocity fluctuations below and above the bubble is obscured by the correlations inside the wake region, in which the velocity fluctuations extend further than in the case of potential flow.

The influence of the void fraction on the spectrum shape is small. Although the value of -1.5 is relatively close to -5/3, this does not show that the cascade and dissipation of the wake is similar to that in single phase flow (the Kolmogorov -5/3 law), as is claimed by Cui and Fan (2004). The slope is in fact caused by the pseudo-turbulence: the passage of structures around the bubble with the bubble rise velocity. These structures do not need to be dissipated or broken down into smaller structures in order to produce a power-law spectrum.

7.6.2. Flow with large scale structures and the hybrid fit technique

Although the entire data set is affected, the correlation of the fluctuations due to the local flow field is limited up to lags around T_{local}. For conditions with large scale structures, this time scale decreases since the typical velocity increases, assuming the bubble-bubble distance does not increase strongly.

Figure 7.55 shows the power spectra of the velocity signals obtained at various distances from the wall l. The variable window technique with κ=3 was used. This leads to some smearing of the

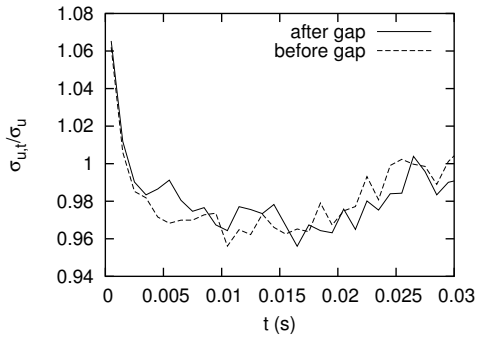

Figure 7.56.: Strength of the fluctuations in the signal as a function of the time from the start or end of the gap. U_g=0.093 m/s, z=0.65 m. T_{mingap}=0.005 s

power at the frequencies below 0.5 Hz. For the study of these lowest frequencies, a higher value for κ or the direct transformation technique should be used. The variation with the distance to the wall is quite small. A slope close to -5/3 is observed in the range 1-10 Hz. One of the signals is examined in more detail: the signal obtained at 7 mm from the wall. Figure 7.56 shows the increased variance level before and after the gaps in the data that are associated with the bubble passage, suggesting a value of 0.005 s for $T_{removal}$. Since the bubbles can move downward due to the vortical structures, increased levels are found before the gaps as well. Figure 7.57(a) shows the autocorrelation function for the shorter time intervals. A clear increase in the slope of the autocorrelation function is observed for τ<0.015 s. This increase is due to the local flow around the bubbles. Removal of the velocity realizations right before and after gaps in the data only reduces this increased correlation level slightly, at the cost of a 50% reduction in data points. This is therefore not an effective method. Another method to reduce the influence of the local flow field on the power spectrum is by fitting the autocorrelation function with a model for τ>0.015 s, and replacing the autocorrelation values for τ<0.015 s with values obtained via extrapolation of this model. This method is named the 'hybrid fit technique': extrapolation of a fit of the autocorrelation function is followed by application of the variable window technique. The effect of the technique is the following:

- For frequencies smaller than 5-10 Hz the technique removes the 'noise' due to the small scale bubble fluctuations.
- At higher frequencies the velocity fluctuations of the cascaded structures and the flow field around the bubble are correlated: the local flow does not simply provide an additional amount of power, independent of the flow at larger scales. Nevertheless, the technique does provide an idea about the amount of power that is due to the larger scale structures that have cascaded to smaller scales.

Figures 7.57(a) and 7.57(b) show the result of a fit with equation 5.23. The fit is performed over the interval 0.015-0.4 s and gives a good approximation. The effect of both procedures on the power spectrum is shown in Figure 7.58. The effect of the removal of velocity realizations

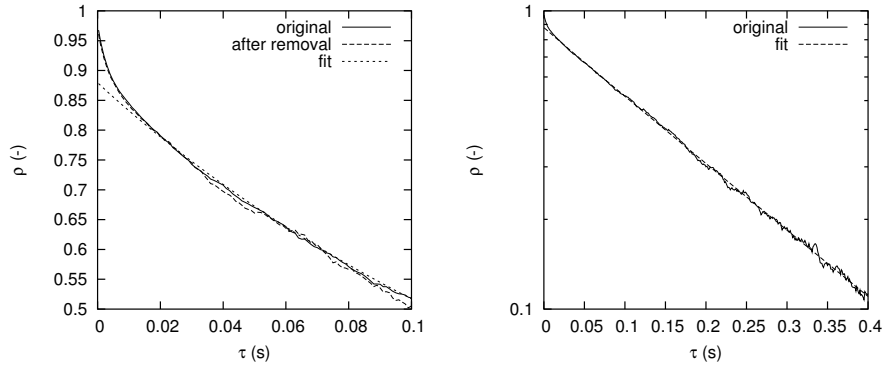

(a) Linear zoom into short time scales (b) Fit

Figure 7.57.: Autocorrelation functions. Removal with T_{mingap}=0.005 s and $T_{removal}$=0.005 s.

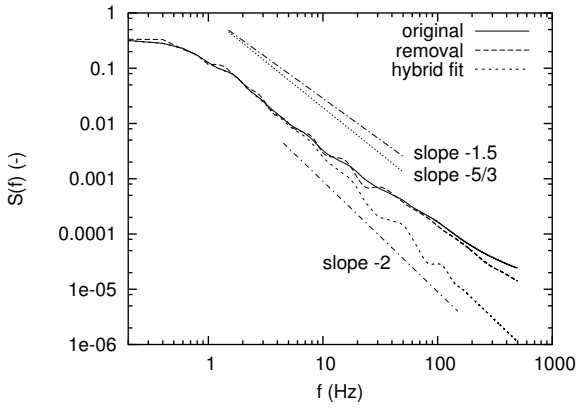

Figure 7.58.: Effect of data removal and autocorrelation fit techniques on the power spectrum estimate.

on the power spectrum is very small. The effect of the fit is much larger. In order to get an idea about the decay of turbulent structures at scales larger than the bubble-bubble distance, the various estimates are compared. The spectra are similar for frequencies smaller than 10 Hz. This shows that, for the present example, for these frequencies the 'noise' contribution of the bubbles is negligible. In the region 2-10 Hz a slope of approximately -5/3 is observed, consistent with experiments for single phase flow. This may suggest the cascade process is similar to that in single phase flow. Beyond 10 Hz, the various curves present a confidence interval: the curves present two extremes. If the decay of the autocorrelation function at the shortest lags is indeed similar to that at the longer lags, a slope close to -2 is present. This would indicate that the rate of dissipation increases somewhat at scales around and smaller than the bubble-bubble distance. Without any further information, however, this remains speculative.

Figure 7.59 shows the effect of an increase in the superficial gas velocity on the power spectrum. For U_g<0.055 m/s no large scale structures are present: the entire spectrum is dominated by the local flow around the bubbles, consequently the spectra are similar. For U_g>0.065 m/s vortical structures are continuously present in the flow. The large scale structures lead to a strong increase in the energy in the low frequencies. For frequencies beyond 20 Hz, the local flow around the bubbles results in a smaller slope. For U_g=0.057 m/s, intermittent behavior is observed: the flow is locally free of vortical structures for a short period, followed by a period of typically 10 seconds during which a large number of vortical structures pass, after which the process repeats itself. As a result, the amount of power in the large scale vortical structures is not large enough to obscure the fluctuations due to the local flow: the cascade of the large scale vortical structures is observed at the lowest frequencies, and the local flow around the bubbles for the high frequencies. For the higher superficial gas velocities, the power due to the structures increases.

For the tangential velocity component flatter spectra are obtained (Figure 7.59(b)) than for the axial component. Figure 7.60 shows the effect of the hybrid fit technique for the tangential velocity component. The results show that the local flow fluctuations provide a relatively larger contribution to the total power for the range of 1-10 Hz than for the axial component. The removal via the fit results in steeper spectra. Although the resulting spectrum is locally still somewhat curved, possibly a -5/3 power law behavior may be present for the tangential component as well.

Figure 7.61 shows the power spectra for non-uniform gas injection as a function of the height in the bubble column. Due to the non-uniform gas injection, dynamic large scale vortical structures are created near the sparger, which decay in strength higher in the bubble column. These result in increased power levels at low frequencies with -5/3 power law behavior. A comparison is shown with the case of uniform gas injection. If measurements are performed higher in the bubble column, the flow dynamics resemble more and more that of homogeneous bubbly flow. The measurements closer to the sparger resemble more and more the spectra obtained at U_g>0.07 m/s with uniform sparging. This suggests that the nature of the cascade process of vortical structures created by the sparger and the cascade process for the structures created by instabilities are similar. The differences that are observed can be explained with different strengths of the vortical structures and the different void fractions.

Figure 7.62 shows the result of the hybrid fit technique for measurements where the power-law behavior due to the local flow around the bubbles and the large scale structures are clearly

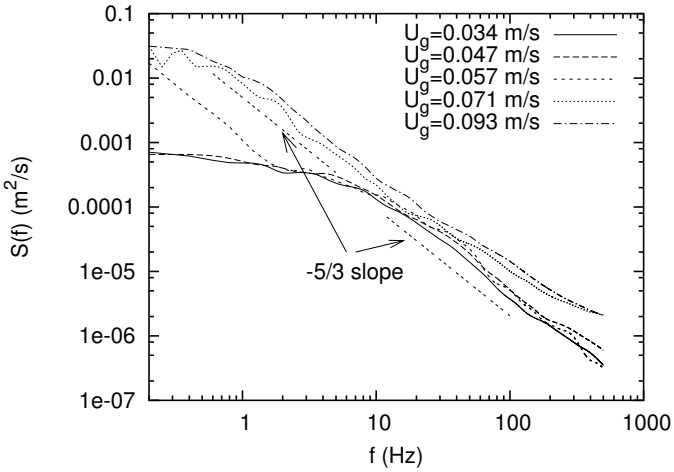

(a) Axial velocity component

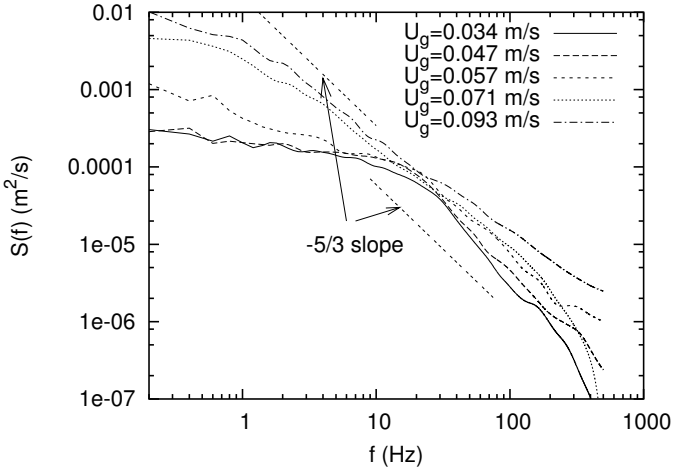

(b) Tangential velocity component

Figure 7.59.: Effect of an increase in the superficial gas velocity (and amount of vortical structures) on the power spectrum. l=7 mm, uniform gas injection. Tap water of one day old was used.

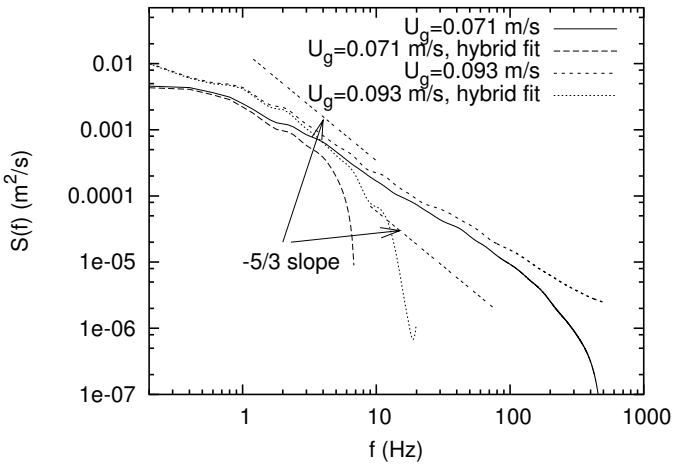

Figure 7.60.: Effect of hybrid autocorrelation fit on the shape of the power spectrum.

separated in frequency. A comparison between uniform gas injection with instabilities and non-uniform gas injection is made. Similar results as in Figure 7.58 are obtained: beyond the frequency where the local flow around the bubbles becomes important the hybrid fit technique gives a power law slope around -2. The behavior is similar for the two flow conditions.

For high superficial gas velocities (U_g>0.07 m/s), which already have large vortical structures in the flow for uniform gas injection, the shape of the power spectra is not affected by the non-uniformity of the gas injection, only a small increase in the magnitude of the velocity fluctuations is obtained. The -5/3 power law behavior that is observed in the various spectra may be an indication that the typical Kolomogorv scaling also appplies to these bubbly flows. This observation was also made by Camussi and Verzicco (2004), Verzicco and Camussi (2003) and Mashiko et al. (2004) for buoyancy driven flows driven by temperature differences.

7.7. Conclusions

Uniform gas injection: flow stability

If uniform gas injection with the needle sparger is used, homogeneous bubbly flow is obtained for low superficial gas velocities; no large scale vortical motion is observed, except for a very weak up flow in the center and down flow in a very narrow region close to the wall. The superficial gas velocity where the first large scale structures are observed, increases with the level of contamination of the tap water. For the highest level of contamination, a maximum void fraction of 55% with homogeneous flow properties is reached. Several strong indications are found that the onset of large dynamical motion is due to the reversal of the sign of the lift force. For low superficial gas velocities, void fraction profiles are very flat, except close to the wall where small peaks are observed, since the flow contains many small bubbles and these small bubbles

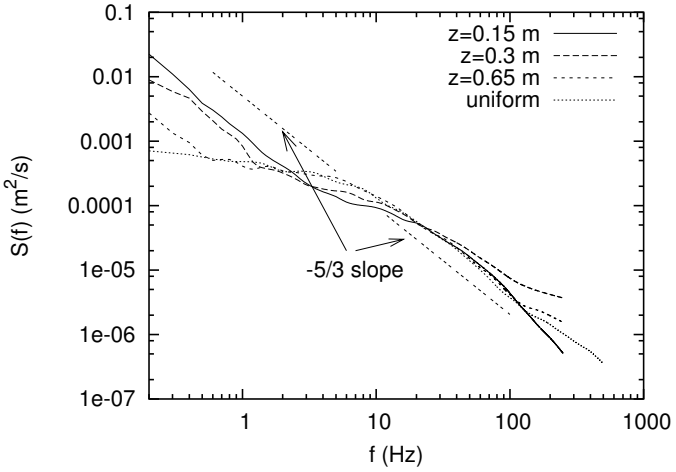

(a) Two rings off

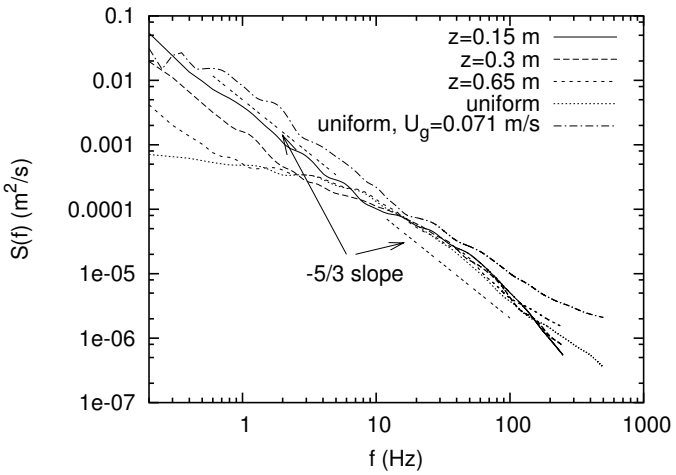

(b) Three rings off

Figure 7.61.: Power spectra for non-uniform gas injection (l=0.01 m). U_g=0.032 m/s, z=0.65 m for uniform gas injection cases.

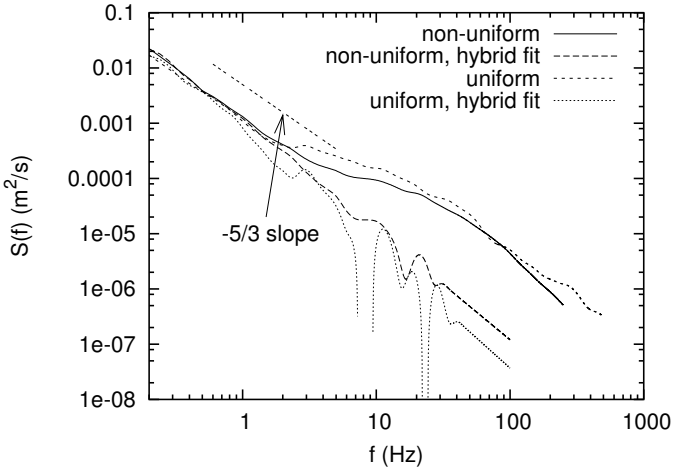

Figure 7.62.: Power spectrum obtained with hybrid fit technique. Uniform gas injection: U_g=0.032 m/s and z=0.65 m. Non-uniform gas injection with two rings off: U_g=0.057 m/s, z=0.15 m.

experience a lift force oriented toward the wall. The wall peak disappears when the transition is approached, since the bubble size increases until eventually the flow contains sufficient bubbles with small or negative lift coefficient. At this point, bubbles will start moving toward the center of the flow and instabilities can grow. The critical diameter where the instability occurs, agrees well with the results of Lucas et al. (2005) and Tomiyama et al. (2002). If the level of contamination of the liquid increases, smaller bubbles in the column result due to decreased coalescence, and the critical diameter is reached for a higher superficial gas velocity. As soon as the flow becomes unstable, the interaction of the vortical structures with the sparger can create intermittent behavior.

Pseudo-turbulence

In the homogeneous regime, the liquid velocity fluctuations are dominated by pseudo-turbulence: the small scale velocity fluctuations induced by the motion of the bubble relative to the liquid. Scaling methods based on the dissipation rate in the flow and on the variation for inviscid flow are considered. Both scaling methods appear more or less equally appropriate.

Non-uniform gas injection

The influence of the uniformity of gas injection is investigated by introducing non-aerated regions in the sparger. If small non-aerated regions are introduced in the sparger, weak static circulation cells result, but no dynamic large scale structures are obtained. If the non-aerated region is introduced at the wall, and its size exceeds a critical value, large scale dynamic structures are found close to the sparger. These generate an entrance region with increased mixing. The

intensity of the associated fluctuations decays exponentially with the height in the column, and at a distance of about 4 column diameters from the sparger the nature of the flow is very similar to that obtained with uniform gas injection, if the transitional regime has not yet been reached. For U_g<0.05 m/s, the intensity of the fluctuations in the entrance region scales with the void fraction, and the rate of decay of the fluctuations is independent of the void fraction: the size and nature of the entrance region mainly depend on the type of gas injection pattern. If the area through which the gas is injected is decreased, eventually a point is reached where the onset of the transitional regime occurs at a lower superficial gas velocity. This is probably due to increased coalescence at the sparger. For all cases, the bubble column can roughly be split in two regions: an entrance region close to the sparger and a bulk region on top with uniform properties (either with or without large vortical structures).

For the pseudo-2D column, the behavior is only investigated for low void fractions, but it looks qualitatively very similar. Again, small non-aerated regions do not produce dynamic behavior, and if the size of the non-aerated region is increased beyond a critical size, suddenly dynamic behavior is obtained.

Power spectra in bubbly flow

Autocorrelation functions and power spectra obtained in the bubbly are determined with the slotting technique, both for homogeneous flow and flow with large dynamic structures. Large dynamic structures are considered both due to non-uniform gas injection and due to instability of the flow. The local flow around the bubbles results in the addition of extra energy to the spectrum, obscuring the turbulent cascade process. Analysis of the autocorrelation functions for homogeneous flow shows that the flow around the bubble is significantly correlated up to intervals corresponding to the bubble-bubble distance. Consequently, removal by rejection of the velocity samples obtained closest to the bubble gives only a partial improvement. Better results are obtained by extrapolating the autocorrelation function for the shortest intervals with the use of a fit technique. The power spectra that are obtained in the transitional regime exhibit a -5/3 slope for the intermediate frequencies, consistent with results for single phase turbulence. Similar results are obtained for the flow dominated by large scale structures generated by the non-uniform gas injection.

List of symbols

Roman symbols

a	bubble semi-major axis length	m
b	bubble semi-minor axis length	m
C_D	drag coefficient	-
C_{kin}	proportionality constant total kinetic energy	-
$C_{kin,a}$	proportionality constant axial component contribution to total kinetic energy	-
C_L	lift coefficient	-
C_p	proportionality constant fluctuations dissipation method	-

C_u	constant describing decay terminal velocity with void fraction	-
c	constant describing decay data rate	-
c_k	constant for kinetic energy due to inviscid flow contribution	-
$c_{k,a}$	constant for axial contribution to kinetic energy due to inviscid flow contribution	-
D_{column}	bubble column diameter	m
d_c	bubble chord length	m
d_b	bubble diameter	m
d_{b-b}	bubble-bubble distance	m
d_{eq}	bubble equivalent diameter	m
f	frequency	s^{-1}
g	gravitational acceleration	$m\ s^{-2}$
l	distance measurement volume to the wall	m
l_w	length scale fluctuations	m
$\dot{N}_1, \dot{N}_2$	frequency scales for bubbly flow data interarrival time distribution	s^{-1}
$\dot{N}_{tot}$	mean data rate	s^{-1}
R	radius bubble column	m
R_{2D}	half width pseudo-2D column	m
R_{depth}	half depth pseudo-2D bubble column	m
R_{uu}	autocovariance function	$m^2\ s^{-2}$
r	radial coordinate	m
S	power spectrum	various
STFT	Short Time Frequency Transform	
T	window duration	s
T_{local}	maximum time lag up to which correlations due to local flow are important	s
T_{mingap}	minimum gap duration in order to associate gap with bubble	s
$T_{removal}$	duration signal segment removed from the signal before/after bubble arrival	s
t	time	s
U_∞	terminal velocity	$m\ s^{-1}$
U_g	superficial gas velocity	$m\ s^{-1}$
U_R	slip velocity	$m\ s^{-1}$
u	axial liquid velocity	$m\ s^{-1}$
u_b	axial bubble velocity	$m\ s^{-1}$
v	tangential liquid velocity	$m\ s^{-1}$
u', v'	axial and tangential velocity fluctuations	$m\ s^{-1}$
$\overline{u_E'^2}$	total liquid kinetic energy	$m^2\ s^{-2}$
w	radial liquid velocity	$m\ s^{-1}$
w_b	radial bubble velocity	$m\ s^{-1}$
x	horizontal coordinate	m
y	horizontal coordinate	m
z	axial coordinate	m

Greek symbols

α	void fraction	-
α_0	void fraction for scaling	-
β_u	bubble selection criterion 1D four point probe algorithm	-
γ	Gaussian window for STFT	-
$\Delta\tau$	slot width	s
ϵ_w	dissipation rate	$m^2\ s^{-3}$
κ	variable window constant	-
ρ	autocorrelation function	-
$\sigma_{u,t}$	strength fluctuations in liquid velocity at time t after end gap in data	$m\ s^{-1}$
τ	lag	s
ϕ	gas flow rate per needle	$m^3\ s^{-1}$
ϕ_1	angle between probe axial direction and velocity vector	rad
ϕ_p	probe inclination angle	rad
ϕ_x	bubble velocity angle	rad

Subscripts

pot	potential flow

8. Conclusions

The aim in the present thesis was to investigate the behavior of dynamic large scale structures in bubble columns. Special attention has been paid to the influence of non-uniformities in the sparger on the creation of these structures and to the changes in the homogeneous flow leading to instability. Both the properties of the pseudo-turbulence (strength of the fluctuations) and the large-scale turbulence (power spectra) have been studied.

First, conclusions are presented of the investigation of the hydrodynamic behavior. Next, the findings of the preparatory studies on the sparger and measurement techniques are discussed.

8.1. Dynamic large scale vortical structures in bubble columns

The main findings of the study are that very homogeneous flow is obtained with uniform gas injection which can be maintained up to very high void fractions for conditions with little coalescence, that non-uniformities in the sparger can only introduce large structures relatively close to the sparger and that the stability of the flow seems to be governed by the bubble size: instability sets in once enough bubbles are present larger than the critical diameter of 5.8 mm given by Tomiyama et al. (2002) for which the lift coefficient changes sign.

Uniform gas injection: flow stability

The very uniform gas injection obtained with the needle sparger produces homogeneous bubbly flow up to the superficial gas velocity where instability sets in. For increasing levels of natural contamination, increasing critical voidages, for which the vortical structures first appear, are found with values up to 55%. Up to this highest void fraction, only very weak up flow (0.01-0.02 m/s) is found in the column center, and down flow is only found in a very narrow region close to the wall. Several indications are found that the onset to the transition regime with large vortical structures is due to reversal of the sign of the lift force. Wall peaking is observed for the lower superficial gas velocities, it disappears at superficial gas velocities right before the onset of the structures. The mean horizontal bubble diameter that is observed around the critical voidage agrees well with the critical diameter given by Tomiyama et al. (2002). For more contaminated water, the coalescence near the sparger decreases, smaller bubbles result and the flow is stable up to a higher voidage. As soon as the flow becomes unstable, the interaction of vortical structures with the sparger can create intermittent behavior due to a time-dependent bubble size generated at the sparger.

Non-uniform gas injection

The introduction of non-aerated regions in the sparger leads to the creation of circulation cells, which can become dynamic if the non-uniformity is big enough. The strength of these large

structures quickly weakens for higher positions in the column: an entrance region is created. Above this entrance region, a bulk region is identified with uniform properties, where dynamic large structures, if present, are due to instability of the flow. For U_g<0.05 m/s, the size and decay of the entrance region are mainly dependent on the gas injection pattern and only little depend on the void fraction. For higher superficial gas velocities, both increased and decreased stability can be obtained due to the non-uniform injection.

Pseudo-turbulence

In the homogeneous regime, the liquid velocity fluctuations are dominated by pseudo-turbulence: the small scale velocity fluctuations induced by the motion of a bubble relative to the liquid. Scaling methods based on the dissipation rate in the flow and on the variation for inviscid flow are considered. Both scaling methods appear more or less equally appropriate and reasonably well describe the experimental data.

Turbulence power spectra

Autocorrelation functions and power spectra obtained in the bubbly flow are determined with the slotting technique, both for homogeneous flow and flow with large dynamic structures. Large dynamic structures are considered both due to non-uniform gas injection and to instability of the flow. Extra energy is added to the spectrum by the local flow around the bubbles, obscuring the turbulent cascade process. Analysis of the autocorrelation functions for homogeneous flow shows that the flow around the bubble is significantly correlated up to intervals corresponding to the bubble-bubble distance. Consequently, removal of the velocity samples obtained closest to the bubble gives only a partial reduction in the amount of extra power due to the local flow. Better results are obtained by extrapolating the autocorrelation function for the shortest intervals with the use of a fit technique. The power spectra that are obtained in the transitional regime exhibit a -5/3 slope for the intermediate frequencies, consistent with results for single phase turbulence. Similar results are obtained for the flow dominated by large scale structures generated by the non-uniform gas injection.

8.2. Sparger, setup, measurement and signal processing techniques

Sparger

For the study of the influence of the gas injection, a special needle sparger was built and the bubble formation at the needles was investigated. This investigation showed that several interaction effects are important for the formation process: both blocking and attraction due to the previously formed bubble are observed. These effects can change the bubble size and result in a size reduction for flow rates beyond a critical flow rate. As a result, strong size fluctuations can be obtained around this critical flow rate if large vortical structures are present. Interaction effects with other needles are quite small.

Optical fiber probes

The use of a single optical fiber probe for the estimation of the void fraction generally leads to underestimation. A study of the piercing process of bubbles with the use of CCD images shows that the so-called Low-Level-Criterion for the processing of signals gives the best match with the actual gas-liquid transition. Additionally, its use results in reduction of the underestimation. Further study of the error sources shows that, for perpendicular piercing, the blinding and crawling effects provide the major inaccuracy. For non-perpendicular piercing, the drifting effect becomes important as well. The magnitude of the inaccuracy is strongly dependent on the piercing conditions, making quantitative prediction difficult for practical conditions.

The inaccuracy of the measurement of the bubble size and 3D bubble velocity with a four point optical fiber probe has been evaluated with the use of simulations of modeled piercing, and with test experiments. This showed that the major error sources are the shape oscillations of the bubbles and probe-bubble interaction effects, and that correction for the bubble curvature is required in order to get reduced inaccuracy. Especially aspect ratio oscillations can produce considerable variations in the bubble velocity and bubble size estimates that can obscure the true distribution. The most important probe-bubble interaction effects are the drifting effect and deformation of the bubble, which create significant inaccuracies in the estimate of the velocity direction. Although, for individual bubbles, the velocity direction estimate is not very precise, the average direction of an ensemble of bubbles can be estimated reasonably accurately. If the bubble moves under an angle with the probe, an underestimation of the velocity magnitude and bubble chordal length is found, as well as an overestimation for the angle between the probe axial direction and bubble velocity vector.

Laser Doppler Anemometry applied to bubbly flows

In order to evaluate and improve LDA applied to bubbly flows, both the signal processing of the velocity signals and the processing of the electronic signals containing the bursts are studied and enhanced. For the signal processing, the focus is on methods how to deal with the random sampling and gaps in the data introduced by the blocking of laser beams by the bubbles, and on the effect of the pseudo-turbulence (local flow around the bubble) on the power spectra.

The study shows that reconstruction based techniques, such as Sample-and-Hold are not suited for use with bubbly flows. The techniques suffer from step noise addition and low-pass filtering. Compared to the effects for single phase flow, the cut-off frequency is, generally, located at a lower frequency. In addition, a second filter operation is created with different cut-off frequency. The interaction of the two filters can result in power-law slopes close to -5/3 in the absence of turbulent behavior. Correction for the artifacts is not possible. Slotting techniques and time-series analysis give good results and have no problems with the extra gaps due to the bubbles.

The pseudo-turbulence results in the addition of extra power in the spectrum, affecting the shape especially at frequencies typically beyond 10 Hz. This obscures the cascade process of the large scale structures. The amount of additional power is larger for reconstruction based techniques than for the slotting technique. The influence may be reduced by rejection of velocity realizations before and after gaps in the data. The improvement is, however, partial and occurs at the cost of an increase of the variance. Less data needs to be rejected if more sophis-

ticated methods are used that employ information about velocity gradients, but correct removal is difficult.

For the processing of the electronic signals obtained in LDA, a dual burst wavelet processor and a dedicated burst detector have been developed, tested and applied to both single phase and bubbly flows. Special attention has been paid on effective ways how to combine the wavelet technique (fitting a model of the burst to the data) and dual burst (i.e. overlapping bursts) processing. The use of this processor results in a 50% smaller dead time, strong reduction of multiple validation, more accurate arrival time and Doppler frequency estimates, and strongly enhanced transparency of the data processing when compared to a traditional commercial hardware processor (TSI IFA-750). Also, for applications with poor SNR, the data rate is strongly enhanced. Smaller bias problems are obtained for the velocity moments. The advantages for estimation of power spectra are, however, limited due to the finite size of the measurement volume, and since the extra information is obtained in the frequency range governed by the pseudo-turbulence. The comparison of the moments of the velocity time series gives clues how to improve the accuracy in the results of the commercial processor: by removal of multiple validation, application of a coincidence window and velocity bias correction much better results are obtained.

8.3. Perspectives and implications

Hydrodynamics

The results for uniform gas injection and non-uniform gas injection show that for numerical work the homogeneous regime still provides an interesting challenge. Correct prediction of the transition to the heterogeneous regime requires good models, the sharp change in entrance region behavior for small changes in the sparger provides additional tough validation cases. So far, no agreement exists about the implementation of the lift force (e.g. Sokolichin et al. (2004)). The present work suggests that it is important, and that the reversal of direction for larger bubbles needs to be taken into account.

It would be interesting to test the stability of flows with wider bubble size distributions than used in the present thesis. This would require a sparger that generates large bubbles in addition to the smaller bubbles. In addition, more details are required about the flow close to the free surface in order to understand the onset of the instability better. The present investigation suggests that instability is mainly due to the lift force reversal. On the other hand, various authors (e.g. Biesheuvel and Gorissen (1990)) suggest another mechanism where the instability of void fraction waves in the axial direction leads to transition. It would be interesting to find out under which conditions this mechanism becomes relevant, and why it underestimates the critical voidage for the present conditions.

In the process industry, there is a trend toward smaller equipment: process intensification. This way, the aspect ratio of the reactors may decrease, increasing the importance of the behavior in the entrance region. The improved understanding of the entrance region obtained in the present investigation may be used for better process design. For instance, the study has shown that gas injection close to the wall is important if the large scale structures should be limited (e.g. mass transfer is the limiting factor and mixing is less important).

The importance of the pressure drop over the gas injector is not clear: clarification is required

into which extent dynamic behavior of the gas injector changes the characteristics of the entrance region. On the other hand, forced dynamic gas injection provides an interesting way to increase the operational space of bubble columns: this way, it may be possible to temporally alternate a dynamic and quiescent entrance region via control and obtain a better compromise between mass transfer and mixing.

For the study of the turbulent behavior, the pseudo-turbulence still presents problems. For the high void fractions in the present work, it appears not possible to fully separate the contributions due to the local flow and the cascade of the large structures. It would be interesting to check if this also holds for the low void fractions, and, if not, from which void fraction this holds. The combination of LDA with a fiber probe close to the measurement volume may provide means for separation, with improved performance when compared to methods employing the signal characteristics.

The -5/3 slope that has been found in the power spectra is consistent with results for single phase flow. Further study should clarify how to interpret this similarity. A comparison with power spectra of velocity time series obtained from Computational Fluid Dynamics studies can show how good the dynamic behavior is predicted by this CFD work. The interpretation of the results of the hybrid fit technique is not yet fully clear. The influence of the bubbles on the cascade process needs further study.

Sparger and measurement techniques

The study of the bubble formation process at the needle sparger showed the importance of bubble-bubble interaction processes. In the bubble column, coalescence near the sparger was found to have a major impact on the hydrodynamics, i.e. the critical voidage where transition occurs. More detailed study of the coalescence during bubble formation and the influence of the level of contamination on this process can provide better predictions for the critical voidage.

Improved accuracy for both the one-point and four-point probes can be achieved with the use of thinner fibers. Similar studies as those presented in chapters 3 and 4 can provide insight how the inaccuracy reduces for these thinner fibers. The use of the so-called 3C (Cone-Cylinder-Cone) geometry for the probe tips may provide additional velocity information, which can be used to reduce the variance in the bubble velocity estimate due to shape oscillations. The results on the lift force show the importance of the measurement of the horizontal bubble diameter, which is not possible using the optical probes. Alternative techniques, such as endoscopic methods may provide this information.

The use of the wavelet processor can provide accurate measurements. This technique may be employed for different flows and can be used to construct low-budget LDA systems. So far the technique was optimized for accuracy. In a next step, more attention can be paid to speed-up the processing.

On the fundamental aspects of the application of LDA to bubbly flows, more attention should be paid to the bias due to temporal variations in void fraction, i.e. the time-dependent data rate for measurements further away from the wall. Perhaps the extent of the problem can be reduced by testing a reference beam technique: the use of only a single beam inside the bubble column may be able to reduce the temporal variations in data rate.

A. Monte Carlo simulation of bubbly flow

The blockage of laser beams by bubbles when LDA is used, has an impact on the data rate and the distribution of the data interarrival times. This has important consequences for, e.g., the estimation of turbulence power spectra (chapter 5). In order to study these effects, artificial data is generated with the use of Monte Carlo techniques. The present appendix discusses these Monte Carlo techniques.

Basically, the simulation is performed by creating a batch of virtual ellipsoidal bubbles with prescribed trajectories. For a given set of arrival times, the algorithm checks whether blockage of the laser beams (modeled as lines) by any of the bubbles occurs. All time instants when there is no blockage, are outputted for further use. In addition, the data set with the positions of the bubbles in time can be used to create artificial signals of potential flow around the bubbles (see section 5.9). The first section describes the check for blockage, the second the batch of virtual bubbles.

A.1. Blockage by bubbles

Bubbles are modeled as ellipsoids with half major axis length a and half minor axis length b. The orientation of the minor axis is specified by the angles ϕ_1 and ϕ_2 (Figure A.1). The center of the bubble is located at (x_0, y_0, z_0). Each laser beam is specified by two planes

$$\begin{cases} a_1 x + b_1 y + c_1 z &= d_1 \\ a_2 x + b_2 y + c_2 z &= d_2 \end{cases} \tag{A.1}$$

In order to determine whether the laser beam intersects with the bubble the equations are transformed to the coordinate system of the bubble (x', y', z'):

$$\begin{cases} a'_1 x' + b'_1 y' + c'_1 z' &= d'_1 \\ a'_2 x' + b'_2 y' + c'_2 z' &= d'_2 \\ \frac{x'^2}{a^2} + \frac{y'^2}{a^2} + \frac{z'^2}{b^2} &= 1 \end{cases} \tag{A.2}$$

using the transformation:

$$\begin{pmatrix} x' \\ y' \\ z' \end{pmatrix} = \begin{pmatrix} cos(\phi_1) & 0 & -sin(\phi_1) \\ 0 & 1 & 0 \\ sin(\phi_1) & 0 & cos(\phi_1) \end{pmatrix} \begin{pmatrix} cos(\phi_2) & sin(\phi_2) & 0 \\ -sin(\phi_2) & cos(\phi_2) & 0 \\ 0 & 0 & 1 \end{pmatrix} \begin{pmatrix} x - x_0 \\ y - y_0 \\ z - z_0 \end{pmatrix} \tag{A.3}$$

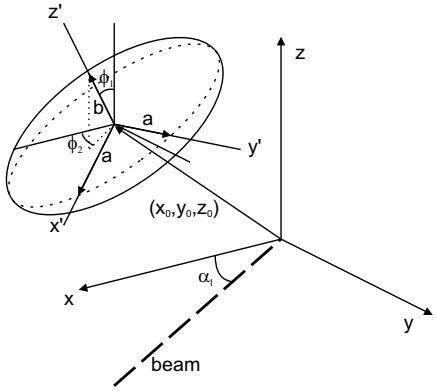

Figure A.1.: Coordinate frames for ellipsoid bubble.

We get:

$$\begin{cases} a_i^{(1)} &= a_i cos(\phi_2) + b_i sin(\phi_2) \\ a'_i &= a_i^{(1)} cos(\phi_1) - c_i sin(\phi_1) \\ b'_i &= -a_i sin(\phi_2) + b_i cos(\phi_2) \\ c'_i &= a_i sin(\phi_1) + c_i cos(\phi_1) \\ d'_i &= d_i - a_i x_0 - b_i y_0 - c_i z_0 \end{cases} \tag{A.4}$$

Equation A.2 have zero, one or two solutions (x'_1, y'_1, z'_1) and (x'_2, y'_2, z'_2). These points are transformed back to the original coordinate system using the inverse of equation A.3: (x_1, y_1, z_1) and (x_2, y_2, z_2). If $0 \leq x_1 < l$ or $0 \leq x_2 < l$ the beam is blocked by the beam. l is the distance of the measurement volume to the wall. Similarly, an overlap of the bubble with the measurement volume can be determined by checking whether $x_1 \leq l \leq x_2$.

A.2. Virtual batch of moving bubbles

We consider a control volume with dimensions Δx_c, Δy_c, Δz_c and volume V_{tot} (Figure A.2). Initially, N_b ellipsoidal bubbles with identical dimensions are placed randomly in it. In order to predict realistic bubble-beam intersection durations, the non-rectilinear bubble motion is modeled. Fan and Tsuchiya (1990) report zig-zag motion for contaminated conditions, therefore the bubble motion is modeled with zig-zagging trajectories with vertical velocity U_z. Bubble i has dimensions a and b and volume V_b, and orientations $\phi_{1,i}(t)$ and $\phi_{2,i}$. The bubble only tilts in the plane in which it moves (Brücker (1999)), and with its minor axis parallel to the velocity vector (De Vries (2001) and Fan and Tsuchiya (1990)). Brücker (1999), Fujiwara et al. (2004) and De Vries (2001) show that the trajectory has a sinusoidal shape. Consequently, the motion

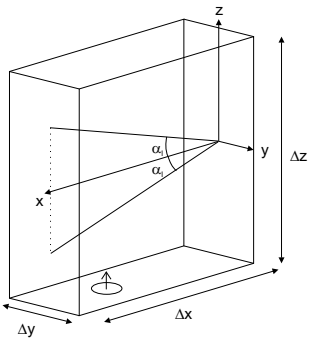

Figure A.2.: Control volume.

of the bubbles is described with:

$$\begin{cases} r_{osc,i}(t) &= R_{osc} sin(\frac{2\pi}{\lambda_{osc}} z_i(t) + \phi_{osc,i}) \\ x_{0,i}(t) &= x_{0c,i} + r_{osc,i}(t) cos(\phi_{2,i}) \\ y_{0,i}(t) &= y_{0c,i} + r_{osc,i}(t) sin(\phi_{2,i}) \\ \phi_{1,i}(t) &= \phi_{1,max} cos(\frac{2\pi}{\lambda_{osc}} z_i(t) + \phi_{osc,i}) \\ z_i(t) &= U_z(t - T_{a,i}) \end{cases} \tag{A.5}$$

The parameters for the motion are obtained from Brücker (1999) and Fan and Tsuchiya (1990). Brücker (1999) investigates the motion of zig-zagging bubbles in water with 6 mm equivalent diameter and aspect ratio of 0.66. These conditions are close to the bubbles observed in the bubble column (4-5 mm, aspect ratio around 0.6-0.65). For these bubbles, Brücker (1999) finds that the oscillation amplitude $R_{osc} = 1.3a$, which agrees approximately with observations in the bubble column. Fan and Tsuchiya (1990) show that the maximum rocking angle $\phi_{1,max} = 25°$ for Re up to approximately 4000. This angle agrees quite well with the data presented in Xue (2004). With the condition of the minor axis parallel to the bubble path, the wavelength of the oscillation is given by $tan(90° - \phi_{1,max}) = \frac{\lambda_{osc}}{2\pi R_{osc}}$. Bubbles with equivalent diameter of 4.5 mm are considered with aspect ratio of 0.65. This gives $R_{osc} = 7$ mm, and $\lambda_{osc} = 0.07$ m, which agrees with the wavelength of 6 cm observed in a bubble plume.

Each new bubble which is given a random position $(x_{0c,i}, y_{0c,i}, -\Delta z/2)$ at the bottom plane of the control volume, random orientation $\phi_{2,i}$ and random oscillation phase $\phi_{osc,i}$. $T_{a,i} = T_{a,i-1} - \Delta T_b ln(RND)$, with RND an uniformly distributed random number between 0 and 1, and ΔT_b the average time between the arrival of two bubble centers in the control volume. The average time is given by:

$$\Delta T_b = \frac{V_{tot}}{\Delta x_c \Delta y_c U_z n_b} \tag{A.6}$$

n_b is the mean number of bubbles inside the control volume over a long period. In order to determine this number, the possible overlap of bubbles due to the random placement has to be taken into account. Due to this overlap, in general the void fraction is smaller than $N_b V_b / V_{tot}$. Prevention of overlap by modified placement of the bubbles at the inlet region (i.e. replacement

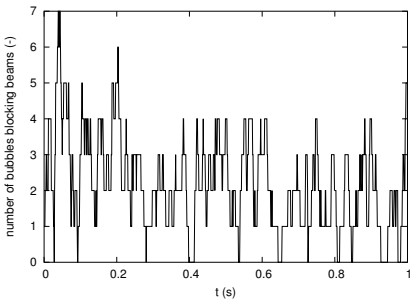

Figure A.3.: Blockage of laser beams by bubbles. $\alpha = 10\%$, $l = 0.04$ m, bubbles $d_{eq} = 4.5\ mm$ with aspect ratio 0.66. $u = 0.2\ m/s$, $f_l = 0.35\ m$.

if an overlap is detected) does not solve the problem because of the zig-zagging motion. Over a long period, the void fraction is on average:

$$\alpha = 1 - (1 - \frac{V_b}{V_{tot}})^{n_b} \tag{A.7}$$

where n_b may be non-integer. So:

$$n_b = \frac{ln(1-\alpha)}{ln(1-\frac{V_b}{V_{tot}})} \tag{A.8}$$

Figure A.3 shows how the number of bubbles that block the beams fluctuates wildly, and that even though on average 2-3 bubbles are blocking the laser beams, still windows allowing for measurements occur.

List of symbols

Roman symbols

a	bubble semi-major axis length	m
$a_1, a_2, b_1, b_2,$ c_1, c_2, d_1, d_2	constants defining laser beams	various
b	bubble semi-minor axis length	m
l	distance measurement volume to wall	m
n_b	mean number of bubbles in control volume	-
R_{osc}	maximum radius bubble path	m
r_{osc}	intantaneous radius bubble path	m
N	number of bubbles	-
T_a	arrival time bubble at bottom control volume	s
t	time	s
U_z	vertical velocity	$m\ s^{-1}$
V_b	bubble volume	m^3
V_{tot}	control volume	m^3

x, y, z	coordinates in lab frame of reference	m
x', y', z'	coordinates in bubble frame of reference	m
x_0, y_0, z_0	coordinates bubble center	m
x_1, y_1, z_1	coordinates first point where laser crosses bubble interface	m
x_2, y_2, z_2	coordinates second point where laser crosses bubble interface	m
z	axial coordinate	m

Greek symbols

α	void fraction	-
$\Delta x_c, \Delta y_c,$ Δz_c	dimensions control volume	m
ΔT_b	average time between arrival bubbles in control volume	s
λ_{osc}	wavelength zig-zag motion	m
ϕ_1	angle between gravity direction and bubble minor axis	rad
$\phi_{1,max}$	maximum for ϕ_1	rad
ϕ_2	angle of projection of the velocity vector on the xy plane to the x-axis	rad
ϕ_{osc}	phase zig-zag path	rad

B. Laser Doppler Anemometry burst detection

In order to get reliable and accurate information from the measured bursts in Laser Doppler Anemometry, a good burst processor is required. The processor that was developed and described in chapter 6, requires, however, a large number of computations and a piece of the signal containing not more than two bursts in order to be successful. Thus, in order to prevent excessive computation times, a separate efficient burst detector is required which provides the burst processor with the approximate location and width of the bursts (Figure B.1). The present appendix describes and discusses the method and algorithms used to detect the bursts. First, the requirements for a good burst detector are discussed. Next, existing methods from literature as well as the new detection algorithms are described. Finally, the optimum setting of the presented algorithm is discussed using artificial signals.

B.1. Requirements burst detector

A number of requirements can be identified for a good burst detector. The importance of the requirements depends on the type of detector/processor combination. For instance, the newly developed detector and processor algorithms employ a final validation step (Figure B.1), whereas the TSI Intelligent Flow Analyzer (IFA) - 750 has no such validation step (Figure B.2). This means that segments with noise that are detected as bursts will generate erroneous velocity realizations for the IFA-750 processor. This is not necessarily so for the new detector/processor algorithms.

- The detector should provide the burst location and duration with reasonable accuracy to the processor. If the duration is underestimated, clipping of the burst occurs, which reduces the accuracy of the Doppler frequency and arrival time estimate: optimal estimation requires the entire burst. If the duration is overestimated, the signal-to-noise ratio of the

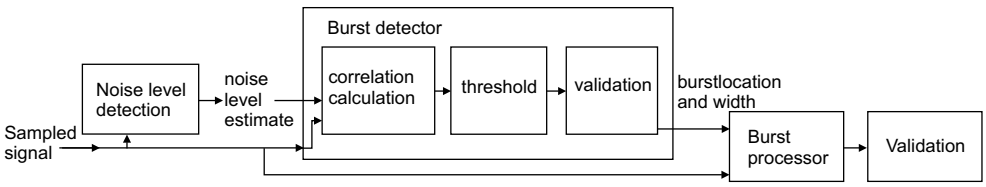

Figure B.1.: Schematic algorithm detection and processing of bursts

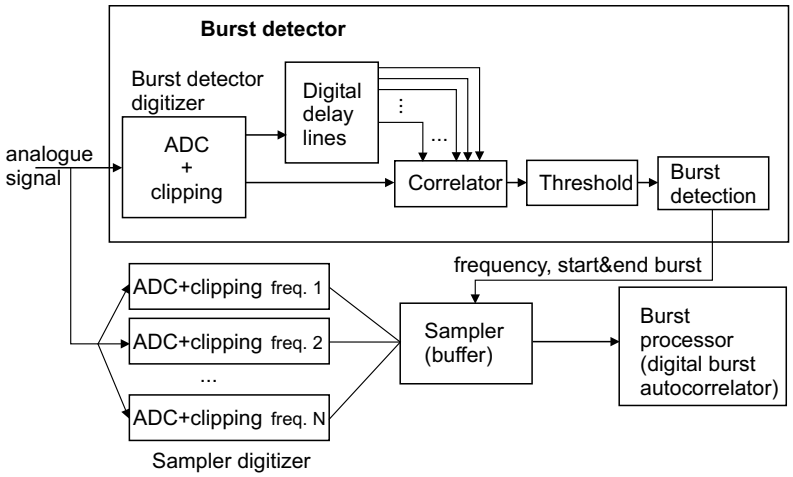

Figure B.2.: Schematic algorithm detection and processing of bursts in TSI IFA-750

signal drops. Although the wavelet technique effectively suppresses the noise outside the burst, this has negative consequences for the pre-estimation that provides first estimates for the Doppler frequency and e.g. for various filters. In addition, the probability of having more than one burst in the selected signal segment increases. Although the algorithm can process dual (overlapping) bursts, the accuracy of the processing of dual bursts is generally smaller than the processing of a single burst. Furthermore, if more than two burst are present in the segment, only two can be processed.

- Associated with this last point is the prevention of multiple validation: if the duration of bursts is underestimated, the probability of multiple validation increases, i.e. the multiple detection of a single burst. Multiple validation can give serious problems with further data processing, since the inaccuracy of the estimates of the burst parameters increases, the accurate estimation of turbulence power spectra up to high frequencies becomes more difficult and velocity moments can get biased.

- The segments of the signal that are provided to the processor should contain bursts that are strong enough to allow for accurate processing. In addition, unwanted low-level coherent signals should not be passed (such as frequency shift bleedthrough). The importance of these points depends on the type of detector/processor. If a segment containing only noise or a very weak burst is passed to the processor, this will lead to an erroneous point in the velocity series in the case of the IFA-processor. In the new dual burst wavelet processor, this point is probably removed by the validation routine, since it has more detailed information about the burst. In addition, velocity realizations due to frequency shift bleedthrough can be removed. Therefore, if such a validation routine is present, the detector can be set more sensitively and higher data rates may be obtained. Of course, a more sensitive setting will lead to more detected burst candidates and therefore to higher computational times.

- The frequency sensitivity of the algorithm should be sufficiently uniform: bursts with different frequencies but identical amplitudes should have similar probabilities of detection. If not, a bias will result.

- The algorithm should be sufficiently fast.

- Some degree of 'intelligence' should be present in the algorithm: if the noise level or other properties of the signal change from one signal to another (within certain limits), the algorithm should adapt.

- The algorithm should be transparent. With the IFA-750 it is hard to check whether the detection step is accurate. The most powerful test is by checking the time between data distribution for the presence of multiple validation. Improvements may be obtained in a new burst detector by adding additional detection information, such as calculated detection signals, thresholds and validation criteria. Problems such as multiple validation or overlapping bursts detected as single bursts are more easily noticed this way.

B.2. Burst detection algorithm

B.2.1. Existing detectors

Albrecht et al. (2003) presents an overview of existing methods for burst detection. These are based on various signal properties: the signal amplitude, the autocorrelation of the signal or the spectrum of the signal. In some cases, the detection is performed as pre-processing, in others the algorithm serves to check whether the processed data contains a valid signal or not.

For the present investigation, TSI equipment is used and the TSI IFA-750 processor is used for many of the experiments described in the present thesis. Figure B.2 shows the schematic operation of the detector in the IFA-750 (TSI Incorporated, 1988). An analogue signal enters the IFA-750. This is the signal of the Photo Multiplier Tube after downmixing and amplification. Inside the IFA-750 the signal is first further amplified and bandpass-filtered to remove noise. Next the signal is digitized with 1 bit digitizers: only the sign bit is determined of the signal (clipping). The sampling is performed in parallel by the burst detector digitizer and the sampler digitizer. The latter performs the sampling at multiple sampling rates. In the burst detector 16 logarithmically spaced autocorrelation coefficients of the 1 bit clipped signal are calculated. Whenever a negative peak in these coefficients drops below a fixed negative threshold, a coherent signal is detected. A rough frequency estimate is obtained from the smallest time-delay coefficient that drops below the threshold. The transit time is determined from the time the coefficients stay below the threshold. The frequency estimate of the detector is used in the sampler to determine which of the multiple sampling rates is best for further processing, the burst location estimate is used to take out the center 256 samples, which are passed to the burst processor.

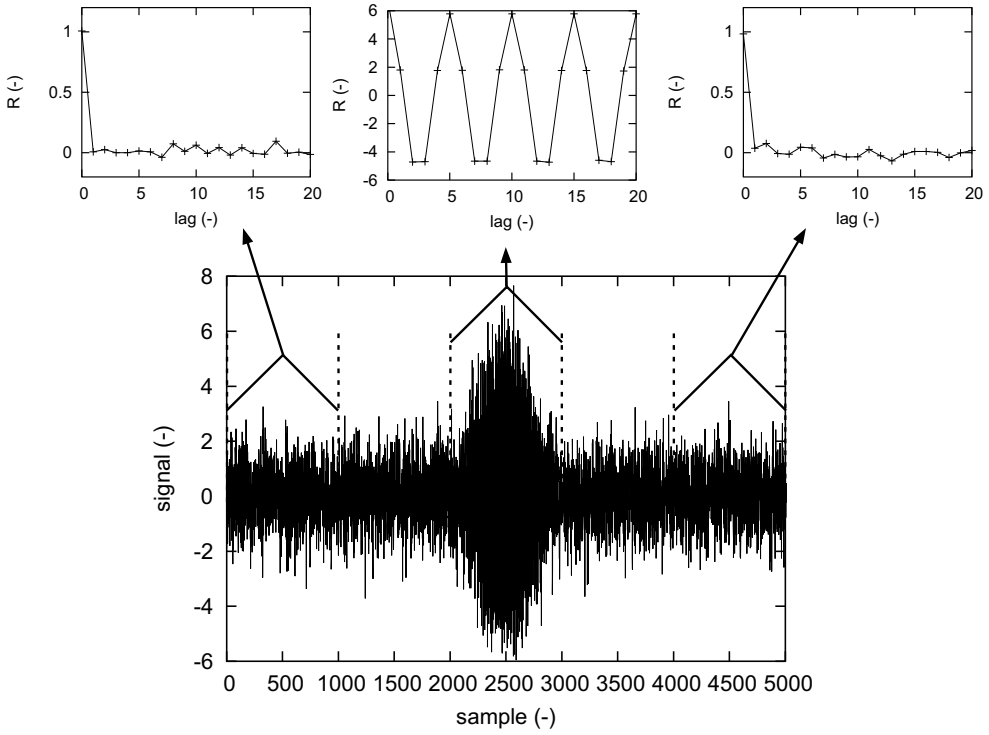

Figure B.3.: Autocovariance of signal segments.

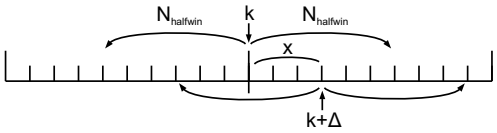

Figure B.4.: Autocovariance of signal segments.

B.2.2. New burst detection algorithm

Autocovariance signal

The burst detector algorithm employs the autocovariance function (ACF) of the signal in a similar way as the IFA-750 detector. However, there are important differences. These are partly due to the fact that the signal has been sampled at a relatively small sampling frequency f_s, typically a factor of 3-10 times the Doppler frequency. In addition, the present detector is more flexible and has been made more sophisticated to provide more sensitivity, accuracy and prevent multiple validation.

Figure B.3 shows an example of a burst immersed in strong noise. The signal has been sampled at 2.5 MHz, the Doppler frequency is 500 kHz, the transit time 0.4 ms. We consider small segments of the signal with length $N_{window} = 2N_{halfwin}+1$ and calculate the autocovariance function of these segments around sample k with (see Figure B.4):

$$R(\Delta, k) = \frac{1}{N_{window}} \sum_{i=k-N_{halfwin}}^{i=k+N_{halfwin}} x(i)x(i+\Delta) \tag{B.1}$$

where Δ is the lag. The autocovariance function is calculated for incremental values of k. By doing this with running sums the computational load remains low. The autocovariance functions of three example segments are shown in Figure B.3 (N_{window}=1001). As can be expected, if a periodical component is present in the signal, strong negative and positive peaks exist in the autocovariance function. Thus, the presence of a burst in the signal can be determined by finding signal segments with strong peaks in the autocovariance function at nonzero lags. In order to get a fast algorithm, the covariance coefficients are only calculated for a small number of lags.

Two types of algorithms are tested: the first detects coherent signals by detecting positive peaks ('maximum algorithm'), the other detects negative peaks ('minimum algorithm'). A range of frequencies $f_{det,low}..f_{det,high}$ where bursts can be expected is selected. Based on this range $N_{det,f}$ lags for the covariance calculation are selected. For the maximum algorithm, this gives the following lags based on the location of the first maximum of the covariance coefficients:

$$\Delta_j \in [\text{floor}(f_s/f_{det,high})...\text{round}(f_s/f_{det,low})] \tag{B.2}$$

where f_s is the sampling frequency. For the minimum algorithm, lags are obtained based on the location of the first minimum of the coefficients:

$$\Delta_j \in [\text{floor}(0.5f_s/f_{det,high}), ..., \text{round}(0.5f_s/f_{det,low})] \tag{B.3}$$

where floor(x) denotes rounding x to the nearest smaller integer, and round(x) denotes rounding x to the nearest integer. Consequently, $N_{det,f}$ lags Δ_j are considered with window sizes $N_{window,j} = 2N_{halfwin,j} + 1$. For each lag Δ_j we calculate the sum of products for a signal segment around sample k:

$$R(\Delta_j, k) = \frac{1}{N_{window,j}} \sum_{i=k-N_{halfwin,j}}^{i=k+N_{halfwin,j}} x(i)x(i+\Delta_j) \tag{B.4}$$

Two approaches will be evaluated for the amount of averaging specified by $N_{window,j}$:

- For each lag, the averaging is performed over approximately the same number of periods:

$$N_{halfwin,j} = \text{round}(0.5N_{periods}\frac{f_s}{f_j}) \tag{B.5}$$

  with $f_j = f_s/\Delta_j$ for the maximum algorithm and $f_j = f_s/(2\Delta_j)$ for the minimum algorithm. Generally, faster particles generate shorter transit times and higher Doppler frequencies. In the absence of a preshift frequency, the number of periods is more or less

constant for each burst and with this method similar fractions of each bursts are considered if the frequency varies.

- The window size is the same for all lags.

$$N_{halfwin,j} = N_{halfwin,constant} \tag{B.6}$$

with $N_{window,constant} = 2N_{halfwin,constant} + 1$. This assumes that the transit time shows little variation from burst to burst.

The largest and smallest values of R for all lags are determined. For the maximum and minimum algorithm the following expressions are obtained:

$$R^{max}(k) = max(R(\Delta_j, k), j = 1..N_{det,f}) \tag{B.7}$$

$$R^{min}(k) = min(R(\Delta_j, k), j = 1..N_{det,f}) \tag{B.8}$$

$R^{max}(k)$ and $R^{min}(k)$ are referred to as the autocovariance signals and are used to detect the bursts. A higher value indicates a higher probability that that the signal segment contains a coherent signal. Examples of these autocovariance signals are shown in Figure B.5a (for fixed $N_{periods}$). The index j where the extreme value is found is referred to as j_{max} (maximum algorithm) or j_{min} (minimum algorithm), see Figure B.5b. For the maximum algorithm, j_{max} is usually close to the period of the signal in the strongest part of the signal. In the weaker parts of the burst j_{max} is usually a multiple of this period and it locks to a higher order maximum of the autocovariance function. This is especially the case for fixed $N_{periods}$, where $N_{window,j}$ is larger for larger j.

The coherent bursts are detected by monitoring two threshold levels: $R_{threshold}$ and $R_{threshold,2}$ (Figure B.6). The start of a potential burst is marked when the covariance signal $R^{max}(k)$ or $R^{min}(k)$ becomes larger ('maximum' algorithm) of smaller ('minimum' algorithm') than the threshold level $R_{threshold}$. When the covariance signal again crosses this threshold level, the end of the burst is marked, except in the following case. If during a time $T_{threshold}$ the autocovariance signal does not cross $R_{threshold,2}$ and again exceeds $R_{threshold}$, the end is not marked, and the search for the end of the burst continues. This second threshold technique is implemented to allow for fluctuations in the autocovariance signal inside the bursts that otherwise might cause multiple validation, especially at higher threshold levels $R_{threshold}$.

Detection threshold level

The noise in the signal causes fluctuations and an offset in the autocovariance signal (visible in Figure B.5a). Consequently, the threshold levels $R_{threshold}$ and $R_{threshold,2}$ have to be set carefully with respect to the magnitude of these fluctuations and the offset. For this reason, the offset μ_R and standard deviation σ_R of $R^{max}(k)$ and $R^{min}(k)$ are investigated for the combination of a sine with amplitude A and white noise with standard deviation σ_{noise}. The values for μ_R and σ_R in the absence of a coherent signal are given by μ_{Rn} and σ_{Rn}, their magnitude determines the threshold level. Empirical relations were found for μ_R, μ_{Rn}, σ_R and σ_{Rn}. For fixed N_{window}

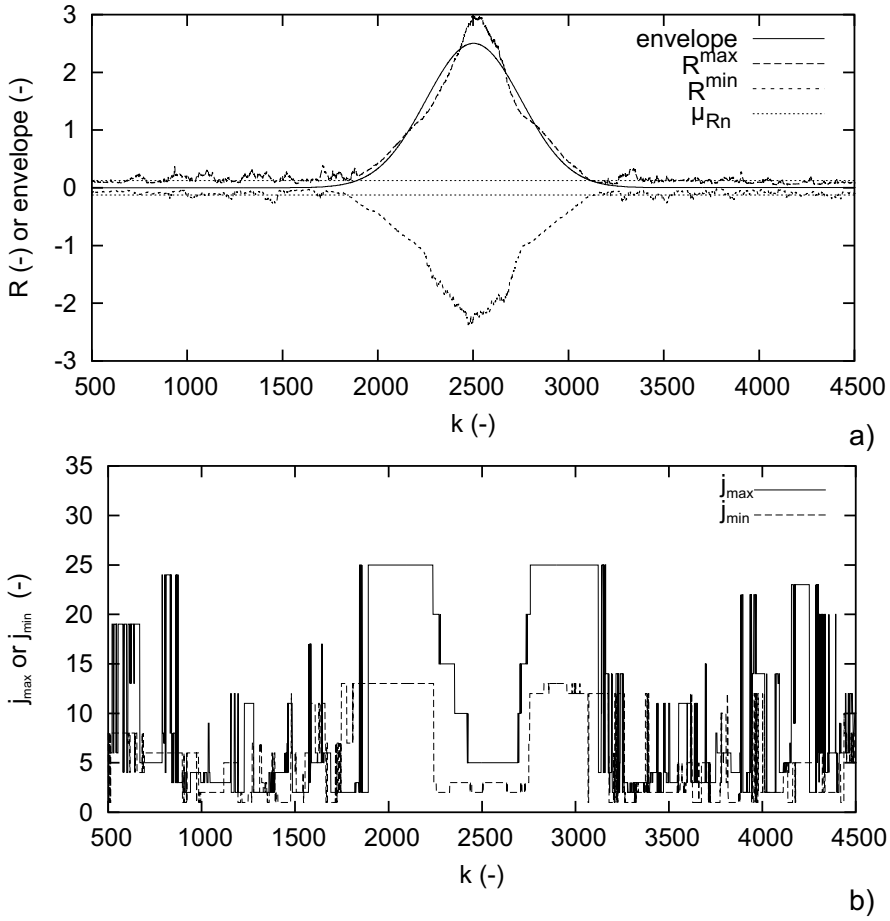

Figure B.5.: a) Autocovariance signals with 'minimum' and 'maximum' algorithms. $N_{periods}$=32, Doppler frequency 500 kHz, f_s=2.5 MHz, $f_{det,low}$=100 kHz, $f_{det,high}$=1000 kHz. b) Lag index where the maximum autocovariance coefficient is obtained.

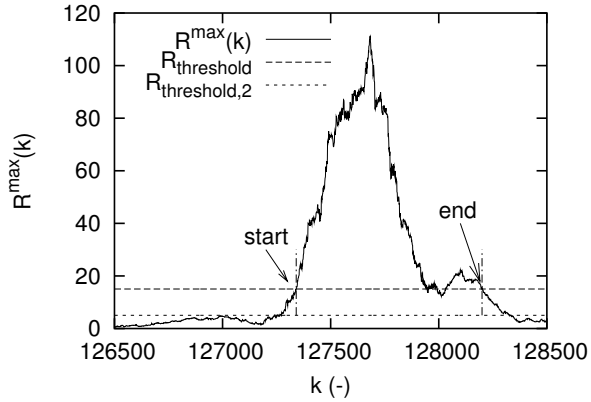

Figure B.6.: Detection thresholds and the detected start and end of the burst ('maximum' algorithm).

(equation B.6):

$$\mu_R \approx \frac{1}{2}A^2 + \mu_{Rn} = \frac{1}{2}A^2 + \frac{\sigma^2_{noise}(0.5ln(N_{det,f}) + 0.32)}{\sqrt{N_{window,constant}}} \tag{B.9}$$

$$\sigma_{noise} >> A \text{ and } N_{det,f} > 10: \quad \sigma_R \approx \sigma_{Rn} = 0.3\mu_R \tag{B.10}$$

For fixed $N_{periods}$ (equation B.5):

$$\sigma_{noise}/A > 3: \quad \mu_R \approx \tfrac{1}{2}A^2 + \mu_{Rn} = \tfrac{1}{2}A^2 + \frac{\sigma^2_{noise}}{\sqrt{N_{window,1}}} \tag{B.11}$$

$$\sigma_{noise}/A < 1: \quad \sigma_R \approx A\frac{\sigma^2_{noise}}{\sqrt{N_{window,j_{max/min}}}} \tag{B.12}$$

$$\sigma_{noise}/A > 6: \quad \sigma_R \approx \sigma_{Rn} = \tfrac{1}{2}\frac{\sigma^2_{noise}}{\sqrt{N_{window,1}}} \tag{B.13}$$

For fixed $N_{periods}$, μ_R and σ_R scale with the window size of the most relevant lag, which in the case of pure noise is the shortest window, with index 1. This explains why if j_{max} or j_{min} increases near the sides of the burst, the magnitude of the fluctuations decreases (Figure B.5).

The mean offset level outside the burst is given by μ_{Rn} (an example is shown in Figure B.5a). For both fixed $N_{periods}$ and fixed N_{window}, the magnitude of the fluctuations in the autocovariance signal outside the burst, σ_{Rn}, scales with the offset μ_{Rn}: $\sigma_{Rn} = constant * \mu_{Rn}$. The threshold levels for detection $R_{threshold}$ and $R_{threshold,2}$ should therefore be chosen proportional with this level:

$$R_{threshold} = \pm C_{threshold}\mu_{Rn} \tag{B.14}$$

$$R_{threshold,2} = \pm C_{threshold,2}\mu_{Rn} \tag{B.15}$$

where the sign is positive for the 'maximum' algorithm and negative for the 'minimum' algorithm. Correct setting of the constants $C_{threshold}$ and $C_{threshold,2}$ is discussed in section B.3. The constants are kept constant for similar flow conditions. If the noise level of the signal varies from measurement to measurement, the threshold is adjusted automatically.

Noise level estimation

In order to set the detection threshold levels with equations B.14 and B.15, an estimate of μ_{Rn} is required. In order to calculate μ_{Rn} a piece of the signal not containing any bursts is required. Next, μ_{Rn} can be either determined from the standard deviation of this signal with equations B.9 or B.11, or by directly calculating the mean of the autocovariance signal of the signal segment. The second method was found to render best results, since usually the noise is not purely white, and the signal also contains stray components, e.g. frequency shift bleeding. Consequently, μ_{Rn} is usually larger than the prediction by equations B.9 and B.11.

The estimation of μ_{Rn} is performed in the noise level detection routine (Figure B.1). The noise level is determined by considering a signal segment, remove possible bursts based on the local probability density function of the signal amplitude and, subsequently, calculate the mean of $R^{max}(k)$ or $R^{min}(k)$ of the remaining signal parts.

The idea behind the burst removal is that for a Gaussian white noise signal x_i with mean μ_{noise} and standard deviation σ_{noise}, the probability $p(\mu_{noise} - C_{clip}\sigma_{noise} < x_i < \mu_{noise} + C_{clip}\sigma_{noise}) = 1 - P_{clip}$, e.g. for $C_{clip} = 2$, $P_{clip} = 0.05$. If the probability density function of a small signal segment is determined and the fraction of values inside the interval $[\mu_{noise} - C_{clip}\sigma_{noise}, \mu_{noise} + C_{clip}\sigma_{noise}]$ is significantly smaller than $1 - P_{clip}$, this segment probably contains a burst.

The mean μ_{noise} and standard deviation σ_{noise} are determined iteratively. As a first guess, the mean and standard deviation of the entire signal are taken: $\mu^{(0)}_{noise} = \text{mean}(x)$ and $\sigma^{(0)}_{noise} = \text{standard deviation}(x)$. Subsequently, these estimates are refined in iteration j. The parts of the signal where potential bursts are located are identified. A window with size $N_{noisewindow}$ is shifted over the signal. When the window is centered around point k, $N_{clip}(k)$ points are found inside the window which have values outside the interval $[\mu^{(j-1)}_{noise} - C_{clip}\sigma^{(j-1)}_{noise}, \mu^{(j-1)}_{noise} + C_{clip}\sigma^{(j-1)}_{noise}]$. Next,

$$\begin{aligned} &\text{if } \tfrac{N_{clip}(k)}{N_{noisewindow}} > C_{noise}: \quad n^{(j)}_k = 0 \\ &\text{if } \tfrac{N_{clip}(k)}{N_{noisewindow}} \leq C_{noise}: \quad n^{(j)}_k = 1 \end{aligned}$$

where C_{noise} is based on P_{clip} but taken somewhat larger to account for the finite window size and deviations from the white noise character. Consequently, $n^{(j)}_k = 0$ in the parts of the signal where a burst may be present. In order to include the weaker tails of the bursts, the zones where $n^{(j)}_i = 0$ are extended in length with a factor $C_{noiseextend}$. Next, the mean and standard deviation of the noise are calculated for $j > 0$ with:

$$\mu^{(j)}_n = \frac{\sum_i x_i n^{(j)}_i}{\sum_i n^{(j)}_i} \tag{B.16}$$

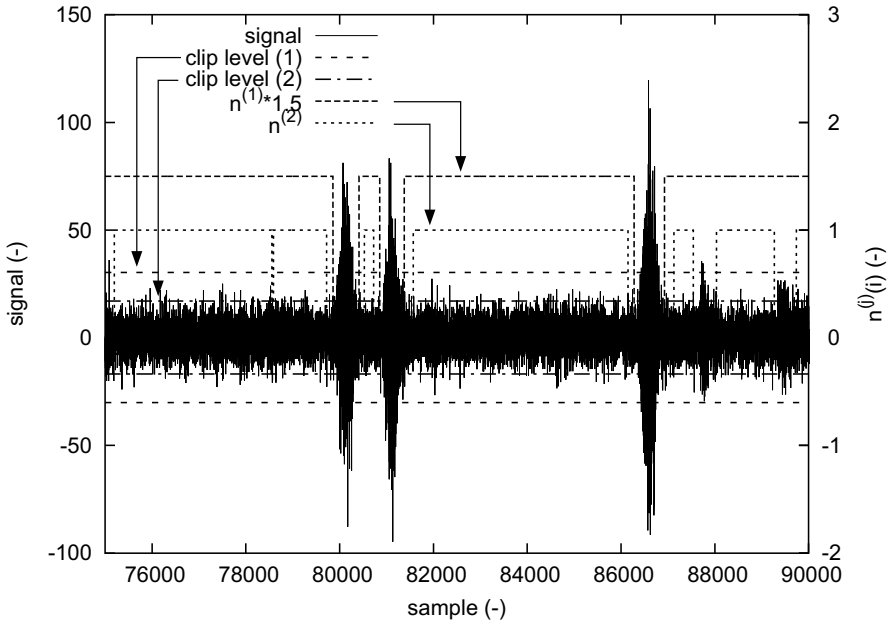

Figure B.7.: Example of burst removal for noise level estimation. Iterations 1 and 2 are shown for the noisy signal from a bubble column.

$$\sigma_n^{(j)} = \sqrt{\frac{\sum_i (x_i - \mu_n^{(j)})^2 n_i^{(j)}}{\sum_i n_i^{(j)}}} \tag{B.17}$$

Typical values that are used (obtained with some trial and error), are $C_{clip} = 2.5$, $C_{noise} = 0.06$, $C_{noiseextend} = 1.4$. A piece of the signal of typically 1 Msamples is used. With these values the algorithm also works well if the noise is not purely white Gaussian and e.g. there is some frequency shift bleeding. Usually 2-3 iterations are enough, with more iterations no further change in the standard deviation is obtained. An example is shown in Figure B.7. The clipping intervals are shown, as well as n_i, for each iteration. After the first iteration ($n^{(1)}$) the strongest parts of the burst have been removed. At this point, the average duration of the gaps T_{gap} is calculated, it can be used as an estimate of the burst duration for the burst detector. After the second iteration ($n^{(2)}$), also the weak bursts and the tails of the strong bursts are removed.

After the removal of the bursts, μ_{Rn} is estimated by directly calculating the mean of $R^{max}(k)$ or $R^{min}(k)$ from the signal parts not containing bursts.

Detected burst validation

Due to the noise, $R^{max}(k)$ or $R^{min}(k)$ regularly crosses the threshold level $R_{threshold}$, also if no burst is present. Similarly, a single burst may be detected multiple times, especially in its weakest parts close to the tails. In order to reduce the number of these false burst detections

some checks are performed on the burst candidate. The burst location and width to the burst are only passed to the processor if the burst satisfies:

- $T_{transit} = (k_{end} - k_{start})/f_s > T_{transit,min}$
- Maximum algorithm:
  - $R_{mean} = \frac{1}{k_{end}-k_{start}+1} \sum_{i=k_{start}}^{k_{end}} R^{max}(k) > R_{mean,threshold}$
  - $R_{peak} = \max(R^{max}(k), k \in [k_{start}, .., k_{end}]) > R_{peak,threshold}$
- Minimum algorithm:
  - $R_{mean} = \frac{1}{k_{end}-k_{start}+1} \sum_{i=k_{start}}^{k_{end}} R^{min}(k) < R_{mean,threshold}$
  - $R_{peak} = \min(R^{min}(k), k \in [k_{start}, .., k_{end}]) < R_{peak,threshold}$

where k_{start} and k_{end} mark the start and end of the burst, and with:

$$R_{mean,threshold} = \pm C_{mean,threshold} \mu_{Rn} \tag{B.18}$$

$$R_{peak,threshold} = \pm C_{peak,threshold} \mu_{Rn} \tag{B.19}$$

similar to equation B.14. The setting of $C_{mean,threshold}$ and $C_{peak,threshold}$ is discussed in section B.3.

Splitting of overlapping bursts

If bursts arrive shortly after one another, there may be an overlap, such that the autocovariance signal does not cross the threshold level(s) in between the bursts. As a result, the detector sees only one long burst (interval AC in Figure B.8). If this occurs with two bursts the dual burst processor can deal with the problem, but if more than two bursts are involved, problems may result. The probability that more than two bursts are involved is dependent on the data rate (seeding density), typical transit time and the detection threshold level. If the signal-to-noise ratio of the LDA signal is increased, the threshold level drops relatively since it is based on the noise level. Consequently, the probability that the detector cannot distinguish the bursts increases. One way to tackle the problem is by increasing the threshold level(s). The example of a burst with relatively large amplitude in Figure B.8 illustrates that the increase of the threshold has to be quite large since the signal to noise ratio varies strongly from burst to burst. This means that weak bursts are no longer detected or detected incorrectly. Therefore, the data rate may drop significantly due to this increase in threshold. For this reason, a different approach is taken.

In order to deal with this problem an optional additional step is included in the algorithm. The part of the autocovariance signal between k_{start} and k_{end} is considered in more detail, and an attempt is made to split it into separate bursts if these are present. A threshold based on R_{peak} is introduced.

$$R_{threshold,split} = C_{threshold,split} R_{peak} \tag{B.20}$$

with $C_{threshold,split}$ typically around 0.2. If $R_{threshold,split} < R_{threshold}$, the burst (pair) is too weak to be splitted and no splitting is performed. The parts of the autocovariance signal are

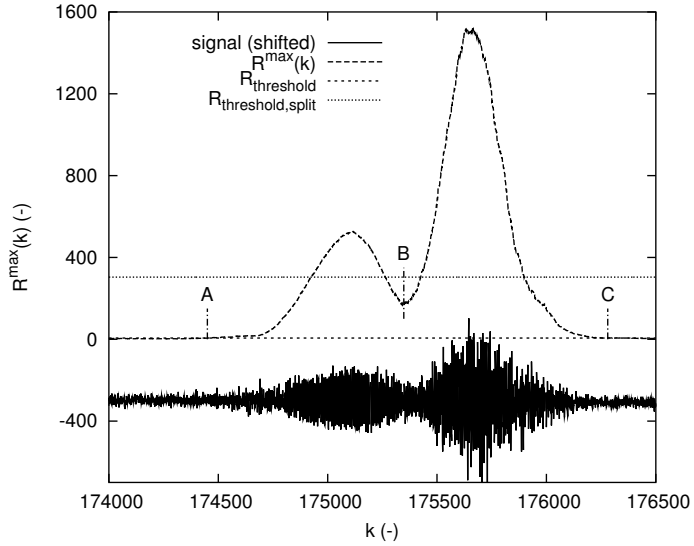

Figure B.8.: Example of overlapping bursts.

identified where the autocovariance signal exceeds $R_{threshold,split}$. The indices where segment i starts and ends are named $k_{splitstart,i}$ and $k_{splitend,i}$. Only segments complying to validation criteria are identified. These validation criteria are similar to those used in the detector burst validation step:

- $(k_{splitend,i} - k_{splitstart,i})/f_s > T_{transit,min}$
- $R^{split}_{mean,i} = \frac{1}{k_{splitend,i}-k_{splitstart,i}+1} \sum_{i=k_{splitstart,i}}^{k_{splitend,i}} R^{max}(k) > R^{split}_{mean,threshold}$
- $R^{split}_{peak,i} = \max(R^{max}(k), k \in [k_{splitstart,i}, .., k_{splitend,i}]) > R^{split}_{peak,threshold}$

with

$$R^{split}_{mean,threshold} = \max(R_{mean,threshold}, R_{threshold,split} + \mu_{Rn}) \tag{B.21}$$

and

$$R^{split}_{peak,threshold} = \max(R_{peak,threshold}, R_{threshold,split} + 4\mu_{Rn}) \tag{B.22}$$

which were obtained empirically. If at least $N_{split,min}$ segments are found, splitting is performed. $N_{split,min}$ is typically set to 3. In this case, the location and width of $N_{split,min}$ bursts are outputted. The start and end of these bursts are given by k_{start}, k_{end} and the locations of the minima of $R^{max}(k)$ between the segments. An example with two segments (i.e. with $N_{split,min}$=2) is shown in Figure B.8: the original interval AC is splitted into AB and BC.

Parameter/method	Description
maximum/minimum algorithm	Detection is based on either the 1st maximum or the 1st minimum of the autocovariance function
fixed $N_{periods}$ or fixed N_{window}	Either the number of periods inside the window is fixed or the window size itself is fixed
$N_{periods}$	Number of periods on which the window size is based
N_{window}	Window size
$f_{det,low}$	Lowest frequency of signals that the detector should be able to detect accurately
$f_{det,low}$	Highest frequency of signals that the detector should be able to detect accurately
f_s	Sampling frequency
$C_{threshold}$	Constant that determines 1st threshold level for burst detection
$C_{threshold,2}$	Constant that determines 2nd threshold level for burst detection
$C_{mean,threshold}$	Constant that determines burst validation threshold for R_{mean}
$C_{peak,threshold}$	Constant that determines burst validation threshold for R_{peak}

Table B.1.: Various methods and parameters in the burst detector

B.3. Optimal setting of burst detector

Good performance of the detector as described in section B.1 requires correct selection of the various methods and setting of the various parameters in the algorithm that was described in section B.2 (see Table B.1). The influence of these parameters and the selection of these methods on the accuracy of the burst location and width, multiple validation and frequency sensitivity is investigated in this section.

B.3.1. Frequency sensitivity

The frequency sensitivity of the burst detection can be tested by calculating R_{peak} for artificial bursts without noise for a range of Doppler frequencies. Strong variations in R_{peak} with the Doppler frequency may indicate a frequency dependent probability of detection, which can lead to bias problems. Artificial bursts are generated with transit time 0.4 ms and Doppler frequencies in the range of 10 kHz-1250 kHz. Figure B.9 shows the frequency sensitivity for the 'maximum' algorithm for decreasing $f_{det,low}$ value. Since only integer lag values are available (equations B.2 and B.3) not every Doppler frequency will give a similar value for R_{peak}. For example, if a sampling frequency of 2.5 MHz is used with the 'maximum' algorithm, a frequency of 500 kHz corresponds exactly to lag 5. The first maximum of the autocovariance function of a burst with a frequency of 714 kHz is not located close to an integer lag but at 3.5. However, it has its second maximum at lag 7. The sum of products for this lag is only considered for the ranges

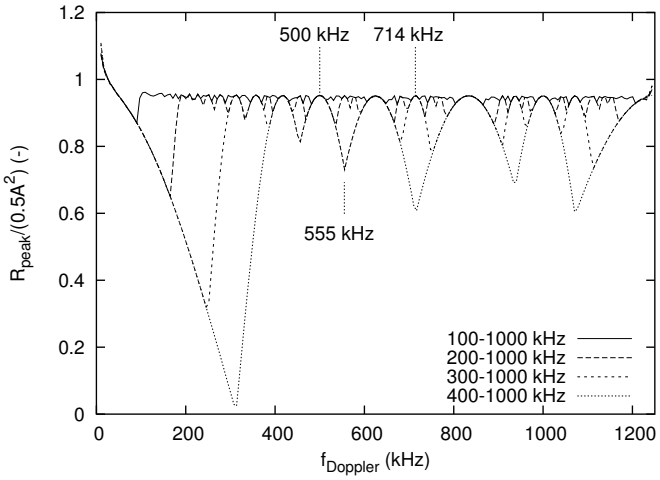

Figure B.9.: Comparison of frequency sensitivity for various $f_{det,low}$ values, $f_{det,high}$=1000 kHz. Settings: maximum algorithm, $N_{window,constant}$=201.

with $f_{det,low} \leq 300$ kHz. Consequently, only for these ranges the sensitivity around 714 kHz is similar to that around 500 kHz. Similarly, the frequency 555 kHz has its second maximum at lag 9, which is included in the calculations for $f_{det,low} \leq 200$ kHz. So for decreasing $f_{det,low}$ the uniformity of the frequency response at higher frequencies improves as well. For $f_{det,low}$ in the range 100-200 kHz the uniformity is quite good.

Since non-uniformities in the sensitivity are caused by the discrete nature and limited number of the lags, an increase in the sampling frequency f_s leads to an improvement in the uniformity of the sensitivity. This is illustrated in Figure B.10. In order to get no more than 10% variation in R_{peak} for different Doppler frequencies, the signal should be sampled at at least 2500 kHz for LDA performed in the 100-1000 kHz range.

The effect of the integer values of the lags becomes even more apparent when the 'minimum' algorithm is used. Figure B.11 compares the sensitivity of the 'minimum' algorithm with the 'maximum' algorithm. Since the 'minimum' algorithm operates at even smaller lag values than the 'maximum' algorithm, stronger gaps appear in the frequency sensitivity (e.g. around 835 kHz). The 'maximum' algorithm has a few small drawbacks: it requires a larger number of lags $N_{det,f}$ to be calculated, which makes the algorithm a bit slower and increases the level μ_{Rn} somewhat (equation B.9). In addition, if a stray signal, such as frequency preshift bleeding, is present, and the burst is weak, the first and second maximum of the autocovariance function may be distorted and therefore smaller. Consequently, the 'minimum' algorithm has a larger sensitivity for the weakest bursts. This difference reduces if $f_{det,low}$ is reduced since the higher order maxima in the autocovariance function are detected as well. However, the bubble column signal generally covers a large frequency range and we want to prevent bias induced by an insensitivity for certain frequencies in the detector. For this reason the 'maximum' algorithm is selected and this is the only algorithm that will be considered in the rest of this section.

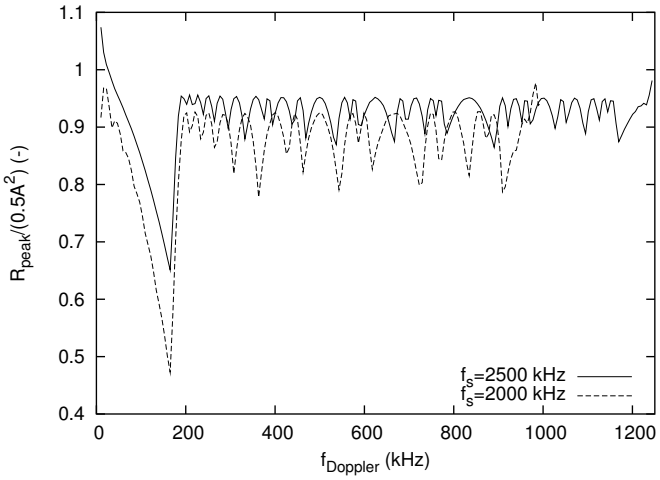

Figure B.10.: Comparison of frequency sensitivity for sampling frequencies of 2 MHz and 2.5 MHz. $N_{window,constant}$=201.

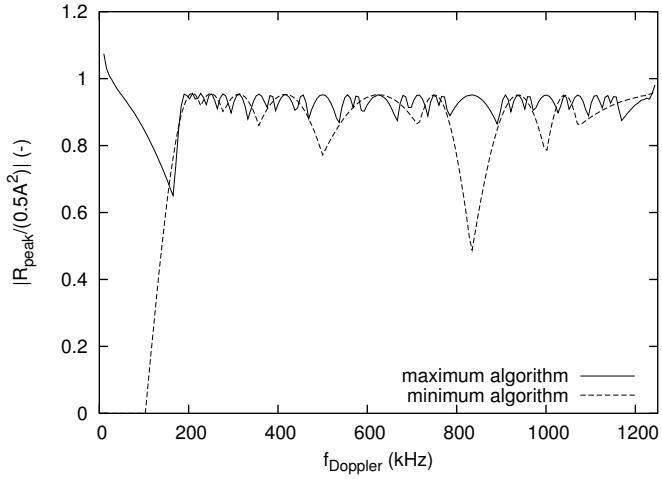

Figure B.11.: Comparison of frequency sensitivity of minimum and maximum algorithms. $N_{window,constant}$=201, $f_{det,low}$=200 kHz, $f_{det,high}$=1000 kHz, f_s=2.5 MHz.

Nevertheless, most results are equally valid for the 'minimum' algorithm.

B.3.2. Multiple validation and accuracy of burst width and location

Multiple validation

The most important parameters for the correct detection of the start and the end of bursts are the amount of averaging when calculating the autocovariance signal $R^{max}(k)$ (set with $N_{periods}$ or $N_{window,constant}$) and the threshold levels $R_{threshold}$ and $R_{threshold,2}$. This is illustrated in Figure B.12. The threshold level $R_{threshold}$ should not be selected too low or too high. If it is taken too low, no bursts are selected, or many parts of the signal not containing any coherent signal are mistaken as bursts. If it is taken too high, a single burst is detected multiple times: multiple validation occurs. Careful setting of $R_{threshold,2}$ can reduce the problem, but not eliminate it fully. In the example in Figure B.12, the burst is detected three to five times for $N_{periods} = 4$. The problem reduces if $N_{periods}$ is increased and more averaging occurs. For $N_{periods} = 32$ one large and one small burst are detected in Figure B.12. Correct setting of the constraints $T_{transit,min}$, $R_{mean,threshold}$ and $R_{peak,threshold}$ will remove these small bursts. When the IFA-750 detector/processor is used, the only possible values for $N_{periods}$ are 4 and 8. A typical burst for LDA in the bubble column contains 100-200 periods (500 kHz, 0.3 ms transit time), which is much larger. This explains the problems with multiple validation if the IFA processor is used for measurements in the bubble column.

$N_{periods}$ or $N_{window,constant}$ should therefore be based on the actual number of periods or samples encountered in the bursts.

Fixed number of periods versus fixed window size

Figure B.13 shows the autocovariance signal of an artificial burst without noise for both constant $N_{periods}$ and constant N_{window}. The Doppler frequency of 500 kHz provides maxima around lag 5, 10, 15, 20 and 25. Since N_{window} is larger for larger lags if fixed $N_{periods}$ is used, the lag Δ_j of the sum of products that determines $R^{max}(k)$ increases in the weaker parts of the burst (see also Figure B.5b). Consequently, the burst shape is smeared in the autocovariance signal. As a result, estimation of its width is difficult and adjacent bursts cannot very well be differentiated. This effect can only be reduced by decreasing $N_{periods}$, which increases the probability of multiple validation. This effects makes it difficult to find an optimal value for $N_{periods}$.

Since the experiments in the bubble column were usually performed with a relatively large preshift frequency, and the flow has a relatively isotropic character, the number of periods varies quite a lot from burst to burst. Combining this with the potential problems due to the smearing effect, constant window size is selected as the preferred method for all bubble column experiments. For this reason, constant N_{window} is the only method that will be considered in the rest of this section.

Selection of N_{window}

The value of N_{window} is a compromise. In order to smooth noise fluctuations, a large value is required for N_{window}. On the other hand smoothing of the burst should be prevented by

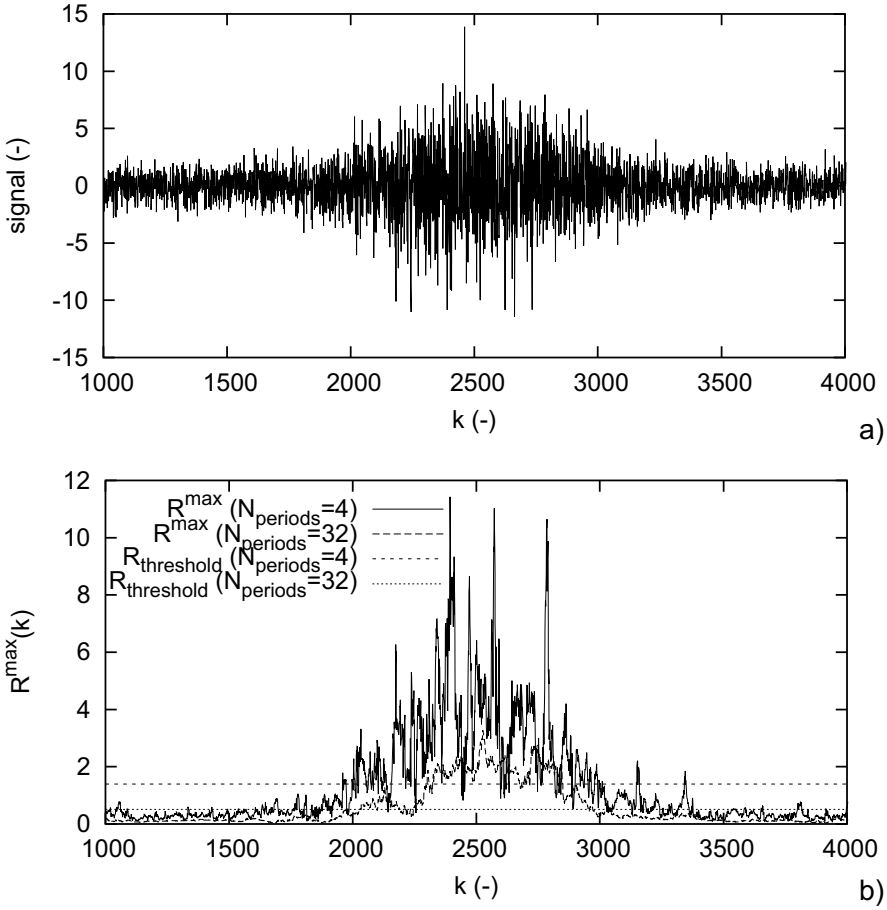

Figure B.12.: a) Signal. b) Autocovariance signals with threshold levels for burst detection, $C_{threshold} = 5$, $f_{det,low}$=200 kHz, $f_{det,high}$=800 kHz, Doppler frequency=500 kHz.

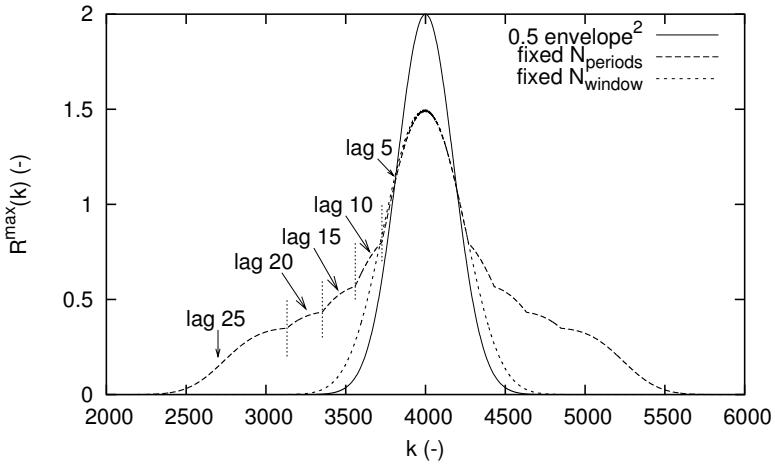

Figure B.13.: Autocovariance signals for fixed $N_{periods}$=100 and fixed N_{window}=501. The lags j of the sum of products $R(\Delta_j, k)$ which locally determines $R^{max}(k)$ are shown for the case with fixed $N_{periods}$. f_D=500 kHz, $f_{det,low}$=100 kHz, $f_{det,high}$=1000 kHz, f_s=2.5 MHz.

keeping N_{window} small. For this reason, the largest possible value is taken for N_{window} where the smoothing of the burst is still acceptable. The smoothing of the burst shape is illustrated in Figure B.14, where C_w is the fraction of the typical burst transit time $T_{t,typical}$ over which the averaging is performed:

$$N_{window} = C_w T_{t,typical} f_s \tag{B.23}$$

This shows that the largest value of C_w where the burst duration can be estimated reliably is around 0.5. Around this value, some overestimation of the burst duration may be induced, but overestimation of the burst duration has much smaller negative consequences than underestimation of the burst duration. The value of 0.5 will be used when possible.

For the typical bubble column experiments, a mean transit time of 0.3 ms is found, and the minimum burst duration is typically set at 0.05 ms. The mean transit time has been estimated as T_{gap} in the noise estimation algorithm. The algorithm is set to process bursts with durations of 50% of this transit time with the optimal factor $C_w = 0.5$. Bursts with duration close to the minimum burst duration should be processed with a factor $C_w = 1$. This gives two values for $N_{window,constant}$, the average is taken:

$$N_{window,constant} = f_s \frac{T_{gap} * 0.25 + T_{transit,min}}{2} \tag{B.24}$$

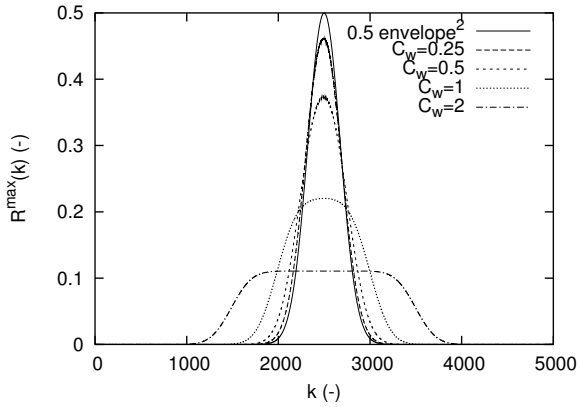

Figure B.14.: Effect of window size N_{window} on the smearing of the burst shape.

Validation criteria and detection thresholds

Tests with artificial signals are used to find optimal setting for $C_{peak,threshold}$, $C_{mean,threshold}$, $C_{threshold}$ and $C_{threshold,2}$. This gives for $C_{threshold,2}$ a value of 1.5 and for the validation criteria:

$$C_{peak,threshold} = C_{threshold} + 4 \tag{B.25}$$

$$C_{mean,threshold} = C_{threshold} + 1 \tag{B.26}$$

For the investigation of $C_{threshold}$ artificial bursts are generated which have relatively small amplitudes. The bursts have frequencies in the range 400-600 kHz and transit times of 0.4 ms. f_s=2.5 MHz, $f_{det,low}$=100 kHz, $f_{det,high}$=1000 kHz, $N_{window,constant}$=156. The amplitudes of the burst A are in the range 0.35-4.0, σ_{noise}=1. $C_{threshold,2}$=1.5 and the validation criteria from equations B.25 and B.26 are used.

The results are shown in Figure B.15. This shows that at very low values of $C_{threshold}$ the burst duration is overestimated and has large fluctuations. The magnitude of the fluctuations decreases if $C_{threshold}$ is increased, but levels off for $C_{threshold}$>1.5. A similar trend is observed for the accuracy of the estimate of the location of the burst center. The mean burst duration estimate continues to decrease if $C_{threshold}$ is increased since the burst is 'cut' at a higher point. Consequently, the duration of the weakest bursts is either underestimated, or these bursts may not be detected at all. Therefore, the best results will be obtained for $C_{threshold}$ in the range 1.5-2.0.

Example

Finally, the performance of the algorithms is evaluated for the parameter settings recommended in the previous sections. A signal was obtained by measuring the axial velocity component in a turbulent pipe flow of water (mean velocity 0.11 m/s, Re=5400). The mean Doppler frequency was close to 300 kHz. The following settings were used: frequency preshift 200 kHz, electronic

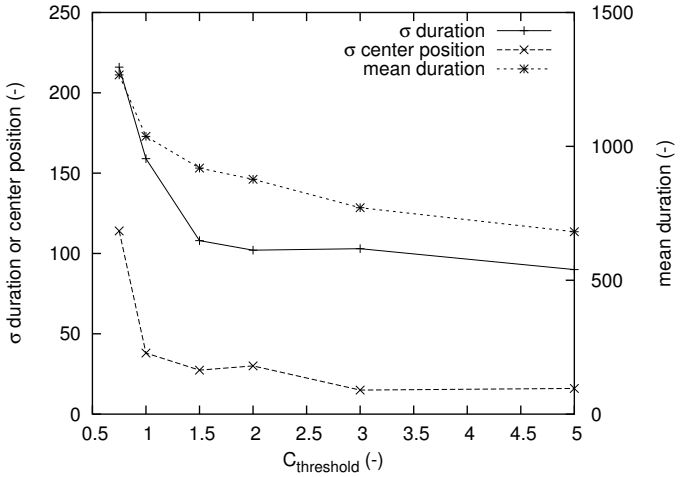

Figure B.15.: Effect of $C_{threshold}$ on the standard deviation and mean of the estimated burst duration and the standard deviation of the estimated position of the burst center. Exact transit time: 1000 samples.

bandpass filter range 100-1000 kHz, f_s=2500 kHz, 'maximum' algorithm, N_{window}=constant (eq. B.24), $f_{det,low}$=100 kHz, $f_{det,high}$=1000 kHz, $C_{threshold}$=2, $C_{threshold,2}$=1.5, $C_{mean,threshold}$=3 (eq. B.26), $C_{peak,threshold}$=6 (eq. B.25), $T_{transit,min}$=0.1 ms.

The result is shown in Figure B.16. The performance is good. This shows that without any user tweaking good results can be obtained. The current settings were based on an analysis of bursts with white noise and allow for the presence of some additional noise inside the bursts. If e.g. the noise is colored or stray signals are present, some small manual adjustments may be required to improve the sensitivity a little further.

List of symbols

Roman symbols

A	amplitude	-
C_{clip}	constant determining interval for clipping	-
$C_{mean,threshold}$	factor for $R_{mean,threshold}$	-
C_{noise}	minimum fraction of time that clipping should occur before signal is considered part of a burst	-
$C_{noiseextend}$	constant determining with which factor noise window length should be multiplied	-
$C_{peak,threshold}$	factor for $R_{peak,threshold}$	-
$C_{threshold}$	constant for setting of $R_{threshold}$	-
$C_{threshold,2}$	constant for setting of $R_{threshold,2}$	-
$C_{threshold,split}$	constant for setting of $R_{threshold,split}$	-

C_w	fraction of burst transit time on which N_{window} is based	-
$f_{det,low}$, $f_{det,high}$	lowest and highest frequency to be detected	s^{-1}
f_s	sample frequency	s^{-1}
j_{max} or j_{min}	index acf for which value of R^{max} or R^{min} is used	-
k	index at center of window for acf calculation	-
k_{end}, k_{start}	indices where end and start of burst are detected	-
$k_{splitstart}$, $k_{splitend}$	indices for splitting of burst	-
N_{clip}	number of points in window which have value outside clipping interval	-
N_{det}	number of lags for which acf is calculated	-
$N_{halfwin}$	half window size acf calculation	-
$N_{noisewindow}$	number of points in window for noise estimation	-
$N_{periods}$	number of periods for acf calculation	-
N_{window}	window size acf calculation	-
n	window function denoting which points are considered as noisy	-
P_{clip}	probability that clipping occurs	-
p	probability	-
R	autocovariance	-
R^{max}	largest autocovariance value	-
R_{mean}	mean R^{max} or R^{min} during burst	-
$R_{mean,threshold}$	threshold R_{mean} for validation	-
R^{min}	smallest autocovariance value	-
R_{peak}	extreme values of R^{max} or R^{min} during burst	-
$R_{peak,threshold}$	threshold R_{peak} for validation	-
R^{split}_{mean}	mean of R^{max} or R^{min} for splitting interval	-
$R^{split}_{mean,threshold}$	threshold for R^{split}_{mean}	-
R^{split}_{peak}	extreme of R^{max} or R^{min} for splitting interval	-
$R^{split}_{peak,threshold}$	threshold for R^{split}_{peak}	-
$R_{threshold}$	threshold for R^{max} or R^{min}	-
$R_{threshold,2}$	second threshold for R^{max} or R^{min}	-
$R_{threshold,split}$	threshold for R^{max} or R^{min} for splitting	-
T_{gap}	estimate burst duration from noise estimator	s
$T_{threshold}$	minimum time that R^{max} or R^{min} should drop below threshold before end of burst is marked	s
$T_{transit}$	estimated burst duration	s
$T_{transit,min}$	minimum burst duration for validation	s
$T_{t,typical}$	typical burst transit time	s

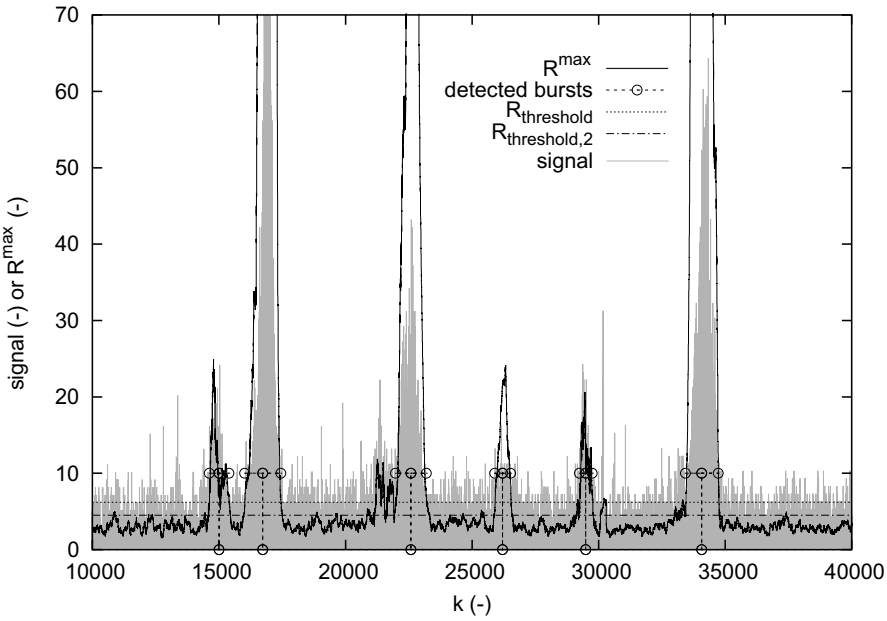

Figure B.16.: Example of burst detection in a signal obtained in turbulent pipe flow.

Greek symbols

μ_R	expectancy R^{max} or R^{min} signal+noise	-
μ_{Rn}	expectancy R^{max} or R^{min} noise only	-
μ_{noise}	mean noise signal	-
σ_{noise}	standard deviation noise	-
σ_R	standard deviation R^{max} or R^{min} signal+noise	-
σ_{Rn}	standard deviation R^{max} or R^{min} noise only	-

C. LDA frequency sensitivity measurements

C.1. Introduction

The range of Doppler frequencies is relatively high for the measurements in bubble columns. Both negative and positive velocities are encountered over a wide range, requiring a relatively large frequency preshift. A relatively small fringe spacing results from the use of a lens with short focal length to reduce the magnitude of the preshift frequency component present in the signal due to reflections. For example, using a lens with 12.2 cm focal length, Doppler frequencies in the range 300 kHz to 800 kHz are obtained. The most suitable bandpass filter in the IFA-750 processor has the range 100 kHz to 1000 kHz, thus a large part of the range of this filter is covered.

Consequently, if the electronic equipment does not amplify all frequencies with the same factor, a bias may result in the liquid velocity moments. This is due to the larger probability for detection and/or validation for weak bursts with frequencies that have the larger amplification factor. The resulting relative error in the mean liquid velocity can be quite large since the mean liquid velocities are often smaller than the standard deviation of these velocities. This is especially the case for the measurements in the homogeneous regime with uniform gas injection.

Therefore, this frequency dependent amplification is investigated for the IFA equipment. A simple tests can show the presence of the frequency dependency. If a LDA signal is determined in a bubbly flow, rotation of the backscatter probe with 180° should only change the sign of the mean velocity if no bias occurs. With this test, velocities that initially give a Doppler frequency of e.g. 700 kHz, now give Doppler frequencies of 300 kHz (in the case of a preshift frequency of 500 kHz). The relative probabilities of detection are strongly modified this way. The test shows that the mean of the velocity is changed with up to 0.05 m/s when the probe is rotated by 180°. This change is of the same order of magnitude as the true mean. Its actual value depends on the signal-to-noise ratio of the signal. Although part of this bias may be due to frequency bias and multiple validation in the IFA-750 detector and/or processor (some of these problems are discussed in Nievaart (2000)), part of the problem lies in the electronic components of the IFA equipment.

Also if wavelet processing is used, the frequency dependent amplification may result in bias. After processing, the validation is based, amongst others, on a signal to noise ratio criterion like:

$$SNR_i = \frac{S_i}{N_i} > SNR_{threshold} \tag{C.1}$$

with S_i the height of the peak in the powerspectrum, and N_i the height of the noise floor in the power spectrum. As was shown, S_i is dependent on the Doppler frequency f_D, whereas tests show that this is hardly the case for N_i. Therefore, a bias may result with this criterion. For this reason, a different criterion is required.

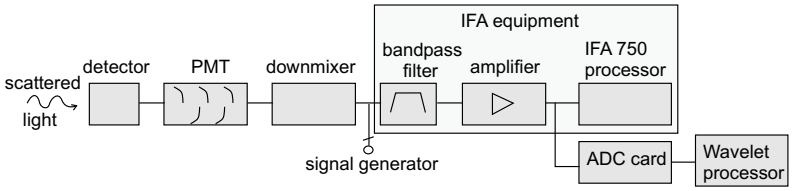

Figure C.1.: The equipment that processes the optical signal before AD conversion.

Suppose two bursts are measured, one with frequency f_D, the other with reference frequency f_0. The bursts have similar intensity I when they arrive at the optical detector. After detection, downmixing, amplification and filtering (Figure C.1), the signals enter the burst detector and processor with amplitudes $A(f_D)$ and $A(f_0)$. Their ratio is given by:

$$C_a(f_D) = \frac{A(f_D)}{A(f_0)} \tag{C.2}$$

With this ratio a correction can be introduced for the SNR criterion:

$$SNR_i^c = \frac{S_i}{C_a^2(f_D)N_i} > SNR_{threshold}^c \tag{C.3}$$

which should no longer suffer from the bias problem, possibly at the cost of a reduction in data rate.

This appendix discusses the experiments performed to determine $C_a(f_D)$. This is performed for the bandpass filter range 100-1000 kHz. In addition, an attempt is made to identify the electronic components which are the biggest source of the variations in $C_a(f_D)$.

C.2. Experiments

$C_a(f_D)$ can be determined by monitoring the amplitude of the signal sampled with the ADC card (Figure C.1) while varying the Doppler frequency. During this experiment, the intensity of the incoming optical signal should be kept constant, as well as the amplification factors inside the electronic equipment.

The optical signal is generated by positioning a rotating surface in the measurement volume, or by placing the measurement volume in a liquid with seeding particles at a point where the velocity is constant in time. The Doppler frequency can be varied by changing the velocity, the probe orientation and/or the preshift frequency. The intensity can be kept constant by ensuring the surface position and passage of seeding particles is not changed if the velocity is changed. To ensure this is the case, two different experiments are performed and the results are compared:

- Histograms of the amplitudes of bursts in a laminar flow are determined with the use of the wavelet processor and compared for different frequencies.
- The amplitude of the signal originating from a rotating disk is measured while its velocity is varied.

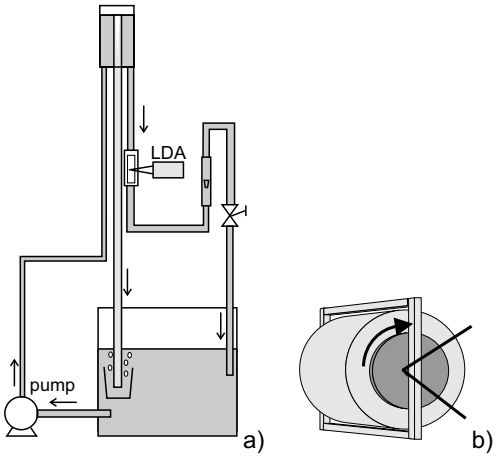

Figure C.2.: Setups. a) Laminar flow experiment b) Rotating disk experiment

C.2.1. Laminar flow experiment

The setup is shown in Figure C.2a and uses an overflow system to keep the velocity constant. The pipe diameter is 0.05 m, the liquid used is a glycerol-water mixture with viscosity close to 35 mPas, ensuring laminar flow at a constant velocity in the range 0-0.2 m/s. The open nature of the system, the high viscosity in combination with the downflow result in problems with tiny bubbles (smaller than 0.5 mm). These bubbles present a second source of scattered light. If the velocity is varied, their size and quantity change, and thus the amplitude of the optical signal is velocity dependent. For this reason, the velocity is kept constant and the Doppler frequency is varied by changing the preshift frequency (0, 100, 200, 500 and 1000 kHz) and the backscatter probe orientation. This way, the Doppler frequencies 100, 200, 300, 400, 600 and 900 are obtained. The amount of small bubbles is minimized, measurements are started after five hours and are performed in a short period, such that the size and concentration of the bubbles have reached an equilibrium and do not change during the experiment.

By sampling and wavelet processing, the amplitudes $A(f_D, i)$ of the bursts are obtained as a function of the Doppler frequency f_D. Next, the histograms of $A(f_D, i)$ are determined, an example is shown in Figure C.3. 600 kHz is taken as a reference frequency. $C_a(f_D)$ is estimated by finding the value where the histograms of $A(600\text{kHz}, i)$ and $C_a(f_D)A(f_D, i)$ have the best match (an example for 400 kHz is given in Figure C.3).

C.2.2. Rotating disk

The measurement volume is aligned on a rotating disk (Figure C.2b). The alignment of the disk and the measurement volume changes slightly when the velocity is changed. This leads to changes in the strength of the optical signal. These changes are minimized by pressing an object against the axis of rotation. In addition, the measurement is performed close to the axis to reduce variations in time due to small changes in the orientation of the disk. The standard

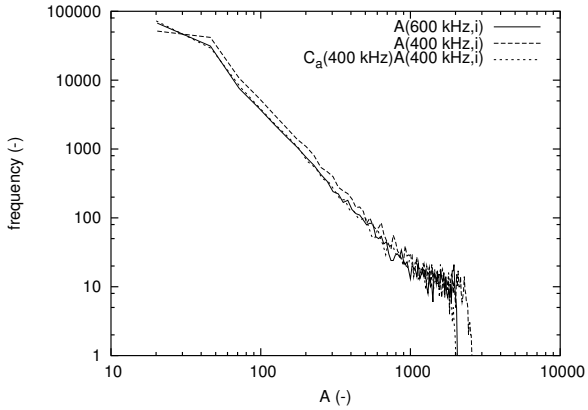

Figure C.3.: Histograms of burst amplitudes for laminar flow experiment.

deviation of the sampled LDA signal is used to determine $C_a(f_D)$. Contributions due to noise are subtracted. A simple test is performed to check the constantness of this standard deviation with time. Initially the laser beams are blocked, next the blockage is removed and the standard deviation is monitored. This shows that the standard deviation is constant for 10-15 seconds, after which both sudden and smooth decreases are observed. These are probably due to automatic stepwise changes in the gain of some amplifiers, as well as possible slow changes in the sensitivity of the photomultiplier tube. After a short period of renewed beam blockage, the same initial high values are obtained. For this reason, the following protocol is used:

- The laser beams are blocked with an object during 15 seconds. This way, all gains and sensitivities are reset to the same initial values. During this time, the speed of the disk is adjusted and has enough time to reach a constant value.
- The object is removed, the standard deviation is determined during 5 seconds. The Doppler frequency is determined from the signal. The laser beams are blocked again after this period.
- The procedure is repeated with different velocities; every fifth measurement the same reference velocity is used to correct for small drifts.

C.2.3. Amplification factors

Figure C.4 shows the results for the laminar flow experiment and the rotating disk. For the rotating disk, two different preshift frequencies were used. The results have been scaled since different reference frequencies were used. For comparison the root of the noise spectrum is shown. This spectrum was determined from spectra of two laminar flow LDA signals with distinct Doppler frequencies, such that contributions due to bursts could be removed. The agreement between the noise spectra, the laminar flow experiment and the rotating disk is good. This suggests that the input noise has a white noise character, and that the noise spectrum is

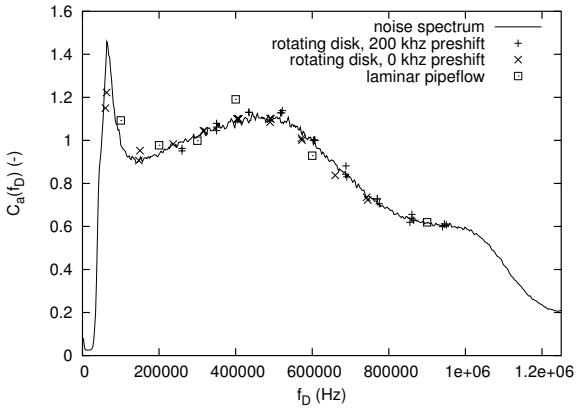

Figure C.4.: Amplification factors $C_a(f_D)$ for various experiments. A comparison with the scaled root of the noise spectrum is shown.

proportional to the amplification function $C_a(f_D)$ of the equipment. This means that $C_a(f_D)$ can also be determined from noise spectrum measurements, greatly facilitating the measurement procedure.

The variations in $C_a(f_D)$ are quite strong over the range 100-1000 kHz. The amplitude of bursts with Doppler frequency 800 kHz is generally a factor 0.6 smaller than bursts with Doppler frequency 500 kHz. Results for the second channel are identical. This explains at least part of the biases observed in the tests where the probe orientation is reversed.

C.2.4. IFA-750 amplifier and bandpass filters

In order to find the electronic component responsible for the strongly non-uniform amplification $C_a(f_D)$ is compared with the amplification in the IFA-750 amplifier and bandpass filter (Figure C.5). This shows that this component is responsible to a large extent for the problem. Different bandpass ranges (30-300 kHz, 300-3000 kHz) exhibit similar behavior. For this reason, dedicated electronic amplifiers and bandpass filters have been built for use with the wavelet processor measurements. The use of these filters ensures a much smaller drop in the amplification factor over the relevant ranges (see Figure C.5, where the relevant range is 300-800 kHz).

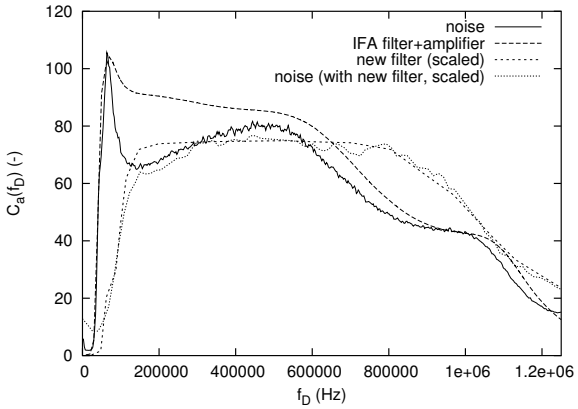

Figure C.5.: Comparison of amplification factors $C_a(f_D)$, the amplification of IFA-750 and the new filter.

List of symbols

Roman symbols

A	amplitude	random
C_a	amplification factor	-
f_0	reference frequency	s^{-1}
f_D	Doppler frequency	s^{-1}
I	intensity	random
N	noise	-
S	signal	-
SNR	signal-to-noise ratio	-
$SNR_{threshold}$	validation threshold signal-to-noise ratio	-

D. The influence of the bubbles on the data rate for Laser Doppler Anemometry in bubbly flow

For the measurement of liquid velocities with LDA, a sufficiently high data rate is essential to get detailed information about the hydrodynamics. In a bubbly flow, much light is blocked due to the presence of the bubbles. This blockage is a strong function of the void fraction α, the bubble size and the path length l of laser beam from the wall to the measurement volume. Measurements further away from the wall, and at higher void fractions are, therefore, severely hampered. The present appendix studies, therefore, how the data rate for LDA in bubbly flow varies with α and l.

The following constraints have to be satisfied in order to get a velocity realization if a particle crosses the measurement volume. First, the laser beams that form the measurement volume should not be blocked in between the measurement volume and the wall. Second, enough light should be able to pass back to the detecting fiber to allow detection of the burst. The influence of these points on the data rate is discussed in the present appendix, starting with the second.

Signal to noise ratio: detection of scattered light

If the measurement volume exists and a particle crosses the measurement volume, light is scattered. This light is collected by the receiving lens and focused on the receiving fiber. Apart from this desired source of light, several other sources of undesired light signals can be identified. If particles pass through the laser beams at positions close to the measurement volume, their light will also be focused on the receiving fiber (i.e. they are inside the 'detection volume', see Figure 6.15(b)). This produces 'noise bursts' with a Gaussian envelope. Second, at the moments when measurements are possible, i.e. when the measurement volume exists, the light reflected by bubbles will always originate from locations behind the measurement volume. This light has, therefore, to cover distances larger than the light from the measurement volume. In addition, contaminations in the water crossing the beams further away from the measurement volume, and light reflected by bubbles produce a 'background' noise level. All noise contributions hamper the detection of coherent bursts, and tests show that the 'noise bursts' produce the major contribution.

If the void fraction, or the distance of the measurement volume to the wall is increased, the amount of light that reaches the detection fiber from the measurement volume decreases. The decrease is, however, approximately similar for both the coherent bursts, the 'noise' bursts and the reflections from bubbles at the moments when the measurement volume exists. The 'background' noise level is found to vary slightly with the distance to the wall, but no clear trend is observed. In addition, the contribution of the background noise level to the total noise level is

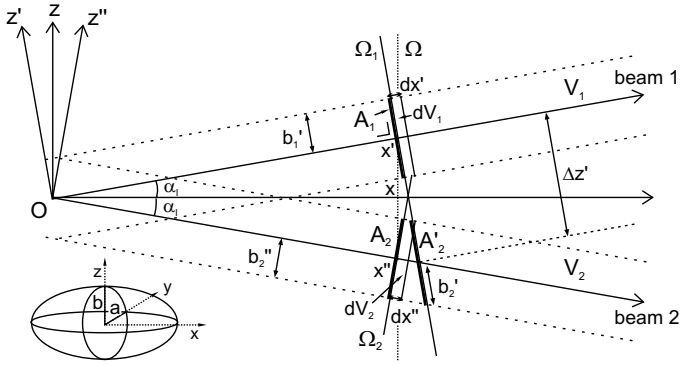

Figure D.1.: Dual beam geometry for the axial component

limited. Its influence on the data rate is, therefore, also small. Consequently, the effect on the data rate is small if the thresholds for detection are adjusted accordingly.

Summarizing, the blockage of light from the measurement volume travelling to the receiving fiber has only a minor influence on the data rate.

Blockage of laser beams

The blockage of the laser beams, however, does play an important role. If the void fraction or the distance to the wall is increased, the probability decreases that the path of the laser beam is not blocked by one or more bubbles. Ohba et al. (1976) showed that this probability decreases exponentially. If the data rate without bubbles is $\dot{N}_0$, the data rate $\dot{N}$ with the bubbles present is given by:

$$\frac{\dot{N}}{\dot{N}_0} = exp(-c\frac{\alpha l}{\overline{d_{SV}}}) \tag{D.1}$$

with $\overline{d_{SV}}$ the mean Sauter diameter (for its calculation the volume-equivalent diameter and the diameter based on the cross-sectional area perpendicular to the beam are used). The coefficient c is $3/2$ for a single beam (Ohba et al. (1976)) and 3 for two beams with independent blockage. Close to the measurement volume, the distance between the beams is smaller than the bubble diameter, and the beam blockage is no longer independent. Consequently the decay is slower. Mudde et al. (1998) report a coefficient c value of 2.4.

In order to accurately predict the decay of the data rate, the blockage of both beams by a single bubble has to be taken into account. Approximately, the situation can be modeled as is shown in Figure D.1. The measurement volume is located in the origin O. Ellipsoidal bubbles without inclination (non-wobbling) are considered, with semi-major axis length a, and semi-minor axis length b. If the center of a bubble is located in the volume V_i, beam i is blocked. These volumes V_i have ellipsoidal cross-sections A_i, i.e. the projection of the bubble if it is observed along the laser beam i. These ellipsoids have dimensions a and b_1' (beam 1) and a and b_2'' (beam 2). Since the bubbles are not inclined, $b_1' = b_2'' = \sqrt{a^2 sin^2(\alpha_l) + b^2 cos^2(\alpha_l)}$.

A period with duration T_0 is considered. $T(x)$ is the amount of time in this period during

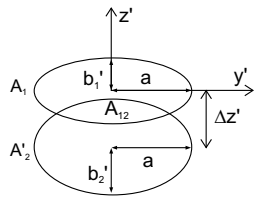

Figure D.2.: Overlapping ellipsoids.

which neither of the beams is blocked in the region between the measurement volume and the plane Ω, which is located at a distance x from the measurement volume. The blocking is modeled by stating that beam 1 is blocked in the portion between x' and $x' + dx'$ if a bubble center is present inside the volume dV_1. The probability that this occurs is given by:

$$P_1(x')dx' = \frac{3}{2}\alpha\frac{d_A^2}{d_V^3}dx' \tag{D.2}$$

with $d_A^2 = 4ab_1'$. Due to symmetry and since $dx' = dx''$, the probability that beam 2 is blocked is identical: $P_1(x')dx' = P_2(x'')dx''$. Part of the volume dV_1 may be located inside volume V_2, i.e. bubbles that are located in this part of the volume block both beams and should therefore be excluded for one of the beams. The overlap in the volumes is determined by calculating the overlap A_{12} of A_1 and A_2', the cross-section of V_2 and plane Ω_1. This is shown in Figure D.2. The dimensions of A_2' are given by: $b_2' = b_2''/cos(2\alpha_l)$ and $\Delta z' = x'tan(2\alpha_l)$. The probability density of blockage of one beam or both beams is given by:

$$P_{blockage}(x') = P_1(x')(2 - f_o(x')) = \frac{3}{2}\alpha\frac{d_A^2}{d_V^3}(2 - f_o(x'))dx' \tag{D.3}$$

with $f_o(x') = A_{12}(x')/A(x')$ and ignoring second order terms. We get:

$$\frac{\dot{N}}{\dot{N}_0} = \frac{T(l)}{T_0} = e^{-\frac{3}{2}\alpha\frac{d_A^2}{d_V^3}\int_0^{l/cos(\alpha_l)}(2-f_o(x'))dx'} \tag{D.4}$$

which is solved numerically.

Figure D.3 shows the prediction by equation D.4 for both the axial and tangential component for a void fraction of 15.6%, probe focal length of 35 cm, beam distance 5 cm and bubbles with diameter 4 mm and aspect ratio 0.65. The ellipsoidal shape of the bubbles results in a smaller loss in data rate for the tangential component. As expected, in the limit of short length l, the slope corresponding to a single beam is found, in the limit of long l the slope of two independent beams is found. Obviously, if the model in equation D.1 is used to fit the data, a coefficient c somewhere in between 1.5 and 3.0 will be found, the value depending on the fit range, lens focal length, bubble size, etc. This explains the value of 2.4 which was reported by Mudde et al. (1998). The value of 1.66, reported by Kulkarni et al. (2001a) is very low, considering the results presented here. The authors use forward scatter, in which case it may be harder to distinguish individual bursts, i.e. the data rate may not represent very well the number of bursts due to

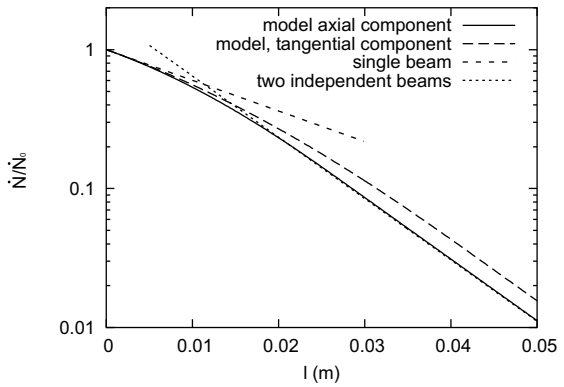

Figure D.3.: Data rate model.

particles passing the measurement volume.

Figure D.4 shows the experimental data rate for the axial component for the 12.2 and 35 cm focal length lenses, for the IFA-750 processor and the wavelet processor, and compares these with model predictions. The experiment was performed for a void fraction of 15.6% and bubbles of 4 mm. The results show that close to the wall a smaller slope is obtained with the 35 cm lens. This is caused by the smaller beam distance close to the measurement volume, i.e. over a longer distance the blocking resembles that of a single beam. Consequently, the data rate attenuation is clearly relatively smaller at larger distances from the wall for the 35 cm lens than for the 12 cm lens. Further away from the wall the data rate decreases according to a straight line on a log scale, the behavior is similar to that of two beams which are blocked independently. The slope according to the model is somewhat smaller than that observed in the experiments. This is probably due to deviations in the bubble diameters, orientations and shapes, which are obviously not constant in the experiment.

List of symbols

Roman symbols

a	bubble semi-major axis length	m
b	bubble semi-minor axis length	m
c	constant describing decay data rate	-
d_{SV}	mean Sauter bubble diameter	m
d_A	area equivalent bubble diameter (in direction laser beam)	m
d_V	volume equivalent bubble diameter (in direction laser beam)	m
f_o	function decribing overlap blockage of beams	-
l	distance measurement volume to the wall	m
$\dot{N}$	mean data rate	s^{-1}
$\dot{N}_0$	mean data rate at wall	s^{-1}

P_1	probability bubble blocking beam 1 at distance x'	-
$P_{blockage}$	probability blockage beam 1 and/or 2 at x'	
$T(x)$	average time at x that neither of the beams is blocked	s
T_0	period of measurement	s
V	small volume considered for bubble presence	m^3
x	horizontal coordinate	m
y	horizontal coordinate	m
z	axial coordinate	m

Greek symbols

α	void fraction	-
α_l	inclination laser beam	rad

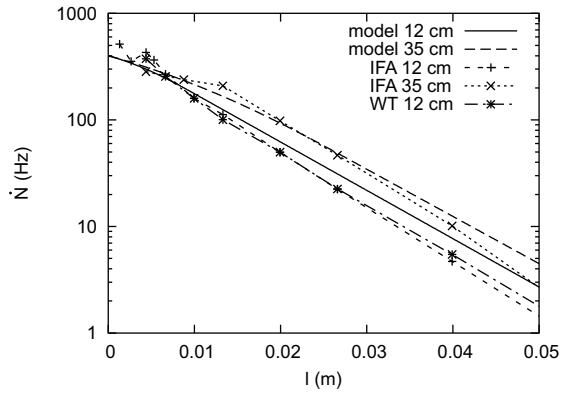

Figure D.4.: Comparison of the change of the data rate with l for the axial component for both experiments and the model. The model data rates at the wall are set to 400 Hz.

E. Experimental techniques

The present appendix provides a description of various practical aspects of the application of the experimental techniques that have been used in the investigations reported in this thesis.

E.1. Laser Doppler Anemometry

The present section describes the LDA technique: the equipment that is used and the data processing that is performed before calculating means, standard deviations and probability density functions. For more general information about LDA, the reader is refered to Albrecht et al. (2003).

The LDA equipment consists of a 4W Spectra-Physics Ar+ laser and a TSI 9201 colorburst multicolor beam separator. Beam pairs are focused using a backscatter probe with a lens of 0.122 m focal length. Detected light is sent to a TSI 9230 colorlink. The axial component is determined with green (λ=514.5 μm) beams, the tangential component using blue (λ=488 μm) beams. The fringe spacings are 1.28 μm (green channel) and 1.22 μm (blue channel). For the measurements in the homogeneous regime and relatively mild structures, a preshift frequency of 500 kHz and bandpass filter range 100-1000 kHz has been used. For measurements in the heterogeneous regime, a preshift frequency of 1 MHz and bandpass filter range of 300-3000 kHz are used. Bursts are processed with the IFA-750 (TSI) processor, controlled by a 486 PC. For test measurements, comparisons have been made with the results of the wavelet processor (chapter 6). The comparison has been used to get improved settings, understanding and data processing. For the majority of the experiments, the use of the wavelet processor is quite impractical due to the huge amounts of data and processing times involved. The flow is seeded with glass particles which were neutrally buoyant and had 10 μm size. The time series obtained has typical lengths of 900 s (cylindrical column) and 300 s (rectangular column).

The short focal length of 0.122 m is used to enable measurements close to the wall (i.e. at distances smaller than 5 mm). With longer focal lengths, strong preshift frequency bleeding is encountered: light is scattered at the positions where the beams cross the vessel walls - close to the wall some of this light is focused on the receiving fiber of the backscatter probe. Shorter focal lengths strongly reduce the amount of focused light.

A number of data-processing steps have been performed on the data before calculating the velocity moments. The presence of the bubbles leads to increased noise levels compared with LDA in single phase flows. The higher noise levels lead to the occurrence of multiple validation, i.e. the multiple detection of the burst caused by a single particle. This may lead to inaccurate velocity estimates or even outliers. The effect has been handled by first rejecting velocity realizations with $|u_i - \overline{u_i}| > 4\sigma$ (σ being the standard deviation of the signal). Next, bursts have been removed which follow other bursts within an interval of 1 ms (see section 6.6.4 for motivation). The effect of these operations on the tangential velocity component is very small: mean velocities

typically decrease by 0.003 m/s, variances increase by typically 2%. The effect on the axial velocity variances is somewhat bigger: these increase by typically 6-9%.

In a time varying flow the instantaneous data rate is generally correlated with the instantaneous liquid velocity. As a result, the higher velocities are usually over-represented in the time signal and the velocity moments are biased if simple arithmetic averaging is used: velocity bias occurs. The results in chapter 6.6.4 indicate the importance of velocity bias correction. The velocity bias correction is performed by so-called $2D^+$ weighing: inversely weighing the data with the velocity (Tummers (1999)). Since only two components are known, the magnitude of the third component is estimated from the variance of the second component: the weighing factor is $\omega = 1/\sqrt{u^2 + v^2 + (d_m/l_m)^2\overline{v'^2}}$ with d_m/l_m the diameter-to-length ratio of the ellipsoidal measurement volume. The use of only two components is justified since the magnitude of the radial and tangential fluctuations will be close, and the influence of the third component is small since d_m/l_m is small. Due to inaccuracies in the burst processing, the axial velocity u and the tangential velocity v are never measured at the exact same time instants. For this reason, pairs of axial and tangential velocity realizations are searched which have arrival times inside coincidence windows with length of 300 μs. This time roughly corresponds to the mean transit time of the seeding particles. Unfortunately, the use of this coincidence window results in a further decrease of the datarate of the velocity signal.

E.2. Particle Image Velocimetry/ Particle Tracking Velocimetry

The large scale structures in the pseudo-2D column can be studied very well with the use of Particle Image Velocimetry (PIV) and Particle Tracking Velocimetry (PTV). For more details about these techniques, the reader is refered to, e.g., Raffel et al. (1998). A CCD camera (Dalsa Inc) with resolution of 512x512 is used to record images of the flow. The lower area (0<z<0.7m) of the column is recorded in two steps, each step imaging an area of 0.24mx0.35m, providing a resolution of 0.64 mm/pixel. Both the PIV and PTV analyses have been performed with the use of DaVis processing software (LaVision). Sequences of images of the bubble motion are recorded and PIV is used to determine the bubble velocities from these sequences. Illumination from the rear is used to obtain bubble shadows over a large area of the column (Figure E.1). This leads to averaging of the bubble velocity over the depth of the column, but does not lead to problems since only large scale structures have to be resolved. Binary images of the bubbles are obtained by applying a threshold algorithm to the greyscale images, from the subsequent images the velocities are obtained using PIV. Interrogation areas of 32x32 pixels have been used with 50% overlap. 50 subsequent images of the bubbly motion have been used (frame rate 150 Hz), the velocities obtained from these images have been averaged. The total time of the image sequence corresponds to 0.33 second, therefore the information about the large structures is preserved since these have a much longer timescale.

The liquid flow is determined by putting tracers in the liquid. The tracer particles need to be distinguished from the bubbles before the PTV algorithms are used. The separation is based on a threshold applied to the greyscales in the image. This requires a large contrast between the shadows of the bubbles and the particles. This has been achieved by optimisation of the lighting conditions and selection of proper tracer particles. Relatively large particles have been selected to

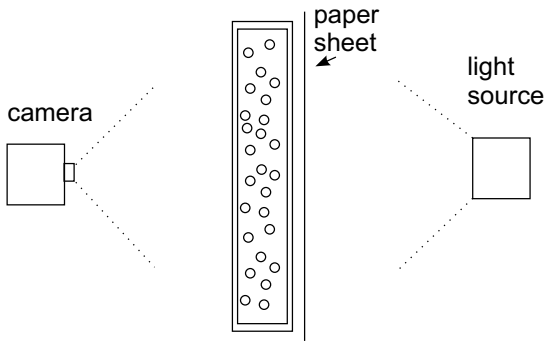

Figure E.1.: PIV/PTV setup.

provide sufficient contrast: polystyrene particles of approximately 2.5 mm size. These have been painted black to give further image contrast enhancement. The relatively large size also results in a homogeneous distribution over the column. Due to the large inertia of the particles only the largest structures were determined, the effect of the smaller structures was filtered out this way. The lighting gave the best contrast results in the center of the image, the corners had somewhat worse contrast. For the PTV analysis, images have been used that were obtained at a framerate of 30 Hz over a period of 0.6 s. Due to the presence of the bubbles, most tracer particles are only visible for short periods. Some particles are visible for long periods. Therefore the amount of vectors per area varies widely. For the sake of clarity, the vector field has been interpolated on a grid. Since the particles are not neutrally buoyant, but have a slip velocity of 0.09 m/s the results must be interpreted with care and give mainly a qualitative impression of the large structures. The PIV and PTV results have been obtained from sets of experiments performed on different days, therefore the vector fields do not correspond to the same time instants and the large scale structures are different.

E.3. Glass fiber probes

The time averaged void fraction is determined by using glass fiber probes (see chapter 3 for more details). Five fiber probes are used simultaneously to measure the void fraction over a line from the center of the column to the wall. If only a single probe would be used it is hard to investigate the uniformity of the flow due to drift of, e.g., the total flow to the sparger. This drift can be bigger than the small gas fraction variations near the column center obtained with uniform gas injection. The technique generally underestimates the void fraction for the present conditions by some 10-20%, depending on the type of signal processing that is used. Chapter 3 has shown that the so-called low level criterion should be used for the processing. This reduces the underestimation to about 10%. The remaining underestimation is caused by the interaction of the probe with the bubble as well as a perturbation of the flow field by the fiber and its holder. Chapter 3 showed that the dominant effects in the probe-bubble interaction are a reduction of the bubble velocity if it is pierced in the center, or a deformation if the bubble is pierced close

to its side. In addition, if the bubble is pierced under an angle the bubble path is altered. The latter two effects result in the underestimation. The underestimation has been quantified in chapter 3 for a bubble formed at a needle. The exact result was found to be dependent on the phase of the bubble oscillation. This phase differs widely in an actual bubble column, and, in addition, bubbles follow zig-zagging paths, leading to a distribution of angles under which the bubble is pierced. Moreover, the bubble motion is affected by the presence of the other bubbles. Consequently, it is not possible to estimate the total underestimation accurately with experiments of bubbles formed at a single needle. Therefore, an empirical correction factor is determined for each probe to compensate for the underestimation.

The void fraction $\alpha_{probe,i}$ is obtained for one probe by integration of the void fraction obtained over the entire column. The void fraction is measured over a horizontal line through the center at z=0.6 m and an axial line through the center (900 s/point). The radial integration is performed by assuming axial symmetry and by using linear interpolation. The void fraction in the region closest to the wall drops to zero, no measurements can be taken in this region due to the size of the probe holder. The void fraction profile is in this region therefore estimated with the assumption that bubbles are randomly distributed, but that bubbles cannot overlap with the wall. This gives an approximately linear profile over a region with thickness equal to the horizontal bubble axis length. For the integration in the axial direction, the assumption of isomorphic profiles is used. The correction factor has been determined for void fractions 6.2%, 7.7% and 11%, the mean has been taken for further use. The correction factors for the other probes have been determined by determining the differences between the underestimation for all probes from a measurement in a homogeneous region with the probes quite close to each other. The mean correction factor of all probes is around 1.1. Tests with experiments over several weeks show that the correction factors are quite reproducible (about 1% variation). The time series in the experiments for the probes have lengths of 1000 s. During this time, typically some 15000 bubbles have been collected per probe (α=20%).

List of symbols

d_m	diameter measurement volume	m
l_m	length measurement volume	m
u	axial liquid velocity	$m\ s^{-1}$
v	tangential liquid velocity	$m\ s^{-1}$
z	axial coordinate	m
α	void fraction	-
α_{probe}	average void fraction entire bubble column from probe measurements	-
λ	laser light wavelength	m
σ	standard deviation	
ω	weight factor velocity bias correction	-

Bibliography

Adrian, R. and Yao, C. (1987). Power spectra of fluid velocities measured by laser doppler velocimetry. *Exp. Fluids*, 5:17–28.

Albrecht, H., Borys, M., Damaschke, N., and Tropea, C. (2003). *Laser Doppler and Phase Doppler Measurement Techniques*. Springer-Verlag.

Antal, S., Lahey, R., and Flaherty, J. (1991). Analysis of phase distribution in fully developed laminar bubbly two phase flow. *Int. J. Multiphase Flow*, 17:635–652.

Bakker, A. (1992). *Hydrodynamics of stirred gas-liquid dispersions*. PhD thesis, Delft University of Technology.

Barnea, E. and Mizrahi, J. (1973). A generalized approach to the fluid dynamics of particulate systems. *Chem. Eng. J.*, 5:171–189.

Barrau, E., Rivière, N., Poupot, C., and Cartellier, A. (1999). Single and double optical probes in air-water two-phase flows: real time signal processing and sensor performance. *Int. J. Muliphase Flow*, 25:229–256.

Becker, S., Sokolichin, A., and Eigenberger, G. (1994). Gas-liquid flow in bubble columns and loop reactors: part II. comparison of detailed experiments and flow simulations. *Chem. Eng. Sci.*, 49:5747–5762.

Benedict, L., Nobach, H., and Tropea, C. (2000). Estimation of turbulent velocity spectra from laser doppler data. *Meas. Sci. Technol.*, 11:1089–1104.

Bhaga, D. and Weber, M. (1980). In-line interaction of a pair of bubbles in a viscous liquid. *Chem. Eng. Sci.*, 35:2467–2474.

Bhavaraju, S., Russell, T., and Blanch, H. (1978). The design of gas sparged devices for viscous liquid systems. *AIChE J.*, 24:454–466.

Bhole, M. and Joshi, J. (2005). Stability analysis of bubble columns: predictions for regime transition. *Chem. Eng. Sci.*, 60:4493–4507.

Biesheuvel, A. and Gorissen, W. (1990). Void fraction disturbances in a uniform bubbly fluid. *Int. J. Multiphase Flow*, 16:211–231.

Bos, R., de Waele, S., and Broersen, P. (2002). Autoregressive spectral estimation by application of the Burg algorithm to irregularly sampled data. *IEEE T. Instrum. Meas.*, 51:1289–1294.

Britz, D. and Antonia, R. (1996). A comparison of methods of computing power spectra of LDA signals. *Meas. Sci. Technol.*, 7:1042–1053.

Broersen, P. (2002). Automatic spectral analysis with time series models. *IEEE T. Instrum. Meas.*, 51:211–216.

Broersen, P. (2005). Time-series analysis for irregularly sampled data. In *Proc. IFAC World Congress (Prague)*. paper 1696.

Broersen, P., de Waele, S., and Bos, R. (2000). The accuracy of time-series analysis for laser doppler velocimetry. In *Proc. 10th int. symposium on applications of laser techniques to fluid mechanics (Lisbon)*.

Broersen, P., de Waele, S., and Bos, R. (2004). Autoregressive spectral analysis when observations are missing. *Automatica*, 40:1495–1504.

Brücker, C. (1999). Structure and dynamics of the wake of bubbles and its relevance for bubble interaction. *Phys. Fluids*, 11:1781–1796.

Buchholz, M. and Auracher, H. (2002). Improved optical probes and their validation for local measurements in two phase flow. In *Proc. of the German-Japanese workshop on Multiphase flow, Karlsruhe, Germany, August 25-27 2002*.

Bunner, B. and Tryggvason, G. (2002). Dynamics of homogeneous bubbly flows. part 2. velocity fluctuations. *J. Fluid Mech.*, 466:53–84.

Burgess, J. and Calderbank, P. (1975). The measurement of bubble parameters in two-phase dispersions. 1: The development an improved technique. *Chem. Eng. Sci.*, 30:743–750.

Camarasa, E., Vial, C., Poncin, S., Wild, G., Midoux, N., and Bouillard, J. (1999). Influence of coalescence behaviour of the liquid and of gas sparging on hydrodynamics and bubble characteristics in a bubble column. *Chem. Eng. Process.*, 38:329–344.

Camussi, R. and Guj, G. (1997). Orthonormal wavelet decomposition of turbulent flows: intermittency and coherent structures. *J. Fluid Mech.*, 348:177–199.

Camussi, R. and Verzicco, R. (2004). Temporal statistics in high Rayleigh number convective turbulence. *Eur. J. Mech. B/Fluids*, 23:427–442.

Carrica, P., Sanz, D., Delgadino, G., Zanette, D., and Marco, P. D. (1995). A contribution to uncertainties estimation of local void fraction measurements in gas-liquid flows. In Celata, G. and Shah, R., editors, *Two-Phase Flow Modelling and Experimentation 1995*, pages 709–714. ETS Pisa.

Cartellier, A. (1990). Optical probes for local void fraction measurements: characterization of performance. *Rev. Sci. Instrum.*, 61(2):874–886.

Cartellier, A. (1992). Simultaneous void fraction measurement, bubble velocity, and size estimate using a single optical probe in gas-liquid two-phase flows. *Rev. Sci. Instrum.*, 63:5442–5453.

Cartellier, A. (2001). Optical probes for multiphase flow characterization: some recent improvements. *Chem. Eng. Technol.*, 24:535–538.

Cartellier, A. and Achard, J. (1991). Local phase detection probes in fluid/fluid two-phase flows. *Rev. Sci. Instrum.*, 62:279.

Cartellier, A. and Barrau, E. (1998a). Monofiber optical probes for gas detection and gas velocity measurements: conical probes. *Int. J. Multiphase Flow*, 24:1265–1294.

Cartellier, A. and Barrau, E. (1998b). Monofiber optical probes for gas detection and gas velocity measurements: optimised sensing probes. *Int. J. Multiphase Flow*, 24:1295–1315.

Chen, R., J., J. R., and Fan, L.-S. (1994). Flow structure in a three-dimensional bubble column and three-phase fluidised bed. *AIChE J.*, 40:1093–1104.

Chesters, A. (1977). An analytical solution for the profile and volume of a small drop or bubble symmetrical about a vertical axis. *J. Fluid Mech.*, 81:609–624.

Chuang, S. and Goldschmidt, V. (1970). Bubble formation due to a submerged capillary tube in quiescent and coflowing streams. *J. Basic Eng.*, 92:705–711.

Clift, R., Grace, J., and Weber, M. (1978). *Bubbles, drops and particles*. Academic Press.

Cui, Z. and Fan, L. (2004). Turbulence energy distributions in bubbling gas-liquid and gas-liquid-solid flow systems. *Chem. Eng. Sci.*, 59:1755–1766.

Daalmans, A. (2005). Laser-doppler anemometry measurements of particle-driven secundary flow in turbulent horizontal pipe-flow. Master's thesis, Delft University of technology.

Davidson, J. and Schüler, B. (1960a). Bubble formation at an orifice in a viscous liquid. *Trans. Inst. Chem. Engrs.*, 38:144–154.

Davidson, J. and Schüler, B. (1960b). Bubble formation at an orifice in an inviscid liquid. *Trans. Inst. Chem. Engrs.*, 38:335–342.

De Vries, A. (2001). *Path and wake of a rising bubble*. PhD thesis, Twente University.

Deckwer, W. (1992). *Bubble column reactors*. John Wiley and Sons.

Dhotre, M., Ekambara, K., and Joshi, J. (2004). CFD simulation of sparger design and height to diameter ratio on gas gold-up profiles in bubble column reactors. *Exp. Therm. Fluid Sci.*, 28:407–421.

Drahos, J., Bradka, F., and Puncochár, M. (1992a). Fractal behavior of pressure fluctuations in a bubble column. *Chem. Eng. Sci.*, 47:4069–4075.

Drahos, J., Zahradník, J., Fialová, M., and Bradka, F. (1992b). Identification and modelling of liquid flow structures in bubble column reactors. *Chem. Eng. Sci.*, 47:3313–3320.

Drahos, J., Zahradník, J., Puncochár, M., Fialová, M., and Bradka, F. (1991). Effect of operating conditions on the characteristics of pressure fluctuations in a bubble column. *Chem. Eng. Process.*, 29:107–115.

Fan, L.-S. and Tsuchiya, K. (1990). *Bubble wake dynamics in liquids and liquid-solid suspensions*. Butterworth-Heinemann.

Farge, M. (1992). Wavelet transforms and their applications to turbulence. *Annu. Rev. Fluid Mech.*, 24:395–457.

Farge, M., Kevlahan, N., Perrier, V., and Goirand, E. (1996). Wavelets and turbulence. *Proc. IEEE*, 84(4):639–669.

Fordham, E., Holmes, A., Ramos, R., Simonian, S., Huang, S.-M., and Lens, C. (1999). Multiphase-fluid discrimination with local fibre-optical probes: I. liquid/liquid flows. *Meas. Sci. Technol.*, 10:1329–1337.

Franz, K., Börner, T., Kantorek, H., and Buchholz, R. (1984). Flow structures in bubble columns. *Ger. Chem. Eng.*, 7:365–374.

Frijlink, J. (1987). *Physical aspects of gassed suspension reactors*. PhD thesis, Delft University of Technology.

Fujiwara, A., Y.Danmoto, Hishida, K., and Maeda, M. (2004). Bubble deformation and flow structure measured by double shadow images and PIV/LIF. *Exp. Fluids*, 36:157–165.

Garnier, C., Lance, M., and Marié, J. (2002). Measurement of local flow characteristics in buoyancy-driven bubbly flow at high void fraction. *Exp. Therm. Fluid Sci.*, 26:811–815.

Geary, N. and Rice, R. (1991). Bubble size prediction for rigid and flexible spargers. *AIChE J.*, 37:161–168.

Groen, J. (2004). *Scales and structures in bubbly flows*. PhD thesis, Delft University of Technology.

Groen, J., Mudde, R., and van den Akker, H. (1999). On the application of LDA to bubbly flow in the wobbling regime. *Exp. Fluids*, 29:435–449.

Guet, S. (2004a). Personal communication.

Guet, S. (2004b). *Bubbly size effect on the gas-lift technique*. PhD thesis, Delft University of Technology.

Guet, S., Fortunati, R., Mudde, R., and Ooms, G. (2003). Bubble velocity and size measurement with a four-point optical fiber probe. *Part. Part. Syst. Char.*, 20:219–230.

Haque, M., Nigam, K., and Joshi, J. (1986). Optimum gas sparger design for bubble columns with a low height-to-diameter ratio. *Chem. Eng. J.*, 33:63–69.

Harper, J. (1997). Bubbles rising in line: why is the first approximation so bad? *J. Fluid Mech.*, 351:289–300.

Hebrard, G., Bastoul, D., Roustan, M., Comte, M., and Beck, C. (1999). Characterization of axial liquid dispersion in gas-liquid and gas-liquid-solid reactors. *Chem. Eng. J.*, 72:109–116.

Hills, J. (1974). Radial non-uniformity of velocity and voidage in a bubble column. *Trans. Inst. Chem. Eng.*, 52:1–9.

Hooper, A. (1986). A study of bubble formation at a submerged orifice using the boundary element method. *Chem. Eng. Sci.*, 41(7):1879–1890.

Ityokumbul, M. T. (1993). Effect of vertical misalignment of liquid dispersion in bubble columns. *Chem. Eng. J.*, 53:151–153.

Jenson, L. (1992). LDV digital signal processor based on autocorrelation. In *Proc. 8th Intl. Symp. On Appl. Of Laser Techniques to Fluid Mechanics, Lisbon, Portugal*.

Johnson, T. and Patel, V. (1999). Flow past a sphere up to a Reynolds number of 300. *J. Fluid Mech.*, 378:19–70.

Joshi, J. and Sharma, M. (1979). A circulation model for bubble columns. *Trans. Inst. Chem. Eng.*, 57:244–251.

Joshi, J., Vitankar, V., Kulkarni, A., Dhotre, M., and Ekambara, K. (2002). Coherent flow structures in bubble column reactors. *Chem. Eng. Sci.*, 57:3157–3183.

Karamanev, D. (1994). Rise of gas bubbles in quiescent liquids. *AIChE J.*, 40(8):1418–1421.

Katz, J. and Meneveau, C. (1996). Wake-induced relative motion of bubbles rising in line. *Int. J. Multiphase Flow*, 22:239–258.

Khurana, A. and Kumar, R. (1969). Studies in bubble formation - III. *Chem. Eng. Sci.*, 69(24):1711–1723.

Kiambi, S. ., Duquenne, A., Dupont, J.-B., C.Colin, Risso, F., and Delmas, H. (2003). Measurements of bubble characteristics: comparison between double optical probe and imaging. *Can. J. Chem. Eng.*, 81:764–770.

Kiambi, S., Duquenne, A., Bascoul, A., and Delmas, H. (2001). Measurements of local interfacial area: application of bi-optical fibre technique. *Chem. Eng. Sci.*, 56:6447–6453.

Krepper, E., Vanga, B. R., Prasser, H.-M., and de Bertodano, M. L. (2004). Experimental and numerical studies of void fraction distribution in rectangular bubble columns. In *Proceedings of the 3rd international symposium on two-phase flow modelling and experimentation*.

Kulkarni, A. (2005a). Personal communication.

Kulkarni, A. (2005b). Effect of sparger design on the local flow field in a bubble column - analysis using LDA. *Chem. Eng. Res. Des.*, 83(A1):59–66.

Kulkarni, A. and Joshi, J. (2004a). The lift force on bubbles in a swarm: experimental analysis using LDA. In *Proc. 3rd int. symp. on two-phase flow modelling and experimentation.*

Kulkarni, A. and Joshi, J. (2004b). Simultaneous measurement of flow pattern and mass transfer coefficient in bubble columns. *Chem. Eng. Sci.*, 59:271–281.

Kulkarni, A., Joshi, J., Kumar, V., and Kulkarni, B. (2001a). Application of multiresolution analysis for simultaneous measurement of gas and liquid velocities and fractional gas hold-up in bubble column using LDA. *Chem. Eng. Sci.*, 56:5037–5048.

Kulkarni, A., Joshi, J., Kumar, V., and Kulkarni, B. (2001b). Identification of the principal time scales in bubble column by wavelet analysis. *Chem. Eng. Sci.*, 56:5739–5747.

Kulkarni, A., Joshi, J., Kumar, V., and Kulkarni, B. (2001c). Wavelet transform of velocity-time data for the analysis of turbulent structures in a bubble column. *Chem. Eng. Sci.*, 56:5305–5315.

Kulkarni, A., Joshi, J., and Ramkrishna, D. (2004). Determination of bubble size distributions in bubble columns using LDA. *AIChE J.*, 50:3068–3084.

Kumar, S., Moslemian, D., and Duducovic, M. (1997). Gas-holdup measurements in bubble columns using computed tomography. *AIChE J.*, 43:1414–1425.

Kyriakidis, N. and Kastrinakis, E. (1997). Bubbling from nozzles submerged in water: transitions between bubbling regimes. *Can. J. Chem. Eng.*, 75:684–691.

la Nauze, R. and Harris, I. (1972). On a model for the formation of gas bubbles at a single submerged orifice under constant pressure conditions. *Chem. Eng. Sci.*, 27:2102–2105.

Lamb, H. (1932). *Hydrodynamics.* Cambridge Univerity Press, sixth edition.

Lance, M. and Bataille, J. (1991). Turbulence in the liquid phase of a uniform bubbly air-water flow. *J. Fluid Mech.*, 222:95–118.

Lapin, A. and Lübbert, A. (1994). Numerical simulation of the dynamics of two-phase gas-liquid flows in bubble columns. *Chem. Eng. Sci.*, 49:3661–3674.

Lathouwers, D. (1999). *Modelling and simulation of turbulent bubbly flow.* PhD thesis, Delft University of Technology.

Léon-Becerril, E., Cockx, A., and Liné, A. (2002). Effect of bubble deformation on stability and mixing in bubble columns. *Chem. Eng. Sci.*, 57:3283–3297.

Léon-Becerril, E. and Liné, A. (2001). Stability analysis of a bubble column. *Chem. Eng. Sci.*, 56:6135–6141.

Liju, P.-Y., Machane, R., and Cartellier, A. (2001). Surge effect during the water exit of an axisymmetric body travelling normal to a plane interface: experiments and BEM simulation. *Exp. Fluids*, 31:241–248.

Lin, T.-J., Juang, R.-C., Chen, Y.-C., and Chen, C.-C. (2001). Predictions of flow transitions in a bubble column by chaotic time series analysis of pressure fluctuation signals. *Chem. Eng. Sci.*, 56:1057–1065.

Lomb, N. (1974). Least-squares frequency analysis of unequally spaced data. *Astrophys. Space Sci.*, 39:447–462.

Longuet-Higgins, M., Kerman, B., and Lunde, K. (1991). The release of air bubbles from an underwater nozzle. *J. Fluid Mech.*, 230:365–390.

Loubière, K. and Hébrard, G. (2003). Bubble formation from a flexible hole submerged in an inviscid liquid. *Chem. Eng. Sci.*, 58:135–148.

Lucas, D., Prasser, H.-M., and Manera, A. (2005). Influence of the lift force on the stability of a bubble column. *Chem. Eng. Sci.*, 60:3609–3619.

Lucas, G. and Mishra, R. (2005). Measurements of bubble velocity components in a swirling gas-liquid pipe flow using a local four-sensor conductance probe. *Meas. Sci. Technol.*, 16:749–758.

Luther, S., Rensen, J., and Guet, S. (2004). Bubble aspect ratio and velocity measurement using a four-point fiber-optical probe. *Exp. Fluids*, 36:326–333.

Mashiko, T., Tsuji, Y., Mizuno, T., and Sano, M. (2004). Instantaneous measurement of velocity fields in developed thermal turbulence in mercury. *Phys. Rev. E*, 68:036306.

Matovic, D. and Tropea, C. (1991). Spectral peak interpolation with application to LDA signal processing. *Meas. Sci. Technol.*, 2:1100–1106.

Mayo, Jr, W., Shay, M., and Ritter, S. (1974). Digital estimation of turbulence power spectra from burst counter LDV data. In *Proc. 2nd int. workshop on laser velocimetry (Purdue university)*, pages 16–26.

McCann, D. and Prince, R. (1969). Bubble formation and weeping at a submerged orifice. *Chem. Eng. Sci.*, 24:801–814.

McCann, D. and Prince, R. (1971). Regimes of bubbling at a submerged orifice. *Chem. Eng. Sci.*, 26:1505–1512.

Meneveau, C. (1991). Analysis of turbulence in the orthonormal wavelet representation. *J. Fluid Mech.*, 232:469–520.

Mishra, R., Lucas, G., and Kieckhoefer, H. (2002). A model for obtaining the velocity vectors of spherical droplets in multiphase flows from measurements using an orthogonal four-sensor probe. *Meas. Sci. Technol.*, 13:1488–1498.

Monahan, S. and Fox, R. (2005). Correlation estimator for two-channel non-coincidence laser-doppler-anemometer. In *Proc. 11th workshop on two-phase flow predictions (Merseburg, Germany)*.

Monahan, S., Vitankar, V., and Fox, R. (2005). CFD predictions for flow-regime transitions in bubble columns. *AIChE J.*, 51(6).

Moore, D. (1965). The velocity of rise of distorted gas bubbles in a liquid of small viscosity. *J. Fluid Mech.*, 23:749–766.

Mouza, A., Dalakoglou, G., and Paras, S. (2005). Effect of liquid properties on the performance of bubble column reactors with fine pore spargers. *Chem. Eng. Sci.*, 60:1465–1475.

Mudde, R. (2005). Gravity driven bubbly flows. *Annu. Rev. Fluid Mech.*, 37:393–423.

Mudde, R., Groen, J., and Van den Akker, H. (1997a). Liquid velocity field in a bubble column: LDA experiments. *Chem. Eng. Sci.*, 52:4217–4224.

Mudde, R., Groen, J., and Van den Akker, H. (1998). Application of LDA to bubbly flows. *Nucl. Eng. Des.*, 184:329–338.

Mudde, R., Lee, D., Reese, J., and L.-S., F. (1997b). Role of coherent structures on Reynolds stresses in a 2-D bubble column. *AIChE J.*, 43:913–926.

Mudde, R. and Saito, T. (2001). Hydrodynamic similarities between bubble column and bubbly pipe flow. *J. Fluid Mech.*, 437:203–228.

Mudde, R. and Simonin, O. (1999). Two- and three-dimensional simulations of a bubble plume using a two-fluid model. *Chem. Eng. Sci.*, 54:5061–5069.

Mudde, R. and Van den Akker, H. (1999). Dynamic behavior of the flow field of a bubble column at low to moderate gas fractions. *Chem. Eng. Sci.*, 54 (21):4921–4927.

Nievaart, V. (2000). Improvement and tailoring for near-wall turbulence measurements in a venturi. MSc thesis. Kramers laboratorium voor Fysische Technologie, Delft University of Technology.

Nobach, H. (2002a). Analysis of dual-burst laser doppler signals. *Meas. Sci. Technol.*, 13:33–44.

Nobach, H. (2002b). Local time estimation for the slotted correlation function of randomly sampled LDA data. *Exp. Fluids*, 32:337–345.

Nobach, H., Muëller, E., and Tropea, C. (1998a). Efficient estimation of power spectral density from laser Doppler anemometer data. *Exp. Fluids*, 24:499–509.

Nobach, H., Müller, E., and Tropea, C. (1998b). Correlation estimator for two-channel non-coincidence laser-Doppler-anemometer. In *Proc. 9th int. symposium on applications of laser techniques to fluid mechanics (Lisbon)*. paper 32.1.

Nobach, H. and van Maanen, H. (2001). LDA and PDA signal analysis using wavelets. *Exp. Fluids*, 30:613–625.

Oels, U., Lucke, J., Buchholz, R., and Schugerl, K. (1978). Influence of gas distributor type and composition of liquid on the behaviour of a bubble column bioreactor. *Germ. Chem. Eng.*, 1:115–129.

Oey, R. (2005). *Gas-liquid flows in a two-fluid formalism - modelling and validation of closure relations*. PhD thesis, Delft University of Tecnology.

Oguz, H. and Prosperetti, A. (1993). Dynamics of bubble growth and detachment from a needle. *J. Fluid Mech.*, 257:111–145.

Oguz, H. and Zeng, J. (1997). Axisymmetric and three-dimensional boundary integral simulations of bubble growth from an underwater orifice. *Eng. Anal. Bound. Elem.*, 19:319–330.

Ohba, K., Kishimoto, I., and Ogasawara, M. (1976). Simultaneous measurement of local liquid velocity and void fraction in bubbly flows using a gas laser- part I: principle and measurement principle. Technol. rep. no. 1328, Osaka University 27.

Park, Y., Tyler, A., and de Nevers, N. (1977). The chamber orifice interaction in the formation of bubbles. *Chem. Eng. Sci.*, 32:907–916.

Pinczewski, W. (1981). The formation and growth of bubbles at a submerged orifice. *Chem. Eng. Sci.*, 36:405–411.

Polli, M., di Stanislao, M., Bagatin, R., Bakr, E. A., and Masi, M. (2002). Bubble size distribution in the sparger region of bubble columns. *Chem. Eng. Sci.*, 57:197–205.

Poulsen, B. and Iversen, J. (1999). Membrane sparger in bubble column, airlift, and combined membrane-ring sparger biorectors. *Biotechnol. Bioeng.*, 64:452–458.

Raffel, M., Willert, C., and Kompenhans, J. (1998). *Particle Image Velocimetry*. Springer Berlin.

Ramakrishnan, S., Kumar, R., and Kuloor, N. (1969). Studies in bubble formation - I bubble formation under constant flow conditions. *Chem. Eng. Sci.*, 69(24):731–747.

Ranade, V. (1993). Numerical simulation of turbulent flow in bubble column reactors. *AIChE symposium series*, 89:61–71.

Ranade, V. and Joshi, J. (1987). Transport phenomena in multiphase systems: momentum, mass and heat transfer in bubble column reactors. In Upadhyay, S., editor, *Transport processes in multiphase systems*, page 113. Banaras Hindu Univ., Varanasi, India.

Ranade, V. and Tayalia, Y. (2001). Modelling of fluid dynamics and mixing in shallow bubble column reactors: influence of sparger design. *Chem. Eng. Sci.*, 56:1667–1675.

Rensen, J. (2003). *Bubbly flow, hydrodynamic forces and turbulence*. PhD thesis, Twente University.

Rensen, J., Luther, S., de Vries, J., and Lohse, D. (2005). Hot-film anemometry in bubbly flow I : bubble-probe interaction. *Int. J. Multiphase Flow*, 31:285–301.

Rice, R., Barbe, D., and Geary, N. (1990). Correlation of nonverticality and entrance effects in bubble columns. *AIChE J.*, 36:1421–1424.

Rice, R. and Howell, S. (1986). Elastic and flow mechanics for membrane spargers. *AIChE J.*, 32:1377–1382.

Rice, R. and Littlefield, M. (1987). Dispersion coefficients for ideal bubbly flow in truly vertical bubble columns. *Chem. Eng. Sci.*, 42:2045–2053.

Roy, M., Kumar, R., Kulkarni, B., Sanderson, J., Rhodes, M., and vander Stappen, M. (1999). Simple denoising algorithm using wavelet transform. *AIChE J.*, 45(11):2461–2466.

Ruff, K. (1972). Bildung von Gasblasen an Dusen bei konstantem Volumendurchsatz. *Chemie-Ing. Techn.*, 44(24):1360–1366.

Ruzicka, M., Drahos, J., Zahradnik, J., and Thomas, N. (1999). Natural modes of multi-orifice bubbling from a common plenum. *Chem. Eng. Sci.*, 54:5223–5229.

Ruzicka, M., Drahos, J., Zahradnik, J., and Thomas, N. (2000a). On bubbles rising in line. *Int. J. Multiphase Flow*, 26:1141–1181.

Ruzicka, M., Drahos, J., Zahradnik, J., and Thomas, N. (2000b). Structure of gas pressure signal at two-orifice bubbling from a common plenum. *Chem. Eng. Sci.*, 55:421–429.

Ruzicka, M. and Thomas, N. (2003). Buoyancy-driven instability of bubbly layers: analogy with thermal convection. *Int. J. Multiphase Flow*, 29:249–270.

Ruzicka, M., Zahradník, J., Drahos, J., and Thomas, N. (2001). Homogeneous-heterogeneous regime transition in bubble columns. *Chem. Eng. Sci.*, 56:4609–4626.

Sankaranarayan, K., Shan, X., Kevrekidis, I., and Sundaresan, S. (2002). Analysis of the drag and virtual mass forces in bubbly suspensions using an implicit formulation of the lattice Boltzmann method. *J. Fluid Mech.*, 452:61–96.

Satyanarayan, A., Kumar, R., and Kuloor, N. (1969). Studies in bubble formation - II bubble formation under constant pressure conditions. *Chem. Eng. Sci.*, 69(24):749–761.

Scargle, J. (1989). Studies in astronomical time series analysis III. Fourier transforms, auto-correlation functions and cross-correlation functions of unevenly spaced data. *Astrophys. J.*, 343:874–887.

Schmitt, A., Hoffmann, K., and Loth, R. (1995). A transputer based measuring system for decentralized signal processing, applied to two-phase flow. *Rev. Sci. Instrum.*, 66(10):5045–5049.

Sene, K. (1984). *Aspects of bubbly two-phase flow.* PhD thesis, University of Cambridge.

Serizawa, A., Kataoka, I., and Michiyoshi, I. (1975). Turbulent structure of air/water bubble flow. *Int. J. Multiphase Flow*, 2:235–246.

Serizawa, A., Tsuda, K., and Michiyoshi, I. (1984). Real-time measurement of two-phase flow turbulence using a dual-sensor anemometry. In Delhaye, J. and Cognet, G., editors, *Measuring techniques in gas-liquid two-phase flows*, pages 495–523. Springer, Berlin.

Shnip, A. I., Kolhatkar, R., Swamy, D., and Joshi, J. (1992). Criteria for the transition from the homogeneous to the heterogeneous regime in two-dimensional bubble column reactors. *Int. J. Multiphase Flow*, 18:705–726.

Simon, L. and Fitzpatrick, J. (2004). An improved sample-and-hold reconstruction procedure for estimation of power spectra from LDA data. *Exp. Fluids*, 37:272–280.

Snabre, P. and Magnifotcham, F. (1998). Formation and rise of a bubble stream in a viscous liquid. *Eur. Phys. J. B*, 4:369–377.

Snape, J., Zahradník, J., Fialová, M., and Thomas, N. (1995). Liquid-phase properties and sparger design effects in an external-loop airlift reactor. *Chem. Eng. Sci.*, 20:3175–3186.

Sokolichin, A., Eigenberger, G., and Lapin, A. (2004). Simulation of buoyancy-driven bubbly flow: established simplifications and open questions. *AIChE J.*, 50:24–45.

Sokolichin, A., Eigenberger, G., Lapin, A., and Lübbert, A. (1997). Dynamic numerical simulation of gas-liquid two-phase flows: Euler/Euler versus Euler/Lagrange. *Chem. Eng. Sci.*, 52:611–626.

Sousa, F., Portela, L., Mudde, R., and Mangiavacchi, N. (2005). Direct numerical simulation of deformable bubbles in wall-bounded shear flows. *submitted to Chem. Eng. Sci.*

Takemura, F. and Magnaudet, J. (2003). The transverse force on clean and contaminated bubbles rising near a vertical wall at moderate Reynolds number. *J. Fluid Mech.*, 495:235–253.

Tang, C. and Heindel, T. (2004). Time-dependent gas holdup variation in an air-water bubble column. *Chem. Eng. Sci.*, 59:623–632.

Theofanous, T. and Sullivan, J. (1982). Turbulence in two-phase dispersed flows. *J. Fluid Mech.*, 116:343–362.

Thorat, B. and Joshi, J. (2004). Regime transition in bubble columns: experimental and predictions. *Exp. Therm. Fluid Sci.*, 28:423–430.

Thorat, B., Shevade, A., Bhilegaonkar, K., Aglawe, R., Veera, U. P., Thakre, S., Pandit, A., Sawant, S., and Joshi, J. (1998). Effect of sparger design and height to diameter ratio on fractional gas hold-up in bubble columns. *Trans. Inst. Chem. Eng.*, 76:823–834.

Tinge, J. and Drinkenburg, A. (1986). The influence of slight departures from vertical alignment on liquid dispersion and gas hold-up in a bubble column. *Chem. Eng. Sci.*, 41(1):165–169.

Titomanlio, G., Rizzo, G., and Acierno, D. (1976). Gas bubble formation from submerged orifices - "simultaneous bubbling" from two orifices. *Chem. Eng. Sci.*, 31:403–404.

Tomiyama, A., Tamai, H., Zun, I., and Hosokawa, S. (2002). Transverse migration of single bubbles in simple shear flows. *Chem. Eng. Sci.*, 57:1849–1858.

TSI Incorporated (1988). *Instruction manual Flow Information Display Software Model IFA 750 Digital Burst Correlator*. TSI Incorporated, 500 Cardigan Road, P.O. Box 64394, St. Paul, MN, USA.

Tummers, M. (1999). *Investigation of a turbulent wake in an adverse pressure gradient using laser Doppler anemometry*. PhD thesis, Delft University of Technology.

Tummers, M. and Passchier, D. (1996). Spectral estimation using a variable window and the slotting technique with local normalisation. *Meas. Sci. Technol.*, 7:1541–1546.

Tummers, M. and Passchier, D. (2001). Spectral analysis of biased LDA data. *Meas. Sci. Technol.*, 12:1641–1650.

Van den Berg, R. (1996). *Interplaying time scales in two-phase flows*. PhD thesis, Delft University of Technology.

Van Maanen, H. (1999). *Retrieval of turbulence and turbulence properties from randomly sampled laser Doppler anemometry data with noise*. PhD thesis, Delft University of Technology.

Van Maanen, H. and Nijenboer, F. (1996). Application of the wavelet transform to laser-Doppler processors. In *Proceedings 8th international symposium on applications of laser techniques to fluid mechanics (Lisbon)*.

Van Maanen, H., Nobach, H., and Benedict, L. (1999). Improved estimator for the slotted autocorrelation function of randomly sampled data. *Meas. Sci. Technol.*, 10:L4–L7.

Van Maanen, H. and Oldenziel, A. (1998). Estimation of turbulence power spectra from randomly sampled data by curve-fit to the autocorrelation function applied to laser-Doppler anemometry. *Meas. Sci. Technol.*, 9:458–467.

Van Maanen, H. and Tummers, M. (1996). Estimation of the autocorrelation function of turbulent velocity fluctuations using the slotting technique with local normalisation. In *Proceedings 8th international symposium on applications of laser techniques to fluid mechanics (Lisbon)*. paper 36.4.

Van Wijngaarden, L. (1998). On pseudo-turbulence. *Theor. Comp. Fluid. Dyn.*, 10:449–458.

Veera, U. P. and Joshi, J. (1999). Measurement of gas hold-up profiles by gamma ray tomography: effect of sparger design and height of dispersion in bubble columns. *Trans. Inst. Chem. Eng.*, 77:303–317.

Venneker, B. (1999). *Turbulent flow and gas dispersion in stirred vessels with pseudoplastic liquids*. PhD thesis, Delft University of Technology.

Verzicco, R. and Camussi, R. (2003). Numerical experiments on strongly turbulent thermal convection in a slender cylindrical cell. *J. Fluid Mech.*, 477:19–49.

Veynante, D. and Candel, S. (1988). Application of non linear spectral analysis and signal reconstruction to LDV. *Exp. Fluids*, 6:534–540.

Vial, C., Camarasa, E., Poncin, S., Wild, G., Midoux, N., and Bouillard, J. (2000). Study of hydrodynamic behaviour in bubble columns and external loop airlift reactors through analysis of pressure fluctuations. *Chem. Eng. Sci.*, 55:2957–2973.

Vial, C., Poncin, S., Wild, G., and Midoux, N. (2001). A simple method for regime identification and flow characterisation in bubble columns and airlift reactors. *Chem. Eng. Proc.*, 40:135–151.

Wild, G., Poncin, S., Li, H.-Z., and Olmos, E. (2003). Some aspects of the hydrodynamics of bubble columns. *Int. J. Chem. React. Eng.*, 1:R7.

Wilkinson, P., Spek, A., and van Dierendonck, L. (1992). Design parameters estimation for scale-up of high-pressure bubble columns. *AIChE J.*, 38:544–554.

Wong, P., Wang, T.-H., and Ho, C.-H. (2002). Optical fiber tip fabricated by surface tension controlled etching. In *Solid state sensor, actuator and microsystems workshop, Hilton Head Island, South Carolina, June 2-6*. http://ho.seas.ucla.edu/publications/2002/Optical_HH02.pdf.

Wraith, A. (1971). Two stage bubble growth at a submerged plate orifice. *Chem. Eng. Sci.*, 26:1659–1671.

Xue, J. (2004). *Bubble velocity, size and interfacial area measurements in bubble columns*. PhD thesis, Washington University.

Xue, J., Al-Dahhan, M., Dudukovic, M., and Mudde, R. (2003). Bubble dynamics measurements using four-point optical probe. *Can. J. Chem. Eng.*, 81 (3-4):375–381.

Yu, Y. and Kim, S. (1991). Bubble properties and local liquid velocity in the radial direction of cocurrent gas-liquid flow. *Chem. Eng. Sci.*, 46:313–320.

Yuan, H. and Prosperetti, A. (1994). On the in-line motion of two spherical bubbles in a viscous fluid. *J. Fluid Mech.*, 278:325–349.

Yuan, Y., Devanathan, N., and Dudukovic, M. (1993). Liquid backmixing in bubble columns via Computer-Automated Radioactive Particle Tracking (CARPT). *Exp. Fluids*, 16:1–9.

Zahradnik, J., Fiavola, M., Ruzicka, M., Drahos, J., Kastanek, F., and Thomas, N. (1997). Duality of the gas-liquid flow regimes in bubble column reactors. *Chem. Eng. Sci.*, 52:3811–3826.

Zhang, L. and Fan, L.-S. (2003). On the rise velocity of an interactive bubble in liquids. *Chem. Eng. J.*, 92:169–176.

Zhang, L. and Shoji, M. (2001). Aperiodic bubble formation from a submerged orifice. *Chem. Eng. Sci.*, 56:5371–5381.

Zhang, W. and Tan, R. (2000). A model for bubble formation and weeping at a submerged orifice. *Chem. Eng. Sci.*, 55:6243–6250.

Zǔn, I., Filipič, V., Perpar, M., and Bombač, A. (1995). Phase discrimination in void fraction measurements via genetic algorithms. *Rev. Sci. Instrum.*, 66(10):5055–5064.

List of Publications

- W.K. Harteveld, R.F. Mudde, H.E.A. van den Akker, Estimation of turbulence power spectra for bubbly flows from Laser Doppler Anemometry signals, Chem. Eng. Sci., 60, 6160, 2005.
- J.E. Juliá, W.K. Harteveld, R.F. Mudde, H.E.A. van den Akker, On the accuracy of the void fraction measurements using optical probes in bubbly flows, Rev. Sci. Instr., 035103, 2005.
- W.K. Harteveld, J.E. Juliá, R.F. Mudde, H.E.A. van den Akker, Large scale vortical structures in bubble columns for gas fractions in the range 5%-25%, proc. 16th international conference on chemical and process engineering, Prague, Czech republic, 2004.
- W.K. Harteveld, R.F. Mudde, H.E.A. van den Akker, Dual burst wavelet LDA processor implemented and tested on real flows, proc. 12th int. symposium on application of laser techniques to fluid mechanics, Lisbon, Portugal, 2004.
- W.K. Harteveld, R.F. Mudde, H.E.A. van den Akker, Dynamics of a bubble column: influence of gas distribution on coherent structures, Can. Journal of Chem. Eng., 81(3-4), 389, 2003.
- T.H.J.J. van der Hagen, W.K. Harteveld, R.F. Mudde, S. Verdoold, Disentangling up and down flow characteristics of a turbulent nuclear fluidized bed by auto-regressive modelling of gamma-transmission fluctuations, proc. Physor 2000, Pittsburgh, Pennsylvania, USA, 2000.
- W.K. Harteveld, P.A. van Halderen, R.F. Mudde, C.M. van den Bleek, H.E.A. van den Akker, B.A. Scarlett, A fast active differentiator capacitance transducer for electrical capacitance tomography, proc. 1st world congress on industrial process tomography, Buxton, greater Manchester, UK, 1999.
- R.F. Mudde, W.K. Harteveld, H.E.A. van den Akker, T.H.J.J van der Hagen, H. van Dam, Gamma radiation densitometry for studying the dynamics of fluidized beds, Chem. Eng. Sci. 54, 2047, 1999.
- T.H.J.J van der Hagen, W.K. Harteveld, R.F. Mudde, H. van Dam, Gamma transmission measurements on core density fluctuations of a fluidized bed nuclear reactor, proc. Informal meeting on reactor noise - IMORN 27, Valencia, Spain, 1999.

- T.H.J.J van der Hagen, H. van Dam, W.K. Harteveld, J.E. Hoogenboom, J.E. Khotylev, R.F. Mudde, Studies on the inhomogeneous core density of a fluidized bed reactor, proc. of the int. conf. on future nuclear systems, Pacifico Yokohama, Japan, 1997.

About the Author

Wouter Harteveld was born on July 1, 1974 in Leidschendam, the Netherlands. In 1992, he graduated from secondary school (VWO) at the St. Janscollege in Den Haag. In 1992, he started studying Applied Physics at the Delft University of Technology, and graduated in 1997 (cum laude). His graduation project was performed at the Kramers Laboratorium voor Fysische technologie in Delft on the topic "Gamma radiation densitometry in turbulent fluidised beds", a joint project with the Reactor Physics group in the Interfacultary Reactor Institute. After his graduation he worked on a joint project of the Kramers Laboratorium and the Particle Technology Group (at Delft ChemTech) on the topic of Electrical Capacitance Tomography for process equipment. This project was part of the Delft Interfacultair Onderzoeks Centrum (DIOC) "Mastering the Molecules in Manufacturing". In April 2001 he started working on his PhD research in the Kramers Laboratorium voor Fysische Technologie. On June 12, 2004 he married Natalie Askamp. After finishing his research he started working as an Engineer Fluid Flow on July 1, 2005 for Shell Global Solutions in Amsterdam.